Investigating the function of the hereditary spastic paraplegia protein spastin in the endomembrane system

Guy James Pearson

Department of Medical Genetics

Cambridge Institute of Medical Research

University of Cambridge

This dissertation is submitted for the degree of Doctor of Philosophy

Jesus College Original Submission: September 2018 – Revised Submission: January 2019

Abstract

Hereditary spastic paraplegias (HSPs) are genetically inherited neurological diseases characterised by the distal axonal degeneration of corticospinal neurons. Of the 80 genes currently associated with HSP, mutations in *SPAST*, encoding the protein spastin, are by far the most common cause of pathology. Spastin functions as a microtubule remodelling enzyme by using energy derived from ATP hydrolysis by its ATPase domain. The location of this activity is governed by spastin's localisation domains which mediate recruitment to membrane sites including endosomes and the ER. In this thesis I aimed to elucidate the function of spastin at these sites, as well as to analyse the resulting effects on the cell surface proteome. Through this work, I have shown that spastin functions to mediate the fission of endosomal recycling tubule and have confirmed spastin's localisation to ER exit sites, but show using synchronised secretion assays that spastin is dispensable for generalised cargo secretion of at least 2 classes of secretory cargo. Finally, through quantitative cell surface proteomics, I show that mutation of spastin's ATPase domain induces substantial remodelling of the cell surface proteome, and through this have generated a list of pathological candidates whose change in surface abundance could drive the pathogenicity of spastin-HSP.

Declaration

I hereby declare that this dissertation is the result of my own work and includes nothing which is the outcome of work done in collaboration except where specifically indicated in the text. The contents of this dissertation are not substantially the same as any that I have submitted, or, is being concurrently submitted for a degree or diploma or other qualification at the University of Cambridge or any other university or similar institution.

The total length of the main body of this dissertation is 55,225 words and therefore does not exceed the limit of 60,000 words for such a dissertation.

Guy Pearson

September 2018

Acknowledgements

Firstly, I would like to thank my supervisor, Evan Reid. Evan's vision and intellect has guided me throughout my PhD, and I thank him for his compassion and understanding, his scientific (and life!) wisdom, and most importantly for having an unwavering sense of humour. In particular, I would like to thank you Evan for making me a scientist, and moreover, for instilling within me an understanding of and appreciation for good scientific practise. Evan's views on collaborations changed my life by allowing me to go to America to work with Jennifer Lippincott-Schwartz; something that would not have been possible without Evan's willingness to share ideas. Evan was hugely important in teaching me the skills of scientific writing during the creation of this viva, and I thank him for going through my writing with a relentless demand for high standards. Finally, and most importantly, I would like to thank Evan for giving me a chance four years ago when no one else was willing to.

The Reid lab as a whole receives all my love. Rachel Allison has taught me almost all the non-microscopy related techniques that I know, and I would like to thank Rachel for being willing to dedicate her time to help me during my rotations and during the first year of my PhD. When it was sometimes just us two in the lab, Rachel's scientific optimism and pragmatism was always comforting when projects were proving challenging. Despite what I often joke, Rachel is not scary, but is kind and generous with her time, and always great company. I would also like to thank Catherine Rodger. Although Catherine hasn't been in the lab for a long time, it's hard to image life in the lab without her having always been here. Thanks for putting up with my crazy ideas and my inane chat, and if your projects work out as well as you plan and organise your science, I am looking forward to your future amazing publication record. Other members of the Reid lab I would like to thank over the years are Vivien Tsang for being great company for a year, and James Connell for his advice at the start and his advice when I was a supervisor.

CIMR is a building full of brilliant people. Of these, I would firstly like to pay tribute to both Niko Amin-Wetzel and Alex Davies who are the fellow intake in my year of the 4-year CIMR PhD programme. Niko has excelled at pretty much everything and has provided a great role model and inspiration over the years. Thanks in particular to Niko for helping me in the year that we were supervising together; if the students could see the time we had put into going through the lectures and coming up with weird and wonderful questions! As for Alex, thank you for the five years. At the beginning you provided me with the support that I needed to get through the rotation year, and it was always nice to go across to get

a Burger King with you, or randomly find a Percy Pig on my desk. The time we had at Leeds together was fantastic, and I'll never forget us putting out fires. Furthermore, thank you for providing healthy competition over the years. By watching your dedication and high standards, it has driven me to work harder just to keep up. I am sure your scientific future will be fantastic, and I'm looking forward to working together in the future.

Special mention has to go to the unrecreatable collective that was the Cell-Tick football team. In particular, Tom O'Loughlin, Paul Manna, Ian Lobb, Colin Davies, and Stephen Burr have my ever-lasting friendship (bad luck guys!) for everything they have done for me over the years. Tom, thank you for providing me with company during late night tissue culture, and for being one of the few people who ever listened to my radio show; I cried when you left. To Paul, thanks for constantly knocking me down to size when I got too high, and for picking me up when I got too low. And to Ian and Stephen, for sharing the same experiences that I went through and being able to laugh about them.

I also want to thank all the other people who make the CIMR such a special place to work. This includes the friendship of people in the Robinson lab, the Buss lab, and the Weekes lab, and my fellow students who have given their time to make the CIMR a welcome non-sterile environment including Fran and Ting for running everything before I took over, and for Anna and Lior for keeping the current CIMR student community vibrant. I would also like to thank Matthew and Mark in microscopy for listening to my ideas, putting up with my moaning, and for teaching me some of the basics of microscopy.

Going to America was a huge turning point in my scientific life, and I would like to thank Jennifer Lippincott-Schwartz for letting me work with her and her lab for 6 wonderful months. In particular, I would like to thank Jennifer for showing me the importance of scientific connections, and how to frame scientific data so that its presentation does not detract from its message. I would like to extend my love to everyone's in Jennifer's lab, but in particular to Carolyn Ott for always being a source of wisdom, to Daniel Feliciano for always giving good advice scientifically and otherwise, Jonny Nixon-Abell for those glasses and that cheeky smile, and to Chris Obara. Chris has changed the way that I think about science, and the has taught me everything I know about microscopy. Thank you Chris for being willing to sit down and explain everything to me, for building fires with me, for your friendship, and for your advice. Thank you also Chris for demanding that I learn to code; I hope we will work together in the future. Thank you also to Tim Harris for keeping me sane by letting me use his boat.

Outside of work, I would like to thank all my friends in Cambridge. Living at Jesus has been an integral part of my life for so long that it's hard to remember what came before. In particular thank you to all my boys at JCBC over the years. Training with JCBC has taught me skills of determination, teamsmanship, humility, and leadership, and every session has been worth it for the indefinite friendships that I have formed. Thanks also go to the badminton core for putting up with my chaotic sporting lifestyle. Thanks also go to Cambridge University Light Entertainment Society for everything they've let me do over the years, and Elizabeth forever has my love. I'd like to thank Tom Edwards in particular for being my best friend in Cambridge for several years, and for having a similar passion for ridiculousness and science. Furthermore, thanks for the friendship from Megan and Caroline and Miriam. I give my love to Silvia Basilico who has nurtured and nourished me for the last three years. Thank you Silvia for having such an inherent joy for life, for an unbounding sense of optimism, for your caring and kindness, your deep sense of right and wrong, and for being there for me.

Jesus Oxford provided me with the opportunity to be here completing my PhD. Whilst there are too many names to thank here, I would like to highlight four people in particular. Thank you firstly to Ellie. Thank you to Andrew Maclean, for always providing me with the competition I needed to achieve the standards that you seemed so effortless capable of; I hope we will be friends again soon. Thirdly, I would like to thank my Oxford supervisor, Graham Taylor, the smartest man I have ever known. Graham has been an inspiration and a scientific role model by his calmness and clarity of thought, and if I can amount to half of what he is, I will be extremely fortunate. Thank you Graham for letting me cry on your table, and for helping me achieve what I wanted even if we did have to take the hard way around. Finally, I want to thank Alex Hannington for being my best friend, now and forever.

Finally, I thank my parents. My life has been a team effort, and this is my team. If I could tell you how much I love you, I'd write forever. You have been my pillar throughout everything in the last 26 years, and I couldn't be luckier to have parents who love so selflessly. Thank you for listening to me and supporting me through both the good times, and the times were things weren't going so well. Your drive has been my drive, and Dad, I am proud that I got to experience Cambridge for you when you weren't able to. Only you guys know the journey that has led to this point, and I'm blessed to have arrived at this point with you.

Papers Arising From This PhD

1. Allison, Rachel et al. 2017. “Defects in ER-Endosome Contacts Impact Lysosome Function in Hereditary Spastic Paraplegia.” *Journal of Cell Biology*. ***joint first author**

Foreword Regarding Movies

In addition to printed figures and tables, this thesis contains movies showing either live cell microscopy data or 3D-reconstructions of fixed cell microscopy data. These movies are provided on the USB stick attached to this thesis, along with a PDF document that contains the movie figure legends. The movies are divided into two folders corresponding to their relevant results chapter. In addition, these movies can be downloaded from the University of Cambridge data repository. The permanent URL link for this is: https://doi.org/10.17863/CAM.28063 and a QR code to download these movies is provided below. In the downloaded version, movies are contained within two .ZIP files corresponding to each chapter, and the movie figure legends are provided as a downloadable PDF. Due to long file names and the large size of some movies, it is recommended that the files are downloaded to the desktop before playback. In total there are 17 movies: 14 from my first results chapter (Chapter 3), and 3 from my second results chapter (Chapter 4).

QR code of the DOI link to download the movies from the University of Cambridge data repository. To use the QR code you will require a QR code scanner application on a smart device (e.g. tablet or phone). The data can also be accessed directly be entering the URL address stated above into a web browser, or by accessing the movies from the provided USB stick.

Abbreviations

AAA+	-	ATPase associated with diverse cellular activities
AcN	-	Acetonitrile
ALS	-	Amyotrophic lateral sclerosis
AP	-	Adaptor protein
ATP	-	Adenosine triphosphate
BCA	-	Bicinchoninic acid
BMP	-	Bone morphogenetic protein
bp	-	Base pair
BSA	-	Bovine serum albumin
CCD	-	Charge-coupled device
CCVs	-	Clathrin-coated vesicles
ChIP	-	Chromatin immunoprecipitation
CHMP	-	Charged multivesicular body proteins
CI-M6PR	-	Cation-independent M6PR
CLEM	-	Correlative light-electron microscopy
CME	-	Clathrin-mediated endocytosis
CMOS	-	Complementary metal-oxide-semiconductor
CMT	-	Charcot-Marie-Tooth disease
DIC	-	Differential interference contrast
DMEM	-	Dulbecco's modified eagle's medium
DMSO	-	Dimethyl sulfoxide
DNA	-	Deoxyribonucleic acid
DTT	-	Dithiothreitol
EB	-	End binding
EDTA	-	Ethylenediaminetetraacetic acid
EGFR	-	Epidermal growth factor receptor
ER	-	Endoplasmic reticulum
ERAD	-	ER-associated protein degradation
ERES	-	ER exit sites
ERGIC	-	ER-Golgi intermediate compartment
ESCRT	-	Endosomal sorting complexes required for transport
FBS	-	Fetal bovine serum
GaAsP	-	Gallium arsenide phosphide
GalT	-	Galactose-1-phosphate uridylyl transferase
GAP	-	GTPase-activating protein
GDP	-	Guanine diphosphate
GEF	-	Guanine nucleotide exchange factor
GFP	-	Green fluorescent protein
GPI	-	Glycosylphosphatidylinositol
GTP	-	Guanosine triphosphate
HBSS	-	Hanks's balanced salt solution
HEPES	-	4-(2-hydroxyethyl)-1-piperazineethanesulfonic acid
HET	-	Heterozygous
HOM	-	Homozygous
HPLC	-	High performance liquid chromatography
HRP	-	Horseradish peroxidase
HSP	-	Hereditary spastic paraplegia
IgG	-	Immunoglobulin G

ILVs	-	Intraluminal vesicles
IPSCs	-	Induced pluripotent stem cells
IRES	-	Internal ribosomal entry site
Kb	-	Kilobase
kDa	-	Kilodaltons
KO	-	Knock out
LB	-	Lysogeny broth
LDLR	-	Low-density lipoprotein receptor
M6PR	-	Mannose-6-phosphate receptors
MEF	-	Mouse embryonic fibroblast
MHC	-	Major histocompatibility complex
MIM	-	Microtubule interacting and trafficking interacting motif
MIT	-	Microtubule interacting and trafficking
MRI	-	Magnetic resonance imaging
mRNA	-	Messenger ribonucleic acid
MTBD	-	Microtubule binding domain
MTOC	-	Microtubule organising centre
MVB	-	Multivesicular body
NCE	-	Normalised collision energy
NGFR	-	Neuronal growth factor receptor
NMD	-	Nonsense mediated decay
NMJs	-	Neuromuscular junctions
NMR	-	Nuclear magnetic resonance
NTP	-	Nucleoside triphosphate
PBS	-	Phosphate buffered saline
PCR	-	Polymerase chain reaction
PDL	-	Poly-D-lysine
PFA	-	Paraformaldehyde
PLS	-	Primary lateral sclerosis
PMT	-	Photomultiplier tube
PVDF	-	Polyvinylidene fluoride
PX	-	Phox homology
RCF	-	Relative centrifugal force
RFP	-	Red fluorescent protein
RNAi	-	Ribonucleic acid interference
RUSH	-	Retention using selective hooks
S.D.	-	Standard deviation
SBP	-	Streptavidin-binding protein
SCX	-	Strong cation exchange
SDS	-	Sodium dodecyl sulfate
SILAC	-	Stable isotope labelling by amino acids in cell culture
SIM	-	Structural-illumination microscopy
siRNA	-	Small interfering ribonucleic acid
SiT	-	Sialyltransferase
SNARE	-	Trans-soluble NSF attachment protein receptor
SNX	-	Sorting nexin
SPG	-	Spastic paraplegia type
SRH	-	Second region of homology
TEMED	-	Tetramethylethylenediamine
TfnR	-	Transferrin receptor
TGN	-	Trans-Golgi network

TIRF	-	Total internal reflection
TMT	-	Tandem mass tags
UTR	-	Untranslated region
UV	-	Ultraviolet
VBA	-	Visual basic for applications
VSVG	-	Vesicular stomatitis virus glycoprotein
VTCs	-	Vesicular tubular clusters
WASH	-	Wiskott-Aldrich syndrome protein and SCAR homolog
WT	-	Wildtype

Table of Contents

List of Figures

List of Tables

Chapter 1 - Introduction

1.1 – Overview

In this thesis I examine the function of the hereditary spastic paraplegia (HSP) protein spastin in the processes of endosomal tubule fission and ER exit, and the consequences of the expression of an ATPase-defective spastin on the cell surface proteome. By way of an introduction to these topics, this introduction will describe the following:

1. Hereditary spastic paraplegia – The history and clinical features of HSP (1.2.1), an overview of the functions of HSP-associated genes (1.2.2), and the relative prevalence of pathogenic mutations in each HSP gene relative to the total HSP cases reported (1.2.3).
2. Spastin – The history and clinical features of spastin-associated HSP (1.3.1), the isoforms of spastin (1.3.2), spastin's functional domains (1.3.3), the mutational distribution in the spastin-encoding gene SPAST (1.3.4), and the cell biological functions of spastin (1.3.5).
3. Endocytic sorting – The identity of the sorting endosome (1.4.1), sorting endosome input pathways (1.4.2), cargo sorting within the sorting endosome (1.4.3), the mechanisms of endosomal recycling tubule formation (1.4.4), and a brief introduction to endosomal tubule fission (1.4.5).
4. Membrane scission – Passive membrane remodelling (1.5.1), and energy-dependent membrane remodelling including the function of cytoskeletal elements (1.5.2) and specific fission machineries (1.5.3).

1.2 – Hereditary Spastic Paraplegia

1.2.1 – History and clinical features of hereditary spastic paraplegias

The first description of hereditary spastic paraplegia (HSP) was by German physician Ernst Adolf von Strümpell in 1880. Upon neurological examination of a patient, he observed degeneration of the lateral corticospinal tract, fasciculus gracilis, and spinocerebellar tract. These descriptions were further developed by Maurice Lorrain. However, the rarity of the disease and the heterogeneity of pathologies presented resulted in an almost 100 year wait for HSPs to be methodologically clinically classified. In 1983, Anita Harding of the University of London defined the term hereditary spastic paraplegia (HSP), differentiating the disease from the phenotypically similar hereditary ataxias (Harding 1983). Harding introduced the classification of HSPs as being either pure or complex, and provided a description of the genetic inheritance patterns of each described subtype of the disease.

The clinical classification of HSPs into pure and complex subtypes remains in use today. HSPs are described as being monogenic disorders characterised by a dysfunction of the longer motor tracts of the spinal cord, resulting in progressive weakness and spasticity of the lower limbs (Faber et al. 2017; Klebe et al. 2015). Pure forms of HSP display only pyramidal dysfunction in association with sphincter disturbances and potentially some deep sensory loss (de Souza et al. 2017). However complex forms of HSP display these symptoms with additional neurological or non-neurological features. These may include cerebellar dysfunction, cognitive impairment, psychiatric disturbances, myopathy, epilepsy, hypomyelination, and non-neurological pathologies such as ophthalmological abnormalities, dysmorphia, skin changes, and orthopaedic abnormalities (de Souza et al. 2017). The age of onset of the disease can range from infancy to more than 70 years old depending on which gene is mutated to cause the HSP, and the nature of the specific mutation (de Souza et al. 2017).

HSPs have been associated with all types of genetic inheritance. In total 80 genes have been associated with HSPs (**Table 1**; de Souza et al. 2017). In addition, there are 15 genomic regions that have been associated with HSP-causing mutations with the causative gene having not been identified (Klebe et al. 2015). In total, 51 genes show autosomal recessive inheritance, 18 genes autosomal dominant, 2 genes autosomal but have no stated inheritance pattern, 3 show X-linked, and 4 are mitochondrially inherited. In addition, 2 genes can present both autosomal dominant and autosomal recessive inheritance (Klebe et al. 2015; de Souza et al. 2017). Autosomal recessive and X-linked HSPs typically present with complex HSP phenotypes, with only 2/51 autosomal recessive and no X-linked HSPs classified as pure HSPs. Conversely, autosomal dominant HSPs present as mainly pure HSPs (12/18).

Mitochondrially inherited HSPs may present as either pure or complex depending on the severity of the phenotype dependent on heteroplasmy rate and the tissue affected (Klebe et al. 2015).

Despite HSPs being described in many different countries, it is difficult to accurately determine their global prevalence. One problem is that detailed analyses of HSP prevalence have been mainly performed in Europe, creating a substantial geographic bias (Ruano et al. 2014). Furthermore, these studies may not necessarily have had the same criteria for patient inclusion, may not have been performed in low prevalence regions, may be skewed by small geographic regions of isolated populations or consanguinity, and sufferers from poor or rural communities may not present for medical care (Klebe et al. 2015). Acknowledging these biases, from a global meta-analysis performed by Ruano et al. (2014), the mean global prevalence of both autosomal recessive and autosomal dominant HSP was 1.8/100,000. However, there was substantial variation depending on survey country. For autosomal recessive HSP, the highest reported prevalence was 5.3/100,000 in Tunisia (Boukhris et al. 2009), and the lowest was 0 from 115,270 in the Valle d'Aosta region in Italy (Leone et al. 2009). For autosomal dominant HSPs, the highest reported prevalence was 5.5/100,000 in Norway (Erichsen et al. 2007), and the lowest was 0.5/100,000 in Tunisia (Boukhris et al. 2009).

The overlap between HSP pathologies and other neurodegenerative diseases make HSP diagnosis challenging (Klebe et al. 2015). Examples of other diseases presenting similar pathologies include hereditary ataxias, amyotrophic lateral sclerosis (ALS), primary lateral sclerosis (PLS), and Charcot-Marie-Tooth disease (CMT). To appropriately diagnose HSP a range of tools are used by clinicians. Familial cases of HSP can by identified by family history. However, for sporadic HSPs techniques such as magnetic resonance imaging (MRI) of the head and spinal cord, a lumbar puncture, and electrophysiological examinations of the upper and lower limbs are typically performed to exclude alternative diagnoses (Klebe et al. 2015). Furthermore, the presence of urinary urgency or incontinence is often symptomatic of pure HSP phenotypes (Fourtassi et al. 2012). It is also important to rule out neurological metabolic disorders such as Krabbe disease and GM1/GM2 gangliosides. This can be performed by blood and serum metabolomics and analysis of specific enzyme abundance and activity (Wang et al. 2011). More recently, 1st line molecular genetic sequencing of HSP gene panels, whole exomes, or genomes, has been used to identify common mutations in known HSP genes (Hensiek et al. 2015).

1.2.2 – Hereditary Spastic Paraplegia associated genes

One of the most distinctive features of HSP is the heterogeneity of protein functions encoded by HSP genes. Despite the presentation of similar HSP disease phenotypes, these functions range from lipid metabolism, mitochondrial function, endocytic and autophagosomal pathways, secretion, regulation of endoplasmic reticulum (ER) morphology, microtubule-dependent trafficking, protein folding and modification, ion and solute transport, cell-cell contact formation, immunity, nucleotide processing, and regulation of axon myelination (**Table 1**). The function and a disease and functional reference for of each gene is presented in **Table 1**, and a brief introduction to each of these major functional themes is provided below.

Protein Name	Gene	SPG Number	Inheritance	Pure or Complex	ER Shaping	Mitochondrial	Lipid Metabolism	Secretory Pathway	Endosomal/Autophagosomal	Immune Related	Myelination	Nascent Protein Processing	Cell-Cell Contacts	Nucleotide Processing	Microtubule Related	Transporters	Protein Function	Disease Reference	Protein Function Reference
Neural cell adhesion molecule L1	L1CAM	SPG1	X	C									✓				Cell surface cell adhesion protein in neurons	Jouet *et al.* 1994	Samatov *et al.* 2016
Myelin proteolipid protein	PLP1	SPG2	X	P/C							✓						Cell surface protein that functions in the myelin sheath to hold together the layers of myelin	Saugier-Veber *et al.* 1994	Griffiths *et al.* 1998
Atlastin-1	ATL1	SPG3	AD	P	✓		✓										GTPase mediating ER tubule fusion. Also functions in BMP signalling.	Zhao *et al.* 2001	Hu & Rapoport 2016
Spastin	SPAST	SPG4	AD	P	✓		✓	✓	✓						✓		ATPase mediating microtubule severing in abscission, nuclear membrane reformation. Also functions in fission of endocytic recycling tubules, neural pruning, and lipid droplet biogenesis	Hazan *et al.* 1999	*Thesis Introduction*
25-hydroxycholesterol 7-alpha-hydroxylase	CYP7B1	SPG5	AR	P/C			✓										Cholesterol enzyme of the ER mediating the formation of 7α,25-dihydroxycholesterol	Tsaousidou *et al.* 2008	Hannedouche *et al.* 2011
NIPA1	NIPA1	SPG6	AD	P					✓								Inhibitor of BMP signalling by promoting BMPRII endocytosis and lysosomal degradation	Rainier *et al.* 2003	Tsang *et al.* 2009
Paraplegin	SPG7	SPG7	AR	P/C		✓											Mitochondrial protein that functions as an AAA metalloprotease and part of the mitochondrial permeability transition pore that triggers apoptosis	Casari *et al.* 1998	Shanmughapriya *et al.* 2015
Strumpellin	KIAA0196	SPG8	AD	P					✓								Part of the WASH complex that interacts with retromer to mediate actin polymerisation on endosomes	Valdmanis *et al.* 2007	Gomez & Billadeau 2009
Aldehyde dehydrogenase 18 family, member A1 (ALDH18A1)	ALDH18A1	SPG9	AD	C		✓											Mitochondrial enzyme that catalyses the reduction of glutamate in proline, orthithine, arginine synthesis	Coutelier *et al.* 2015	Baumgartner *et al.* 2000
Kinesin heavy chain isoform 5A (KIF5A)	KIF5A	SPG10	AD	P		✓		✓	✓						✓		Neuron specific microtubule plus end directed motor with functions in endosomal transport, secretion, and mitochondrial positioning	Reid *et al.* 2002	Hirokawa *et al.* 2010; Campbell *et al.* 2014

Protein Name	Gene	SPG Number	Inheritance	Pure or Complex	ER Shaping	Mitochondrial	Lipid Metabolism	Secretory Pathway	Endosomal/Autophagosomal	Immune Related	Myelination	Nascent Protein Processing	Cell-Cell Contacts	Nucleotide Processing	Microtubule Related	Transporters	Protein Function	Disease Reference	Protein Function Reference
Spatacsin	SPG11	SPG11	AR	C					✓								Endosomal protein that functions with AP5 to mediate endocytic traffic. Also functions in autophagic lysosome reformation	Stevanin *et al.* 2007	Vantaggiato *et al.* 2018
Reticulon-2	RTN2	SPG12	AD	P	✓												ER shaping protein shaping highly curved ER tubules	Montenegro *et al.* 2012	Shibata *et al.* 2008
Chaperonin	HSPD1	SPG13	AD	P		✓											Mitochondrial heat shock protein mediating the folding of imported mitochondrial proteins	Hansen *et al.* 2002	Levy-Rimler *et al.* 2001
Spastizin	ZFYVE26	SPG15	AR	C					✓								Endosomal protein that functions with AP5 to mediate endocytic traffic. Also functions in autophagosome-lysosome fusion and au tophagic lysosome reformation	Hanein *et al.* 2008	Vantaggiato *et al.* 2018
Seipin	BSLC2	SPG17	AD	P			✓										ER protein mediating the formato n of lipid d roplets	Windpassinger *et al.* 2004	Wang *et al.* 2016
Erlin 2	ERLIN2	SPG18	AR	C	✓		✓					✓			✓		ER protein part of Erlin1/Erlin2 complex that mediates ER-associated degradation of inositol 1,4,5-trisphosph ate receptors (IP3Rs). Functions in lipogenesis. Also functions in the cell cycle by functioning as a microtubule interacting protein.	Alazami *et al.* 2011	Pearce *et al.* 2009; Zhang *et al.* 2015
Spartin	SPG20	SPG20	AR	C		✓	✓		✓								Mediates lipid droplet biogenesis and endocytic trafficking of epidermal growth factor (EGF). Functions as an inhibitor of bone morphogenic signalling. Also functions in mitochondrial traffi king	Patel *et al.* 2002	Lu *et al.* 2006; Zhao & Hedera, 2015
Maspardin	SPG21	SPG21	AR	C					✓								Endosomal protein that regulates EGF induced growth and maturation of primary cortical n eurons	Simpson *et al.* 2003	Davenport *et al.* 2016
Monocarboxylate transporter 8	SLC16A2	SPG22	X	C												✓	Cell surface neuron specific thyroid transporter	Schwartz *et al.* 2005	Heuer *et al.* 2005
Beta-1,4 N-acetylgalactosaminyltransferase 1	B4GALNT1	SPG26	AR	C			✓				✓						Catalyses the transfer of N-acetylgalactosamine in ganglioside biosynthesis, crucial in myelin formation	Boukhris *et al.* 2013	Schnaar *et al.* 2010

Protein Name	Gene	SPG Number	Inheritance	Pure or Complex	ER Shaping	Mitochondrial	Lipid Metabolism	Secretory Pathway	Endosomal/Autophagosomal	Immune Related	Myelination	Nascent Protein Processing	Cell-Cell Contacts	Nucleotide Processing	Microtubule Related	Transporters	Protein Function	Disease Reference	Protein Function Reference
Phospholipase DDHD1	DDHD1	SPG28	AR	P/C			✓										Functions in the synthesis of arachidonic acid-containing lysophosphatidylinositol in lipid metabolism	Tesson *et al.* 2012	Yamashita *et al.* 2010
Kinesin-like protein KIF1A	KIF1A	SPG30	AR	P/C				✓							✓		Microtubule plus end directed motor that functions in the transport of post-Golgi dense core vesicles and synaptic vesicles	Erlic *et al.* 2011	Stucchi *et al.* 2018
REEP1	REEP1	SPG31	AD	P	✓	✓	✓										ER shaping protein shaping highly curved ER tubules. Also functions in lipid droplet formation, ER stress, and ER-mitochondrial contact formation	Zuchner *et al.* 2006	Zheng *et al.* 2018
Fatty acid 2-hydroxylase	FA2H	SPG35	AR	C			✓				✓						Functions in the synthesis of 2-hydroxysphingolipids involved in myelination	Dick *et al.* 2010	Maldonado *et al.* 2008
Neuropathy target esterase	PNPLA6	SPG39	AR	C			✓	✓									ER protein that functions as a phospholipase that deacetylates phosphatidylcholine for plasma membrane maintenance	Rainier *et al.* 2008	Zaccheo *et al.* 2004
Acetyl coenzyme A transporter 1	SLC33A1	SPG42	AD	P												✓	ER protein mediating the import of Acetyl-CoA into the lumen of the ER for Nε-lysine acetylation of ER proteins	Lin *et al.* 2008	Jonas *et al.* 2010
Protein C19orf12	C19ORF12	SPG43	AR	C		✓											ER and mitochondrial protein that potentially functions in mediating response to oxidative stress	Landoure *et al.* 2013	Venco *et al.* 2015
Connexin 47	GJC2	SPG44	AR	C									✓				Cell membrane proteins that function in gap junction formation allowing cytoplasmic exchange of ions and metabolites between neighbouring cells	Orthmann-Murphy *et al.* . 2009	Goodenough & Paul 2009
Non-lysosomal glucosylceramidase	GBA2	SPG46	AR	C			✓										Cell surface enzyme functioning in lipid metabolism in the non-lysosomal conversion of glucosylceramide to free glucose and ceramide. Is also linked to sphingomyelin generation.	Martin *et al.* 2013	Boot *et al.* 2007
AP-4 complex subunit beta-1	AP4B1	SPG47	AR	C				✓	✓								Golgi recruited adaptor protein that functions in Golgi to endosome cargo trafficking	Abou Jamra *et al.* 2011	Hirst *et al.* 2013
AP-5 complex subunit zeta-1	AP5Z1	SPG48	AR	P/C					✓								Endocytic protein that functions in late endosome to Golgi retrieval	Slabicki *et al.* 2010	Hirst *et al.* 2018
Tectonin beta-propeller repeat-containing protein 2	TECPR2	SPG49	AR	C				✓	✓								ER localised protein that functions in the formation of autophagosomes from ER exit sites (ERES)	Oz-Levi *et al.* 2012	Stadel *et al.* 2015
AP-4 complex subunit mu-1	AP4M1	SPG50	AR	C				✓	✓								Golgi recruited adaptor protein that functions in Golgi to endosome cargo trafficking	Verkerk *et al.* 2009	Hirst *et al.* 2013

Protein Name	Gene	SPG Number	Inheritance	Pure or Complex	ER Shaping	Mitochondrial	Lipid Metabolism	Secretory Pathway	Endosomal/Autophagosomal	Immune Related	Myelination	Nascent Protein Processing	Cell-Cell Contacts	Nucleotide Processing	Microtubule Related	Transporters	Protein Function	Disease Reference	Protein Function Reference
AP-4 complex subunit epsilon-1	AP4E1	SPG51	AR	C				✓	✓								Golgi recruited adaptor protein that functions in Golgi to endosome cargo trafficking	Abou Jamra et al. 2011	Hirst *et al.* 2013
AP-4 complex subunit sigma-1	AP4S1	SPG52	AR	C				✓	✓								Golgi recruited adaptor protein that functions in Golgi to endosome cargo trafficking	Abou Jamra et al. 2011	Hirst *et al.* 2013
Vacuolar protein sorting 37 homolog A	VPS37A	SPG53	AR	C					✓								Cytosolic protein that forms part of the ESCRT-I complex that functions in multivesicular body (MVB) formation in the endocytic pathway	Zivony-Elboum *et al.* 2012	Okumura *et al.* 2014
Phospholipase DDHD2	DDHD2	SPG54	AR	C			✓										Functions as a neuron specific triglyceride lipase. Also functions in the formato n of lipid d roplets	Schuurs-Hoeijmakers *et al.* 2012	Inloes *et al.* 2014
Probable peptide chain release factor C12orf65, mitochondrial	C12ORF65	SPG55	AR	C		✓								✓			Mitochondrial protein that functions as a codon independent translation receptor factor in mitochondrial protein synthesis	Shimazaki *et al.* 2012	Antonicka *et al.* 2010
Cytochrome P450 2U1	CYP2U1	SPG56	AR	P/C		✓	✓										Mitochondrial and ER protein that functions in the hydroxylation of unsaturated fatty acids and long saturated fatty acids	Tesson et al. 2012	Dhers *et al.* 2017
TRK Fused Gene 1	TFG	SPG57	AR	C				✓									ER protein that functions at ERES to regulate ER-Golgi-intermediate compartment structure and procollagen transport	Ishiura *et al.* 2012	McCaughey *et al.* 2016
Kinesin-like protein KIF1C	KIF1 C	SPG58	AR	P/C				✓							✓		Microtubule plus end directed motor that localises at the Golgi and functions in intra and post Golgi vesicle transport	Dor *et al.* 2014	Lee *et al.* 2015
Ubiquitin carboxyl-terminal hydrolase 8	USP8	SPG59	AR	C					✓								Cytosolic deubiquitin ates that interacts with ESCRT-III proteins on endosomes to regulate the stability and ubiquitin aton status of ESCRT-0 proteins and CHMP1B ubiquitin aton	Novarino *et al.* 2014	Crespo-Yanez *et al.* 2018
WD repeat-containing protein 48	WDR48	SPG60	AR	C													Recruits UPS12 deubiquitin ase to remove ubiquitin chains from PHLPP1 that functions in the phosphatid ylinositol 3-kinase/Akt pathway in cell survival	Novarino *et al.* 2014	Gangula & Maddika 2013
ADP-ribosylation factor-like protein 6-interacting protein 1	ARL6IP1	SPG61	AR	C	✓												ER protein that functions in the shaping of highly curved tubular ER	Novarino *et al.* 2014	Yamamoto *et al.* 2014
Erlin 1	ERLIN1	SPG62	AR	P	✓							✓					ER protein part of Erlin1/Erlin2 complex that mediates ER-associated degradation of inositol 1,4,5-trisphosph ate receptors (IP3Rs).	Novarino *et al.* 2014	Pearce *et al.* 2009

Protein Name	Gene	SPG Number	Inheritance	Pure or Complex	ER Shaping	Mitochondrial	Lipid Metabolism	Secretory Pathway	Endosomal/Autophagosomal	Immune Related	Myelination	Nascent Protein Processing	Cell-Cell Contacts	Nucleotide Processing	Microtubule Related	Transporters	Protein Function	Disease Reference	Protein Function Reference
AMP deaminase 2	AMPD2	SPG63	AR	C										✓			Cell surface enzyme that functions in purine nucleotide metabolism to deamination AMP	Novarino *et al.* 2014	Akizu *et al.* 2014
Ectonucleoside triphosphate diphosphohydrolase 1	ENTPD1	SPG64	AR	C						✓				✓			Cell surface enzyme that catalyses the phosphohydrolysis of extracellular ATP and ADP in inflammaton and cell injury	Novarino *et al.* 2014	Takenaka *et al.* 2016
Cytosolic purine 5'-nucleotidase	NT5C2	SPG65	AR	P/C										✓			Cytosolic nucleotidase that functions in the homeostasis of intracellular nucleotide pools by clearance of excess purine nucleotides	Novarino *et al.* 2014	Dieck *et al.* 2018
Arylsulfatase I	ARSI	SPG66	AR	C					✓								Lysosomal enzymes that catalyses the hydrolysis of sulfate esters and sulfamates	Novarino *et al.* 2014	Oshikawa *et al.* 2009
GPI inositol-deacylase	PGAP1	SPG67	AR	C			✓					✓					ER localises protein that catalyses the removal of an acyl chain on the GPI inositol on nascent GPI anchored proteins	Novarino *et al.* 2014	Liu *et al.* 2018
Leucine-rich repeat transmembrane protein FLRT1	FLRT1	SPG68	AR	C									✓				Cell surface protein that functions as a guidance factor for vascular and neural development by promoting cell adhesion or repulsion	Novarino *et al.* 2014	Jackson *et al.* 2016
Rab3 GTPase-activating protein non-catalytic subunit	RAB3GAP2	SPG69	AR	C	✓			✓									Part of the RAB3GAP1/RAB3GAP2 complex that functions as a Rab18 GEF and a Rab3 GAP. This regulates synaptic vesicle trafficking, autophagosome formation, and ER structure regulation	Novarino *et al.* 2014	Kern *et al.* 2015
Methionine-tRNA ligase, cytoplasmic	MARS	SPG70	AR	C										✓			Cytoplasmic enzyme that ligates methionine with its appropriate tRNA	Novarino *et al.* 2014	Popow *et al.* 2012
Zinc finger RNA-binding protein	ZFR	SPG71	AR	P						✓				✓			Enzyme that functions to regulate alternative splicing of mRNA. This may function in regulation of interferon in the immune response	Novarino *et al.* 2014	Haque *et al.* 2018
Receptor expression-enhancing protein 2 (REEP2)	REEP2	SPG72	AD/AR	P	✓												ER localises protein that facilitates the formation of high curvature on the ER at ER tubules	Esteves *et al.* 2014	Esteves *et al.* 2014
Carnitine palmitoyl transferase IC	CPT1C	SPG73	AD	P			✓										ER localised neuron specific enzyme that catalyses the transfer of acyl moieties from acyl-CoA to carnitine or choline	Carrasco *et al.* 2013	van der Hoek *et al.* 2018
IBA57	IBA57	SPG74	AR	C		✓											Mitochondrial enzyme part of the iron-sulfur cluster that catalyses heme biosynthesis	Lossos *et al.* 2015	Lossos *et al.* 2015
Dynamin-2	DNM2	-	AD	C		✓			✓								Cytosolic GTPase that functions in membrane fission	Sambuughin *et al.* 2015	Neumann *et al.* 2013

Protein Name	Gene	SPG Number	Inheritance	Pure or Complex	ER Shaping	Mitochondrial	Lipid Metabolism	Secretory Pathway	Endosomal/Autophagosomal	Immune Related	Myelination	Nascent Protein Processing	Cell-Cell Contacts	Nucleotide Processing	Microtubule Related	Transporters	Protein Function	Disease Reference	Protein Function Reference
Plasma membrane calcium-transporting ATPase 4	PMCA4	-	AD	?												✓	Cell surface protein that couples ATP hydrolysis to cellular calcium export	Ho *et al.* 2015	Adamo *et al.* 1995
β-Tubulin class IVA	TUBB4A	-	AD	C											✓		Brain specific tubulin monomer for microtubule formaton	Kancheva *et al.* 2015	Vulinovic *et al.* 2018
Interferon-induced helicase C domain-containing protein 1	IFIH1	-	AD	C						✓							Cytoplasmic protein that functions as a sensor of viral nucleic acids in innate immune response	Crow *et al.* 2014	Pichlmair *et al.* 2009
Double-stranded RNA-specific adenosine deaminase	ADAR	-	AD	P										✓			Nuclear enzyme that catalyses the hydrolytic deamination of adenosine to inosine in dsRNA	Crow *et al.* 2014	Kim *et al.* 1994
ATPase family AAA-domain containing protein 3A	ATAD3A	-	AD	C		✓											Mitochondrial inner membrane AAA+ protein with an unknown function	Cooper *et al.* 2017	Cooper *et al.* 2017
Lysosomal-trafficking regulator	LYST	-	AR	C					✓	✓							Cytoplasmic protein that regulates endolysosomal responses to Toll Like Receptor (TLR) 3 and TLR4 induced signalling pathways in the immune response	Shimazaki *et al.* 2014	Westphal *et al.* 2017
Myelin-associated glycoprotein	MAG	-	AR	C							✓		✓				Cell surface glycoprotein that functions in the myelin sheath to mediate glia-neuron interactions to cell maintenance and survival	Novarino et al. 2014	Quarles *et al.* 2007
T-complex protein 1 subunit epsilon	CCT5	-	AR	C								✓					ER protein that functions ensuring the efficient folding of nascent and stress-denatured proteins	Bouhouche *et al.* 2006	Pereira *et al.* 2017
Exosome component 3	EXOSC3	-	AR	C					✓					✓			Part of the multisubunit RNA exosome complex that functions in RNA degradaton	Zanni *et al.* 2013	Mitchell *et al.* 1997
Phenylalanine--tRNA ligase, mitochondrial	FARS2	-	AR	C		✓								✓			Mitochondrial enzyme that functions in ligating phenylalanine to phenylalanine tRNA	Yang *et al.* 2016	Elo *et al.* 2012
Alsin	ALS2	-	AR	C		✓			✓								Protein that functions as a Rab5 GEF regulating Rab5-bound endosome dynamics and localisation including recruitment to damaged mitochondria. Also functions as an activator of Rac1 GTPase	Eymard-Pierre *et al.* 2002	Lai *et al.* 2009; Hsu *et al.* 2018
Kinesin light chain 2	KLC2	-	AR	C											✓		Microtubule plus end directed motor that functions in protein, vesicular, ribonuclear protein, and organelle transport	Macedo-Souza *et al.* 2009	Yip *et al.* 2016
L-glutamate-L-decarboxylase type 1	GAD1	-	AR	C			✓	✓									Golgi localised enzyme that functions to synthesis the neurotransmitter y-aminobutyric acid (GABA) in neurons	McHale *et al.* 1999	Dirkx Jr. *et al.* 1995

Protein Name	Gene	SPG Number	Inheritance	Pure or Complex	ER Shaping	Mitochondrial	Lipid Metabolism	Secretory Pathway	Endosomal/Autophagosomal	Immune Related	Myelination	Nascent Protein Processing	Cell-Cell Contacts	Nucleotide Processing	Microtubule Related	Transporters	Protein Function	Disease Reference	Protein Function Reference
Kinesin light chain 4	KLC4		AR	C											✓		Microtubule plus end directed motor that functions in protein, vesicular, ribonuclear protein, and organelle transport	Bayrakli *et al.* 2015	Yip *et al.* 2016
Reticulophagy regulator 1	RETREG1	-	AR	C					✓								ER localised protein that mediates ER turnover by acting as an a receptor for components of the ER-phagy machinery	Ilgaz Aydinlar *et al.* 2014	Islam *et al.* 2018
Protein bicaudal D homolog 2	BICD2	-	AD/AR	C				✓	✓						✓		Cytosolic adaptor protein that interacts with the dynein-dynactin complex and Rab6 to facilitate Golgi to ER trafficking and mRNA transport	Oates *et al.* 2013	Matanis *et al.* 2002
Glutamate receptor ionotropic delta 2	GRID2	-	A?	C					✓								Cell surface receptor for glutamate that promotes synaptogenesis and AMPA receptor endocytosis	Maier *et al.* 2014	Elegheert *et al.* 2016
Ribonuclease H2 subunit B	RNASEH2B	-	A?	P										✓			Nuclear enzyme that catalyses the degradation of RNA of RNA:DNA hybrids	Crow *et al.* 2014	Figiel *et al.* 2011
Cytochrome c oxidase subunit 3, mitochondrial	MT-CO3	-	M	P/C		✓											Mitochondrial enzyme of the electron transport chain of complex 4 that reduces oxygen and transports hydrogen across the mitochondrial membrane	Tiranti *et al.* 2000	Castresana *et al.* 1994
Transfer RNA, mitochondrial, isoleucine	MT-TI	-	M	P/C		✓								✓			Mitochondrial transfer RNA of isoleucine	Corona *et al.* 2002	Anderson *et al.* 1981
Complex V, ATP synthase, subunit ATPase 6	MT-ATP6	-	M	P/C		✓											Mitochondrial ATP synthase	Verny *et al.* 2011	Kucharczyk *et al.* 2009
NADH-ubiquinone oxidoreductase chain 4	MT-ND4	-	M	P/C		✓											Mitochondrial enzyme of the electron transport chain of complex 1 that transports electrons from NADH to ubiquinone	Clarencon *et al.* 2006	De Vries *et al.* 1996

Table 1 - **The HSP genes and their functions**. All the identified HSP genes are listed with their function. Column order is: (1) Protein name; (2) Gene name; (3) Inheritance pattern (AD = autosomal dominant; AR = autosomal recessive; A? = autosomal but unclear dominant or recessive; AD/AR = both autosomal dominant and recessive depending on the mutation; M = mitochondrially inherited; X = X-linked); (4) Pure or complex HSP pathology; (5-16) Groups of HSP functions; (17) Protein function; (18) Disease reference; (19) Protein function reference. Data from Lo Giudice et al. 2014; Klebe et al. 2015.

Endosomal or autophagosomal

The endosomal pathway will be described in more detail in Introduction Section 1.4. Briefly however, cell surface cargos can be internalised by endocytosis into endosomes. Cargos are then either redistributed via endocytic recycling tubules or are degraded in the lysosome (Maxfield and McGraw 2004)(McNally and Cullen 2018). In macroautophagy, autophagosomal membranes engulf proteins or organelles to be degraded before then fusing with the lysosome to mediate their degradation (Pavel and Rubinsztein 2017). HSP proteins associated with either endocytic and autophagosomal trafficking pathways constitute the largest group of HSP proteins, with 24/80 associated HSP proteins functioning in these pathways. Functions include mediating Golgi to endosome traffic (SPG47, SPG50, SPG51, SPG52), mediating endocytic recycling (SPG4, DNM2, SPG8, SPG11, SPG15, SPG48, SPG20), mediating endosomal sorting complex required for transport (ESCRT) activity (SPG53, SPG59), mediating endosome motility (SPG10), mediating autophagosome formation (SPG49), and in lysosome function (SPG4, SPG8, SPG31, SPG11, SPG15, SPG66). Of note is that several proteins such as spartin, spastin, NIPA1 function in mediating the recycling of bone morphogenic protein II (BMPRII). It should be noted that along with spastin, spartin, dynamin-2, and strumpellin, the ER shaping proteins are involved in the process of endocytic recycling by ER-endosome contacts facilitating endosomal tubule fission (Rowland et al. 2014). Membrane trafficking pathways are often interdependent, meaning that some proteins may have described functions in more than one of these membrane sites, with primary defects having knock-on effects on downstream pathways.

Mitochondrial

Mitochondrial function in cells includes ATP synthesis, metabolite and lipid synthesis, heat production, apoptosis, and lipid synthesis. The proteins which drive these functions are either encoded by the mitochondrial genome or encoded by the nuclear genome and imported as proteins into the mitochondria (Osellame et al. 2012). This category represents the second largest grouping of HSP proteins, with 18/80 HSP proteins associated with mitochondrial function. These include proteins that function within the mitochondria such as in the electron transport chain (MIT-CO3, MT-ATP6, MT-ND4), in mitochondrial translation (SPG55, FARS2, MT-TI), and mitochondrial metabolite synthesis (SPG56, SPG9, SPG74). In addition, it also includes cytoplasmic mitochondrially related proteins such as those involved in mitochondrial fission (SPG31, DNM2), mitochondrial positioning (SPG10, SPG20), and mitochondrial turnover (ALS2). Of note also is paraplegin (SPG7), a protein that functions as part of the mitochondrial AAA metalloprotease, as it is the most commonly mutated mitochondrial protein to cause HSP.

Lipid metabolism

Lipids are essential components of all cells as they function in membrane formation, energy storage, and extracellular and intracellular signalling (Welte and Gould 2017). Lipid metabolism is the third largest grouping of HSP genes, with 17/80 HSP genes associated with the processing of lipids. Lipid-related HSP proteins function in a diverse range of lipid metabolism activities, including cholesterol synthesis (SPG5), ganglioside and sphingolipid synthesis for myelination (SPG26, SPG35) and inositol processing (SPG18, SPG28, SPG67). Another theme that emerges is the involvement of several HSP proteins with lipid droplet biogenesis. This includes the proteins atlastin-1 (SPG3), spastin (SPG4), seipin (SPG17), spartin (SPG20), REEP1 (SPG31), and phospholipase DDHD2 (SPG54). Lipid droplets are crucial in every cell type to provide a storage of energy. These can be synthesised or hydrolysed during times of energy surplus or deficiency respectively. In addition, lipid droplets can also function as storage sites for signalling precursors and vitamins, to mitigate the effects of ER and oxidative stress, and in protein maturation, storage, and turnover (Welte and Gould 2017).

Secretory pathway

After being correctly folded in the ER, proteins destined for the Golgi apparatus, the cell surface, the endocytic pathway, or secretion enter the secretory pathway (Presley et al. 1997). This pathway describes export from the ER, transition to the Golgi, and transport away from the Golgi. Proteins involved in secretion form the fourth largest cluster of HSP proteins, with 14/80 HSP proteins associated with secretion. This includes proteins that function as motor proteins or motor adaptors in vesicle trafficking (SPG30, SPG10, SPG58, BICD2), cargo transport away from the Golgi apparatus (SPG47, SPG50, SPG51, SPG52, SPG69), and at ER exit sites (ERES; SPG4, SPG49, SPG57). Of note is that 4 subunits of AP4 complex involved in Golgi to endosome traffic are HSP proteins.

Nucleotide processing

Nucleotides are essential molecules for life as they provide information and temporary energy and phosphate storage. Proteins involved in nucleotide processing form the fifth largest group of HSP associated proteins, with a total of 11/80 HSP associated proteins. This includes proteins that function in mitochondrial and cytoplasmic translation (FARS2, MI-TI, SPG55, SPG70), RNA degradation (EXOSC3, RNASEH2E), and purine metabolism (SPG63, SPG65, ADAR).

Microtubule related

Microtubules are cytoskeletal elements that function in long range vesicular transport, cell division, cilia and flagella formation, and cell motility. Vesicular transport is mediated by microtubule motor proteins dynein and kinesin that travels towards and away from the nucleated minus end of microtubule respectively (Janke and Chloë Bulinski 2011). In total 9/80 HSP proteins are microtubule associated. These include motor proteins (SPG10, SPG30, SPG58, KLC2, KLC4), and adaptor proteins linking vesicle transport to microtubules (BICD2, SPG18). Spastin (SPG4) is unique among these proteins in its ability to regulate microtubule architecture by regulating microtubule stability and severing (Vemu et al. 2018).

ER shaping

The ER is composed of a continuous network of hollow membranes that take the shape of distinct tubules, dense tubular matrices, or sheets (Nixon-Abell et al. 2016). The architecture of the ER is generated by ER shaping proteins that control the formation of ER junctions and tubule/sheet ratio. In total, 9/80 HSP proteins function in ER shaping. This includes the GTPase atlastin-1 (SPG3) that mediates ER junction formation. Many of these HSP proteins contain long hydrophobic domains that allow them to embed into the outer leaflet of the ER membrane, acting as a hydrophobic wedge to mediate its curvature. These include spastin (SPG4), REEP1 (SPG31), reticulon-2 (SPG12), protrudin (SPG33), ADP-ribosylation factor-like protein 6-interacting protein 1 (SPG61), and REEP2 (SPG72). Spastin, atlastin, reticulons and REEPs are thought to interact in the ER to form an ER morphogen complex (Blackstone et al. 2011).

Immune related

The immune system is responsible for protecting the body against infection. 4/80 HSP proteins are involved in immunity. All these proteins were only recently associated with HSP (Lo Giudice et al. 2014). These include interferon-induced helicase C domain-containing protein 1 (IFIH1) and lysosomal-trafficking regulator (LYST) that function as a sensor of viral nucleic acids and as receptors or Toll Like Receptor (TLR) 3 and 4 activation respectively (Pichlmair et al. 2009; Westphal et al. 2017). In addition, zinc finger RNA-binding protein (SPG71) functions in alternative mRNA splicing in interferon regulation (Haque et al. 2018), and ectonucleoside triphosphate diphosphohydrolase 1 (SPG64) functions at the cell surface to hydrolyse ATP and ADP during cell injury and inflammation (Takenaka et al. 2016).

Cell-cell contacts

Cell-cell contacts are important in mediating the rapid exchange of solutes between cells, as well as in cell guidance and signalling. Four HSP proteins are associated with cell-cell contact formation. These include myelin-associated glycoprotein (MAG) that functions in glia-neuron interactions (Quarles 2007), neural cell adhesion molecule L1 (SPG1) that functions in neuronal adhesion (Samatov et al. 2016), connexin 47 (SPG44) that functions in gap junction formation (Goodenough and Paul 2009), and leucine-rich repeat transmembrane protein FLRT1 (SPG68) that functions in neuronal guidance (Jackson et al. 2016).

Myelination

The myelination of axons is essential to provide the fast transmission of action potentials in the axon. Rather than action potentials having to continuously move down the entire length of the axon membrane, they are able to jump between unmyelinated breaks in the axon by saltatory conduction, thereby dramatically increasing conduction speed (Schnaar 2010). Only 4 HSP proteins are directly associated with myelination. These include the lipid synthesis proteins fatty acid 2-hydoxylase (SPG35) and beta-1,4 N-acetylgalactosaminyltransferase 1 (SPG26), and myelin sheath associated proteins myelin proteolipid protein (SPG2), and myelin-associated glycoprotein (MAG). Of note is that myelin proteolipid protein (SPG2) is the major myelin protein in the central nervous system.

Nascent protein processing

In the secretory pathway proteins must be correctly folded and postranslationally modified before they are secreted. Any protein that fails this process is degraded in the ER-associated degradation (ERAD) pathway (Benham 2012). Four HSP proteins are associated with ER-based protein modification, folding, or degradation. These include Erlin 1 (SPG62) and Erlin 2 (SPG18) which function in ERAD of inositol 1,4,5-trisphosphate receptors (Pearce et al. 2009), T-complex protein 1 subunit epsilon (CCT5) that functions in protein folding (Pereira et al. 2017), and GPI inositol-deacetylase (SPG67) that functions in GPI anchor modification on nascent GPI anchored proteins (Liu et al. 2018).

Transporters

Non-cell permeable solutes and ions that move across membranes must do so through channels, or proteins that facilitate diffusion or active transport. This activity is essential for the homeostatic balance of all cellular compartments and in cell signalling. Only 3 HSP proteins have been associated with transport across membranes. These include monocarboxylate transporter 8 (SPG22) that functions in thyroid hormone transport (Heuer et al. 2005), acetyl coenzyme A transporter 1 (SPG42) that functions in the import of acetyl-CoA into the ER (Jonas et al. 2010), and plasma membrane calcium transporting ATPase 4 (PMCA4) that functions in ATP-dependent calcium export (Filoteo 1995).

A diverse set of proteins related to the same disease

How can mutations in such a diverse set of proteins lead to a similar pathology? Two non-mutually exclusive possibilities have been proposed. One possibility is that there is a unifying molecular biological process involving all or many proteins. Previous suggestions have included dysfunctional BMP signalling (Blackstone et al. 2011) and lysosome dysfunction (Allison et al. 2017). Although it is currently unclear how these processes may apply to all HSP proteins, precedent has suggested that seemingly diverse HSP proteins can function in a common pathway. One example is the discovery that ER architecture is essential for the fission of endosomal recycling tubules, with mutations in either sets of proteins leading to lysosome dysfunction (Allison et al. 2017; Rowland et al. 2014). This therefore united the HSP proteins involved in endolysosomal pathways with those involved in ER shaping. Other hints that there may be only one or a few core mechanisms of HSP are provided by several HSP proteins appearing in multiple functional groups, such as the proteins involved in both membrane traffic and lipid biology. An intermediate model in which pathology results from a collection of distinct unifying pathways perhaps is the most likely.

The alternative possibility is that instead of a common molecular pathway, HSP proteins are components of multiple pathways that are united only by their requirement for axonal health and the disproportionate effect that their pathogenic mutations have upon corticospinal neurons. Corticospinal neurons are unique by their length, with axons able to grow to 1m in length (Blackstone et al. 2011). This allows the rapid transmission of action potentials, but also creates high demands on cellular processes such as axonal transport, homogenously distributed energy production, lipid synthesis, and myelination. This demand may render these neurons vulnerable to even small deviations in molecular efficiency. By contrast, the same loss of inefficacy may result in a negligible effect on cell types with less extreme morphology.

1.2.3 – Relative contribution of each gene to overall HSPs

The majority of familial and sporadic HSP are caused by mutations in only a few genes (**Figure 1**; Lo Giudice et al. 2014; Klebe et al. 2015). From data from Lo Giudice et al. (2014), these include the genes encoding spastin (SPG4), atlastin-1 (SPG3), kinesin heavy chain isoform 5A (SPG10), REEP1 (SPG31), 25-hydroxycholesterol 7-alpha-hydroxylase (SPG5), paraplegin (SPG7), spatacsin (SPG11), spastizin (SPG15), and neural cell adhesion molecule L1 (SPG1). ~20% of familial HSP and ~50% of sporadic HSP were caused by mutations in unmapped genetic loci in 2014.

By far the most common cause of HSP is mutation in the *SPAST* gene (SPG4) encoding the protein spastin. Mutations in *SPAST* are the single largest cause of HSP in both familial and sporadic HSP, accounting for ~40% of all familial HSP cases, and ~20% of all sporadic HSPs. This accounts for more than double the contribution of any other HSP gene to the incidence of HSP in both familial and sporadic HSP. Research into understanding the function of spastin is therefore critical to understanding the pathology of HSP.

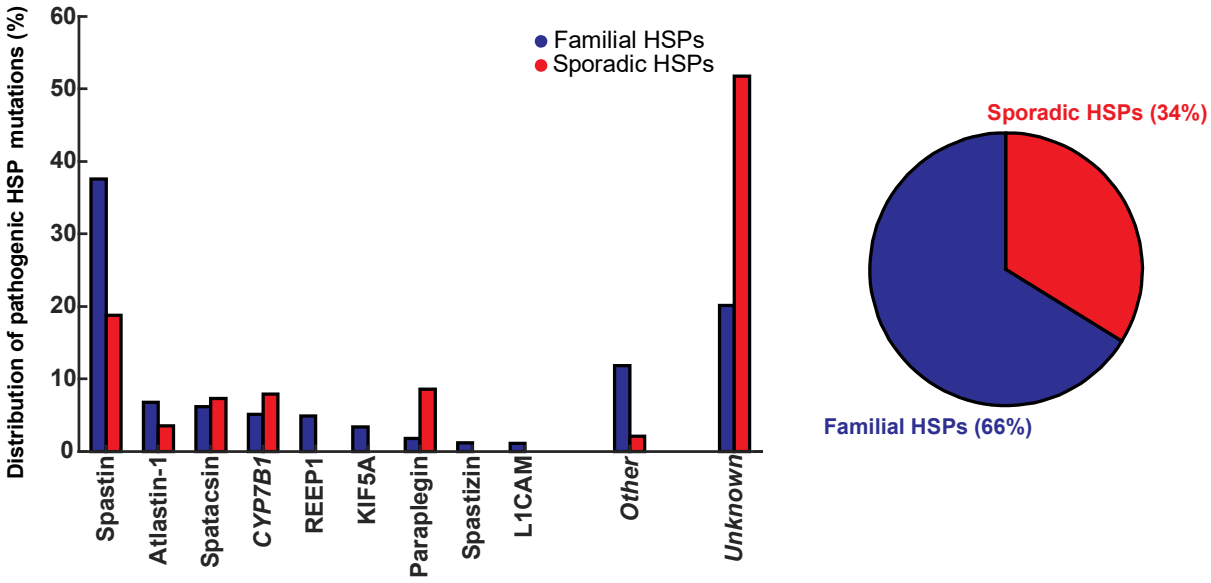

Figure 1 - **Prevalence of familial and sporadic pathogenic mutations in HSP genes by gene.** Bar chart showing the relative contribution of pathogenic inherited or sporadic mutations in HSP-associated proteins against the total reported cases of HSP. Inherited mutations and sporadic mutations are displayed by blue and red bars respectively. Only the most common proteins mutated in HSP pathogenesis are displayed. The pie chart shows the proportion of pathogenic HSP mutations that are caused by genetically inherited or sporadic mutations. Data adapted from Lo Giudice et al. (2014).

1.3 – Spastin

1.3.1 – Historical and clinical features of spastin-related HSP

The *SPAST* gene encodes the protein spastin. *SPAST* was first discovered as an HSP gene in 1999 by a positional cloning approach on the SPG4 locus, the position on chromosome 2p21-22 known to be responsible for a considerable proportion of autosomal dominant HSP (Hazan et al. 1999; Raskind et al. 1997). Since this discovery, 467 papers have been published with keywords SPG4, SPAST, or spastin (**Figure 2**). These papers include clinical reports of novel and reoccurring *SPAST* mutations from every continent, as well as structural and functional studies. Of the major HSP genes contributing to familial or sporadic HSP (**Figure 1**), spastin is the second most researched protein behind L1CAM (**Figure 2**).

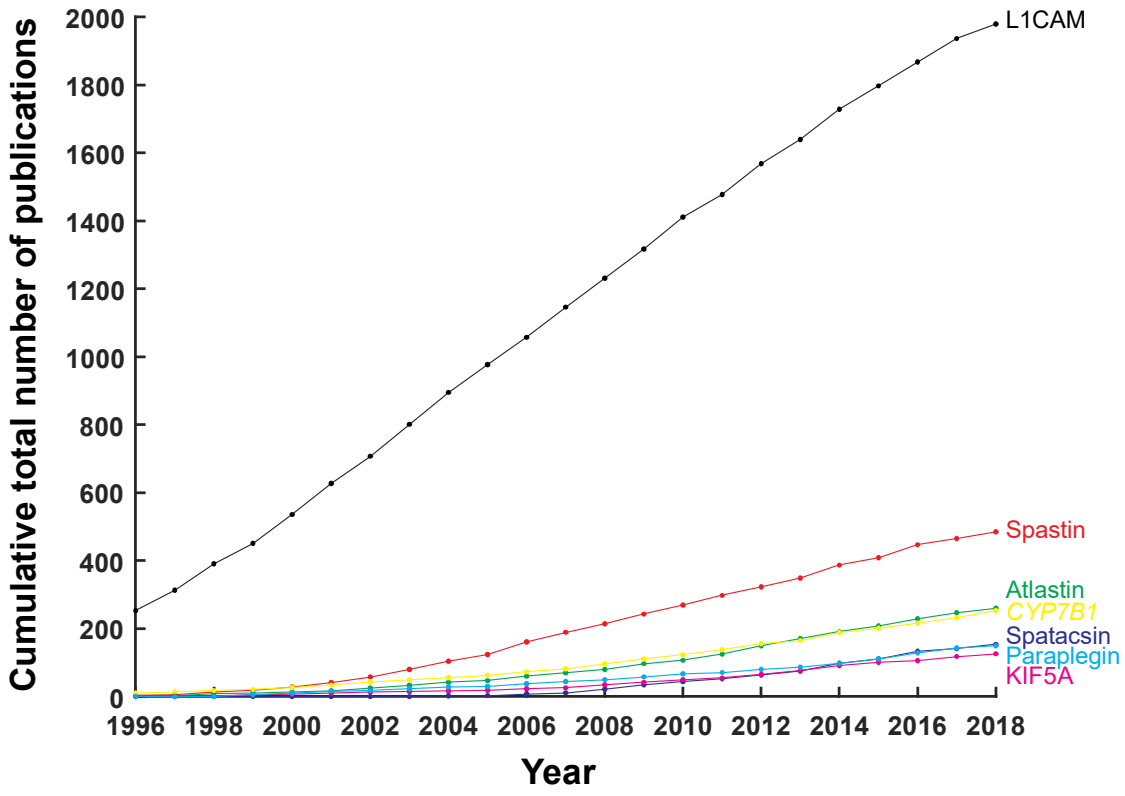

Figure 2 - **Publication history of most commonly mutated HSP genes.** Cumulative line plot showing the cumulative total number of publications for the most commonly mutated HSP genes causing HSP from 1996 to 2018. Publication counts were generated by searching the NCBI PubMed database for the protein (including synonyms), gene name, or HSP reference name (e.g. spastin/SPAST/SPG4). Data accurate to August 2018.

SPAST-associated HSP is an autosomal dominant pure form of spastic paraplegia. The major disease phenotype is a progressive bilateral lower limb spasticity. This is often associated with brisk reflexes, ankle clonus, and involuntary movement of the toes upon stroking the underside of the foot (Babinski

sign). More than 50% of patients have proximal weakness in the lower libs, and 33% have urinary urgency or incontinence (Reid 1999). Subtle cognitive impairment has been reported in some cases (Byrne et al. 1998; Reid et al. 1999; Tisher and Salardini 2016; Webb and Hutchinson 1998), and depression has been reported in 41% of cases (du Montcel et al. 2008). Onset occurs mostly in early adult life but can vary between infancy to old age (Fonknechten et al. 2000). Age of onset can be accelerated by epistatic mutations in the contiguous gene *DPY30* (Newton et al. 2018). Life expectancy is not affected by the disease. Currently there are no etiological treatments. However symptomatic treatments include use of antispastic drugs for leg spasticity, anticholinergic antispasmodic drugs for urinary urgency, and physiotherapy for stretching spastic muscles (Dürr et al. 2003; Reid et al. 1999). In addition, botulinum toxin injections may be given to severe patients (Rousseaux et al. 2007). ~40% patients also use assisted walking, including wheelchair use (Reid et al. 1999). *SPAST* mutations causing HSP have been described globally. The prevalence of *SPAST* associated HSP varies by country but is estimated to be between 2/100,000 and 6/100,000 for most countries (Durr et al. 1993).

1.3.2 – Spastin isoforms

SPAST has homologs in all vertebrates including sea squirts (e.g. *Ciona intestinalis*), the arthropods (e.g. *Drosophila melanogaster*), nematodes (e.g. *Caenorhabditis elegans*), as well as in yeast (e.g. *Saccharomyces cerevisiae*; Ensembl, 2018). In humans it is located on chromosome 2 at band 2p22-23. It is composed of 17 exons and is ~94kb in length (Ensembl). The gene contains two promoters: a TATA-less promoter 310bp upstream of the first ATG (Canbaz et al. 2011; Mancuso and Rugarli 2008), and a cryptic promoter that covers the 5'-untranslated region (UTR) and part of exon 1 (Mancuso and Rugarli 2008). The TATA-less promoter contains a CAAT box and a CpG island and appears able to bind transcription factor Elk1 (Canbaz et al. 2011).

The presence of these two promoters drives the production of two of four main spastin transcripts (**Figure 3A**). The long 'M1 spastin' transcript encodes a protein 616 amino acids in length and is driven by the TATA-less promoter upstream of the first ATG. The short 'M87 spastin' transcript, driven by the cryptic protomer, encodes a protein 530 amino acids in length. These two transcripts also have further variety by the alternative splicing of exons 4, 8, or 15, although of these, only exon 4 spliced spastin is expressed at significant levels (Svenson et al. 2001). In addition to these transcriptional mechanisms for generation spastin isoforms, a poor Kozak sequence surrounding the first ATG codon leads to leaky scanning of the 40S ribosomal subunit through to the strong Kozak sequence at initiation codon M87, causing some M87 spastin to be translated from M1 spastin transcript (CLAUDIANI et al. 2005). These mechanisms result in M87 spastin being expressed at a higher level than M1 spastin (Solowska et al. 2008, 2010). Both M1 and M87 isoforms are expressed in all tissues but M1 spastin is specifically enriched in the brain and spinal cord (Charvin 2003; CLAUDIANI et al. 2005; Solowska et al. 2010).

1.3.3 – Spastin functional domains

The properties of a protein are conferred by its functional domains. Spastin contains five different domains: a hydrophobic hairpin-loop domain, nuclear localisation and export motifs, a microtubule interacting and trafficking (MIT) domain, a microtubule binding domain (MTBD), and an ATPases associated with diverse cellular activities (AAA+) domain (**Figure 3**). All domains except the hydrophobic hairpin-loop and the nuclear export motif are contained by both M1 and M87 isoforms of the protein. The hydrophobic hairpin-loop and the nuclear export motif are encoded in exon 1 so are excluded from the M87 isoform of spastin.

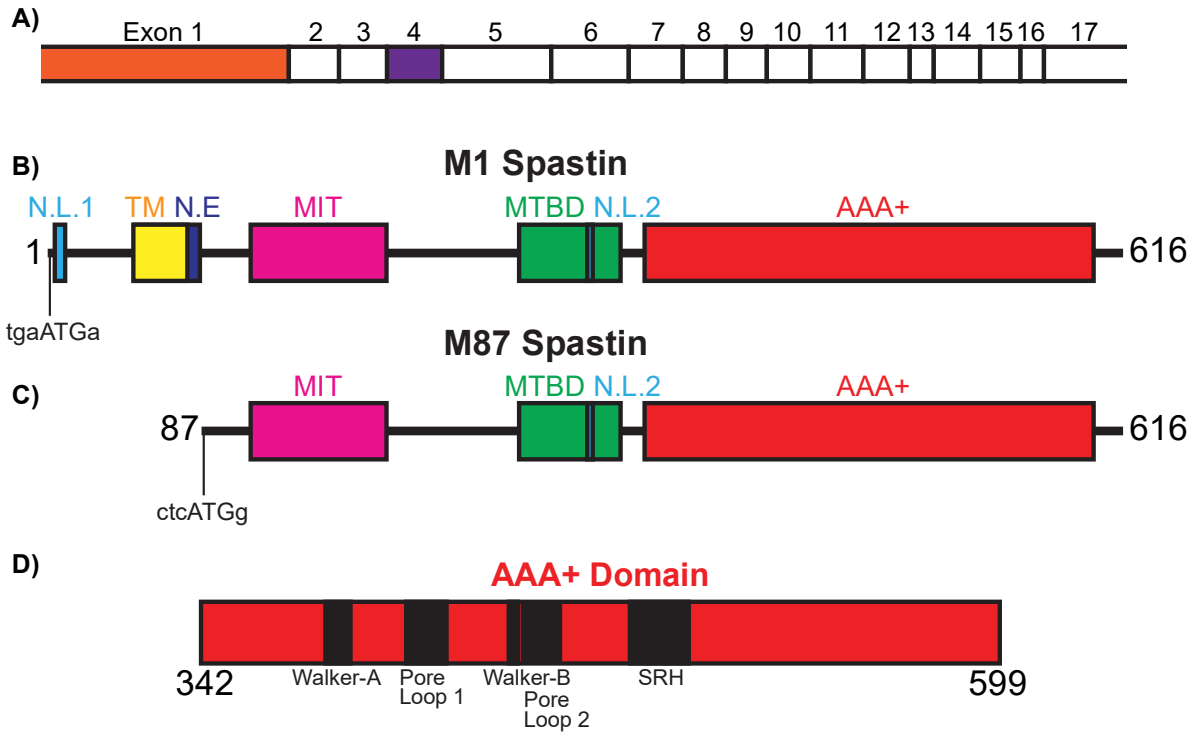

E)

Domain	Start	End
Nuclear Localisation 1 (N.L.1)	4	10
Hydrophobic Hairpin Loop (TM)	49	80
Nuclear Export (2 Motifs) (N.E.)	50	87
Microtubule Interacting and Trafficking (MIT)	116	194
Microtubule Binding Domain	270	328
Nuclear Localisation 2 (N.L.2)	309	312
ATPases Associated with diverse cellular Activites (AAA+)	342	599

AAA+ Motif	Start	End
Walker-A	382	390
Pore Loop 1	408	421
Walker-B	441	444
Pore Loop 2	445	458
SRH	480	499

Figure 3 - **Aligned exon and domain structure of SPAST and M1 and M87 spastin isoforms**. (A) Exon structure of spastin mature transcript, scaled to the number of amino acids in each exon, and in line with the below M1 and M87 spastin domains. Exon 4 is highlighted as it may be alternatively spliced, and exon 1 as it contains a cryptic promoter. (B) Size-proportionate domain cartoon of M1 and M87 spastin. M1 spastin contains a weak Kozak sequence at its N-terminus (tgaATGa), causing leaky scanning of the 40S ribosomal subunit to a second start site encoding a stronger Kozak sequence (ctcATGg: M87). In order, M1 spastin contains: a nuclear

localisation sequence (4-10), a hydrophobic hairpin transmembrane domain (49-80), two nuclear export sequences (in total between 50-87), an microtubule interacting and trafficking (MIT) domain (116-194), a microtubule binding domain (MTBD) (270-328), a second nuclear localisation sequence (309-312), and a ATPase associated with diverse cellular activities (AAA+) domain (324-599). (C) M87 spastin also has a unique transcript due a cryptic promoter in exon 1. M87 spastin lacks all domains N-terminally of M87. (D) Size-proportionate motif cartoon of the AAA+ domain. In order, the AAA+ domain contains: Walker-A motif (382-390), Pore Loop 1 (408-421), Walker-B motif (441-444), Pore Loop 2 (445-458), and a Second Region of Homology (SRH) domain (480-499). (E) Table showing the amino acid start and end positions of spastin domains and motifs in the AAA+ domain.

Hydrophobic hairpin-loop

The hydrophobic hairpin-loop, which is only present in the full 616 amino acid M1 isoform of spastin, is encoded by exon 1 and is located between amino acids 49-80. This motif allows the M1 spastin isoform to be localised to the ER by insertion into the outer leaflet of the ER membrane, making M1 spastin an integral membrane protein (Chang et al. 2013; Connell et al. 2009; Park et al. 2010). Due to the hairpin nature of the hydrophobic motif, the N and C termini are cytoplasmic (Chang et al. 2013; Park et al. 2010). The precise mechanism of how M1 spastin is inserted into the ER membrane has not been investigated. However, by homology of hydrophobic hairpin-loop to that of Arl6IP1 and the reticulons, it is possible that the insertion of M1 spastin may be mediated by either the translocon or a PEX3-PEX19 posttranslational insertion pathway (Yamamoto and Sakisaka 2018).

The hydrophobic hairpin of M1 spastin is similar to that of other HSP proteins (Yamamoto et al. 2014). These include atlastin-1 (SPG3), protrudin (SPG33), reticulon-2 (SPG12), REEP1 (SPG31), REEP2 (SPG72), and ARL6IP1 (SPG61). Through this domain, spastin is able to interact with atlastin-1 (Evans et al. 2006; Park et al. 2010; Sanderson et al. 2006), REEP1 (Park et al. 2010), protrudin (Chang et al. 2013), and reticulon-1 (Mannan et al. 2006; Montenegro et al. 2012). These proteins are thought to work together in an 'ER-morphogen complex' to regulate the morphology of the ER (Blackstone et al. 2011). This complex is able to generate curvature of ER membranes through hydrophobic wedging (Shibata et al. 2009; Voeltz et al. 2006), thereby allowing the formation of the tubular ER network. In addition, the M1 domain of spastin allows it to interact with the centrosomal protein NA14 (Errico 2004).

Nuclear localisation and export domains

Spastin was hypothesised to be a nuclear protein upon its discovery (Hazan et al. 1999). This was based upon the presence of an RGKKK putative nuclear localisation signal in amino acids 7-11 of the M1 isoform of spastin. However, this signal sequence was later disregarded as it did not cause exclusive import of spastin into the nucleus (Beetz et al. 2004). Instead, spastin was confirmed to have two functional nuclear localisation signals: PGGRGKK in exon 1 at amino acid positions 4-10, and RKKK in exon 6 at amino acid positions 309-312 (Beetz et al. 2004). In addition, spastin contains two overlapping nuclear export signals located between amino acids 50 to 87 in exon 1 (CLAUDIANI et al. 2005).

The combination of these motifs results in M1 spastin containing two nuclear localisation signals and two nuclear export signals, and M87 spastin containing one nuclear localisation signal but no nuclear export signal. As a result, M1 spastin is not localised in the nucleus (CLAUDIANI et al. 2005; Connell et al. 2009). Due to lack of an export signal, M87 spastin however is localised both cytoplasmically and in the nucleus (Beetz et al. 2004; CLAUDIANI et al. 2005; Connell et al. 2009). This difference in isoform localisation helps explain initially conflicting observations regarding the cytoplasmic or nuclear localisation of spastin (Charvin 2003; Errico 2002, 2004; McDermott et al. 2003; Reid et al. 2005; Wharton et al. 2003). Despite extensive research into the cytoplasmic function of spastin, there is currently only one publication suggesting an intranuclear function for spastin (Daftary et al. 2011).

The microtubule interacting and trafficking (MIT) domain

The microtubule interacting and trafficking (MIT) domain of spastin was first identified in 2003 (Ciccarelli et al. 2003). This was discovered by comparisons between a non-redundant protein database and the N-terminal of spartin (SPG20). This analysis identified conserved domains in the proteins spartin, spastin, sorting nexin 15, RPK118, SKD1, VPS4, and calpain-7, of approximately 80 amino acids overlapping with the previously termed ESP domain. This list of MIT domain containing proteins was later expanded to include the VPS4 cofactor LIP5 (Shim et al. 2008), deubiquitinating enzymes AMSH (Solomons et al. 2011; Tsang et al. 2006) and USP8 (Row et al. 2007), autophagy initiation protein ULK1 (Fujioka et al. 2014), and microtubule interacting and trafficking domain containing protein 1 (MITD1; Tsang et al. 2006).

The MIT domain of spastin is located between amino acids 116 and 194 and is encoded by exons 1, 2, and 3. It is therefore present in both M1 and M87 spastin isoforms. The structure of MIT domains was identified by nuclear magnetic resonance (NMR) spectroscopy and x-ray crystallography

of the VPS4 MIT domain. It was shown to consist of three α-helices arranged asymmetrically, with the α-helices 1 and 3 running parallel, and antiparallel to helix 2 (Obita et al. 2007; A. Scott et al. 2005; Takasu et al. 2005). Spastin's MIT domain was shown to be structurally similar to that of VPS4 (Yang et al. 2008).

MIT domains specifically interact with MIT-interacting motifs (MIMs), primarily found in endosomal sorting complexes required for transport (ESCRT)-III proteins, typically located at the C-terminus (Kieffer et al. 2008; Schöneberg et al. 2017; A. Scott et al. 2005). Proteins may either contain a single MIM (e.g. Charged multivesicular body protein (CHMP) 1, CHMP2, CHHMP5, CHMP7) or MIMs in tandem (e.g. CHMP4, Increased sodium tolerance 1 (IST1); Schöneberg et al. 2017). Currently there are five different described modes of MIT-MIM interaction (**Table 2**). Typically, MIMs interact in a groove created by the MIT α-helices, lying parallel to the orientation of the first MIT helix. These interaction modes are displayed in **Figure 4** and described in **Table 2**.

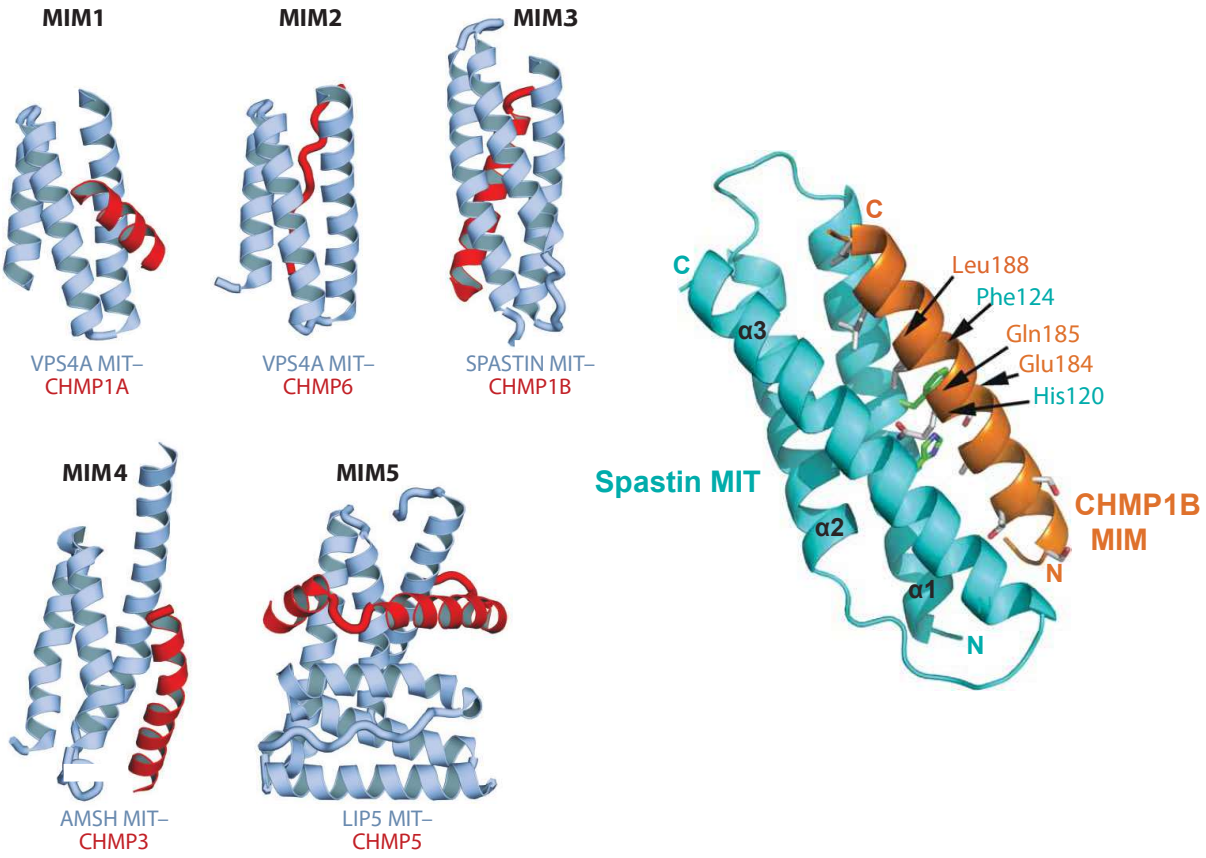

Figure 4 - **MIT-MIM interaction modes and spastin MIT-CHMP1B MIM interaction**. (Left) The different MIT-MIM interaction modes. A detailed description of each mode is provided in proceeding table (**Table 2**). Protein structures from McCullough et al. (2018). (Right) Interaction structure of spastin's MIT domain and the MIM of CHMP1B. The MIM of CHMP1B sits in a groove between α-helices 1 and 3 of spastin's MIT domain. Key residues mediating the interaction are displayed, with blue and orange indicating residues from the MIT domain and MIM respectively. Structure adapted from Yang et al. (2008).

MIT-MIM Interaction	Example Complex	Location of MIM	Binding Type	Reference
MIT-MIM Mode 1	VPS4-VP2 VPS4-CHMP1A	MIM1 lies in a groove between MIT helices 2 and 3	Hydrophobic interactions and salt bridges	Obita *et al.*, 2007 Stuchell-Brereton *et al.*, 2007
MIT-MIM Mode 2	VPS4-CHMP6	MIM2 lies in a groove between MIT helices 1 and 3	Hydrophobic interactions, salt bridge formation, hydrogen bonding	Kieffer *et al.*, 2008
MIT-MIM Mode 3	Spastin-CHMP1B Spastin-IST1	MIM3 lies in a groove between MIT helices 1 and 3. Differs to MIM2 as the interaction domain is longer	Hydrophobic interactions, salt bridge formation, hydrogen bonding	Yang *et al.*, 2008 Sundquist Lab, unpublished
MIT-MIM Mode 4	AMSH-CHMP3	MIM4 lies in a groove between MIT helices 2 and 3. Differs to MIM1 as forms a more extended helix with polar interactions.	Polar interactions	Solomons *et al.*, 2011
MIT-MIM Mode 5	LIP5-CHMP5	MIM5 wraps around the MIT outside MIT grooves in a 'Leucine Collar'.	Hydrophobic interactions, salt bridges, and hydrogen bonding	Skalicky *et al.*, 2012

Table 2 – **Table showing the different MIT-MIM modes of interaction**.

The MIT domain of spastin allows it to specifically interact with the ESCRT-III proteins CHMP1B and IST1. These interactions were first identified by yeast two-hybrid experiments and were confirmed by coimmunoprecipitation, microscopy and structural studies (Allison et al. 2017; Reid et al. 2005; Renvoisé et al. 2010; Yang et al. 2008).

The MIT-MIM interaction between spastin and CHMP1B has been mapped by x-ray crystallography at 2.5-Å resolution (Yang et al. 2008). This revealed that spastin interacts with CHMP1B through a unique mode of MIT-MIM interaction (mode 3), with CHMP1B's MIM filling a 30-Å groove between spastin's MIT α-helices 1 and 3 that runs the entire length of the MIT domain. This interaction was mediated by leucine residues in the CHMP1B MIM binding to a hydrophobic pocket in spastin's

MIT groove consisting of phenylalanine124, leucine127, and isoleucine131 of spastin's MIT domain α-helix 1, and methionine187 of spastin's MIT domain α-helix 3 (**Figure 4**). In addition, the MIT-MIM interaction is also facilitated by salt-bridge formation and hydrogen bonding. Recently, it has been shown that spastin's MIT domain interacts with the MIMs of IST1 using the same MIM3 mode of interaction (*BioRxiv non-peer reviewed* - Talledge et al. 2018). This binding is proposed to be in a near identical position as the spastin-CHMP1B MIT-MIM interaction, preventing the same spastin monomer from being able to bind both CHMP1B and IST1 simultaneously.

IST1 and CHMP1B ESCRT-III proteins are similar in structure, with both proteins containing the six α-helices typical of ESCRT-III proteins as well as an additional helix, αA. However, IST1 contains an additional short helix αB as well as two MIMs compared to CHMP1B's single MIM. CHMP1B and IST1 interact to form a double-stranded heteropolymeric helical tube in vitro (**Figure 5;** McCullough et al. 2015; *BioRxiv non-peer reviewed* - Talledge et al. 2018). In this complex, IST1 is present in a closed folded conformation, mediated by a long N-terminal hairpin that packs against helices 3, 4, and 5 (McCullough et al. 2015). CHMP1B however is present in a hyperextended open conformation, with both helices 1-3 and helices 4 and A forming extended structures (McCullough et al. 2015). The complex itself is formed by salt bridge interactions between CHMP1B's extended helix 4 and IST1's helix 1 (McCullough et al. 2015), as well as the MIM of CHMP1B binding to the IST1 helices 1 and 2 on the outside of the complex (Talledge et al. 2018).

Despite IST1 and CHMP1B existing in closed and open confirmations respectively, both are able to form homomeric polymers: IST1 via its N-C terminal interactions of helix 2, and CHMP1B prolifically interacting with eight other CHMP1B subunits via multiple hydrophobic interaction sites (McCullough et al. 2015; Talledge et al. 2018). As a result, IST1 closed conformation polymers form the outer layer of the helical tube IST1-CHMP1B complex, and the CHMP1B extended conformation polymers form the inner layer. In this conformation, CHMP1B's highly basic helix 1 lines the inside of the helix, allowing interaction with electronegative phospholipid heads of membranes. Furthermore, the MIMs of each of the CHMP1B subunits are able to protrude through the IST1 outer layer, making both CHMP1B and IST1 MIMs available for binding by spastin's MIT domain (Talledge et al. 2018). The binding of spastin to CHMP1B and IST1 however is mutually exclusive in the same spastin molecule, as the CHMP1B and IST1 MIMs bind spastin's MIT domain in the same location (Talledge et al. 2018). The binding of spastin to the CHMP1B MIM dissociates CHMP1B MIM-IST1 binding, destabilising the CHMP1B-IST1 polymer, priming it for remodelling or disassembly (Talledge et al. 2018).

The structure of the CHMP1B-IST1 copolymer means that it binds positively curved membrane within the lumen of the helix (McCullough et al. 2015). Due to the curvature required, this complex is likely to form on the outside of membranes, differing from canonical ESCRT-III formation on the inside of membrane necks (Schöneberg et al. 2017). As ESCRT-III complexes typically cause membrane constriction and fission, the structural model of the CHMP1B-IST1 complex therefore predicts it to function in the fission of membrane tubules. This data supports *in vivo* data that shows that a spastin-IST1 interaction is required for the fission of endosomal recycling tubules, localising at endosomal tubule constrictions (Allison et al. 2013, 2017). In addition, this interaction is also required for localising spastin to the nuclear envelope during nuclear envelope reformation (Vietri et al. 2015), and to the zone of abscission (Connell et al. 2009; Yang et al. 2008).

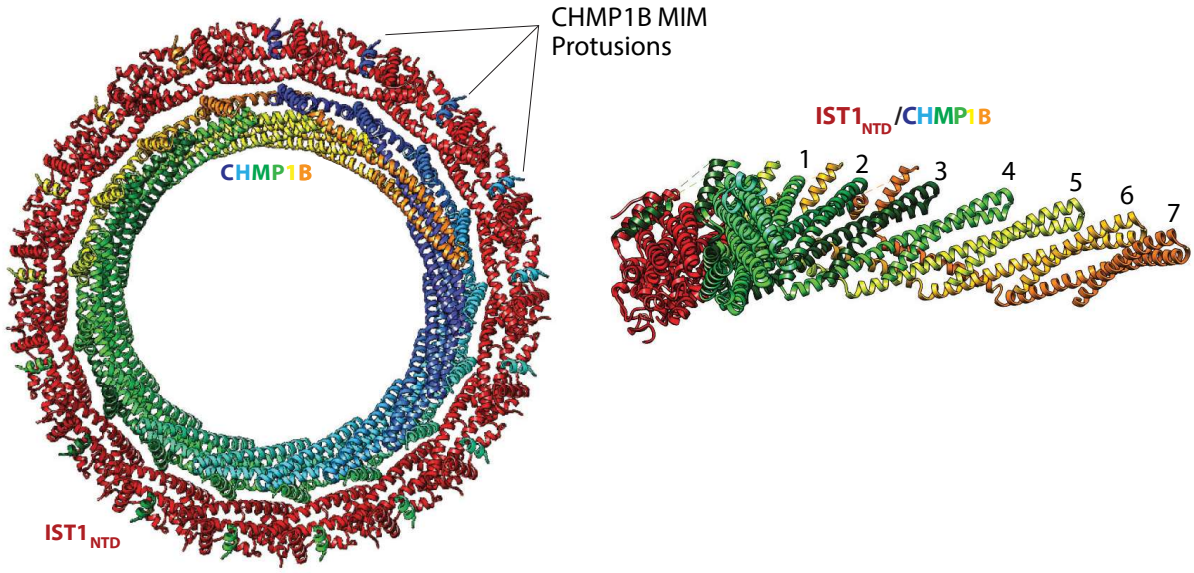

Figure 5 - **IST1-CHMP1B co-polymer filament.** (Left) End on view of a turn of the IST1-CHMP1B co-polymer assembled on a lipid bilayer. The N-terminal IST1 polymer is formed on the outside of the IST-CHMP1B complex, and the multicoloured CHMP1B polymer is formed on the inside to interact with the lipid bilayer. The MIM domain protrusions of CHMP1B through the IST1 structure are displayed. (Right) Side view of a section of the IST1-CHMP1B co-polymer viewed from the membrane. Seven interacting CHMP1B subunits are displayed (although CHMP1B has recently been shown to form 8 other CHMP1B interactions (Talledge et al., 2018)), and the CHMP1B MIM protruding through the IST1 monomer. Only a single IST1 is displayed for viewing clarity. Structures from McCullough et al. (2015).

Microtubule binding domain

The earliest studies of spastin showed that it is able to interact with microtubules (Errico 2002, 2004; McDermott et al. 2003; Sherwood et al. 2004; Trotta et al. 2004). This interaction was originally mapped to the N-terminal transmembrane domain of spastin (Errico 2002), but both the N-terminus and the MIT domain was later shown to be dispensable for spastin-microtubule interaction (Roll-Mecak and Vale 2005). Spastin was revealed to have two distinct interaction domains with microtubules (White et al. 2007). One interaction is mediated at the microtubule binding domain (MTBD), and one is within the C-terminal ATPases associated with diverse cellular activities (AAA+) domain.

The MTBD spans between 270-328 amino acids and is encoded by exons 5 and 6. It is present in both the M1 and M87 isoforms of spastin. The domain itself has proved hard to crystallise (Taylor et al. 2012), meaning there is no confirmed structure. It has been proposed that the MTBD interacts with microtubules through an essential RKKK motif (Eckert, Le, et al. 2012). However, despite its discovery in 2007, the specific biology of the MTBD has not been extensively studied. Instead the majority of research investigating spastin-microtubule interactions have focussed on the AAA+ domain.

AAA+ domain

Spastin was identified as a member of the AAA (ATPases associated with diverse cellular activities) protein family upon its discovery (Hazan et al. 1999). This family, now called the AAA+ proteins, is a subset of the p-loop nucleotide triphosphate (NTP)ase protein superfamily that use the hydrolysis of an NTP to generate mechanical work (Hanson and Whiteheart 2005). The AAA+ proteins specifically do this via the hydrolysis of adenosine triphosphate (ATP). The AAA+ protein family is large and diverse, functioning in processes such as protein folding and degeneration, DNA replication and recombination, peroxisome biogenesis, ESCRT complex disassembly, motor protein transport, and microtubule severing (Miller and Enemark 2016; Snider et al. 2008).

Spastin's AAA+ domain is encoded by exons 7 to 16 and is located between amino acids 342 to 599. It is therefore present in all spastin isoforms. The AAA+ domain allows spastin to bind ATP and hexamerise on microtubules to mediate microtubule severing and microtubule GTP-island formation (Eckert, Link, et al. 2012; Hinnerwisch et al. 2005; Roll-Mecak and Vale 2008; Taylor et al. 2012; Vemu et al. 2018; White et al. 2007). This complex process requires the coordination of microtubule binding,

ATP binding and hydrolysis, and hexamer formation (Roll-Mecak and Vale 2008; Zehr et al. 2017). The spastin hexamer itself forms an asymmetrical ring with a central pore (**Figure 6**; Roll-Mecak and Vale 2008; Zehr et al. 2017).

Spastin is able to bind polymerised microtubules via its AAA+ domain in addition to via its MTBD (White et al. 2007). This occurs via an interaction with acidic C-terminal tubulin tails that emanate from each microtubule α/β-tubulin dimer (Roll-Mecak and Vale 2008; White et al. 2007). In each spastin hexamer, each spastin monomer projects two peptide loops into the centre of the hexamer pore that interacts with the C-terminal tubulin tails (White et al. 2007). One pore loop is encoded between amino acids 407-421 and contains the conserved YVG sequence. Mutation of the aromatic tyrosine residue blocks tubulin binding (White et al. 2007). The second pore loop is encoded between amino acids 445 and 459 and contains basic amino acids that enable binding to the acidic tubulin tails (White et al. 2007).

Posttranslational modifications of these C-terminal tubulin tails can aid in spastin binding (Lacroix et al. 2010; Valenstein and Roll-Mecak 2016). In particular, polyglutamylation increases spastin-microtubule binding by increasing the acidity of the tails (Lacroix et al. 2010). Spastin's microtubule severing activity shows a graded response to the amount of C-terminal tubulin glutamylation, although excess glutamylation inhibits severing (Valenstein and Roll-Mecak 2016). It is worth noting that in addition to this C-terminal interaction, spastin binds microtubules independently of C-terminal tails via its MTBD (Eckert, Link, et al. 2012). This interaction is thought to stabilise spastin-microtubule interactions to facilitate spastin's AAA+ domain to bind the tubulin tails (White et al. 2007).

The ATPase function of spastin has largely been extrapolated from other AAA+ domain containing proteins. Spastin binds and hydrolyses ATP via conserved AAA+ domain components. These include the N-linker, the Walker-A motif, the Walker-B motif, the Second Region of Homology (SRH) motif that contains Sensor 1 and the Arginine fingers, and Sensor 2 (Monroe and Hill 2016). ATP binding is mediated by four motifs: the N-terminal linker, the Walker-A motif, the SRH motif, and Sensor 2. The N-terminal linker forms part of adenosine binding pocket (Smith et al. 2004). The Walker-A motif binds the phosphate of ATP via a conserved lysine (Hanson and Whiteheart 2005). Similarly, the arginine fingers at the C-terminus of the SRH and the arginine of Sensor 2 use the same mode of interaction to bind the phosphate of the ATP (Müller and Schulz 1992; Wendler et al. 2012). However, the arginine fingers differ in that they contact ATP molecules that are located in the binding pocket of adjacent spastin subunits of the spastin hexamer (Wendler et al. 2012).

ATP hydrolysis is mediated by the nucleophilic attack of the ATP phosphate by an activated water molecule. This is mediated by the Walker-B motif and Sensor 1 of the SRH motif. The Walker-B motif coordinates Mg^{2+} via its C-terminal aspartate residue, and this in addition to an adjacent glutamate residue facilitate water activation for nucleophilic attack (Story and Steitz 1992). Sensor 1 of the SRH motif functions as part of hydrogen-bonding network that positions the water molecule in relation to the phosphate of ATP via its polar residues (Lenzen et al. 1998).

The AAA+ domain facilitates spastin's hexamerisation. This is a key characteristic of the meiotic clade of AAA+ proteins that along with spastin include the microtubule severing enzymes katanin, fidgetin, and the ESCRT-III remodelling and disassembly protein Vps4 (Monroe and Hill 2016). Hexamer formation generates the central pore through which substrates can be translocated to be disassembled and is essential for catalytic activity (White et al. 2007). Each subunit of the spastin hexamer contacts two other subunits of the spastin hexamer (Roll-Mecak and Vale 2008; Zehr et al. 2017). This interaction is mediated by multiple locations of contact, including by the N-terminal linker (Roll-Mecak and Vale 2008; Wendler et al. 2012; Zehr et al. 2017). It is worth noting that as M1 and M87 spastin's AAA+ domains are the same, hexamer formation also allows M1 spastin to localise M87 spastin to biologically relevant locations for microtubule severing (Allison et al. 2017).

By homology to katanin, a change in spastin's hexamer conformation is proposed to drive microtubule severing (Zehr et al. 2017). The asymmetric spastin hexamer is proposed to cycle between two different conformations: an open spiral, and a closed ring. In its ATP bound form, the hexamer exists as a spiral and binds tubulin in the first spastin subunit. Upon the hydrolysis of ATP, the hexamer reforms into a ring, thereby translocating the tubulin from the first subunit to the pore loops of the second spastin subunit. Upon ATP binding, the structure then resets to its spiral conformation, allowing a previously unbound region of tubulin to be accessed by the first spastin subunit. This cycle of hexamer spiral-ring conformational change coupled to ATP hydrolysis and tubulin translocation is proposed to pull the tubulin dimer off the polymerised microtubule, mediating microtubule severing (**Figure 6**; Roll-Mecak and Vale 2008; White et al. 2007; Zehr et al. 2017).

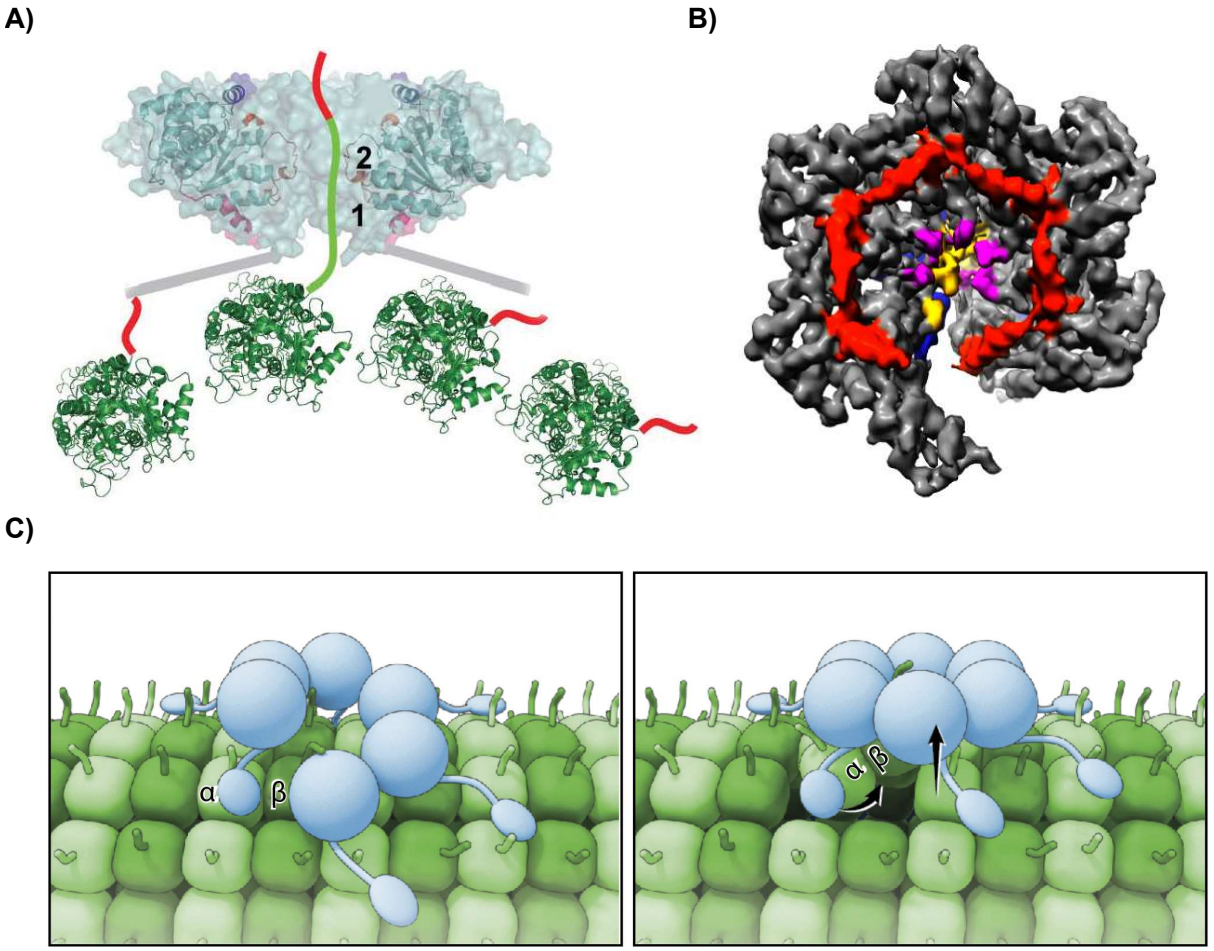

Figure 6 - **Spastin hexamer structure and proposed conformational changes during microtubule severing**. (A) The C-terminal tails (red) of tubulin (green) are fed through the spastin hexamer (cyan). This is mediated by the bound tubulin passing between the pore loops of each spastin subunit. The two pore loops in spastin are labelled by numbers. The grey bars emanating from the hexamer indicate the MTBD. (B) The density map of the open spiral conformation of katanin. The pore loops that bind tubulin are shown in yellow and purple (Pore loop 1 = yellow; Pore loop 2 = purple). This structure of katanin is likely to also resemble that of the spastin hexamer. (C) A cartoon of the conformational changes of spastin facilitating tubulin dimer removal. The spastin hexamer is assembled in its open spiral conformation in its ATP bound form. The c-terminal tail of β-tubulin of an α/β-tubulin dimer binds the pore loops of a single spastin protein within the hexamer. (Right) ATP hydrolysis induces a conformation change in hexamer, leading to the formation of a closed ring structure. This translocates tubulin-tail to the pore loops of the next spastin protein in hexamer. Repeated action generates tension on the tubulin dimer, removing it from the polymerised microtubule, inducing either GTP-tubulin repair, or microtubule severing. **Figure A** was adapted from Roll-Mecak and Vale 2008, and **Figures B and C** were adapted from Zehr et al. 2017.

1.3.4 – Spastin mutational distribution

Pathogenic mutations in *SPAST* are both numerous and diverse (Ensembl 2018; Fonknechten et al. 2000; Hazan et al. 1999; Shoukier et al. 2009; Solowska and Baas 2015). From the Ensembl database, 460 *SPAST* transcript variants are recorded that contain pathogenic mutations affecting *SPAST* exons (Ensembl, August 2018). These variants encode 368 unique mutations in spastin. These include missense mutations, insertions and deletions, splice site mutations, and nonsense mutations. In addition, *SPAST* is susceptible to Alu-mediated genomic rearrangements due to its Alu-rich genomic architecture (Beetz et al. 2006; Boone et al. 2014; Depienne et al. 2007; Jahic et al. 2016). These results in large deletions which are generally predicted to cause degradation of transcripts via nonsense-mediated decay (NMD; Jahic et al. 2016; Solowska and Baas 2015).

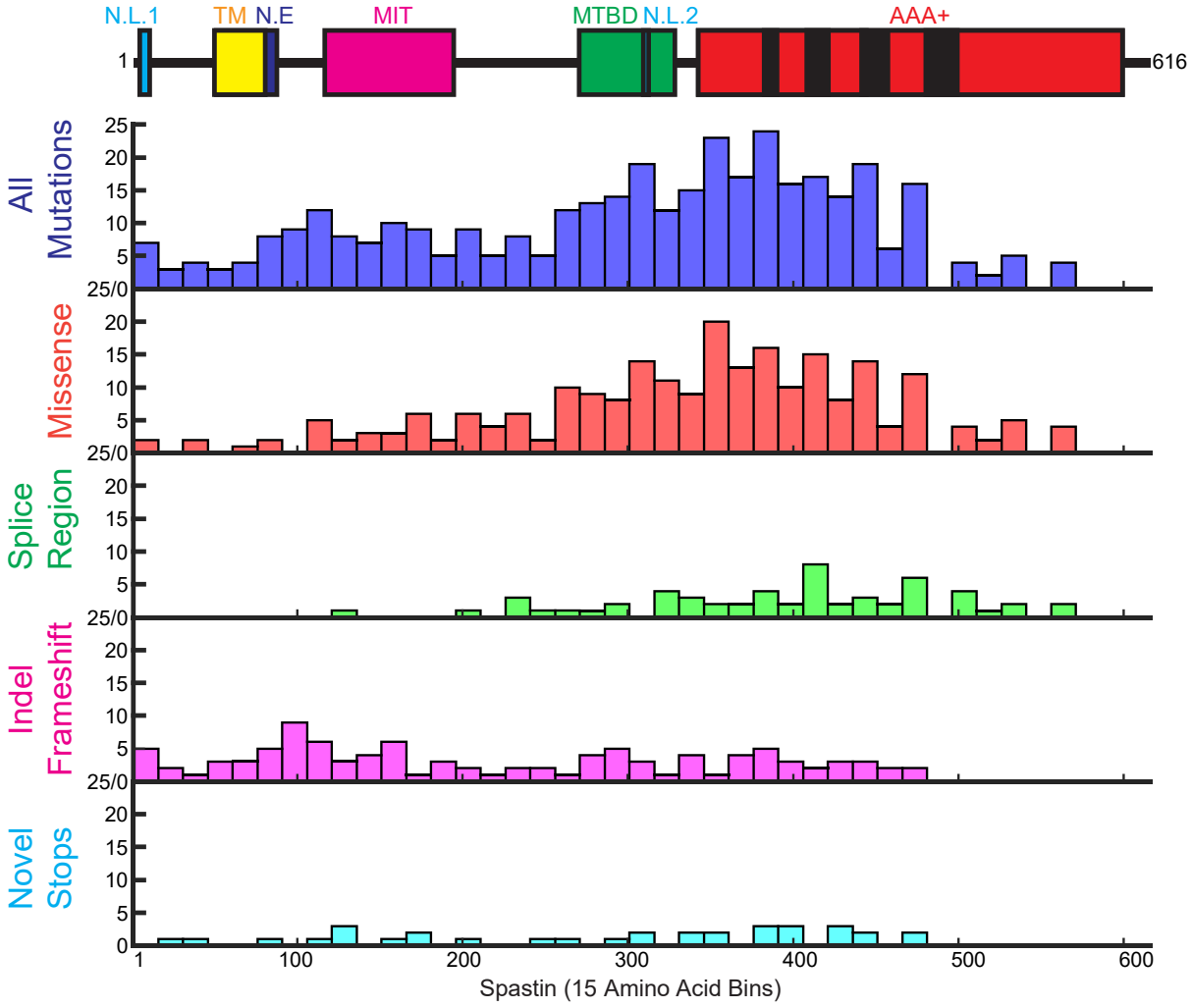

Figure 7 - **Distribution of reported mutations relative to spastin's domain architecture.** Published pathogenic exon mutations in SPAST were obtained from Ensembl, filtered to remove duplicate listed mutation, and categorised into 15 amino acid bins based on their position within spastin. Resulting histograms were aligned against the domain structure of spastin (including the AAA+ domain motifs), and plotted for all reported mutations (top), missense mutations (second row), splice region mutations (third row), indel frameshift causing mutations (fourth row), novel stop causing mutations (bottom row). Mutation data accurate to August 2018.

Unique protein mutations were identified in every functional domain of spastin (**Figure 7**). Out of 368 unique mutations in the Ensembl database (August 2018), 81% mapped to a functional domain. 47% of all unique mutations localised to the AAA+ domain, 15% to the MTBD, and 11% to the MIT domain. These figures are similar to those reported from a study of 200 unique HSP mutations by Shoukier et al. (2009).

The largest group of unique mutations in *SPAST* are missense mutations; single amino acids changes in the spastin protein. Out of the 368 unique mutations, 53% were missense mutations. Remarkably, 56% of these localised to the AAA+ domain, whilst only 17% localised to the MTBD, and 7% localised to the MIT domain. Of the 131 unique missense mutations in the AAA+ domain, 33% mapped to either the Walker A/B motifs, the SRH, or the pore loops.

The majority of mRNA transcripts that contain either frameshift-inducing insertions or deletions, or premature stop codons are degraded by NMD mRNA processing machinery (Gatfield 2003). As a result, no protein is produced from these transcripts. Out of the 368 unique mutations, 20% were frameshift-inducing insertions or deletions. These mutations showed a relatively even distribution across *SPAST*, but with an increased proportion in the N-terminal region. In addition, 27 single nucleotide polymorphisms were identified that would give rise to a novel premature stop codon. It is likely that these would also result in NMD, although they could theoretically result in spastin truncation products (Solowska et al. 2014; Solowska and Baas 2015). Such truncated products however have never been identified in physiological samples.

Truncated spastin protein variants could also be formed through in-frame insertions or deletions, or splice-site mutations. This has in vivo relevance as truncated spastin mRNA was observed in a spastin mouse model with a splice site mutation resulting in the loss of exon 7, although this did not produce spastin protein (Kasher et al. 2009). No in-frame insertions or deletions were identified from the 368 unique spastin mutations recorded. However, 47 splice site mutations were identified. These localised almost predominantly to the AAA+ domain (70%) and the MTBD (11%).

The inheritance pattern and mutational spectrum in *SPAST* suggests that disease is often caused by loss of function haplo-insufficiency (Denton et al. 2014; Fonknechten et al. 2000; Shoukier et al. 2009). In this model, a decreased concentration of spastin would result in inefficient cellular functions, such as microtubule severing. NMD is likely to result in a lack of spastin protein produced from *SPAST* that contained either frameshifting insertions or deletions, or premature stop codons (Riano et al. 2009). Furthermore, the mutational spectrum includes whole gene deletions and deletion of exon 1, preventing the production of any spastin protein. In addition, mutated spastin that is successfully

translated may not interact with appropriate binding partners, or may have defective ATP binding, ATP hydrolysis, hexamer formation, all leading to inability of spastin to severe microtubules.

In addition to a direct correlation between expression of mutated spastin and loss of protein activity, it is possible that some missense mutations may also generate dominant negative loss of function effects. In the case of microtubule severing by the AAA+ domain, the C-terminal tail of tubulin is translocated through the spastin hexamer pore by being passed between spastin monomers (Zehr et al. 2017). If only one of these spastin monomers was dysfunctional, the entire complex may fail. This would therefore lead to only a small amount of mutated protein displaying a disproportionately large loss of function effect. However, such missense mutations have never been identified as causing a more severe phenotype than other mutational classes.

It has been proposed that some *SPAST* mutations lead to a toxic gain of function (Leo et al. 2017; Solowska et al. 2014; Solowska and Baas 2015). For example, it was shown their either premature stop mutations or missense mutations in M1 spastin lead to a decrease in fast axonal transport in giant axoplasm. However, all experiments investigating a toxic gain of function for spastin have used over-expression of exogenous truncated proteins which have never been identified physiologically.

1.3.5 – The cell biology of spastin

The domain architecture of spastin facilitates its biological function. The AAA+ domain allows spastin to function as a microtubule remodelling enzyme. However, the subcellular location of this activity is mediated by spastin's hydrophobic hairpin, nuclear localisation, MIT, and MTBD localisation domains. These allow monomeric spastin to concentrate in specific locations, thereby likely facilitating hexamer formation and localised microtubule severing. These localisation domains therefore directly regulate the biological function of spastin. Furthermore, as the ATPase activity of spastin is not dependent on any of these domains, they are free to recruit spastin to different subcellular locations working either in isolation or simultaneously without affecting ATPase activity. In addition, spastin may function independently of its AAA+ domain, mediating its effects by presence in a membrane or complex.

Spastin has been reported to function in at least 10 different biological processes (**Figure 8**). A detailed analysis of each of these functions is provided below.

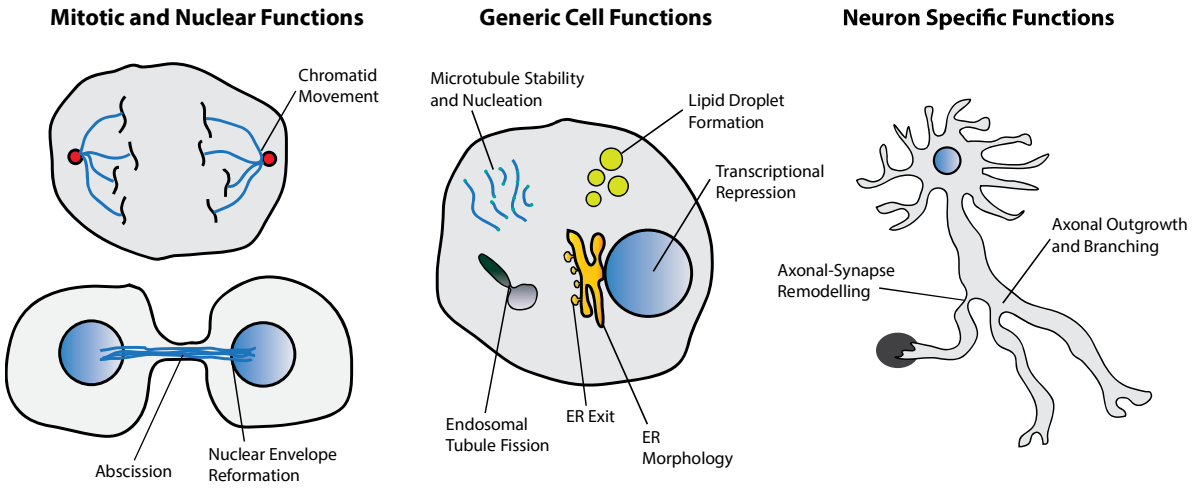

Figure 8 - **Diversity of spastin functions**. (Left). The published mitotic and nuclear functions of spastin include chromatid movement, abscission, and nuclear envelope reformation. (Middle). Published growth phase generic functions of spastin include regulation of microtubule stability and nucleation, lipid droplet formation, transcriptional repression, ER morphology regulation, in ER exit, and in endosomal tubule fission. (Right) Published neuron specific functions of spastin include regulation of axonal outgrowth and branching, and axonal-synapse remodelling. Details of each function are provided in the text.

Microtubule stability and nucleation

Microtubules are essential cytoskeletal components that facilitate the long-range transport of cargos via molecular motor proteins kinesins and dyneins. Microtubules may exist as either stable arrays or dynamic filaments. The architecture of microtubules is mediated by the action of enzymes that regulate microtubule-end polymerisation and depolymerisation, cross-linking, and microtubule severing by controlling the tubulin composition and post-translational modification of the microtubule polymer (Janke and Chloë Bulinski 2011).

The individual tubulin dimer subunit (α/β-tubulin) can either exist in a GTP or GDP bound state. During microtubule polymerisation, the GTP-bound α-tubulin protomer of the assembled microtubule binds the β-tubulin of an GTP-bound α/β-tubulin dimer. This causes the GTP in the binding site between the two tubulin dimers to be hydrolysed to GDP (Mitchison and Kirschner 1984). If the GTP on the α-tubulin monomer at the tip of the polymerised microtubule hydrolyses to GDP, the microtubule is prone to spontaneously disassemble by shrinkage (a catastrophe) (Carlier and Pantaloni 1981). This depolymerisation either continues in the minus-end direction until the microtubule completely disassembles or is halted by either the plus-end tip regaining a GTP cap (a rescue), or the depolymerising microtubule reaching a trapped pocket of unhydrolysed GTP (Aumeier et al. 2016; Dimitrov et al. 2008). As a result, the higher the proportion of GTP incorporated into a microtubule polymer, the higher its stability. Due to the slow acting nature of tubulin post-translational modification enzymes on polymerised microtubules, stable microtubules often accumulate post-translational modifications on their C-terminal tails such as detyrosination followed by glutamylation or acetylation (Janke and Chloë Bulinski 2011).

Microtubule length and site of nucleation is also relevant to its function. In neurons for example, tubulin nucleation from the microtubule organising centre (MTOC) in the soma would likely limit the neuron's ability to rapidly remodel during injury or development (Roll-Mecak and Vale 2006). Instead, new microtubules could be nucleated from small microtubule oligomers or severed microtubules in the location where microtubule reorganisation was relevant (Kalil et al. 2000; Keating and Borisy 1999). Importantly, the microtubule severing enzyme katanin has this function in *Arabidopsis* (Lindeboom et al. 2013), where it was shown that microtubule severing by katanin led to an increase in microtubule mass by nucleating the growth of new microtubules from severed microtubule ends. This accounted for ~80% of all new longitudinal microtubule growth, showing microtubule severing to be a mechanism for rapidly increasing microtubule populations.

Recently spastin has been shown to function in the nucleation of new microtubules by microtubule severing, and the increase in microtubule stability by mediating the formation of GTP-islands (Vemu et al. 2018). Previous studies had shown that spastin functions to increase microtubule mass. A loss of spastin in *Drosophila* neurons was shown to result in a sparse disorganised microtubule network in axons at NMJs (Sherwood et al. 2004; Trotta et al. 2004). The same effect was also observed in zebrafish axons (Wood 2006) and mammalian cells (Schiel et al. 2011). This phenotype was similar to that observed upon depletion of katanin (Burk 2002; Lindeboom et al. 2013; Srayko et al. 2006).

Vemu et al. (2018) have recently shown the mechanism by which spastin mediates microtubule nucleation and enhanced stability. Spastin (and katanin) causes nanoscale damage ('bites') along the length of microtubule polymers by removing tubulin dimers via ATP hydrolysis (**Figure 9**). The amount of nanoscale damage along the microtubule is dependent on the concentration of spastin. This damage can be repaired by the incorporation of new GTP-bound tubulin dimers, creating GTP-tubulin islands within the polymerised microtubule. This results in a ~5x increase in probability of a microtubule rescue and regrowth during catastrophe *in vitro*, thereby increasing microtubule stability. However, if the rate of tubulin extraction by spastin (or katanin) exceeds the rate of tubulin incorporation, a severing event occurs. The severed microtubule has GTP bound at either end, protecting it from depolymerisation. This allows it to polymerise, meaning that each microtubule severing event increases microtubule number and mass.

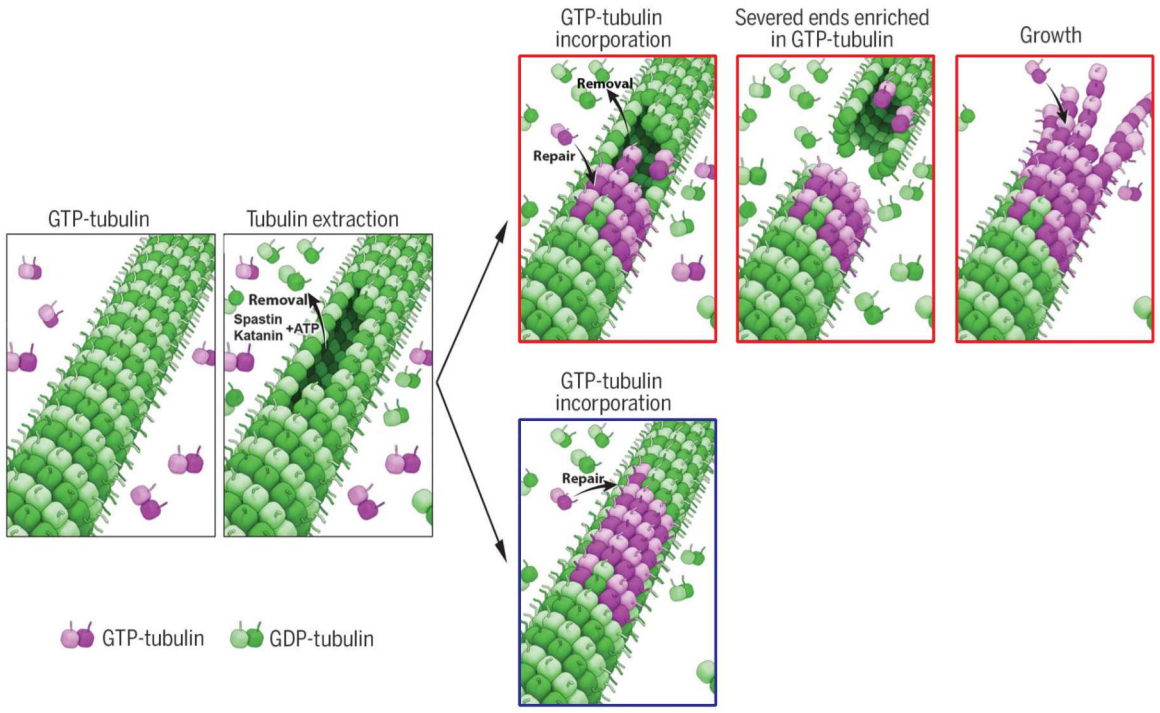

Figure 9 - **Spastin 'biting' or 'severing' microtubules**. Spastin (and katanin) form hexamers and use their AAA+ domain to remove tubule dimers from polymerised microtubules. These removed dimers are repaired by GTP-bound tubulin. If the rate of tubulin removal is lower than the rate of tubulin incorporation, the area is repaired (blue box). If the rate of tubulin removal is higher than the rate of tubulin incorporation, the microtubule severs (red boxes). The severed microtubule is capped by GTP-bound tubulin, allowing the regrowth of the microtubule by polymerisation. Adapted from Vemu et al. (2018).

The regulation of microtubule stability or new microtubule growth through microtubule severing is likely to drive some of the spastin-dependent biological processes associated with microtubule dynamics. However most functional studies have not differentiated between whether the AAA+ function of spastin depends on increased stability (via 'biting') or new microtubule formation (via 'severing'). One recent study however has shown that increased microtubule stability is important for normal peroxisome trafficking in the axon-like processes of olfactory neurosphere-derived stem cells (Wali et al. 2016). Spastin mutant patient-derived cells showed a decreased number of fast-moving peroxisomes, leading to oxidative stress. By comparison with the effect of microtubule stabilising drug Epothilone D on peroxisome movement, it was argued that spastin mediates peroxisome movement by stabilising microtubules (Wali et al. 2016). However, it is also important to note that the physical act of breaking the microtubule is likely to be the crucial element in other processes. Biological processes requiring these functions of spastin are described below.

Axon outgrowth and branching

The unique highly elongated morphology of neurons facilities their function in the transmission of nervous impulses. Dendrites surrounding the neuron soma receive electrical impulses from synaptic connections with the axon terminals of other neurons. These impulses are then rapidly transmitted down the length of the neuron's axon by saltatory conduction, before being converted into neurotransmitter signals at the axon terminal's synaptic connections.

Axonal and dendritic morphology is important in regulating the connectivity of the neural network. This morphology can be maintained upon neuronal damage, with neurons displaying abilities to regrow both axons and dendrites. This extensive cell remodelling requires dramatic reshaping of the underlying microtubule cytoskeleton. Examples of reshaping events include the replacement of long stable microtubules with short microtubules, with this facilitated by microtubule severing (Hu et al. 2008; Yu et al. 2008, 1994).

Spastin has been shown to function in regulating the morphology of neurons, both during development and during neuronal regeneration (Butler et al. 2010; Jinushi-Nakao et al. 2007; Rao et al. 2016; Riano et al. 2009; Stone et al. 2012; Wood 2006; Yu et al. 2008; Zhang et al. 2012). Wood et al. (2006) reported that both branchiomotor neurons and spinal motor neurons in zebrafish had a significant reduction in axon outgrowth upon spastin depletion. This was shown to lead to a disruption of axonal networks and neuromuscular synapse formation. This effect on axon outgrowth was later confirmed in both cultured rat and mouse hippocampal neurons depleted of spastin by siRNA (Riano et al. 2009; Yu et al. 2008). Later research showed that a depletion of spastin led to a strong reduction in microtubule-associated end-binding (EB) comets that mark the growing plus ends of microtubules in axonal growth cones, suggesting the necessity of microtubule remodelling in axonal growth (Butler et al. 2010). This suggests that this function of spastin may involve microtubule severing rather than biting. Furthermore, spastin was shown to interact and facilitate the function of protrudin in mediating neurite extension in PC12 cells and motor neuron axon outgrowth in zebrafish embryos (Zhang et al. 2012).

In addition, spastin siRNA depletion led to a reduction in axonal branch frequency by 45% in rat hippocampal neurons (Yu et al. 2008). Overexpression of spastin led to a 70% increase in the number of neuronal processes, including a dramatic increase in axonal branching (Yu et al. 2008). Spastin was shown to concentrate both at the axonal growth cone and axonal branch points in 10 day cultured hippocampal neurons (Yu et al. 2008), in agreement with previous localisation studies (Errico 2004; Svenson et al. 2005). Of note also is that the level of spastin expression has been shown to have

differing effects on axonal morphology (Jinushi-Nakao et al. 2007; Riano et al. 2009). Whilst spastin loss leads to reduced neurite outgrowth, strong spastin overexpression also recreates the same effect, and subtle increases in spastin expression can lead to enhanced axon elongation and branching (Jinushi-Nakao et al. 2007; Riano et al. 2009). In *Drosophila* neurons, spastin levels are regulated by the transcription factor Knot (Jinushi-Nakao et al. 2007). The regulation of spastin's expression by Knot was shown to regulate spastin's activity at neurite arbours by microtubule severing (Jinushi-Nakao et al. 2007).

Spastin is also required for axon regeneration (Rao et al. 2016; Stone et al. 2012). RNAi depletion of spastin in *Drosophila* neurons led to a significant reduction in the regeneration of axons from dendrites and axon stumps after proximal axotomy (Rao et al. 2016; Stone et al. 2012). The loss of one spastin allele by using the *Drosophila* mutant $spastin^{5.75}$ led to the complete abolition of both types of regeneration (Stone et al. 2012). This however has been debated as Rao et al. (2016) showed that this effect was dependent on the overexpression of EB proteins. The overexpression of spastin also led to inefficient axonal regeneration, overall indicating that regeneration is sensitive to spastin dosage. These effects were not related to the reversal of microtubule polarity typically associated with axonal regeneration (Stone et al. 2010, 2012), but are likely to be related to microtubule dynamics (Rao et al. 2016). The effect of spastin on neurite regeneration is specific to axons as spastin depletion had no effect on dendrite regeneration (Rao et al. 2016).

Axonal-synapse remodelling

During embryonic development multiple neuronal axons form synaptic contacts at neuromuscular junctions (NMJ; Meltzer and Schuldiner 2016). However, in the early postnatal period, axonal pruning occurs so that only a single axon remains connected to the NMJ. Pruning occurs as a result of competition between NMJ axons, with the losing axon branch being shed from its parent neuron (Bishop et al. 2004; Brill et al. 2016; Walsh and Lichtman 2003). In addition, neuronal rewiring away from the NMJ also requires synapse elimination as well as formation (Destexhe and Marder 2004).

Brill et al. (2016) show that spastin functions in pruning of motor neurons at NMJs. By fluorescence microscopy and CLEM, it was shown that there was a substantial loss of microtubules specifically in axonal branches retreating from NMJs. These axon branches specifically showed high levels of EB protein compared to the stem axon, suggesting a highly localised dynamic remodelling of the cytoskeleton caused by severing. Stabilisation of these microtubules by Epothilone prevented axonal pruning and was phenocopied in spastin knockout (KO) neurons, which showed a significant reduction in the rate of axonal retraction, and an inhibition of NMJ synapse elimination. These

retreating axon microtubules showed an ~8x increase in polyglutamylation, suggesting a mechanism by which spastin could specifically be recruited to axonal branches to be pruned to mediate microtubule severing (Brill et al. 2016; Lacroix et al. 2010; Valenstein and Roll-Mecak 2016).

Spastin has also been shown to function in the synaptic remodelling of GABAergic dorsal D-type neurons in *C.elegans* (Kurup et al. 2015). Although most of the research was focused upon the action of the Mitogen-activated protein kinase kinase kinase Dlk-1, it was shown that spastin (and also kinesin-13) depletion led to impaired remodelling of D-type neurons. It was proposed that Dlk-1 may activate spastin to increase microtubule dynamicity, allowing new synapse formation (Kurup et al. 2015).

Chromatid movement

During mitotic anaphase, chromosomes are separated into chromatids and are moved to opposite sides of the cell towards the centrioles. This movement is facilitated by microtubules that are bound to the centrioles at their minus-end and the kinetochore at the centromere of the chromatid at their plus-end. The chromatid moves towards the centriole via a two-part mechanism termed 'Pacman-Flux' (Rogers et al. 2004; Zhang et al. 2007). For the Pacman mechanism, microtubules are actively depolymerised by the kinetochore at their plus end, allowing the chromatids to move towards the centrioles by 'chewing up' the microtubule (Gorbsky 1987; Mitchison et al. 1986). For the Flux mechanism, chromatids are pulled towards the poles by depolymerisation of the microtubule from their minus-end at the centriole (Mitchison 1989).

Spastin, along with katanin and fidgetin, has been shown to function in the Pacman-flux mechanism of chromatid movement (Zhang et al. 2007). This provided functional relevance to the early localisation studies that showed spastin localises to centrosomes and spindle poles in mammalian cells (Errico 2004; Svenson et al. 2005). Zhang et al. (2007) showed that *Drosophila* spastin also localised to centrosomes. Significantly, inhibition of spastin by RNAi led to a decrease in the rate of poleward chromatid flux in both metaphase and anaphase. Spastin likely mediates this by facilitating the turnover of tubulin at the centrosome via microtubule severing. This releases the microtubule minus end from the nucleating complex, allowing it to be depolymerised by kinesin-13. Despite this work however, no other studies have been performed to further elucidate the mechanism of spastin function in chromatid migration.

Nuclear envelope reformation

In mitotic prometaphase the nuclear envelope breaks down to allow the attachment of microtubule spindle fibres to the kinetochores of chromatids. After chromatid separation in anaphase, the nuclear envelope reforms in telophase, but requires the spindle fibres that connect the chromatids to the centrioles to be removed to allow the complete nuclear membrane sealing (Vietri et al. 2015). In addition, small gaps in the nuclear envelope are closed by ESCRT-III proteins, in particular CHMP7 (Olmos et al. 2015).

Spastin functions to disrupt spindle microtubules at the nuclear envelope to allow nuclear envelope reformation (Vietri et al. 2015). Vietri et al. (2015) show by siRNA depletion and fluorescence microscopy that CHMP7 facilitates the recruitment of CHMP4B to the nuclear envelope during anaphase. By correlative light and electron microscopy (CLEM) and super resolution structural illumination microscopy (SIM), CHMP4B was shown to localise specifically to sites of unclosed nuclear envelope that also contained microtubules. Depletion of other ESCRT-III components CHMP2A and IST1 impaired the disassembly of these microtubules, suggesting their function at the site of microtubule-nuclear envelope interface. Either depletion of spastin or mutation of IST1's MIMs led these microtubules to persist at these sites. Furthermore, by confocal imaging, live-cell imaging, and SIM, both M1 and M87 spastin was shown to localise directly to these sites. Together, this implies that spastin is recruited by ESCRT-III proteins to sever these nuclear-envelope protruding microtubules to allow nuclear envelope closure. Remarkably, the MTBD was not required for this process, further showing that not all of spastin's localisation domains need to function simultaneously to localise spastin for its severing activity.

Abscission

During mitotic telophase, the two daughter nuclei are physically separated by cleaving the cytoplasmic join at the centre of the mother cell. This separation is termed cytokinesis and is a complex process requiring the coordinated spatio-temporal recruitment of abscission machinery. These function to contract the membrane surrounding the site of abscission (the midbody) until the two edges of the cell membrane touch and the two daughter cells separate. An important process during abscission is the removal of cytoskeletal elements (e.g. microtubules) from the midbody to allow complete cleavage (Steigemann and Gerlich 2009).

Spastin functions at cytokinetic midbodies to facilitate abscission (Connell et al. 2009; Goliand et al. 2018; Guizetti et al. 2011). Spastin shows a strong specific recruitment to the midbody in cells undergoing cytokinesis (Connell et al. 2009; Errico 2004; Yang et al. 2008), forming a double ring

structure (Connell et al. 2009). By siRNA depletion experiments, the ESCRT-III protein CHMP1B was shown to be essential for spastin's recruitment via interacting with spastin's MIT domain (Yang et al. 2008). The importance of spastin's MIT domain in recruitment was also shown by the expression of a spastin mutant lacking the N-terminus and the MIT domain (Connell et al. 2009).

Depletion of spastin using siRNAs revealed that spastin was essential for efficient cytokinesis (Connell et al. 2009). This was also observed by RNAi experiments studying abscission in the trypanosome *Trypanosoma brucei* (Benz et al. 2012). Depletion of spastin in mammalian cells led to the formation of extended cytokinetic bridges containing tubulin that took an abnormally long time to break (Connell et al. 2009). This was also confirmed in spastin KO cells, and it was shown that when cytokinetic bridge is finally cleaved, it is cleaved adjacent to one of the cells rather than at the typical constriction zone (Goliand et al. 2018).

Spastin's role in abscission is suggested to be via its microtubule severing activity. By the expression of a Walker-A AAA+ domain K338R spastin mutant, it was shown that extended cytokinetic bridges also formed upon impaired spastin ATPase activity (Connell *et al.*, 2009). This was confirmed by Guizetti et al. (2011) who showed both that the timing of abscission correlates with microtubule disassembly, and that this microtubule disassembly is driven by spastin. It was further shown that there is strong high resolution colocalisation between spastin and the ESCRT-III machinery to facilitate membrane constriction, indicating both a spatial and temporal coordination between microtubule severing and membrane constriction (Guizetti et al. 2011). This however contradicts evidence by Schiel et al. (2011) who show that spastin depletion did not induce microtubule severing at the abscission site, but rather led to highly disordered microtubule arrays. Additionally, it was shown recently in spastin KO cells that spastin is required for helical ESCRT-III polymers to appropriately compress to constrict the cytokinetic bridge (Goliand et al. 2018). This is suggested to be due to a failure of the underlying microtubules being severed.

Lipid droplet formation and metabolism

Cells store neutral lipids such as cholesterols and triacylglycerols in the form of lipid droplets (Fujimoto and Parton 2011). These form from the ER membrane and are either found attached to the ER or unattached in the cytoplasm. They are able to vary in size dramatically based on whether depending on the cellular balance of lipid synthesis and hydrolysis, with proteins on the surface of the lipid droplet mediating lipid metabolism (Welte 2015).

Papadopoulos et al. (2015) show that both overexpressed and endogenous M1 spastin recruits to lipid droplets. This colocalisation increased after cells were treated with oleic acid to stimulate lipid droplet biosynthesis. Mutation experiments showed that the localisation of overexpressed M1 spastin on lipid droplets was mediated by the hydrophobic hairpin-loop domain and is dependent upon an arginine at amino acid 65. As a result, M87 spastin does not recruit to lipid droplets. High levels of spastin expression led to fewer but larger lipid droplets in both mammalian cells and *Drosophila*. Depletion of spastin in *Drosophila* and *C.elegans*, but not mammalian cell cultures, led to a reduction in lipid droplets. In addition, the MTBD of spastin was required to avoid the nuclear clustering of lipid droplets.

Despite this work, the precise mechanism of spastin's function in lipid droplet biology remains to be elucidated. The decrease in lipid droplet formation observed upon the depletion of spastin in *Drosophila* and *C.elegans* implies it may function in lipid droplet formation. This would place spastin with other HSP proteins involved in lipid droplet metabolism such as seipin, spartin, REEP1, and DDHD2.

ER morphology regulation

The ER is a continuous membrane that links the nuclear envelope and peripheral ER by a series of tubules, tubular matrices, and sheets (Nixon-Abell et al. 2016; Schwarz and Blower 2016). ER morphology is essential for its function in forming ER-organelle contacts (Rowland et al. 2014; Wu et al. 2018). ER morphology is controlled by a large number of proteins, including the atlastins and lunapark which mediate ER-tubule junction formation and stabilisation, the REEPs, reticulons and protrudin which mediate ER-tubule curvature, Climp63 which mediates sheet formation, and ER-microtubule interacting proteins such as STIM1 (Schwarz and Blower 2016).

M1 spastin has been shown to interact with the ER shaping proteins atlastin-1 and REEP1 (Park et al. 2010; Sanderson et al. 2006), protrudin (Chang et al. 2013; Mannan et al. 2006; Zhang et al. 2012), and reticulon-1 and reticulon-2 (Mannan et al. 2006; Montenegro et al. 2012). These

interactions require the N-terminal hydrophobic hairpin-loop (Chang et al. 2013; Park et al. 2010). These hydrophobic hairpins insert into the outer leaflet of the ER lipid bilayer and have been shown to be necessary to generate membrane bending required for ER tubule formation (Goyal and Blackstone 2013).

Despite the interaction with ER shaping proteins, it is unclear therefore whether M1 spastin regulates ER morphology physiologically. ER architecture is regulated by microtubule dynamics and motors (Goyal and Blackstone 2013), and overexpression of ATPase defective mutant spastin led to a dramatic redistribution of ER onto bundled microtubules (Connell et al. 2009), suggesting that microtubule severing by spastin was important in regulating ER architecture. In addition to working enzymatically, spastin may also provide a mechanism of facilitating ER-microtubule interaction by simultaneously binding the ER via its hydrophobic hairpin-loop domain, and microtubules via its MTBD. In addition, spastin was shown to function in the recruitment of ER to the tip of axons regenerating from axonal damage (Rao et al. 2016).

EMX2 transcriptional corepression

Early studies of spastin identified M87 spastin both in the cytoplasm and the nucleus (Beetz et al. 2004; CLAUDIANI et al. 2005; Connell et al. 2009). This is mediated by the presence of a nuclear localisation signal but no export signal (as described in Section 1.3.3).

To date, only one publication has shown a functional effect of spastin in the nucleus. Daftary et al. (2011) reported that endogenous spastin was co-immunoprecipitated with the nuclear transcription complex HOAX10 by mass spectrometry in uterine epithelial Ishikawa cells. This was also verified by co-immunoprecipitation and western blotting using a spastin antibody. By chromatin immunoprecipitation (ChIP), spastin was shown to specifically bind to the HOAX10-binding *EMX2* promoter element. Spastin likely functions as a corepressor of *EMX2*, as siRNA depletion of spastin led to a significantly increased expression of *EMX2*. This was also validated in a breast adenocarcinoma cell line BT-20. In addition, Daftary et al. (2011) showed by mutation experiments that the nuclear localisation signal of spastin was required for its function in *EMX2* repression.

Despite the relative lack of research of spastin's function in the nucleus, this is an area worthy of revisiting. For example, despite Daftary et al. (2011) characterising spastin-HOAX10 function on *EMX2* repression in uterine cells, *EMX2* has been shown to play an important role in neuronal development and in the cerebral cortex (Desmaris et al. 2018; Falcone and Mallamaci 2015; Ji et al. 2018; Zhang et al. 2018). Furthermore, spastin's ESCRT-III interacting protein CHMP1B localises to the

nucleus (Reid et al. 2005), and recently in a non-peer-reviewed paper, Talledge et al. (2018) show that the spastin-interacting CHMP1B-IST1 complex is able to bind nucleic acids.

ER exit

Proteins that are correctly folded in the ER are transported from the ER to the Golgi via COPII-coated vesicles that form at ER exit sites (ERES; Venditti, Wilson, and De Matteis 2014). M1 spastin localises to ERES, and overexpressed ATPase defective spastin, but not spastin depletion, was shown to impair cargo secretion (Connell et al. 2009). As a result, the function of spastin at ERES is currently unclear. This unknown function of spastin is the topic of investigation in Chapter 4.

Endosomal tubule fission

Cargos in the endocytic pathway may either be degraded in the lysosome or are retrieved from degradation and recycled back to the site of origin. This recycling occurs via the fission of endosomal tubules from the sorting endosome (Maxfield and McGraw 2004). Depletion of spastin, or mutations in spastin's MIT or AAA+ domains, lead to the formation of abnormally long endosomal tubules, and cause the mistrafficking of typically recycled cargos such as transferrin receptor (TfnR; Allison et al. 2013). It was predicted that elongated tubules resulted from a failure in endosomal tubule fission, but this was not tested experimentally. This unknown function of spastin in endosomal tubule fission is the topic of investigation in Chapter 3, and an introduction to the sorting endosome and membrane fission mechanisms are provided below.

1.4 – Endocytic Recycling

The first results chapter of this thesis investigates the function of spastin in the fission of endosomal recycling tubules from sorting endosomes (Chapter 3). The key features of sorting endosome biology and membrane fission are reviewed below.

1.4.1 – Sorting endosome identity

The sorting endosome is an intermediary endocytic structure that is at the centre of fate decisions in the endocytic pathway. The sorting endosome receives input from both the cell surface and the Golgi apparatus, and sorts cargo to be transported either back to the cell surface, to the Golgi apparatus, to specialised organelles such as melanosomes, or to the lysosome via multivesicular body (MVB) formation (McNally and Cullen 2018).

The sorting endosome is in a constant state of flux, being continuously formed through the maturation and homotypic fusion of plasma membrane-derived vesicles and fusion with Golgi-derived vesicles, and dismantled by membrane export through recycling tubule fission and MVB formation (**Figure 10**). As a result, it is typically characterised by its acidity, its membrane composition, and the identity of associated proteins (Naslavsky and Caplan 2018).

As endocytosed cargo moves from the plasma membrane to the lysosome, the lumenal environment of the endosome becomes increasingly acidified (Mellman et al. 1986). This is mediated by the action of vacuolar H+-ATPases (V-ATPase), and in early endosomes by the a2-isoform of the V-ATPase (Hurtado-Lorenzo et al. 2006). This acidity increase facilitates the dissociation of cargo from their receptors, allowing cargo to be degraded in the lysosome, and their receptors to be recycled (Mellman 1992). The sorting endosome is typically at ~pH6.2, more basic than late endosomes (<pH 5.5) and lysosomes (as low as pH 4.6) (Mellman 1992).

The sorting endosome also has a distinct membrane lipid composition, typified by enriched presence of PI3P (Corvera et al. 1999), although other phosphoinositides such as PI4P and PI(4,5)P_2 have also been identified on endosome subdomains (Dong et al. 2016; Yoshida et al. 2017). This confers distinct membrane identity, differentiating the sorting endosome from the plasma membrane and late endosomes, typically characterised by the enriched presence of PI(4,5)P_2 and PI(3,5)P_2 respectively (Balla 2013; Corvera et al. 1999; Shaw et al. 2003). The enrichment of PI3P on sorting endosomes is mediated by the activity of class III PI3 kinases on phosphatidylinositol (Murray et al. 2002). The high composition of PI3P on endosomes is important as it facilitates the binding of effector proteins that contain FYVE and phox homology (PX) domains (Kanai et al. 2001; Xu et al. 2001).

Examples of these proteins include early endosome antigen 1 (EEA1) and rabenosyn-5 which both bind Rab5 (Nielsen et al. 2000).

The Rab-GTPases (Rabs) are crucial proteins in defining membrane identity (Wandinger-Ness and Zerial 2014). Rabs are numerous and diverse, with each functioning as an effector to mediate the activity of the bound organelle or vesicle. Rabs exist either in their cytosolic inactive GDP-bound state, or their membrane-bound active GTP-bound state (Progida and Bakke 2016). Transition between different Rabs on endocytic membranes is a key characteristic of endosome maturation. The early endocytic pathway is characterised by the presence of Rab5, Rab4, and Rab11 (Bucci et al. 1992; van der Sluijs et al. 1992; Ullrich et al. 1996), and is distinct from the late endosome/MVB which is characterised by Rab7 (Feng et al. 1995). In addition, Rab13, Rab22, Rab35, Rab15, and Rab17 are all associated with endocytic recycling from the sorting endosome (Wandinger-Ness and Zerial 2014). Rab proteins mediate their effects via effector proteins that can influence diverse processes such as phosphoinositide metabolism, microtubule motor protein activation, and complex recruitment such as retromer (Wandinger-Ness and Zerial 2014). Due to the central position between the early endocytic pathway, the late endocytic pathway, and the recycling pathways, the sorting endosome can have multiple Rab identities, although these divide into spatially-separate subdomains (Sönnichsen et al. 2000).

1.4.2 – Sorting endosome input pathways

Sorting endosomes predominantly receive their cargo and membrane input from the cell surface and from the Golgi apparatus (**Figure 10**). At the cell surface, endocytosis facilitates the internalisation of external cargo into the cell. There are different modes of endocytosis, including macropinocytosis, phagocytosis, and via caveolae, but the major route of the internalisation of many cargos is via clathrin-mediated endocytosis (CME) (Kaksonen and Roux 2018). CME facilitates the internalisation of transmembrane proteins typically bound to extracellular ligands. One example is endocytic internalisation of transferrin receptor upon its binding to an extracellular transferrin-iron complex. During endocytosis, the binding of cargo to its receptor leads to the clustering of coat proteins on the cytoplasmic side of the plasma membrane. This is mediated by adaptor proteins such as adaptor protein 2 (AP2) and clathrin assembly lymphoid myeloid leukaemia protein (CALM). This leads to membrane bending to form a cargo filled clathrin-coated pit which is then scissioned by Bin/Amphiphysin/Rvs (BAR) domain-containing proteins such as FCH domain only 1 (FCHO1) and endophilin, and the GTPase dynamin. The clathrin-coat of clathrin-coated vesicles (CCVs) rapidly

disassembles, allowing the maturation of the vesicle to an early endosome/sorting endosome by Rab5 recruitment (Kaksonen and Roux 2018).

The second input pathway for sorting endosomes is from the trans-Golgi network (TGN). This route is used by proteins such as the hydrolytic lysosomal cathepsin enzymes, and the lysosome-associated membrane proteins (LAMPs), via their interaction with transmembrane sorting receptors such as mannose-6-phosphate receptor (M6PR) and sortilins (Progida and Bakke 2016). In the example of M6PR-dependent transport, newly synthesised soluble lysosomal enzymes are glycosylated with mannose-6-phosphate in the Golgi, allowing them to interact with M6PR. In a manner similar to CME, once these receptor-ligand interactions have formed, adaptor proteins such as ADP-ribosylation-factor-binding proteins (GGAs) and adaptor protein 1 (AP1) lead clathrin coat requirement, and ultimately the formation of endosome-directed CCVs (Progida and Bakke 2016). This is facilitated by the PI4P composition of the TGN (J. Wang et al. 2007) and Rabs such as Rab31 and Rab9 (Rodriguez-Gabin et al. 2009). It is worth noting that M6PRs exist as both cation-independent (CI-M6PR) and cation-dependent (CD-M6PR) forms. These have distinct but similar functions in Golgi to endosome trafficking, but CI-M6PR has additional functionality at the cell surface (Ghosh et al. 2003). In addition, there are M6PR-independent TGN to endosome transport pathways. LAMPs, for example, are trafficked independently of M6PR via adaptor protein 3 (AP3) (Pols et al. 2013).

Vesicles derived from the cell surface and the TGN converge via microtubule-based transport at sorting endosomes. A crucial process is the fusion of these vesicles to generate sorting endosomes with a similar membrane identity. Vesicle fusion is mediate by the formation of trans-soluble NSF attachment protein receptors (SNAREs) complexes. SNAREs involved in endocytic vesicle fusion include syntaxin 6 and syntaxin 13 (McBride et al. 1999; Simonsen et al. 1999) via EEA1-dependent recruitment (Gorvel et al. 1991). TGN-derived vesicles containing LAMPs contain hVPs41 and VAMP7 SNARES to mediate their fusion with endosomes via endosomal syntaxin 7 and syntaxin 8 (Dingjan et al. 2018; Pols et al. 2013). In addition, TGN-derived vesicles use VAMP4 to associate with early endosomes (Steegmaier et al. 1999).

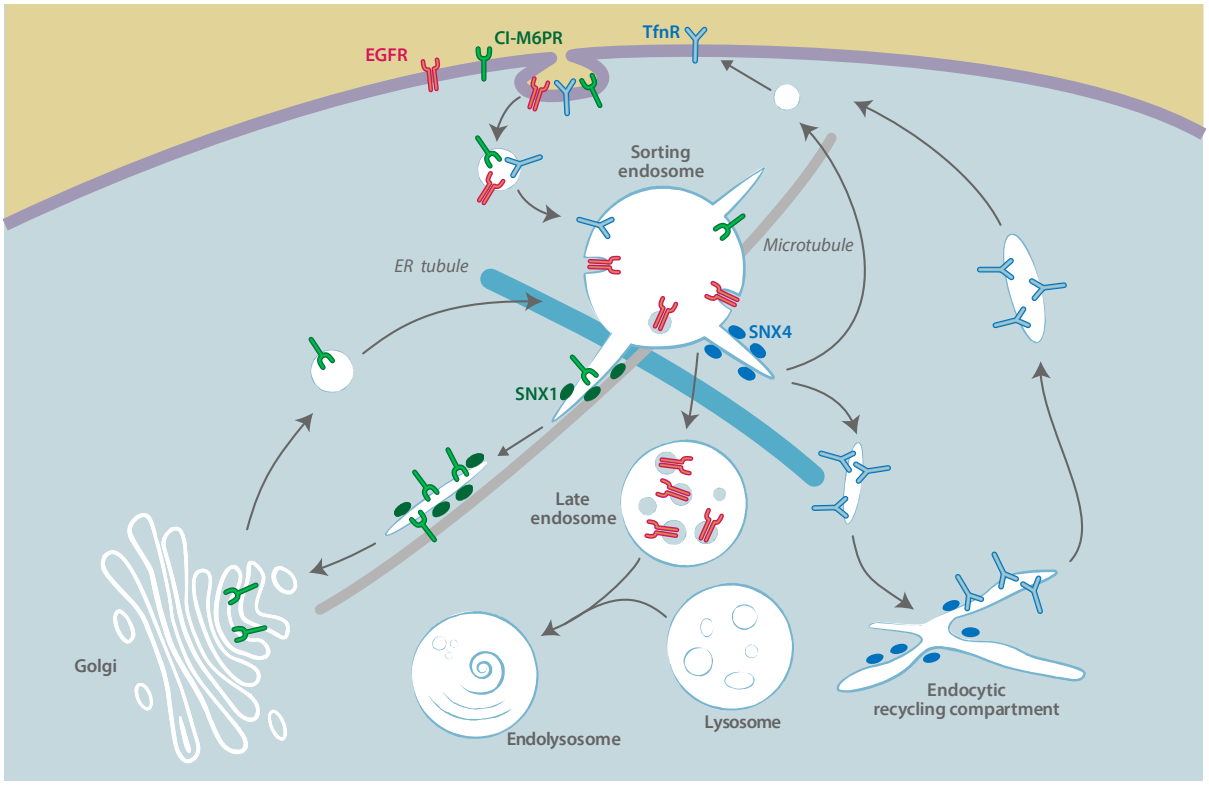

Figure 10 - **Cargo sorting in the endocytic pathway.** Cargo predominantly arrives at the sorting endosome via two main pathways: from the plasma membrane via endocytosis (e.g. EGFR, CI-M6PR, TfnR), and from the TGN via M6PR-dependent or independent Golgi to endosome traffic (e.g. lysosomal hydrolases). Cargo that recycles back to the cell surface can do so via SNX4-dependent trafficking, either via a direct pathway, or via the endocytic recycling compartment. Cargo that recycles back to TGN is typically associated with SNX1-coated endosomal tubules. The fission of endosomal recycling tubules occurs at sites of ER-endosome contact, and the fissioned tubule is transported on microtubules via microtubule motors. Cargo that is not recycled is internalised into MVBs and is ultimately degraded in the endolysosome. Cartoon adapted from Allison et al. (2017).

1.4.3 – Cargo sorting within the sorting endosome

Once the receptor-ligand complex has dissociated, endosomal cargos must be separated between those destined for degradation or recycling. Further complexity is added as recycling pathways have multiple destinations such as the TGN or cell surface, and multiple recycling pathways exist for different cargos recycled to the same destination (Hsu et al. 2012).

An original mechanism proposed for the separation of recycled *vs* degraded cargo was 'geometric-based sorting' (Maxfield and McGraw 2004). This model worked on the basis that: 1) receptor-ligand complexes disassemble as a result of increased acidity in the sorting endosome, leaving a to-be-recycled membrane fraction, and a to-be-degraded luminal fraction; 2) membranous tubules protrude from the body of the sorting endosome are required for recycling (Marsh et al. 1986); and 3) these tubules have high surface area and low volume. Therefore, by repeated formation and

scission of these tubules, recycled cargo could be separated from degraded cargo (Dunn 1989; Maxfield and McGraw 2004).

However, it is now clear that this model is inadequate in accommodating recycling pathway diversity. In addition, it fails to explain how integral membrane proteins are lysosomally degraded. Instead, it has now been shown that cargo sorting is facilitated by sequence-dependent cargo capture by multimeric protein complexes on sub-domains of the sorting endosome (Hsu et al. 2012; McNally and Cullen 2018). These complexes include retromer, retriever, the CCDC22, CCDC93, and COMMD (CCC) complex, and the Wiskott-Aldrich syndrome protein and SCAR homolog (WASH) complex (**Figure 11**). These function to concentrate cargo to be recycled in a specific subdomain of the sorting endosome that ultimately becomes the endosomal recycling tubule.

Lysosomal degradation

Cargos destined for lysosomal degradation are internalised into intraluminal vesicles (ILVs) within the sorting endosome. This internalisation blocks the ability of transmembrane receptors such as EGFR from signalling to the cytosol (Raiborg and Stenmark 2009). The sorting endosome progressively matures into a multivesicular body (MVB) as recycled cargos are removed from the sorting endosome in endosomal tubules and cargos-to-be-degraded are internalised into ILVs. Cargo degradation occurs when the MVB fuses with a lysosome to form an endolysosome, with lysosomal lipases digesting the membrane of the ILVs to expose transmembrane proteins to lysosomal proteases (Raiborg and Stenmark 2009; **Figure 10**).

Cargo internalisation into ILVs is mediated by the action of ubiquitin ligases and the ESCRT-0, -I, -II, -III complexes. Cargos destined for degradation are tagged with polyubiquitin lysine-63 chains by E3 ubiquitin ligases during the cargo's endocytosis and residency in the sorting endosome, with one example being the ubiquitination of EGFR by c-Cbl (Duan et al. 2003; Grøvdal et al. 2004; Ravid et al. 2004). This ubiquitination attracts the binding of ESCRT-0 proteins such as Hrs and STAM which contain ubiquitin-binding motifs in their VHS domains (Ren and Hurley 2010). In addition, the ESCRT-0 proteins contain clathrin-binding domains, helping form clathrin-rich microdomains on the endosomal membrane to cluster ubiquitinated cargos (Raiborg 2001; Sachse et al. 2002). Importantly, the ESCRT-0 proteins facilitate the localisation of ESCRT-I proteins to the ubiquitinated cargo, with this allowing the subsequent recruitment of ESCRT-II proteins. Both ESCRT-I and ESCRT-II proteins are able to bind the endosome membrane, and the ESCRT-I complex has been suggested to begin the membrane deformation to generate invaginations in which cargos-to-be-degraded are concentrated

(Kostelansky et al. 2007). ESCRT-II proteins facilitate the binding of ESCRT-III complexes such as CHMP2 and CHMP3 proteins. These ESCRT-III proteins form extended polymers that contain large regions of basic amino acids allowing a strong interaction with the phospholipid-rich membrane (Williams and Urbé 2007). ILVs are then generated by the continued invagination of the membrane and their eventual closure mediated by the joint action of ESCRT-III proteins and the ATPase VPS4 (Raiborg and Stenmark 2009). The proposed mechanism of ESCRT-III mediated membrane deformation and scission is discussed in Introduction Section 1.5.

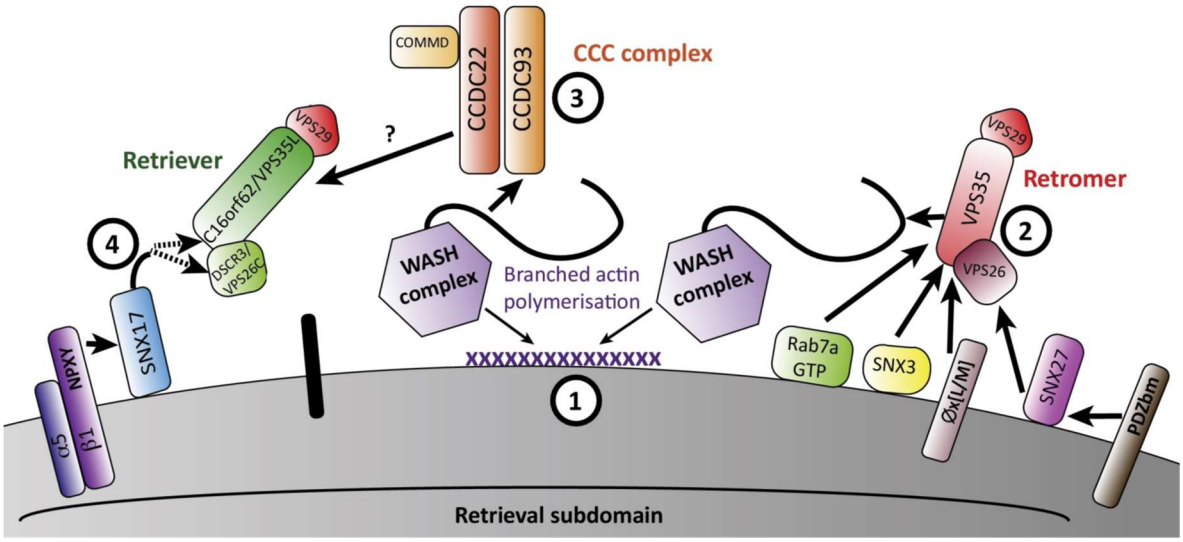

Figure 11 - **Cargo sorting machinery of the sorting endosome**. (1) The WASH complex facilitates the polymerisation of branched actin on the endosome membrane via WASH1 and is recruited to the endosome by its FAM21 tail, either by direct binding to the membrane, or by interaction with endosomal proteins such as retromer. This FAM21 tail also facilitates its interaction with the CCC complex. (2) The heterotrimer retromer is recruited to the endosomal membrane by interaction with Rab7 and SNX3. SNX3 and SNX27 act as cargo adaptors allowing it to bind to additional cargo. Cargo with ϕxL/M (ϕ = aromatic amino acid; x = any amino acid) can bind directly to retromer. Retromer interacts with FAM21 of WASH via VPS35. (3) The CCC complex interacts with the FAM21 tail of WASH and retriever through an unknown mechanism. It may also bind cargo directly. (4) The heterotrimer retriever is recruited to membrane via interaction with WASH, mediated by the CCC complex, although its interaction site with the CCC complex is not known. It uses SNX17 as a cargo adaptor, allowing the sorting of cargo with NPxY or NPxF motifs. Cartoon adapted from McNally & Cullen, 2018.

Cargo recycling

The pentameric WASH complex is composed of WASH1, FAM21, CCDC53, strumpellin, and strumpellin and WASH interacting protein (SWIP; Derivery et al. 2009). The WASH complex is recruited to the endosome membrane through FAM21 which can both directly bind PI3P on the endosome membrane (Derivery et al. 2009), or bind endosomal proteins such as FK506-binding protein 15 (FKBP15) (Harbour et al. 2010), RME-8 (Freeman et al. 2014), and the VPS35 subunit of retromer (Harbour et al. 2012; McGough et al. 2014). The WASH complex is essential for the recycling of many cargos, including

cation-independent M6PR (CI-M6PR) (Gomez and Billadeau 2009), transferrin receptor (TfnR) (Derivery et al. 2009), and β2-adrenergic receptor (Puthenveedu et al. 2010).

WASH has several functions in mediating cargo sorting. The first is in the polymerisation of branched actin on the endosome surface. This is mediated by WASH1 which functions as a nucleation promoting factor for the actin polymerising enzyme Arp2/3 (Puthenveedu et al. 2010). The branched actin has two purposes: to generate distinct retrieval subdomains on the endosome (Derivery et al. 2012); and to help generate and stabilise endosomal recycling tubules (Puthenveedu et al. 2010). Actin polymerisation by WASH is initiated by PI4P and was recently shown to be regulated by ER-endosome contact formation, with these contacts allowing endosomal PI4P to be removed by ER-resident PI4P phosphatase Sac1 in conjunction with oxysterol-binding protein 1 (OSBP1) (Dong et al. 2016). The second function for WASH in mediating cargo sorting is by acting as a scaffold for the recruitment of multimeric retrieval complexes. For example, WASH facilitates the recruitment of the CCC complex and retriever onto endosomal membranes (McNally et al. 2017).

Retromer is involved in the retrograde transport of cargo back to the TGN (Seaman et al. 1998) and recycling of cargo to the cell surface (Steinberg et al. 2013). In mammals, retromer is formed of a hetero-trimer of vacuolar protein sorting-associated 26 (VPS26), VPS35, and VPS29 (Seaman et al. 1997). This can bind directly to cargo via motifs in cargo's cytosolic tails, with examples including the ϕxL/M motif (ϕ=aromatic AA, x=any AA) of iron transporter diavalent metal transporter 1 (DMT1-II) (Tabuchi et al. 2010), and the FANSHY motif of sortilin-related receptor L (SORL1) (Fjorback et al. 2012). In addition, retromer can bind cargo adaptors to increase the range of cargo it can interact with (Lucas et al. 2016). Examples include the binding of SNX3, allowing retromer interaction with DMT1-II (Lucas et al. 2016) and the recycling of Wnt sorting receptor Wntless (Harterink et al. 2011), and the binding of SNX27, allowing retromer interaction with PDZbm domain-containing proteins such as glucose transporter GLUT1 and B2-adrenoreceptor that interact with SNX27's PDZ domain, and with NPxY-NxxY motif-containing proteins that bind SNX27's FERM-like domain (Ghai et al. 2011; Lauffer et al. 2010; Steinberg et al. 2013). The binding of retromer to SNX3 and Rab7 facilitates its binding to the endosome membrane (Rojas et al. 2008; Seaman et al. 2009).

In addition, retromer is able to interact with the SNX-BAR family of proteins (Hierro et al. 2007). These proteins form hetero-dimers composed of either SNX1 or SNX2 and SNX5, SNX6, or SNX32 (Wassmer et al. 2006; van Weering et al. 2012). These proteins contain a BAR domain that are able to sense and induce membrane curvature, allowing the formation of endosomal recycling tubules (Carlton et al. 2004; Peter 2004). Their interaction with retromer couples both tubule formation and

cargo selection, allowing recycled cargo to be packaged into recycling tubules. In addition, these SNX-BAR proteins are also able to directly interact with cargos such as CI-M6PR and insulin-like growth factor 1 receptor (Kvainickas et al. 2017; Simonetti et al. 2017).

The recently discovered retriever complex bears similarities to retromer (McNally et al. 2017). It is a hetero-trimer composed of the retromer component VPS29, the VPS26 paralog Downs syndrome critical region 3 (DSCR3), and C16orf62 (McNally et al. 2017). Like retromer, retriever interacts with WASH, and also interacts with SNX17 and the CCC complex. The binding of retriever to SNX17 facilitates cargo recruitment via its FERM-like domain binding cargos such as $\alpha_5\beta_1$ and T-cell receptor that contain NPxY or NPxF motifs (McNally et al. 2017; Osborne et al. 2015). SNX17 is able to bind membrane via its PX domain but also localises to endosomal membranes via the CCC complex which interacts with the WASH component FAM21 (McNally et al. 2017).

The CCC complex is a three-protein complex composed of the heterodimer of coiled-coil domain-containing protein 22 (CCDC22), and CCDC93, and a member of the copper metabolism MURR1 domain-containing (COMMD) protein family (Phillips-Krawczak et al. 2015). It is able to interact with membrane by binding to FAM21 of the WASH complex, and retriever (McNally and Cullen 2018). In this way, it facilitates the action of retriever in cargo retrieval and recycling. Indeed, when depleted, integrin $\alpha_5\beta_1$ trafficking is impaired (McNally et al. 2017).

In addition to its function in a complex with WASH and retriever, it is likely that the CCC is also able to independently bind cargo (Bartuzi et al. 2016; Li et al. 2015). A CCC complex containing COMMD9 was shown to function in the retrieval and recycling of developmental receptor Notch 2 (Li et al. 2015), and a complex containing COMMD1 was shown to function in the recycling of ATP7A and low-density lipoprotein receptor (LDLR) (Bartuzi et al. 2016; Phillips-Krawczak et al. 2015).

1.4.4 – Endosomal recycling tubule formation

Recycled cargos are physically partitioned into long sorting endosome membrane protrusions. These protrusions, ‘endosomal recycling tubules’, undergo fission away from the main body of the sorting endosome, allowing microtubule-based transport of recycled cargos to either the cell surface, the TGN, or other destinations. Due to the hydrophobic effect, the structure of the high surface area low volume endosomal tubule is energetically unfavourable compared to the spherical parent sorting endosome (Qualmann et al. 2011). As a result, energy is required to deform the sorting endosome

membrane into tubules. This deformation is mediated by the sorting nexins (SNXs), and cytoskeletal elements actin, microtubules, and motor proteins.

An important subgroup of SNX proteins involved in endosomal tubule formation is the SNX-BAR proteins. These, like all SNX proteins, contain a phosphoinositide-binding PX domain, but at their C-terminal contain a BAR domain (Carlton et al. 2004). SNX-BAR proteins dimerise to form a rigid curved structure. Rigidity is conferred by a tightly-packed 6 helix central bundle, and the curvature can range from 10^{o} at the lowest (e.g. F-Bar proteins), to 30^{o} (N-Bar proteins) (Qualmann et al. 2011). In addition, SNX-BAR proteins are able to self-associate to form large lattice structures, mediated by 'tip-to-tip' contact between the BAR-domain tip loop of different SNX proteins (Dislich et al. 2011; van Weering et al. 2012). The banana-shaped BAR module displays positive charges on its membrane binding surface, facilitating interaction with the negatively charged phospholipids of the endosomal membrane (Peter 2004). In total, these properties allow SNX-BAR proteins to bind curved membrane, but due to the protein's rigidity and self-associating lattice formation this also means that bound membrane is deformed to the shape of the protein (Qualmann et al. 2011). In addition, the presence of a N-terminal amphipathic helices in the N-BAR subset of proteins facilitates additional membrane bending by the partial embedding into the membrane bilayer, in a manner similar to that proposed in ER shaping (Gallop et al. 2006).

By *in vitro* experiments not all SNX-BAR proteins induce membrane curvature (van Weering et al. 2012). However, many SNX-BAR proteins that do not induce membrane curvature heterodimerise with proteins that are able to induce curvature. These include SNX1, SNX2, and SNX4 (van Weering et al. 2012). As a result of curvature-inducing SNX-BAR lattice formation, the relatively low-curvature of the sorting endosome membrane is modelled into the high curvature structure characteristic of an endosomal tubule (van Weering et al. 2012). In addition to being able to directly bind cargo (Kvainickas et al. 2017), these SNX-BAR proteins are recruited by retromer to the site of cargo capture. This allows the site of the tubule formation to be correlated with a high concentration of cargo to be recycled. It should be noted however that not all endosomal tubules contain the same SNX-BAR proteins. For example, SNX1-containing endosomal tubules recycle cargo to the TGN (Carlton et al. 2004), whereas SNX4-containing endosomal tubules recycle to the plasma membrane via a perinuclear endosomal compartment termed the recycling endosome (Traer et al. 2007).

Actin polymerisation by WASH is also thought to stabilise the formation of endosomal tubules (Dong et al. 2016; Puthenveedu et al. 2010). Endosomal tubules can be observed to be decorated in a highly localised actin cytoskeleton, and inhibition of actin led to a 25% reduction in the number of endosomal tubules (Puthenveedu et al. 2010). WASH also binds to tubulin, potentially helping coordinate actin and microtubule recruitment onto endosomal tubules (Gomez and Billadeau 2009).

Microtubules have an important role in endosomal tubule formation (Hunt et al. 2013). *In vitro* studies show that kinesins are able to pull tubules from liposomes (Roux et al. 2002), and electron microscopy shows endosomal tubules in close proximity to microtubules (Friedman et al. 2013). The microtubule motor dynein is required for the formation of transferrin-positive endosomal tubules (Horgan and McCaffrey 2011; Palmer et al. 2009). Microtubule motors can couple to SNX proteins of endosomal tubules (Hunt and Stephens 2011; Wassmer et al. 2009; van Weering et al. 2010), with one example being the coupling of SNX5 to dynein via the dynactin complex (Hong et al. 2009). Hunt et al. (2013) define dynein-1 and kinesin-1 motors associating with SNX1 labelled membranes, and dynein-1 and kinesin-2 motors for SNX4 labelled membranes. In addition, the microtubule motor kinesin 13A (KIF13A) localises to endosomal tubules, and its depletion leads to a reduction in the number of recycling tubules that emanate from the sorting endosome (Delevoye et al. 2014). Conversely, overexpression of KIF13A leads to a dramatic endosomal tubulation (Delevoye et al. 2014).

1.4.5 – Endosomal tubule fission

The first results chapter of my thesis provides a detailed discussion of endosomal tubule fission. In addition, a more general introduction to membrane scission mechanisms is provided in the following section (Introduction Section 1.5).

1.5 – Membrane scission

Membrane scission describes the process where two edges of a continuous lipid membrane come together resulting in the production of two distinct lipid membrane structures. This process is ubiquitous in eukaryotes, facilitating processes such as cellular abscission, MVB formation, endocytosis, viral exit, mitochondrial division, ER remodelling, and endosomal tubule fission (Shibata et al. 2009). This process may be driven by two types of process: 1) passive remodelling by processes such as amphipathic helix insertion; or 2) NTP-hydrolysing processes such as by scission machinery dynamin or ESCRT, or by cytoskeletal polymers actin or microtubules (Renard et al. 2018). Spastin has been associated with both types of membrane remodelling.

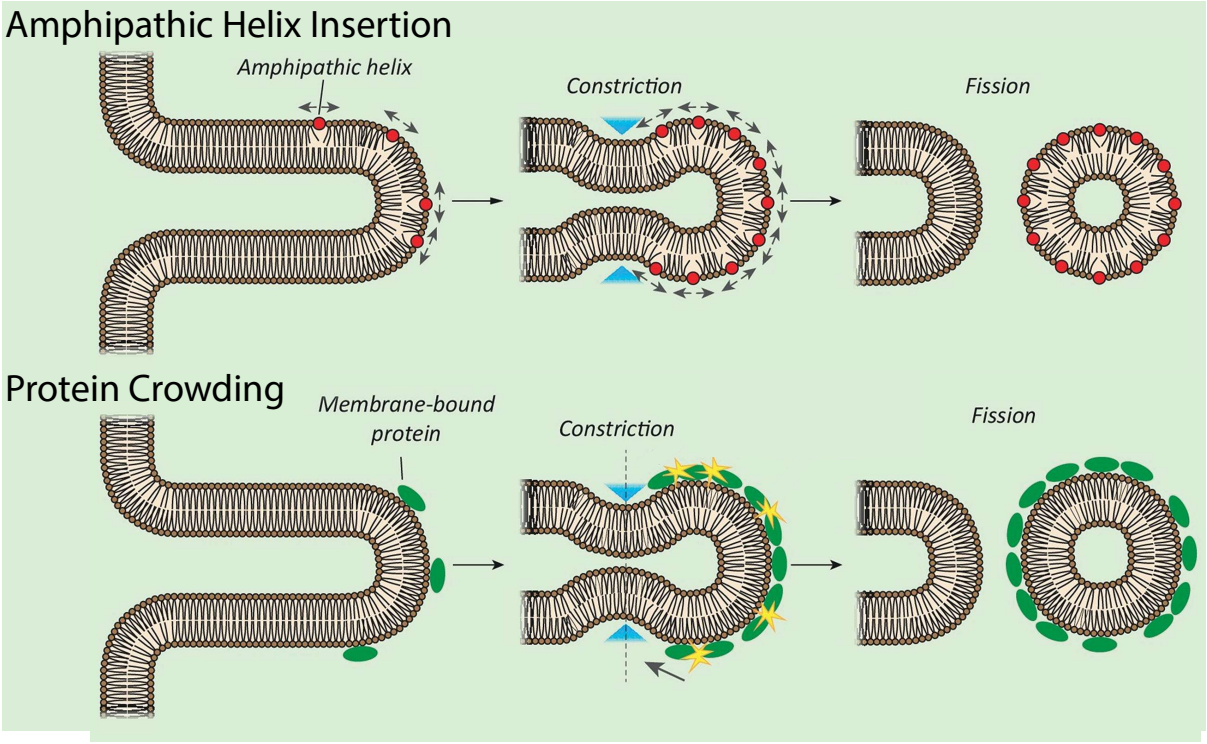

Figure 12 - **Modes of passive membrane scission.** (Top) Amphipathic helix insertion into the outer leaflet of the lipid bilayer induces curvature due an increase in surface area of the outer leaflet compared to the inner leaflet. If insertion is at a high concentration, scission can occur. (Bottom) The insertion or binding of a high density of proteins to the outer leaflet of a lipid bilayer can induce membrane deformation and fission. This occurs by the repulsion forces between bound/inserted proteins. Cartoon adapted from Renard et al. (2018).

1.5.1 – Passive membrane remodelling

Passive membrane remodelling describes the spontaneous reorganisation of lipids that leads to constriction without a direct use of NTP hydrolysis (Renard et al. 2018). Proposed passive remodelling mechanisms include amphipathic helix insertion and protein crowding (**Figure 12**). It should be noted that these proposed mechanisms have been largely generated by *in vitro* and *in silico* experiments and remain to be tested in cells (Renard et al. 2018).

Amphipathic helix insertion

The shallow insertion of hydrophobic domains (e.g. amphipathic helices) into the outer leaflet of the lipid bilayer leads to membrane bending by 'membrane wedging' (Drin and Antonny 2010). This is caused by the increase of surface area of the outer membrane leaflet compared to the lipid bilayer midplane and inner leaflet. If the density of wedging is high enough, it leads to the formation of a membrane neck which can spontaneously resolve, causing membrane scission (Campelo et al. 2008). Boucrot et al. (2012) showed *in vitro* that the insertion of hydrophobic helices of epsin into liposomes can lead to vesiculation, and simultaneously showed that epsin and the amphipathic helix of BAR containing proteins function in CCV fission during endocytosis. Amphipathic helix insertion has also been proposed as the mechanism by which Sar1 drives the fission of COPII vesicles during ER exit (Lee et al. 2005). Sar1 was shown to induce membrane tubulation and vesiculation of liposomes, and mutations of hydrophobic residues prevented this effect. This however has not been shown *in vivo*.

Protein crowding

Membrane deformation by protein crowding bears some similarities to deformation by amphipathic helix insertion. The insertion or binding of a high density of proteins to the outer leaflet of a lipid bilayer can result in repulsion effects between the bound proteins. As these proteins are attached to the membrane, the repulsion leads to the underlying membrane bending. This however assumes that the inner leaflet has a lower number of similar opposing repulsion effects occurring (Snead et al. 2017; Stachowiak et al. 2010). It has been shown that as little as 20% coverage of membrane in proteins lacking intrinsic bending properties (e.g. green fluorescent protein (GFP)) can result in membrane bending (Stachowiak et al. 2012). Snead et al. (2017) showed that an increase in protein coverage of a membrane, or an increase in protein size can lead to the fission of tubules from liposomes. It is unclear however whether protein crowding to cause fission occurs *in vivo*.

1.5.2 – Active membrane remodelling: cytoskeleton-induced scission

Actin

The cytoskeletal element actin is able to induce membrane bending effects by the formation of rigid polymerised actin arrays to constrict membrane, or the action of myosin motor proteins to push or pull membranes. High membrane tension during endocytosis caused by osmotic swelling can lead to a stalling of CCV formation (Boulant et al. 2011). In these circumstances, the polymerisation of actin can allow the continued invagination of the vesicle, although it is not clear if this occurs by neck constriction or by pushing the plasma membrane away from the vesicle (Boulant et al. 2011). In yeast, actin polymerisation is also required for endocytosis by working in concert with dynamin (Palmer et al. 2015). Actin polymerisation has also been shown necessary for endosomal tubule fission. A burst of actin polymerisation is observed at the fission location during tubule fission (Puthenveedu et al. 2010), occurs at ER-endosome contacts which marks the endosomal fission location (Dong et al. 2016; Rowland et al. 2014), and depletion of WASH component strumpellin leads to aberrantly long endosomal tubules implying a defect in fission (Harbour et al. 2010). In addition, polymerisation of actin at the TGN has also been implicated in the formation of post-Golgi vesicles (Salvarezza et al. 2009).

Actin-based myosin motors are also important in membrane scission. For example, myosin II was implicated in the fission of Rab6 positive post-Golgi vesicles from the TGN (Miserey-Lenkei et al. 2010). In addition, myosin plays an important role during mitochondrial fission. Actin depolymerisation inhibits dynamin recruitment to the mitochondria resulting in defective mitochondrial fission (De Vos et al. 2005). Furthermore, depletion of myosin regulatory light chain or myosin heavy chain II, or myosin drug-inhibition results in aberrant mitochondrial elongation, suggesting a fission defect (DuBoff et al. 2012; Korobova et al. 2014).

Microtubules

Microtubule motor proteins are able to generate pulling forces on membranes to induce scission (Day et al. 2015). An important requirement for this process is that the neck of the tubule or invagination is stabilised to prevent increased lipid diffusion into the tensioned area (Renard et al. 2015), and in the case of endosomal tubule fission, that the whole body of the endosome is prevented from moving. Stabilisation of the membrane body can be done by opposing cytoskeletal elements such as actin filaments at the cell surface (Flanagan and Koch 1978), or microtubules on sorting endosomes (Friedman et al. 2013). BAR containing proteins (e.g. SNX-BAR proteins) are able to prevent lipid

diffusion by forming scaffolds around membrane necks (Simunovic et al. 2016, 2017). This process is sometimes termed friction-driven scission (Renard et al. 2018).

Microtubule-induced scission is proposed to occur in clathrin-independent endocytosis and endosomal tubule fission. During clathrin-independent endocytosis, dynein-mediated pulling leads to membrane fission upon membrane necks being scaffolded by BAR protein endophilin-A2 (Renard et al. 2015). In endosomal tubule fission, the endosomal tubule is also scaffolded by BAR containing proteins, suggesting a pulling force could also generated scission (van Weering et al. 2012). Spastin's microtubule severing activity may induce motor protein loading at the endosomal tubule to generate pulling forces (Allison et al. 2013), and various kinesin and dynein motor proteins have been shown to be required for endosomal tubule formation (see Introduction Section 1.4.4).

1.5.3 – Active membrane remodelling: scission enzymes

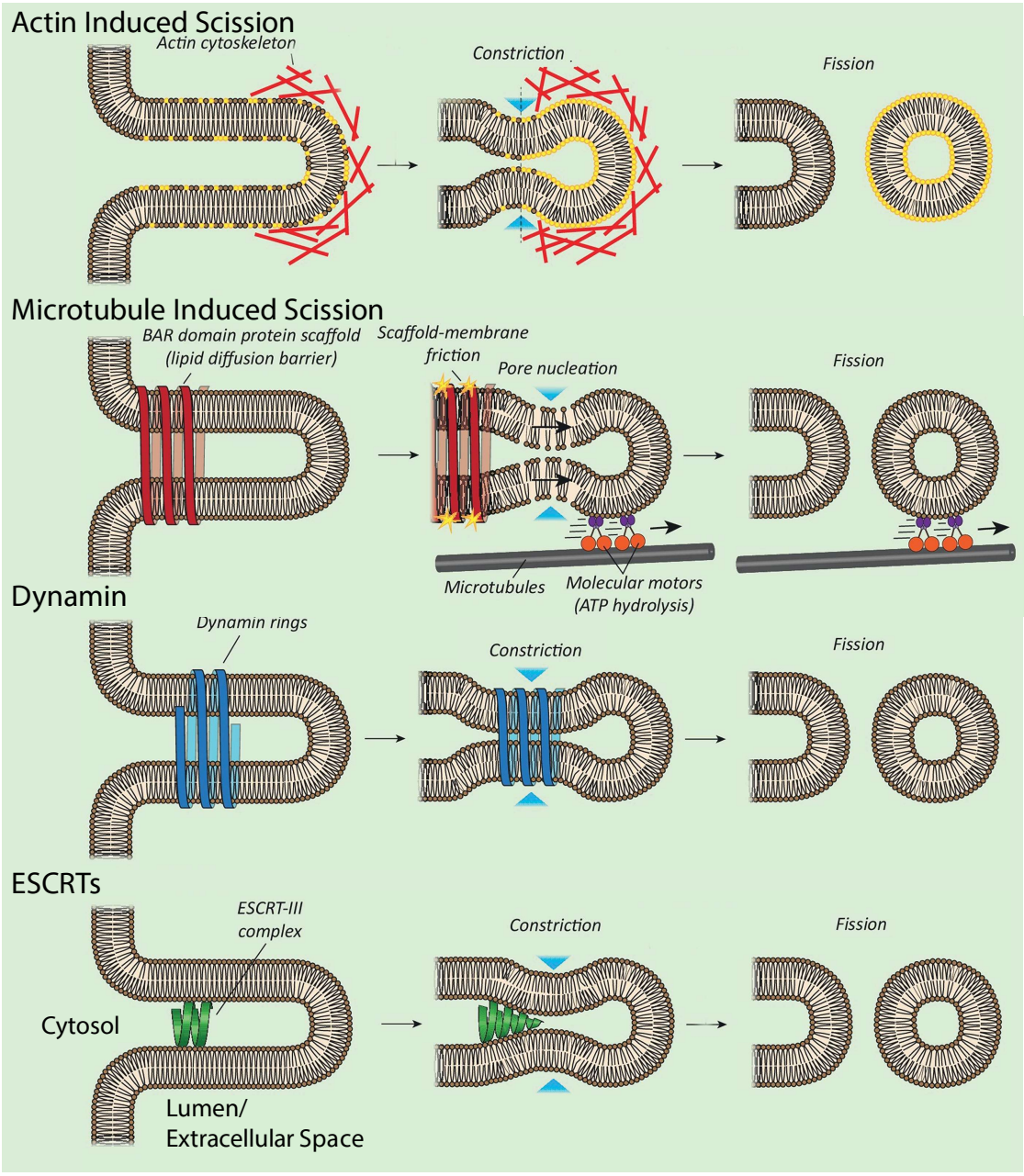

Figure 13 - **Modes of active membrane scission**. (Top) The polymerisation of actin can induce membrane constriction and fission by the formation of filamentous actin scaffolds or via myosin motor proteins generating a pushing or pulling force. (Second row) Microtubule motors can exert a pulling force on membranes to induce membrane constrictions. This depends on scaffolding beyond the neck of the constriction to stop lipid diffusion, and attachment of the body of the membrane to stop transport of the entire lipid structure. (Third row) The GTPase dynamin forms helical polymers which are able to contract in a ratchet mechanism upon GTP hydrolysis. This leads to membranes constricting to form a state of hemi-fission, where the membrane can spontaneously undergo fission. (Bottom) Inside-out example of ESCRT-III polymer formation leading to membrane constriction. No consensus view exists of the mechanism by which ESCRT-III polymers drive membrane fission. Supported models for scission include the formation of increasingly tight helical spirals, and spontaneous buckling to alleviate energetic unfavorability in the assembled ESCRT-III polymer. In all figures the membrane tubulates into the cytosol with the exception of the ESCRT figure where the membrane tubulates into the lumen or extracellular space. Cartoon adapted form Renard et al. (2018).

Dynamin

The GTPase dynamin is expressed as three isoforms: dynamin 1 and 3 are neuron specific, while dynamin 2 is ubiquitously expressed (Antonny et al. 2016). It is composed of a GTPase domain, a central four helix bundle stalk, a flexible linker domain (the bundle signalling element), and a $PI(4,5)P_2$ binding pleckstrin homology (PH) domain. GDP bound dynamin is able to oligomerise into a 50nm cylindrical helix on membranes (Hinshaw and Schmid 1995), with PH domains and GTPase domains on the inside and outside of the helix respectively (Zhang and Hinshaw 2001). Oligomerisation is driven by protein-protein interactions in the helical stalk (Faelber et al. 2011).

The function of dynamin is to fission membrane tubules from the outside (Antonny et al. 2016). Depletion of dynamin leads to defective fission of clathrin-coated pits (Raimondi et al. 2011), and expression of GTPase defective dynamin blocks transferrin internalisation and increases clathrin residence on the plasma membrane (Marks et al. 2001; Taylor et al. 2011). GTP hydrolysis causes a constriction of the dynamin helical oligomer. Expression of a GTPase mutant dynamin leads to extended membrane necks during endocytosis (Takei et al. 1995) and endosomal recycling tubule formation (Chi et al. 2014; Derivery et al. 2009), and during GTP hydrolysis membrane necks are more constricted (Sweitzer and Hinshaw 1998). Constriction occurs via the twisting of the helical collar of dynamin (Morlot et al. 2012), powered by GTP hydrolysis causing adjacent turns of the dynamin helix to slide over one another (Chappie et al. 2011). This leads to the formation of a hemi-fission state, where the tubule is constricted to a radius of 1.9nm and composed of a single lipid layer (Sundborger et al. 2014). This hemi-fission state then undergoes spontaneous and stochastic complete fission (Mattila et al. 2015), which can be accelerated by membrane tension (Cocucci et al. 2014; Roux et al. 2006).

Dynamin has been shown to be required for CME, mitochondrial fission, and endocytic recycling (Antonny et al. 2016). In all of these processes, dynamin is thought to work in concert with other constriction proteins help constrict the membrane neck of the tubule to a diameter than can be bound by dynamin (Roux et al. 2010). For example, in mitochondrial fission, dynamin requires the action of actin and Drp1 to constrict mitochondria division points before it can bind (Ji et al. 2015; Korobova et al. 2013). In endocytosis, dynamin requires the action of BAR containing proteins such as endophilin-A2 (Renard et al. 2015).

ESCRTs

The ESCRT machinery comprises a large set of cytosolic proteins that are coordinated to mediate membrane scission (Christ et al. 2017). This is typically mediated on the inside of membrane necks to 'pull shut' membrane, with examples including during MVB formation, cytokinesis, and viral budding. It can also form on the outside of membranes to constrict membranes during endosomal tubule fission (McCullough et al. 2018). The core ESCRT machinery consists of ESCRT-I, ESCRT-II, and ESCRT-III complexes, Alix protein, and VPS4-LIP5 (Schöneberg et al. 2017). Proteins of these groups interact to form large hetero-polymer complexes that mediate membrane fission. Fission itself is carried out by the ESCRT-III proteins in association with the ATPase VPS4 (Adell et al. 2017; Mierzwa et al. 2017). The function of the other ESCRT machinery components are to recruit ESCRT-III to an appropriate site of action and initiate membrane bending (McCullough et al. 2018).

ESCRT-III can be recruited to membranes by two different modes. The 'canonical recruitment' pathway' is mediated by heterotetrametric ESCRT-I and ESCRT-II complexes that interact with a 1:1 stoichiometry (Schöneberg et al. 2017). This is observed in processes such as MVB formation (Babst 2011) and cytokinesis (Goliand et al. 2014). The alternative pathway is via the Alix protein, which allows direct binding to ESCRT-III protein CHMP4 (McCullough et al. 2008), and typically observed during viral budding (Strack et al. 2003). There is however redundancy in these pathways (Tang et al. 2016). During MVB formation, ESCRT-I is recruited to ubiquitinated proteins by the ESCRT-0 protein Hrs, which also binds the PI3P rich membrane of the endosome (Christ et al. 2017).

ESCRT-III complexes drive membrane remodelling via polymerising into helical spirals or conical configurations (Hanson et al. 2008; Lata et al. 2008). ESCRT-III polymerisation is mediated by ESCRT-II proteins by removing ESCRT-III autoinhibition (Bajorek et al. 2009). This allows the ESCRT-III protein to convert from a closed monomeric soluble state into a membrane bound configuration that is capable of polymerisation. These polymer configurations have inherently curved structures, with the membrane interacting region decorated in basic amino acids. For most ESCRT-III proteins this is on the convex surface of the complex (Im *et al.*, 2009), but for the proposed constriction fission ESCRT complex of IST1-CHMP1B, these are on the concave face (see Introduction Section 1.3.3; McCullough et al. 2015). ESCRT-III proteins typically containing MIMs, facilitating their interaction with MIT-domain-containing proteins such as VPS4 and spastin (see Introduction Section 1.3.3).

Despite their evident importance in membrane scission, a consensus model of how ESCRT-III proteins induce scission has not been established (Schöneberg et al. 2017). One set of models, proposes that ESCRT-III polymers may form on membranes with an energetically unfavourable

underbent conformation (Fabrikant et al. 2009). The ESCRT-III polymer resolves this energetic unfavorability by forming restricting spirals, driving membrane constriction and fission by tight association between ESCRT-III and the membrane. Extensions of this model include the ESCRT-III subunits being replaced with those of tighter curvature as the membrane constrictions (Fabrikant et al. 2009), potentially by the action of VPS4 (Adell et al. 2017; Mierzwa et al. 2017).

The alternative most supported model is the buckling/spiral spring model (Chiaruttini et al. 2015; Lenz et al. 2009; Schöneberg et al. 2017; Shen et al. 2014). This model is able to explain both inside-out and outside-in membrane fission (Schöneberg et al. 2017). In this model, ESCRT-III polymers form either at the neck of membranes or on flat membrane surfaces and grow with increasingly wide ESCRT-III subunits. This results in high energetic unfavorability, with some regions of the polymer being underbent and some overbent. Continued polymerisation drives this unfavorability to a critical point whereby the ESCRT-III filament buckles, releasing energy to deform the membrane (McCullough et al. 2018; Schöneberg et al. 2017).

1.6 – Thesis Aims

This thesis investigates the function of spastin in endosomal tubule fission and cargo export from the ER. As highlighted above (Section 1.3), spastin has been associated with these processes but a direct functional relationship has not been shown (Allison et al. 2013; Connell et al. 2009). In addition, I quantify the effect of a spastin ATPase mutation on the cell surface proteome, with an idea to identifying candidate proteins whose altered endomembrane transport could lead to the axonopathy observed in HSP. Each of these aims is discussed in more detail below.

The function of spastin in endosomal tubule fission (Chapter 3)

Allison et al. (2013) reported that a depletion of spastin or IST1, or mutation in spastin's MIT or AAA+ domains, led to the formation of abnormally elongated endosomal SNX1 and SNX4 recycling tubules. This suggested that spastin functions in mediating the fission of endosomal recycling tubules from the sorting endosome via an ESCRT-III interaction and microtubule remodelling. However, several unanswered questions remain: 1) whether the aberrantly long endosomal tubules formed are in fact due to defective tubule fission; 2) whether spastin and IST1 localise to endosomal tubules or enact their endocytic function from alternative locations; and 3) how spastin's microtubule remodelling activity relates to endosomal tubule dynamics. These topics are investigated in my first results chapter.

The function of spastin in the early secretory pathway (Chapter 4)

Connell et al. (2009) showed that M1 spastin recruited to ERES, and overexpression of an ATPase defective spastin, but not spastin depletion, led to impaired export of cargo from the ER. This therefore left the function of spastin at ERES ambiguous. My second results chapter investigates the localisation of spastin to ERES and investigates the function of spastin in cargo secretion.

The impact of ATPase defective spastin on the cell surface proteome (Chapter 5)

Due to the central role of spastin in microtubule remodelling (Vemu et al. 2018), endocytic cargo recycling (Allison et al. 2013, 2017), and lysosome function (Allison et al. 2017), it can be predicted that a loss of functional spastin may have dramatic downstream consequences. One predicted outcome is a change in the trafficking of proteins to and from the cell surface. This would likely lead to a remodelling of the cell surface proteome, as shown by investigations that have blocked endocytic cargo retrieval during endocytic recycling (McNally et al. 2017; Steinberg et al. 2013). Such changes

may impact the interaction of a cell and its environment, potentially leading to pathology such as the axonopathy observed in HSP. In my third results chapter, I use quantitative cell surface proteomics to explore the effect of spastin loss of function in mouse embryonic fibroblasts (MEFs) and primary cortical neurons. This was performed with the dual of aim of firstly exploring whether spastin loss of function remodels the cell surface proteome, and secondly aiming to identify pathological candidates in spastin-HSP.

Chapter 2 - Materials and Methods

2.1 – Cell Culture Techniques

2.1.1 – List of cells used

Cell Line	Original Tissue	Obtained From	Advantages	Stable Cell Line Variants
MRC5	Human lung fibroblasts	Nick Morrell (Department of Medicine, Cambridge)	Diploid, large with easy-to-image ER and microtubules, easy to culture and transfect/transduce	GFP-SNX1-I-NeoR; EGFP-Spastin M87A mt 1,3-I-Hygro; EGFP-Spastin M87A mt 1,3-I-Hygro and mCherry-SNX1-I-NeoR
HeLa-M	Human cervical cancer epithelial cells	N/A	Easy to culture and transfect	None
HeLa-M RUSH Cells	Human cervical cancer epithelial cells	Franc Perez (Institute Curie, Paris)	Stably express RUSH reporter and hook; previously verified and published RUSH assay cells	TNFα-SBP-GFP KDEL-Streptavidin; GPI-SBP-GFP KDEL-Streptavidin
SPG4$^{-/-}$ (WT) immortalised mouse embryonic fibroblasts (MEFs)	Mouse embryonic fibroblasts	Own production immortalised using pEF321-T plasmid	Easy to culture and transfect/transduce, direct association with spastin mutation-induced pathology	GFP-SNX1-I-NeoR
SPG4$^{N384K/-}$ (HET) immortalised mouse embryonic fibroblasts (MEFs)	Mouse embryonic fibroblasts	Own production immortalised using pEF321-T plasmid	Easy to culture and transfect/transduce, direct association with spastin mutation-induced pathology	GFP-SNX1-I-NeoR

Cell Line	Original Tissue	Obtained From	Advantages	Stable Cell Line Variants
SPG4$^{N384K/N384K}$ (HOM) immortalised mouse embryonic fibroblasts (MEFs)	Mouse embryonic fibroblasts	Own production immortalised using pEF321-T plasmid	Easy to culture and transfect/transduce, direct association with spastin mutation-induced pathology	GFP-SNX1-I-NeoR
COS7	Monkey kidney fibroblasts	Paul Lehner (Cambridge Institute of Medical Research, CIMR)	Diploid, very large and very flat with ideal ER for imaging, easy to culture and transfect/transduce	GFP-SNX1-I-NeoR
Phoenix cells (HEK293T retroviral producer line)	Human embryonic kidney epithelial Cell	Paul Luzio (Cambridge Institute of Medical Research, CIMR)	Large production of retrovirus with the stable expression of gag-pol and envelope proteins	None
SPG4$^{-/-}$ (WT) embryonic primary cortical neurons	Primary E16 mouse cortical neurons	Own production	Direct association with spastin mutation-induced pathology; the tissue affected by HSP	None
SPG4$^{N384K/-}$ (HET) embryonic primary cortical neurons	Primary E16 mouse cortical neurons	Own production	Direct association with Spastin mutation-induced pathology; the tissue affected by HSP	None
SPG4$^{N384K/N384K}$ (HOM) embryonic primary cortical neurons	Primary E16 mouse cortical neurons	Own production	Direct association with Spastin mutation-induced pathology; the tissue affected by HSP	None

Table 1 - **Table of cell lines**

2.1.2 – Cell maintenance

Cell line maintenance

Cell lines were cultured in Dulbecco's Modified Eagle's Medium (DMEM (Sigma-Aldrich – D6546)) or DMEM without Phenol Red (Sigma-Aldrich – D5921) supplemented with 10% Foetal Bovine Serum (FBS (Sigma-Aldrich – F7524)), 2mM L-Glutamine (Sigma-Aldrich – G7513), and 100µg/mL Penicillin-Streptomycin (Sigma-Aldrich – P0781). DMEM lacking Phenol Red was used for cells cultured for live cell imaging to avoid autofluorescence. For the selection of stable cell lines, media was supplemented with 200µg/mL Gentamicin (Sigma-Aldrich – G1397), or 190µg/mL Hygromycin-B (ThermoFisher – 10687010) depending on the selection cassette expressed. All cells were grown at 37°C and 5% CO_2.

To remove adherent cells from the growth surface, cells were washed once with phosphate buffered saline (PBS) lacking $MgCl_2$ and $CaCl_2$ (Sigma-Aldrich – D8637)) and incubated with 0.05% Trypsin-EDTA (Sigma-Aldrich - T3924) for ~5mins with gentle tapping to help loosen adhered cells. Before being replated, trypsinised cells were resuspended in growth media to neutralise the trypsin, and then centrifuged and the pellet suspended in fresh media. Cell counting was performed using a haemocytometer (Hausser Scientific – 3720).

Maintenance of E16 mouse neurons

Primary neurons extracted from E16 mice cortices were cultured in 10cm^2 dishes coated with 0.05mg/mL Poly-D-Lysine (Sigma-Aldrich – 6407) allowing for full extension of neurites. Neurons were cultured in neuronal culture media consisting of Neurobasal Media minus Phenol Red (ThermoFisher – 12348017) supplemented with GIBCO 50x, serum free B-27 (ThermoFisher - A3582801), 0.5mM GlutaMAX (ThermoFisher – 35050061), 1mM sodium pyruvate (ThermoFisher – 11360070), and 100µg/mL Penicillin-Streptomycin (Sigma-Aldrich – G1397). Neurons were maintained in culture for 14 days, with half the culture media replaced every three days with fresh media.

Freezing and thawing cell lines

To freeze cell lines, a cell pellet was resuspended in a freeze medium consisting of 50% FBS, 40% growth media, and 10% dimethyl sulfoxide (DMSO (Sigma-Aldrich – D8418)). The resuspended cells were then aliquoted into 1.8mL Cryotubes (ThermoFisher – 377267) and placed onto dry ice before being stored at -80°C. After several days, the Cryotubes were transferred to liquid nitrogen-cooled cell banks for long-term storage. To defrost cells, the Cryotube was opened and a small volume of pre-warmed growth media was pipetted into the vial, defrosting a small volume of the frozen cell pellet.

This defrosted volume was extracted and pipetted into a T25 flask pre-filled with growth media. This process was repeated until the entire frozen cell suspension was defrosted and transferred to the T25 flask. The following day, the media was replaced with fresh growth media.

2.1.3 – Primary cortical neuron extraction

Poly-D-lysine coating

Poly-D-Lysine (PDL) was used to coat cell culture plastic and coverslip glass to allow neurites to form. The day before neural dissection, Poly-D-Lysine Hydrobromide (Sigma-Aldrich - 6407) was resuspended in 50mL sterile H_2O (100µg/mL) and added to a 15cm^2 dish for 2hrs before being recollected back into a 50mL Falcon tube, thus removing any undissolved toxic PDL from the solution. The solution was then diluted to its working concentration of 50µg/mL with sterile H_2O. This solution was then added to 10cm^2 dishes and glass coverslips placed within the wells of a 6-well plate (with enough to cover the surface of the dish/wells) and the dishes/plates incubated in an incubator overnight at 37^{o}C. The following morning, the PDL was removed, and plates were washed 3xs with sterile H_2O, with the final wash kept on the plate for 1hr before being removed. After the final H_2O wash had been removed, 10mL of neuronal growth media was added to each dish and 2mL of neuronal growth media was added to each well of the 6-well plate, and both were warmed in a cell incubator at 37^{o}C.

Dissection of cortices

All elements of the dissection protocol were performed as quickly as possible to ensure maximum neuron viability post-dissection. Apart from where stated, all tissue was kept in ice-cold phenol-red-free Hanks Balanced Salt Solution (HBSS (ThermoFisher - H6648)) before and duration dissection.

The pre-dissected uterus was placed in a 15cm^2 dish, and each individual embryo was obtained. Using scissors, each embryo was decapitated, with the heads collected in a 15mL Falcon tube. Each head was placed in a 10cm^2 dish so that the top of the head was facing upwards. With forceps inserted through the nose, the skin was pealed back from the top of the skull using scissors to create an incision along the length of the top of the head, and forceps to peel back the skin. This method was then used to cut through the soft skull of the embryo for the same effect to reveal the brain. The flat of the forceps was then used to gently push the brain towards the back of the neck, thereby dislodging the brain from the head. The entire brain was then transferred to a new 10cm^2 dish

to ensure the brain could be kept ice-cold. A small section of skin was kept and transferred to an Eppendorf tube for use in DNA extraction and genotyping.

Once the brain had been extracted, the cerebellum, medulla oblongata, and olfactory lobes were removed by using scissors, leaving just the cerebral hemispheres. The two hemispheres were separated by cutting between them. For each hemisphere in turn, forceps were used to carefully peel back the meninge coating so that it was removed completely as one membrane. Using forceps, the hippocampus was then removed, leaving just the cortices of each hemisphere. The two dissected cortices were then placed back on ice in a 15mL Falcon tube.

Dissociation of neurons

Once all embryos had been dissected, the HBSS was removed and replaced with 1mL 0.25% Trypsin-EDTA (ThermoFisher – 25200056) with 0.1% DNase (ThermoFisher – EN0521), and the tube placed in a 37^{o}C waterbath for 15mins with the tube inverted every 3mins. During this period, 3 Pasteur glass pipettes per embryo were occluded so each had progressively smaller diameter holes. After 15mins, the trypsin mixture was removed without disturbing the cortices and replaced with 1mL pre-warmed HBSS supplemented with 10% FBS (Sigma-Aldrich – F7524). After 2mins, this solution was removed and replaced with fresh pre-warmed HBSS to wash the cortices. This liquid was then removed and replaced with 1mL neuronal culture media. Using the pre-occluded Pasteur pipettes, the cortex was then homogenised by sucking the cortex into the pipette and expelling it 10 times using each pipette starting from the pipette with the widest diameter, careful to avoid bubble formation. The homogenised cortices were then pipetted through a 70µm cell strainer and the resulting solution added to the pre-warmed media of the PDL-coated 10cm^2 dishes, with a small amount also added to similarly prepared glass coverslips placed within a 6-well plate. After ~4hrs, all the media was removed and replaced with pre-heated fresh neuronal growth media.

2.1.4 – Transfection and transduction

Transfection

Cells were transfected with either Lipofectamine 2000 (ThermoFisher - 11668019) or Lipofectamine 3000 (ThermoFisher - L3000008) transfection reagents using the manufacturer's protocol. For both methods for one well of a 6-well plate, 250µL Opti-MEM (ThermoFisher – 31985062) was mixed with 5µL Lipofectamine reagent, and in a separate tube 250µL Opti-MEM was mixed with 1000ng DNA (for Lipofectamine 3000 reactions, also 5µL of P3000 reagent), and incubated separately for 5mins. After the elapsed time, both tubes were mixed and incubated for 10mins. In this time, cells were washed twice with PBS (Sigma-Aldrich – D8637) and 2mL of fresh growth media was added to the well. After the elapsed 10mins, 500µL transfection mixture was added dropwise to the well. After transfection, cells were typically used within 24hrs to prevent cell mortality from severe overexpression of the protein of interest. No washing steps were performed for the transfection of cells previously transfected using siRNA oligonucleotides.

Transduction

All transductions were performed using either pLXIN or pBMN retroviral vectors transfected into the Phoenix retrovirus producer HEK 293T cell lines using the methods detailed by the Nolan lab (Stanford University). Firstly, Phoenix cells were plated at $1x10^6$ in $10cm^2$ dishes. The following day, the cells were transfected with the retroviral vector containing the desired gene for stable expression. This media was replaced the next morning with fresh growth media and the cells transferred to a viral incubator at 32°C to allow virus production to occur. On the next day, the cells to be transduced were trypsinised and $2x10^6$ cells were pelleted, the media removed, and the pellet resuspended in the remaining media droplet followed by the addition of Polybrene (Sigma-Aldrich - H9268) to a working concentration of 4µg/mL. The viral media from the Phoenix cells was then collected and filtered through a 0.45µm filter into the 15mL Falcon tube containing the cells to be transduced. The viral media and cells were then mixed, before the cells were transferred to a T75 growth flask and grown at 37°C overnight. The next day, the viral media was removed from the cells and the transduced cells were grown in selection-free media. When the cells had grown to confluency, they were split into 4 $10cm^2$ dishes and grown in media supplemented with selective agents.

siRNA knockdowns

siRNA knockdowns were performed using Oligofectamine reagent (ThermoFisher – 12252011) following the manufacturer's protocol with siRNAs typically used at a final concentration of either 10nM or 20nM (Dharmacon). For one well of a 6-well plate, cells were plated at $4x10^4$ cells (for microscopy) or $1x10^5$ (for lysis and western blotting). The following day, two solutions for both mock and knockdown treatments were made: 1) 5µL H_2O or 5µL siRNA (at 4µM resuspended in H_2O) with 165µL Opti-MEM (ThermoFisher – 31985062); 2) 5µL Oligofectamine reagent with 25µL Opti-MEM. These were mixed gently and incubated at room temperature for 5mins. After the elapsed time, 30µL of each Oligofectamine solution was mixed with the appropriate mock (H_2O) and knockdown (siRNA) solutions and incubated at room temperature for 20mins. After the incubation, the 200µL volume for each solution was transferred into a different tube and 800µL Opti-MEM was added to each and mixed by inversion. Cells were then washed twice in PBS (Sigma-Aldrich – D8637) and the 1mL mixture was added dropwise to the cells. This 1mL volume was then supplemented with 1mL 20% FBS growth media (the standard growth media with double the concentration of FBS) and incubated for 72hrs before being used in experimentation. The efficacy of knockdown was verified by cell lysis and western blotting.

Target Gene	**Oligonucleotide Name**	**Oligonucleotide Sequence**	**Manufacturer**
SPAST	Spastin siRNA '1'	GAACUUCAACCUUCUAUAA	Dharmacon
SPAST	Spastin siRNA '3'	UAUAAGUGCUGCAAGUUUA	Dharmacon
IST1	IST1 siRNA '1'	CCAAGUAUAGCAAGGAAUA	Dharmacon

Table 2 - **Table of siRNAs**

2.1.5 – Cell sorting

All cell sorting was performed by the CIMR Flow Cytometry team using a Becton Dickinson Influx cell sorter and was used to isolate either single cells or populations of cells from cell lines stably expressing fluorescent proteins. To prepare cells for sorting, cells were trypsined, pelleted, and the trypsin neutralised as previously described, before an appropriate number of cells were pelleted again and resuspended in 2.5mL of growth media in 5mL Polystyrene Round-Bottom Falcon tubes. A non-fluorescent cell sample was then loaded onto the cell sorter and the laser voltage was adjusted to set any signal from these cells to almost zero. The fluorescent cells to be sorted were then loaded and the same laser voltages applied. After gating for singlets, the fluorescent population (or a subset) was gated and sorted into polystyrene tubes prefilled with growth media or 96-well plates (for clonal expansion). Cells sorted into tubes were pelleted and resuspended in fresh media before being replated to minimise potential contamination.

2.2 – Molecular Biology

2.2.1 – Cloning Methods

Polymerase chain reaction (PCR)

All PCR reactions were performed using the Phusion polymerase (New England Biolabs - M0530) in 50µL volumes using the PCR mixture described in **Table 3**. For negative controls, H_2O was added instead of DNA to check against DNA contamination. A range of DMSO concentrations were often used for primers with strong secondary structure. PCR thermocycling was performed as stated in **Table 4**. Primer annealing temperatures were calculated using the online Tm Calculator tool, or for Gibson Assembly PCR from the online tool NEBuilder® Assembly Tool (detailed below).

Name	**Volume (for a single 50µL mixture)**
GC-Rich Phusion Buffer	10µL
10mM dNTPs	1µL
10µM Forward Primer	2.5µL
10µM Reverse Primer	2.5µL
DMSO	1.5µL
H_2O	27µL
Phusion Polymerase	0.5µL
DNA @ 50ng/µL	5µL

Table 3 - **Table of the Phusion PCR mixture**. All components purchased from New England Biolabs (E0553).

Stage	**Duration**	**Temperature**
1. Initial Denaturation	30secs	98°C
2a. Denaturation	8secs	98°C
2b. Annealing	20secs	Variable
2c. Elongation	22secs per kb	72°C
	35 cycles	
3. Final elongation	8mins	72°C

Table 4 - **Table of PCR thermocycling conditions when using Phusion polymerase**.

Restriction enzyme digest

For the digestion of plasmids, 5µg of plasmid DNA was incubated with 2µL of each restriction enzyme and 5µL of the appropriate NEB Buffer, with the final volume made to 50µL with H_2O. For the restriction digest of PCR products, the protocol was the same but 30µL of the PCR product DNA was used instead. Digestions were performed at 37°C for 3hrs.

DNA dephosphorylation and phosphorylation

DNA dephosphorylation was performed when a single restriction site was used during cloning to prevent undesired plasmid reannealing during ligation. In a reaction volume of 30µL, 3µL of Alkaline Phosphatase Buffer (New England Biolabs - M0290) was mixed with 1µL Alkaline Phosphatase (New England Biolabs - M0290) and 26µL of DNA. For insertion of PCR fragments into dephosphorylated DNA the PCR product must be phosphorylated. For a reaction volume of 30µL, 3µL of T4 DNA Ligase Buffer (New England Biolabs - B0202) was mixed with 1µL T4 DNA Kinase (New England Biolabs - M0201) and 26µL DNA. To proceed, both reactions were then heated at 37°C for 1hr before being heated at 65°C for 10mins to denature the enzymes.

DNA ligation

The DNA ligation protocol was performed for all cloning where Gibson Assembly was not used and performed between plasmids and DNA fragments digested using the same restriction enzymes. For a 20µL ligation, 2µL of a 1:20 and a 1:50 dilution of the digested vector DNA was incubated with 10µL of digested DNA fragment to be inserted, 2µL of NEB T4 Ligase Buffer (New England Biolabs - B0202), and 1µL of T4 DNA Ligase (New England Biolabs – M0202), with the total volume made to 20µL with H_2O. Two comparable control reactions were set up with 10µL H_2O in place of the DNA insert. For the reaction to proceed, the two solutions were mixed by vortexing and the solution was left at room temperature overnight.

Bacterial transformations and clone amplification

For bacterial transformations, competent XL-10 Gold bacteria stored at -80°C were defrosted on ice for 20mins. Once defrosted, 50µL of bacteria were mixed with 2µL plasmid DNA and incubated on ice for 25mins with occasional gentle shaking. The bacterial solutions were then heat-shocked at 42°C for 1min before being placed back onto ice. After several minutes, the bacteria were then plated and spread on Lysogeny broth (LB) plates with the appropriate selection antibiotic, and the plates were incubated at 37°C overnight. For bacterial clone amplification, either a single bacterial colony or a sweep of identical bacterial clones were collected using a pipette tip and placed in either a 15mL Falcon tube containing 5mL of LB (for single colonies) or a 250mL conical flask containing 100mL LB (large amplification of multiple clones). Inoculated LB was then heated overnight at 37°C in a shaking incubator. All LB plates and media were prepared by the CIMR core team. The LB formulation used was 0.5% NaCl, 1% Bacto Peptone, 1% yeast extract (and 1.5% Bacto Agar for LB plates). Either 100mg/ml ampicillin or 30mg/ml kanamycin antibiotics were added for selection.

DNA agarose purification

DNA agarose gel purification was used to extract DNA fragments separated by agarose gel electrophoresis. DNA purification from agarose was performed by using a QIAquick DNA Gel Extraction Kit (Qiagen – 28704) following the manufacturer's protocol. To dissolve isolated agarose, the agarose containing the DNA of interest was weighed and incubated with 3x the weight in volume of QG Buffer and heated at 50°C for 10mins. After the agarose had dissolved, an equivalent volume of isopropanol (Sigma-Aldrich – 190764) to the mass of the original agarose was added, and the mixed solution poured into a QIAquick spin column and centrifuged at 17900RCF for 1min. The column membrane was then washed with 750µL PE buffer and centrifuged again. The column was then dried by further centrifugation, before 30µL H_2O was added to the membrane and the tube centrifuged as before to elute the DNA.

DNA concentration measurement

DNA concentrations were measured using the ratio of optical absorbance at 260nm and 280nm wavelengths using a Nanodrop 200C spectrophotometer (ThermoFisher - ND-2000).

Gibson assembly

For all Gibson Assembly reactions, the destination vector backbone was linearised using restriction enzymes, and all DNA inserts were generated using PCR using Phusion polymerase (New England Biolabs - M0530), with initial primer design performed using the online NEBuilder® Assembly tool. The section of primers that annealed to the desired PCR insert were checked through the online tool Primer3Plus to verify the quality of the suggested primer. If Primer3Plus highlighted potential problems with the primers (e.g. primer self-complementarity), the length of the annealing section was adjusted. Digested vector and PCR products were then run through an agarose gel, and size-appropriate DNA bands were then cut from the agarose. After purification, DNA concentration was measured, and vector backbone and PCR inserts were mixed with Gibson Assembly Master Mix (New England Biolabs - E2611) made to 20µL with H_2O. DNA concentration in pmols was calculated using the below equation (1) and mixed in the below ratio (2).

1. pmols = ((weight in ng) *1000)/ (base pairs x 650)
2. (Backbone Vector) 100ng vector: (PCR Insert) 3*pmols of 100ng vector

The reaction mixture was then heated to 50°C for 1hr allowing the Gibson Assembly reactions to occur. After 1hr, 2µL Gibson mixture was transformed into bacteria by 42°C heat shock, and bacteria were then plated on LB plates with the appropriate bacterial selection matching the resistance conveyed by the plasmid.

Small-scale preparation of DNA

The small-scale preparation of plasmid DNA was performed from overnight 5mL bacterial cultures using the QIAGEN Spin Miniprep Kit (Qiagen – 27104). The bacterial culture was centrifuged at 2350RCF for 15mins, and the pellet was resuspended in 250µL P1 buffer which had been premixed with LyseBlue reagent and RNase A solution. This suspension was transferred to 1.5mL Eppendorf tubes and 250µL P2 lysis buffer was added and the solution was mixed. After 5mins, 350µL N3 buffer was added and the solution mixed until it became homogenously white. The solution was then centrifuged at 17900RCF for 10mins, and the supernatant applied to a QIAGEN spin column by decanting. The column was then spun for 1min at 17900RCF and washed with 750µL PE buffer. The column was then spun twice more, and the plasmid was eluted by the addition 50µL H_2O followed by centrifugation at 17900RCF.

Large-scale preparation of DNA

The large-scale preparation of plasmid DNA was performed from overnight 100mL bacterial cultures using the QIAfilter Plasmid Midi Kit (Qiagen – 12243). The bacteria were pelleted by centrifugation at 2350RCF for 30mins. The pellet was resuspended in 4mL P1 buffer which had been premixed with LyseBlue and RNase A buffer. 4mL of P2 buffer was added and the tube mixed until it became homogenously blue and left to stand for 5mins. During this time, a QIAGEN tip column was equilibrated using 4mL QBT buffer. After 5mins, 4mL of ice-cold P3 buffer was added to the lysed bacteria and mixed until the solution turned white. This was then applied to a capped QIAfilter cartridge and left to stand for 5mins. The cap was then removed, and the solution pushed through the cartridge resin by a plunger, with the solution entering the equilibrated QIAGEN tip column. After this solution had passed through the QIAGEN tip column, the tip was washed twice with 10mL QC buffer and the DNA was eluted by the addition of 5mL QF buffer. The eluted DNA was precipitated by the addition of 3.5mL isopropanol (Sigma-Aldrich – 190764) and centrifuged at 4^{o}C for 1hr at 2350RCF. The solution was then decanted to leave the DNA pellet which was washed with 2mL 70% ethanol (Sigma-Aldrich – 51976). The resuspended DNA was then centrifuged at 15000RCF for 10mins before the supernatant was removed and the pellet allowed to airdry. The dried pellet was then resuspended in 200µL H_2O.

Tissue DNA extraction and spastin mouse genotyping

DNA extraction using the Dneasy Blood and Tissue Kit (Qiagen – 69504) was used to obtain DNA from tissue or cells for genotyping. Ear punches or skin (e.g. from neural dissections) were incubated in 180µL ATL buffer and 20µL Proteinase K at 56^{o}C until the tissue was completely lysed. The lysate was then vortexed and 200µL AL buffer and 200µL 100% ethanol (Sigma-Aldrich – 51976) were added. This mixture was then vortexed and pipetted into a DNeasy Mini Spin Column and centrifuged at 6000RCF for 1min. The column was then washed with 500µL AW1 buffer and centrifuged as before. 500µL AW2 buffer was then added and the column dried by centrifugation at 20000RCF for 3mins. DNA was eluted by the addition of 100µL AE buffer and centrifugation at 6000RCF. For DNA extraction from cells, a maximum of 5x10^{6} cells were pelleted and resuspended in 200µL AL buffer, 20uL Proteinase K and 200µL PBS (Sigma-Aldrich – D8637) and heated at 56^{o}C for 10mins. 200µL 100% ethanol (Sigma-Aldrich – 51976) was then added, and the protocol continued as above.

For genotyping, 'Spastin Forward/Reverse Genotyping' primers were used to amplify around intron 4 of spastin using PCR. This allowed the identification of the presence/absence of an inserted

loxP site in the spastin-mutated alleles. PCR products were run on a 1% gel, with the WT bands at 707bp and mutated spastin bands at 899bp.

Name	Sequence
Spastin Forward Genotyping	TTGAACCGCCCTACTTGCCT
Spastin Reverse Genotyping	TAAGGGGTCTTTCCTCTTCGG

Table 5 - **Table of spastin genotyping primers**

2.2.2 – List of plasmids and donors

Vector Backbone	Generated Constructs	Bacterial Resistance	Promotor	Description
pIRES	pIRESneo2-myc-GFP-Spastin M87A mt 1,3	Ampicillin	CMV	Used as a mammalian expression vector with the additional optional function of adding a selection element downstream of an Internal Ribosomal Entry Site (IRES).
pBMN-I-Hygro	pBMN-GFP-Spastin M87A mt 1,3-I-Hygro;	Ampicillin	Viral 5' LTR	Used to generate retrovirus that incorporates a gene of interest followed by an IRES element and a Hygromycin B resistance gene into transduced cells. Typically used with Phoenix retroviral packaging cell lines that stably express viral envelope proteins
pLXIN-I-NeoR	pLXIN-GFP-SNX1-I-NeoR; pLXIN-mCherry-SNX1-I-NeoR	Ampicillin	Viral 5' LTR	Used to generate retrovirus that incorporates a gene of interest followed by an IRES element and a Neomycin (G418) resistance gene into transduced cells. Typically used with Phoenix retroviral packaging cell lines that stably express viral envelope proteins.
pmCherry	pmCherry-SNX1; pmCherry-Sec23; pmCherry-EB3	Kanamycin	CMV	Used as a mammalian expression vector to express a protein of interest fused to mCherry fluorescent protein.
pmFusionRed	pmFusionRed-SIT	Kanamycin	CMV	Used as a mammalian expression vector to express a protein of interest fused to mFusionRed fluorescent protein.
pmRFP	pmRFP-KDEL	Kanamycin	CMV	Used as a mammalian expression vector to express a protein of interested fused to mRFP fluorescent protein.

Vector Backbone	Generated Constructs	Bacterial Resistance	Promotor	Description
pEF321-T	pEF321-T	Ampicillin	EF-1α	Used to immortalise primary fibroblasts.

Table 6 - **Table of vector backbones and plasmids**

Plasmid Name	Donor	Reference
pIRESneo2-myc-spastin M87A mt 1,3	R. Allison	Allison et al. 2013
pIRES GFP-SNX1	M. Seaman	Harbour, Breusegem, and Seaman 2012
pmCherry-Sec23	J. Lippincott-Schwartz	NA
pmFusionRed-SIT	J. Lippincott-Schwartz	NA
pmRFP-KDEL	J. Lippincott-Schwartz	Altan-Bonnet 2005
EB3-mCherry	J. Lippincott-Schwartz	NA
pEF321-T expressing SV40 large T antigen	S. Sugano	Kim et al. 1990

Table 7 - **Table of plasmids obtained from donors**

2.2.3 – Plasmid construction

pLXIN-GFP-SNX1-I-NeoR

GFP-SNX1 was PCRed from pIRES GFP-SNX1 (Harbour et al. 2012) using 'Sal1 GFP Forward' and 'Not1 SNX1 Reverse' oligonucleotide primers. These primers introduced a Sal1 restriction site at the 5' end and a Not1 restriction site at the 3' end of the GFP-SNX1 PCR product. The GFP-SNX1 PCR product and a pLXIN-I-NeoR plasmid were digested using Sal1 (New England Biolabs - R3138) and Not1 (New England Biolabs - R3189) restriction enzymes, and GFP-SNX1 was then ligated into the digested pLXIN-I-NeoR plasmid. The ligated plasmid was amplified in bacteria selected with ampicillin, and bacterial clones were selected by DNA extraction and diagnostic digest using BglII (New England Biolabs - R0144). In clones positive for pLXIN-GFP-SNX1-I-NeoR, the GFP-SNX1 insert was checked for mutations by Sanger sequencing using the oligonucleotide primers listed in **Table 8**.

pmCherry-SNX1

SNX1 was PCRed from pIRES GFP-SNX1 using 'BglII SNX1 Forward' and 'Sal1 SNX1 Reverse' oligonucleotide primers. These primers introduced a BglII restriction site at the 5' end and a Sal1 restriction site at the 3' end of the SNX1 PCR product. The SNX1 PCR product and a pmCherry plasmid were digested using BglII (New England Biolabs - R0144) and Sal1 (New England Biolabs - R3138) restriction enzymes, and SNX1 was then ligated into the digested pmCherry plasmid. The ligated plasmid was amplified in bacteria selected with kanamycin, and bacterial clones were selected by DNA extraction and diagnostic digest using Bts1 (New England Biolabs – R0614) restriction enzyme. In clones positive for pmCherry-SNX1, the SNX1 insert was checked for mutations by Sanger sequencing using the oligonucleotide primers listed in **Table 8**.

pLXIN-mCherry-SNX1-I-NeoR

pLXIN-mCherry-SNX1-I-NeoR was generated by Gibson Assembly. mCherry-SNX1 was PCRed from pmCherry-SNX1 using 'Gibson mCherry-SNX1 Forward' and 'Gibson mcherry-SNX1 Reverse' oligonucleotide primers, and pLXIN-I-NeoR was digested using Sal1 (New England Biolabs - R3138) and Not1 (New England Biolabs - R3189) restriction enzymes. PCRed mcherry-SNX1 and digested pLXIN-I-NeoR were then mixed with Gibson Assembly master mix leading to the formation of pLXIN-mCherry-SNX1-I-NeoR. The ligated plasmid was amplified in bacteria selected with ampicillin, and bacterial clones were selected by DNA extraction and diagnostic digest using BsrGI (New England Biolabs – R3575) restriction enzyme. In positive clones for pLXIN-mCherry-SNX1-I-NeoR, the SNX1 insert was checked for mutations by Sanger sequencing using the oligonucleotide primers listed in **Table 8**.

pIRESneo2-myc-GFP-Spastin M87A mt1,3 (M1 expression only, siRNA resistant)

GFP without its stop codon was PCRed from GFP-SNX1 using 'Nhe1 GFP Forward' and 'Nhe1 GFP Reverse' oligonucleotide primers. These primers introduced a Nhe1 restriction site at the 5' and 3' ends of the GFP PCR product. The GFP PCR product and a pIRESneo2-myc-spastin M87A mt1,3 plasmid obtained from Rachel Allison (Allison et al. 2013) were digested using the Nhe1 (New England Biolabs - R3131) restriction enzyme, opening the pIRESneo2-Myc-Spastin M87A mt 1,3 plasmid between myc and spastin. The digested plasmid was then dephosphorylated and the GFP PCR product was phosphorylated. The GFP PCR product was then ligated into the digested pIRESneo2-Myc-Spastin M87A mt 1,3 plasmid. The ligated plasmid was amplified in bacteria selected with ampicillin, and bacterial clones were selected by DNA extraction and diagnostic digest using BsrGI (New England Biolabs – R3575) restriction enzyme. In positive clones for pIRESneo2-myc-GFP-Spastin M87A mt1,3,

the GFP insert was checked for mutations by Sanger sequencing using the oligonucleotide primers listed in **Table 8**.

pBMN-GFP-Spastin M87A mt1,3-I-Hygro

GFP-spastin M87A mt1,3 was PCRed from pIRESneo2-myc-GFP-Spastin M87A mt1,3 using 'BamH1 GFP-M1 Spastin Forward' and 'GFP-M1 Spastin Reverse' oligonucleotide primers. These primers introduced a BamH1 restriction site at the 5' and retained a BamH1 restriction site at the 3' end of the GFP-spastin M87A mt1,3 sequence. The GFP-spastin M87A mt1,3 PCR product and a pBMN-I-Hygro plasmid were digested using BamH1 (New England Biolabs - R3136) restriction enzyme, the digested PCR product was phosphorylated and the pBMN-I-Hygro plasmid was dephosphorylated, and GFP-spastin M87A mt1,3 was ligated into the digested pBMN-I-Hygro plasmid. The ligated plasmid was amplified in bacteria selected with ampicillin, and bacterial clones were selected by DNA extraction and diagnostic digest using Xho1 (New England Biolabs –R0146) restriction enzyme. In clones positive for pBMN-GFP-Spastin M87A mt1,3-I-Hygro, the GFP-spastin M87A mt1,3 insert was checked for mutations by Sanger sequencing using the oligonucleotide primers listed in **Table 8**.

Plasmid Being Generated	**Oligonucleotide Name**	**Purpose**	**Sequence**
pLXIN-GFP-SNX1-I-NeoR	Sal1 GFP Forward	PCR Primer	TAGGGAGTCGACATGGTGAGCAAGGGCGAGGA
	Not1 SNX1 Reverse	PCR Primer	TCCCTAGCGGCCGCAGGGCTAAGTCCAGCCAAGG
	GFP Forward	Sequencing Primer	GGACGACGGCAACTACAAGA
	GFP Reverse	Sequencing Primer	TTCTGCTTGTCGGCCATGAT
	SNX1 (Mouse) Middle Forward	Sequencing Primer	TTCATTGTGCCTCCTCCAC
	SNX1 (Mouse) Middle Forward 2	Sequencing Primer	GGTAGAGTGTGAGGAGCAGC
	SNX1 (Mouse) Start Reverse	Sequencing Primer	ATTCTGTGTGCTGTCCAGGG
	SNX1 (Mouse) End Forward	Sequencing Primer	AGAGTGGGAATCTCGGGTGA
pmCherry-SNX1	BglII SNX1 Forward	PCR Primer	TAGGGAAGATCTATGGATCCGGAGTCGGAAGG

Plasmid Being Generated	Oligonucleotide Name	Purpose	Sequence
	Sal1 SNX1	PCR Primer	ATCCCTGTCGACTCAGGAGATGGCCTTTGCCTC
	SNX1 (Mouse) Middle Forward	Sequencing Primer	TTCATTGTGCCTCCTCCAC
	SNX1 (Mouse) Middle Forward 2	Sequencing Primer	GGTAGAGTGTGAGGAGCAGC
	SNX1 (Mouse) Start Reverse	Sequencing Primer	ATTCTGTGTGCTGTCCAGGG
	SNX1 (Mouse) End Forward	Sequencing Primer	AGAGTGGGAATCTCGGGTGA
	CMVF_pCDNA3	Sequencing Primer	CAACGGGACTTTCCAAAATG
pLXIN-mCherry-SNX1-I-NeoR	Gibson mCherry-SNX1 Forward	Gibson PCR Primer	*CCGGAATTCGTTAACG*ATGGTGAGCAAGGGCGAG
	Gibson mCherry-SNX1 Reverse	Gibson PCR Primer	*GAGGGGCGAATTTGCTTATCACTA*TCAGGAGATGGCCTTTGC
	SNX1 (Mouse) Start Reverse	Sequencing Primer	ATTCTGTGTGCTGTCCAGGG
	SNX1 (Mouse) Middle Forward	Sequencing Primer	TTCATTGTGCCTCCTCCAC
	SNX1 (Mouse) Middle Forward 2	Sequencing Primer	GGTAGAGTGTGAGGAGCAGC
	SNX1 (Mouse) End Forward	Sequencing Primer	AGAGTGGGAATCTCGGGTGA
pIRESneo2-myc-GFP-Spastin M87A mt1,3	Nhe1 GFP Forward	PCR Primer	TAGGGAGCTAGCATGGTGAGCAAGGGCGAGGA
	Nhe1 GFP Reverse	PCR Primer	ATCCCTGCTAGCCTTGTACAGCTCGTCCATGCC
	GFP Forward	Sequencing Primer	CATGGTCCTGCTGGAGTTCGT G
	GFP Reverse	Sequencing Primer	GTTCAGGGGGAGGTGTG
pBMN-GFP-Spastin M87A mt1,3-I-Hygro	BamH1 GFP Forward	PCR Primer	TAGGGAGGATCCGCTAGCATGGTGAGCAAGGG

Plasmid Being Generated	Oligonucleotide Name	Purpose	Sequence
	Downstream of M1 Spastin Reverse	PCR Primer	GGAGTACTCACCCCAACAGC
	GFP Forward	Sequencing Primer	CATGGTCCTGCTGGAGTTCGT G
	GFP Reverse	Sequencing Primer	GTTCAGGGGGAGGTGTG
	Spastin Start Forward	Sequencing Primer	GCGCATCGATGAGGATGAGA
	Spastin Start Reverse	Sequencing Primer	ACACTGTTCACCTTGTCCTGT
	Spastin 734 Forward	Sequencing Primer	CACTGCCTCGTTCAAAAACA
	Spastin 1122 Forward	Sequencing Primer	TGCCAGAGGGCTGTTACTCT

Table 8 - **Oligonucleotide table of PCR and sequencing primers.** Underlined sequences indicate a restriction site, and italic sequences in Gibson Assembly primers indicate the region of the primer that is complementary to the destination of the PCR product.

2.2.4 – *In silico* DNA analysis

- **Gibson Assembly Design**: All Gibson Assembly design was performed using NEBuilder® Assembly Tool (http://nebuilder.neb.com/). Preferences were left as default, with Phusion and GC Buffer selected as the PCR product group. Where necessary, bases were added to the forward or reverse primers generated to ensure that all inserts were in the appropriate codon frame in the vector backbone. All suggested annealing sequences were analysed using the 'Check Primers' task on Primer3Plus (http://www.primer3plus.com/cgi-bin/dev/primer3plus.cgi). If the annealing region of the suggested primers were poor, the length of the annealing region was varied, with each length of primer checked through Primer3Plus. Of the variants, the nucleotide length that gave the lowest Penalty score was used as the annealing nucleotides of the Gibson PCR primer.
- **Primer Selection**: The online web application Primer3Plus (http://www.primer3plus.com/cgi-bin/dev/primer3plus.cgi) was used to generate optimal primers from a DNA region, or to check pre-selected primers against characteristics which would be detrimental to any PCR reactions to be performed. Example primer features that Primer3Plus evaluates are dimer formation, primer hairpin formation, primer 3' stability, and template mispriming.

- **DNA Sequencing**: Source BioScience Sanger Sequencing was used for the sequencing of all plasmids. Plasmid DNA was provided at 100ng/µl, with at least 5µL provided per reaction. Primers were supplied at 3.2pmol/µL with at least 5µL provided per reaction.
- **DNA Sequencing Chromatogram Analysis**: The free software Finch TV (Geospiza, Inc) was used to analyse the chromatogram generated by DNA Sanger Sequencing. In particular, chromatograms were checked for mixed traces indicating DNA contamination, and used to give an estimate of the confidence of a generated DNA sequence.
- **DNA Sequencing Viewing**: The free software Serial Cloner 2.6 was used to view, annotate, and store all DNA sequences. This tool also allowed identification of restriction sites for cloning and diagnostic digest. It was also used to align DNA sequences (e.g. for comparison between a sequenced plasmid and a predicted plasmid sequence) using the 'Align two sequences' function to identify any replication errors generated during PCR during plasmid generation.
- **DNA Sequence Lookup:** To search for DNA sequences, the online databases Ensembl (http://www.ensembl.org/index.html) or NCBI (https://www.ncbi.nlm.nih.gov/) were used.
- **Nucleotide Queries:** To match DNA sequences against annotated genomes, the online tool BLAST (https://blast.ncbi.nlm.nih.gov/Blast.cgi) was used.

2.3 – Protein Techniques

2.3.1 – Antibody-based protein detection

Cell lysis

For each well of a 6-well dish, cells were washed twice with ice-cold PBS (Sigma-Aldrich – D8537), with the PBS completely aspirated before continuing. After aspiration, chilled 50µL NP-40 lysis buffer (**Table 9**) supplemented with Protease Inhibitors (Sigma-Aldrich – COEDTAF-RO Roche) was added to each well, cells scraped using a cell scraper, and the lysates pipetted into chilled Eppendorf tubes. The tubes were kept on ice for 15mins with frequent vortexing to allow complete cell lysis. The lysates were then centrifuged at 10000RCF for 10mins at 4°C to pellet the nuclear fraction. The supernatant was kept and frozen at 20°C for short-term storage.

Name	Concentration	Manufacturer
TRIS pH7.5	10nM	CIMR Core Stock
NaCl	150mM	CIMR Core Stock
EDTA	0.5mM	CIMR Core Stock
IGEPAL CA-630	0.5%	Sigma-Aldrich - I8896

Table 9 - **NP-40 lysis buffer formulation**

Bicinchoninic acid (BCA) assay and protein normalisation

The BCA assay was used to normalise protein concentrations and performed using Pierce BCA reagents (ThermoFisher – 23225). Dilutions of Bovine Serum Albumin (BSA (ThermoFisher – BP1605-100)) at 0, 0.1, 0.2, 0.5, 1, 1.5, 2, 2.5 mg/mL were prepared, and 10µL was pipetted in triplicate into a 96-well plate. The sample was diluted ten-fold and 10µL was pipetted in triplicate into the 96-well plate. With the plate on ice, 200µL of BCA solution was added to each well, with the plate then incubated for 30mins at 37°C. The optical absorbance of each well at 562nm was determined, and the protein concentrations of each sample determined by comparing to a standard curve generated from the BSA standards.

Normalised protein concentrations were typically made up in a volume of 75µL, with 25µL of this volume consisting of 3x DTT SDS-Sample Buffer (**Table 10**). The remaining 50µL was composed of a combination of protein lysate and PBS in a proportion that allowed each sample to have an equivalent maximum concentration of protein. The volume of lysate in each sample was made in relation to the concentration of protein in the least concentrated sample if 50µL lysate volume was used. This was determined using the following equation:

C = (Lv*Lcmin)/Dv

where lysate volume (Lv) = 50µL; desired volume (Dv) = 75µL; C = final concentration; Lc = lysate protein concentration; Lcmin = lowest lysate protein concentration

Name	Concentration	Manufacturer
Glycerol	20%	ThermoFisher – G/P460/53
Tris pH6.8	100mM	CIMR Core Team
Sodium dodecyl sulphate (SDS)	140mM	ThermoFisher – S/P530/53
Dithiothreitol (DTT)	200mM	ThermoFisher – R0861
Bromophenol Blue	0.04%	VWR – 97061-690

Table 10 - **3x DTT SDS-Sample Buffer formulation**

SDS-polyacrylamide gel electrophoresis (SDS-PAGE)

SDS-PAGE using the BioRad Mini-PROTEAN system was used to separate denatured proteins on a polyacrylamide gel based on their molecular weight. 10% polyacrylamide gels were cast for separation of proteins between 30-100kDa. For a 1mm-thick 10% polyacrylamide gel, a resolving buffer-acrylamide solution (**Table 11**) was poured between 1mm spacer BioRad glass plates placed in a casting frame to leave a ~2cm gap at the top of the plates, with a layer of isopropanol (Sigma-Aldrich – 190764) added to prevent the top of the gel from drying. After the gel had set, the isopropanol was discarded, and the top of the gel was washed several times with H_2O. A stacking buffer-acrylamide solution (**Table 12**) was then poured onto the set resolving gel to fill the glass plates, and a 10-well comb was placed in the stacking gel to create the lanes for protein loading. After the gel was set, the plate was placed within the BioRad Electrode Assembly unit, and the Mini Tank filled to the appropriate height with SDS-Electrophoresis Buffer (**Table 13**). The well comb was then removed to form the protein loading lanes. 20µL See Blue Plus 2 Prestained protein ladder (ThermoFisher – LC5925) was added into the first lane, and 30µL of DTT SDS-Sample Buffer lysates that been boiled at 98^{o}C for 10mins were loaded, with blank lanes filled with 30µL 1x DTT SDS-Sample Buffer. The gel was then run at 100V for an appropriate time.

Name	Concentration	Manufacturer
Acrylamide Bis-Acrylamide Solution (Ratio 37.5:1)	34%	Severn Biotech – 20-2100-10
Resolving gel buffer	25%	See below
Ammonium persulfate	1.75mM	Sigma-Aldrich – A3678
Tetramethylethylenediamine (TEMED)	0.15%	Sigma-Aldrich –T9281
Resolving gel buffer (pH8.8)	-	-
Tris	1.5M	Sigma-Aldrich – T1503
Sodium dodecyl sulphate (SDS)	0.4%	ThermoFisher – S/P530/53

Table 11 - **10% polyacrylamide resolving gel formulation**

Name	Concentration	Manufacturer
Acrylamide Bis-Acrylamide Solution (Ratio 37.5:1)	13%	Severn Biotech – 20-2100-10
Resolving gel buffer	25%	See below
Ammonium persulfate	1.75mM	Sigma-Aldrich – A3678
Tetramethylethylenediamine (TEMED)	0.15%	Sigma-Aldrich –T9281
Stacking gel buffer (pH6.8)	-	-
Tris	0.5M	Sigma-Aldrich – T1503
Sodium dodecyl sulphate (SDS)	0.4%	ThermoFisher – S/P530/53

Table 12 - **Polyacrylamide stacking gel formulation**

Name	Concentration	Manufacturer
Tris	2.5mM	Sigma-Aldrich – T1503
Glycine	1.92mM	ThermoFisher – G/0800/60
Sodium dodecyl sulphate (SDS)	0.01%	ThermoFisher – S/P530/53

Table 13 - **1x SDS-electrophoresis buffer**

Western blotting and antibody labelling

After proteins were separated using SDS-PAGE, proteins were transferred onto polyvinylidene fluoride (PVDF) membranes. To do this, a transfer sandwich was constructed in a BioRad Mini Gel Holder Cassette consisting of: a foam pad, two pieces of 10cm x 8cm chromatography filter paper (Whatman – 3030-917), the polyacrylamide gel, a 9cm x 7cm PVDF membrane (Millipore – IPVH00010) pre-activated by incubation with methanol (ThermoFisher – M/4056/17), two pieces of 10cm x 8cm chromatography filter paper (Whatman – 3030-917), and a foam pad. The closed cassette was placed within the Mini Trans-Blot Central Core which was placed within the Mini Tank. The tank was filled using SDS Transfer Buffer (**Table 14**) and the system run at 100V for 75mins. The membrane was then blocked using 5% skimmed milk (Marvel) in TBS-Tween (**Table 15**) for 1hr at room temperature before being incubated in primary antibody (**Table 16**) diluted in 5% skimmed milk overnight at 4°C. The

following day, the membrane was washed three times for 5mins in TBS-Tween (**Table 15**) before the addition of secondary antibody (**Table 16**) diluted in 5% skimmed milk for 1hr at room temperature. After this time, the membrane was washed 3 times for 5mins in TBS-Tween and placed onto 2mL aliquots of pre-mixed SuperSignal West Pico Chemiluminescent Substrate (ThermoFisher – 34578) on clingfilm for 5mins. The membrane was then gently blotted to remove excess liquid, wrapped in clingfilm, and placed in a Hypercasette (ThermoFisher – RPN11649) where it used expose Fuji Super RX X-Ray film (FUJIFILM – 4741019289) which was then developed.

Name	**Concentration**	**Manufacturer**
Tris	48mM	Sigma-Aldrich – T1503
Glycine	39mM	ThermoFisher – G/0800/60
Sodium dodecyl sulphate (SDS)	0.0375%	ThermoFisher – S/P530/53
Methanol	20%	ThermoFisher – M/4056/17

Table 14 - **1x SDS-transfer buffer**

Name	**Concentration**	**Manufacturer**
10x Tris-buffer saline (TBS)	10%	See below
Polyoxyethylene-20 (Tween-20)	0.0001%	NBS Biologicals – TB0560
10x Tris-buffer saline (pH7.4)	-	-
NaCl	0.9%	Sigma-Aldrich –71387
Tris	10mM	Sigma-Aldrich – T1503

Table 15 - **TBS-Tween formulation**

Name	Antigen	Host	IgG Type	Dilution	Source/Reference
GAPDH (14C10)	Carboxy terminus of GAPDH	Rabbit	Rabbit monoclonal IgG	1:5000	Cell Signalling - 2118
Spastin	Amino acids 86-340 of M1 spastin	Rabbit	Rabbit polyclonal IgG	1:500	Allison et al. 2013
OLC1 (IST1)	hIST1-GST Fusion Protein (Proteintech Ag0721)	Rabbit	Rabbit polyclonal IgG	1:1000	Proteintech – 51002-1-AP
SNX1	GST-SNX1 Fusion Protein	Rabbit	Rabbit polyclonal IgG	1:1000	Seaman 2004
Donkey anti-rabbit peroxidase	Rabbit IgG	Donkey	-	1:150000	Sigma-Aldrich – SAB3700934

Table 16 - **Primary and secondary western blotting antibodies**

2.3.2 – Plasma membrane profiling

Cell surface biotinylation

The procedure of cell surface biotinylation is detailed by Zeng et al. 2009. This uses sodium periodate to oxidise glycosylated (sialylated) proteins to produce aldehyde groups and, in the presence of the catalyst Aniline, the compound aminooxy-biotin then forms stable oxime linkage hence biotinylating cell surface proteins. At 4°C, the sodium periodate and/or aminooxy-biotin are cell impermeable, hence allowing the procedure to specifically biotinylate cell surface proteins.

Firstly, the pre-made biotinylation mixture (**Table 17**) was activated by the addition of 4.2mL 10x Sodium Periodate (**Table 17**), with this active mixture kept at 4°C under foil and used within 10mins. Cells were washed twice with ice-cold PBS (Sigma-Aldrich – D8662), with this wash solution completely aspirated from the dish before continuing. The washed cells were then biotinylated by the addition of 6mL activated biotinylation mix to each dish which was placed on a rocker for 30mins at 4°C in the dark. During this incubation time, the lysis buffer with iodoacetamide was prepared (**Table 18**). After the biotinylation incubation, the reaction was quenched by the addition of 1.5mL 5mM glycerol (ThermoFisher – G/P460/53) dissolved in PBS (Sigma-Aldrich – D8662). The cells were then washed twice with ice-cold PBS (Sigma-Aldrich – D8662), with this removed completely after the second wash. 1mL of the lysis buffer was added to each dish, the cells scraped, and lysates were transferred to chilled Eppendorf tubes and kept on ice for 30mins. The lysates were then centrifuged

at 13000RCF at 4°C for 5mins with the supernatant kept. This process was repeated 3x and the final supernatant snap frozen in liquid nitrogen and stored at -80°C.

Name	Concentration	Manufacturer
Aminooxy-biotin	97µM	Biotium – 90113
Aniline (dissolved in PBS pH6.7)	0.095%	Acros Organics – 423425000
10x Sodium periodate (added last)	10%	See below
10x Sodium periodate dissolved in PBS (Sigma-Aldrich - D8662) pH6.7	10mM	ThermoFisher – 20504

Table 17 - **Biotinylation mixture formulation.** The mixture is made using PBS (Sigma-Aldrich – D8662), with the 10X sodium periodate added immediately before starting the biotinylation reaction.

Name	Concentration	Manufacturer
Tris	10mM	Sigma-Aldrich – T1503
Triton X-100	1.6%	ThermoFisher – 28314
NaCl	150mM	Sigma-Aldrich – 71387
Roche Protease Inhibitor Cocktail Tablet	1 per 10mL	Sigma-Aldrich - COEDTAF-RO Roche
Iodoacetamide	5µM	Sigma-Aldrich – I1149

Table 18 - **Biotinylation reaction lysis buffer formulation.**

Biotinylated protein pulldown and digestion (Performed by Weekes Lab)

Streptavidin beads (ThermoFisher – 65601) were prepared by removing 500µL beads and pipetting into a 10mL Polyprep column (BioRad – 731-1550) placed on a vacuum manifold and washing 4 times with 800µL ice-cold 1% lysis buffer (as **Table 18**, but with 1% Triton-X100). Once washed, 600µL 1% lysis buffer was added to the beads. Previously biotinylated lysates were thawed on ice and protein pulldown was performed by mixing 95µL of resuspended streptavidin bead solution to each lysate and rotating the solution at 4°C for 75mins. After the elapsed time, the beads were washed. To do this, the entire contents of the bead-incubated lysates were transferred to new Polyprep vacuum columns (with 500µL 1% lysis buffer used to wash the bead incubation tube and added to the column to ensure complete transfer) and washed using 9 sequential wash/incubation steps (**Table 19**).

Tryptic digest was then performed. The washed beads were resuspended in 600µL HPLC-grade H_2O (WVR – 23595.328) and transferred to a spin column in a microcentrifuge tube, ensuring that all resuspended beads were transferred to the column. Samples were then centrifuged at 2000RCF for 1min, the spin column transferred to a new microcentrifuge tube and the bottom of spin column screwed on and digested by the addition of 35µL Trypsin-HEPES solution (0.8% Trypsin (ThermoFisher

– 90305)) in 200mM HEPES (Sigma-Aldrich – H0887) dissolved in PBS (Sigma-Aldrich – D8537)) and shook at 37°C for 3hrs. The caps were then removed, and the columns centrifuged at 2000RCF for 1min to obtain the digested samples.

Wash Step	**Solution Component**	**Concentration**	**Manufacturer**	**Incubation Time (if applicable)**
1. 4 washes in 1% lysate buffer	1% lysate buffer	See **Table 18**	See **Table 18**	NA
2. 4 washes in 1mL PBS-SDS-DTT solution	Solution made up in PBS (Sigma-Aldrich - D8537)			
	Dithiothreitol	*100mM*		*NA*
	Sodium dodecyl sulphate (SDS)	*0.5%*	*ThermoFisher – S/P530/53*	*NA*
3. Incubation with 500µL PBS-SDS-DTT solution				20mins RT
4. 8 washes with 1.5mL urea solution	Solution made up in HPLC-grade H_2O (WVR – 23595.328)			
	Urea	*6M*	*CalBiochem – 9530*	*NA*
	Tris	*0.1M*	*Sigma-Aldrich – T1503*	*NA*
5. 1 wash with 10mL urea solution				
6. Incubation with 500µL urea solution with Iodoacetamide	Urea solution with iodoacetamide	Iodoacetamide concentration - 500µM	Sigma-Aldrich – I1149	20mins RT in dark
7. 2 washes with 1.5mL urea solution				
8. 3 washes with 1.5mL HPLC-grade H_2O (WVR – 23595.328)				
9. 1 wash with 10mL HPLC-grade H_2O (WVR – 23595.328)				

Table 19 - **Washing protocol of the streptavidin beads with bound biotinylated proteins**. 9 sequential steps are required for the washing of the streptavidin-biotinylated protein bead conjugates. Where solution formulations are required, they are noted underneath each washing step.

TMT labelling and SepPak peptide purification (Performed by Weekes Lab)

After the elution of the digested peptides, 10µL of 100% acetonitrile (AcN; Acros Organics – 364311000) was added to each sample, followed by incubation for 1hr at room temperature with 6µL of TMT reagent (ThermoFisher – 90111 and A34807) resuspended in 100% AcN, with different TMT labels added to each sample. After the TMT labels had bound the peptides, a 'Single Shot' sample was extracted by removing a 5µL aliquot from each sample. The Single Shot extraction allowed a quick determination of whether the TMT labelling had been successful and the relative abundances of the samples. The extracted samples were then mixed separately with 0.55µL 5% hydroxylamine (Sigma-Aldrich – 467804) made in 200mM HEPES (Sigma-Aldrich – H0887) pH8.5 to quench the TMT reaction, before being combined into a single tube. 1.9mL of 1% formic acid (ThermoFisher – 85178) was then added to acidify the combined samples and bring the AcN concentration below 3%. Excess salt was then removed using SepPak C18 columns (Waters – WAT05960), with columns equilibrated by washing 2 times with 1mL 70% AcN (Acros Organics – 364311000), followed by 3 washes with 1mL 1% formic acid (ThermoFisher – 85178). The peptide mixture was then added to the column to bind the peptides to the C18 resin. The column was then washed 3 times with 1% formic acid (ThermoFisher – 85178) to remove any salt residues, before being eluted in 700µL of buffer composed of 70% AcN (Acros Organics – 364311000) and 1% Formic acid (ThermoFisher – 85178). This eluate was then dried completely using a centrifugal evaporator, with the dried sample then resuspended in 10µL of a buffer composed of 4% AcN (Acros Organics – 364311000) and 5% formic acid (ThermoFisher – 85178) for mass spectrometry.

After the Single Shot data had been acquired, the remaining eluate from the individually labelled TMT samples were quenched by the addition of 3.3µL 5% hydroxylamine (Sigma-Aldrich – 467804), and the samples were combined, ensuring that the combined volume contained a roughly equal proportion of peptide from each sample. This combined sample was then dried, acidified, removed of salt contaminants using the SepPak C18 column as previously described, and dried completely before being fractionated.

Strong-cation-exchange (SCX) peptide fractionation (Performed by Weekes Lab)

SCX fractionation was used to separate the TMT-labelled peptides into subsets based on peptide hydrophobicity. To begin, the SCX resin filter was constructed by removing the filter from a P10 pipette tip and inserting it into a P200 tip and adding 150µL of Polysulfoethyl A resin (The Nest Group – BMSE2003). The tip was then washed and equilibrated by using 800µL SCX Buffer A, 400µL SCX Buffer B, and finally 1.6mL SCX Buffer A again, with the key difference in the buffers being their concentration

of KCl (**Table 20**). The dried peptide sample was then resuspended in 400µL SCX Buffer A and added to the SCX filter tip, with run through collected in a microcentrifuge tube labelled 0, with all peptides binding to the SCX resin. The tip was then washed with 150µL '0' buffer into the same tube (**Table 21**). The tip was then moved to another microcentrifuge tube, the '10' wash buffer applied to elute the first fraction, and eluate collected, with this process repeated using the different wash buffers until all fractions had been collected, with the '150' buffer eluting all remaining peptides. When all fractions had been collected, the peptides were dried completely using a centrifugal evaporator. To remove high salt concentrations, dried fractionated peptides had to be washed before being loaded into the mass spectrometer. This was done using an identical method to the SepPak method described above.

Name	**Concentration**	**Manufacturer**
SCX Buffer A (pH2.8)		
Acetonitrile (AcN)	30%	Acros Organics – 364311000
Potassium phosphate	7mM	Sigma-Aldrich – P0662
SCX Buffer B (pH2.8)		
Acetonitrile (AcN)	30%	Acros Organics – 364311000
Potassium phosphate	7mM	Sigma-Aldrich – P0662
Potassium chloride	350mM	Sigma-Aldrich – P9541

Table 20 - **SCX buffer formulations.** All buffers were made in HPLC-grade H_2O (WVR – 23595.328)

Wash Buffer Name	**Proportion of SCX Buffer B**	**Proportion of SCX Buffer A**
Wash Buffer '0'	0%	100%
Wash Buffer '10'	2.9%	97.1%
Wash Buffer '25'	7.1%	92.9%
Wash Buffer '40'	11.4%	88.6%
Wash Buffer '60'	17.1%	82.9%
Wash Buffer '90'	25.7%	74.3%
Wash Buffer '150'	42.9%	57.1%

Table 21 - **SCX wash buffer formulations.**

Mass spectrometry (Performed by CIMR Proteomics Core)

Resuspended peptides were analysed by Liquid Chromatography Tandem Mass Spectrometry (LC-MS/MS) using a Thermo Orbitrap Fusion Lumos (ThermoFisher) coupled to an RSLC3000 nanoUPLC (ThermoFisher). Peptides were fractionated using a 75cm Acclaim PepMap column (ThermoFisher) with solvent A (0.1% formic acid) and B (80% MeCN, 0.1% formic acid) at a flow rate of 250nl/min. Single shot analyses used a gradient rising from 3-37% B by 180mins, and SCX fractions used 3-37% B by 120mins with MS spectra acquired using an MS3-TMT strategy. MS2 spectra were obtained by CID

fragmentation (normalized collision energy (NCE) 35) with ion trap scanning in turbo mode. MS3 acquisition used Synchronous Precursor Selection of the top six MS2 ions for HCD fragmentation (NCE 65). Fragments were scanned in the Orbitrap at 60,000 resolution and were not accumulated for all parallelisable time. The entire MS/MS/MS cycle had a target time of 3s with dynamic exclusion for 70s. The six SCX fractions and the Single Shot data were processed together in the final data set using a Sequest-based-in-house software pipeline, using the mouse Uniprot database (January 2017).

2.4 – Microscopy

2.4.1 – List of microscopes used

Microscope Base Unit	Vendor	Imaging Type	Light Source	Fixed/Live	Objective	Camera	Other
Axio Observer Z1	Zeiss	Widefield	Metal Halide	Fixed + Live	Plan-Apochromat 100x/1.40 Oil DIC M27; Plan-Apochromat 63x/1.40 Oil DIC	sCMOS ORCA Flash 4 v2 (1024x1024)	Definite Focus.2
LSM 780	Zeiss	Laser Scanning Confocal	Laser	Live	Plan-Apochromat 63x/1.4 Oil DIC M27	QUASAR GaAsP Array	Definite Focus.2
LSM 880	Zeiss	Laser Scanning Confocal	Laser	Fixed + Live	Plan-Apochromat 63x/1.40 Oil DIC M27	PMT Detectors	Definite Focus.2
LSM 880	Zeiss	Airyscan	Laser	Fixed + Live	Plan-Apochromat 63x/1.4 NA Oil DIC M27	Zeiss Airyscan FAST GaAsP Detectors	Definite Focus.2
Axio Observer Z1	Zeiss	Spinning Disk Confocal	Laser	Live	Plan-Apochromat 63x/1.40 Oil DIC	Andor iXON Ultra 897 EM-CCD (512x512)	CSU-X1A Yokogawa Scanhead; 1.6x Tubelens Optivar
Nikon Eclipse Ti	Nikon	Spinning Disk Confocal	Laser	Live	Apochromat CFI Apo SR TIRF 100X/1.49NA Oil	3x Andor iXON Ultra 897 EM-CCD (512 × 512)	CAIRN MultiCam Beam-splitter; Perfect Focus; CSU-X1A Yokogawa Scanhead
Thermo EVosFL	Thermo Fisher	Widefield	LED Illumination	Fixed + Live	AMG LPLAN 10x/0.25; AMG LPLAN 20x/0.4; AMG LPLANFl 40x/0.65	Sony ICX285AL CCD (1360x1024)	-

Table 22 - **List of microscopes used.**

2.4.2 – General microscopy techniques

Cell plating

For fixed cell microscopy, cells were plated on 10mm coverslips within a 6-well plate. For super resolution microscopy, cells were grown on high precision MatTek glass bottom dishes (MatTek – P35G-0.170-14-C). For live cell microscopy, cells were plated on MatTek glass bottom dishes (MatTek – Part # P35G-1.5-20-C). Typically dishes and coverslips were left uncoated, however for imaging the ER, coverglasses were coated with 500µg/mL Matrigel (Corning – 354277). All cells were seeded to achieve a ~60% confluency at the time of imaging.

Fixation and permeabilisation

Cells were washed once with PBS (Sigma-Aldrich – D8537) before the addition of 3.6% paraformaldehyde (PFA; VWR – 20909.290) made in PBS (Sigma-Aldrich – D8537) per well for 20mins at room temperature. After 20mins, the PFA was aspirated and the cells were washed with PBS three times. For the fixed ER imaging, the 3.6% PFA was supplemented with 0.1% glutaraldehyde (Sigma-Aldrich – G5882), with the fixation and PBS washes performed with simultaneous aspiration and solution addition to ensure cells were kept moist. After fixation, cells to-be-permeabilised were treated with 0.1% Triton-X100 (ThermoFisher – 28314) for 4mins at room temperature, and the cells washed three times with PBS (Sigma-Aldrich – D8537).

Immunostaining

For cells grown on coverslips, after permeabilisation coverslips were blocked by the transferring the coverslip cell-side-down onto Parafilm (Sigma-Aldrich – P7793) dotted with 100µL FBS blocking solution (10% FBS (Sigma-Aldrich – F7524)) in PBS (Sigma-Aldrich – D8537) for 1hr at room temperature. Coverslips were then transferred to a new 100µL dot of primary antibody diluted in FBS blocking buffer (**Table 23**) and incubated for 1hr at room temperature. The coverslips were then washed by immersing the coverslip twice in FBS blocking solution, twice in PBS (Sigma-Aldrich – D8537) and twice in H_2O, with the process repeated 6 times. The coverslips were then placed cell-side-down onto a 100µL dot of secondary antibody (**Table 23**) diluted in FBS blocking buffer for 1hr at room temperature. The coverslips were then washed as before, and mounted cell-side-down onto microscope slides dotted with ProLong Gold Antifade mountant (ThermoFisher – P36930/P36936). For cells grown in MatTek dishes, cells were blocked, treated with primary antibody, washed and

treated with secondary antibody as above, but with a sufficient volume added to the dish to cover the embedded glass slide during each stage. Cells were then imaged in PBS (Sigma-Aldrich – D8537).

Name	Antigen	Host	IgG Type	Dilution	Source/Reference
OLC1 (IST1)	hIST1-GST Fusion Protein (Proteintech Ag0721)	Rabbit	Rabbit monoclonal IgG	1:100	Proteintech – 51002-1-AP
A-tubulin	Sarkosyl-resistant filaments from Strongylcentrotus purpuratus sperm axonemes	Mouse	Mouse monoclonal IgG1	1:2000	Sigma-Aldrich – T5168
Goat anti-rabbit Alexa Fluor 405	Rabbit IgG	Goat	NA	1:300	ThermoFisher – A-31556
Donkey anti-mouse Alexa Fluor 647	Mouse IgG	Donkey	NA	1:300	ThermoFisher – A-31571

Table 23 - **List of primary and secondary antibodies used for immunofluorescence**

2.4.3 – Live cell imaging methods

Retention using selective hooks (RUSH) assay

Two HeLa stable cell lines expressing the RUSH system were obtained from the Perez Lab (Curie Institute, Paris): TNFα-SBP-GFP KDEL-Streptavidin and GPI-SBP-GFP KDEL-Streptavidin. Upon receipt, cells were sorted by flow cytometry to enrich GFP-high populations to aid signal detection during live cell imaging.

For siRNA depletion experiments, cells were plated on MatTek dishes and in a 6-well plate for knockdown validation by lysis and western blotting. The following day, cells were transfected with siRNA. This protocol was similar to the one described above, but the transfection mixture was made using FBS-free growth media rather than Opti-MEM as Opti-MEM contains biotin that leads to the aberrant release of the reporter, and FBS blocks oligonucleotide-lipid complex formation. Once the oligonucleotide-lipid complex had formed, the mixture was combined with regular growth media for addition to the cells as in the standard protocol. The following day, cells were transfected with SiT-FusRed to highlight the Golgi, with the transfection method similar that previously described, but using FBS-free growth media rather than Opti-MEM. This mixture was then added directly onto the siRNA-

mixture already on the cells without washing the cells. 6hrs post transfection, the media on the cells was completely changed and replaced with 2mL normal growth media.

RUSH imaging was performed the following morning using a LSM780 confocal with an 63x objective, autofocus, heated stage, and CO_2 incubation (**Table 22**). A dish was loaded onto microscope and 10 healthy cells with bright reticular GFP signal and low background Golgi signal were selected and stored as positions. The imaging was set to move between the 10 positions and image in both channels before returning to the first position and repeating the process with no delay. ~200 cycles were imaged with ~40secs between each cycle. After several repeated cells to image the cell without biotin addition, the CO_2 incubator lid was removed and 2mL of 2x preheated 80µM biotin (Sigma-Aldrich – B4639) in growth media was added dropwise whilst the imaging was occurring, with the cycle and position number recorded of when the biotin was added. The CO_2 lid was then replaced, and the imaging allowed to continue. After the imaging was complete, a new dish was imaged using the same process. Per experimental repeat, 3 dishes of each treatment were imaged, with 10 cells imaged per dish. After imaging, both the imaged cells and the cells plated in the 6-well dish were lysed for knockdown validation. A handwritten ImageJ and Visual Basic for Applications Excel code was used to measure the secretion dynamics of the RUSH cargos.

RUSH assay positive control

During the RUSH assay, secretory transport was artificially disrupted by using H-89 dihydrochloride hydrate (Lee & Linstedt, 2000). Cells were plated at 350,000, 400,000 and 450,000 cells per dish with two sets of dishes per condition. The following day, media was replaced with 1mL fresh media. For cells with the H89 treatment, 1mL of 200µM (2x) H89 (Sigma-Aldrich – B1427) dissolved in fresh media was then added 30mins before imaging, with untreated cells having 1mL growth media added. After 30mins, the RUSH assay was performed as described above.

Live cell imaging of endosomal tubules

Cells expressing GFP-SNX1 were plated in triplicate on 25mm coverslips in a 6-well plate at 30,000 cells per well per experimental condition, with 1250,000 cells also plated in a separate 6-well plate for lysis to validate the efficacy of knockdown. The following day, cells were transfected with siRNAs as previously described. After 72hrs, cells were washed in PBS before being imaged using an AxioObserverZ1 inverted microscope fitted with a spinning disk scanhead (**Table 22**) for 3mins at 400ms per frame. Images were processed in ImageJ using a Single Pixel Filter and a mild Gaussian Blur

to help remove hot pixels. Concurrently with imaging, cells plated for knockdown verification were lysed and processed. The quantification of GFP-SNX1 endosomal tubule dynamics was done manually, with filenames coded using a random number generator to avoid measurement biases. Tubules were defined as stated in **Figure 3** of Chapter 3. Tubules were only counted if they were not present at the start or end of the acquired movie.

Live cell imaging of ER-endosome contacts

ER-endosome contacts were imaged in cells stably expressing GFP-SNX1 and transiently expressing RFP-KDEL. Cells for imaging were grown on MatTek dishes, with cells also plated in 6-well dishes for lysis and knockdown verification. The following day, cells were transfected as previously described, and after 48hrs, cells were transfected with RFP-KDEL as previously described. Cells were imaged in growth media 72hrs post-siRNA transfection. Imaging was performed using a Nikon Eclipse Ti microscope fitted with a spinning disk, a beamsplitter, and two cameras (**Table 22**). Imaging was performed at 400ms per frame simultaneously in both colours. The quantification of ER-endosome contacts was done manually, with filenames coded using a random number generator. 15 GFP-SNX1 tubules were identified in regions of the cell with resolvable ER tubules per cell, and five cells were measured per condition per experimental repeat. To avoid bias, the endosomal tubules were identified first without the ER channel visible, with this only displayed after the 15 endosomal tubules had been selected. ER-endosome contacts were defined as when the two organelles overlapped.

Live cell imaging of EB comets

Cells for imaging were plated in MatTek dishes and cells for knockdown verification were plated in 6-well plates as previously described. The following day, cells were treated with siRNAs as appropriate (e.g. not during the imaging of MEFs). 72hrs after plating, cells were transfected with EB3-mCherry as previous described. 6hrs after transfection, the media was completely removed from the cells, the cells washed twice with PBS (Sigma-Aldrich – D8537), and 2mL growth media was added to the cells. The cells were imaged 18hrs after their transfection, with the concurrent lysis of the cells designated for knockdown verification. Imaging was performed using an AxioObserverZ1 widefield microscope (**Table 22**), at 500ms per frame continuously for 90secs. A minimum of 15 cells were recorded for each experimental repeat per condition.

For image analysis, images were pre-processed with ImageJ before being analysed by particle tracking using Imaris 9.1.0 software (Bitplane, Inc.). In ImageJ, a region of interest was generated and

saved that only contained one successfully transfected cell. These processed images were then analysed using the 'Spots' tool of the Imaris software, with the parameters used described in **Table 24**. In Imaris, the region of interest selected was a rectangle within the ImageJ processed image. Spot filtering was typically performed using the automatic 'quality' metric, but this was adjusted if obvious errors occurred, and additional filters were applied to repress noise where necessary. Statistics were exported from Imaris, and track filtering and summary statistics generation was performed using a custom-made MATLAB script, with tracks filtered using the parameters listed in **Table 25**.

Imaris Spot Wizard Parameters	**Value (if applicable)**
Segment only a Region of Interest	TRUE
Track Spots (over Time)	TRUE
Estimated XY Diameter	0.65µm
Spot Filtering	Quality (automatic)
Tracking Method	Autoregressive Motion
Maximum Distance	0.75µm
Maximum Gap Size	3 frames

Table 24 - **Imaris spot detection parameters.**

MATLAB Filter Parameter	**Value**
Track Straightness	0.4 < **X** < 1
Track Duration	3.75secs < **X** < 45secs
Track Length	**X** > 2.5µm
Track Speed	0.05µm/s < **X** < 0.35µm/s
Track Speed Variation	0.1 < **X** < 0.85

Table 25 - **MATLAB track filtering parameters.**

2.5 – Data Processing

2.5.1 – Image processing

ImageJ software

Image processing was performed primarily using the Fiji distribution of image processing freeware ImageJ2 (Rueden et al. 2017; Schindelin et al. 2012). Raw microscopy formats (e.g. Zeiss's .czi or Nikon's .nd2 format) were batch pre-converted into 16-bit TIFF file format using a custom macro making use of the OME Bio-Format plugin for ImageJ. Images were then manipulated as appropriate, with common manipulations including: adjusting brightness/contrast, adding or removing channels, bleach correction (histogram matching), thresholding, adjusting look-up-tables, resizing, cropping, image transformations, pixel value subtraction/addition/multiplication/division, and application of gaussian blur and/or single pixel filters to supress high noise. Images were then either analysed for quantification or finalised into exported images or movies. For image quantification, the 'Measure' tool on regions of interest, and the 'Analyse Particles' tool for thresholded images was used extensively, with several custom-made macros designed to efficiently make use of these features. All 2D movies were created in ImageJ, making use of the Stack Tools such as 'Combine' to place different images in panels, 'Concatenate' to merge multiple image stacks, 'Insert' to add an image stack overlay into an existing image stack, 'Z-project' to merge multiple Z-positions into a single Z plane, and 'Time Stamper' and 'Text' and 'Draw' to overlay a time stamp and labels on the movie. To finalise and export movies or images, images were converted to RGB format and saved as either TIFF or AVI formats as appropriate.

Imaris 9.1.0 software

Imaris 9.1.0 (Bitplane, Inc.) software was used for particle tracking and for the visualisation and movie creation of 3D data sets. Images imported into Imaris were either raw microscopy format images, or pre-processed TIFF files. The 'Spots' tool was used extensively for measuring the dynamics of EB comets by particle tracking, the 'Surface' tool was used for 3D structure segmentation, and the 'Animation' tool was used for the generation of 3D movies.

Huygens Professional software

Huygens Professional (Scientific Volume Imaging) software was used for high-quality microscopy deconvolution, bleach correction, background elimination, Z-drift correction, and for judging Nyquist sampling rate for images taken with either widefield, spinning disk, or confocal microscopes. For each image to be deconvolved, the theoretical point-spread-function based on the microscope and fluorophore parameters was used, with the deconvolution parameters adjusted to produce a sharp but low artefact image.

2.5.2 – Data processing

Microsoft Excel 2016 software

Most of medium and small data handling and processing tasks was performed in Microsoft Excel 2016. This included the manual input of quantification data, the concatenation of multiple data sets, and the production of summary data using the Analysis ToolPak Excel add-in (e.g. averages, standard errors, and statistical tests). For more time-consuming repetitive tasks, several custom-built Visual Basic for Applications (VBA) macros were written to allow semi-automated data entry, manipulation, and output generation.

MATLAB R2018a

MATLAB software (MathWorks) was used for data handling and processing tasks involving large numerical datasets. This included the simultaneous extraction of data from multiple Microsoft worksheets, concatenation into single matrices, data filtering and manipulation, summary statistic generation, and data export. Custom-built MATLAB scripts were used for these tasks. MATLAB was used extensively in the analysis and filtering of cell surface proteomics data and EB comet data. MATLAB was also used for hierarchical clustering using a Euclidean pairwise distance method using the ‘clustergram’ function. All scripts were written using Notepad++ software.

DAVID analysis

Gene ontology enrichment analysis was performed using DAVID 6.8 (Huang et al. 2009b, 2009a). The input was set as a filtered gene list (e.g. by relative fold change), the background set to the entire list of proteins identified by the proteomics, and searches performed against a mouse background.

Statistical tests

Statistical tests such a paired and unpaired one and two tail t-tests were typically performed either in Microsoft Excel 2016 manually, using the Analysis ToolPak add-in, PRISM 7 software, or JMP 10 (SAS) statistical software. All critical alpha values were set at 0.05, with the Bonferroni correction or Benjamini-Hochberg correction used to adjust the alpha value when performing multiple t-tests.

2.5.3 – Data presentation

MATLAB R2018a

All graphs were produced using MATLAB R2018a software. This including the plotting of grouped and individual bar charts with standard errors, boxplots, XY scatter plots, line plots, cumulative line plots, histograms, pie charts, and heatmaps. XY scatter plots with ellipses were generated using the 'ellipsate' MATLAB plugin with standard deviation set to 1.

Adobe Illustrator and Photoshop CS6

Multipart figures were constructed using Adobe Illustrator CS6 (Adobe). This included the organisation of images and graphs into a complete figure, the addition of labels, inserts, and text onto images, the export of the complete figure into a graphics file that could be inserted into presentation or text document and imported PDF editing. Adobe Photoshop CS6 (Adobe) was used for the brightness/contrast editing of some images, as well as the generation of high-quality image crops to be used as zoom inserts.

Microsoft Word 2016

Thesis writing was prepared using Microsoft Word 2016.

Chapter 3 – The function of spastin in endosomal tubule fission

3.1 – Introduction

3.1.1 – The function of spastin in endocytic recycling

Endocytic recycling

As reviewed in the Introduction (Section 1.4 and Section 1.5), endocytic sorting is a fundamental cellular process that facilitates the separation of lysosomally degraded cargos from those that are recycled. Cargo that is destined for recycling is retrieved from degradation in the sorting endosome by the action of multimeric cargo sorting machineries such as retromer, retriever, the CCC complex, the WASH complex, and their associated accessory proteins (McNally and Cullen 2018). These retained cargos are sorted into tubules that undergo WASH and dynamin-dependent fission from the sorting endosome body. Fissioned endosomal tubules then traffic along microtubules to their target destinations which include the cell surface (e.g. the route of TfnR), or the TGN (e.g. the route of M6PR; Maxfield and McGraw 2004).

Spastin functions in endocytic recycling

Several HSP proteins have been associated with endosomal sorting and recycling, including the WASH component strumpellin and the membrane scission enzyme dynamin-2 (reviewed in Introduction Section 1.2.2). The first evidence for a potential endosomal function for spastin came through the observed colocalisation between endogenous spastin and GFP-tagged mutant VSP4-E235Q (Connell et al. 2009). This ATP hydrolysis-defective VPS4 functions as a dominant negative and prevents the disassembly of ESCRT complexes on endosomal membranes (Bishop and Woodman 2000; Stuchell-Brereton et al. 2007). The localisation between spastin and VPS4 therefore revealed that spastin could be dynamically recruited to endosomes, and that spastin was likely to have a relationship with ESCRT proteins.

Spastin was later shown to have an endocytic function. Allison et al. (2013) showed that depletion of spastin or spastin's ESCRT-III interaction partner IST1 in HeLa cells led to the aberrant

elongation of SNX1 and SNX4-positive endosomal tubules and the mistrafficking of TfnR to the lysosome. This endosomal elongation phenotype was also observed in spastin depleted zebrafish neurons and could not be rescued by the reintroduction of siRNA-resistant spastin mutants that were ATPase defective (K388R) or unable to bind to ESCRT-III binding partners via a mutation in spastin's MIT domain (F124D). Collectively, this suggested that spastin depletion or loss of function inhibited endosomal recycling by causing defective endosomal tubule fission that is typically driven by spastin's ESCRT-III interaction and microtubule remodelling activity. This proposed role for the spastin-IST1 interaction is consistent with the model of the ESCRT-III IST1-CHMP1B copolymer assembling on tubular membranes to mediate fission (reviewed in Introduction Section 1.3.3 and 1.5.3). However, the function of spastin or IST1 in endosomal tubule fission was not formally proven, nor was the nature of spastin's microtubule remodelling activity during endosomal tubule fission.

Endosomal tubule fission events have been shown to occur at sites of ER-endosome contact (Rowland et al. 2014). This provided a potential explanation of the somewhat puzzling observation that ER-localised M1 spastin was able to rescue the endosomal tubule elongation phenotype (Allison et al. 2013). Specifically, the necessity for ER-endosome contacts raised the hypothesis that M1 spastin may be located at these sites of ER-endosome contact to function in endosomal tubule fission. This however has not been tested.

3.1.2 – Experimental approach

Two outstanding questions surround the function of spastin in endocytic recycling: 1) do spastin and IST1 mediate endosomal tubule fission; and 2) what are the mechanisms by which spastin mediates its endosomal tubule function? In relation to this second question, areas of enquiry included investigating whether spastin or IST1 need to localise to endosomal tubules to mediate their fission, whether spastin participates in ER-mediated endosomal tubule fission, and whether tubule fission is driven by spastin's ATPase domain and its microtubule remodelling function.

In this results chapter, I investigate these questions using high spatial and temporal resolution fixed and live cell microscopy. This was performed to generate a large dataset of endosomal tubule fission dynamics in cells with and without spastin or IST1. In addition, microscopy was used to investigate whether spastin or IST1 localised to endosomal tubules, whether this localisation was associated with tubule constriction, and whether spastin's recruitment to endosomal tubules temporally and spatially correlated with endosomal tubule fission. Finally, two-colour live cell imaging was used to test whether spastin promotes ER-mediated endosomal tubule fission, and whether microtubule severing drives the fission of endosomal tubules. As each of these methods depend on

the extensive use of microscopy techniques, a brief introduction to the microscopy methods used is provided below.

3.1.3 – Microscopy approaches

The experimental aims generated two main microscopy problems. In the study of endosomal tubule dynamics, a challenge was that tubules form and undergo fission in timescale of seconds and are thin (<1µm). This therefore required that high spatial and temporal resolution microscopy was used to adequately sample endosomal tubule dynamics. In particular, the imaging rate must be high enough to differentiate between endosomal tubules with normal or abnormal fission dynamics. This was achieved using spinning disk microscopy (described below).

Secondly, in studies of the localisation of spastin on endosomal tubules in living cells, it was necessary to express a fluorescently tagged spastin construct. Due to the cytosolic localisation of M87 spastin and the punctate localisation of M1 spastin on the ER (Connell et al. 2009), M1 spastin was chosen for fluorescent tagging. However, overexpression of spastin can result in substantially altered microtubule dynamics due to the increased severing of microtubules (Roll-Mecak and Vale 2005). It was therefore required to express GFP-M1 spastin at a low level to avoid overexpression artefacts, but this led to dim spastin signal. This required microscopy with increased signal to noise capabilities to accurately observe M1 spastin's live cell dynamics, with this achieved by using Airyscan microscopy (detailed below).

Spinning disk microscopy

In spinning disk microscopy, two rapidly rotating discs are placed between the light source and the sample. The second of these discs contains thousands of 50µm confocal pinholes which allow multiple parallel light beams to illuminate the image plane near-simultaneously. This light is then passed back through the objective and the confocal pinholes of the disk and is detected using high sensitivity cameras. Once through the disk, the light can be split using dichroic mirrors and sent to different cameras, meaning that multiple excited fluorophores with different spectral properties can be acquired simultaneously (**Figure 1A**).

The key advantage of this method is that it allows confocal sampling of the entire field of view near-simultaneously. This differs from the raster scanning method employed in conventional confocal microscopy. As the imaging plane is illuminated in millisecond timescales, this imaging modality can achieve speeds of up to 1000 frames per second whilst simultaneously blocking out-of-focus light from

other axial planes. This makes this methodology a suitable tool for imaging the growth and fission of endosomal tubules on the second timescale range.

Airyscan microscopy

Despite the benefits of confocal microscopy in achieving axial image resolution, the presence of a pinhole also limits the amount of light that reaches the detector, ultimately resulting in dim signal even for bright fluorophores. The pinhole can be opened to increase the proportion of light received by the detector, but only at the expense of axial image resolution. Airyscan microscopy circumvents this problem by removing the physical pinhole, allowing a much higher proportion of light emitted from each fluorophore to be captured (Korobchevskaya et al. 2017). The light is collected by a radial array of detectors, and computationally integrating and reassigning the signal from each detector to the central detector results in a well resolved bright image (**Figure 1B**).

The major benefit of this method over conventional confocal microscopy is that by removing the physical pinhole, a far greater proportion of the emitted light is collected. This allows even dim samples to be represented with a high signal to noise ratio. In addition, as the light collected contains more high spatial frequency information (represented in the angle of light emitted from a fluorophore), the image itself is of higher resolution compared to conventional confocal microscopy. This therefore makes it well suited to study the dim expression of GFP-tagged M1 with high resolution in both fixed and live cells.

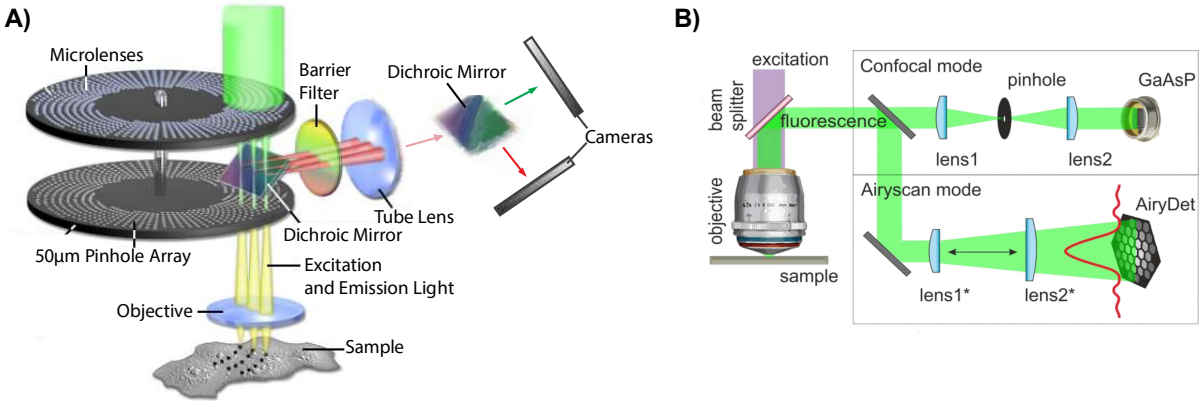

Figure 1 - **Spinning disk and Airyscan microscopy.** (A) The light pathway of the spinning disk microscopy used. Light from the laser source passes through a rotating disk that contains a radial array of microlenses. These separate the light into light beams which are then passed through a dichroic mirror and into a second disk which contains a radial array of pinholes which spins relative to the first disk. This light then passes through the objective and illuminates the sample causing fluorophores to emit light. This light then passes back through the objective onto the spinning disk. Out-of-focus light is blocked by the confocal pinholes, leaving only in-focus light to hit the dichroic mirror. This causes the light (which is a longer wavelength than the excitation light due to the

Stokes Shift) to be reflected towards the camera. A dichroic beam-splitter splits the light depending on its wavelength, allowing light emitted from different fluorophores with different emission wavelengths to be detected by each camera. The information from both cameras then represents two channels in the final image and can be aligned spatially. (B) The light path of the Airyscan microscope. The light from laser passes onto the sample via the objective and is deflected via a dichroic mirror towards the detectors. The top path represents the light path in confocal microscopy, with out-of-focus light being filtered by a confocal pinhole before being detected using a single photomultiplier detector. The bottom light path represents the Airyscan detection mode. The light is spread using mirrors of a variable distance and projected on a radial array of photomultiplier detectors. The strongest signal is detected in the centre of the array, but the light that would have been blocked by the confocal pinhole is also collected. The red line is a representation of the brightness of signal at relative positions of the detector. Whilst being the dimmest, the edges of the array receive information with the highest spatial information. As this area of light is detected rather than excluded by a pinhole, it means that once the signal information is reassigned, the image is both brighter and of a higher spatial resolution.

Image (A) adapted from http://zeiss-campus.magnet.fsu.edu/tutorials/spinningdisk/yokogawa/indexflash.html; Image (B) adapted from Korobchevskaya et al. (2017).

3.2 – Results

3.2.1 – Spastin is necessary for efficient fission of SNX1 tubules in MRC5 cells

Generation of GFP-SNX1 expressing cell lines

To determine whether spastin promotes endosomal tubule fission it was necessary to visualise SNX1 dynamics. Therefore, cell lines were retrovirally transduced to stably express N-terminally tagged GFP-SNX1 at low levels (see Materials and Methods – Section 2.2.3 for cloning methods). Human lung fibroblast MRC5 cells and money kidney fibroblast COS7 cells were chosen as an appropriate cell model. This was because are both relatively flat when adhered to glass, meaning that a large volume of the cell could be resolved in a thin axial plane making them suitable for imaging the ER. MRC5 cells are also known to have a relatively sparse microtubule network, making them suitable for imaging microtubule dynamics. Also transduced were immortalised embryonic fibroblasts derived from either wildtype or spastin^{N384K} mice that were heterozygous or homozygous for a mutation in spastin's ATPase domain that made the protein ATPase defective (Connell et al. 2016). These mouse embryonic fibroblasts (MEFs) are referred to as WT (spastin$^{WT/WT}$), HET (spastin$^{WT/N384K}$, and HOM (spastin$^{N384K/N384K}$).

In the mixed clonality populations used for experimentation, the abundance of GFP-SNX1 was below endogenous SNX1 abundance in all three MEF cell genotypes, equal to endogenous SNX1 abundance in COS7 cells, and somewhat increased above the abundance of endogenous SNX1 in the MRC5 cell line (**Figure 2**).

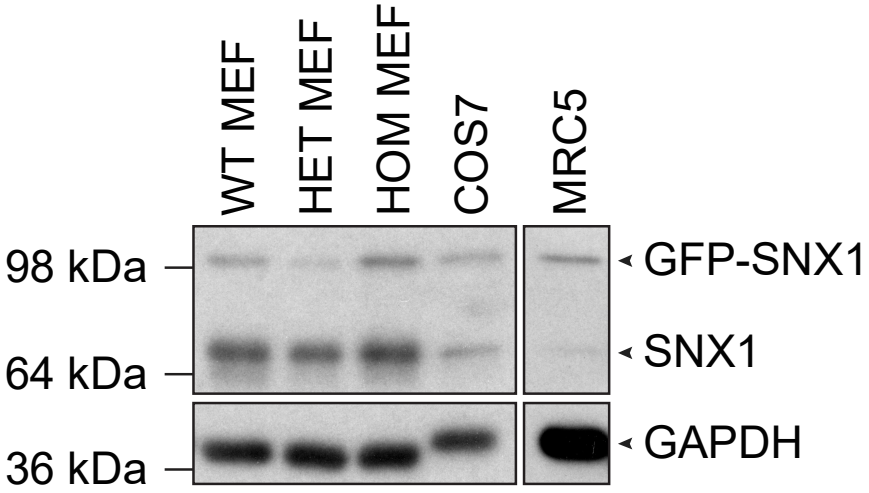

Figure 2 - **GFP-SNX1 expression levels in MEF, COS7 and MRC5 cells**. WT, HET, HOM MEFs, and COS7 and MRC5 cell lines were retrovirally transduced to express N-terminally tagged GFP-SNX1. Lysates from the clonal populations were collected and the relative abundance of GFP-SNX1 to endogenous SNX1 was determined by western blotting and probing with an antibody against SNX1.

Imaging and quantification of GFP-SNX1 dynamics in mock and spastin depleted MRC5 cells

Spinning disk live cell imaging of GFP-SNX1 dynamics was performed in mock treated MRC5 cells and MRC5 cells depleted of spastin using a pool of two different spastin siRNAs. This revealed a dramatic difference in the dynamics of GFP-SNX1 endosomal tubules in mock versus spastin siRNA depleted cells (**Movie 1** and **Figure 3A**). Tubules in spastin depleted cells appeared to grow for a longer period of time before fission, with more tubules fissioning along the length of the tubule or collapsing back into the parent endosome without fission. Growth rates however appeared unchanged (**Movie 1**).

To quantify these differences, the maximum length, total duration, and fate of each endosomal tubule was manually measured and recorded. An endosomal tubule was defined as a SNX1-positive tubular protrusion of >1µm emerging from a roughly spherical SNX1 labelled punctum. The definitions of maximum length, total duration and tubule fate are defined in the **Figure 3B** legend.

There was a statistically significant increase in the length of endosomal tubules between mock and spastin depleted cells (**Figure 3Bi**), confirming the effect observed in HeLa cells by Allison et al. (2013). Importantly, there was also a significant increase in the duration of endosomal tubules between mock and spastin depleted cells (**Figure 3Bii**), highly suggestive of defective fission in spastin depleted cells.

It was also possible to compare the tubule fates between mock and spastin depleted cells. For the efficient recycling of sorted endosomal cargo, it would be expected for tubules to fission at the endosome body to allow the largest possible amount of cargo to be recycled. However, spastin depleted cells showed a significant reduction in the percentage of tubules that underwent fission at the endosome body (**Figure 3Biii**). Instead there was a significantly increased proportion of tubules that underwent fission along the tubule or which collapsed back into the parent endosome, suggesting that inefficient or failed fission was more common in spastin depleted cells.

By plotting all duration against length data for mock and spastin siRNA treated cells and plotting the 1 standard deviation ellipse lines that contained 68% of all data points (**Figure 3C**), it can be observed that there was a correlation between tubule duration and length, and that the shape of both data sets was similar in their directionality. Ellipse directionality can be used to get an impression of tubule growth rates, but it should be noted that correlation coefficients were not calculated as tubule growth rates cannot be calculated directly from this data as maximum tubule length and tubule duration was recorded and plotted. This data therefore does not consider whether the tubule growth was continuous or intermittent, or even whether the tubule had other behaviours such as semi-collapsing before continued growth and fission. Overall the data showed that spastin depleted cells

were on average longer with a longer duration and suggested that mock treated and spastin depleted cells had similar rates of growth. This overall pattern also held approximately true when subdividing data by their fission fates, with all fates showing longer length tubules that persisted for longer in spastin depleted cells compared to mock cells (**Figure 3D**). This showed that all GFP-SNX1 tubules were affected by depletion of spastin irrespective of fission fate. For all experiments, the siRNA treatment was shown to strongly reduce the cellular abundance of spastin (**Figure 3E**).

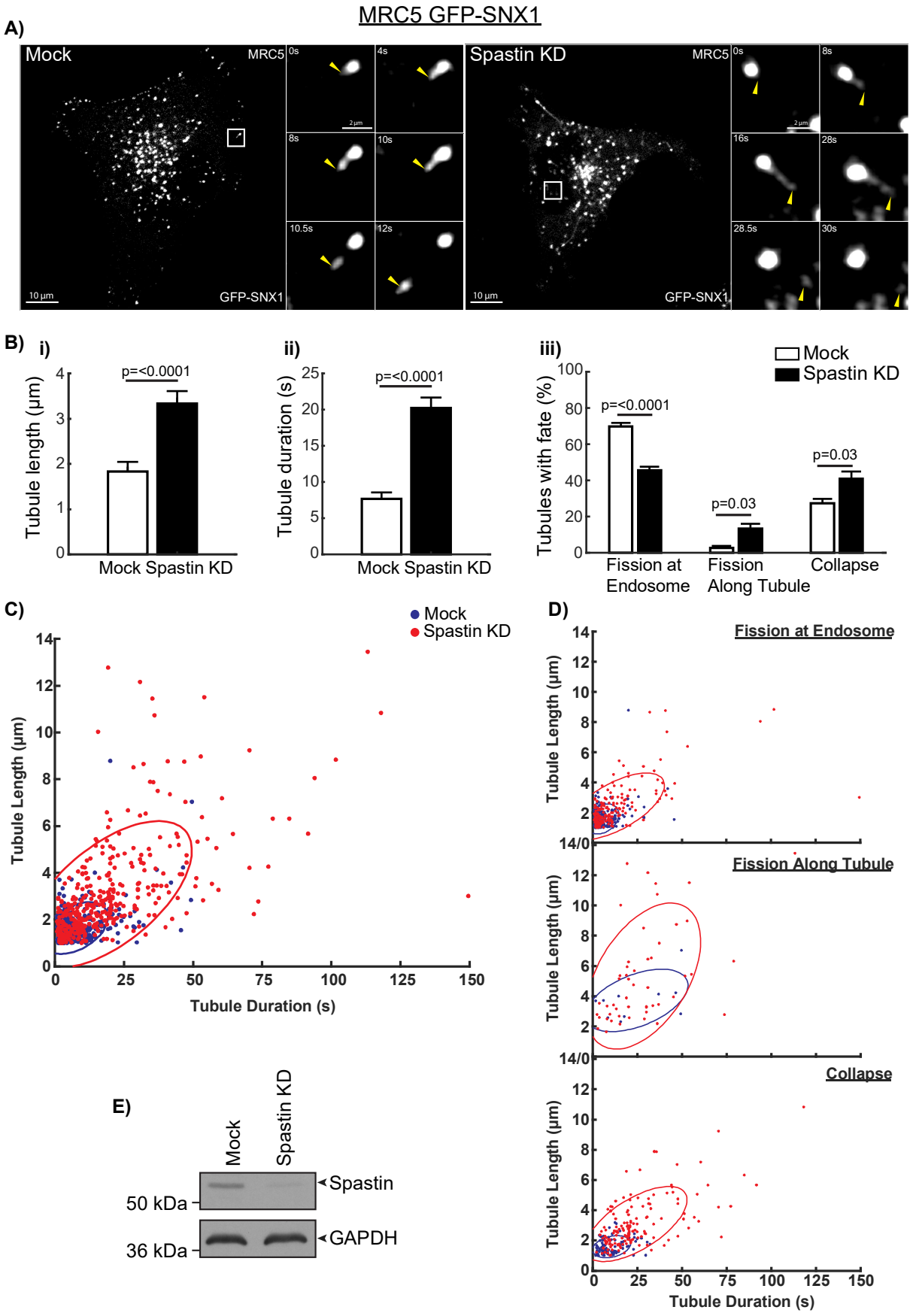
A)
MRC5 GFP-SNX1
Mock
MRC5
GFP-SNX1
10 µm
Spastin KD
B) i)
Tubule length (µm)
p=<0.0001
Mock Spastin KD
ii)
Tubule duration (s)
p=<0.0001
iii)
Tubules with fate (%)
Mock
Spastin KD
p=<0.0001
p=0.03
p=0.03
Fission at Endosome
Fission Along Tubule
Collapse
C)
Mock
Spastin KD
Tubule Length (µm)
Tubule Duration (s)
D)
Fission at Endosome
Fission Along Tubule
Collapse
E)
Mock
Spastin KD
Spastin
GAPDH
50 kDa
36 kDa

Figure 3 - Live cell microscopy of GFP-SNX1 shows spastin to be required for efficient endosomal tubule fission in MRC5 cells.

A) **Whole cell and zoom images of GFP-SNX1 tubule dynamics in mock and spastin siRNA depleted MRC5 cells** – MRC5 cells stably expressing GFP-SNX1 were treated with either mock or spastin siRNA and imaged using live-cell spinning disk microscopy to visualise endosomal tubule fission dynamics. Imaging was performed at 400ms per frame for 3 minutes. The main panels show an overview of the mock and spastin depleted cells, with the small panels showing a tubule fission sequence at the location highlighted by the box in the main panels. Time 0 corresponds to the frame in which the highlighted tubule first emerges. Yellow arrows show the tip of the growing or fissioned tubule. Of note is the difference in time between initial tubule growth and fission between the mock and spastin depleted cells. Scale bar in the overview and zoom images represents 10µm and 2µm respectively. This image accompanies **Movie 1**.

B) **Bar charts showing the quantification of GFP-SNX1 tubule dynamics in mock and spastin siRNA depleted MRC5 cells** – GFP-SNX1 tubule dynamics were manually quantified from the live-cell imaging of mock and spastin siRNA depleted stably expressing GFP-SNX1 MRC5 cells. Tubule length (i) was defined as the maximum distance between the tubule forming edge of the endosome body and the tip of the tubule before fission or collapse. Tubule duration (ii) was defined as the time between the first emergence of the tubule from the endosome body until the frame of fission or complete collapse back into the endosome body. Fission at the endosome (iii) was defined as a tubule fissioning from the endosome body less than 1.5µm from the near edge of the endosome body, fission along the tubule (iii) was any fission event that occurred more than 1.5µm from the near edge of the endosome body, and collapse (iii) was defined as a tubule that did not undergo fission but instead retracted back into the endosome body. 15 tubules were quantified per cell, with 5 cells per condition, and 6 experimental repeats performed (5 for the fission fate data). P values were generated by paired two-tail t-tests, with error bars indicating standard error of the mean.

C) **Scatter plot showing all length and duration data for GFP-SNX1 tubules quantified in mock and spastin siRNA depleted GFP-SNX1 stably expressing MRC5 cells** – The length (Y-axis) and duration (X-axis) data was plotted for each endosomal tubule quantified in all cells from all six experimental repeats in mock and spastin siRNA depleted cells. Blue and red dots show mock and spastin siRNA depleted data respectively. Ellipses contain 68% of each respective population (1 standard deviation). Mock N = 401, spastin KD N = 437.

D) **Scatter plots showing length and duration data for GFP-SNX1 tubules quantified in mock and spastin siRNA depleted GFP-SNX1 stably expressing MRC5 cells separated by tubule fate** – The length (Y-axis) and duration (X-axis) data was plotted for tubules that underwent fission at the endosome (top), along the tubule (middle), or collapsed (bottom) from all five experimental repeats in mock and spastin siRNA depleted cells. Blue and red dots show mock and spastin siRNA depleted data respectively. Ellipses contain 68% of each respective population (1 standard deviation). Fission at endosome mock N = 257, spastin KD N = 171, fission along tubule mock N = 10, spastin KD N = 50, collapse mock N = 101, spastin KD N = 154.

E) **Western blot showing spastin protein abundance in mock and spastin siRNA depleted MRC5 cells** – MRC5 cells treated with mock or spastin siRNA were lysed and proteins separated by SDS-PAGE, with proteins transferred onto PVDF membrane by western blotting. The abundance of spastin was detected by the use of a spastin antibody. Equal loading between lanes was verified by also blotting for the housekeeping protein GAPDH.

3.2.2 – Spastin is necessary for efficient fission of endosomal SNX1 tubules in COS7 cells

To verify that a depletion of spastin leads to inefficient SNX1 tubule fission in another cell type, the analogous experimental procedures were repeated using COS7 cells. As with MRC5 cells, spastin depleted COS7 cells showed a marked difference in GFP-SNX1 endosomal tubule dynamics compared to mock treated cells (**Movie 2** and **Figure 4A**). Spastin depleted cells subjectively appeared to have longer tubules that had a longer duration, with no clear difference in growth rate, and also appeared to have fewer tubule fission events occurring at the endosome body (**Movie 2** and **Figure 4A**).

The mean tubule length of spastin depleted cells was significantly increased (**Figure 4Bi**), although more subtly than in MRC5 cells, with spastin depleted COS7 tubules being on average 1µm shorter than their MRC5 equivalents. Similarly, GFP-SNX1 tubule duration was significantly increased in spastin depleted cells, but once again showed a subtler increase compared to the MRC5 cells, with tubule duration lasting on average 10s less than the MRC5 cells with the same treatment (**Figure 4Bii**). Furthermore, there were no statistically significant changes in the proportion of tubules that underwent each fission fate (**Figure 4Biii**), although there were clear trends of a reduced fission at the endosome body, increased fission along the tubule, and increased collapse events in spastin depleted cells.

The plot of duration by length data for all endosomal tubules illustrated the subtle but significant inefficient fission of endosomal tubules in spastin depleted COS7 cells (**Figure 4C**). The distribution of the data, marked by the ellipses, was similar to the MRC5 data in that it showed an equal increase in both tubule length and tubule duration in spastin depleted cells compared to mock cells, with the directionality of the ellipses suggesting similar rates of growth (**Figure 4C** and **Figure 4D**). However, a marked difference between the MRC5 and COS7 data is that in the COS7 spastin depleted data there were far fewer extreme values, with few tubules growing beyond 25s or more than 3µm. Despite the smaller effect, the COS7 data showed that spastin was required for efficient endosomal tubule fission, verifying the MRC5 data. For all experiments, the siRNA treatment was shown to strongly reduce the cellular abundance of spastin (**Figure 4E**).

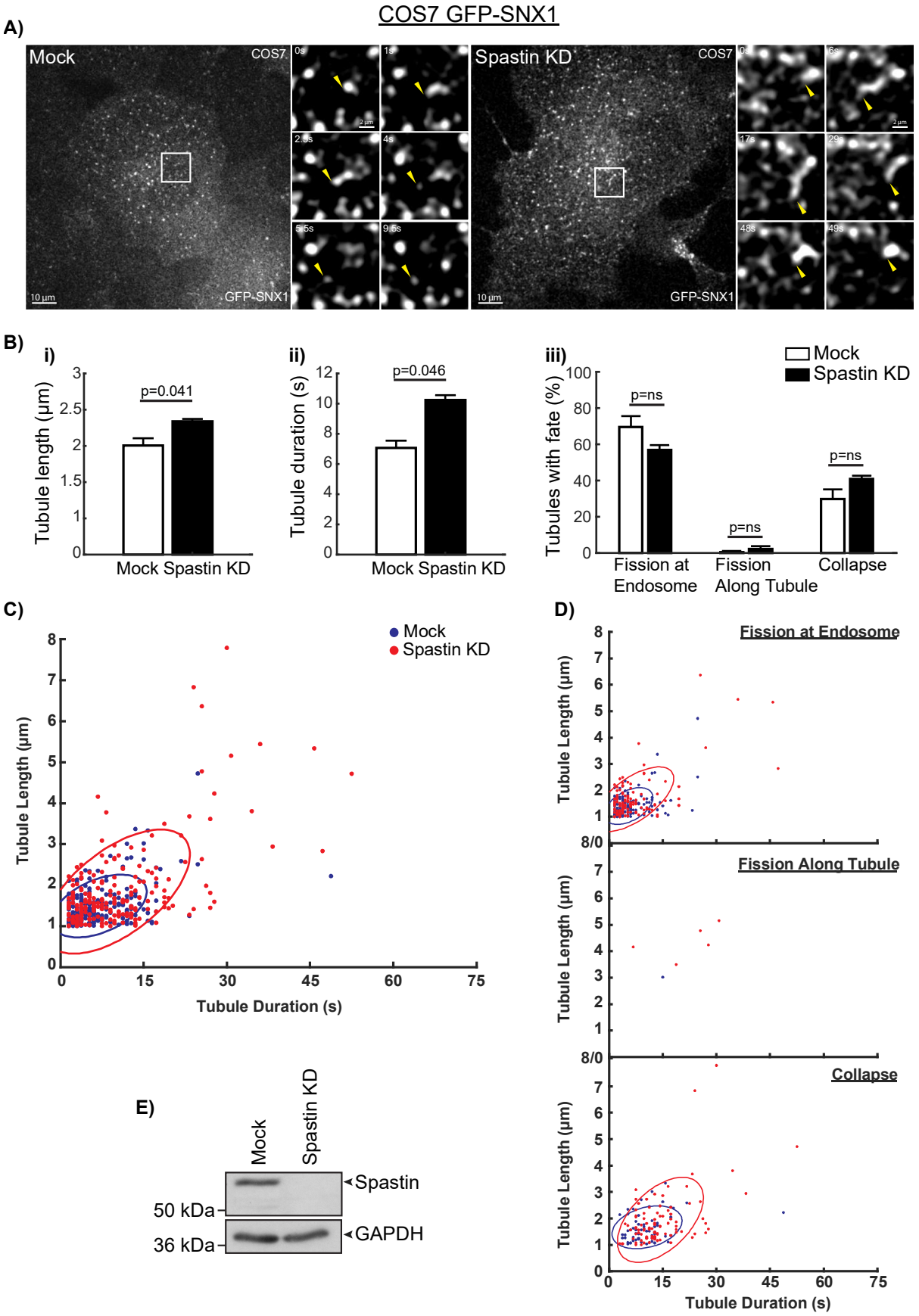
A)
COS7 GFP-SNX1
Mock
COS7
GFP-SNX1
Spastin KD
COS7
GFP-SNX1
B)
i)
Tubule length (µm)
p=0.041
Mock Spastin KD
ii)
Tubule duration (s)
p=0.046
Mock Spastin KD
iii)
Mock
Spastin KD
Tubules with fate (%)
p=ns
p=ns
p=ns
Fission at Endosome
Fission Along Tubule
Collapse
C)
Mock
Spastin KD
Tubule Length (µm)
Tubule Duration (s)
D)
Fission at Endosome
Fission Along Tubule
Collapse
Tubule Length (µm)
Tubule Duration (s)
E)
Mock
Spastin KD
Spastin
GAPDH
50 kDa
36 kDa

Figure 4 - Live cell microscopy of GFP-SNX1 shows spastin to be required for efficient endosomal tubule fission in COS7 cells.

A) **Whole cell and zoom images of GFP-SNX1 tubule dynamics in mock and spastin siRNA depleted COS7 cells** – COS7 cells stably expressing GFP-SNX1 were treated with either mock or spastin siRNA and imaged using live-cell spinning disk microscopy to visualise endosomal tubule fission dynamics. Imaging was performed at 400ms per frame for 3 minutes. The main panels show an overview of the mock and spastin depleted cells, with the small panels showing a tubule fission sequence in the mock cell and a tubule collapse sequence in the spastin depleted cell, both at the location highlighted by the box in the main panels. Time 0 corresponds to the frame in which the highlighted tubule first emerges. Yellow arrows show the tip of the growing, collapsing, or fissioned tubule. Of note is the difference in time between initial tubule growth and fission and tubule grown and collapse between the mock and spastin depleted cells. Scale bar in the overview and zoom images represents 10µm and 2µm respectively. This image accompanies **Movie 2**.

B) **Bar charts showing the quantification of GFP-SNX1 tubule dynamics in mock and spastin siRNA depleted COS7 cells** – GFP-SNX1 tubule dynamics were manually quantified from the live-cell imaging of mock and spastin siRNA depleted stably expressing GFP-SNX1 COS7 cells. Definitions of quantifications of tubule length (i), duration (ii), and fates (iii) were as previously described in **Figure 3B**. 15 tubules were quantified per cell, with 5 cells per condition, and 3 experimental repeats performed. P values were generated by paired two-tail t-tests, with error bars indicating standard error of the mean.

C) **Scatter plot showing all length and duration data for GFP-SNX1 tubules quantified in mock and spastin siRNA depleted GFP-SNX1 stably expressing COS7 cells** – The length (Y-axis) and duration (X-axis) data was plotted for each endosomal tubule quantified in all cells from all three experimental repeats in mock and spastin siRNA depleted cells. Blue and red dots show mock and spastin siRNA depleted data respectively. Ellipses contain 68% of each respective population (1 standard deviation). Mock N = 210, spastin KD N = 225.

D) **Scatter plots showing length and duration data for GFP-SNX1 tubules quantified in mock and spastin siRNA depleted GFP-SNX1 stably expressing COS7 cells separated by tubule fate** – The length (Y-axis) and duration (X-axis) data was plotted for tubules that underwent fission at the endosome (top), along the tubule (middle), or collapsed (bottom) from all three experimental repeats in mock and spastin siRNA depleted cells. Blue and red dots show mock and spastin siRNA depleted data respectively. Ellipses contain 68% of each respective population (1 standard deviation). No ellipse was drawn for fission along tubule data due to low number of data points. Fission at endosome mock N = 148, spastin KD N = 128, fission along tubule mock N = 1, spastin KD N = 5, collapse mock N = 61, spastin KD N = 92.

E) **Western blot showing spastin protein abundance in mock and spastin siRNA depleted COS7 cells** – COS7 cells treated with mock or spastin siRNA were lysed and proteins separated by SDS-PAGE, with proteins transferred onto PVDF membrane by western blotting. The abundance of spastin was detected by the use of a spastin antibody. Equal loading between lanes was verified by also blotting for the housekeeping protein GAPDH.

3.2.3 – Spastin's ESCRT-III binding partner IST1 is necessary for efficient fission of endosomal SNX1 tubules in MRC5 cells

Allison et al. (2013) showed that depletion of IST1 causes increased endosomal tubulation, and that rescue of this phenotype required IST1's ability to bind to spastin. It was therefore investigated whether IST1 was also required for endosomal tubule fission.

When GFP-SNX1 MRC5 cells were depleted of IST1 using siRNA, IST1 depleted cells develop abnormally elongated endosomal tubules that had increased durations between formation and resolution, and often collapsed or underwent fission along the tubule length (**Movie 3** and **Figure 5A**). Quantifying this as previously described, tubule length and duration was significantly increased in the IST1 depleted cells **(Figure 5Bi** and **Figure 5Bii**). These effects however were not as large as those observed with spastin depletion in MRC5 cells. Interestingly, there were some further differences compared to the spastin data. As for spastin, there was a significant decrease in the proportion of endosomal tubules that underwent fission at the base of endosomal tubules and this was accompanied by a significant increase in the proportion of fission along the tubule events, however, unlike spastin, there was no increase in collapse events (**Figure 5Biii**).

The plots of duration against length data for mock and IST1 depletion GFP-SNX1 tubules showed no discernible differences in the rate of tubule growth as determined by the relative directionality of the 1 S.D. ellipses (**Figure 5C**). This was also seen when subdividing this data by fate (**Figure 5D**), with this data also showing that tubules that underwent fission at the endosome and fission along the tubule had longer length and durations in the IST1 depleted cells. This was also seen for tubules that collapsed, with the position of the ellipse showing that these tubules were relatively longer with a longer duration on average compared to their mock counterparts, despite there being no increase in the proportion of collapsed tubules between the two treatments overall. Altogether, these data appear similar to the spastin depletion data in MRC5 and COS7 cells, and therefore indicate that IST1 also functions in endosomal tubule fission. For all experiments, the siRNA treatment was shown to strongly reduce the cellular abundance of IST1 (**Figure 5E**).

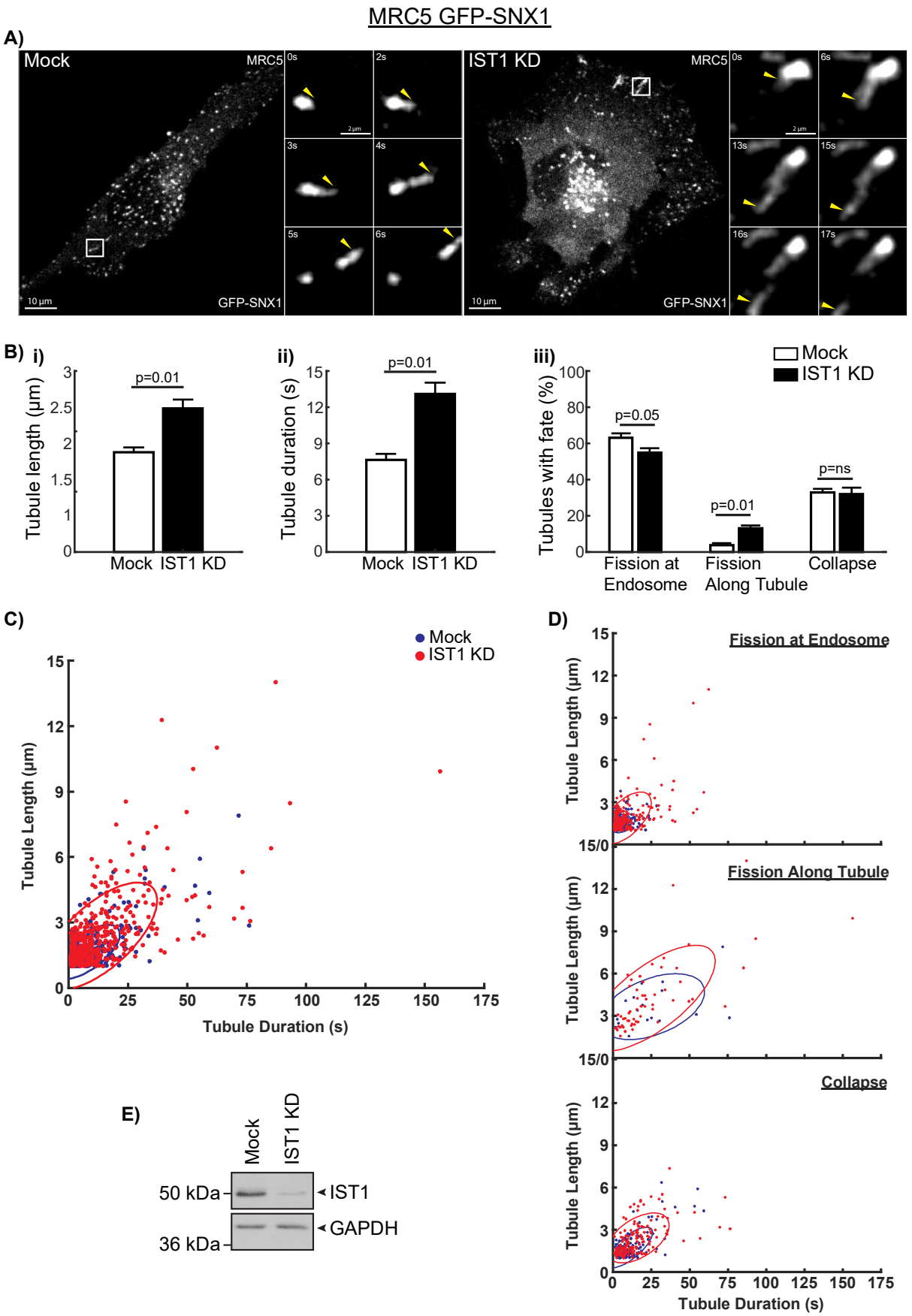
MRC5 GFP-SNX1
A)
Mock
MRC5
GFP-SNX1
IST1 KD
0s
2s
3s
4s
5s
6s
13s
15s
16s
17s
10 µm
B)
i)
Tubule length (µm)
p=0.01
Mock IST1 KD
ii)
Tubule duration (s)
p=0.01
iii)
Tubules with fate (%)
p=0.05
p=0.01
p=ns
Fission at Endosome
Fission Along Tubule
Collapse
C)
Tubule Length (µm)
Tubule Duration (s)
D)
Fission at Endosome
Fission Along Tubule
Collapse
E)
50 kDa
36 kDa
IST1
GAPDH

Figure 5 - Live cell microscopy of GFP-SNX1 shows the spastin interaction partner IST1 to be required for efficient endosomal tubule fission in MRC5 cells.

A) **Whole cell and zoom images of GFP-SNX1 tubule dynamics in mock and IST1 siRNA depleted MRC5 cells** – MRC5 cells stably expressing GFP-SNX1 were treated with either mock or IST1 siRNA and imaged using live-cell spinning disk microscopy to visualise endosomal tubule fission dynamics. Imaging was performed at 400ms per frame for 3 minutes. The main panels show an overview of the mock and IST1 depleted cells, with the small panels showing a tubule fission sequence at the location highlighted by the box in the main panels. Time 0 corresponds to the frame in which the highlighted tubule first emerges. Yellow arrows show the tip of the growing or fissioned tubule. Of note is the difference in time between initial tubule growth and fission between the mock and IST1 depleted cells. Scale bar in the overview and zoom images represents 10µm and 2µm respectively. This image accompanies **Movie 3**.

B) **Bar charts showing the quantification of GFP-SNX1 tubule dynamics in mock and IST1 siRNA depleted MRC5 cells** – GFP-SNX1 tubule dynamics were manually quantified from the live-cell imaging of mock and IST1 siRNA depleted stably expressing GFP-SNX1 MRC5 cells. Tubule length (i), duration (ii), and fates (iii) were measured as previously described. 15 tubules were quantified per cell, with 5 cells per condition, and 5 experimental repeats performed. P values were generated by paired two-tail t-tests, with error bars indicating standard error of the mean.

C) **Scatter plot showing all length and duration data for GFP-SNX1 tubules quantified in mock and IST1 siRNA depleted GFP-SNX1 stably expressing MRC5 cells** – The length (Y-axis) and duration (X-axis) data was plotted for each endosomal tubule quantified in all cells from all five experimental repeats in mock and IST1 siRNA depleted cells. Blue and red dots show mock and IST1 siRNA depleted data respectively. Ellipses contain 68% of each respective population (1 standard deviation). Mock N = 448, IST1 KD N = 450.

D) **Scatter plots showing length and duration data for GFP-SNX1 tubules quantified in mock and IST1 siRNA depleted GFP-SNX1 stably expressing MRC5 cells separated by tubule fate** – The length (Y-axis) and duration (X-axis) data was plotted for tubules that underwent fission at the endosome (top), along the tubule (middle), or collapsed (bottom) from all five experimental repeats in mock and IST1 siRNA depleted cells. Blue and red dots show mock and IST1 siRNA depleted data respectively. Ellipses contain 68% of each respective population (1 standard deviation). Fission at endosome mock N = 283, IST1 KD N = 247, fission along tubule mock N = 17, IST1 KD N = 59, collapse mock N = 148, IST1 KD N = 144.

E) **Western blot showing IST1 protein abundance in mock and IST1 siRNA depleted MRC5 cells** – MRC5 cells treated with mock or IST1 siRNA were lysed and proteins separated by SDS-PAGE, with proteins transferred onto PVDF membrane by western blotting. The abundance of IST1 was detected by the use of an IST1 antibody. Equal loading between lanes was verified by also blotting for the housekeeping protein GAPDH.

3.2.4 – Efficient SNX1 endosomal tubule fission requires spastin's ATPase activity

Spastin functions as an enzyme, with its C-terminal ATPase domain converting the release of energy from ATPase hydrolysis into a mechanical force that severs microtubules (Roll-Mecak and Vale 2008). It is possible that this function of microtubule severing may be relevant to the tubule fission mechanism, as endosomal tubules have an inherent relationship with the microtubule network (Granger et al. 2014). Furthermore, Allison et al. (2013) showed that ATPase defective spastin was unable to rescue the abnormal SNX1 endosomal tubule phenotype observed upon spastin depletion in HeLa cells. Thus, it was tested whether the ATPase domain of spastin was important for its function in endosomal tubule fission.

This was tested using WT, HET and HOM MEFs stably expressing GFP-SNX1 (detailed in Section 3.2.2). The HET and HOM MEF are heterozygous and homozygous respectively for a spastin^{N384K} mutation that renders the ATPase domain of spastin catalytically null (Connell et al. 2016). Live cell imaging revealed both HET and HOM spastin mutants to display GFP-SNX1 endosomal tubules that were longer and persisted for a longer duration than WT MEFs, with apparently more collapse and fission along the tubule events (**Movie 4** and **Figure 6A**). Quantification confirmed these observations. There was a significant increase in GFP-SNX1 tubule length in the HOM compared to the WT MEFs, with a similar although non-significant trend seen between the HET and WT MEFs (**Figure 6Bi**). Similarly, there was a significant increase in the total duration of tubules between the HOM and WT MEFs, with a similar non-significant trend seen when comparing the HET and WT MEFs (**Figure 6Bii**). For tubule fission fates, both HET and HOM MEFs had small but significant reductions in the proportion of GFP-SNX1 tubules that underwent fission at the endosome body (**Figure 6Biii**). This was accompanied by non-statistically significant increases in the proportion of fission events along the tubule and collapse events.

Duration against length plots showed a strong pattern of similarity between the HET and HOM MEFs, with a near identical overlap between the 1 S.D. ellipse plots, with both elongated compared to WT data (**Figure 6C**). The directionality of the ellipses suggested that the rate of tubule growth was similar between the three conditions, with a minor deviation towards slower growth in the spastin mutant MEFs. When segregating the data by fate, this pattern was mirrored closely when looking at tubules that underwent fission at the endosome body or collapse. However, there did appear to be some differences in ellipse directionality for tubules that underwent fission along the tubule, with tubules from wildtype animals appearing to have a much slower rate of growth than heterozygous or homozygous mutant MEFs (**Figure 6D**). It is worth noting however that out of the three fission fates, fission along the tubule had the fewest collective data points, potentially limiting the representativeness of this data.

In summary, MEFs expressing ATPase-defective spastin had impaired endosomal tubule fission, with the effects of the mutation roughly mirroring the effects of spastin depletion in MRC5 and COS7 cells, and IST1 depletion in MRC5 cells. Thus, spastin requires a functional ATPase domain to mediate endosomal tubule fission.

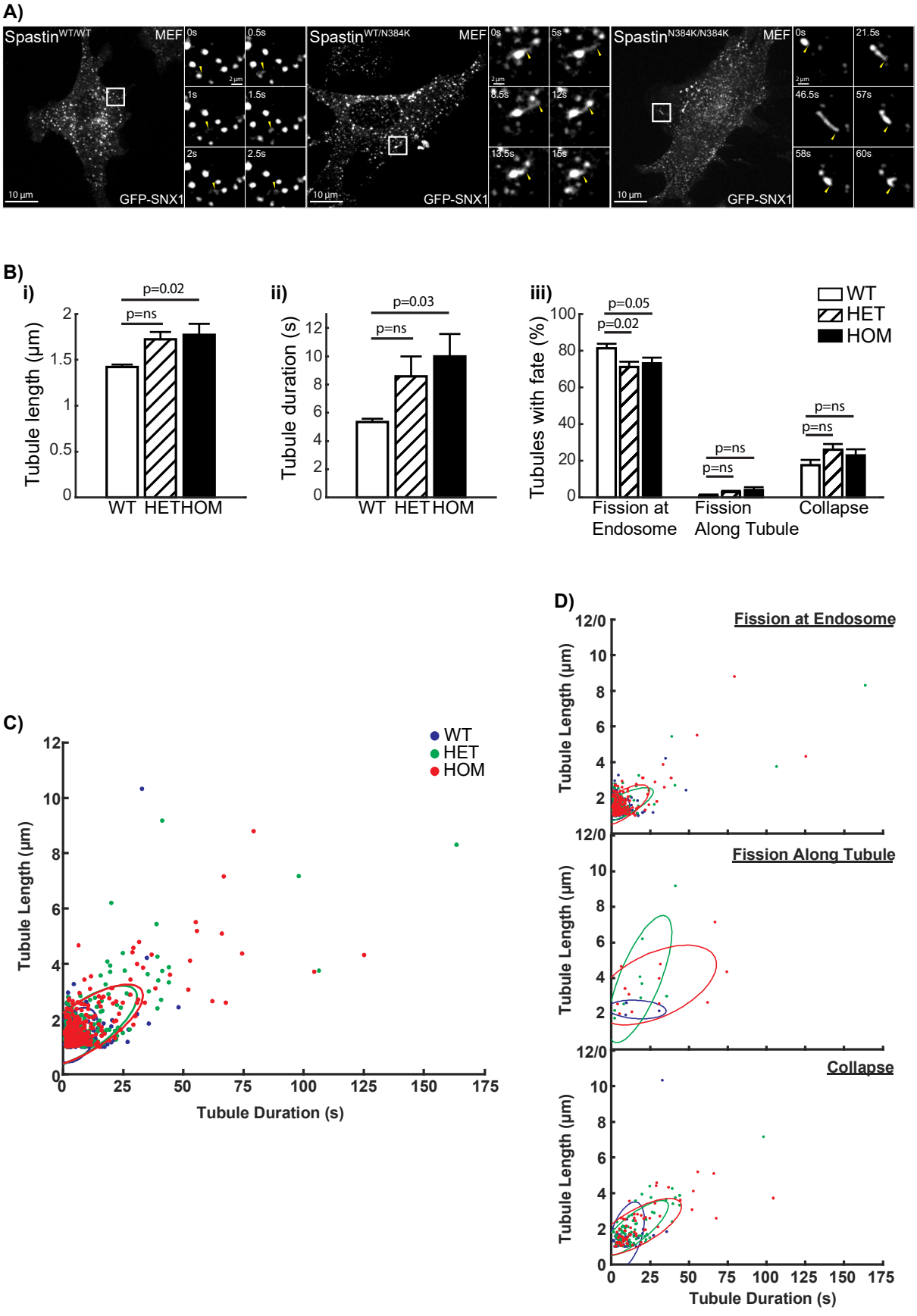
A)
Spastin WT/WT
MEF
GFP-SNX1
Spastin WT/N384K
Spastin N384K/N384K
10 µm
B)
i)
Tubule length (µm)
p=0.02
p=ns
WT HET HOM
ii)
Tubule duration (s)
p=0.03
p=ns
iii)
Tubules with fate (%)
p=0.05
p=0.02
WT
HET
HOM
Fission at Endosome
Fission Along Tubule
Collapse
C)
Tubule Length (µm)
Tubule Duration (s)
D)
Fission at Endosome
Fission Along Tubule
Collapse

Figure 6 - Live cell microscopy of GFP-SNX1 shows that spastin requires a functional ATPase domain for its role in efficient endosomal tubule fission in immortalised mouse embryonic fibroblasts (MEFs).

A) **Whole cell and zoom images of GFP-SNX1 tubule dynamics in spastin$^{WT/WT}$ (WT), spastin$^{WT/N384K}$ (HET), and spastin$^{N384K/N384K}$ (HOM) immortalised MEFs** – SV-40 immortalised MEFs stably expressing GFP-SNX1 were imaged using live-cell spinning disk microscopy to visualise endosomal tubule fission dynamics. Imaging was performed at 400ms per frame for 3 minutes. Each of the large images shows an overview of the spastin$^{WT/WT}$, spastin$^{WT/N384K}$, and spastin$^{N384K/N384K}$ cells, with the small panels showing a tubule fission event in the case of wildtype and homozygous mutant cells, and a tubule collapse event in the case of heterozygous mutant cells, at the location highlighted by the white box in the overview images. Time 0 corresponds to the frame in which the highlighted tubule first emerges. Yellow arrows show the tip of the growing, collapsing, or fissioned tubule. Of note is the difference in time between the tubule growth and fission or collapse between the wildtype and spastin mutants. Scale bars in the overview and zoom images represent 10µm and 2µm respectively. This image accompanies **Movie 4**.

B) **Bar charts showing the quantification of GFP-SNX1 tubule dynamics in spastin$^{WT/WT}$ (WT), spastin$^{WT/N384K}$ (HET), and spastin$^{N384K/N384K}$ (HOM) immortalised MEFs** – GFP-SNX1 tubule dynamics were manually quantified from the live-cell imaging of spastin wildtype (WT), heterozygous mutant (HET), and homozygous mutant (HOM) MEFS stably expressing GFP-SNX1. Tubule length (i), duration (ii), and fates (iii) were measured as previously described. 15 tubules were quantified per cell, with 5 cells per condition, and 4 experimental repeats performed per spastin mutant type. P values were generated by paired two-tail t-tests with Tukey-Kramer correction applied to correct for multiple testing with error bars indicating standard error of the mean.

C) **Scatter plot showing all length and duration data for GFP-SNX1 tubules quantified in spastin$^{WT/WT}$ (WT), spastin$^{WT/N384K}$ (HET), and spastin$^{N384K/N384K}$ (HOM) immortalised MEFs** – The length (Y-axis) and duration (X-axis) data was plotted for each endosomal tubule quantified in all cells from all four experimental repeats in wildtype, heterozygous, and homozygous spastin mutant GFP-SNX1 stably expressing immortalised MEFs. Blue, green, and red dots show wildtype, heterozygous, and homozygous spastin mutant data respectively. Ellipses contain 68% of each respective population (1 standard deviation). WT N = 300, HET N = 300, HOM N = 300.

D) **Scatter plot showing all length and duration data for GFP-SNX1 tubules quantified in spastin$^{WT/WT}$ (WT), spastin$^{WT/N384K}$ (HET), and spastin$^{N384K/N384K}$ (HOM) immortalised MEFs by tubule fate** – The length (Y-axis) and duration (X-axis) data was plotted for tubules that underwent fission at the endosome (top), along the tubule (middle), or collapsed (bottom) from all four experimental repeats in wildtype, heterozygous, and homozygous spastin mutant GFP-SNX1 stately expressing MEF cells. Blue, green, and red dots show wildtype, heterozygous, and homozygous spastin mutant data respectively. Ellipses contain 68% of each respective population (1 standard deviation). Fission at endosome WT = 244, HET = 213, HOM = 219, fission along tubule WT = 3, HET = 9, HOM = 12, collapse WT = 53, HET = 78, HOM = 69.

3.2.5 – Spastin and IST1 localise to SNX1 tubules at tubule constrictions, and spastin spatio-temporally localises to sites of endosomal tubule fission

Having established spastin and IST1 to be required for endosomal SNX1 tubule fission, it was investigated whether spastin and IST1 are located at sites of tubule fission. This was done by using both fixed and live cell imaging, with fixed cell imaging used to investigate the spatial localisation of spastin and its binding partner IST1 in relation to SNX1 tubules, and live cell imaging used to visualise whether spastin was spatio-temporally present at the location of endosomal tubule fission.

To achieve this, a new set of MRC5 cell lines were generated via retroviral transduction that stably expressed N-terminally tagged GFP-M1 spastin (the isoform of spastin that localises to the ER at steady state). A clonal GFP-M1 cell line was selected which expressed GFP-M1 spastin at very low levels to avoid artefacts of spastin overexpression (**Figure 7A**). From these clonal cells, retroviral transduction was used to produce a double stable cell line that expressed both GFP-M1 spastin and a mixed population of mCherry-SNX1. Imaging was performed on these cells using Airyscan microscopy, necessary given the low expression of the GFP-M1 spastin (reviewed in Section 3.1.3).

Fixed cell localisation of GFP-M1 spastin and IST1 on mCherry-SNX1 tubules

Four-colour fixed cell Airyscan microscopy showed a clear association between GFP-M1 spastin and endogenous IST1 on mCherry-SNX1 tubules that grew along α-tubulin labelled microtubules (**Movie 5** and **Figure 7B**). From the high spatial resolution imaging, GFP-M1 spastin was seen as constrictions along mCherry-SNX1 tubules (**Figure 7B**), with it clear in the 3D reconstruction that spastin was wrapping around the tubule at a constriction near the tubule base (**Movie 5**). At this point and also at other constrictions, IST1 was shown to be in close proximity to spastin, with the whole structure placed along a microtubule that was aligned in the direction of the endosomal tubule (**Figure 7B**). Thus, spastin and IST1 colocalise at likely sites of endosomal tubule fission.

Live cell visualisation of GFP-M1 spastin's localisation on mCherry-SNX1 tubules during tubule fission

To test whether spastin localises to pre-formed SNX1 constrictions or drives constriction formation, live cell microscopy was performed imaging GFP-M1 spastin and mCherry-SNX1 to visualise endosomal tubule fission events. Imaging was performed using Airyscan imaging at 2.88 second per frame in both colours simultaneously at a higher resolution than standard confocal microscopy.

The imaging showed that spastin was present at the spatial and temporal location of endosomal tubule fission (**Movie 6** and **Figure 7C**), with the highlighted tubule showing GFP-M1

spastin puncta localising to the tubule when and where it underwent fission. From the selected endosomal tubule, spastin did not appear to recruit to preformed constrictions, with spastin present near the endosome body during growth of the tubule. By looking at a change in the RGB intensity plots through the growth and fission path of the tubule, there appeared to be a direct correlation between an increase in GFP-M1 spastin and a decrease in mCherry-SNX1 signal, suggesting that an increase in spastin concentration along the tubule led to a tubule constriction. Interestingly however, the increase in spastin concentration and the constriction event did not lead to an immediate fission of the endosomal tubule, with spastin intensity not increasing, nor mCherry-SNX1 signal decreasing, for 5.5s after the formation of the constriction. This relationship between GFP-M1 spastin recruitment and mCherry-SNX1 tubule constriction and subsequent fission is representative of the appearance seen in multiple endosomal tubule fission events. This however was not quantified. Overall this suggests that spastin induces constriction formation and fission at constriction sites, but the recruitment of spastin does not perfectly temporally correlate to fission.

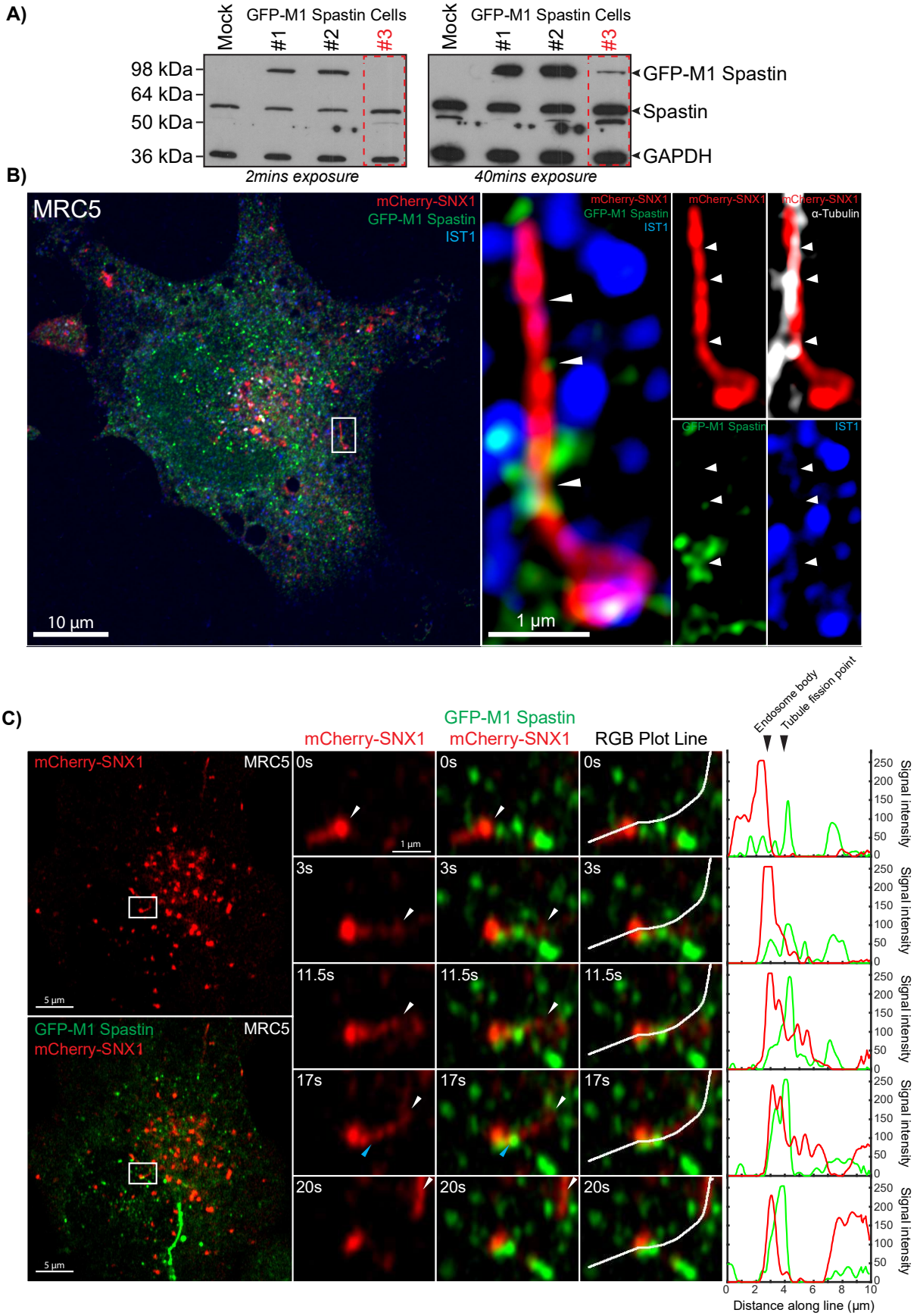
A)
Mock
GFP-M1 Spastin Cells
#1
#2
#3
98 kDa
64 kDa
50 kDa
36 kDa
2mins exposure
40mins exposure
GFP-M1 Spastin
Spastin
GAPDH
B)
MRC5
mCherry-SNX1
GFP-M1 Spastin
IST1
α-Tubulin
10 µm
1 µm
C)
mCherry-SNX1
GFP-M1 Spastin
RGB Plot Line
Endosome body
Tubule fission point
0s
3s
11.5s
17s
20s
5 µm
Signal intensity
Distance along line (µm)

Figure 7 - Fixed and live cell Airyscan imaging shows spastin to spatio-temporally localise to the location of endosomal tubule fission.

A) **Western blot showing GFP-M1 spastin protein abundance in stably expressing GFP-M1 spastin MRC5 cells** – Mock and GFP-M1 spastin stably expressing MRC5 cells were lysed, proteins separated by SDS-PAGE, and proteins transferred onto PVDF membrane by western blotting. The 6C6 spastin antibody was used to show the relative abundance of GFP-M1 spastin and endogenous isoforms of spastin, with the GFP-M1 spastin band inferred by the known sizes of GFP and M1 spastin. The red dashed box indicates the GFP-M1 spastin clone that was used for imaging. The left and right blots show a 2 minute and 40 minute exposure respectively.

B) **Fixed 4 colour Airyscan imaging of GFP-M1 spastin, mCherry-SNX1, IST1, and α-tubulin in MRC5 cells** – MRC5 cells stably expressing GFP-M1 spastin and mCherry-SNX1 were fixed and stained using IST1 and α-tubulin antibodies, before being imaged using Airyscan microscopy. The large overview panel shows mCherry-SNX1, GFP-M1 spastin, and IST1 channels, with α-tubulin not displayed. Smaller panels show a zoom of an mCherry-SNX1 endosomal tubule with a variety of colour channel combinations displayed. Scale bars on the overview and large zoom image represent 10µm and 1µm respectively. White arrows on the zoom images show locations of constrictions on the mCherry-SNX1 endosomal tubule. The white box on the overview image indicates the zoom region. This image accompanies **Movie 5**.

C) **Live cell 2 colour Airyscan imaging of GFP-M1 spastin and mCherry-SNX1 in MRC5 cells** – MRC5 cells stably expressing GFP-M1 spastin and mCherry-SNX1 were imaged using live cell Airyscan microscopy. Imaging was performed at 2.88 seconds per frame for 2 minutes in both channels simultaneously. The two large images on the left show an overview of the highlighted cell, with the top panel displaying only mCherry-SNX1 and the bottom panel displaying GFP-M1 spastin and mCherry-SNX1. The smaller central images show a time-lapse of an endosomal tubule fission event (by row), with the first column panels showing mCherry-SNX1 alone, the second column panels showing both GFP-M1 spastin and mCherry-SNX1, and the third column panels showing the RGB plot line used to measure the RGB intensity profile through the endosomal tubule during the tubule fission event. The final column shows RGB intensity (Y-axis) plots along the length of the RGB plot line (X-axis) through the tubule, with the red and green plot lines indicating the intensity of the mCherry-SNX1 and GFP-M1 spastin signal along the length of the line respectively. Black arrows on the RGB plots indicate the location of the endosome body and the tubule fission point along the RGB line. White arrows on the zoom panels show the tip of the endosomal tubule. White boxes on the overview panels show the location of the zoom panels. Scale bars of the overview and zoom panels represent 5µm and 1µm respectively. This image accompanies **Movie 6**.

3.2.6 – The function of spastin in SNX1 tubule fission is not related to the formation of ER-endosome contacts

ER-endosome contacts are important for endosomal tubule fission (Rowland et al. 2014). Spastin is able to associate with both ER and endosome membranes, with the hydrophobic domain of M1 spastin being required to localise it to the ER (Connell et al. 2009), while the MIT domain allows it to localise to endosomal membranes via an interaction with IST1 (Allison et al. 2013). It is therefore possible that spastin may function in the formation of these contacts, with a potential reason for impaired endosomal tubule fission upon spastin depletion being the inefficient formation of endosome-ER contacts.

ER-endosomal tubule contacts form in fixed cells despite spastin depletion

Fixed and live cell imaging was used to investigate the function of endosomal SNX1 tubules in relation to ER dynamics. Imaging was performed in MRC5 and COS7 cells stably expressing GFP-SNX1 and transiently expressing RFP-KDEL to visualise the endoplasmic reticulum. The close spatial association between endosomal tubules and the endoplasmic reticulum was initially verified by use of fixed cell super resolution structural illumination microscopy that allowed a spatial resolution of 100nm laterally, and 280nm axially. In spastin depleted MRC5 cells, endosomal tubules had many points of contact between the endosomal tubule and the endoplasmic reticulum (**Figure 8A**).

ER-endosomal tubule contacts form in live cells despite spastin depletion

Live cell imaging was then performed to visualise endosomal tubule fission in relation to the ER network. Imaging of the GFP-SNX1 and RFP-KDEL expressing mock transfected and spastin siRNA depleted MRC5 and COS7 cells was performed using spinning disk microscopy. This revealed that in both mock transfected and spastin depleted cells there was still a strong overlap between endosomal SNX1 tubules and the ER, with the formation of potential endosomal tubule-ER contacts subjectively appearing unaffected by spastin depletion, but with GFP-SNX1 tubules taking longer to undergo fission or collapse after initial contact in spastin depleted cells (**Movie 7** and **Figure 8B**).

This observation was quantified manually by measuring the proportion of SNX1 tubules that underwent fission at the point of contact with an ER tubule, as well as measuring the total duration from the formation of an endosomal tubule-ER contact to either endosomal tubule fission or collapse. Potential endosomal tubule-ER contacts were defined as when the two organelles had clear colocalisation. In both MRC5 and COS7 cells, this analysis showed no significant difference between

mock or spastin depleted cells in the proportion of GFP-SNX1 tubules that underwent fission on an ER tubule (**Figure 8C**). Reassuringly, the percentage of tubules breaking at the ER for mock and spastin depleted cells was ~80%, similar to figures published by Rowland et al. (2014).

Spastin depletion causes a delay in the fission of endosomal tubules upon ER-endosome contact formation

Interestingly, spastin-depleted MRC5 cells had a longer duration between organelle contact formation and endosomal tubule fission or collapse (**Figure 8D**). A similar non-significant trend was also observed in COS7 cells. Overall, this implies that impairment of endosomal tubule fission upon spastin depletion is not caused by a failure of ER-endosome tubule contact formation.

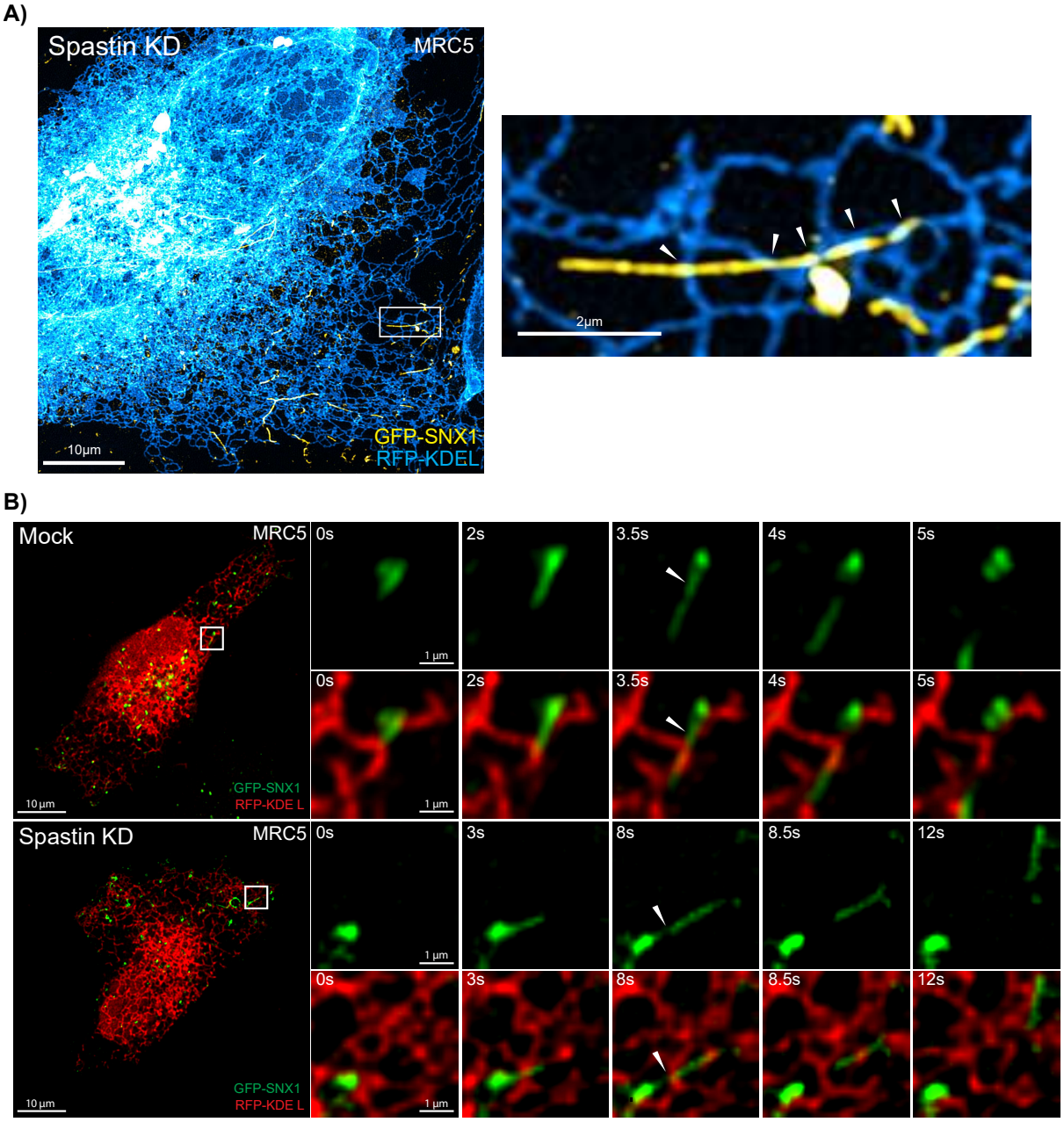
A)
Spastin KD
MRC5
10µm
GFP-SNX1
RFP-KDEL
2µm
B)
Mock
MRC5
0s
2s
3.5s
4s
5s
1 µm
10 µm
GFP-SNX1
RFP-KDE L
Spastin KD
MRC5
0s
3s
8s
8.5s
12s
C)
GFP-SNX1 tubule fission on an ER tubule (%)
100
80
60
40
20
0
p=ns
p=ns
Mock Spastin KD
MRC5
Mock Spastin KD
COS7
D)
Duration of ER-endosome contact before fission/collapse (s)
8
6
4
2
0
p=0.04
p=ns
Mock Spastin KD
MRC5
Mock Spastin KD
COS7

Figure 8 - Spastin depletion does not impair the formation of ER-endosome contacts but delays endosomal tubule fission once contacts are formed.

A) **Maximum intensity Z-projection of fixed super-resolution 3D-Structural Illumination Microscopy of GFP-SNX1 and RFP-KDEL in MRC5 cells** – Spastin siRNA treated GFP-SNX1 stably expressing MRC5 cells were transfected with RFP-KDEL and fixed before being imaged using 3D-Structural Illumination Microscopy to visualise endosome-endoplasmic reticulum (ER) colocalisation. The images displayed shows a maximum intensity Z-projection of a Z stack taken ranging from the top to bottom of the cell. The left large image shows an overview of the highlighted cell, and the right image shows a zoom of the endosomal tubule highlighted by the white box in the overview image. Cyan and yellow colour schemes were chosen to allow best visualisation of the complex ER ultrastructure, with the cyan colour scheme ranging from blue to white depending on signal intensity. White arrows on the zoom image show points of potential contact between the SNX1 endosomal tubule and the ER. The scale of the overview and zoom images were 10µm and 2µm respectively.

B) **Live cell imaging of GFP-SNX1 and RFP-KDEL in mock and spastin siRNA depleted MRC5 cells** – MRC5 cells stably expressing GFP-SNX1 were treated with either mock or spastin siRNA and transfected with RFP-KDEL before being imaged by spinning disk live cell microscopy. Imaging was performed at 400ms per frame simultaneously for both colour for three minutes. The top half of the figure shows an overview and a zoom from a mock treated cell, and the bottom half the same for a spastin siRNA treated cell. The left large images show images of the mock and spastin depleted cell, with the right smaller panels showing a time-lapse (by column) of an endosomal tubule fission event in relation to an ER tubule. The location for these events was marked by the white boxes on the overview images. Both top and bottom halves of the zoom panels display GFP-SNX1 alone in the top half of each panel and both GFP-SNX1 and RFP-KDEL in the second half. The white arrows in the zoom boxes indicate the point of endosomal tubule fission. Scale bars in the overview and zoom images represent 10µm and 2µm respectively. Of note is the difference in duration between tubule formation and fission in the mock and spastin depleted cell. This image corresponds to **Movie 7**.

C) Bar charts showing the quantification of percentage of GFP-SNX1 tubules that undergo fission on an ER tubule in MRC5 and COS7 cells – Endosomal tubule-ER interactions were manually quantified from the live cell imaging of GFP-SNX1 and RFP-KDEL in mock and spastin siRNA depleted GFP-SNX1 stably expressing MRC5 and COS7 cells. The left bar charts show the proportion of GFP-SNX1 endosomal tubule fission that occurred on an ER tubule in MRC5 cells, with the right bar charts showing the equivalent in COS7 cells. Approximately 15 endosomal tubules in areas of resolvable ER tubules were counted per cell, with 5 cells counted per experimental repeat, and 3 experimental repeats performed for mock and spastin depleted conditions for both cell types. Statistical testing was performed using paired two-tailed t-tests, with error bars showing standard error of the mean.

D) Bar charts showing the quantification of duration of ER-endosome contacts before tubule fission or collapse in MRC5 and COS7 cells – Endosomal tubule-ER interactions were manually quantified from the live cell imaging of GFP-SNX1 and RFP-KDEL in mock and spastin siRNA depleted GFP-SNX1 stably expressing MRC5 and COS7 cells. The left bar charts show the duration of endosome-ER contact before either tubule fission or collapse in mock and spastin depleted MRC5 cells, and the right bar charts show the equivalent in COS7 cells. The number of events quantified, and the details of statistical testing are as described in **Figure 8C**.

3.2.7 – Investigating the role of microtubule severing in endosomal tubule fission

The spastin ATPase domain is required for microtubule remodelling where it can introduce GTP-tubulin islands to increase microtubule stability or sever microtubules to facilitate the nucleation of new microtubules (reviewed in Introduction – Section 1.3.5.; Vemu et al. 2018). As spastin's ATPase domain was required for efficient endosomal tubule fission, this raised the possibility that spastin's role in endosomal tubule fission was via microtubule severing. To test this, I investigated whether microtubule severing could be visualised in relation to endosomal tubule fission. Live cell imaging was therefore performed attempting to visualise the relationship between endosomal tubule fission and microtubule dynamics.

SiR-tubulin dose optimisation

Microtubules were imaged in GFP-SNX1 stably expressing MRC5 cells using the dye SiR-tubulin. This provided a bright photostable far-red probe for investing the microtubule cytoskeleton that had good spectral separation from the GFP fluorophore of GFP-SNX1. This docetaxel-based dye is reported to have little effect on cytoskeletal dynamics in HeLa cells (Lukinavičius et al. 2014), but it was important to verify this in MRC5 cells.

A dosage experiment was used to determine a concentration of SiR-tubulin that would allow the imaging of the dynamics of the microtubule network with a high signal to noise ratio. This was performed using spinning disc microscopy and revealed very similar results for the 100nM to 25nM dilutions, with the microtubule network being continuous, very brightly labelled, and with almost no background fluorescence (**Movie 8** and **Figure 9A**). Whilst the 5nM and 1nM dilutions also had a good signal to noise ratios, the microtubule labelling appeared punctate rather than the continuous microtubule network seen with higher concentrations. The 10nM dilution was similar to the 25nM dilution, although slightly dimmer. For this reason, a 25nM dilution of SiR-tubulin was used in all future experiments. This was 4-fold lower than the manufacturer's recommended dilution, giving further confidence that this concentration would have a limited impact on microtubule dynamics.

SIR-tubulin does not block microtubule severing

Having chosen an appropriate working concentration, it was important to verify that spastin was still able to sever 25nM SiR-tubulin labelled microtubules. Therefore, MRC5 cells were labelled with 25nM SiR-tubulin dye and transiently transfected with mEmerald-M87 spastin, allowing the effect of increasing expression of spastin on the SiR-tubulin labelled microtubule network to be revealed by live cell imaging. **Movie 9** and **Figure 9B** show that SiR-tubulin labelled microtubules are still able to undergo microtubule severing by spastin, as there was a progressive loss of microtubule label in the cells that had increasing spastin concentrations. This validated the use of SIR-tubulin to investigate the relationship between endosomal tubule fission and microtubule severing.

GFP-SNX1 endosomal tubules can grow, fission, and be transported on SiR-tubulin labelled microtubules

To verify that GFP-SNX1 tubules have typical dynamics on SIR-tubulin labelled microtubules, GFP-SNX1 and 25nM SiR-tubulin labelled microtubules were imaged using spinning disk microscopy. Endosomal tubules were able to undergo fission in GFP-SNX1 SiR-tubulin treated MRC5 cells, with tubules observed to grow along a microtubule, fissioning along a microtubule, and travelling along a microtubule after fission as expected (**Movie 10** and **Figure 9C**). Quantifying this, ~80% of GFP-SNX1 tubules formed and fissioned on SIR-tubulin labelled microtubules (**Figure 9Di** and **Figure 9Dii**), and 90% of tubules travelled along microtubules after fission (**Figure 9Diii**). These proportions match previous descriptions of the intimate association between endosomal growth and transport dynamics and the microtubule network (Granger et al. 2014).

GFP-SNX1 endosomal tubule fission does not correlate with visible microtubule severing

Spinning disk imaging of stably expressing GFP-SNX1 cells treated with 25nM SiR-tubulin was used to determine whether there was a correlation between endosomal tubule fission and microtubule severing. Microtubule severing events were defined as occurring when a continuous section of microtubule was broken into two.

Quantification of the imaging revealed that almost no GFP-SNX1 tubule fission events correlated with microtubule severing events (**Movie 10** and **Figure 9E**). In fact, it was had to visualise any microtubule severing events at all in MRC5 cells and they were much less frequent that endosomal tubule fission events. This difference between the rate of endosomal tubule fission events and microtubule severing events was also indicative of the lack of correlation between the two processes.

This therefore implied that microtubule severing is not required for the fission of endosomal tubules. However, the possibility that microtubule severing is coupled to tubule fission in a manner not observable from this form of imaging could not be excluded.

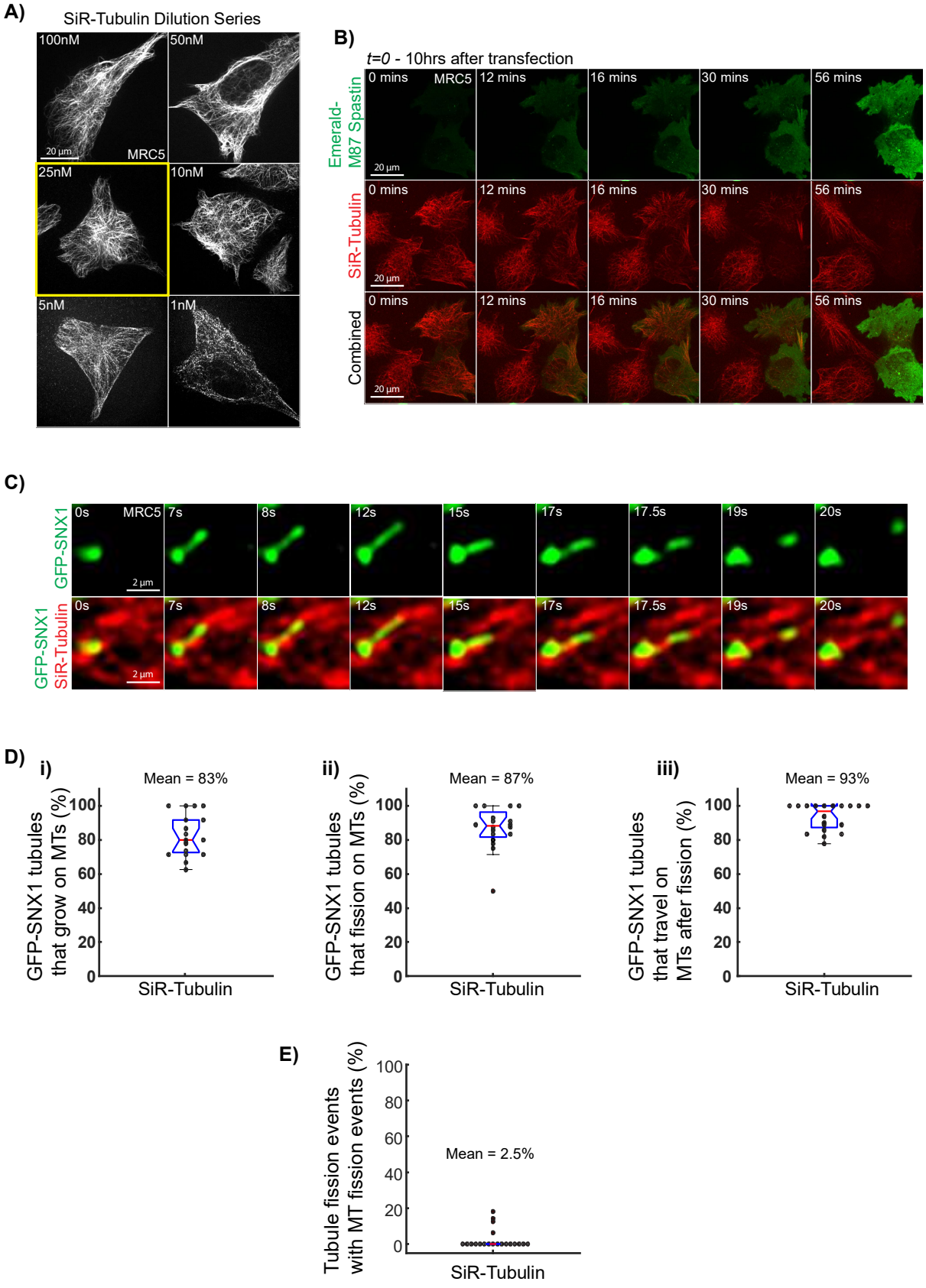
A)
SiR-Tubulin Dilution Series
100nM
50nM
25nM
10nM
5nM
1nM
MRC5
20 µm
B)
t=0 - 10hrs after transfection
Emerald-M87 Spastin
SiR-Tubulin
Combined
0 mins
12 mins
16 mins
30 mins
56 mins
MRC5
C)
GFP-SNX1
GFP-SNX1 SiR-Tubulin
0s
7s
8s
12s
15s
17s
17.5s
19s
20s
2 µm
D)
i)
ii)
iii)
Mean = 83%
Mean = 87%
Mean = 93%
GFP-SNX1 tubules that grow on MTs (%)
GFP-SNX1 tubules that fission on MTs (%)
GFP-SNX1 tubules that travel on MTs after fission (%)
SiR-Tubulin
E)
Tubule fission events with MT fission events (%)
Mean = 2.5%
SiR-Tubulin

Figure 9 - Live cell microscopy of GFP-SNX1 and microtubule dye SiR-tubulin shows endosomal tubule fission to have no correlation with observable microtubule severing in MRC5 cells.

A) **Whole cell images of a dilution series of SiR-tubulin to identify the appropriate concentration of SiR-tubulin used to label microtubules for live-cell imaging in MRC5 cells** – MRC5 cells were treated with 100nM, 50nM, 25nM, 10nM, 5nM, 1nM SiR-tubulin for 8hrs before being imaged using live-cell spinning disk microscopy at 450ms per frame. Each image represents a still image from the imaging series. 25nM, identified by the yellow box, was chosen as the concentration of SiR-tubulin to give good microtubule labelling at the lowest concentration. Scale bars for images represent 20µM. This image accompanies **Movie 8**.

B) **Live-cell imaging of the effect of increasing M87 spastin concentration on SiR-tubulin labelled microtubules to verify labelled microtubules can still be severed** – MRC5 cells were transfected with mEmerald-M87 spastin and after 2 hrs were treated with 25nM SiR-Tubulin for 8hrs. 10 hrs after transfection, Emerald-M87 spastin and SiR-tubulin was imaged, with imaging performed simultaneously in both channels at 2 minutes per frame for 24 hours. Panels show a time-series (by column) of the increasing expression of Emerald-M87 spastin and the effect on the SiR-tubulin microtubules. Top panels show Emerald-M87 spastin alone, middle panels show SiR-tubulin alone, and bottom panels show both channels combined. Time 0 represents 10hrs after transfection. Scale bars represent 20µM. This image accompanies **Movie 9**.

C) **Live-cell imaging of the GFP-SNX1 and SiR-tubulin labelled microtubules in MRC5 cells to verify endosomal tubule fission still occurs on labelled microtubules** – MRC5 cells stably expressing GFP-SNX1 were treated with 25nM SiR-tubulin microtubule dye for 8 hours. Cells were then imaged using spinning disk live cell microscopy, with imaging performed at 200ms per frame for 3 minutes. Images show a time-lapse of a GFP-SNX1 endosomal tubule growth and fission event in relation to a SiR-tubulin labelled microtubule. Image sequence by column. Top panels show GFP-SNX1 alone, bottom panels show both GFP-SNX1 and SiR-tubulin. Scale bar represents 2µM. This image accompanies **Movie 10**.

D) **Box plots of GFP-SNX1 endosomal tubule dynamics in relation to SiR-tubulin labelled microtubules in MRC5 cells** – Endosomal tubule dynamics in relation to SiR-tubulin labelled microtubules were manually quantified from the live cell imaging of GFP-SNX1 stably expressing MRC5 cells treated with 25nM SiR-tubulin dye. Plots show the percentage of GFP-SNX1 tubules that grow on SiR-tubulin labelled microtubules (i), fission on SiR-tubulin labelled microtubules (ii) and travel on SiR-tubulin labelled microtubules (iii). Black dots indicate the averaged endosomal tubule data from each cell, the red line on the box plot denotes the median, the blue edges of the box indicate the 25^{th} and 75^{th} percentiles, and the whiskers represent the most extreme data points not considered outliers. Approximately 15 endosomal tubules were counted in regions of resolvable microtubules in 20 cells.

E) **Box plot of GFP-SNX1 endosomal tubule fission dynamics in relation to SiR-tubulin labelled microtubule fission dynamics in MRC5 cells** – The spatio-temporal correlation between GFP-SNX1 endosomal tubule fission and SiR-tubulin labelled microtubule severing from the live-cell imaging of GFP-SNX1 stately expressing MRC5 cells treated with 25nM SiR-tubulin was counted manually. Fission with a microtubule severing event was defined as there being a low/no SiR-tubulin signal in the frame after endosomal tubule fission at the point of endosomal tubule fission. Graph plotting details as previously described in **Figure 9D**. Approximately 15 endosomal tubules were counted in regions of resolvable microtubules for 20 cells.

3.2.8 – Fission of SNX1 tubules is unrelated in space and time to the formation of a new microtubule plus-end

A resolution problem in live cell microtubule imaging

An inherent problem with the imaging of microtubules using non-super resolution methods is the difference between the resolution required to appropriately visualise microtubule filaments and the maximum resolution provided by diffraction limited microscopy. Microtubule filaments have a width of 24nm, whilst the lateral resolution limit for a far-red fluorophore using confocal microscopy is 231nm. This large discrepancy means that it is not possible to know whether SiR-tubulin labelled microtubules imaged exist as individual filaments, or rather bundles of multiple parallel microtubules. If microtubule severing only occurred on a single filament along a bundle, it would not be possible to identify a severing event, but this could still result in functional consequences that drive endosomal tubule fission.

The use of plus-end binding proteins (EB proteins) as a surrogate of microtubule severing

A surrogate marker that would identify a breakage event involving a subset of microtubules in a bundle was required to address this potential problem. Previous unpublished work in the Reid lab had shown that depletion of spastin in HeLa cells led to a reduction in the rate of microtubule plus end formation suggesting that microtubule severing by spastin lead to the formation of new microtubule plus ends. Furthermore, spastin regulates the number of microtubule plus-ends in neurite extensions and axons (Fassier et al. 2013; Riano et al. 2009). These plus ends can be visualised by fluorescently tagged end binding (EB) proteins, and thus, the recruitment of these EB proteins at the site of endosomal tubule fission would provide evidence of microtubule severing driving tubule fission.

Spastin depletion decreases the rate of microtubule plus-end formation

First, experiments were performed to verify the Reid lab's unpublished data that depletion of spastin reduces the number of cellular plus-ends. This was done by the live cell imaging of EB3-mCherry dynamics in mock and spastin siRNA transfected MRC5 and HeLa cells, and in spastin ATPase mutant MEFs. After imaging, plus-end dynamics were analysed by automated particle tracking before being represented as the number of formed comets per μm^2 per minute, with normalisation for area.

In MRC5 cells, depletion of spastin led to a ~30% reduction in the rate of comet formation (**Movie 11** and **Figure 10A**). Similar findings were also obtained in HeLa cells (**Movie 12** and **Figure 10B**). However, this pattern was not observed in ATPase spastin^{N384K} mutant MEFs, where there was no significant difference in the rate of comet formation between WT, HET or HOM MEFs (**Movie 13**

and **Figure 10C**). Of note was that the rate of comet formation in all MEF genotypes was substantially lower than that observed in the MRC5 or COS7 cells. Given the ATPase domain's function in microtubule severing, this result is somewhat surprising and might perhaps be explained by compensation in this cell line (e.g. by an upregulation in other microtubule severing enzymes). However, given both the substantial effects of comet formation rate from siRNA-induced reduction of spastin in MRC5 and HeLa cells, it was concluded that spastin's microtubule severing function likely did induce microtubule plus-end formation *in vivo*.

EB3-mCherry does not localise to the spatial and temporal site of GFP-SNX1 tubule fission

Next, live cell spinning disk imaging was performed to investigate whether there was a correlation between GFP-SNX1 endosomal tubule fission and the formation of EB3-mCherry labelled microtubule plus-ends. Initial subjective observations suggested little correlation between the spatio-temporal location of GFP-SNX1 tubule fission and EB3-mCherry plus-end formation (**Movie 14** and **Figure 10D**). Upon quantification, the data showed decisively that bright EB3-mCherry puncta did not form at the location of endosomal tubule fission (**Figure 10F**). Thus, combined with the results on SiR-tubulin-labelled microtubules, these experiments provided no evidence that endosomal tubule fission is spatially or temporally related to microtubule severing.

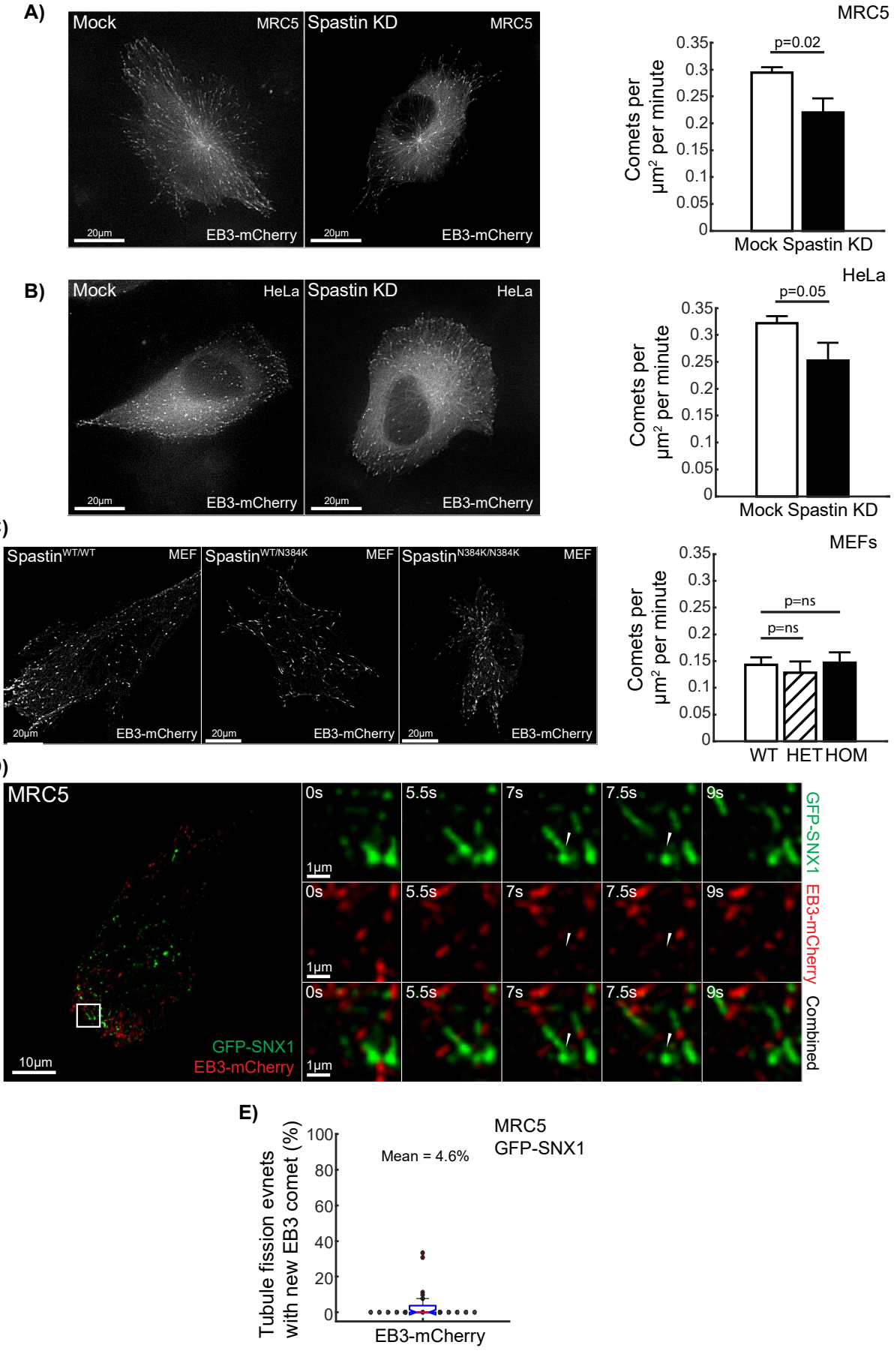
A)
Mock
MRC5
Spastin KD
MRC5
20µm
EB3-mCherry
MRC5
p=0.02
Comets per µm² per minute
Mock Spastin KD
B)
Mock
HeLa
Spastin KD
HeLa
HeLa
p=0.05
C)
SpastinWT/WT
MEF
SpastinWT/N384K
SpastinN384K/N384K
MEFs
p=ns
p=ns
WT HET HOM
D)
MRC5
0s
5.5s
7s
7.5s
9s
1µm
GFP-SNX1
EB3-mCherry
Combined
10µm
E)
MRC5
GFP-SNX1
Mean = 4.6%
Tubule fission evnets with new EB3 comet (%)
EB3-mCherry

Figure 10 - Live cell imaging of GFP-SNX1 and EB3-mCherry shows that microtubule plus end formation does not spatio-temporally correlate with endosomal tubule fission, but spastin depletion impairs microtubule plus end formation in MRC5 cells.

A) **Whole cell still image of live-cell imaging and quantification of EB3-mCherry dynamics in MRC5 cells treated with mock or spastin siRNA** – MRC5 cells were treated with mock or spastin siRNA and transfected with EB3-mCherry and imaged using live-cell widefield microscopy. Imaging was performed at 0.5 seconds per frame for three minutes. Scale bars represent 20µm in both images. EB comet particle tracking was performed using Imaris 9.1.0 and cell area measured using ImageJ, allowing the plot (right) of the number of comets formed per μm^2 per minute in mock and spastin siRNA treated cells. The comets were analysed from approximately 15 cells per mock and spastin siRNA depletion experiment, with four experimental repeats. The bar graph shows the mean of the four experiments for mock and spastin siRNA treated cells, with error bars showing standard error of the mean. P values were generated by paired one-tail t-tests. This image accompanies **Movie 11**.

B) **Whole cell still image of live-cell imaging and quantification of EB3-mCherry dynamics in HeLa cells treated with mock or spastin siRNA** – HeLa cells were treated with mock or spastin siRNA and transfected with EB3-mCherry and imaged using live-cell widefield microscopy. Imaging was performed at 0.5 seconds per frame for three minutes. Scale bars represent 20µm in both images. EB comet tracking, bar chart plots, and number of cells analysed were as described in **Figure 10A**. This image accompanies **Movie 12**.

C) **Whole cell image of live-cell imaging and quantification of EB3-mCherry dynamics in spastin$^{WT/WT}$ (WT), spastin$^{WT/N384K}$ (HET), and spastin$^{N384K/N384K}$ (HOM) immortalised MEFs** – Wildtype, heterozygous, and homozygous spastin mutant MEFs were transfected with EB3-mCherry and imaged using live-cell spinning disk microscopy. Imaging was performed at 0.46 frames per second for three minutes. Scale bars represent 20µm in all images. EB comet tracking and bar chart plots were as described as in **Figure 10A**. The comets were analysed from 5 cells per spastin mutant cell type, with six experimental repeats. This image accompanies **Movie 13**.

D) **Live cell imaging of GFP-SNX1 endosomal tubules and EB3-mCherry microtubule plus ends in MRC5 cells to visualise the spatio-temporal correlation between endosomal tubule fission and EB comet formation** – MRC5 cells stably expressing GFP-SNX1 were transfected with EB3-mCherry and imaged using live cell spinning disk microscopy. The large image (left) shows an overview of a cell with both GFP-SNX1 and EB3-mCherry displayed. The zoom images show a time-series of an GFP-SNX1 endosomal tubule fission event in relation to EB3 microtubule plus ends (by column). The top row shows only GFP-SNX1, the middle row shows only EB3-mCheerry, and the bottom row shows both GFP-SNX1 and EB3-mCherry channels. White arrows show the location of fission of the GFP-SNX1 endosomal tubule. The white box on the large image shows the zoom image location. The scale bars of the overview and zoom images represent 10µm and 1µm respectively. This image accompanies **Movie 14**.

E) **Box plot showing the quantification of the proportion of GFP-SNX1 endosomal tubules that had an EB-mCherry microtubule plus end form at the point of fission** – The number of GFP-SNX1 endosomal tubules that had an EB3-mCherry comet form at the same time and space as endosomal tubule fission was manually scored from live cell movies of GFP-SNX1 stably expressing MRC5 cells transiently expressing EB3-mCherry. 15 endosomal tubules were scored per cell, with 20 cells analysed in total. Box plot details as described in **Figure 9D**.

3.3 – Discussion

3.3.1 – Summary of results

High spatial and temporal resolution microscopy was used to investigate the role of spastin in endosomal tubule dynamics. These experiments showed spastin and its ESCRT-III interaction partner IST1 to be required for the efficient fission of SNX1 endosomal tubules. These proteins colocalised together at sites of tubule constrictions and marked the location of fission. Spastin did not function in the formation of ER-endosome contacts. However, the ATPase domain of spastin was required for tubule fission, suggesting a necessity for microtubule remodelling. There was no direct evidence of a correlation between microtubule severing and SNX1 tubule severing. Furthermore, despite microtubule severing leading to the formation of new microtubule plus-ends, no correlation was observed between SNX1 tubule fission and plus end formation, making it unlikely that the fission of endosomal tubules requires microtubule severing. Altogether, these results provide new insights into the mechanisms of endocytic recycling and endosomal tubule fission, as well as providing new insight into the mechanisms of HSP.

3.3.2 – Spastin and IST1 function in endosomal tubule fission after ER-endosome contact formation

A spastin-IST1 interaction mediates endosomal tubule fission

Depletion of spastin and IST1 in HeLa cells leads to the formation of abnormally long endocytic recycling tubules (Allison et al. 2013). These tubules were hypothesised to result from the failure of endosomal tubule fission. The visualisation of IST1 assembling on positive curvature membranes (such as those found on endosomal tubules) *in vitro* strengthened this hypothesis, with IST1 being likely to form part of a machinery that promotes endosomal tubule constrictions (McCullough et al. 2015).

The research performed supports these hypotheses. Spastin depletion in MRC5 and COS7 cells led to endosomal tubule elongation caused by a delay in tubule fission. The effects of this delay on endocytic trafficking were compounded by the resulting decrease in proportion of successful fission events. Upon spastin depletion, there was an increase in the proportion of tubules that either underwent fission along the length of the endosomal tubule, causing cargo packaged between the fission site and the body of the endosome to not be recycled. Furthermore, tubule collapse events were more common. These represent a major failure of endocytic recycling, with packaged cargo reabsorbed into the endosome body rather than being transported away from lysosomal degradation. Significantly, IST1 depletion led to a near identical phenotype, confirming that both spastin and IST1 function in endosomal tubule fission. Considered with experiments showing that a spastin-IST1

interaction was required to prevent abnormal tubule elongation (Allison et al. 2013), this suggests that tubule fission requires and is driven by a spastin-IST1 interaction.

Further evidence supporting a role of spastin and IST1 in tubule fission came through the use of high sensitivity high spatial resolution Airyscan imaging. In line with predictions from McCullough et al. (2015), spastin and IST1 were shown to localise to sites of tubule constrictions. By live cell imaging, M1 spastin was shown to localise to sites of tubule constriction formation, with these constrictions marking the location of subsequent tubule fission.

A model for spastin-IST1 mediated endosomal tubule fission in the context of known endosomal tubule fission machinery

The mechanism by which spastin and IST1 drive endosomal tubule fission, and how spastin-induced fission fits with other mechanisms known to function on the endosomal tubule is unclear. One established requirement for tubule fission is the formation of contact sites between the tubule and the ER (Rowland et al. 2014). Given that M1 spastin can both bind the ER through its hydrophobic hairpin (Connell et al. 2009), and interact with endosomes through its IST1 and CHMP1B binding MIT domain (Allison et al. 2013; Connell et al. 2009), it was hypothesised that spastin may facilitate contact formation.

However, live cell microscopy shows that spastin does not mediate the formation of ER-endosome contacts. In spastin depleted MRC5 and COS7 cells, the same proportion of endosomal tubule fission events occurred at sites of overlap with the ER as in mock cells. Although the axial resolution of live cell microscopy cannot rule out that these two membranes are close or just overlap without contact formation, electron microscopy in spastin depleted cells showing an increase in membrane contact formation makes this unlikely (Allison et al. 2017). Significantly, depletion of spastin in both MRC5 and COS7 cells led to an extended duration of contact between the endosome and the ER before either a fission or collapse event. This data suggests a model where spastin acts after ER-endosome contact formation in mediating endosomal tubule fission.

How then may spastin-mediated fission at ER-endosome contact sites function in relation to other known fission components? An essential component in endosomal tubule fission is the WASH complex (Derivery et al. 2009; Dong et al. 2016; Gautreau et al. 2014; Puthenveedu et al. 2010). As introduced in Introduction Section 1.4.3, WASH functions to facilitate the nucleation of actin on the sorting endosome and endosomal tubules and supports cargo sorting by mediating the endosomal

recruitment of components of the cargo sorting machinery. Depletion of WASH components impairs endocytic recycling, as shown by the formation of abnormally elongated endosomal tubules and CI-M6PR mistrafficking (Harbour et al. 2010). In addition, an intense burst of actin is observed at the spatial and temporal location of endosomal tubule fission, with this likely mediated by WASH (Puthenveedu et al. 2010).

WASH has also been connected with other proposed components of the endosomal tubule fission machinery. Firstly, it was shown that ER-endosome contacts involving VAP-A and SNX2 lead to the inhibition of WASH-dependent actin polymerisation on endosomal tubules (Dong et al. 2016). Secondly, WASH directly interacts with other proposed endosomal tubule membrane scission enzymes such as dynamin (Derivery et al. 2009), and the dynamin activating protein ATPase Eps15 homology domain (EHD1; Gokool, Tattersall, and Seaman 2007; Jakobsson et al. 2011). Like WASH and spastin, dynamin has been shown to localise to tubulo-vesicular structures in HeLa cells. In addition, expression of a dominant dynamin leads CI-M6PR to mislocalise to lysosomes (Nicoziani et al. 2000), and inhibits the endosome to Golgi transport of endocytosed ricin (Llorente et al. 1998). Furthermore, endosomal recycling tubules elongate upon dynamin inhibition by Dynasore (Derivery et al. 2009), and in yeast, absence of the dynamin ortholog vps1 leads SNX1-coated endosomal tubules to have an extended duration between growth and fission, as well as frequently collapsing back into the mother endosome (Chi et al. 2014). Likewise, depletion of EHD1 led to impaired endosome to plasma membrane recycling of TfnR (Rapaport et al. 2006), and impaired endosome to Golgi traffic of Shiga toxin (McKenzie et al. 2012).

How may spastin and IST1 function in tubule fission in relation to WASH and dynamin activity? One possibility is that spastin-IST1 mediated tubule fission may occur separately to dynamin-mediated tubule fission, potentially separated by cell type, or by acting on different subsets of endosomal tubules. This however seems unlikely, as WASH and dynamin depletion, as well as disruption of ER-endosome contacts, led to the same phenotypes of endocytic mistrafficking as observed with spastin depletion in similar cell types (Dong et al. 2016; Nicoziani et al. 2000; Puthenveedu et al. 2010). Moreover, mutations in spastin, the WASH component strumpellin, or dynamin all result in HSP (Hazan et al. 1999; Sambuughin et al. 2015; Valdmanis et al. 2007). Given that HSP specifically affects cortical neurons, this makes it unlikely that two systems are separated by cell type.

A model is therefore required of how spastin and IST1 may work cooperatively in endosomal tubule fission with WASH and dynamin. A suggestion of how this may occur comes by analogy to mitochondrial fission. Like endosomal tubules, mitochondria also require the formation of ER-

endosome contacts to mediate membrane fission, with fission occurring at the location of contact (Friedman et al. 2011). Intriguingly, like on endosomal tubules, the formation of this organelle-organelle contact leads to a localised burst of actin polymerisation, with this causing the formation of an initial small constriction on the mitochondrion, marking the location of fission (Korobova et al. 2013). This facilitates the recruitment of mitochondrial division dynamin Drp1 to the constriction sites which greatly tightens the constriction (Ji et al. 2015), allowing the recruitment of dynamin-2 which causes membrane cleavage by GTP hydrolysis (J. E. Lee et al. 2016).

Interestingly, whilst dynamin-2 facilitates the final cleavage of the mitochondrion, due to its molecular structure, dynamin-2 is unable to polymerise on membranes that have not already been substantially constricted to a minimum of 30nm (Roux et al. 2010). Thus, dynamin-2 is dependent on an earlier constriction process. The endosomal equivalents of the initial and final stage of mitochondrial fission have been discovered: ER-endosome contacts facilitate an initial burst of actin polymerisation by WASH activation; and dynamin-2 is required for endocytic recycling. Crucially, the endosomal equivalent of Drp1 has not been identified. A spastin-IST1 interaction could do this; through the spastin-mediated action of the IST1-CHMP1B copolymer, endosomal tubules could constrict to a radius that allows dynamin-2 to facilitate the final stages of scission (**Figure 11** (located after Section 3.3.3)). The precise role for spastin in mediating the action of ESCRT-III in endosomal tubule fission however remains to be elucidated (discussed below). A recent significant finding that provides a potential molecular link between these processes is the discovery that WASH recruitment to the endosome is facilitated by the ESCRT-0 protein hepatocyte growth factor-regulated tyrosine kinase substrate (HRS; MacDonald et al. 2018). This therefore suggests a mechanism whereby ESCRT-III/spastin and WASH fission mechanisms can be coordinated.

3.3.3 – Spastin requires its ATPase for fission, but fission is not driven by microtubule severing

Spastin's ATPase domain is required for endosomal tubule fission

A crucial component of the above model is that spastin functions at ER-endosome contacts to generate constrictions on the endosomal tubule. Through its AAA+ domain, spastin is able to convert the hydrolysis of ATP into mechanical force, providing a mechanism by which energy could be conferred to deforming the tubule membrane. An important test of this model would therefore be whether spastin required the function of its ATPase domain to facilitate endosomal tubule fission. Experiments from cells derived from the spastin^{N384K} ATPase-defective mutant mouse showed that this was the case.

Spastin-induced microtubule severing does not drive endosomal tubule fission

One microtubule remodelling function of spastin is the severing of microtubules. Microtubule severing could be envisaged to lead to tubule constriction formation by several mechanisms. Firstly, microtubule severing could lead to the rapid shortening of microtubules at either site of the severing location. If these microtubules were attached to different areas of the endosomal tubule membrane, it could generate tension on the tubule, leading to constriction formation.

An alternative hypothesis is that microtubule severing could lead to an increase of microtubule motor protein loading at the GTP-tubulin rich microtubule severed ends. For example, the microtubule dynein motor has been shown to localise to GTP-tubulin rich microtubule plus ends (Lenz et al. 2006; Vaughan et al. 1999; Wassmer et al. 2009), either via the EB-dependent recruitment of dynactin (Moughamian et al. 2013; Watson 2006), or by kinesin-dependent trafficking moving dynein to plus-ends against its canonical direction of travel (Bieling et al. 2007; Roberts et al. 2014). This increased microtubule loading could lead to an increase in membrane tension via a pulling force, hence generating tubule constrictions. Of relevance is that depletion of p150^{glued} component of the dynein-linker complex dynactin leads to aberrant endosomal tubulation (Wassmer et al. 2009).

Against this background, it was tested whether microtubule severing was visible during endosomal tubule fission. Remarkably, using either microtubule labelling or EB3 as a marker of new microtubule plus-end formation, no microtubule severing events were shown to occur at the position of endosomal tubule fission.

What then is spastin's role in tubule fission if it does not involved microtubule severing at the fission point? A possible explanation is that spastin's AAA+ domain is facilitating the formation of small

microtubule 'bites' along the microtubule that leads to increased GTP-tubulin incorporation into the microtubule without severing (reviewed in Introduction 1.3.5; Vemu *et al*, 2018). Although these GTP-tubulin islands recruit EB proteins (Vemu et al. 2018), it is probable that these could not be visualised by the microscopy performed as the few EB proteins recruited to each 'bite' would likely give a subthreshold signal. Importantly these bites could still be active in recruiting microtubule motors, with the EB-dependent recruitment of dynein still possible, and with kinesin-1 motors (e.g. KIF5A) having been shown to preferentially recruit to GTP-tubulin bound microtubules (Nakata et al. 2011). Thus, spastin's microtubule 'biting' function could potentially induce motor protein loading to generate tubule constrictions via membrane tension (**Figure 11**). As stated, the temporal sequence of this event in relation to ESCRT-III mediated activity is not known, but it may be that this function of spastin occurs after ESCRT-III mediated constriction formation to further reduce the diameter of the endosomal tubule to facilitate dynein loading, and to ensure that the fissioned endosomal tubule can be rapidly transported away from the location of fission.

A more extreme model of spastin's role is that it acts as an alternative VPS4. Spastin and VPS4 have homology, with both proteins having an MIT domain for ESCRT-III binding and an ATPase AAA+ domain (Anna Scott et al. 2005). During membrane constriction, the MIT domain of VPS4 interacts with MIMs of ESCRT-III proteins that generate curvature by forming polymerised filaments (reviewed in Introduction 1.3.3 and 1.5.3). Despite previous dogma that VPS4 recruits to ESCRT-III to facilitate its disassembly (Lata et al. 2008), it has been shown recently that VPS4 and ESCRT-III spatially and temporally localise to generate membrane constrictions, with VPS4 working to facilitate the continued polymerisation of the ESCRT-III constriction polymer (Mierzwa et al. 2017). By analogy, spastin could conceivably function as an alternative VPS4 in endosomal tubule fission, thereby facilitating endosomal tubule constriction by facilitating the non-stalling polymerisation of the IST-CHMP1B copolymer.

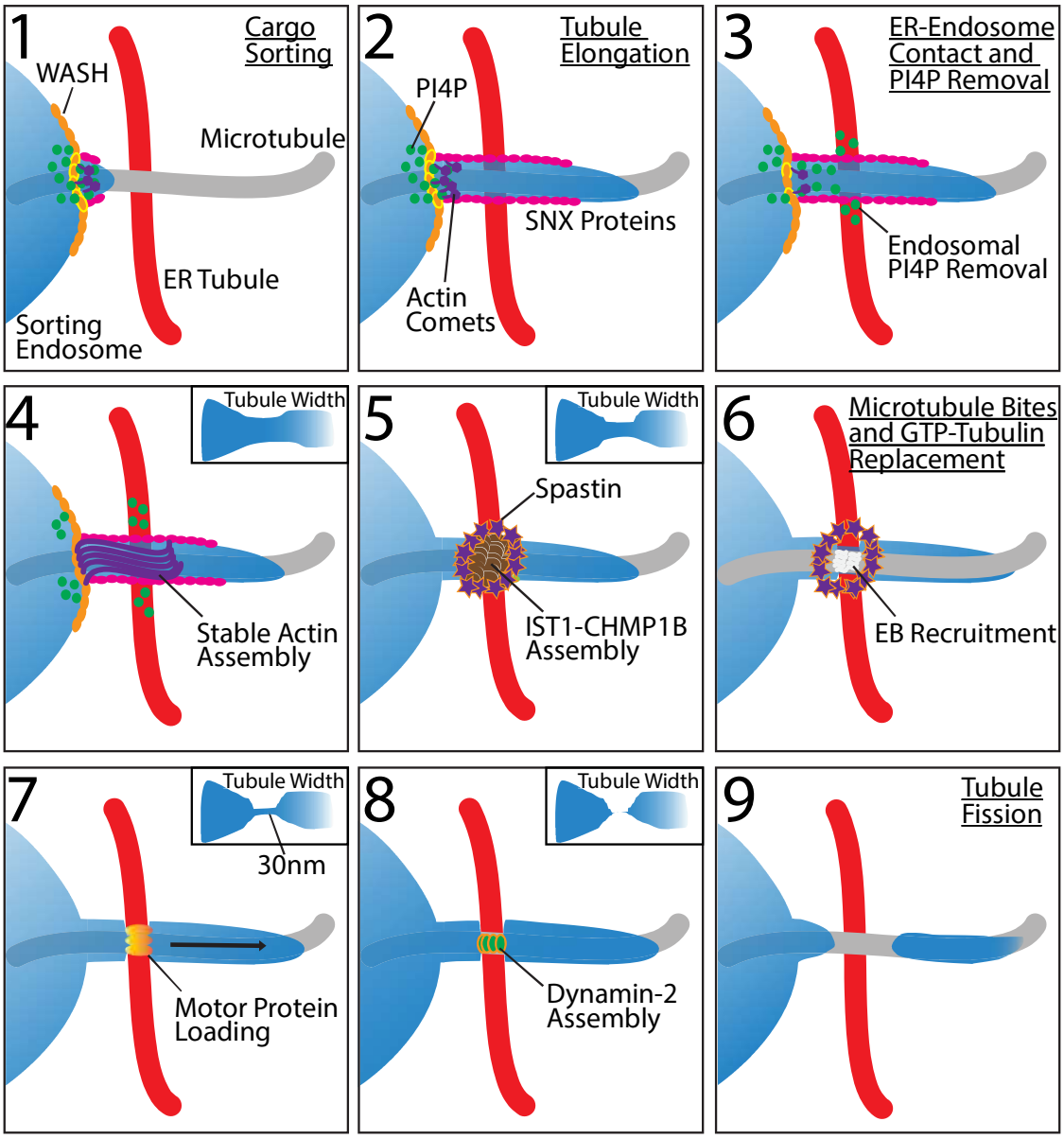

Figure 11 - **Model for spastin-mediated endosomal tubule fission.** (1) Cargo to-be-recycled is retrieved from degradation at the sorting endosome (blue) by cargo sorting machinery such as retriever, retromer, the CCC complex and WASH (orange). These cargos are sorted into tubular projections that grow along microtubules (grey) and by chance may happen to grow across ER tubules (red). This growth is stimulated by fast-polymerising actin comets (purple comets). (2) Increased cargo sorting is coupled to the growth of the endosomal tubule, with SNX-BAR proteins facilitating the high curvature formation of the tubule. (3) An unknown protein mediates the contact of an ER tubule and the endosomal tubule allowing an interaction between ER-localised VAP-A and endosome-localised SNX2 (not shown) allowing OSBP and Sac1 on the ER membrane to remove PI4P from the endosome membrane. (4) PI4P removal inhibits WASH-induced actin comet formation, allowing the formation of stable actin arrays (purple lines) which generate the first sign of tubule constriction. (5) Spastin (stars) and the IST1-CHMP1B (brown) copolymer assembles on the endosomal tubule membrane in an unknown sequence. The IST1-CHMP1B copolymer drive endosomal tubule constriction. (6) Microtubule remodelling by spastin at the site of ER-endosome contacts induces GDP-tubulin to be replaced by GTP-tubulin leading to increased EB recruitment (white). (7) Microtubule remodelling induces microtubule motor protein (orange) loading onto the microtubule beneath the endosomal tubule. This generates tension on the microtubule, causing further constriction to a critical diameter of 30nm. (8). Dynamin-2 polymers (green) are able to assemble on the 30nm endosomal tubule, and through a ratchet mechanism lead to the formation of a hemi-fission state. (9) This single lipid layer hemi-fission state spontaneously resolves, causing endosomal tubule fission. The fissioned endosomal tubule is then transported along microtubules by microtubule motors.

3.3.4 – The implications for the disease mechanism of HSP

Simultaneously with this research, members of the Reid lab were investigating the effect of impaired endosomal tubule fission on the endocytic pathway (Allison et al. 2017). It was shown that inefficient endosomal tubule fission upon spastin or IST1 depletion led to a mistrafficking of CI-M6PR, with a decreased localisation of the receptor at the Golgi apparatus and an increased lysosomal localisation. This was shown to be dependent on spastin's ATPase capability and an ability of spastin and IST1 to interact, mirroring the requirements for endosomal tubule fission. As a result of mistrafficked M6PR, M6P-tagged cargos that typically traffic from the Golgi to endosome (such as lysosomal hydrolase cathepsin D) was aberrantly secreted from the cell. As a likely result of this mistrafficking, lysosomes showed gross changes in their morphology and biology. Lysosomes in spastin depleted cells and cells from patients with spastin-mutation-induced spastic paraplegia had dramatically enlarged lysosomes many of which contained storage membrane. These were also shown to be abnormally acidic. Despite active research, it is not currently understood how lysosomal dysfunction could result in neurodegeneration observed in hereditary spastic paraplegia. Potential mechanisms could include failure in autophagy, failure in autophagic lysosomal reformation, or failure in the breakdown and consequent recycling of lipids and proteins (reviewed in Final Discussion – Section 6.2).

3.3.5 – Future experimental plans

The temporal relationship between spastin, IST1, and other endosomal tubule fission proteins

The temporal relationship between the endosomal tubule fission components is currently unclear. This includes whether spastin recruits to the endosomal tubule before or after IST1, and whether the spastin-IST1 endosomal tubule interaction occurs before or after actin polymerisation by WASH or the endosomal tubule recruitment of dynamin. These experiments could be performed using live cell microscopy, for example by looking at the relationship between the recruitment of pairs of proteins to the endosomal tubule in relation to the fission event. In addition, bespoke microscopy designs could be used that allow 5 or 6-colour live cell imaging (Cohen et al. 2018; Valm et al. 2017). More simply, this could also be performed using a series of siRNA depletion experiments in combination with the live cell imaging of the protein of interest's recruitment to the endosomal tubule. For example, the temporal recruitment of dynamin-2 in relation to spastin or IST1 could be investigated by depleting cells of spastin or IST1 and observing whether dynamin-2 could still recruit to endosomal tubules. This logic can be applied to any pair of endosomal tubule fission machinery components.

The recruitment of microtubule motors to the endosomal tubule fission sites

One hypothesis for how spastin mediates endosomal tubule fission is by recruiting microtubule motors to newly incorporated GTP-tubulin at repaired microtubule bites. This could be very difficult to prove, but approaches could include: 1) the use of fixed cell microscopy to visualise EB patches at the base of endosomal tubules, with the signal amplification provided by antibody labelling providing more sensitivity than live cell; 2) microtubule bites along the endosomal tubule could be visualised *in vivo* using serial-section scanning transmission electron microscopy (STEM), or focussed ion beam scanning electron microscopy (FIB-SEM). The location of these bites could also then be correlated with endosomal tubule constrictions by correlative light electron microscopy (CLEM) approaches. In addition, it might be possible to observe the recruitment of fluorescently labelled motor proteins (e.g. GFP-dynein) at the site of endosomal tubule fission.

Validation in neuronal cells

Given that HSP is caused by the axonal degeneration of cortical neurons, it is important to verify whether the role of spastin and IST1 in endosomal tubule fission also applies in neurons. A major technical difficulty in achieving this is the visualisation of endosomal tubule fission events in the axon which is both thin and may have a high density of cargos. Two potential live cell microscopy approaches could be used: 1) the use of live cell Airyscan may provide the spatial resolution increase required to visualise distinct fission events in the axon; 2) more demandingly, live cell super resolution techniques such as live-cell SIM could be used resolve axonal tubule fission events. These approaches could also be used in combination with a bright endosomal tubule marker expressed at extremely low levels to only label a small subset of endosomal tubule fission events.

Chapter 4 – The function of spastin in the early secretory pathway

4.1 - Introduction

4.1.1 – Overview of the secretory pathway and COPII-coated vesicles

The early secretory pathway

Newly synthesised proteins that are destined for secretion, the cell surface, the endocytic pathway, or other membrane-bound organelles, are translated into the endoplasmic reticulum (ER) where they are folded and glycosylated (Palade 1975). These proteins are then exported from the ER at specialised export locations called ER exit sites (ERES). Proteins leaving these sites travel short distances to fuse with vesicular and tubular membrane clusters (VTCs) that surround each exit site (Bannykh 1996; Hobman et al. 1998). From here, these proteins are transported via microtubule motors in either vesicular or tubular membranes to the microtubule organising centre (MTOC)-localised Golgi apparatus (Presley et al. 1997; Watson et al. 2005). In the Golgi, these proteins may be processed further (e.g. O-linked glycosylation) before being sorted into vesicles that transport cargo to the endocytic pathway (e.g. lysosomal hydrolases), back to the ER, to the cell surface, or to other locations. Collectively these trafficking pathways are defined as the secretory pathway (**Figure 1**).

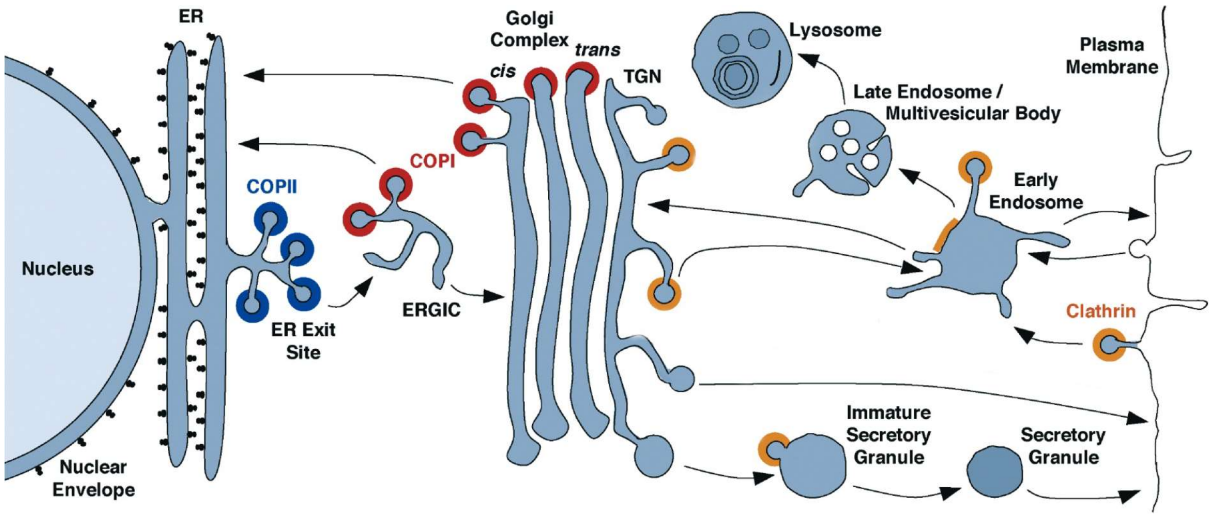

Figure 1 - **Schematic to show cargo trafficking in the early secretory pathway.** Cargo is folded in the ER before being exported in COPII-coated vesicles (blue) to the ER-Golgi intermediate compartment (ERGIC), comprised of VTCs. Here cargo may either be retrieved back to the ER in COPI vesicles (red), with the remaining cargo entering the cis-Golgi complex. This cargo is modified in the Golgi (e.g. glycosylation) before being exported in the TGN. Export routes include transport directly to the cell surface, transport to immature secretory vesicles, or transport to the endocytic pathway. Cargo sorting in the endocytic pathway is also shown. Orange highlights indicate the location of clathrin. Cartoon adapted from Bonifacino and Glick 2004.

COPII-coated vesicle formation and budding

The majority of cargo that leaves the ER is transported in COPII-coated vesicles (Hanna et al. 2016). The formation of a COPII vesicle at an ERES is promoted by the integral ER membrane glycoprotein guanine nucleotide exchange factor (GEF) Sec12 which catalyses the exchange of GDP for GTP on the cytosolic GTPase Sar1 (d'Enfert 1991). This induces the release of an N-terminal amphipathic helix from Sar1 that allows it to integrate into the outer leaflet of the ER membrane (Bielli et al. 2005). The localisation of Sar1 onto the ER induces binding of the Sec23-Sec24 dimer (Barlowe 1994) that serves as a key location of cargo interaction via Sec24 (Miller et al. 2002). Most transmembrane proteins are able to interact directly with Sec24 through amino acid motifs (e.g. DxE) or folded epitopes (Miller et al. 2003), whilst soluble proteins and GPI-anchored proteins rely on membrane adaptor proteins such as ERGIC-53 (Nyfeler et al. 2008) and p24 (Takida et al. 2008) to allow their interaction with Sec24. Together Sec23-Sec24 with bound cargo makes up the inner layer of the coat. Sec23-Sec24 then recruit Sec13-Sec31 to form the outer layer of the COPII coat (Fath et al. 2007). A cartoon of COPII-coated vesicle formation is shown in **Figure 2**.

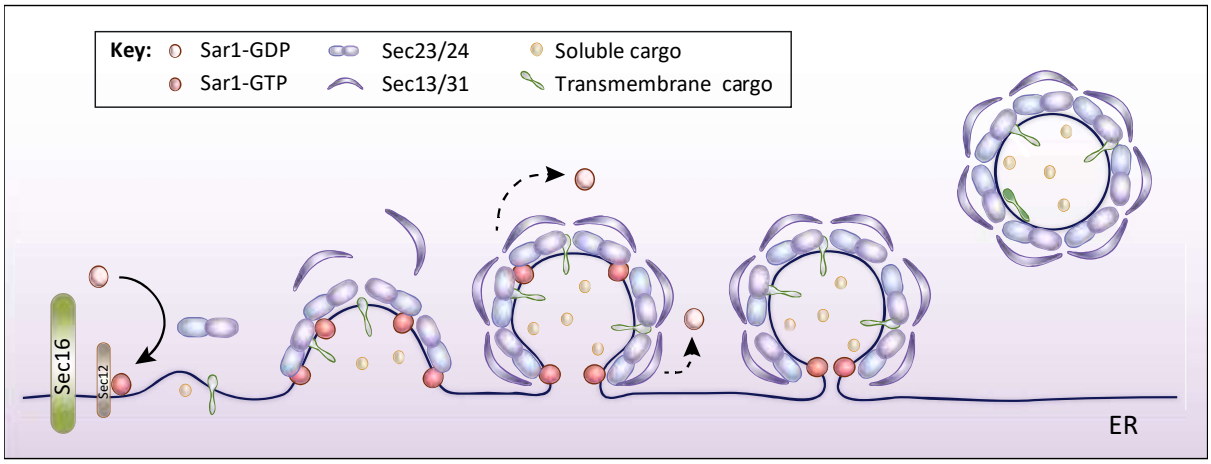

Figure 2 - **A schematic of COPII vesicle formation**. The GTPase Sar1 is recruited to the ER membrane by Sec12. This induces the recruitment of Sec23/Sec24 inner coat proteins which facilitate cargo recruitment, and in turn allow the recruitment of the Sec13/Sec31 outer coat. Sar1 then initiates vesicle neck constriction and cargo budding. Schematic obtained from Venditti, Wilson, and De Matteis 2014.

Although these components form the basic machinery of COPII mediated ER exit, additional ERES proteins aid in the formation of the COPII bud. One example is Sec16, which functions in scaffolding the COPII coat during its assembly, as well as regulating the GTPase-activating protein (GAP) activity of Sec31 to facilitate the formation of vesicles of different sizes (Kung et al. 2012). For example, proteins exiting the ER can have a range of different sizes, with proteins such as procollagen being far larger than the typical 60-90nm size of COPII vesicles. COPII is able to accommodate this large cargo by the action of ERES associated proteins Tango1 and cTage5 (Saito et al. 2011; Wilson et al. 2011). cTage5 binds Tango1 and localises Sec12 to the nascent COPII bud, stimulating the increased recruitment of Sec23-Sec24 by Sar1-GTP, allowing the bud to increase beyond normal size (Saito et al. 2014).

Fission of the nascent COPII bud requires the neck of the COPII vesicle to be constricted. The action of the outer coat proteins Sec13-Sec31 is thought to bend the ER membrane to constrict the neck of the COPII vesicle by the interaction of basic amino acids with the acidic phospholipids of the ER membrane (Bi et al. 2002). The deformation of the ER membrane is also driven by Sar1 as its N-terminal amphipathic helix is able to asymmetrically distort the two layers of the ER lipid bilayer so causing membrane bending (Bielli et al. 2005; Lee et al. 2005). As Sec12 remains localised at the ERES, Sar1-GTP is continually recruited to the COPII bud (Lindroth et al. 2004), despite the GAP activities of Sec23 and Sec31. This is thought to gradually increase the bending of the neck of the COPII vesicle. In addition, it has recently been suggested that Sar1 is able to bind more avidly to bent membrane, ultimately driving an accelerating cycle of Sar1-induced membrane bending and Sar1 recruitment (Hanna et al. 2016). Together these processes lead to COPII fission, with suggestions that Sar1

functions as the ER exit equivalent of dynamin in clathrin mediated endocytosis (Long et al. 2010). It is worth noting however that whilst Sar1 has been shown to induce membrane constrictions, the function of Sar1 in directly causing membrane fission has never been shown *in vivo*.

4.1.2 – The potential role for spastin in ER exit

Whilst ER exit does not appear to require any additional machinery to drive COPII vesicle fission, it is intriguing that the endosomal tubule fission protein spastin (Allison et al. 2017) has been associated with ER exit (Connell et al. 2009). This has been shown by making use of a GFP-tagged temperature sensitive vesicular stomatitis viral glycoprotein (VSVG). The temperature sensitive mutation in VSVG means that it misfolds at 39.5^{o}C, blocking its exit from the ER (Lafay 1974). However, if cells expressing VSVG are cooled to 32^{o}C, VSVG folds correctly and can be exported. This allows the cargo export of VSVG to be synchronised, with the visualisation of the trafficking of VSVG providing an insight into the dynamics of secretion (Presley et al. 1997). Connell et al. (2009) showed that a null mutation in the ATPase domain of spastin led to the impaired trafficking of GFP-tagged temperature-sensitive VSVG from the ER to the Golgi. Furthermore, it was shown that the ER-resident M1 isoform of spastin colocalised with temperature sensitive VSVG at early timepoints of its release from the ER, suggesting spastin to localise to components of the early secretory pathway.

There is additional circumstantial supporting evidence for the involvement of spastin in ER exit. Mass spectrometry of proteins bound to endogenously immunoprecipitated spastin identified the protein TRK-fused gene 1 (TFG; unpublished, Reid lab), with this also confirmed by yeast two-hybrid interaction studies (unpublished, Sanderson lab). TFG functions at ERES to organise the apposition between ERES and the VTCs that form the ER-Golgi intermediate compartment (ERGIC) and is important for efficient procollagen secretion (McCaughey et al. 2016). Spastin's ESCRT-III interacting protein IST1 was also suggested to interact with TFG with high confidence in a large scale human interactome study (Hein et al. 2015). Furthermore, mutations in TFG have recently been shown to result in autosomal recessive complex hereditary spastic paraplegia (Elsayed et al. 2017; Tariq and Naz 2017). Given this data and the similarities in membrane topology between endosomal tubules and COPII buds, as well as the requirement of microtubules for ER to Golgi transport (Gurel et al. 2014), it is tempting to speculate that spastin could also function as a fission enzyme in ER exit.

4.1.3 – Experimental approach

Despite the work of Connell et al. (2009), no experiments have been performed directly looking at the localisation of spastin or IST1 onto ER exit machinery, nor at the effect of spastin or IST1 depletion in the secretion of cargo. Here, I directly test whether spastin and IST1 localise to ERES through the use of high spatial resolution fixed cell Airyscan microscopy and live cell spinning disk microscopy. Furthermore, the role of spastin and IST1 in the efficient trafficking of cargo in the early secretory pathway is tested by imaging the live cell secretion dynamics of TNFα-GFP and GFP fused to a GPI anchor (GFP-GPI). This was performed using the retention using selective hooks (RUSH) assay, allowing cargo release to be synchronised from the ER without the need for unphysiological temperature shifts (discussed below).

4.1.4 – Assays of ER exit and secretion

Traditional experimental methods

Temperature-sensitive VSVG was one of the first tools to study the dynamics of secretion (Lafay 1974; Presley et al. 1997). As described previously, this assay makes use of the temperature-sensitive folding properties of a VSVG mutant to synchronise the export of VSVG from the ER. The synchronised release of VSVG can thereby be visualised, providing a kinetic insight into flux through the secretory pathway. Alternatively, secretory transport can be blocked by cooling cells to 15^{o}C, with export resumed as cells are warmed to 37^{o}C (Matlin and Simons 1983).

Alternative methods include expressing horseradish peroxidase (HRP) or luciferase fused to a signal peptide under a metallothionein promotor. When copper sulphate is added to the cell, it causes transcription and secretion of the HRP/luciferase, and the media of the cell can be regularly sampled and assayed for luminescence activity as a readout of the relative dynamics of the secretory pathway (Bard et al. 2006; Wendler et al. 2010).

In addition, protein export from the ER can synchronised through the use of reversible aggregation (Gordon et al. 2010; Rivera 2000). This method makes use of mutant FK506 binding proteins (FKBP) fused to a cargo of interest. Under steady state conditions, these fusion proteins form ligand-reversible dimers which cannot be secreted. However, upon the addition of FKBP ligand AP21998, the aggregates are solubilised and the cargo-FKBP fusion protein is exported in a synchronised pulse from the ER.

The Retention Using Selective Hooks (RUSH) assay

The RUSH assay is a novel method to synchronise cargo export (Boncompain et al. 2012). This technique relies on the use of two proteins: a hook protein that is resident in the ER (or another organelle if desired), and a reporter protein that is a fluorescently tagged secreted protein of interest. The hook protein is fused to streptavidin and the reporter is fused to streptavidin binding protein, with the interaction between these two proteins sufficient to keep the reporter in the ER under steady-state conditions. However, upon the addition of biotin, the biotin outcompetes the streptavidin binding protein for streptavidin, dissociating the reporter from the hook, allowing it to exit the ER and traffic through the secretory pathway in a synchronised pulse.

Benefits of the RUSH assay

The RUSH assay has benefits over its predecessor techniques (Boncompain et al. 2012). These are: 1) no reliance on unphysiological temperature shifts to induce cargo synchronisation (not possible with the VSVG assay and cooling assay); 2) No delay between stimulus and cargo secretion (not possible with the VSVG, cooling, and HRP/luciferase assays); 3) Fluorescent-tagging of the reporter allowing live cell imaging of the reporters trafficking dynamics (not possible with the HRP/luciferase assays); 4) No upregulation of the unfolded protein response as is possible with the aggregation assay (Boncompain et al. 2012; Perez lab, personal communication). In addition, the reporter can be varied to study the trafficking dynamics of different proteins of interest. In the context of investigating the function of spastin in the secretory pathway, this was crucial as it allowed the effects of spastin on multiple trafficking pathways to be investigated.

4.1.5 – Summary of aims

The experiments in this chapter aimed to address the following questions:

1. Does spastin and IST1 localise to ER exit machinery?
2. Is spastin or IST1 required for efficient ER exit?

4.2 – Results

4.2.1 – Summary of methods

The function of spastin in the early secretory pathway was investigated by using fixed and live cell imaging. Airyscan microscopy were used to investigate the localisation of spastin and IST1 at ERES with high spatial resolution, with the dynamics of spastin localisation at ERES investigated using live cell microscopy. The function of spastin and IST1 in ER exit was investigated by using the RUSH assay to monitor the secretory dynamics of TNFα-GFP and GFP-GPI RUSH cargo reporters.

4.2.2 – Spastin and IST1 localise on ER exit sites in MRC5 cells

Previous investigations of the ER localised M1 isoform of spastin had shown it to colocalise with temperature sensitive viral glycoprotein (VSVGtsO45) in HeLa cells very shortly after its release from the ER (Connell et al. 2009). This suggested that spastin may localise to ER exit sites and so may function in cargo exit from the ER. However, localisation experiments of spastin or its ESCRT-III binding partner IST1 onto ERES machinery were not performed.

To investigate the localisation of spastin and IST1 on ERES machinery, high spatial resolution fixed cell Airyscan imaging was performed in MRC5 cells stably expressing GFP-M1 spastin, transiently expressing mCherry-Sec23, and antibody labelled for endogenous IST1. The GFP-M1 spastin cell lines used were the same as used for experiments of GFP-M1 spastin and IST1 localisation on endosomal tubules detailed in Chapter 3. The imaging showed clear 3-way colocalisation between GFP-M1 spastin, mCherry-Sec23, and IST1 (**Figure 3A**). This colocalisation was observed predominately in the perinuclear and central areas of the cell, with fewer examples of all three proteins colocalising in the cell periphery. Whilst there were many examples of all three proteins localising together, there were instances where GFP-M1 spastin and mCherry-Sec23 were colocalised without IST1, and instances were IST1 and mCherry-Sec23 were colocalised without GFP-M1 spastin. There were also many mCherry-Sec23 puncta that were not colocalised with either protein. Overall however, the high-resolution imaging showed clear examples of spastin, IST1, and Sec23 colocalisation, providing new insight into ESCRT-III biology and confirming previous suggestions about M1 spastin localisation.

The fixed cell imaging could not reveal whether spastin and Sec23 had transient or stable colocalisation. To address this, high temporal resolution live cell spinning disk microscopy of MRC5 cells stably expressing GFP-M1 spastin and transiently expressing mCherry-Sec23 was performed. Confirming the fixed cell imaging, there was a large amount of colocalisation observed between GFP-M1 spastin and mCherry-Sec23 in the central regions of the cell, with less colocalisation observed at

the cell periphery (**Movie 1**, **Figure 3B**). Significantly, the colocalisation of GFP-M1 spastin and mCherry-Sec23 appeared highly stable. For example, in **Movie 1**, all mCherry-Sec23 puncta that were colocalised with a GFP-M1 spastin puncta maintained that colocalisation for the full 30 second duration of the movie. Furthermore, although most GFP-M1 spastin and mCherry-Sec23 puncta were static (even when colocalised), some puncta were highly dynamic in the cell with the colocalisation of GFP-M1 spastin and mCherry-Sec23 maintained despite these rapid movements (white arrows in **Figure 3B**). Overall therefore, this indicated a stable association between GFP-M1 spastin and mCherry-Sec23.

A)

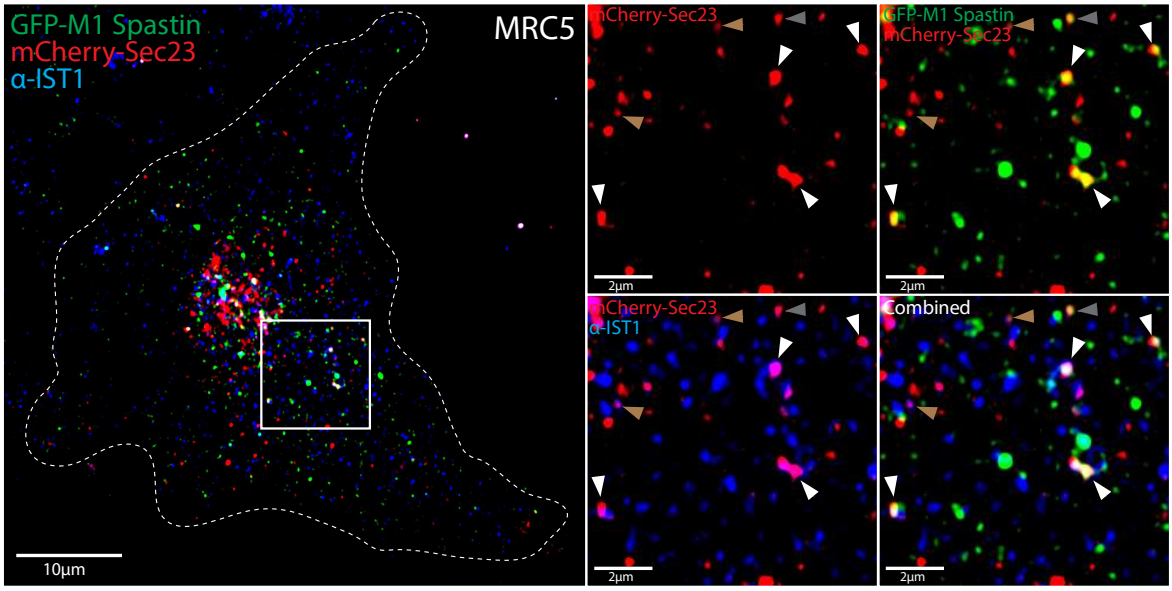

B)

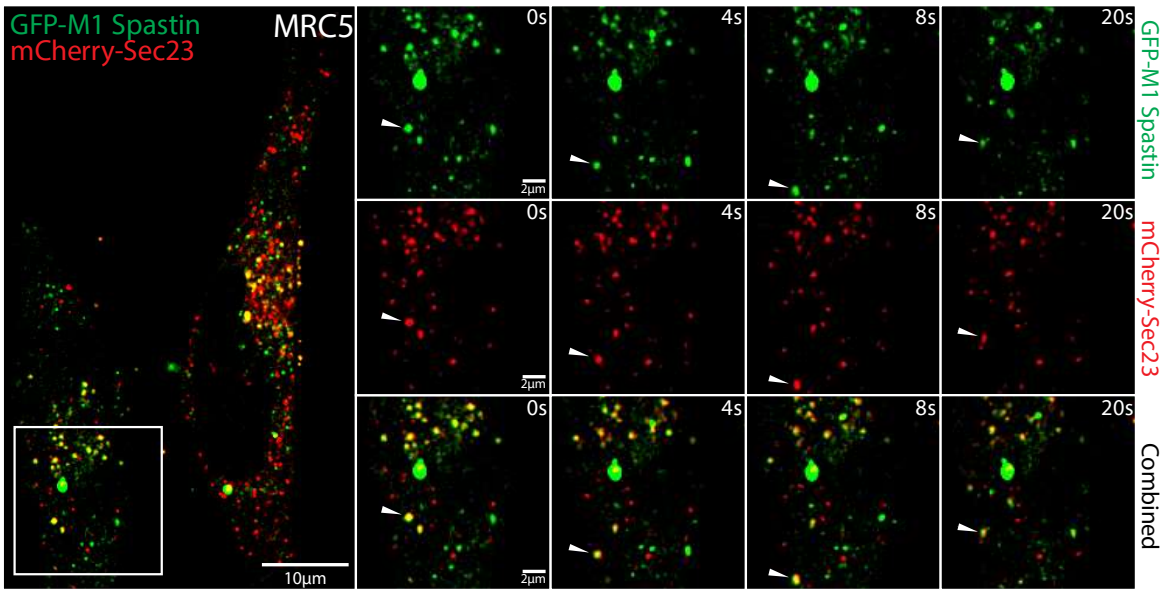

Figure 3 - Spastin and IST1 localise on Sec23-labelled ER exit sites.

A) **Fixed cell Airyscan microscopy of GFP-M1 spastin, mCherry-Sec23, and IST1 in MRC5 cells** – MRC5 cells stably expressing GFP-M1 spastin were transfected with mCherry-Sec23, fixed, and stained with fluorescent antibodies against IST1. Cells were then imaged using high resolution Airyscan microscopy. The left panel shows an overview of a cell, with the white dotted line indicating the outline of the cell. The smaller panels show a zoom of the region highlighted by the white square in the overview image, with the top left showing mCherry-Sec23 alone, top right showing GFP-M1 spastin and mCherry-Sec23, bottom left showing mCherry-Sec23 and IST1, and bottom right showing a merge of all three channels. White arrows indicate Sec23 puncta with both GFP-M1 spastin and IST1 colocalisation, grey arrows indicate Sec23 puncta that exclusively colocalise with GFP-M1 spastin, and orange arrows indicate Sec23 puncta that exclusively colocalise with IST1. Scales for the overview and zoom images represent 10µm and 2µm respectively. See Chapter 3 for GFP-M1 spastin expression blots to show the level of GFP-M1 spastin expressed in this cell line.

B) **Live cell imaging of GFP-M1 spastin and mCherry-Sec23 in MRC5 cells** – MRC5 cells stably expressing GFP-M1 spastin were transfected with mCherry-Sec23 and imaged using spinning disk microscopy. Imaging was performed at 420ms per frame for three minutes simultaneously in both channels. The large left panel shows an overview of two cells. The right smaller panels show a zoom of the region marked by the white square in the overview image. The top panels show GFP-M1 spastin alone, the middle panels show mCherry-Sec23 alone, and the bottom panels show both channels merged. The white arrow tracks a colocalised GFP-M1 spastin and mCherry-Sec23 puncta that moves dramatically in the cell. Scales of the overview and the zoom images represent 10µm and 2µm respectively. This figure corresponds to **Movie 1**.

4.2.3 – Spastin and IST1 depletion have no effect on the synchronised export of RUSH reporter TNFα-GFP from the ER to the Golgi

Previous investigations of spastin had shown transient over-expression of ATPase defective spastin to impair the release and trafficking of VSVG-GFP from ERES to the Golgi apparatus (Connell et al. 2009). However, spastin depletion did not affect VSVG traffic (Connell et al. 2009). Both of these assays relied on using unphysiological temperature shifts to control the synchronised release of VSVG from the ER, and only looked at the trafficking of one cargo. To mitigate these problems, the RUSH assay was used to investigate the effect of spastin and IST1 function in the trafficking of multiple cargos in the early secretory pathway without the need for temperature shifts.

The effect of spastin and IST1 depletion on the ER to Golgi export dynamics of the type-II transmembrane protein TNFα were studied in HeLa cells coexpressing TNFα-SBP-GFP reporter and KDEL-Streptavidin hook. Cells were depleted of either spastin or IST1 using siRNAs, transfected with sialyltransferase fluorescently tagged with FusRed (SiT-FusRed) to label the Golgi apparatus, treated with biotin to induce reporter release, and imaged using live cell confocal microscopy. In addition, a set of TNFα RUSH cells were treated with Sar1-GTPase inhibitor H89 to provide a positive control of impaired ER exit. This imaging appeared to reveal little effect of spastin or IST1 depletion on TNFα trafficking between the ER, Golgi, and the plasma membrane (**Movie 2** and **Figure 4A**). In mock, spastin depleted, and IST1 depleted cells, TNFα-GFP appeared to be localised in small punctate structures at 5 minutes (likely to be ERES), have high colocalisation with SiT-FusRed at 15 minutes (Golgi), and have a diffuse localisation at 60 minutes (likely to be the cell surface). However, a substantial delay in TNFα-GFP trafficking was observed in cells treated with the Sar1-GTPase inhibitor H89. By 15 minutes, there was some colocalisation of TNFα-GFP with SiT-FusRed labelled Golgi, but also much of the GFP signal was still in the form of small puncta, suggesting a block in ER exit. At 60 minutes, most of the TNFα-GFP signal remained colocalised with SiT-FusRed, also suggesting a delay in export from the Golgi.

TNFα-GFP dynamics in mock, spastin depleted, IST1 depleted, and H89 treated RUSH cells were quantified to provide a detailed description of TNFα-GFP trafficking in the early secretory pathway. To quantify TNFα-GFP dynamics, the Golgi apparatus was automatically segmented using the SiT-FusRed signal, and the amount of TNFα-GFP signal in this defined region was measured in each frame of each cell. This was normalised by the total segmented area of the Golgi to control for Golgi size variations. For each cell, the value of signal in the Golgi was expressed as a percentage of the maximum Golgi signal recorded. This allowed a detailed plot of the increase and decrease of TNFα-

GFP localisation in the Golgi region as the cargo exits the ER, enters the Golgi apparatus, and leaves the Golgi apparatus for the cell surface with 1 minute temporal resolution.

The effect of spastin depletion on TNFα-GFP secretory dynamics

There were no observable differences in the TNFα-GFP trafficking dynamics into and out of the Golgi in mock and spastin depleted cells over three experimental repeats (**Figure 4B**). No statistically significant differences in the TNFα-GFP signal in the Golgi region were observed for any time points for the 90 minute duration plotted between the two treatments. Moreover, the time for the maximum TNFα-GFP signal to appear in the Golgi was similar in mock and spastin depleted cells (**Figure 4C**), despite a strong reduction in spastin protein abundance in spastin siRNA treated cells (**Figure 4D**). Both mock and spastin depleted cell TNFα-GFP dynamics closely mirrored those observed by Boncompain et al. (2012) for wildtype cells. This therefore clearly strongly suggested that spastin is not required for the normal trafficking of TNFα-GFP RUSH cargo in the early secretory system.

The effect of IST1 depletion on TNFα-GFP secretory dynamics

The same analysis and quantification were also applied to TNFα-GFP RUSH cells treated with either mock or IST1 siRNAs. From one experimental repeat there was no observable difference in TNFα-GFP trafficking into and out of the Golgi between the two treatments, mirroring the effect seen with spastin depletion (**Figure 4E**). This was reflected in the near identical time for the maximum TNFα-GFP signal to appear in the Golgi region between the mock and IST1 depleted cells (**Figure 4F**), despite IST1 siRNA treated cells having a reduction in IST1 abundance (**Figure 4G**). This showed that, like spastin, IST1 depletion had no effect on the trafficking of TNFα-GFP RUSH cargo in the early secretory pathway.

The effect of H89 treatment on TNFα-GFP secretory dynamics

TNFα-GFP RUSH cells were also treated with H89 as a positive control to show that a perturbation of ER export machinery would lead to changes in the trafficking of TNFα-GFP into and out of the Golgi apparatus (**Figure 4H**). In H89 treated cells there was a substantial delay in the time for maximum TNFα-GFP signal to appear in the Golgi region, with maximum signal in the Golgi approximately 10 minutes later than in mock cells (**Figure 4H**, **Figure 4I**). Furthermore, the rate of TNFα-GFP signal increase into the Golgi and decrease out of the Golgi was substantially lower than in mock cells (**Figure 4H**), confirming initial observations (**Movie 2**, **Figure 4A**). This therefore showed than Sar1-GTPase inhibition led to an impairment of TNFα-GFP trafficking in the early secretory pathway. This confirmed

that manipulations in ER exit machinery could cause an observable change in trafficking of this RUSH assay cargo.

A)

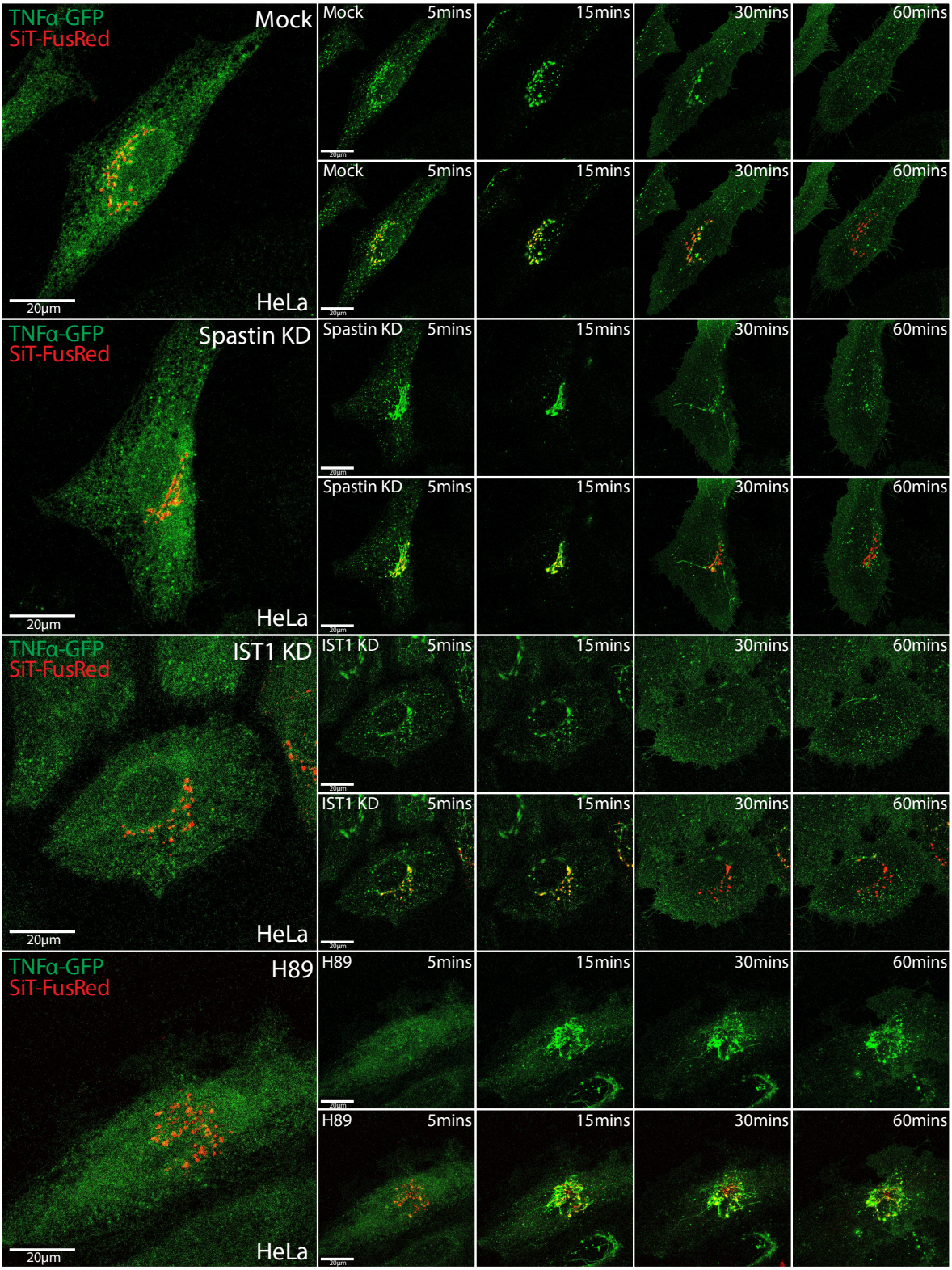
TNFα-GFP
SiT-FusRed
Mock
HeLa
20µm
Mock 5mins
15mins
30mins
60mins
Spastin KD
IST1 KD
H89

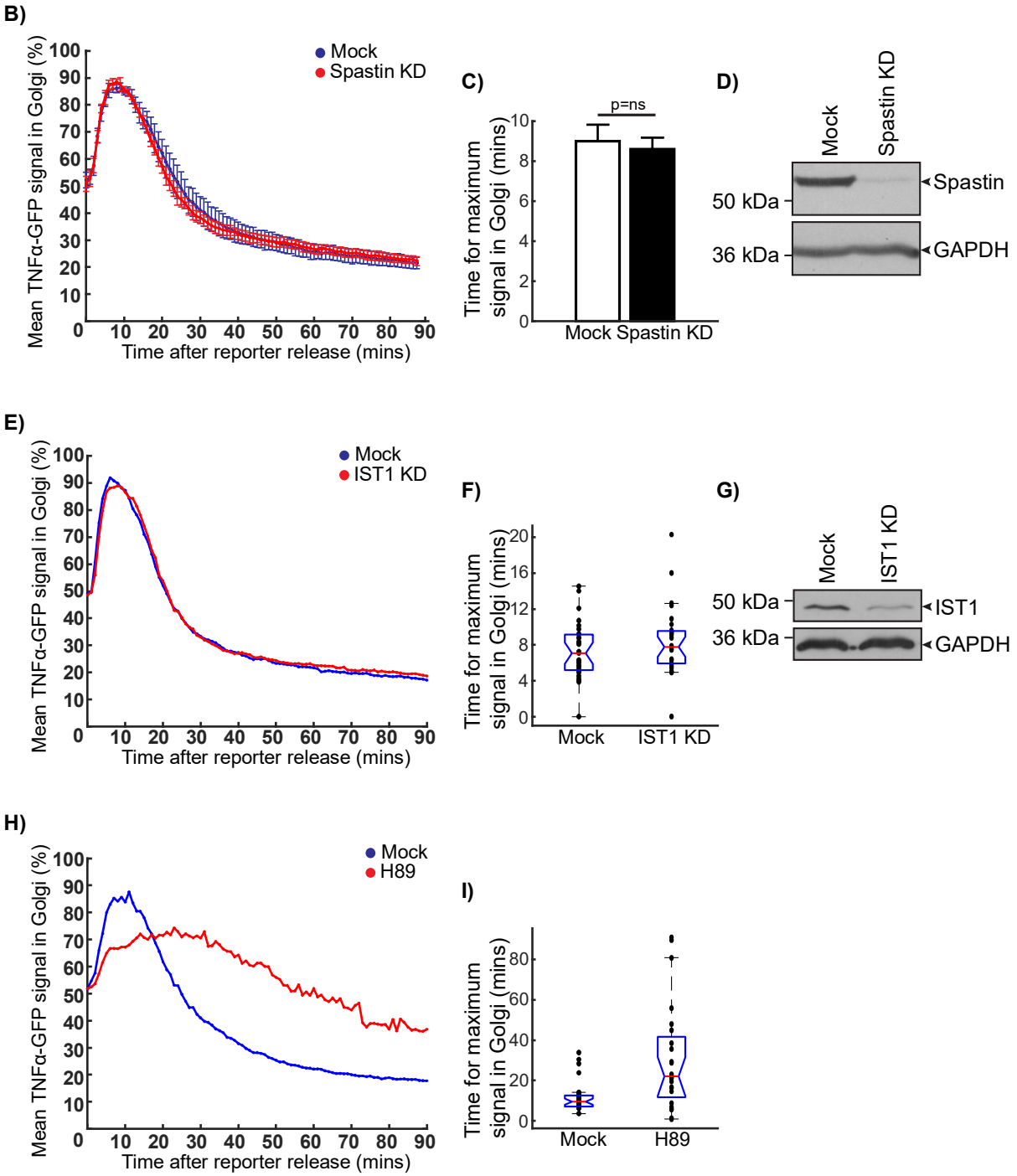
B)
Mock
Spastin KD
Mean TNFα-GFP signal in Golgi (%)
Time after reporter release (mins)
C)
p=ns
Time for maximum signal in Golgi (mins)
Mock Spastin KD
D)
Mock
Spastin KD
50 kDa
36 kDa
Spastin
GAPDH
E)
Mock
IST1 KD
Mean TNFα-GFP signal in Golgi (%)
Time after reporter release (mins)
F)
Time for maximum signal in Golgi (mins)
Mock IST1 KD
G)
Mock
IST1 KD
50 kDa
36 kDa
IST1
GAPDH
H)
Mock
H89
Mean TNFα-GFP signal in Golgi (%)
Time after reporter release (mins)
I)
Time for maximum signal in Golgi (mins)
Mock H89

Figure 4 - Spastin and IST1 depletion does not impair TNFα-GFP RUSH cargo trafficking from the ER to the Golgi apparatus.

A) **Live cell imaging of TNFα-GFP cargo release and trafficking through the secretory pathway upon spastin and IST1 depletion and H89 treatment in TNFα-SBP-GFP KDEL-Streptavidin RUSH HeLa cells** – HeLa cells stably coexpressing TNFα-SBP-GFP RUSH reporter and KDEL-Streptavidin RUSH hook were transfected using spastin siRNAs, IST1 siRNAs, or treated with 100μM H89, and transfected with SiT-FusRed to label the Golgi apparatus. Cells were then imaged using live cell confocal microscopy at ~40 seconds per frame for 90 minutes. The release of TNFα-SBP-GFP from KDEL-Streptavidin was stimulated using 40μM biotin solution, with time 0 corresponding to the time of biotin addition. The different sets of panels show mock treated cells (top main row), spastin depleted cells (2nd main row), IST1 depleted cells (3rd main row), and H89 treated positive control cells (bottom main row). In each main panel, the image on the left shows both TNFα-GFP and SiT-FusRed channels for the frame of biotin addition (t=0). The smaller right panels show 5, 15, 30, and 60 minutes after biotin addition, with the top and bottom panels showing TNFα-GFP alone, and both channels merged respectively. Scale bars for all images represent 20μm. This figure corresponds to **Movie 2**.

B) **Graph of TNFα-GFP signal in the SiT-FusRed labelled Golgi after reporter release in mock and spastin depleted TNFα-SBP-GFP KDEL-Streptavidin RUSH HeLa cells** – HeLa cells stably coexpressing TNFα-SBP-GFP RUSH reporter and KDEL-Streptavidin RUSH hook were treated with either mock or spastin siRNAs and transfected with SiT-FusRed to highlight the Golgi apparatus. Cells were treated with 40μM biotin to induce reporter release and imaged using live cell confocal microscopy at ~40s per frame for 90 minutes. After imaging, images were processed automatically to threshold the SiT-FusRed labelled Golgi apparatus and determine the total TNFα-GFP signal in the defined area. This data was then processed automatically to calculate the signal per Golgi area for each frame of each image, and then calculate the signal in the Golgi for each frame normalised to the frame with the maximum signal for each cell. ~30 cells were imaged per treatment per experimental repeat, with three experimental repeats performed in total. The graph shows the mean normalised TNFα-GFP signal in the Golgi region during the biotin-induced release of the TNFα-GFP reporter over the three experimental repeats for each treatment. Time 0 corresponds to the addition of the biotin. Error bars at each minute represent standard error of the mean. Blue and red lines/bars show mock and spastin siRNA treated cells respectively.

C) **Bar chart showing the time for maximum localisation of TNFα-GFP signal in the SiT-FusRed defined Golgi region in mock and spastin depleted TNFα-SBP-GFP KDEL-Streptavidin RUSH HeLa cells** – Live cell imaging and image analysis was performed on TNFα-SBP-GFP KDEL-Streptavidin RUSH HeLa cells treated with either mock or spastin siRNAs and transfected with SiT-FusRed as described in **Figure 4A** and **Figure 4B**. The time after biotin addition for the maximum localisation of TNFα-GFP signal in the SiT-FusRed defined Golgi region was recorded for each mock and spastin depleted cell. This data was averaged between the three experimental repeats for each treatment. Error bars indicate standard error of the mean. P values were generated by using paired two-tailed t-tests.

D) **Western blot showing spastin protein abundance in mock and spastin siRNA deleted TNFα-SBP-GFP KDEL-Streptavidin RUSH HeLa cells** - TNFα-SBP-GFP KDEL-Streptavidin RUSH HeLa cells treated with mock or spastin siRNA were lysed and proteins separated by SDS-PAGE, with proteins transferred onto PVDF membrane by western blotting. The abundance of spastin was detected by using a spastin antibody. Equal loading between lanes was verified by also blotting for the housekeeping protein GAPDH.

E) **Graph of TNFα-GFP signal in the SiT-FusRed labelled Golgi after reporter release in mock and spastin depleted TNFα-SBP-GFP KDEL-Streptavidin RUSH HeLa cells** – HeLa cells stably expressing TNFα-SBP-GFP RUSH reporter and KDEL-Streptavidin RUSH hook were treated with either mock or IST1 siRNA and transfected with SiT-FusRed to highlight the Golgi apparatus. Cells were then treated with biotin,

imaged, and analysed as described in **Figure 4B**. ~30 cells were imaged per treatment, with one experimental repeat performed. The graph shows the mean normalised TNFα-GFP signal in the Golgi region during the biotin-induced release of the TNFα-GFP reporter for each treatment. Time 0 corresponds to the addition of the biotin. Blue and red lines show mock and IST1 siRNA treated cells respectively.

F) **Box plots showing the time for maximum localisation of TNFα-GFP signal in the SiT-FusRed defined Golgi region in mock and IST1 depleted TNFα-SBP-GFP KDEL-Streptavidin RUSH HeLa cells** – Live cell imaging and image analysis was performed on TNFα-SBP-GFP KDEL-Streptavidin RUSH HeLa cells treated with either mock or IST1 siRNAs and transfected with SiT-FusRed as described in **Figure 4A** and **Figure 4B**. The time after biotin addition for the maximum localisation of TNFα-GFP signal in the SiT-FusRed defined Golgi region was recorded for each mock and IST1 depleted cell and are depicted by black dots. The box plot red bar shows the median, the edges of the blue box show the 25th and 75th percentiles, and the whiskers extend the most extreme points not considered outliers (2.7 standard deviations).

G) **Western blot showing spastin protein abundance in mock and IST1 siRNA deleted TNFα-SBP-GFP KDEL-Streptavidin RUSH HeLa cells** - TNFα-SBP-GFP KDEL-Streptavidin RUSH HeLa cells treated with mock or IST1 siRNA were lysed and proteins separated by SDS-PAGE, with proteins transferred onto PVDF membrane by western blotting. The abundance of IST1 was detected by using an IST1 antibody. Equal loading between lanes was verified by also blotting for the housekeeping protein GAPDH.

H) **Graph of TNFα-GFP signal in the SiT-FusRed labelled Golgi after reporter release in mock and H89 treated TNFα-SBP-GFP KDEL-Streptavidin RUSH HeLa cells** – HeLa cells stably expressing TNFα-SBP-GFP RUSH reporter and KDEL-Streptavidin RUSH hook were treated with either mock or 100μM H89 and transfected with SiT-FusRed to highlight the Golgi apparatus. Cells were then treated with biotin, imaged, and analysed as described in **Figure 4B**. ~30 cells were imaged per treatment, with one experimental repeat performed. The graph shows the mean normalised TNFα-GFP signal in the Golgi region during the biotin-induced release of the TNFα-GFP reporter for each treatment. Time 0 corresponds to the addition of the biotin. Blue and red lines show mock and H89 treated cells respectively.

I) **Box plots showing the time for maximum localisation of TNFα-GFP signal in the SiT-FusRed defined Golgi region in mock and H89 depleted TNFα-SBP-GFP KDEL-Streptavidin RUSH HeLa cells** – Live cell imaging and image analysis was performed on TNFα-SBP-GFP KDEL-Streptavidin RUSH HeLa cells treated with either mock or 100μM H89 and transfected with SiT-FusRed as described in **Figure 4A** and **Figure 4B**. The time after biotin addition for the maximum localisation of TNFα-GFP signal in the SiT-FusRed defined Golgi region was recorded for each mock and H89 treated cell and are depicted by black dots. Box plot description as in **Figure 4F**.

4.2.4 - Spastin depletion has no effect on the synchronised export of RUSH reporter GFP-GPI from the ER to the Golgi

To investigate whether spastin depletion affected the trafficking of a different secretory cargo, the same assays were performed on HeLa cells expressing the GPI-anchored protein SBP-GFP-GPI reporter and KDEL-Streptavidin hook. This allowed the synchronised trafficking of GFP-GPI in the early secretory pathway to be imaged and quantified in mock and spastin siRNA depleted cells.

Once again, initial visual observations suggested little difference in the early secretory pathway trafficking of GFP-GPI in mock and spastin depleted cells, although trafficking appeared impaired in H89 treated cells (**Movie 3** and **Figure 5A**). In mock and spastin depleted cells, strong colocalisation between the GFP-GPI reporter and SiT-FusRed was observed between 15 and 30 minutes, with the colocalisation decreasing and the GFP-GPI signal becoming more diffuse after 60 minutes. This contrasted to H89 treated cells where there was only limited colocalisation between GFP-GPI and SiT-FusRed after 30 minutes, and little diffuse localisation of the GFP-GPI signal after 60 minutes, with the majority of the signal remaining in the Golgi. Interestingly, the dynamics of GFP-GPI signal at the Golgi in mock, spastin depleted, and H89 treated cells appeared generally delayed compared to cells expressing TNFα-GFP reporter (**Movie 3** and **Figure 4A**). This provided good evidence of the difference in trafficking dynamics between different secretory cargo and supported using GFP-GPI in addition to TNFα-GFP to study the effect of spastin depletion on potentially different modes of export in the early secretory pathway.

The effect of spastin depletion on GFP-GPI secretory dynamics

The movement of GFP-GPI into and out of the Golgi in mock, spastin depleted, and H89 treated GFP-GPI RUSH cells was quantified to provide a detailed kinetic description of GFP-GPI trafficking in the early secretory pathway. This was performed as detailed before, using transiently transfected SiT-FusRed to allow segmentation of the Golgi region and imaging using live cell confocal microscopy at 1 minute temporal resolution.

From 3 experimental repeats, little difference in the early secretory dynamics of GFP-GPI between mock and spastin depleted cells was observed (**Figure 5B**). Both treatments showed a near identical rate of increase of GFP-GPI signal in the Golgi region. Spastin depleted cells showed a slight trend toward a decrease in the amount of time for the maximum GFP-GPI signal to occur in the Golgi, but this difference was not statistically significant (**Figure 5C**). In addition, spastin depleted cells showed a trend towards an increased rate of export from the Golgi compared to mock cells, but at no

time point was there a statistically significant difference in the signal in the Golgi between the two treatments (**Figure 5B**). These similarities were observed despite a substantial reduction in spastin abundance in spastin siRNA treated cells (**Figure 5D**). Overall therefore, the data showed that spastin depletion had no effect on the trafficking of synchronously released GFP-GPI RUSH cargo in the early secretory pathway.

The effect of H89 treatment on GFP-GPI secretory dynamics

As in the TNFα-GFP assays, GFP-GPI RUSH cells were also treated with H89 as a positive control to confirm that a perturbation of ER export machinery would lead to changes in the trafficking of GFP-GPI into and out of the Golgi apparatus. As seen when TNFα-GFP RUSH cells were treated with H89, the reporter signal accumulated in the Golgi region at a substantially decreased rate compared to mock cells and had substantial impairment in its export from the Golgi (**Figure 5E**). The time for the maximum GFP-GPI signal to occur in the Golgi region was approximately 10 minutes later than in mock treated cells (**Figure 5F**). This together showed that Sar1-GTPase inhibition led to impairment GFP-GPI trafficking in the early secretory pathway, further validating that manipulations in the ER exit machinery could cause observable changes in the trafficking of RUSH assay cargo.

A)

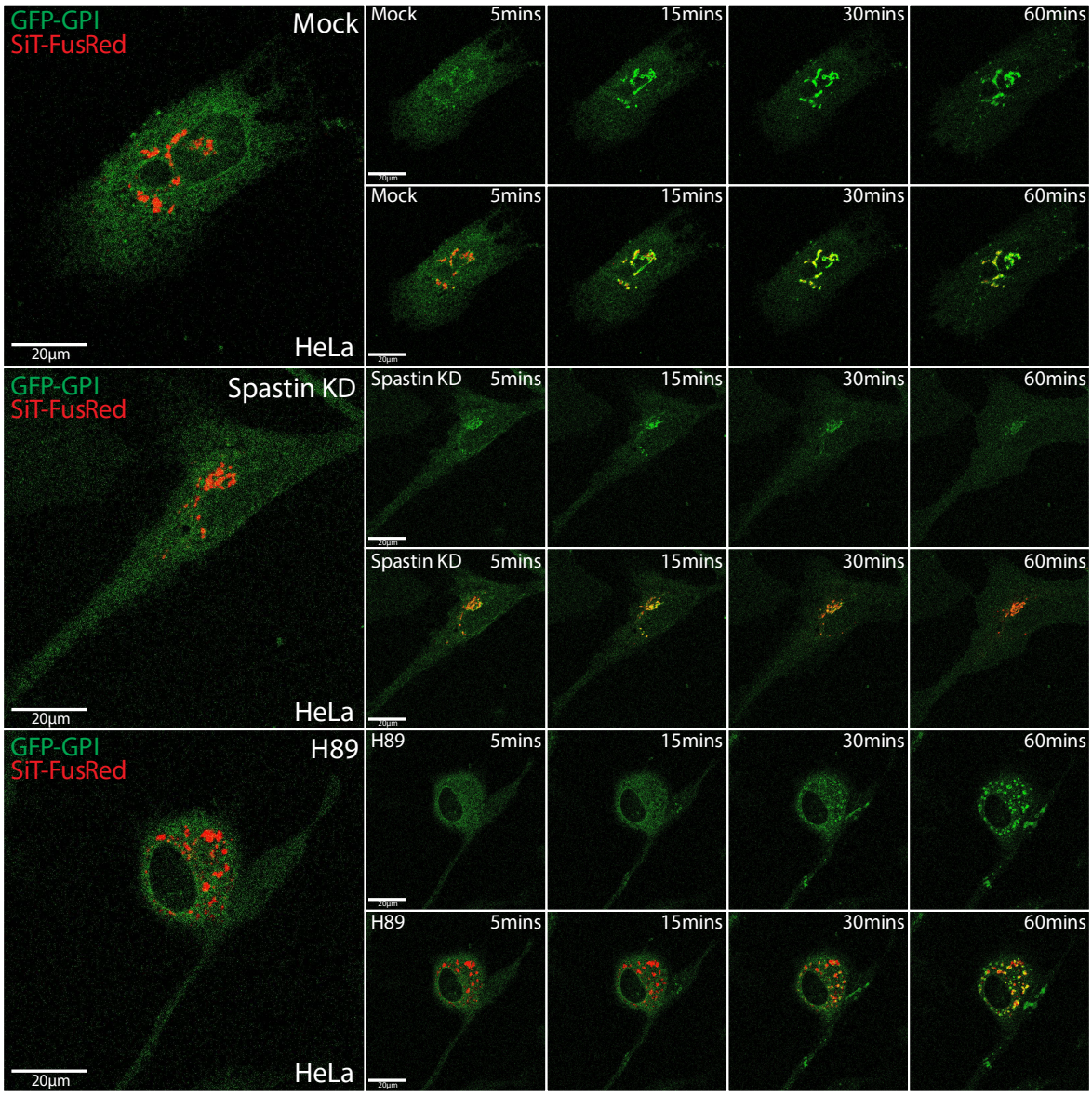
GFP-GPI
SiT-FusRed
Mock
HeLa
20µm
Mock 5mins
15mins
30mins
60mins
Mock 5mins
15mins
30mins
60mins
GFP-GPI
SiT-FusRed
Spastin KD
HeLa
20µm
Spastin KD 5mins
15mins
30mins
60mins
Spastin KD 5mins
15mins
30mins
60mins
GFP-GPI
SiT-FusRed
H89
HeLa
20µm
H89 5mins
15mins
30mins
60mins
H89 5mins
15mins
30mins
60mins

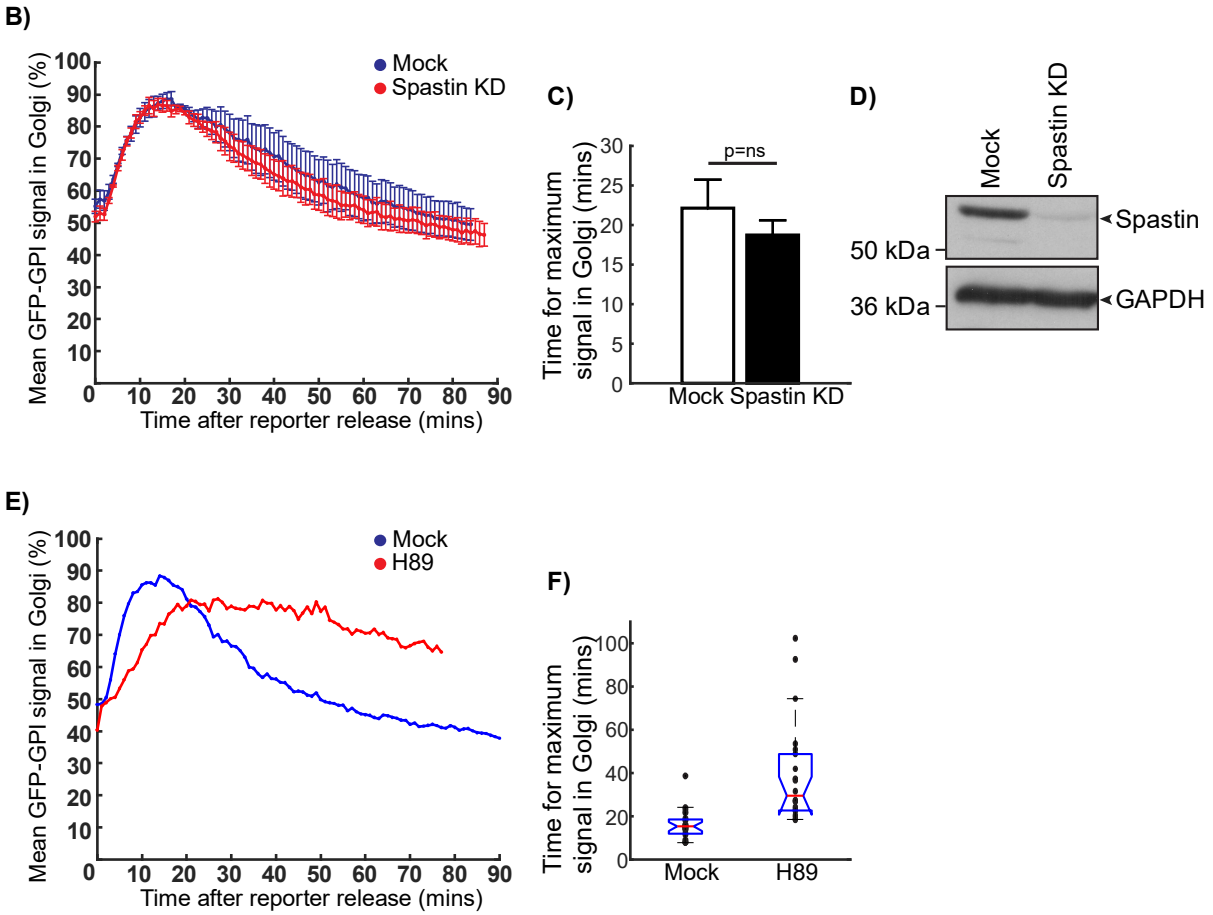

Figure 5 - Spastin depletion does not impair GFP-GPI RUSH cargo trafficking from the ER to the Golgi apparatus.

A) **Live cell imaging of GFP-GPI cargo release and trafficking through the secretory pathway upon spastin depletion and H89 treatment in SBP-GFP-GPI KDEL-Streptavidin RUSH HeLa cells** – HeLa cells stably coexpressing SBP-GFP-GPI RUSH reporter and KDEL-Streptavidin RUSH hook were transfected using spastin siRNAs or treated with 100µM H89 and transfected with SiT-FusRed to label the Golgi apparatus. Cells were then imaged using live cell confocal microscopy at ~40 seconds per frame for 90 minutes. The release SBP-GFP-GPI from KDEL-Streptavidin was stimulated using 40uM biotin solution, with time 0 corresponding to the time of biotin addition. The different sets of panels show mock treated cells (top main row), spastin depleted cells (2nd main row), and H89 treated positive control cells (bottom main row). In each main panel, the image on the left shows both GFP-GPI and SiT-FusRed channels for the frame of biotin addition (t=0). The smaller right panels show 5, 15, 30, and 60 minutes after biotin addition, with the top and bottom panels showing GFP-GPI alone, and both channels merged respectively. Scale bars for all images represent 20µm. This figure corresponds to **Movie 3**.

B) **Graph of GFP-GPI signal in the SiT-FusRed labelled Golgi after reporter release in mock and spastin depleted SBP-GFP-GPI KDEL-Streptavidin RUSH HeLa cells** – HeLa cells stably expressing SBP-GFP-GPI RUSH reporter and KDEL-Streptavidin RUSH hook were treated with either mock or spastin siRNA and transfected with SiT-FusRed to highlight the Golgi apparatus. Cells were then treated with biotin, imaged, and analysed as described in **Figure 4B**. ~30 cells were imaged per treatment per experimental repeat, with three experimental repeats performed in total. The graph shows the mean normalised GFP-GPI signal in the Golgi region during the biotin-induced release of the GFP-GPI reporter over the three experimental repeats for each treatment. Time 0 corresponds to the addition of the biotin. Error bars at each minute represent standard error of the mean. Blue and red lines/bars show mock and spastin siRNA treated cells respectively.

C) **Bar chart showing the time for maximum localisation of GFP-GPI signal in the SiT-FusRed defined Golgi region in mock and spastin depleted SBP-GFP-GPI KDEL-Streptavidin RUSH HeLa cells** – Live cell imaging and image analysis was performed on SBP-GFP-GPI KDEL-Streptavidin RUSH HeLa cells treated with either mock or spastin siRNAs and transfected with SiT-FusRed as described in **Figure 5A** and **Figure 5B**. The time after biotin addition for the maximum localisation of GFP-GPI signal in the SiT-FusRed defined Golgi region was recorded for each mock and spastin depleted cell. This data was averaged between the three experimental repeats for each treatment. Error bars indicate standard error of the mean. P values were generated by using paired two-tailed t-tests.

D) **Western blot showing spastin protein abundance in mock and spastin siRNA deleted SBP-GFP-GPI KDEL-Streptavidin RUSH HeLa cells** - SBP-GFP-GPI KDEL-Streptavidin RUSH HeLa cells treated with mock or spastin siRNA were lysed and proteins separated by SDS-PAGE, with proteins transferred onto PVDF membrane by western blotting. The abundance of spastin was detected by using a spastin antibody. Equal loading between lanes was verified by also blotting for the housekeeping protein GAPDH.

E) **Graph of GFP-GPI signal in the SiT-FusRed labelled Golgi after reporter release in mock and H89 treated SBP-GFP-GPI KDEL-Streptavidin RUSH HeLa cells** – HeLa cells stably expressing SBP-GFP-GPI RUSH reporter and KDEL-Streptavidin RUSH hook were treated with either mock or 100µM H89 and transfected with SiT-FusRed to highlight the Golgi apparatus. Cells were then treated with biotin, imaged, and analysed as described in **Figure 5B**. ~30 cells were imaged per treatment, with one experimental repeat performed. The graph shows the mean normalised GFP-GPI signal in the Golgi region during the biotin-induced release of the GFP-GPI reporter for each treatment. Time 0 corresponds to the addition of the biotin. Blue and red lines show mock and H89 treated cells respectively.

F) **Box plots showing the time for maximum localisation of GFP-GPI signal in the SiT-FusRed defined Golgi region in mock and H89 depleted SBP-GFP-GPI KDEL-Streptavidin RUSH HeLa cells** – Live cell imaging and image analysis was performed on SBP-GFP-GPI KDEL-Streptavidin RUSH HeLa cells treated with either mock or 100µM H89 and transfected with SiT-FusRed as described in **Figure 5A** and **Figure 5B**. The time after biotin addition for the maximum localisation of GFP-GPI signal in the SiT-FusRed defined Golgi region was recorded for each mock and H89 treated cell and are depicted by black dots. Box plot description as in **Figure 5F**.

4.3 – Discussion

4.3.1 – Spastin and IST1 localise to ERES but are not required for the efficient secretion of TNFα-GFP or GFP-GPI RUSH cargo

The background to this investigation was two observations from a publication by Connell et al. (2009). These were: 1) that the ER-localised M1 isoform of spastin colocalises with temperature sensitive VSVG at early timepoints during VSVG secretion; and 2) that overexpression of AAA+ domain mutant spastin blocks VSVG secretion from the ER. This suggested that M1 spastin may localise to components of the ER exit machinery (or ERGIC) and regulate secretion. Interaction studies of spastin and IST1 have strengthened this hypothesis, as both proteins have been suggested to interact with the accessory protein TFG (unpublished, Reid lab; Hein et al. 2015), which itself interacts and localises with the COPII coat proteins at ERES (Hanna et al. 2017; Johnson et al. 2015; McCaughey et al. 2016).

Fixed cell imaging supported a role for spastin at ERES. Using high spatial resolution Airyscan microscopy, M1 spastin was shown to colocalise with Sec23 in the perinuclear and central regions of the cell, but not at the cell periphery. By spinning disk microscopy this interaction was seen to be stable, with M1 spastin remaining colocalised to both static Sec23-labelled ERES, and highly dynamic Sec23 puncta. Spastin's ESCRT-III interacting protein IST1 was also shown to localise to Sec23-labelled ERES. Significantly, this is the first time that IST1 has been shown to localise to ER exit machinery. However, neither spastin nor IST1 depletion was shown to have any effect on ER to Golgi trafficking of TNFα-GFP or GFP-GPI RUSH cargos.

The model for spastin and IST1's function in cargo secretion

It was hypothesised that spastin and IST1 may function in regulating secretion. One dominant theme of spastin and IST1 colocalisation is that the two proteins interact to drive membrane remodelling. Examples of this include the cofunction of IST1 and spastin in abscission (Guizetti et al. 2011), during nuclear pore formation (Vietri et al. 2015), and in endosomal tubule fission (Chapter 3; Allison et al. 2017).

In the context of ERES, one such membrane remodelling event is the fission of cargo-containing ER membranes. One of the major membrane fission events that occurs at ERES is the fission of COPII vesicles to transport cargo to the ERGIC and ultimately to the Golgi on microtubules. There are parallels between this process and endosomal tubule fission. For example, topologically the processes are the same, with both cargo carriers being membranous cargo-filled protrusions emanating into the cytosol. Additionally, COPII vesicles can adopt tubular conformations. For example,

tubular COPII vesicles are commonly observed during the secretion of collagen (Raote et al. 2017; Venditti et al. 2012) and tubular carriers are observed during the transport of other cargos such as VSVG (Presley et al. 1997), E-cadherin and TNFα (Boncompain et al. 2012). In addition, in vitro COPII coat reconstitution experiments have showed the ability of COPII to generate tubules (Zanetti et al. 2013).

The integral function of microtubules in both endosomal tubule fission and secretion provides further support to a putative role for spastin and IST1 in the fission of COPII vesicles. For example, the protein p150^{Glued} of the dynein-dynactin complex is important in both pathways to maintain efficient membrane trafficking (Wassmer et al. 2009; Watson et al. 2005). In secretion, p150^{Glued} was shown to interact with Sec23 of the COPII coat and upon its depletion impair the ER to Golgi trafficking of temperature sensitive VSVG (Watson et al. 2005). Similar to fissioned SNX1 tubule trafficking from endosomes to the Golgi (Jin and Snider 1993), cargo exiting the ER for the Golgi apparatus travels on microtubules and can be blocked by microtubule depolymerisation using nocodazole (Presley et al. 1997). Furthermore, ERES and VTCs localise to microtubules (Mizuno and Singer 1994; Ralston et al. 2001; Saraste and Svensson 1991; Watson et al. 2005), similar to the intimate localisation of endosomes and microtubules (Friedman et al. 2013; Nielsen et al. 1999). Therefore, it is plausible that a spastin-IST1 interaction may facilitate COPII vesicle fission, potentially working in combination with the established COPII neck constriction GTPase Sar1 (Bielli et al. 2005; Hanna et al. 2016; Lee et al. 2005; Long et al. 2010).

The evidence against spastin and IST1's function in cargo secretion

If spastin or IST1 was essential in COPII vesicle fission, it would be expected that cargo flux from the ER to Golgi would be delayed in cells depleted of spastin or IST1. However, this was categorically not the case in live cell RUSH assays measuring the synchronised ER export of TNFα-GFP and GFP-GPI. The kinetics of TNFα-GFP ER to Golgi transport was almost identical in spastin depleted, IST1 depleted and mock cells. Furthermore, this was also true for GFP-GPI transport in mock and spastin depleted cells. Significantly, GPI cargos have a different mode of transport from type II transmembrane proteins such as TNFα, requiring adaptor proteins such as p24 for their internalisation into COPII vesicles (Schimmöller et al. 1995; Takida et al. 2008) and exiting the ER in a distinct subset of exit sites (Bonnon et al. 2010). Spastin therefore appears to have no role in at least two different ER exit processes.

These results are arguably not discordant with those from Connell et al. (2009). Although an effect on VSVG traffic was observed with an ATPase mutant form of M1 spastin, no effect on VSVG traffic was observed when spastin was depleted using siRNAs. Furthermore, the interpretation of

spastin's involvement in ER exit based on the use of the ATPase null isoform of spastin can be questioned. Substantial non-physiological microtubule bundling was observed upon the overexpression of ATPase mutant spastin, causing a dramatic loss of reticular ER architecture (Connell et al. 2009). Both microtubule and ER architecture are essential for secretory cargo transport (Okamoto et al. 2012; Presley et al. 1997; Watson et al. 2005), with high curvature ER tubules important for ERES organisation (Okamoto et al. 2012). Therefore, from these experiments it is hard to deconvolve spastin's potential involvement in cargo secretion from the inhibitory effects of microtubule and ER architecture disruption generated through the overexpression of the spastin ATPase mutant. Overall, considering this with my experiments, it seems very unlikely that spastin functions in either TNFα, GPI anchored protein, or VSVG cargo transport between the ER and the Golgi.

4.3.2 – Potential functions of spastin and IST1 at ERES

In light of these results, what might be spastin's function at ERES? Three models are discussed below: 1) spastin functions in the secretion of selected cargos such as procollagens; 2) spastin functions in generalised cargo secretion, but these effects were not revealed by the RUSH assay; and 3) spastin has a function independent of conventional secretion at ERES.

Procollagen secretion

A clue to the function of spastin and IST1 at ERES may come from better understanding the functional interaction between spastin, IST1 and ERES accessory protein TFG. Like spastin and IST1, TFG was shown to localise to ERES but upon depletion had no effect on the trafficking of RUSH cargos such as mannosidase II, VSVG, E-cadherin, and galactose-1-phosphate uridylyl transferase (GalT; McCaughey et al. 2016). Although debated (Hanna et al. 2017), TFG was suggested to function specifically in the secretion of procollagen (McCaughey et al. 2016).

The function of IST1 or spastin depletion on procollagen secretion has not yet been investigated, and lack of spastin function in VSVG, TNFα, and GPI-anchored protein traffic should not be assumed to apply to procollagen secretion. Procollagens are unique from other COPII cargo by their size, with procollagens able to form up to 400nm (Malhotra and Erlmann 2015). This is substantially larger than the typical 60-90nm diameter of COPII vesicles. As a result, specific machinery is required to distend the COPII vesicle to allow procollagen secretion (Bard et al. 2006; Raote et al. 2017; Saito et al. 2009, 2011). Furthermore, COPII vesicles containing procollagen form tubular structures (Raote et al. 2017, 2018; Venditti et al. 2012) reminiscent of endosomal tubules that form during endocytic

recycling. Given spastin and IST1's potential interaction with TFG and the unique nature of COPII vesicles in procollagen secretion, it would be worth testing whether spastin functions in procollagen secretion.

TFG is able to mediate procollagen secretion by regulation of ERES morphology (McCaughey et al. 2016). Upon TFG depletion, ERES become fragmented into smaller structures resolvable by super resolution light microscopy. This fragmentation is thought to have no effect on smaller cargos, but potentially provide inefficient platforms for procollagen secretion. Given the putative interaction between spastin, IST1, and TFG, and given the function of spastin and IST1 in membrane remodelling, it is possible that spastin may function to remodel the structure of ERES themselves rather than directly mediating the scission of COPII vesicles. This however remains to be tested.

The effect of spastin or IST1 depletion on cargo secretion may be hidden by the RUSH assay

Before discounting any role for spastin or IST1 in generalised cargo export from the ER however, it is worth examining the caveats of the RUSH assay. One of the problems of trying to observe cargo flux through a dynamic system is the difficulty in distinguishing the rate of transport of individual proteins. To address this, a pulse of label can be applied to the system at a defined time, allowing the flux of labelled proteins to be differentiated and measured against the background of unlabelled protein. In the case of the RUSH assay (and temperature sensitive VSVG release assay), this pulse comes by synchronising the release of a fluorescently labelled reporter cargo from the ER. However, a fundamental assumption of these assays is that the pulse (e.g. the synchronisation step in the RUSH assay) does not impact the normal physiology of the system being measured.

In the case of the RUSH assay, the synchronous release of cargo from the ER represents a non-physiological situation. By the synchronous dissociation of RUSH reporter from the ER-resident hook, a high concentration of protein must flux through the early secretory pathway in a short amount of time. The cell has adaptions to respond to high cargo load, with one example being an increase in the number of ERES (Forster et al. 2006; Guo and Linstedt 2006; Stephens 2003). However, given the almost instantaneous action of biotin in the dissociation of the RUSH reporter from the hook (Boncompain et al. 2012), there is a likely temporal mismatch between the time between biotin addition and cargo export and cellular acclimation to high cargo load.

How may ER export accommodate such a high demand on ER exit machinery? One possibility is that a backlog of cargo accumulates in the ER, waiting to be exported. Live cell imaging of TNFα-GFP and GFP-GPI does not rule out this hypothesis as there is a clear temporal delay between the first and

last reporter proteins arriving at the Golgi apparatus. However, an alternative possibility is that pressure on the secretory system is relieved through non-canonical ER export (Benham 2012). Significantly, the function of COPII is not essential for the secretion of all cargo (Mironov 2014). For example, siRNA depletion of all Sar1 and Sec23 isoforms leads to a delay but not a complete block in secretion of all cargos excluding procollagen (Cutrona et al. 2013; Townley et al. 2008). This can also be seen in trafficking of TNFα-GFP and GFP-GPI here when Sar1 was inhibited by H89, and in the trafficking of voltage-sensitive potassium channel 4 (Kv4) upon expression of a dominant negative Sar1 (Hasdemir et al. 2005). This suggests that most cargo (excluding procollagen) is able to export from the ER using an inefficient alternative to COPII-mediated export.

Although much of the machinery of COPII-independent export is unknown (Barlowe and Helenius 2016; Grieve and Rabouille 2011; Nickel and Rabouille 2009), the existence of multiple exit pathways at the ER is significant in the interpretation of data from RUSH or VSVG assays. An untested possibility is that the effect of spastin or IST1 depletion could be masked by the high export load created by the synchronous release of RUSH cargo. If as a result of this atypical load a significant proportion of RUSH cargo was exiting the ER through spastin-IST1 independent pathways, depletion of spastin or IST1 might only have a minimal effect on ER-Golgi traffic. In effect, the alternative export pathways of the ER would compensate for the pressure generated by inadequate COPII-mediated export.

Although never tested directly, there is circumstantial evidence supporting these arguments. Firstly, no studies have ever shown cargo export in the RUSH assay to be fully blocked by disruption of COPII machinery. As described above, the addition of Sar1 inhibitor H89 merely caused a delay in cargo export from the ER to the Golgi. In addition, similar experiments performed with and without the RUSH assay have yielded significantly different results. One example is in the functional analysis of TFG. Whilst McCaughey et al. (2016) observed TFG depletion to have no effect on the secretion of all tested RUSH cargo, Hanna et al. (2017) showed that TFG depletion did have an effect on the secretion of both large cargos such as E-cadherin and small cargos such as the transmembrane domain of mannosidase II. Significantly, Hanna et al. (2017) did not use synchronisation-based methods. Although no literature has cited problems using RUSH previously, given the atypical load of cargo exiting the ER and the availability of other modes of ER exit, it would be useful to analyse the effects of spastin and IST1 depletion on secretion using synchronisation-independent methods.

Functions for spastin and IST1 at ERES independent of conventional secretion

Finally, it is worth speculating briefly that spastin and IST1 may function at ERES in processes unrelated to generalised cargo export. For example, ERES have also been suggested to function as the platform for the formation of autophagosome precursor membranes (Carlos Martín Zoppino et al. 2010; Ge et al. 2013; Ishihara et al. 2001; Reggiori et al. 2004; Sanchez-Wandelmer et al. 2015). Despite recent work identifying the proteins Serca and Vmp1 as important in ER-derived autophagosome biogenesis (Zhao et al. 2017, 2018), the fission mechanism central to autophagosome release from the ER has not yet been identified. Potentially significant is that both autophagosome proteins and ESCRT proteins were recently shown to be required for the secretion of cystic fibrosis transmembrane conductance regulator (CTFR) protein (Noh et al. 2018). Due to the topology of ER-derived autophagosome membranes, any ESCRT-III proteins recruited from the cytosol would have to form on the outside neck of the membrane bud. Of the ESCRT-III proteins, currently only IST1 and CHMP1B have been identified as being able to adopt these conformations (McCullough et al. 2015) and significantly, both of these proteins are interactors of spastin (Reid et al. 2005; Renvoisé et al. 2010; Yang et al. 2008). Despite the circumstantial nature of this evidence, it would therefore be interesting to investigate whether a spastin-IST1 interaction was required for ER-derived autophagosome biogenesis.

4.3.3 – Future experimental plans

Verifying the localisation of endogenous spastin on ERES

The localisation of M1 spastin on ERES was shown through stably expressed N-terminally GFP-tagged M1 spastin. However, experiments localising endogenous spastin on ERES were not performed, although previous members of the Reid lab have observed antibody-labelled endogenous spastin to colocalise with the COPII-coat component Sec31 by confocal microscopy (unpublished data, Reid lab). These experiments require validation, and high resolution (Airyscan or SIM) microscopy could be used to more accurately define the position of spastin on ERES.

Verifying the lack of effect of spastin and IST1 on ER exit

One important future set of experiments is to validate the negative data from the RUSH assay using methods that do not generate a high load on the secretory pathway. Despite the criticisms presented above, this could be done using the RUSH assay. For example, a non-saturating concentration of biotin could be used to only release a small proportion of reporter from the ER. Similarly, a light-dependent caged biotin molecule could be used whose gradual release could be controlled by modulating laser intensity (Terai et al. 2011). Alternatively, rather than modulating the simultaneously release of reporter cargo, the volume of cargo could be reduced by endogenous expression of the RUSH constructs under low expression promoters or by endogenous tagging. A combination of these methods would act to overall reduce the simultaneously load on the secretory pathway.

New developments in protein tagging biology make the synchronous release of reporter unnecessary for the tracking of secreted cargo. Instead, light activation can be used to tag proteins in ER undergoing secretion. This would enable flux through the secretory pathway to be measured in near-endogenous environments. One method is to use photoswitchable proteins. These are proteins which are able to change their fluorescence emission upon irradiation by UV light (Shcherbakova et al. 2014). One example of such a protein is moxDendra2, unique among green to red photoswitchable proteins in its ability to function in the oxidising environment of the secretory pathway (Kaberniuk et al. 2017). By the coexpression of moxDendra2 fused to a secretory protein (e.g. TNFα) and a fluorescent marker of the ER or ERES, a pulse of UV light could be specifically applied to the tagged secretory protein in the ER. This would cause moxDendra2 to switch fluorescence from green to red, allowing the flux of the photoswitched protein to be measured against the background of unconverted proteins.

The use of fluorescence uncaging would also achieve a similar outcome. Like photoswitchable proteins, caged fluorophores rely on the impulse of UV light to cause a change in their fluorescent properties (Politz 1999). However, typically this would be a transition from a dark state to a light state, generated by the UV-induced cleavage of the cage component. Importantly, these caged fluorophores can be directed to a protein of interest by use of protein-specific attachment sites (Hauke et al. 2017). By fusing the protein of interest to such a tag (e.g. HaloTag) and adding the caged fluorophore covalently bound to the tag ligand (e.g. Halo-ligand) to the cell, the protein of interest would be labelled by the non-fluorescing caged fluorophore. Upon an organelle-directed pulse of UV light, it would allow the tagged secretory proteins in the ER to fluorescence. This would allow their flux through the secretory pathway to be imaged. In both this method and the photoswitching method, the tagged secretory proteins could be expressed endogenously, further ensuring negligible impact on the secretory pathway.

Testing functions of spastin at ERES that are independent of generalised cargo secretion

The function of spastin at ERES outside general protein secretion also needs to be tested. An important experiment is to validate the interaction between spastin and TFG. This could be performed using coimmunoprecipitation and colocalisation experiments. If an interaction between spastin and TFG was observed, based on the observations of McCaughey et al. (2016), the role of spastin in procollagen secretion or ERES reorganisation could be investigated. The rate of procollagen secretion can be determined by ascorbic acid addition (Graham et al. 1995). Ascorbic acid greatly increases the production of procollagen, allowing the rate of procollagen increase on the cell to be used as a surrogate of the rate of procollagen secretion. The cell surface abundance increase of collagen could then be compared by antibody detection and fluorescence microscopy between mock and spastin depleted cells. Light microscopy could also be used to measure the number of ERES in mock and spastin depleted cells, providing information as to spastin's role in ERES remodelling.

Finally, the putative role of spastin and IST1 in ER-derived autophagosome biogenesis could be tested. This again could be examined using light microscopy, with experiments aiming to visualise whether ERES localised spastin and IST1 also colocalised with early markers of ER-derived autophagosome biogenesis such as Dfcp1 (Hayashi-Nishino et al. 2009).

Chapter 5 – The impact of ATPase-defective spastin on the cell surface proteome

5.1 - Introduction

5.1.1 – The cell surface proteome as a clue to mechanisms of HSP

The importance of cell surface proteins

Cell surface proteins facilitate the interaction between a cell and its environment. This includes the bidirectional transport of ions and nutrients by ion channels, solute transporters, secretion machinery, and endocytic machinery; signal transduction in development or immunity by receptor proteins; and migration and adhesion by proteins that bind the extracellular matrix. Maintaining a homeostatic balance of this protein landscape is therefore essential to maintaining cellular function (Apaja and Lukacs 2014).

An aberrant change in the cell surface proteome can lead to disease. In antigen presenting immune cells, a loss of major histocompatibility complex (MHC) class II at the cell surface leads to a loss of antigen presentation, resulting in diseases such as bare lymphocyte syndrome (Reith and Mach 2001). In cancer development, changes in the abundance of cell adhesion proteins facilitate cancer metastasis (Okegawa et al. 2004), and changes in receptor abundance facilitates uncontrolled growth (Witsch et al. 2011). In neurons, a loss of myelination proteins at the cell surface results in neurological diseases, including Charcot-Marie-Tooth disease (Berger et al. 2002) and Devic's disease (Wingerchuk et al. 2006). In addition, remodelling of the neurotransmitter landscape is common during drug addiction (Volkow et al. 2016), and toxins such as clostridial cytotoxins can specifically act to prevent neuroreceptor localisation on the cell surface (Popoff and Poulain 2010).

Cell surface protein homeostasis

The cell surface proteome is maintained in a dynamic equilibrium, with proteins being continuously added or removed at the plasma membrane by the fusion or fission of protein-containing vesicles. Proteins added to the cell surface may either be newly synthesised proteins, or proteins that have already been internalised and have been recycled. Proteins are typically removed from the cell surface through endocytic pathways, including clathrin-mediated endocytosis, macropinocytosis and via caveolae (reviewed in Introduction Section 1.4.2).

Newly synthesised proteins are typically derived from the secretory pathway as a result of vesicle trafficking from the TGN to the cell surface. However, newly synthesised proteins that are trafficked from the TGN to the lysosome via sorting endosomes can also reach the cell surface. This occurs via these 'secretory lysosomes' fusing with the plasma membrane, typically during times of stimulation such as during infection (Stinchcombe 2004). In addition, cell surface proteins that have been endocytically internalised can be trafficked back to the cell surface. These proteins are retrieved away from degradation at the sorting endosome and are packaged into endosomal recycling tubules. These tubules then bud away from the endosome body and are transported by microtubule motors to the plasma membrane (reviewed in Introduction Section 4).

Disruption of these transport processes can lead to large changes in the protein landscape at the cell surface. For example, depletion of the secretory protein TFG leads to a loss of extracellular collagen (McCaughey et al. 2016). In endocytosis, the expression of a scission-defective dynamin leads to increased residence of TfnR on the cell surface (Marks et al. 2001). In secretory lysosome fusion, overexpression of synaptotagmin II results in inhibition of Ca^{2+} triggered exocytosis of lysosomes (Baram et al. 2001). In endocytic recycling, inhibition of the SNX-retromer complex by depletion of SNX27 or VPS35 leads to a substantial change in the cell surface proteome, with a particular effect on glucose and metal ion transporters (Steinberg et al. 2013). In addition, it was recently shown that inhibition of the retriever-interacting SNX protein, SNX17, also led to large changes in the surface proteome, with a particular effect on integrin abundance (McNally et al. 2017).

A potential role of spastin in cell surface protein homeostasis

Spastin is an important protein in the endocytic pathway (Allison et al. 2017). Depletion of spastin leads to the formation of long endosomal tubules as a result of impaired endosomal tubule fission (Chapter 3; Allison et al. 2017). This results in inefficient cargo recycling, both from the endosome to the cell surface (Allison et al. 2013), and from the endosome back to the TGN (Allison et al. 2017). As a result, typically recycled receptors such as TfnR and M6PR have decreased abundance at the cell surface and TGN respectively, and have an increased lysosomal localisation (Allison et al. 2013, 2017). In addition, spastin depleted cells and cells expressing ATPase-defective spastin, or MIT domain-mutated spastin, display lysosomal abnormalities (Allison et al. 2017). These cells contain abnormally acidic lysosomes that are swollen in size and contain undigested membranes (Allison et al. 2017). IPSC-derived neurons from patients with spastin-induced HSP also display the same phenotype (Allison et al. 2017). This suggests that spastin mutation or depletion not only disrupts the endocytic pathway by blocking recycling, but also by causing lysosomal dysfunction.

It can therefore be predicted that a loss of functional spastin would result in dramatic changes in the cell surface proteome. These changes could occur through a direct failure of endosome to plasma membrane recycling, but also as a result of wider-ranging consequences of lysosomal dysfunction. Although this has never been systematically studied, supporting evidence is that depletion of spastin leads to a reduction of TfnR at the cell surface (Allison et al. 2013). Moreover, if spastin was important in the homeostatic maintenance of the cell surface protein landscape, plasma membrane proteome changes upon spastin loss-of-function could drive disease pathology. Pathology could be caused either by the specific effect on one or a small group of proteins having an altered cell surface abundance, or by the combined effect of multiple proteins.

5.1.2 – Experimental approach

I aimed to test whether a loss of functional spastin led to changes in the cell surface proteome. This was done with the added aim of potentially identifying proteins with large changes in abundance that may help explain the mechanisms of spastin-HSP pathology. This was performed using quantitative mass spectrometry of cell surface isolated proteins, with peptide labelling performed using Tandem-Mass-Tag labelling (detailed below and see Materials and Methods).

The cells used were obtained from a spastin mouse model that contained a N384K mutation in the phosphate binding site of the Walker-A motif of spastin's AAA+ domain (Connell et al. 2016). The use of cells from this mouse conferred physiological relevance to any findings, as the human mutational equivalent (N386K) missense mutation was shown to cause HSP (Fonknechten et al. 2000), and the mouse model develops a gait phenotype typical of HSP (Connell et al. 2016). Mouse embryonic fibroblasts (MEFs) and embryonic primary cortical neurons were used for cell surface proteome analysis. MEFs were used initially as proof of concept and allowed comparisons between data previously collected using the spastin N384K MEF cells (e.g. Chapter 3; Allison et al. 2017). Primary cortical neurons were used to increase physiological relevance of any findings to the disease, as HSP is a specific axonopathy of corticospinal neurons. These experiments represent the first time that cell surface proteomics has been performed on neurons, and the first example of systematically analysing the cell surface proteome for clues into the mechanisms of a neurological disease.

5.1.3 – Benefits of TMT labelling

Introduction to quantitative proteomic labelling

A labelling strategy is typically required to compare between different quantitative proteomic samples. This label is specific to the peptides of each sample, allowing all the peptides of multiple samples to be combined and run in a single mass spectrometry experiment. The abundances of each identified protein can then be assigned to the appropriate sample. Two basic labelling strategies exist: SILAC (isotopic) and TMT (isobaric).

In SILAC labelling, cells are cultured in the presence or absence of amino acids that have substituted isotopic nuclei, such as ^{13}C or ^{15}N. During repeated rounds of growth and cell division, these heavy amino acid isotopes are imported into the cell and incorporated into proteins. After an extended period of time, all proteins will contain a heavy amino acid label. Cells with and without the label (e.g. a control and a treatment) can then be lysed, combined, and processed for mass spectrometry. The relative abundance of each peptide can be assigned to the appropriate sample by small shifts in the mass/charge ratios obtained in the presence of the SILAC label.

In TMT labelling, cells are cultured in normal growth media until the time of lysis. Cells are then lysed, and the proteins of each sample kept separate during peptide digestion. These peptides are then labelled using isobaric chemical tags which bind to the N-terminus or a lysine residue in the digested peptide. These tags have different combinations of ^{13}C and ^{15}N substitutions in their 'mass region', allowing the peptides of each sample to have a unique identity. Labelled peptides are then mixed and processed together in a single mass spectrometry run.

Benefits of TMT labelling

The use of TMT labelling was advantageous in my work. SILAC has benefits in that it has a simple workflow, with the samples grown in the different SILAC media combined upon lysis. This potentially reduces experimental variability due to operational mistakes (e.g. pipetting errors, etc.). However, an important limitation is that SILAC labelling requires cells to undergo cell division for incorporation of the amino acid isotopes. Neurons do not undergo cell division, and hence could not be labelled by traditional SILAC labelling. TMT labelling however does not have this problem, as proteins are labelled post-peptide digestion.

In addition, due to the variety of TMT labels available, up to 11 samples can be compared simultaneously in a single mass spectrometry run. For SILAC, the maximum comparison is three (unlabelled, ^{13}C, ^{15}N). Thus, with the TMT approach, more samples or multiple experimental repeats can be processed in the same mass spectrometry run, reducing experimental variability due to potential mass spectrometry run differences.

5.1.4 – Summary of aims

1. What is the impact of ATPase defective spastin on the cell surface proteome of MEFs and primary cortical neurons?
2. How do these changes compare with other unbiased studies that have investigated the effects of defective endosomal recycling on the cell surface proteome?
3. Can the changes observed elucidate mechanisms of axonopathy observed in HSP?

5.2 – Results

5.2.1 – Summary of methods

The effect of the spastin^{N384K} ATPase mutation on the mouse cell surface proteome was investigated by cell surface proteomics. This was performed using selective labelling and isolation of cell surface proteins, TMT peptide labelling, and high sensitivity quantitative mass spectrometry. Two different cell types were used: SV-40 immortalised MEFs, and embryonic primary cortical neurons. These were processed in two separate experiments. Each mass spectrometry run quantified peptides from samples extracted from wildtype (spastin$^{wt/wt}$; 'WT'), spastin heterozygous mutant (spastin$^{wt/N384K}$; 'HET'), and spastin homozygous mutant (spastin$^{N384K/N384K}$; 'HOM'), allowing a direct comparison between different spastin^{N384K} genotypes.

5.2.2 – MEF plasma membrane proteomics selectively quantified cell surface proteins and showed the spastin^{N384K} mutation drives intergenotypic differences

An outline of the experimental protocol is shown in **Figure 1A**, as described in Materials and Methods (Section 2.3.2). In brief, three samples of WT, HET, and HOM MEFs were grown to confluency in 10cm dishes, and their cell surface biotinylated. Following cell lysis, biotinylated proteins were isolated by streptavidin pull-down, washed, digested to produce peptide fragments that were then labelled with TMT reagents. A unique TMT label was used for each sample. Labelled peptides were then combined and analysed by liquid chromatography tandem mass spectrometry using a rising acetonitrile (AcN) gradient.

Out of the 837 proteins identified, 594 (71%) were annotated with plasma membrane terms based on the Swiss-Prot protein annotated database (**Figure 1B**). Five different plasma membrane terms were used to avoid incorrectly ignoring poorly annotated proteins. Proteins with multiple plasma membrane terms were only allocated to one category (see **Figure 1B** legend for details). Of the remaining proteins, 33 (4%) solely nuclear proteins were identified, and 209 (25%) proteins were identified that were identified as neither plasma membrane or nuclear. These enrichment proportions were similar to other published TMT cell surface proteomics experiments using unfractionated samples (Weekes et al. 2014). Collectively this shows the technique to have yielded a strong enrichment of plasma membrane proteins.

Hierarchical clustering of the 9 samples was performed (**Figure 1C**). This generated a dissimilarity score based on the relative abundance of each protein between each sample which was used to link samples of similar scores (see **Figure 1C** legend for clustering details). This was performed to assess the validity of investigating intergenotypic differences between the WT and spastin^{N38K} mutant samples. Encouragingly, there was strong intragenotypic clustering, with the samples of each genotype preferentially clustering with each other and separate from samples of the other two genotypes. Looking intergenotypically, HET samples preferentially clustered with WT samples rather than HOM samples (see **Figure 1C** dendrogram). This suggested differences in the cell surface proteome changes driven by the heterozygous and homozygous spastin^{N384K} mutation in MEFs.

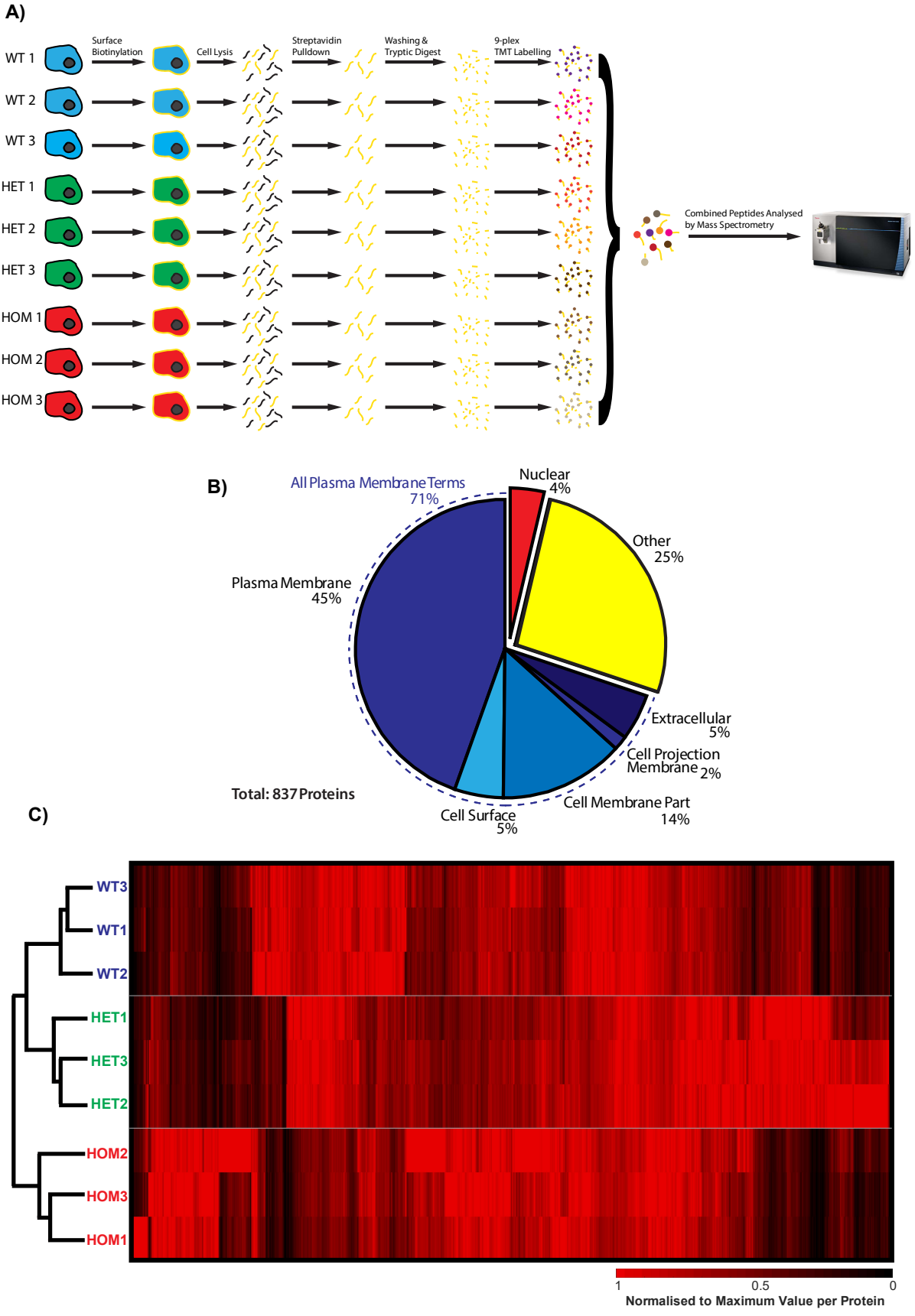
A)
WT 1
WT 2
WT 3
HET 1
HET 2
HET 3
HOM 1
HOM 2
HOM 3
Surface Biotinylation
Cell Lysis
Streptavidin Pulldown
Washing & Tryptic Digest
9-plex TMT Labelling
Combined Peptides Analysed by Mass Spectrometry
B)
All Plasma Membrane Terms 71%
Nuclear 4%
Other 25%
Plasma Membrane 45%
Extracellular 5%
Cell Projection Membrane 2%
Cell Membrane Part 14%
Cell Surface 5%
Total: 837 Proteins
C)
WT3
WT1
WT2
HET1
HET3
HET2
HOM2
HOM3
HOM1
1
0.5
0
Normalised to Maximum Value per Protein

Figure 1 - Overview of cell surface proteomics on WT (spastin$^{wt/wt}$), HET (spastin$^{wt/N384K}$), HOM (spastin$^{N384K/N384K}$) Mouse Embryonic Fibroblasts (MEFs).

A) **Schematic of cell surface proteomic protocol** – Triplicates of WT, HET, and HOM MEFs were grown to confluency and surface proteins biotinylated. Cell lysates were generated, and biotinylated proteins extracted using streptavidin pull down. Isolated proteins were washed extensively before being tryptically digested, with digested proteins from each sample then labelled with a unique Tandem Mass Tag (TMT) label. Labelled peptides were then combined and analysed by Liquid Chromatography Tandem Mass Spectrometry with a rising gradient of MeCN for 180 minutes in a Thermo Orbitrap Fusion Lumos mass spectrometer.

B) **Cell compartment analysis of identified proteins** – All proteins identified from mass spectrometry analysis were annotated with their subcellular location by comparison against the mouse Uniprot (Swiss-Prot) subcellular location database. Plasma membrane terms were defined as annotations of 'plasma membrane', 'cell surface', 'cell membrane part', 'cell projection membrane', and 'extracellular', with 'nuclear' annotations also recorded. If multiple annotations existed for any protein, they were given only one label of the first occurring term in the above list.

C) **Clustergram analysis to show intragenotypic and intergenotypic clustering** – Peptide counts for each sample for each identified protein were normalised by the ratio of peptide counts for each sample summated over all proteins. These peptide counts were then normalised to the maximum peptide count for each protein, with the maximum value for each identified protein set to 1. A clustergram representing the hierarchical clustering of the protein set based on a Euclidean pairwise distance metric and an unweighted average distance linkage method was generated with the heatmap showing samples by row, and individual proteins by column. The heatmap scalebar ranges from bright red (1) for the maximum quantified value to black (0), with dark regions showing fewer detected peptides. The clustergram analysis shows strong intragenotypic clustering, indicating consistent trends of intergenotypic difference.

5.2.3 – Heterozygous and homozygous spastin^{N384K} mutation drive significant changes in the MEF cell surface proteome

For each spastin mutant genotype, the mutant vs wildtype fold change for each protein was plotted against its Benjamini-Hochberg adjusted p-value (**Figure 2**). This provided a representation of the magnitude and variability of the plasma membrane protein landscape changes driven by the spastin^{N384K} mutation. Heterozygous and homozygous spastin^{N384K} mutant MEF data were plotted separately, with separate plots also produced for all proteins and those only annotated to be on the cell surface.

Many proteins had significantly increased or decreased cell surface abundance in the HET MEFs compared to WT MEFs (**Figure 2A**). Using a threshold cut-off of a 2-fold increase or a 2-fold decrease (0.5-fold change) and an adjusted p-value of less than 0.01, 36 proteins (6%) had increased abundance at the cell surface compared to 22 proteins with decreased abundance (4%). Highlighting the six proteins within this grouping with the most statistically significant change in cell surface abundance, all 6 proteins with increased cell surface abundance were enriched at least 5-fold, and 6 proteins with decreased abundance were depleted at least 3-fold (**Figure 2B**).

Similarly, the WT vs HOM comparison showed many proteins with an increased or decreased surface abundance (**Figure 2C**). Using the same thresholds as before, 44 proteins (7%) had increased surface abundance and 54 proteins (9%) had decreased surface abundance in the HOM MEFs compared to the WT MEFs. The most statistically robust proteins with increased cell surface abundance all showed at least a 4-fold enrichment in their typical abundance, and those with a decreased abundance showed at least a 5-fold depletion from the cell surface (**Figure 2D**).

These figures were also reproduced ignoring the subcellular location annotation filter (**Figure 2E** and **Figure 2F**). This was provided as a reference as poor or incorrect protein annotations could lead to plasma membrane proteins being falsely ignored. It is worth noting that the shape of both data sets was similar to the respective plasma membrane plots, and reassuringly, the proteins with the largest fold changes were proteins with plasma membrane annotations.

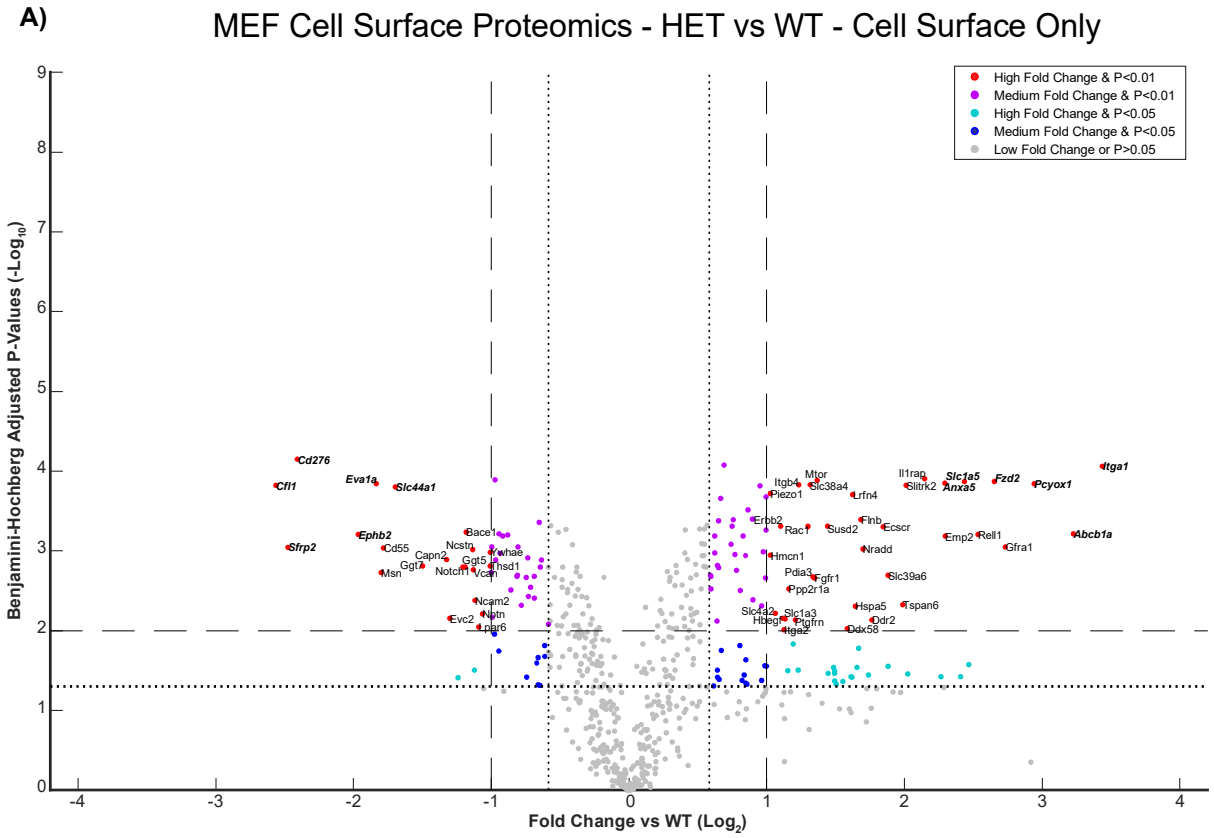
A)
MEF Cell Surface Proteomics - HET vs WT - Cell Surface Only
High Fold Change & P<0.01
Medium Fold Change & P<0.01
High Fold Change & P<0.05
Medium Fold Change & P<0.05
Low Fold Change or P>0.05
Benjamini-Hochberg Adjusted P-Values (-Log10)
Fold Change vs WT (Log2)
Cd276
Cfl1
Eva1a
Slc44a1
Sfrp2
Ephb2
Itga1
Abcb1a
Pcyox1
Fzd2
Slc1a5
Anxa5

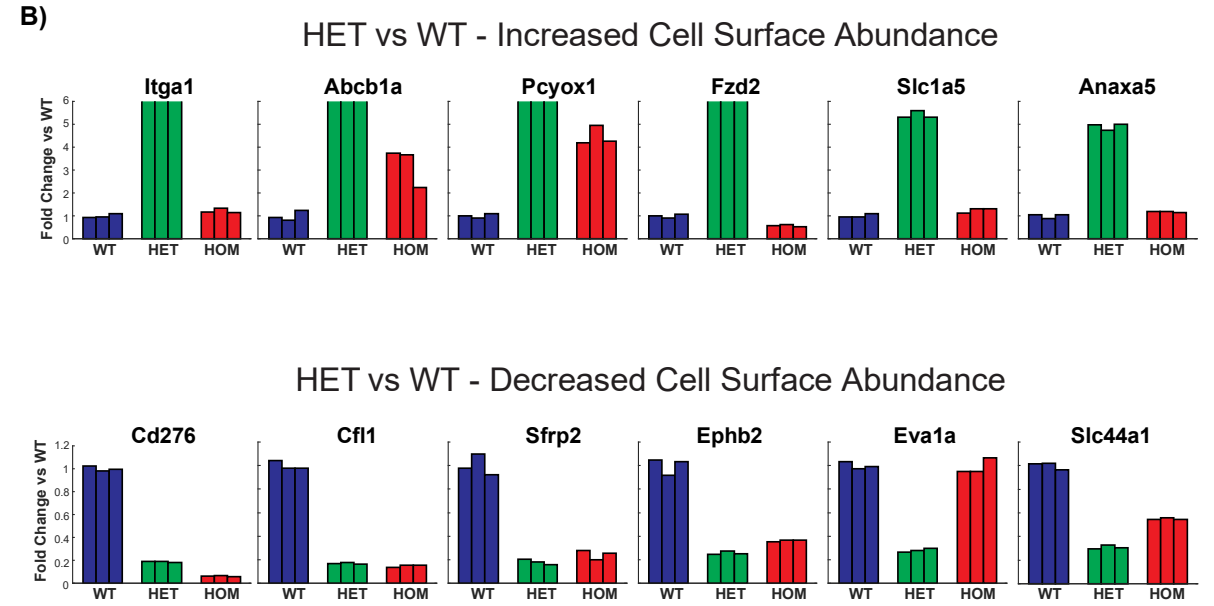
B)
HET vs WT - Increased Cell Surface Abundance
Itga1
Abcb1a
Pcyox1
Fzd2
Slc1a5
Anxa5
Fold Change vs WT
WT
HET
HOM
HET vs WT - Decreased Cell Surface Abundance
Cd276
Cfl1
Sfrp2
Ephb2
Eva1a
Slc44a1

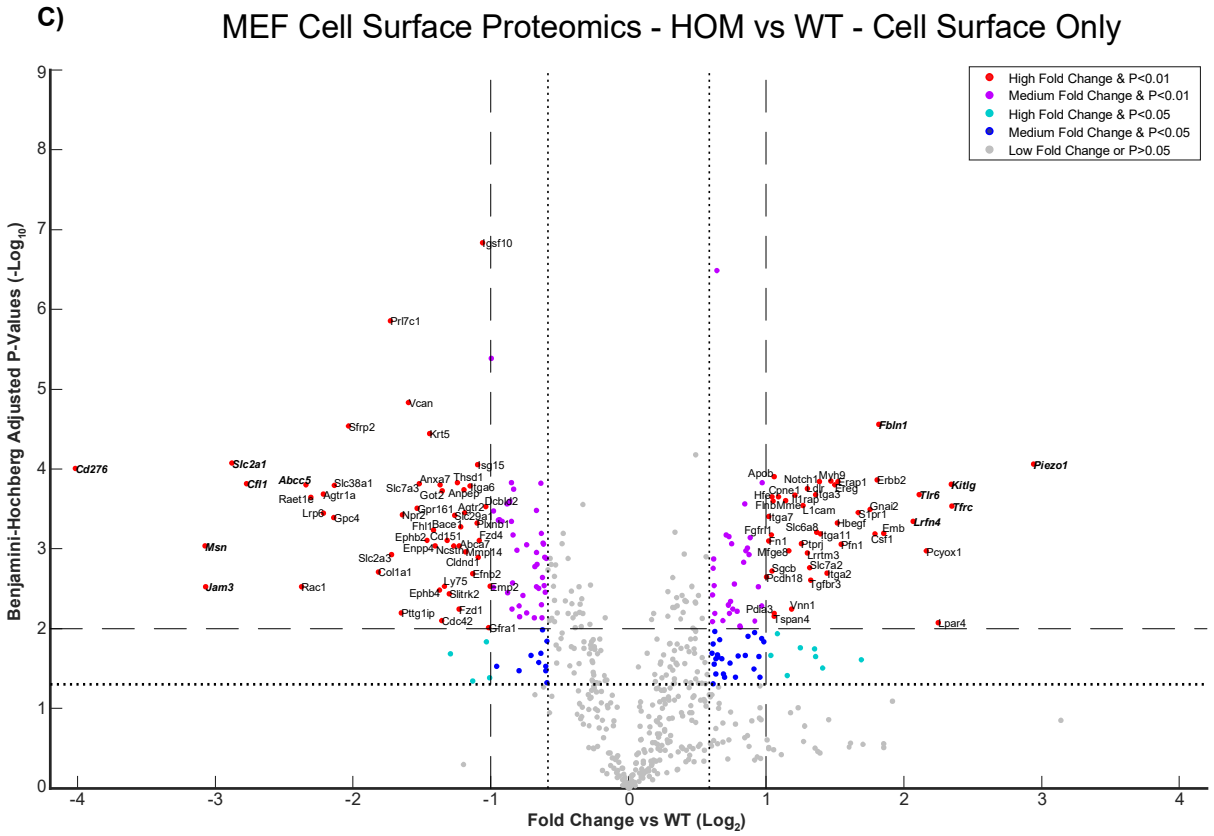
C)
MEF Cell Surface Proteomics - HOM vs WT - Cell Surface Only
High Fold Change & P<0.01
Medium Fold Change & P<0.01
High Fold Change & P<0.05
Medium Fold Change & P<0.05
Low Fold Change or P>0.05
Benjamini-Hochberg Adjusted P-Values (-Log10)
Fold Change vs WT (Log2)
Cd276
Slc2a1
Cfl1
Abcc5
Msn
Jam3
Fbln1
Piezo1
Kitlg
Tfrc
Tlr6
Lrfn4
Lpar4
Dsf10
Prl7c1
Vcan
Sfrp2
Krt5

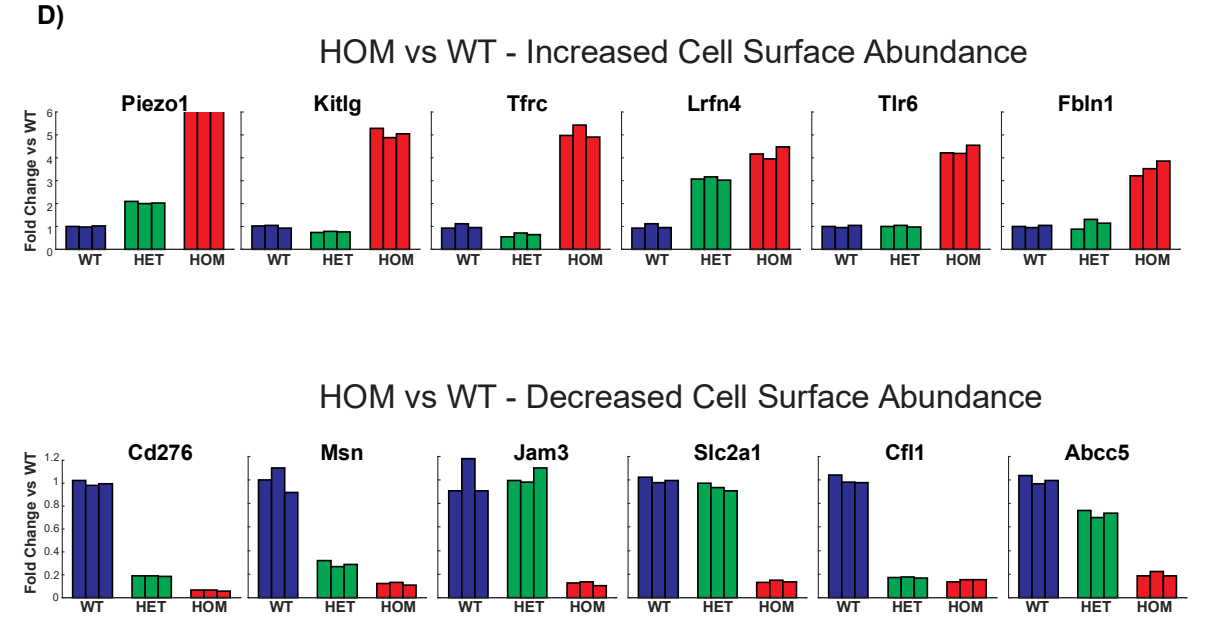
D)
HOM vs WT - Increased Cell Surface Abundance
Piezo1
Kitlg
Tfrc
Lrfn4
Tlr6
Fbln1
Fold Change vs WT
WT
HET
HOM
HOM vs WT - Decreased Cell Surface Abundance
Cd276
Msn
Jam3
Slc2a1
Cfl1
Abcc5

E)

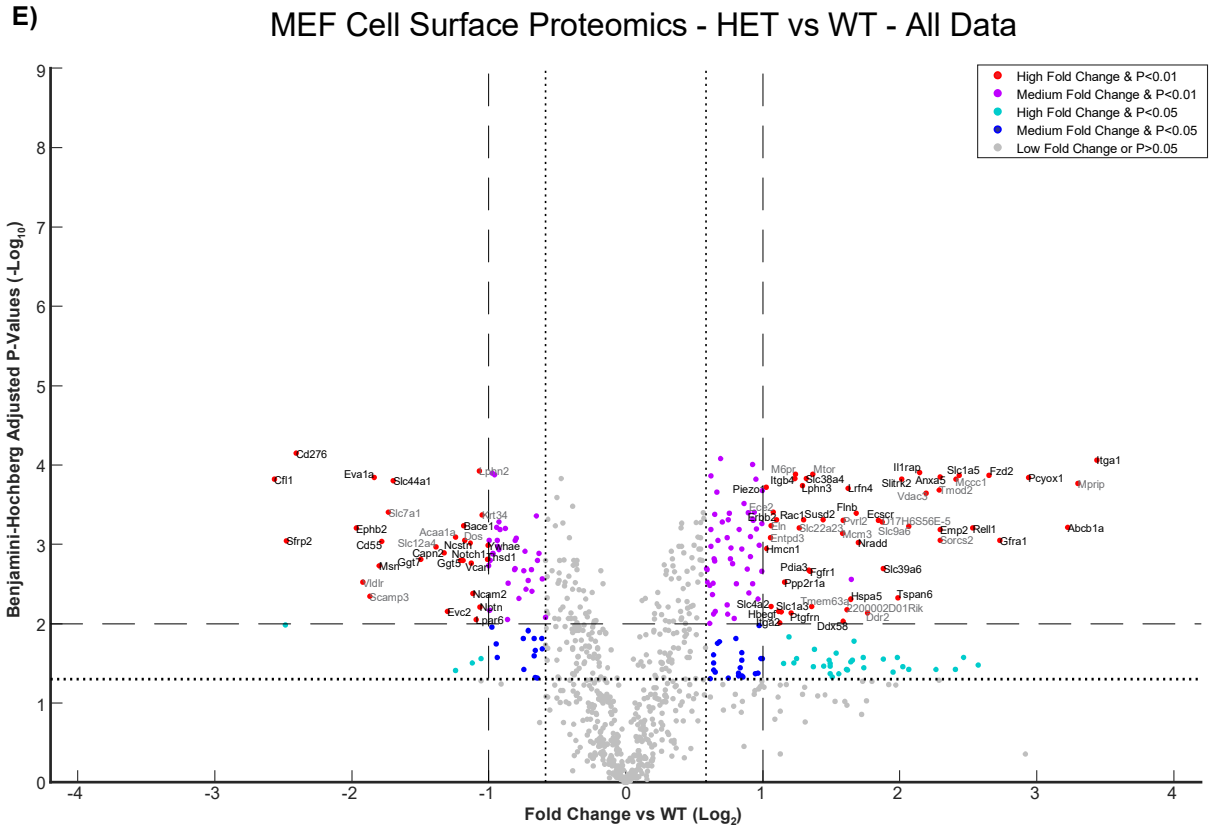
MEF Cell Surface Proteomics - HET vs WT - All Data
High Fold Change & P<0.01
Medium Fold Change & P<0.01
High Fold Change & P<0.05
Medium Fold Change & P<0.05
Low Fold Change or P>0.05
Benjamini-Hochberg Adjusted P-Values (-Log10)
Fold Change vs WT (Log2)

F)

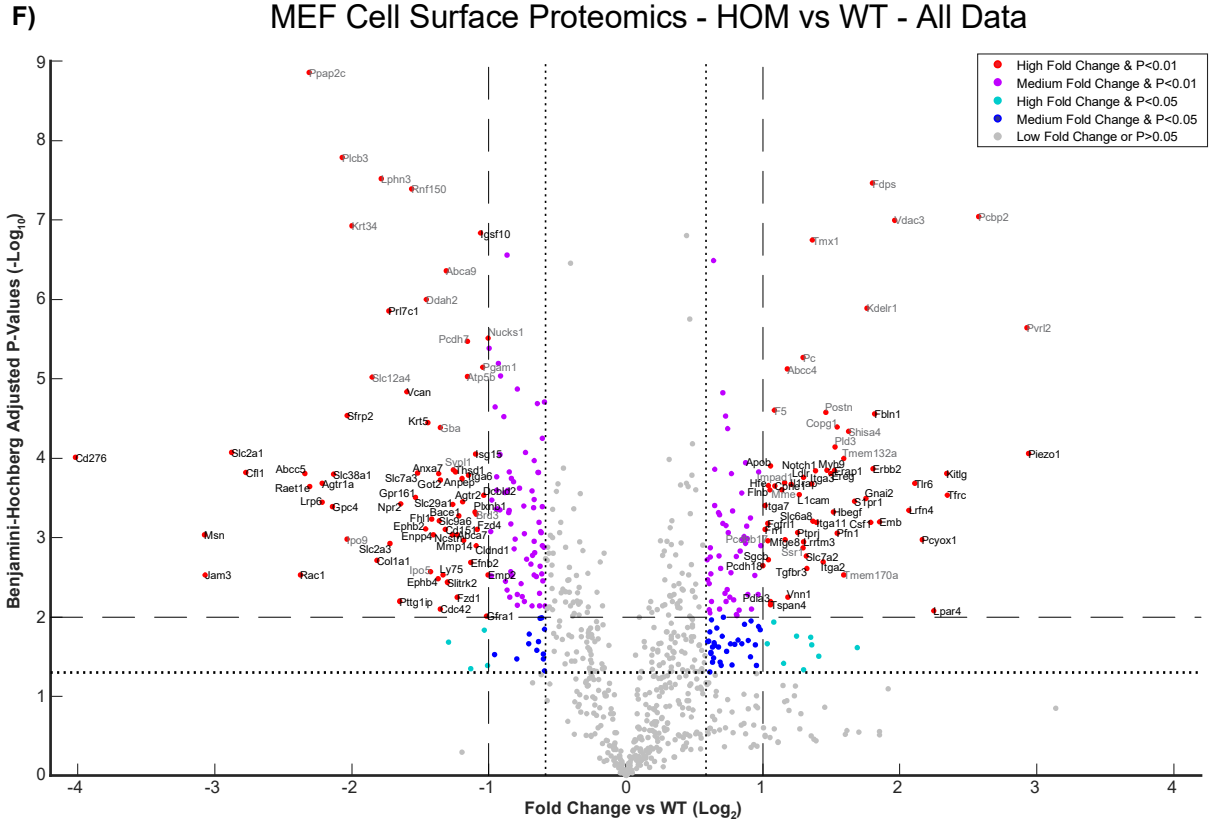
MEF Cell Surface Proteomics - HOM vs WT - All Data
High Fold Change & P<0.01
Medium Fold Change & P<0.01
High Fold Change & P<0.05
Medium Fold Change & P<0.05
Low Fold Change or P>0.05
Benjamini-Hochberg Adjusted P-Values (-Log10)
Fold Change vs WT (Log2)

Figure 2 - Volcano plots reveal that both heterozygous and homozygous spastin^{N384K} mutations drive significant changes in protein cell surface abundance in MEFs.

A) **Volcano plot showing changes in the cell surface abundance of plasma membrane annotated proteins driven by the heterozygous spastin^{N384K} mutation** – The mean HET vs mean WT peptide abundance for each plasma membrane annotated protein was plotted against its Benjamini-Hochberg adjusted p-value (generated from unpaired two-tail t-tests between HET vs WT samples). Fold change (x) was plotted on a $\log_2$ scale, and adjusted p-value (y) plotted on a $-\log_{10}$ scale. Horizontal lines indicate p-values of 0.05 and 0.01 respectively, and vertical lines indicate fold changes of 0.5, 0.67, 1.5, 2 respectively. Proteins with a p-value of lower than 0.01 and less/more 0.5/2-fold change are named, with bold italic names given to proteins with plotted bar charts.

B) **Bar charts of proteins with the largest cell surface increase/decrease driven by the heterozygous spastin^{N384K} mutation** – 6 plasma membrane proteins with the largest HET-WT fold increase/decrease with the lowest HET-WT Benjamini-Hochberg adjusted p-values were selected, and the fold change relative to the mean WT peptide abundance for each sample was plotted for each protein. Chart axes show linear fold change, with axes maxima set to a 6-fold increase for increased abundance samples, and 1.2-fold for decreased abundance samples. Samples exceeding these values were denoted by having open bars.

C) **Volcano plot showing changes in the cell surface abundance of plasma membrane annotated proteins driven by homozygous spastin^{N384K} mutations** – The mean HOM vs mean WT peptide abundance for each plasma membrane annotated protein was plotted against its Benjamini-Hochberg adjusted p-value (generated from unpaired two-tail t-tests between HOM vs WT samples). Chart details as in **Figure 2A**.

D) **Bar charts of proteins with the largest cell surface increase/decrease driven by the homozygous spastin^{N384K} mutation** – 6 plasma membrane annotated proteins with the largest HOM-WT fold increase/decrease with the lowest HOM-WT Benjamini-Hochberg adjusted p-values were selected, and the fold change relative to the mean WT peptide abundance for each sample was plotted for each protein. Chart details as in **Figure 2B**.

E) **Volcano plot showing changes in the cell surface abundance of all detected proteins driven by the heterozygous spastin^{N384K} mutation** – As in **Figure 2A** ignoring subcellular location annotations. Grey text indicates non-plasma membrane annotated proteins.

F) **Volcano plot showing changes in the cell surface abundance of all detected proteins driven by homozygous spastin^{N384K} mutations** – As in **Figure 2C**, ignoring subcellular location annotations. Grey text indicates non-plasma membrane annotated proteins.

5.2.4 – Comparisons between heterozygous and homozygous spastin^{N384K} mutant MEFs reveals proteins with common cell surface abundance changes

Having analysed abundance changes between HET vs WT and HOM vs WT, proteins that showed similar fold changes in both HET and HOM samples were identified. This was performed to identify a set of proteins in which there was a high confidence that their plasma membrane abundance was altered by the spastin mutation. This was performed for proteins with a plasma membrane annotation (**Figure 3A**) and all proteins (**Figure 3B**).

For plasma membrane annotated proteins, there was a weak positive correlation between the fold change of the heterozygous and homozygous spastin^{N384K} mutants (**Figure 3A**). Low fold change proteins in both genotypes tended to be evenly distributed around the origin, with only a weak bias for similar fold change trends between the HET and HOM samples. However, fold change similarities were more apparent at extreme fold change values. Examples of this include the proteins Pcyox1 and Cd276 which had the respective biggest increased and decrease in abundance at the cell surface in both mutant genotypes. **Figure 3B** shows the same plot ignoring subcellular localisation annotations. The pattern of data is consistent with that of **Figure 3A** and shows the proteins with the largest common fold changes to be plasma membrane annotated proteins.

Attention was then focussed on the plasma membrane annotated proteins with a threshold 1.5-fold decreased (0.67-fold change) or increased abundance at the cell surface in both HET and HOM samples (**Figure C-E** for depleted proteins, **Figure F-H** for enriched proteins).

31 proteins were depleted from the cell surface more than 1.5-fold in both mutant genotypes (**Figure 3C**). This represented 48% and 28% of all plasma membrane annotated proteins depleted more than 1.5-fold from the cell surface in heterozygous and homozygous spastin^{N384K} mutant genotypes respectively. These 31 proteins show high homogeneity of fold change between samples intragenotypically, and between the two mutant genotypes (**Figure 3D**). The proteins from this list with the most statistically confident cell surface decreases include the immune regulator Cd276 and proteins regulating cytoskeletal organisation such as Cfl1 (**Figure 3E**; see **Table 1** (located after **Figure 3** figure legends)). Investigations into the functions of these proteins revealed a diverse set of biological functions, including immune regulation, cell adhesion, and Wnt signalling (**Table 1**).

38 proteins were enriched at the cell surface more than 1.5-fold in both mutant genotypes (**Figure 3F**). This represented 30% and 25% of all plasma membrane annotated proteins enriched more

than 1.5-fold at the cell surface in heterozygous and homozygous spastin^{N384K} mutant genotypes respectively. The relative fold change of these proteins is displayed in **Figure 3G**, showing low intragenotypic variability for some proteins, but not a strong fold change correlation between the two spastin mutant genotypes. The proteins from this list with the lowest adjusted p-values include mechanosensitive ion channel Piezo 1 and cytoskeletal organisation proteins such as Erbb2 (**Figure 3H**; see **Table 2** (located after **Figure 3** figure legends). These proteins are reported to function in ion exchange, cytoskeletal reorganisation, and brain development.

A)

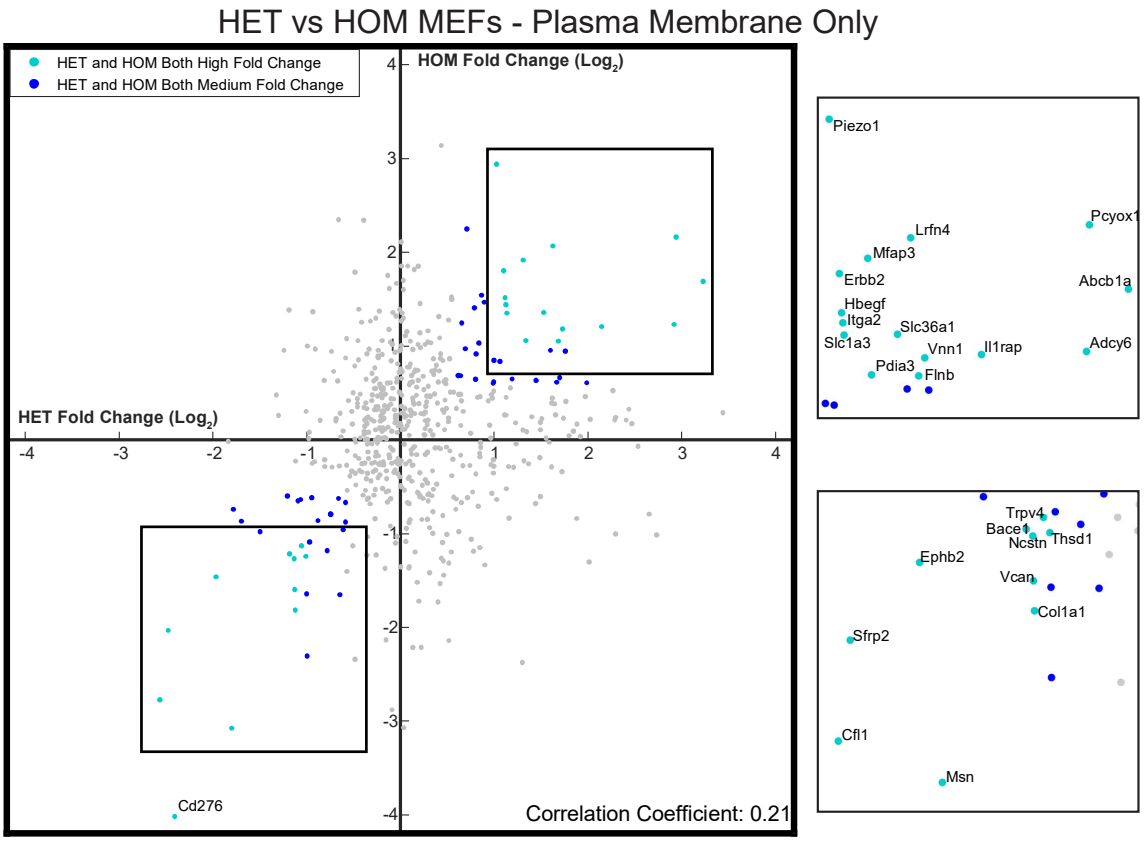
HET vs HOM MEFs - Plasma Membrane Only
HET and HOM Both High Fold Change
HET and HOM Both Medium Fold Change
HOM Fold Change (Log2)
HET Fold Change (Log2)
Cd276
Correlation Coefficient: 0.21
Piezo1
Pcyox1
Lrfn4
Mfap3
Erbb2
Abcb1a
Hbegf
Itga2
Slc36a1
Slc1a3
Vnn1
Il1rap
Adcy6
Pdia3
Flnb
Trpv4
Bace1
Ncstn
Thsd1
Ephb2
Vcan
Col1a1
Sfrp2
Cfl1
Msn

B)

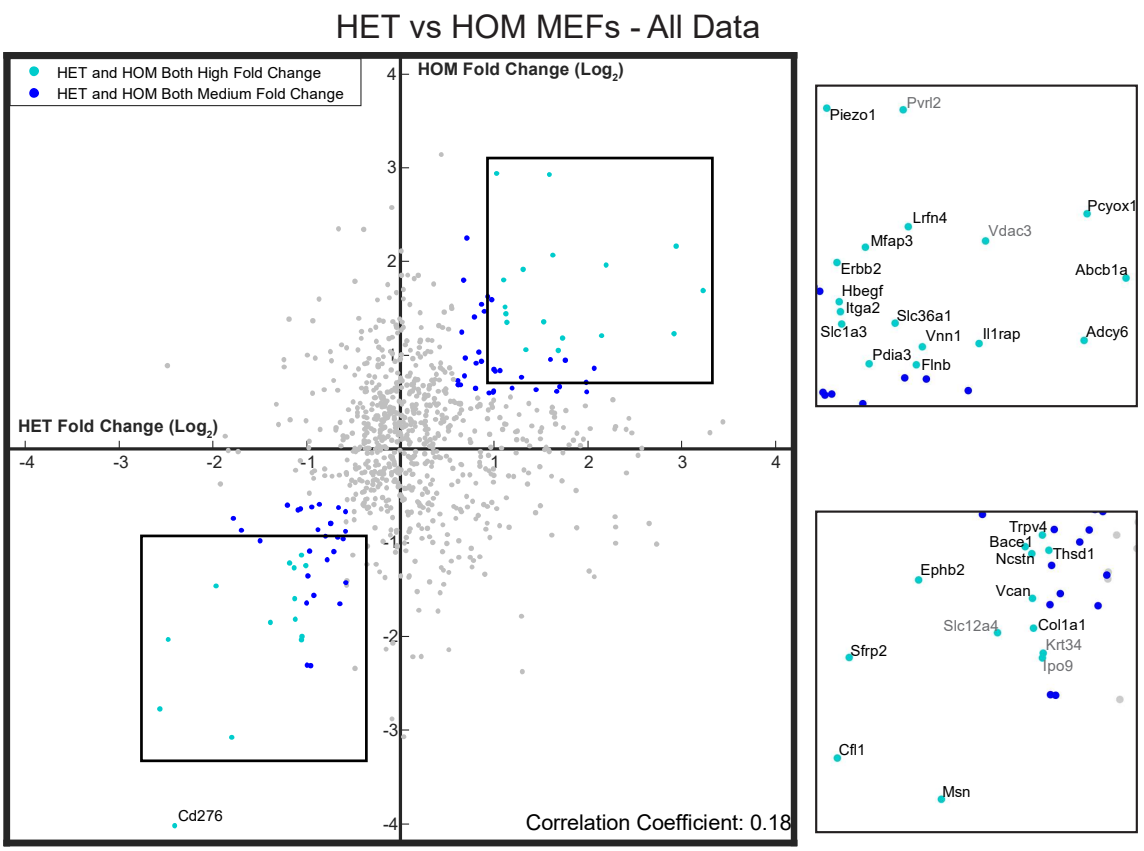
HET vs HOM MEFs - All Data
HET and HOM Both High Fold Change
HET and HOM Both Medium Fold Change
HOM Fold Change (Log2)
HET Fold Change (Log2)
Cd276
Correlation Coefficient: 0.18
Piezo1
Pvrl2
Pcyox1
Lrfn4
Vdac3
Mfap3
Erbb2
Abcb1a
Hbegf
Itga2
Slc36a1
Slc1a3
Vnn1
Il1rap
Adcy6
Pdia3
Flnb
Trpv4
Bace1
Ncstn
Thsd1
Ephb2
Vcan
Slc12a4
Col1a1
Krt34
Sfrp2
Ipo9
Cfl1
Msn

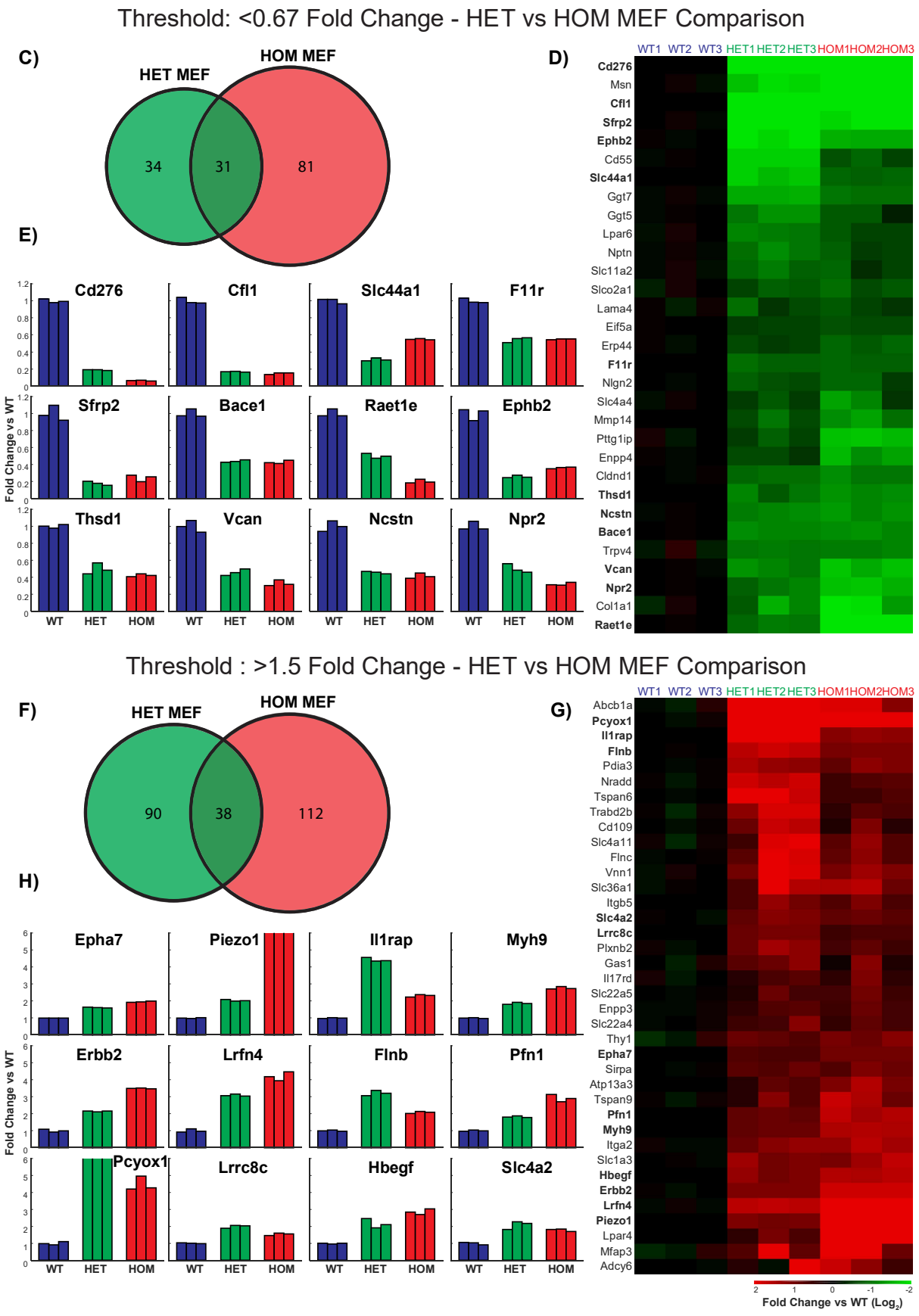
Threshold: <0.67 Fold Change - HET vs HOM MEF Comparison
C)
HET MEF
HOM MEF
34
31
81
D)
WT1 WT2 WT3 HET1 HET2 HET3 HOM1 HOM2 HOM3
Cd276
Msn
Cfl1
Sfrp2
Ephb2
Cd55
Slc44a1
Ggt7
Ggt5
Lpar6
Nptn
Slc11a2
Slco2a1
Lama4
Eif5a
Erp44
F11r
Nlgn2
Slc4a4
Mmp14
Pttg1ip
Enpp4
Cldnd1
Thsd1
Ncstn
Bace1
Trpv4
Vcan
Npr2
Col1a1
Raet1e
E)
Cd276
Cfl1
Slc44a1
F11r
Sfrp2
Bace1
Raet1e
Ephb2
Thsd1
Vcan
Ncstn
Npr2
Fold Change vs WT
WT HET HOM
Threshold : >1.5 Fold Change - HET vs HOM MEF Comparison
F)
HET MEF
HOM MEF
90
38
112
G)
WT1 WT2 WT3 HET1 HET2 HET3 HOM1 HOM2 HOM3
Abcb1a
Pcyox1
Il1rap
Flnb
Pdia3
Nradd
Tspan6
Trabd2b
Cd109
Slc4a11
Flnc
Vnn1
Slc36a1
Itgb5
Slc4a2
Lrrc8c
Plxnb2
Gas1
Il17rd
Slc22a5
Enpp3
Slc22a4
Thy1
Epha7
Sirpa
Atp13a3
Tspan9
Pfn1
Myh9
Itga2
Slc1a3
Hbegf
Erbb2
Lrfn4
Piezo1
Lpar4
Mfap3
Adcy6
2 1 0 -1 -2
Fold Change vs WT (Log2)
H)
Epha7
Piezo1
Il1rap
Myh9
Erbb2
Lrfn4
Flnb
Pfn1
Pcyox1
Lrrc8c
Hbegf
Slc4a2
Fold Change vs WT
WT HET HOM

Figure 3 - Comparison between heterozygous and homozygous spastin^{N384K} mutant MEFs reveal common proteins that have cell surface abundance changes in both genotypes.

A) **Scatter plot showing cell surface abundance fold change of heterozygous spastin^{N384K} mutant MEFs against homozygous spastin^{N384K} mutant MEFs for plasma membrane annotated proteins** – The mean HET vs mean WT peptide abundance for each plasma membrane annotated protein was plotted against the mean HOM vs mean WT peptide abundance for the same protein. Fold change (x,y) was plotted on a $\log_2$ scale. Blue and cyan circles indicate proteins with both a HET-WT and HOM-WT fold change of <0.67/>1.5 and <0.5/>2 respectively. Proteins with both a HET-WT and HOM-WT fold change of <0.5/>2 are named within zoom panels.

B) **Scatter plot showing cell surface fold change of heterozygous spastin^{N384K} mutant MEFs against homozygous spastin^{N384K} mutant MEFs for all identified proteins** – Methods as in **Figure 3B** but ignoring subcellular location annotations. Grey text within zoom panels indicates non-plasma membrane annotated proteins.

C) **Analysis showing a common group of proteins reduced at the cell surface in both heterozygous and homozygous spastin^{N384K} mutant MEFs** – Two lists of plasma membrane annotated proteins with mean HET-WT and mean HOM-WT fold change of <0.67 were generated and plotted in a Venn diagram.

D) **Heatmap showing common proteins reduced at the cell surface in both heterozygous and homozygous spastin^{N384K} MEFs** – The fold change of each sample relative to the mean WT peptide abundance was calculated for each protein. The heatmap displays these values for plasma membrane annotated proteins commonly reduced from the cell surface <0.67 fold in both HET and HOM MEFs identified in **Figure 3C**. Data was plotted on a $\log_2$ scale, with the maximum values set at 2 and -2 (equivalent of 4-fold increase and 0.25-fold decrease) to aid data visualisation. Bold names indicate the 12 proteins from the list with the lowest summed HET-WT and HOM-WT Benjamini-Hochberg adjusted p-values.

E) **Bar charts of plasma membrane annotated proteins with the lowest Benjamini-Hochberg adjusted p-values commonly reduced from the cell surface in heterozygous and homozygous spastin^{N384K} mutant MEFs** – Bar charts of the 12 proteins plasma membrane annotated with the lowest HET-WT and HOM-WT Benjamini-Hochberg adjusted p-values identified in **Figure 3D** were plotted. The chart axes show linear fold change relative to the mean WT peptide abundance.

F) **Analysis showing a common group of proteins increased at the cell surface in both heterozygous and homozygous spastin^{N384K} MEFs** – Two lists of plasma membrane annotated proteins with mean HET-WT and mean HOM-WT fold change of >1.5 was generated and plotted in a Venn diagram.

G) **Heatmap showing common proteins increased at the cell surface in both heterozygous and homozygous spastin^{N384K} MEFs** – Methods as in **Figure 3D**, but with the heatmap displaying plasma membrane annotated proteins commonly increased at the cell surface >1.5 fold in both HET and HOM MEFs identified in **Figure 3D**.

H) **Bar charts of proteins with the lowest Benjamini-Hochberg adjusted p-values commonly increased at the cell surface in heterozygous and homozygous spastin^{N384K} mutant MEFs** – Bar charts of the 12 plasma membrane annotated proteins with the lowest HET-WT and HOM-WT Benjamini-Hochberg adjusted p-values identified in **Figure 3G** were plotted. Chart maxima were set at a linear 6-fold increase, with samples exceeding these values denoted by having open bars.

Gene Name	Protein Function	Reference	Proteomics Results (Fold Change)
Cd276	T cell immune response regulator	Prasad et al. 2004	**Decrease** – HET: 0.19 HOM: 0.06
Cfl1	Cytoskeletal rearrangement regulation	Gohla, Birkenfeld, and Bokoch 2005	**Decrease** – HET: 0.17 HOM: 0.15
Slc44a1	Choline transporter ion channel	Michel and Bakovic 2009	**Decrease** – HET: 0.31 HOM: 0.55
F11r	Epithelial tight junction formation	Itoh et al. 2001	**Decrease** – HET: 0.54 HOM: 0.55
Sfrp2	Modulator of Wnt signalling	Jin et al. 2017	**Decrease** – HET: 0.18 HOM: 0.24
Bace1	Proteolytic processing of amyloid precursor protein	Okada et al. 2010	**Decrease** – HET: 0.44 HOM: 0.43
Raet1e	Natural killer cell cytotoxicity regulator	Bacon et al. 2004	**Decrease** – HET: 0.50 HOM: 0.20
Ephb2	Ephrin-b receptor mediating synaptic transmission and plasticity	Alapin et al. 2018	**Decrease** – HET: 0.26 HOM: 0.36
Thsd1	Nascent focal adhesion regulation	Rui et al. 2017	**Decrease** – HET: 0.50 HOM: 0.42
Vcan	Extracellular matrix assembly and cell adhesion regulation	Damasceno et al. 2016	**Decrease** – HET: 0.46 HOM: 0.33
Ncstn	Member of gamma secretase complex to process Notch and Wnt signalling receptors	Yu et al. 2000	**Decrease** – HET: 0.46 HOM: 0.42
Npr2	Regulates axon bifurcation in dorsal root ganglion axons	Schmidt et al. 2002	**Decrease** – HET: 0.50 HOM: 0.32

Table 1 - **Common proteins depleted from the cell surface in HET and HOM spastin^{N384K}MEFs**. The proteins described are the proteins listed in **Figure 3E**.

Gene Name	Protein Function	Reference	Proteomics Results (Fold Change)
Epha7	Brain development by modulating cell-cell adhesion and synaptic terminal stabilisation	Beuter et al. 2016	**Increase** – HET: 1.60 HOM: 2.00
Piezo1	Mechanosensitive ion channel	Lacroix, Botello-Smith, and Luo 2018	**Increase** – HET: 2.00 HOM: 7.68
Il1rap	Regulation of T cell and mast cell immune response	Ali et al. 2007	**Increase** – HET: 4.43 HOM: 2.31
Myh9	Myosin involved in cytoskeleton reorganisation and focal contact formation	Pecci et al. 2018	**Increase** – HET: 1.86 HOM: 2.77
Erbb2	Regulates outgrowth and stabilisation of peripheral microtubules	Li et al. 2011	**Increase** – HET: 2.14 HOM: 3.49
Lrfn4	Promotes neurite outgrowth in hippocampal neurons	Wang and Wenthold 2009	**Increase** – HET: 3.08 HOM: 4.19
Flnb	Connects cell membrane to actin cytoskeleton	Nakamura, Stossel, and Hartwig 2011	**Increase** – HET: 3.21 HOM: 2.07
Pfn1	Regulator of actin polymerisation	Alkam et al. 2017	**Increase** – HET: 1.82 HOM: 2.91
Pcyox1	Processing of prenylated proteins	Herrera-Marcos et al. 2018	**Increase** – HET: 7.68 HOM: 4.48
Lrrc8c	Volume regulated anion channel	Voss et al. 2014	**Increase** – HET: 2.00 HOM: 1.53
Hbegf	Growth factor that functions in forebrain development	Shim et al. 2016	**Increase** – HET: 2.17 HOM: 2.86
Slc4a2	Anion exchanger	Coury et al. 2013	**Increase** – HET: 2.09 HOM: 1.79

Table 2 - **Common proteins increased at the cell surface in HET and HOM spastin^{N384K}MEFs**. The proteins described are the proteins listed in **Figure 3H**.

5.2.5 – Heterozygous and homozygous spastin^{N384K} mutations drive alterations in focal adhesion pathways in MEFs

Gene ontology analysis allows common subcellular localisations, molecular properties, or biological functions to be highlighted from a list of proteins. Gene ontology analysis using the DAVID resource (Huang et al. 2009b, 2009a) allowed the identification of cell surface pathways significantly affected by the spastin^{N384K} mutation. From this analysis, only proteins involved in focal adhesions (GO:0005925) were highlighted as being significantly enriched in both HET and HOM samples (**Figure 4A**). Analysis of HOM samples alone gave similar results to the HET and HOM samples combined (data not shown).

The fold change magnitude and variation for the focal adhesion identified proteins were examined across the samples from both mutant genotypes (**Figure 4B**). 22 proteins were identified as having annotations of both involvement in focal adhesions and plasma membrane annotations (4% of all plasma membrane proteins). However less than half of the identified proteins had strong fold changes compared to WT MEFs. 8 proteins with the largest fold changes were identified (**Figure 4C**). This showed the proteins Itgb5, Itga2, Flnb, and Flrt2 to have a greater than 1.5-fold increase in abundance at the cell surface in both mutant genotypes. Msn and Trpv4 were also reduced at the cell surface more than 1.5-fold in both mutant genotypes.

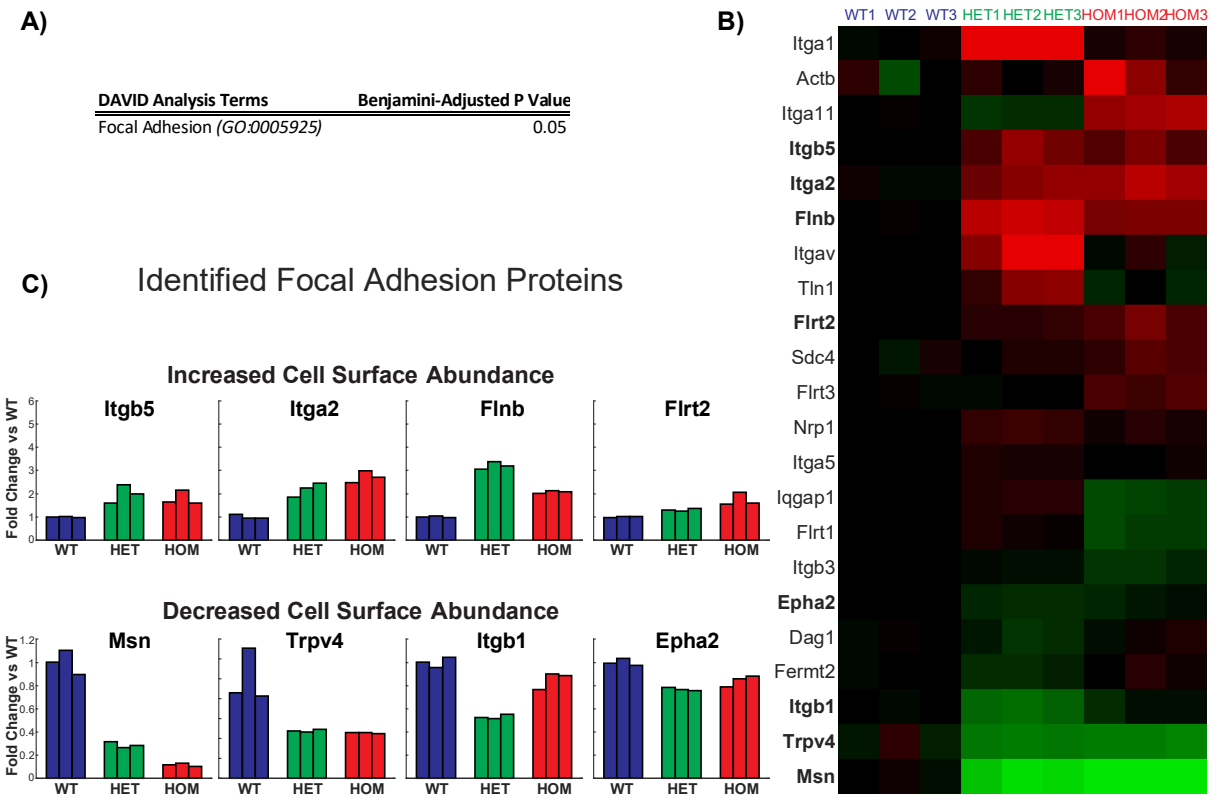

Figure 4 - DAVID analysis reveals heterozygous and homozygous spastin^{N384K} mutations to significantly alter the cell surface abundance of Wnt signalling and focal adhesion proteins in MEF.

A) **DAVID gene ontology analysis of proteins reduced <0.67 or increased >1.5 at the cell surface in both heterozygous and homozygous spastin^{N384K} mutant MEFs** – DAVID enrichment analysis was performed on proteins with a 1.5-fold increase or decrease in both spastin^{N384K} mutant genotypes against a background of all plasma membrane identified proteins.

B) **Heatmap of all identified plasma membrane annotated focal adhesion proteins** – The fold change of each sample relative to mean WT cell surface abundance was plotted for all plasma membrane annotated proteins annotated with the 'Focal Adhesion' (GO:0005925) term. Data was plotted on a $\log_2$ scale, with maximum and minimum values set at 2 and -2 to aid data visualisation. Bold names indicate four proteins with a common increased/decreased abundance at the cell surface in both heterozygous and homozygous spastin^{N384K} mutant MEFs.

C) **Bar charts of focal adhesion proteins commonly increased/decreased at the cell surface in heterozygous and homozygous spastin^{N384K} mutant MEFs** – Bar charts of four Focal Adhesion annotated proteins with an increased/decreased cell surface abundance in both heterozygous and homozygous spastin^{N384K} mutant MEFs from **Figure 4B** were plotted. The chart axes show linear fold change relative to the mean WT peptide abundance

5.2.6 – Primary cortical neuron plasma membrane proteomics selectively quantified cell surface proteins, showing the spastin^{N384K} mutation to drive intergenotypic differences

Having piloted the methods and analysis in an easily manipulable cell line, quantitative cell surface proteomics was next performed using primary embryonic cortical neurons from heterozygous and homozygous spastin^{N384K} mutant mice. This allowed both a comparison with the MEF proteomic data and provided insight into a model system that better resembled the neuron-specific pathology of HSP. This allowed the identification of neuron-specific proteins that could be relevant to the axonal degeneration of HSP.

The experimental protocol used was similar to that for the MEF proteomics. Primary cortical neurons were dissected from spastin^{N384K} mutant E16 foetuses and grown in 10cm^2 dishes for 14 days. Due to the current maximum of 11-plex TMT labelling, 4 WT, 3 HET, and 4 HOM samples were used. Samples were only used if they showed no signs of glial contamination or neurite fragmentation visible by light microscopy (**Figure 5A**). The experimental methodology also involved an addition step as labelled peptide samples were fractionated by strong cation exchange (SCX) fractionation. This allowed enhanced detection of low abundance proteins as it reduced the risk of masking by high abundance peptides. The resulting 6 fractions were analysed separately by mass spectrometry, and the output from all 6 runs was combined for final analysis (**Figure 5B**).

2009 proteins were quantified in total, a 2.4-fold increase compared the MEF proteomics data (**Figure 5C**). This was likely due to the increased sensitivity gained from the SCX fractionation. Of these proteins, 1125 (56%) were annotated with plasma membrane associated terms, 743 (37%) were annotated as being uniquely nuclear, and 141 (7%) were not categorised in either of these categories. Although the proportion of plasma membrane to nuclear proteins was lower than in the MEF data, this result is in line with other published TMT cell surface proteomics experiments that used fractionated samples (Weekes et al. 2014). However, the benefit of using this method was clear, as there was a 1.9-fold increase in the number of plasma membrane quantified proteins in the neuron proteomics compared to the MEF proteomics. Collectively, this indicated that the plasma membrane enrichment protocol had been successful.

Hierarchical clustering of the 11 samples was performed. As before, this allowed an assessment of the validity of investigating the intergenotypic differences between the wildtype and spastin^{N384K} mutant samples. For the most part there was good intragenotypic clustering, with 3 of the WT samples clustering, 2 of the HET samples clustering, and HOM samples either clustering with each other or with

the HET samples (**Figure 5D**). Two samples, 'HET2' and 'WT4' did not cluster with any other samples apart from each other. As a result, these samples were excluded in all future analysis. The analysis also revealed the HET and HOM samples to preferentially cluster compared to the WT cluster. The 'HOM2' sample was seen to cluster with the HET mutant cluster preferentially over the other HOM samples. Together, this suggests overall strong similarities between the cell surface proteome alterations driven by the two spastin^{N384K} mutant genotypes.

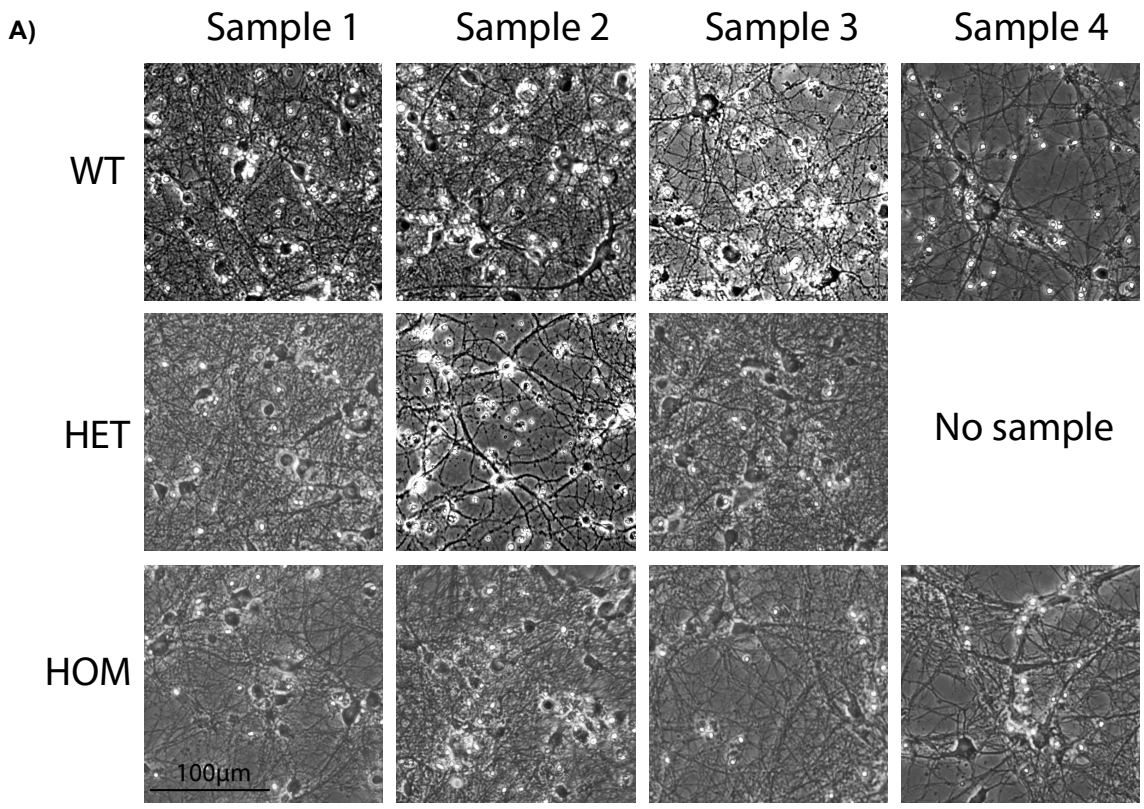
A)
Sample 1
Sample 2
Sample 3
Sample 4
WT
HET
HOM
No sample
100µm

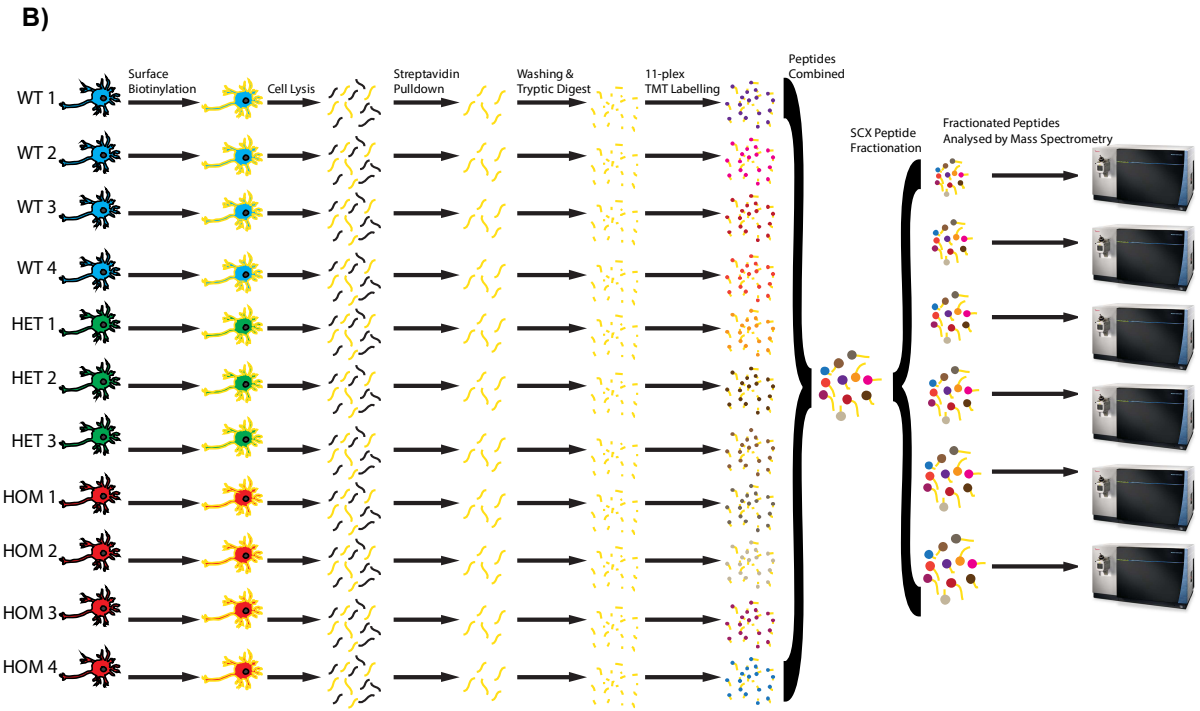
B)
WT 1
WT 2
WT 3
WT 4
HET 1
HET 2
HET 3
HOM 1
HOM 2
HOM 3
HOM 4
Surface Biotinylation
Cell Lysis
Streptavidin Pulldown
Washing & Tryptic Digest
11-plex TMT Labelling
Peptides Combined
SCX Peptide Fractionation
Fractionated Peptides Analysed by Mass Spectrometry

C)

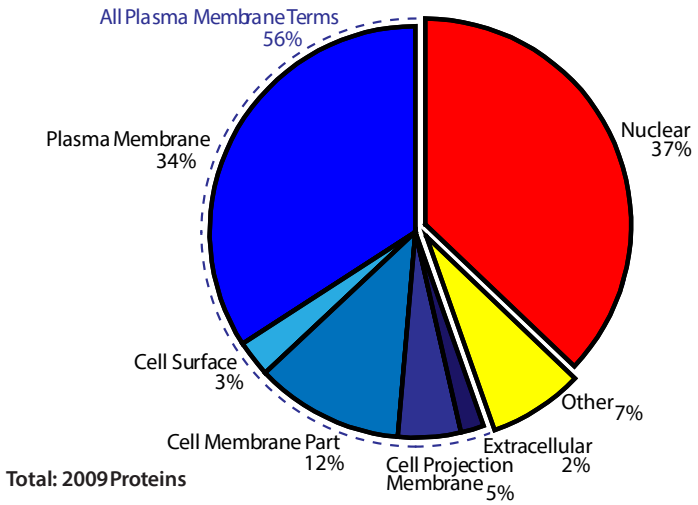
All Plasma Membrane Terms
56%
Plasma Membrane
34%
Nuclear
37%
Cell Surface
3%
Other
7%
Cell Membrane Part
12%
Extracellular
2%
Cell Projection
Membrane
5%
Total: 2009 Proteins

D)

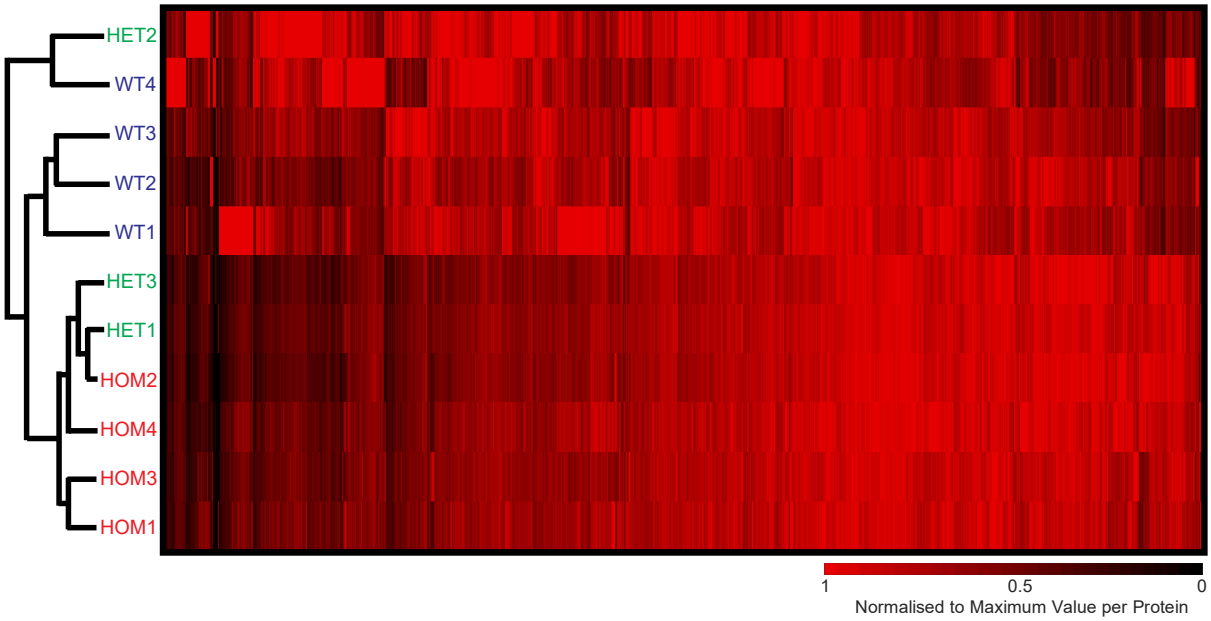
HET2
WT4
WT3
WT2
WT1
HET3
HET1
HOM2
HOM4
HOM3
HOM1
1
0.5
0
Normalised to Maximum Value per Protein

Figure 5 - Overview of cell surface proteomics on WT (spastin$^{wt/wt}$), HET (spastin$^{wt/N384K}$), HOM (spastin$^{N384K/N384K}$) primary cortical neurons.

A) **Microscopic imaging to verify the purity and health of the primary neuron cultures** – Primary neuron samples were imaged using phase contrast microscopy 2 hours before cell surface biotinylation to verify a high purity of primary neurons. Phase contrast imaging was performed using a Thermo EVOS widefield microscope with a 20x/0.65NA objective. Scale bars indicate 100µm.

B) **Schematic of cell surface proteomic protocol** – 4 WT, 3 HET, and 4 HOM primary neuron samples were grown for 14 days and their cell surface proteins biotinylated. Cells lysates were generated, and biotinylated proteins extracted using streptavidin pull down. Isolated proteins were washed extensively before being tryptically digested, with digested proteins from each sample labelled with a different Tandem Mass Tag (TMT) label. Labelled peptides were then combined before being fractionated using Strong Cation Exchange (SCX) peptide fractionation to generate 6 fractions of differing hydrophobicity. These 6 fractions were then run separately using Liquid Chromatography Tandem Mass Spectrometry with a rising gradient of MeCN for 180 minutes in a Thermo Orbitrap Fusion Lumos mass spectrometer. Obtained data was then pooled for analysis.

C) **Cell compartment analysis of identified proteins** – All proteins identified from mass spectrometry analysis were annotated with their subcellular location by comparison against the mouse Uniprot (Swiss-Prot) subcellular location database. Plasma membrane terms were defined as annotations of 'plasma membrane', 'cell surface', 'cell membrane part', 'cell projection membrane', and 'extracellular', with 'nuclear' annotations also recorded. If multiple annotations existed for any protein, they were given only one label of the first occurring term in the above list.

D) **Clustergram analysis showing intragenotypic and intergenotypic sample clustering** – Peptide counts for each sample for each identified protein were normalised by the ratio of peptide counts for each sample summated over all proteins. These peptide counts were then normalised to the maximum peptide count for each protein, with the maximum value for each identified protein set to 1. A clustergram representing the hierarchical clustering of the protein set based on Euclidean pairwise distance analysis was generated with the heatmap showing samples by row, and individual proteins by column. The heatmap scalebar ranges from bright red (1) for the maximum quantified value to black (0), with dark regions showing fewer detected peptides. The clustergram shows both intragenotypic clustering for most samples, and that sample 'HET2' and 'WT4' fail to cluster with their respective genotypes.

5.2.7 – Heterozygous and homozygous spastin^{N384K} mutation drive significant changes in the cell surface proteome of primary cortical neurons

As for the MEF proteomics, cell surface protein abundance changes in the spastin^{N384K} mutant genotypes was assessed by plotting the mutant vs wildtype fold change for each protein against its adjusted p-value. This was done for both mutant genotypes including and excluding filtering for plasma membrane proteins.

For the WT vs HET comparisons, no proteins had significantly increased or decreased cell surface abundance compared to the wildtype samples (**Figure 6A**). This result can be attributed to the exclusion of the 'WT4' and 'HET2' samples, resulting in t-tests with low statistical power due to the 3 vs 2 sample comparison. Despite this, using the adjusted p-values provided a measure of sample variation and allowed the identification of proteins with large fold changes at the cell surface with low intersample variation. Ignoring the adjusted p-value and considering only plasma membrane annotated proteins, using a threshold of a 2-fold change, 15 proteins (1%) had an increased abundance at the cell surface, and 44 proteins (4%) had a decreased abundance at the cell surface. Selecting the highest changers with the lowest p-values, all the 12 highlighted proteins had at least a 2.5-fold increased or decreased abundance at the cell surface (**Figure 6B**). Overall, there was good consistency between the fold changes of HET and HOM spatin^{N384K} neurons for the highlighted proteins (**Figure 6B**).

The WT vs HOM comparison did not have the same sample number problem as the WT vs HET comparison, and there were a modest number of proteins with a significantly increased or decreased cell surface abundance compared to the wildtype condition (**Figure 6C**). Filtering for proteins that had at least a 2-fold change, a plasma membrane annotation, and an adjusted p-value of 0.01, 9 proteins (1%) had a decreased abundance at the cell surface, and only 1 protein had an increased abundance at the cell surface. When relaxing the criteria to a 1.5-fold fold change, 31 proteins (3%) had decreased cell surface abundance, and 11 proteins (1%) had increased cell surface abundance. Selecting the proteins with the most statistically significant fold changes, all the 12 highlighted proteins had at least a 2-fold increased or decreased abundance at the cell surface (**Figure 6D**). Overall there was good consistency between the mean fold changes of the HET and HOM spastin^{N384K} mutant neurons, with very little intragenotypic variation (**Figure 6D**).

As for the MEF proteomics, plots were also produced for the HET and HOM mutant data without the filter of a plasma membrane annotation (**Figure 6E** and **Figure 6F**). Both plots show very similar distributions to their respective plasma membrane partners, and do not reveal any proteins

without plasma membrane annotations to have both a very high fold change and statistical significance.

A)

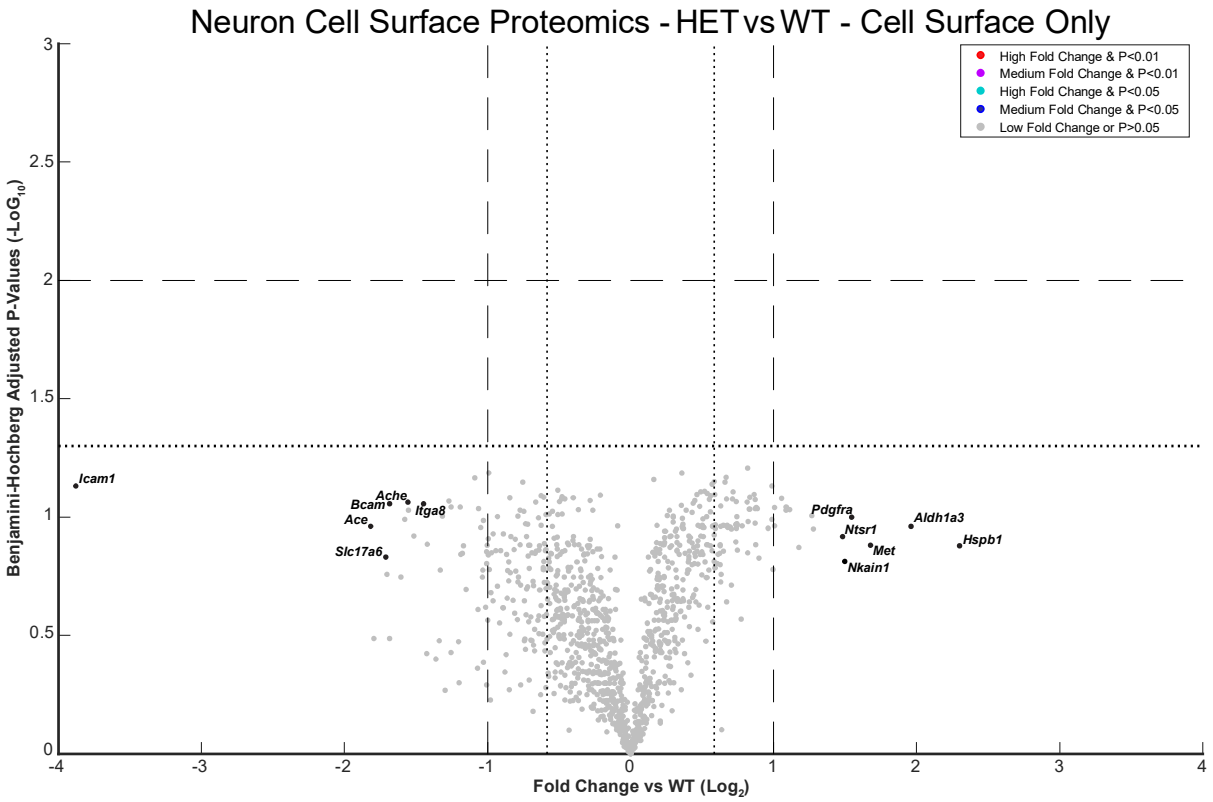
Neuron Cell Surface Proteomics - HET vs WT - Cell Surface Only
High Fold Change & P<0.01
Medium Fold Change & P<0.01
High Fold Change & P<0.05
Medium Fold Change & P<0.05
Low Fold Change or P>0.05
Benjamini-Hochberg Adjusted P-Values (-LoG10)
Fold Change vs WT (Log2)
Icam1
Ache
Bcam
Itga8
Ace
Slc17a6
Pdgfra
Aldh1a3
Ntsr1
Met
Hspb1
Nkain1

B)

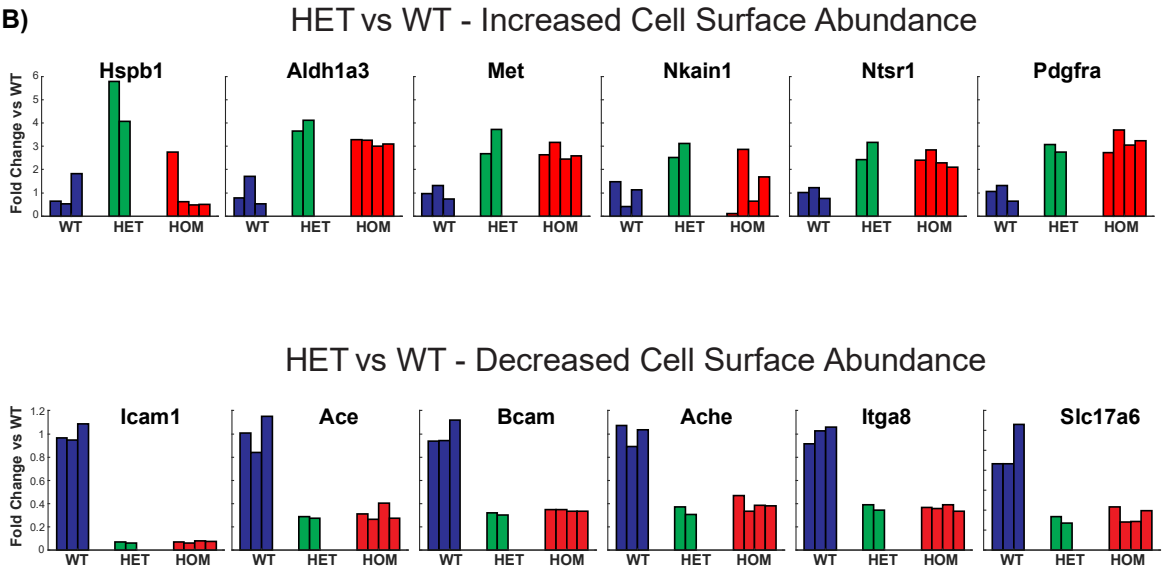
HET vs WT - Increased Cell Surface Abundance
Fold Change vs WT
Hspb1
Aldh1a3
Met
Nkain1
Ntsr1
Pdgfra
WT
HET
HOM
HET vs WT - Decreased Cell Surface Abundance
Icam1
Ace
Bcam
Ache
Itga8
Slc17a6

C)

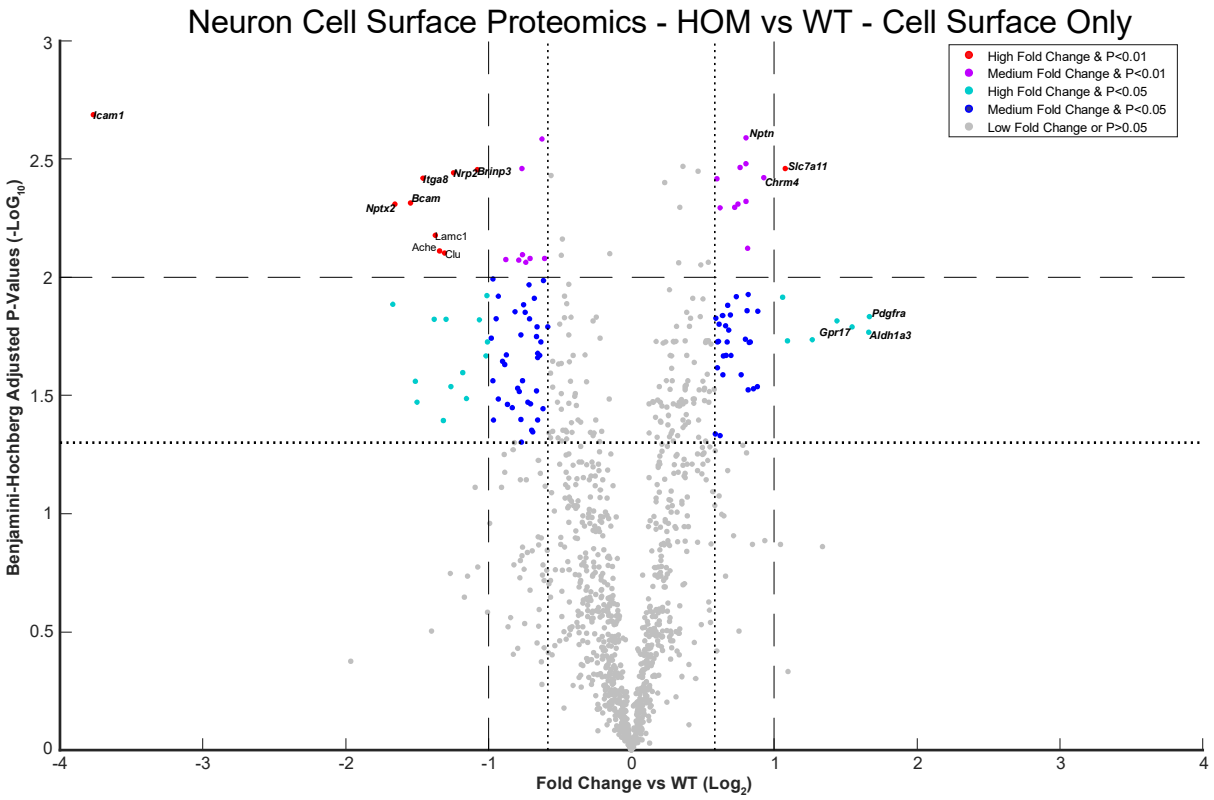
Neuron Cell Surface Proteomics - HOM vs WT - Cell Surface Only
High Fold Change & P<0.01
Medium Fold Change & P<0.01
High Fold Change & P<0.05
Medium Fold Change & P<0.05
Low Fold Change or P>0.05
Benjamini-Hochberg Adjusted P-Values (-LoG10)
Fold Change vs WT (Log2)
Icam1
Nptn
Slc7a11
Chrm4
Itga8
Nrp2
Brinp3
Nptx2
Bcam
Lamc1
Ache
Clu
Pdgfra
Gpr17
Aldh1a3

D)

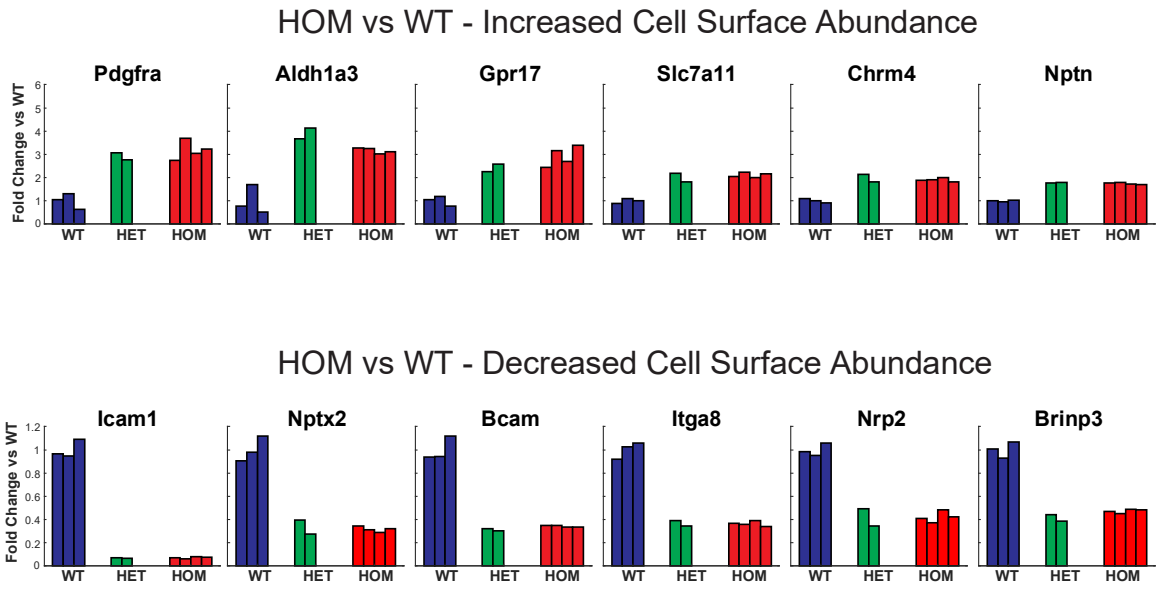
HOM vs WT - Increased Cell Surface Abundance
Pdgfra
Aldh1a3
Gpr17
Slc7a11
Chrm4
Nptn
Fold Change vs WT
WT
HET
HOM
HOM vs WT - Decreased Cell Surface Abundance
Icam1
Nptx2
Bcam
Itga8
Nrp2
Brinp3

E)

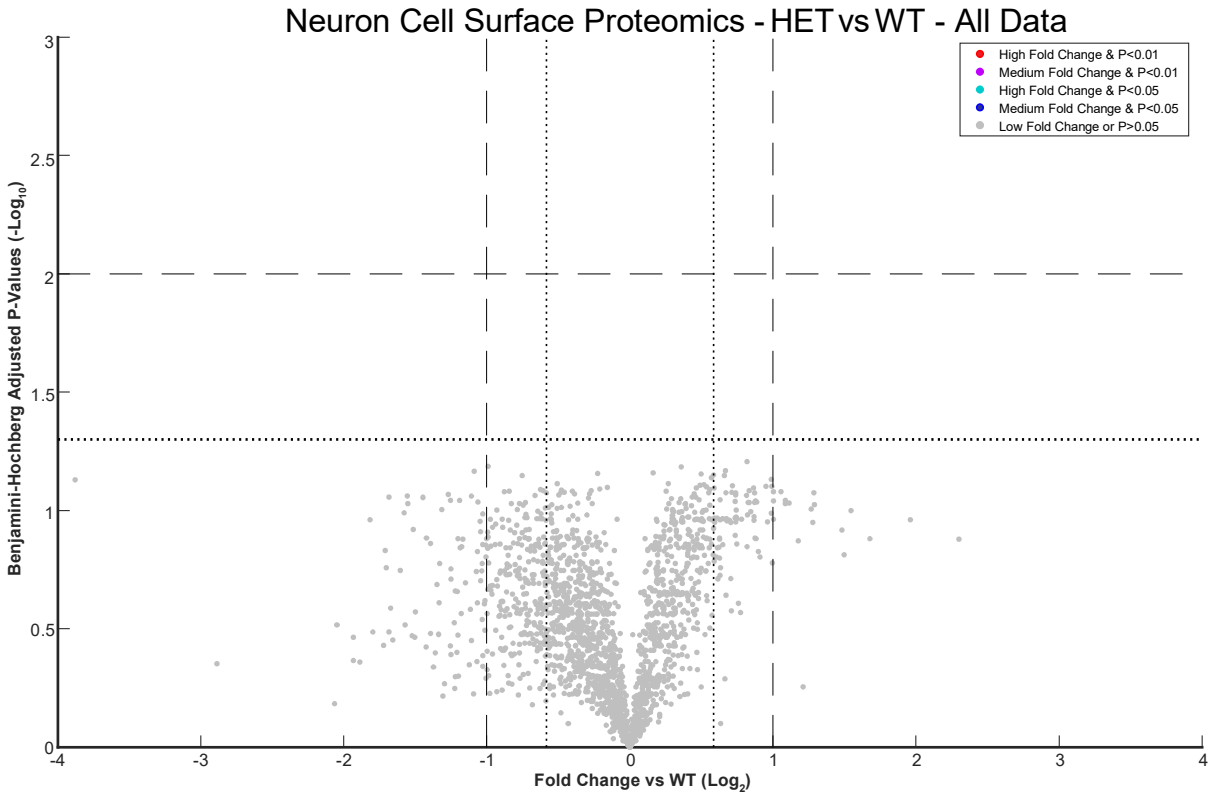
Neuron Cell Surface Proteomics - HET vs WT - All Data
High Fold Change & P<0.01
Medium Fold Change & P<0.01
High Fold Change & P<0.05
Medium Fold Change & P<0.05
Low Fold Change or P>0.05
Benjamini-Hochberg Adjusted P-Values (-Log10)
Fold Change vs WT (Log2)

F)

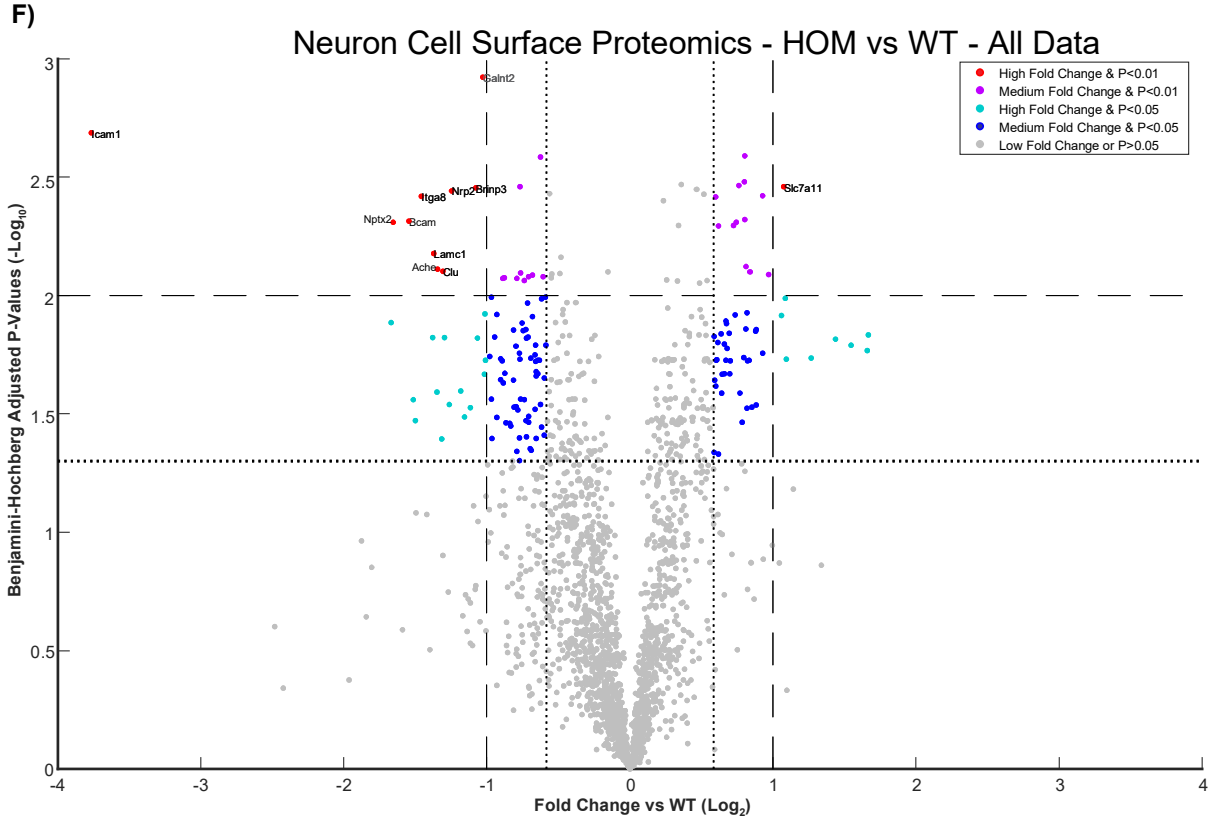
Neuron Cell Surface Proteomics - HOM vs WT - All Data
High Fold Change & P<0.01
Medium Fold Change & P<0.01
High Fold Change & P<0.05
Medium Fold Change & P<0.05
Low Fold Change or P>0.05
Benjamini-Hochberg Adjusted P-Values (-Log10)
Fold Change vs WT (Log2)
Slc7a11
Nptx2
Bcam
Lamc1
Clu

Figure 6 - Volcano plots reveal the changes in protein cell surface abundance driven by heterozygous and homozygous spastin^{N384K} mutations in primary cortical neurons.

A) **Volcano plots showing changes in the cell surface abundance of plasma membrane annotated proteins driven by the heterozygous spastin^{N384K} mutation** – The mean HET vs mean WT peptide abundance for each plasma membrane protein was plotted against its Benjamini-Hochberg adjusted p-value (generated from unpaired two-tail t-tests between HET vs WT samples). Due to poor hierarchical clustering, samples 'WT4' and 'HET2' were excluded from calculations, resulting in low overall statistical power. Fold change (x) was plotted on a $\log_2$ scale and adjusted p-value (y) plotted on a $-\log_{10}$ scale. Horizontal lines indicate p-values of 0.05 and 0.01 respectively, and vertical lines indicate fold changes of 0.5, 0.67, 1.5, 2 respectively. 6 proteins with the lowest p-value and less/more 0.5/2-fold change are named with bar charts plotted below.

B) **Bar charts of proteins with the largest cell surface increase/decrease driven by the heterozygous spastin^{N384K} mutation** – 6 plasma membrane annotated proteins with the largest HET-WT fold increase/decrease with the lowest HET-WT Benjamini-Hochberg adjusted p-values were selected, and the fold change relative to the mean WT peptide abundance for each sample was plotted for each protein. Due to poor hierarchical clustering, samples 'WT4' and 'HET2' were excluded. Chart axes show linear fold change.

C) **Volcano plot showing changes in the cell surface abundance of plasma membrane annotated proteins driven by homozygous spastin^{N384K} mutations** – The mean HOM vs mean WT peptide abundance for each plasma membrane protein was plotted against its Benjamini-Hochberg adjusted p-value (generated from unpaired two-tail t-tests between HOM vs WT samples). Due to poor hierarchical clustering, sample 'WT4' was excluded from calculations. 6 proteins with low p-values and low/high fold changes are named, with bold italic names given to proteins with plotted bar charts. Other chart details as in **Figure 6A**.

D) **Bar charts of proteins with largest cell surface increase/decrease driven by homozygous spastin^{N384K} mutations** – 6 plasma membrane annotated proteins with the largest HOM-WT fold increase/decrease with the lowest HOM-WT Benjamini-Hochberg adjusted p-values were selected, and the fold change relative to the mean WT peptide abundance for each sample was plotted for each protein. Due to poor hierarchical clustering, samples 'WT4' and 'HET2' were excluded. Chart axes show linear fold change.

E) **Volcano plot showing changes in the cell surface abundance of all detected proteins driven by the heterozygous spastin^{N384K} mutation** – As in **Figure 6A** but ignoring subcellular location annotations.

F) **Volcano plot showing changes in the cell surface abundance of all detected proteins driven by homozygous spastin^{N384K} mutations** – As in **Figure 6C** but ignoring subcellular location annotations. Only proteins with a p-value of lower than 0.01 and less/more 0.5/2-fold change are named. Grey text indicates non-plasma membrane annotated proteins.

5.2.8 - Comparisons between heterozygous and homozygous spastin^{N384K} mutant primary cortical neurons reveals proteins with common cell surface abundance changes

Comparisons of the cell surface protein abundance changes from the HET and HOM spastin^{N384K} primary cortical neuron proteomics were performed to analyse correlations in protein abundance. This was performed as described for the MEF proteomics.

There was a remarkably strong positive correlation between the fold changes of the spastin^{N384K} mutant genotypes filtered for plasma membrane annotated proteins (**Figure 7A**). This was also true when ignoring the subcellular localisation annotation (**Figure 7B**). Few dramatic outliers were revealed by the data, with the exception of the cell adhesion molecule Icam1 which had a fold reduction in both mutant genotypes far in excess of any other protein. Overall, the data contrasted sharply to the data distribution produced for the MEF proteomics data. This indicated a stronger intergenotypic consistency between the spastin mutants in the neuron data compared to the MEF data. Overall, this showed that the HET and HOM spastin^{N384K} mutations drove similar size alterations in the cell surface proteome of cortical neurons.

Cell surface proteins most dramatically affected by the spastin^{N384K} mutation in both mutant genotypes were highlighted by focussing on plasma membrane annotated proteins with at least a 1.5-fold change. 105 proteins (9%) were reduced more than 1.5-fold at the cell surface in both mutant genotypes (**Figure 7C**). This was 69% and 90% of all the plasma membrane proteins with a minimum fold change of 1.5 in the HET and HOM samples respectively. The 105 proteins showed a low intragenotypic and intergenotypic variation (**Figure 7D**). The proteins from this list with the most statistically confident fold changes include the cell adhesion molecule Bcam and Icam1 (**Figure 7E**). The functions of the 12 proteins with the most statistically significant reduction in their cell surface abundance (**Figure 7E**) were examined (**Table 3** (located after **Figure 7** figure legends)). This revealed two main groups of proteins: those involved in cell adhesion and migration, and those involved in neuronal signalling, development and survival (**Table 3**).

53 proteins (5%) had an increased cell surface abundance of more than 1.5-fold in both heterozygous and homozygous spastin^{N384K} mutant genotypes (**Figure 7F**). These 53 proteins comprised 70% and 90% of all HET and HOM mutant primary neuron proteins increased at the cell surface respectively. With few exceptions, the 53 identified proteins showed low intragenotypic and intergenotypic variation between the mutant genotypes (**Figure 7G**). The overall magnitude of fold change was smaller for this group compared to their equivalents that were lost at the cell surface.

Proteins from this list with the most statistically confidence cell surface abundance increases include the neurotransmitter regulating proteins Chrm1 and Slc6a11 (**Figure 7H**). Investigating the functions of the top 12 proteins with the most statistically significant increase at the cell revealed mostly neuron-specific proteins that were involved in cell adhesion and maintenance, synaptic transmission, and ion transport (**Table 4** (located after **Figure 7** legends)).

A) HET vs HOM Neurons - Plasma Membrane Only

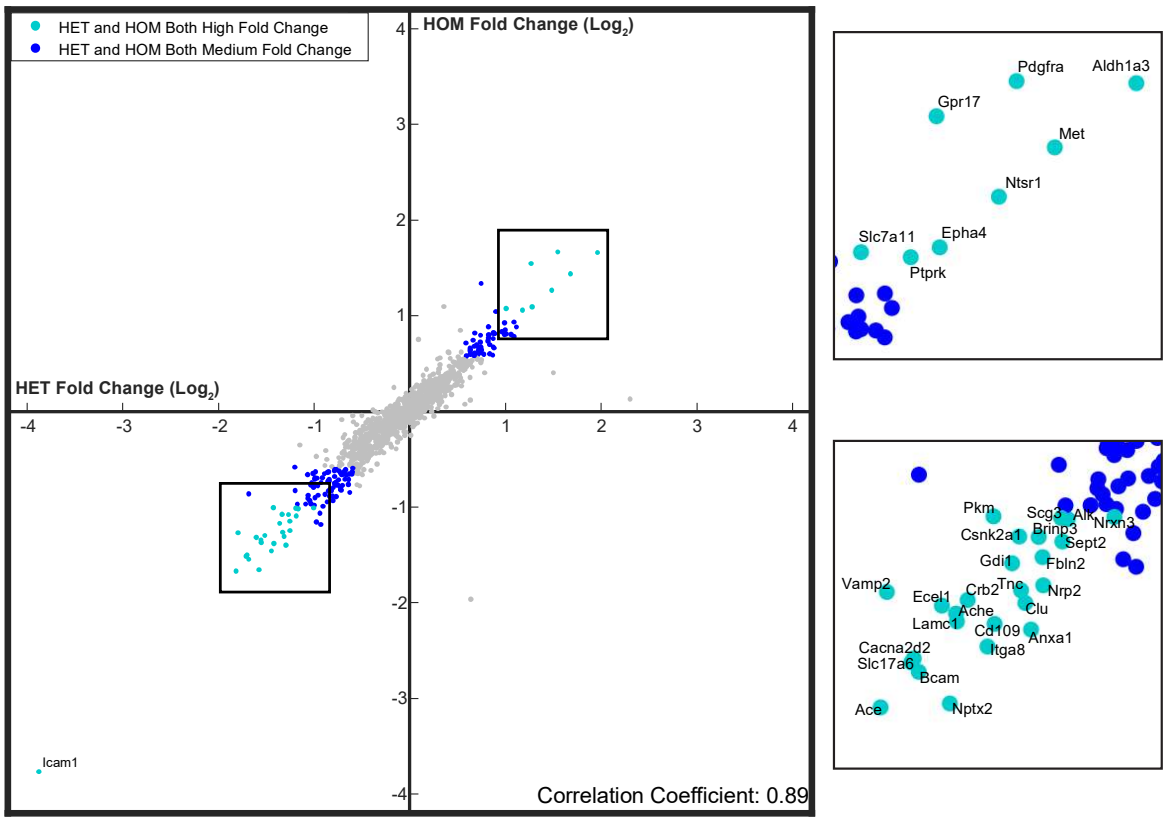

B) HET vs HOM Neurons - All Data

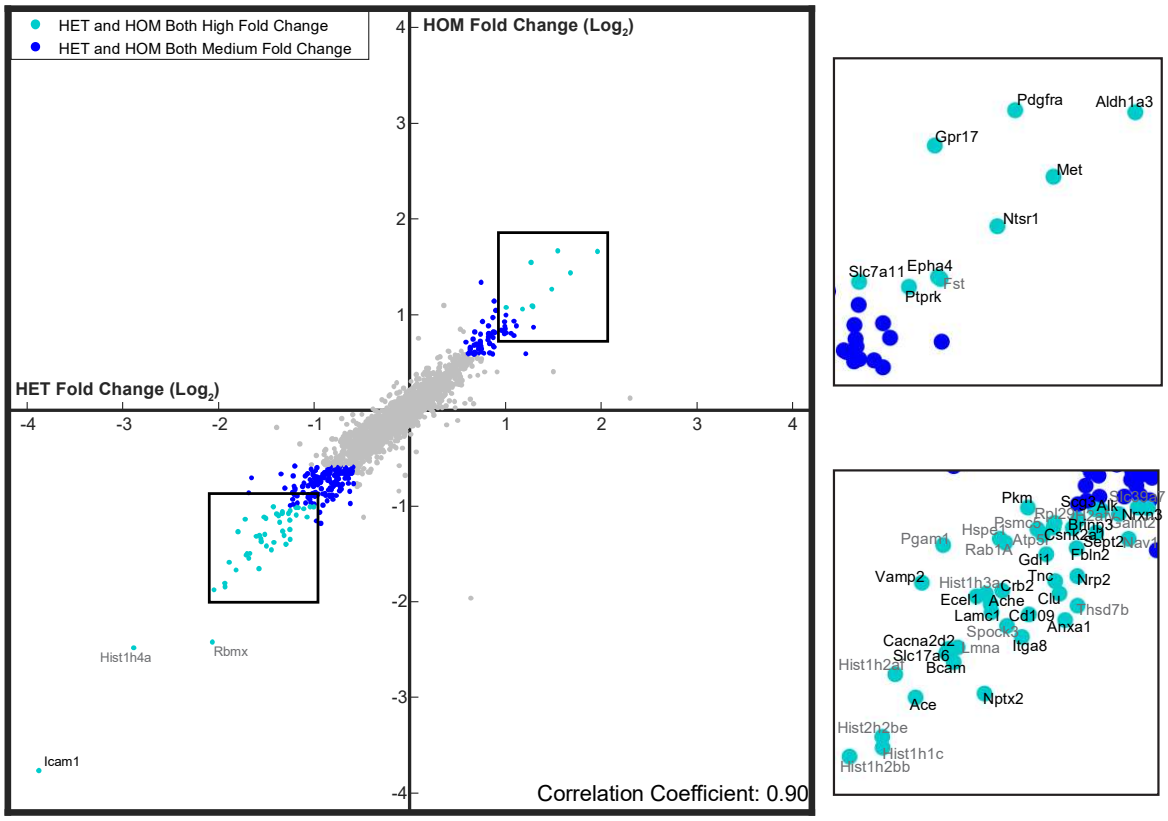

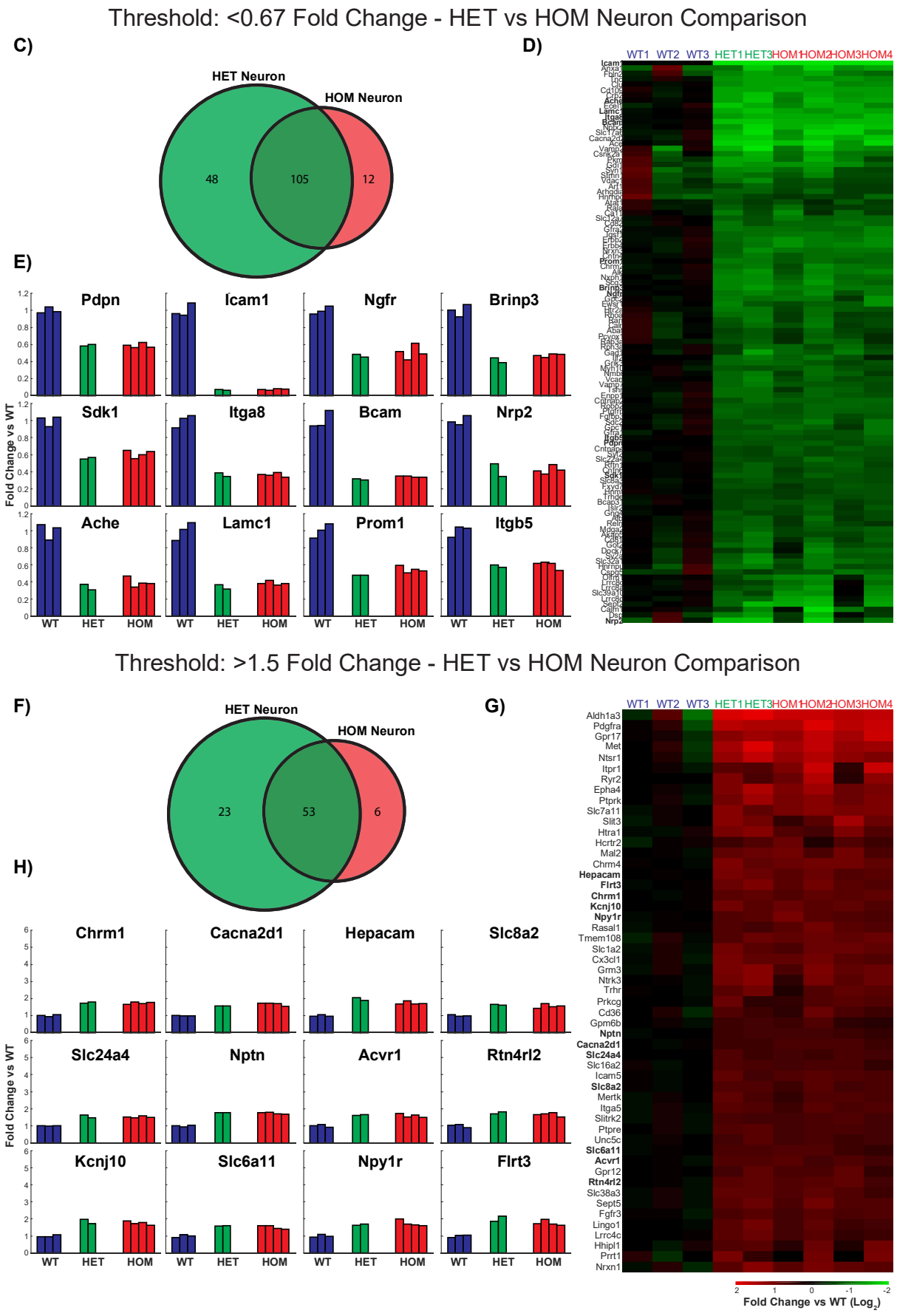
Threshold: <0.67 Fold Change - HET vs HOM Neuron Comparison
C)
HET Neuron
HOM Neuron
48
105
12
D)
WT1 WT2 WT3 HET1 HET3 HOM1 HOM2 HOM3 HOM4
E)
Pdpn
Icam1
Ngfr
Brinp3
Sdk1
Itga8
Bcam
Nrp2
Ache
Lamc1
Prom1
Itgb5
Fold Change vs WT
WT HET HOM
Threshold: >1.5 Fold Change - HET vs HOM Neuron Comparison
F)
HET Neuron
HOM Neuron
23
53
6
G)
H)
Chrm1
Cacna2d1
Hepacam
Slc8a2
Slc24a4
Nptn
Acvr1
Rtn4rl2
Kcnj10
Slc6a11
Npy1r
Flrt3
Fold Change vs WT
WT HET HOM
Fold Change vs WT (Log2)

Figure 7 - Comparison between heterozygous and homozygous spastin^{N384K} mutant primary cortical neurons reveal common proteins that have strong cell surface abundance changes in both genotypes.

A) **Scatter plot showing cell surface abundance fold change of heterozygous spastin^{N384K} mutant primary cortical neurons against homozygous spastin^{N384K} mutant primary cortical neurons for plasma membrane annotated proteins** – The mean HET vs mean WT peptide abundance for each plasma membrane annotated protein was plotted against the mean HOM vs mean WT peptide abundance for the same protein. Fold change (x,y) was plotted on a $\log_2$ scale. Blue and cyan circles indicate proteins with both a HET-WT and HOM-WT fold change of <0.67/>1.5 and <0.5/>2 respectively. Proteins with both a HET-WT and HOM-WT fold change of <0.5/>2 are named within zoom panels. Due to poor hierarchical clustering, samples 'WT4' and 'HET2' were excluded from calculations.

B) **Scatter plot showing cell surface fold change of heterozygous spastin^{N384K} mutant primary cortical neurons against homozygous spastin^{N384K} mutant primary cortical neurons for all identified proteins** – Methods as in **Figure 7A** but ignoring subcellular location annotations. Grey text within zoom panels indicates non-plasma membrane annotated proteins.

C) **Analysis showing a common group of proteins lost at the cell surface in both heterozygous and homozygous spastin^{N384K} mutant primary cortical neurons** – Two lists of plasma membrane annotated proteins with a mean HET-WT and mean HOM-WT fold change of <0.67 were generated and plotted in a Venn diagram. Due to poor hierarchical clustering, samples 'WT4' and 'HET2' were excluded from calculations.

D) **Heatmap showing common proteins lost at the cell surface in both heterozygous and homozygous spastin^{N384K} primary cortical neurons** – The fold change of each sample relative to the mean WT peptide abundance was calculated for each protein. The heatmap displays these values for plasma membrane annotated proteins commonly lost from the cell surface <0.67 fold in both HET and HOM primary cortical neurons identified in **Figure 7C**. Data was plotted on a $\log_2$ scale, with the maximum values set at 2 and -2 (equivalent to a 4-fold increase and a 0.25-fold decrease) to aid data visualisation. Bold names indicate the 12 proteins from the list with the lowest summed HET-WT and HOM-WT Benjamini-Hochberg adjusted p-values. Due to poor hierarchical clustering, samples 'WT4' and 'HET2' were excluded.

E) **Bar charts of proteins with the lowest Benjamini-Hochberg adjusted p-values commonly lost from the cell surface in heterozygous and homozygous spastin^{N384K} mutant primary cortical neurons** – Bar charts of the 12 plasma membrane annotated proteins with the lowest summed HET-WT and HOM-WT Benjamini-Hochberg adjusted p-values identified in **Figure 7C-D** were plotted. Chart axes show linear fold change relative to the mean WT peptide abundance. Due to poor hierarchical clustering, samples 'WT4' and 'HET2' were excluded.

F) **Analysis showing a common group of proteins gained at the cell surface in both heterozygous and homozygous spastin^{N384K} mutant primary cortical neurons** – Two lists of plasma membrane annotated proteins with mean HET-WT and mean HOM-WT fold change of >1.5 were generated and plotted in a Venn diagram. Due to poor hierarchical clustering, sample 'WT4' was excluded from calculations.

G) **Heatmap showing common proteins gained at the cell surface in both heterozygous and homozygous spastin^{N384K} primary cortical neurons** – Methods as in **Figure 7D**, but with the heatmap displaying plasma membrane annotated proteins commonly gained at the cell surface >1.5 fold in both HET and HOM identified in **Figure 7F**.

H) **Bar charts of proteins with the lowest Benjamini-Hochberg adjusted p-values commonly gained at the cell surface in heterozygous and homozygous spastin^{N384K} mutant primary cortical neurons** – Bar charts of 12 plasma membrane annotated proteins with the lowest HET-WT and HOM-WT Benjamini-Hochberg adjusted p-values identified in **Figure 7F-G** were plotted. Chart axes show linear fold change relative to the mean WT peptide abundance. Due to poor hierarchical clustering, samples 'WT4' and 'HET2' were excluded.

Gene Name	Protein Function	Reference	Proteomics Results (Fold Change)
Pdpn	Functions in cell migration, adhesion, and protrusion formation	Martín-Villar et al. 2005	**Decrease** – HET: 0.59 HOM: 0.59
Icam1	Endothelial cell adhesion during immune response	Smith et al. 1989	**Decrease** – HET: 0.07 HOM: 0.07
Ngfr	Neurotrophin receptor regulating axonal health	Johnson et al. 1986	**Decrease** – HET: 0.47 HOM: 0.51
Brinp3	Bone morphogenic protein inducible inhibition of neuronal proliferation	Kawano et al. 2004	**Decrease** – HET: 0.41 HOM: 0.48
Sdk1	Cell adhesion protein promoting synaptic connectivity	Yamagata, Weiner, and Sanes 2002	**Decrease** – HET: 0.56 HOM: 0.61
Itga8	Integrin functioning cell mediation of cell-cell interaction, cell recruitment, and neurite outgrowth regulation	Denda et al. 1998	**Decrease** – HET: 0.37 HOM: 0.36
Bcam	Laminin receptor functioning in cell adhesion	Udani et al. 1998	**Decrease** – HET: 0.31 HOM: 0.34
Nrp2	Regulates axon bifurcation in dorsal root ganglion axons	Schmidt et al. 2002	**Decrease** – HET: 0.42 HOM:0.42
Ache	Terminates signal transduction at neuromuscular junction by acetylcholine hydrolysis	Whittaker 1990	**Decrease** – HET: 0.34 HOM: 0.39
Lamc1	Laminin that mediates cell adhesion and migration during development	Simon-Assmann 2013	**Decrease** – HET: 0.34 HOM: 0.39
Prom1	Regulation of cell differentiation and proliferation, and regulation of neurite extension	Takenobu et al. 2011	**Decrease** – HET: 0.49 HOM: 0.54
Itgb5	Integrin involved in cell adhesion, migration and proliferation	Desgrosellier and Cheresh 2010	**Decrease** – HET: 0.59 HOM: 0.60

Table 3 - **Common proteins depleted from the cell surface in HET and HOM spastin^{N384K} primary cortical neurons**. The proteins described are the proteins listed in **Figure 7E**.

Gene Name	Protein Function	Reference	Proteomics Result (Fold Change)
Chrm1	Acetylcholine receptor with excitatory influence	Carr and Surmeier 2007	**Increase** – HET: 1.76 HOM: 1.74
Cacna2d1	Voltage dependent calcium channel	Gao et al. 2000	**Increase** – HET: 1.58 HOM: 1.68
Hepacam	Cell-cell junction mediation	Wu, Moh, and Schwarz 2016	**Increase** – HET: 1.98 HOM: 1.74
Slc8a2	Sodium/calcium exchanger protein crucial in synaptic plasticity, learning and memory	Jeon et al. 2003	**Increase** – HET: 1.64 HOM: 1.56
Slc24a4	Sodium/potassium/calcium exchanger crucial in nervous impulse termination	Stephan et al. 2012	**Increase** – HET: 1.55 HOM: 1.51
Nptn	Homophilic cell adhesion protein important for long-term potentiation of synapses	Smalla et al. 2000	**Increase** – HET: 1.48 HOM: 1.45
Acvr1	Activin receptor that mediates Bone Morphogenic Protein signalling for development and repair	Kishigami et al. 2004	**Increase** – HET: 1.64 HOM: 1.60
Rtn4rl2	Nogo receptor that inhibits neurite outgrowth, and dendrite spine and synapse formation, but facilitates axon migration	Wills et al. 2012	**Increase** – HET: 1.76 HOM: 1.66
Kcnj10	Potassium channel associated with epilepsy	Nwaobi et al. 2016	**Increase** – HET: 1.85 HOM: 1.76
Slc6a11	GABA transporter terminating the action of GABA at the synaptic cleft	Clarkson et al. 2010	**Increase** – HET: 1.59 HOM: 1.51
Npy1r	Neuropeptide Y receptor that functions in stress, pain perception and circadian rhythm control	Tatemoto 2004	**Increase** – HET: 1.67 HOM: 1.74
Flrt3	Cell adhesion, cell migration, and axon guidance, mediating spatial organisation of neurons, and mediates neurite number and length	Tsuji et al. 2004	**Increase** – HET: 2.00 HOM: 1.75

Table 4 - **Common proteins increased at the cell surface in HET and HOM spastin^{N384K} primary cortical neurons**. The proteins described are the proteins listed in **Figure 7H**.

5.2.9 - Heterozygous and homozygous spastin^{N384K} mutations drive alterations in cell adhesion and nervous system development pathways in primary cortical neurons

DAVID gene ontology enrichment analysis was used to identify cell surface pathways that may be specifically affected by the spastin^{N384K} mutation in primary neurons. Using a similar strategy to that described for the MEF proteomics, DAVID analysis was performed on proteins that had a 1.5-fold increase or decrease at the cell surface in both mutant genotypes. This revealed an enrichment of proteins with annotations related to cell adhesion (GO:0007155) and nervous system development (GO:0007399; **Figure 8A**).

In total, 194 plasma membrane annotated proteins also had an annotation of being involved in cell adhesion (**Figure 8B**). Out of these, 22 proteins (11%) were identified with more than 1.5-fold increased abundance at the cell surface, and 13 proteins (7%) were identified with more than 1.5-fold decreased abundance at the cell surface. These high fold change proteins showed a low variability in fold change between samples intragenotypically and intergenotypically. Out of the top four proteins identified that had the highest statistically significant increase at the cell surface, all had at least a 2-fold increased abundance in both mutant genotypes (**Figure 8C**). Likewise, of the top four proteins that had the highest statistically significant decrease at the cell surface, all had at least a 2-fold reduction in cell surface abundance in both mutant genotypes. This group included Icam1 which was the protein identified with the largest fold change out of all analysed proteins.

DAVID analysis revealed 32 plasma membrane annotated proteins that were also annotated to be involved in nervous system development (**Figure 8D**). Out of these, 6 proteins (19%) had at least a 1.5-fold reduction in cell surface abundance, and 2 proteins (6%) had at least a 1.5-fold increase in cell surface abundance. These proteins showed a low variability in fold change intragenotypically and intergenotypically. The top 4 proteins with the most statistically significant increase and decrease at the cell surface are presented in **Figure 8E**.

A)

DAVID Analysis Terms	Benjamini-Adjusted P Value
Cell Adhesion (GO:0007155)	0.014
Nervous System Development (GO:0007399)	0.026

B)

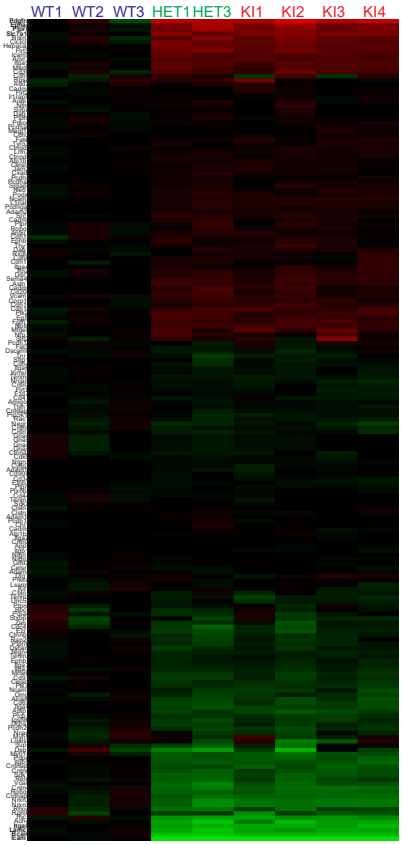

Identified Cell Adhesion Pathway Genes

C)

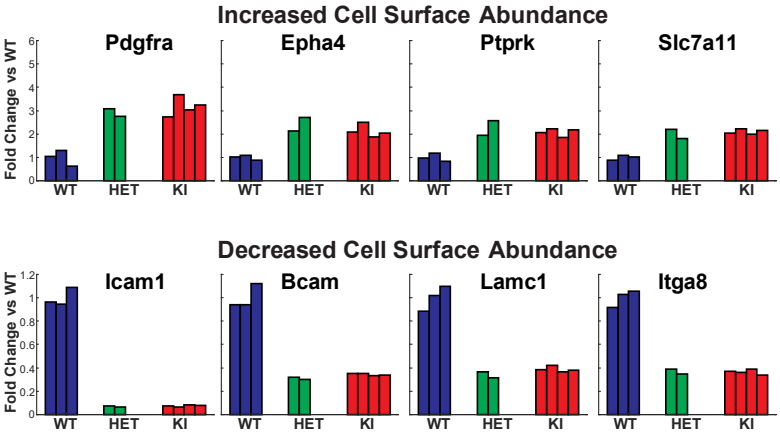

D)

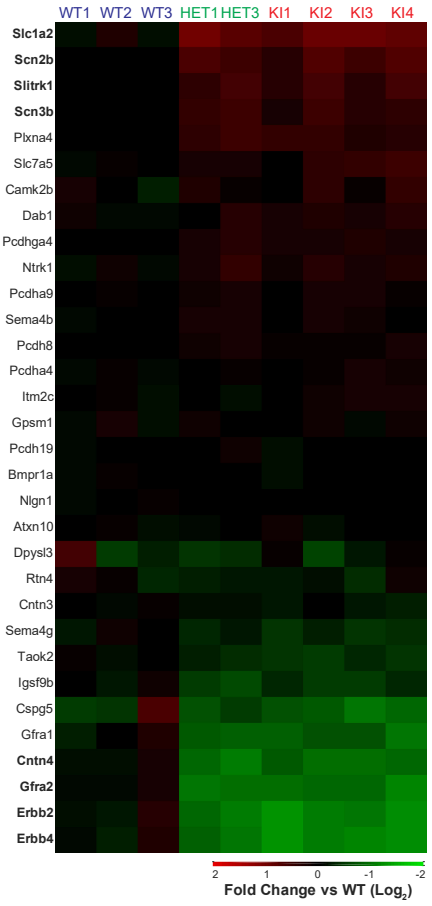

Identified Nervous System Develpment Genes

E)

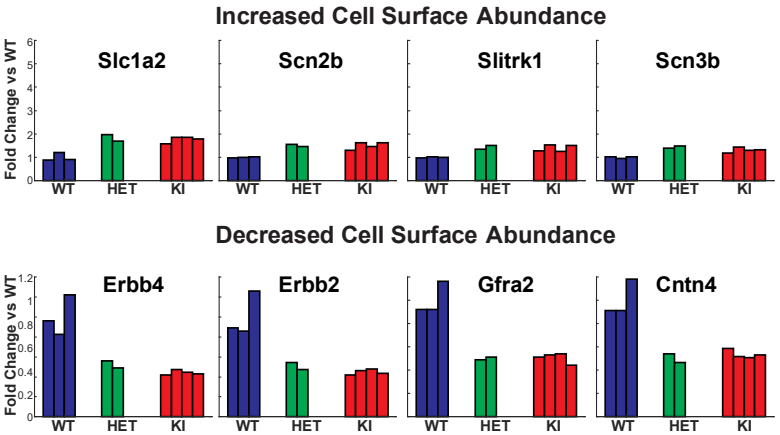

Figure 8 - DAVID analysis reveals heterozygous and homozygous spastin^{N384K} mutations to significantly alter the cell surface abundance of cell adhesion and nervous system development proteins in primary cortical neurons.

A) **DAVID gene ontology analysis of proteins reduced <0.67 or increased >1.5 at the cell surface in both heterozygous and homozygous spastin^{N384K} mutant primary cortical neurons** – DAVID enrichment analysis was performed on proteins with a 1.5-fold increase or decrease in both spastin^{N384K} mutant genotypes against a background of all plasma membrane identified proteins.

B) **Heatmap of all identified plasma membrane annotated cell adhesion proteins** – The fold change of each sample relative to mean WT cell surface abundance was plotted for all plasma membrane annotated proteins annotated with the 'cell adhesion' (GO:0007155) term. Data was plotted on a $\log_2$ scale, with maximum and minimum values set to 2 and -2 to aid data visualisation. Bold names indicate four proteins with a common increased/decreased abundance at the cell surface in both heterozygous and homozygous spastin^{N384K} mutant primary cortical neurons.

C) **Bar charts of focal adhesion proteins commonly increased/decreased at the cell surface in heterozygous and homozygous spastin^{N384K} mutant primary cortical neurons** – Bar charts of four focal adhesion annotated proteins with an increased/decreased cell surface abundance in both heterozygous and homozygous spastin^{N384K} mutant primary cortical neurons from **Figure 8B** were plotted. The chart axes show linear fold change relative to the mean WT peptide abundance.

D) **Heatmap of all identified plasma membrane annotated nervous system development proteins** – Methods as in **Figure 8B**, but with fold change of each sample relative to mean WT cell surface abundance plotted for all plasma membrane annotated proteins annotated with the 'Nervous System Development' (GO:0007399) term.

E) **Bar charts of nervous system development proteins commonly gained/lost at the cell surface in heterozygous and homozygous spastin^{N384K} mutant primary cortical neurons** – Methods as in **Figure 8C**, but with bar charts were plotted of the four nervous system development annotated proteins with an increased/decreased cell surface abundance in both heterozygous and homozygous spastin^{N384K} mutant primary neurons.

5.2.10 – Comparisons between spastin^{N384K} mutant MEFs and primary cortical neurons reveals proteins with common cell surface abundance changes in both cell types

A comparison between the MEF and primary cortical neuron proteomics data was made to highlight proteins that had similar fold changes in both cell types. This would represent a set of proteins in which there was a very high confidence that their plasma membrane abundance was influenced by spastin. 366 plasma membrane annotated proteins were common to the MEF and neuron proteomics analysis. This represented 63% of the MEF plasma membrane proteomics data and 33% of the neuron plasma membrane proteomics data.

Focussing on proteins that were commonly reduced more than 1.5-fold from the cell surface, only 1 protein, Vcan, was reduced from the cell surface in all MEF spastin mutant samples and neuron spastin mutant samples (**Figure 9A** and **Figure 9B**). Vcan had low fold change variability between all the HET and HOM samples in both the MEF and neuron data (**Figure 9C**), with at least a 1.7-fold reduction in cell surface abundance in all samples. 7 proteins were identified when considering proteins that were more than 1.5-fold at the cell surface in 3/4 of the mutant samples (**Figure 9B**). The largest group of these was where these three sample types were the HOM MEFs, HET neurons, and HOM neurons. The function of the proteins with at least a 1.5-fold reduction in cell surface abundance in at least 3 mutant samples was investigated (**Table 5** (located after **Figure 9** legends)). This revealed a diverse set of proteins involved in ion transport, adhesion, and neuronal survival.

No plasma membrane annotated proteins had a greater than 1.5-fold increase in cell surface abundance in all 4 mutant samples (**Figure 9D** and **Figure 9E**). However, 4 proteins were identified that had more than a 1.5-fold increase at the cell surface in the HET MEFs, HET neurons, and HOM neurons grouping, and 4 identified in the HOM MEFs, HET neurons, and HOM neurons grouping (**Figure 9E**). Investigations into the functions of these proteins showed them to have a connection to neuronal health (e.g. Slitrk2, Flrt3, Unc5c), but also function in general cell maintenance (e.g. Pdgfra, Mertk) and transport across membranes (e.g. Slc7a11, Cacna2d1) as shown in **Table 6** (located after **Figure 9** legends). These proteins generally showed low fold change variability both intragenotypically and intergenotypically (**Figure 9C**).

MEF vs Neuron Comparison

Threshold: <0.67 Fold Change

A)

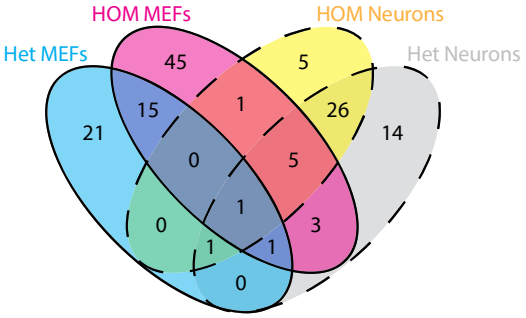

B)

	Het MEFs	HOM MEFs	Het Nrns	HOM Nrns	Total Proteins	Protein Names
i	+	+	+	+	1	**Vcan**
ii	+	+	+	-	1	**Slc11a2**
	+	+	-	+	0	-
iii	+	-	+	+	1	**Slc39a10**
iv	-	+	+	+	5	**Heg1, Got2, Gfra1, Anxa1, Calr**
	+	-	+	-	0	-
	+	-	-	+	0	-
v	-	+	+	-	3	Krt5, Slc29a1, Lypd6
vi	-	+	-	+	1	Slc39a6

Threshold: >1.5 Fold Change

D)

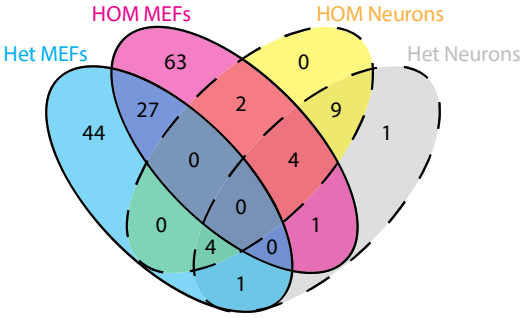

E)

	Het MEFs	HOM MEFs	Het Nrns	HOM Nrns	Total Proteins	Protein Names
	+	+	+	+	0	-
	+	+	+	-	0	-
	+	+	-	+	0	-
vii	+	-	+	+	4	**Slitrk2, Slc7a11, Pdgfra, Unc5c**
viii	-	+	+	+	4	**Cacna2d1, Acvr1, Flrt3, Mertk**
ix	+	-	+	-	1	Ramp2
	+	-	-	+	0	-
x	-	+	+	-	1	Atp2a2
xi	-	+	-	+	2	Tfrc, Mfge8

C)

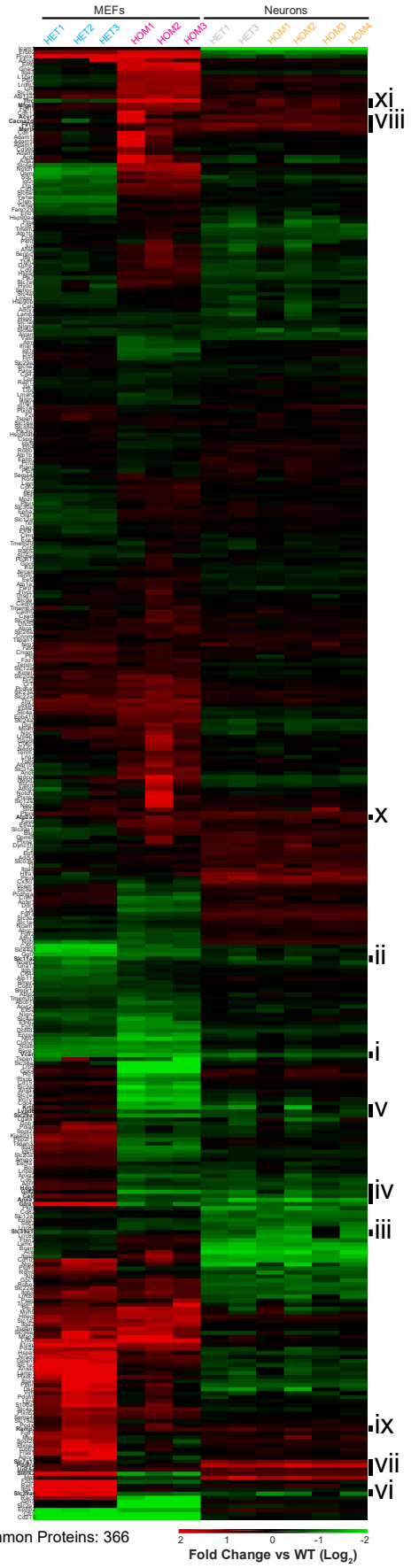

Figure 9 - Comparisons between heterozygous and homozygous spastin^{N384K} mutant MEFs and heterozygous and homozygous spastin^{N384K} mutant primary cortical neurons reveal common proteins with cell surface abundance changes both cell types.

A) **Analysis showing the common groups of proteins reduced at the cell surface when comparing heterozygous/homozygous spastin mutant MEFs/primary cortical neurons** – A list of proteins identified in both the MEF sample proteomics and the neuron sample proteomics was compiled. From this list, lists of plasma membrane annotated proteins with mean HE-WT and mean HOM-WT fold change <0.67 from both MEF and neuron data was generated and plotted in a Venn diagram. Due to poor hierarchical clustering, 'WT4' and 'HET2' from the neuron data set were excluded from calculations.

B) **Table showing the outcome of Figure 9A** – The proteins determined from **Figure 9A** are identified in the table shown. Roman numerals correspond to areas defined in the heatmap (**Figure 9C**).

C) **Heatmap showing all plasma membrane proteins common to both MEF proteomics and neuron proteomics** – The fold change of each sample relative to the mean WT peptide abundance was plotted for MEF and neuron samples, with the heatmap only displaying proteins with a plasma membrane annotation. Data was plotted on a $\log_2$ scale, with maximum/minimum values set at 2 and -2 (equivalent of a 4-fold increase and a 0.25-fold decrease) to aid data visualisation. Line markers and roman numerals indicate regions of proteins identified in **Figure 9A,B,D,E**. Bold names indicate highlighted proteins. Due to poor hierarchical clustering, 'WT4' and 'HET2' from the neuron data set were excluded.

D) **Analysis showing the common groups of proteins increased at the cell surface when comparing heterozygous/homozygous spastin mutant MEFs/primary cortical neurons** – Methods as in **Figure 9A**, but lists of plasma membrane annotated proteins with mean HET-WT and mean HOM-WT fold change >1.5 from both MEF and neuron data was generated and plotted in a Venn diagram.

E) **Table showing the outcome of Figure 9D** – The proteins determined from **Figure 9D** are identified in the table shown. Roman numerals correspond to areas defined in the heatmap (**Figure 9C**).

Gene Name	Protein Function	Reference	Proteomics Result (Fold Change)
Vcan	Extracellular matrix assembly and cell adhesion regulation	Damasceno et al. 2016	**Decrease** – MEF HET: 0.46 MEF HOM: 0.33 Neuron HET: 0.49 Neuron KI: 0.59
Slc11a2	Divalent metal-ion transporter	Mackenzie et al. 2007	**Decrease** – MEF HET: 0.52 MEF HOM: 0.65 Neuron HET: 0.67 Neuron HOM: 0.82
Slc39a10	Zinc influx transporter	Kagara et al. 2007	**Decrease** – MEF HET: 0.67 MEF HOM: 0.92 Neuron HET: 0.61 Neuron HOM: 0.57
Heg1	Regulation of endothelial cell-cell junctions for heart formation and blood vessels	Kleaveland et al. 2009	**Mixed** – MEF HET: 1.51 MEF HOM: 0.65 Neuron HET: 0.66 Neuron HOM: 0.68
Got2	Long-chain free fatty acid uptake	Zhou et al. 1998	**Decrease** – MEF HET: 1.07 MEF HOM: 0.39 Neuron HET: 0.50 Neuron HOM: 0.65
Gfra1	Receptor for glial cell line-derived neurotrophic factor that functions in neuronal survival and differentiation	Konishi et al. 2014	**Mixed** – MEF HET: 6.64 MEF HOM: 0.49 Neuron HET: 0.57 Neuron HOM: 0.56
Anxa1	Regulator of immunity by actin cytoskeleton rearrangement	D'Acquisto et al. 2007	**Mixed** – MEF HET: 1.23 MEF HOM: 0.67 Neuron HET: 0.41 Neuron HOM: 0.38
Calr	Chaperone to promote protein folding in the ER	Nauseef, McCormick, and Clark 1995	**Mixed** – MEF HET: 0.56 MEF HOM: 0.60 Neuron HET: 0.56 Neuron HOM: 0.60

Table 5 - **Common proteins reduced at the cell surface in HET and HOM spastin^{N384K} MEFs and primary cortical neurons, or from 3/4 of these categories**. The proteins described are the proteins listed in **Figure 9B**.

Gene Name	Protein Function	Reference	Proteomics Result (Fold Change)
Slitrk2	Promotes excitatory synapse differentiation and supresses neurite outgrowth	Beaubien et al. 2016	**Mixed** – MEF HET: 4.04 MEF HOM: 0.41 Neuron HET: 1.55 Neuron HOM: 1.58
Slc7a11	Anionic amino acid transporter	Gasol et al. 2004	**Mixed** – MEF HET: 1.80 MEF HOM: 0.91 Neuron HET: 2.00 Neuron HOM: 2.10
Pdgfra	Tyrosine-protein kinase essential in regulation of embryonic development, cell proliferation and survival	Vantler et al. 2006	**Increase** – MEF HET: 1.56 MEF HOM: 1.11 Neuron HET: 2.92 Neuron HOM: 3.18
Unc5c	Netrin receptor required in axonal guidance in the corticospinal tract	Finger et al. 2002	**Increase** – MEF HET: 1.56 MEF HOM: 1.40 Neuron HET: 1.63 Neuron HOM: 1.51
Cacna2d1	Voltage dependent calcium channel	Gao et al. 2000	**Increase** – MEF HET: 1.02 MEF HOM: 3.04 Neuron HET: 1.58 Neuron HOM: 1.68
Acvr1	Activin receptor that mediates Bone Morphogenic Protein signalling for development and repair	Kishigami et al. 2004	**Mixed** – MEF HET: 0.96 MEF HOM: 1.91 Neuron HET: 1.38 Neuron HOM: 1.28
Flrt3	Cell adhesion, cell migration, and axon guidance, mediating spatial organisation of neurons, and mediates neurite number and length	Tsuji et al. 2004	**Mixed** – MEF HET: 0.97 MEF HOM: 1.54 Neuron HET: 2.00 Neuron HOM: 1.75
Mertk	Tyrosine-protein kinase essential for maintenance and survival of a wide variety of mammalian tissues	Dransfield and Farnworth 2016	**Increase** – MEF HET: 1.07 MEF HOM: 1.50 Neuron HET: 1.67 Neuron HOM: 1.56

Table 6 - **Common proteins increased at the cell surface in HET and HOM spastin^{N384K} MEFs and primary cortical neurons, or from 3/4 of these categories.** The proteins described are the proteins listed in **Figure 9E**.

5.2.11 – Comparison between spastin^{N384K} mutant MEFs/primary cortical neurons with SNX17 and SNX27 depletion data reveals proteins with common cell surface abundance changes in plasma membrane recycling

Previous experiments have been performed investigating the effect of depletion of retromer and retriever cargo recruitment components on the cell surface proteome (McNally et al. 2017; Steinberg et al. 2013). By comparing the spastin mutation data to the SNX17 or SNX27 depletion data, it could provide clues as to which recycling pathways the spastin^{N384K} mutation could be affecting.

It should be noted that whilst similarities may be revealing, a lack of similarity would be hard to interpret. This is as a result of several factors: 1) the SNX17 and SNX27 proteomic experiments were performed using a different peptide labelling method, namely SILAC rather than TMT; 2) the SNX17 and SNX27 experiments were performed using a different cell type and species (HeLa rather than MEFs or neurons); and 3) the effect of the spastin mutation is likely to affect the endocytic pathway more generally than by just blocking endocytic recycling (as discussed in Chapter 5 Introduction – Section 5.1.1).

The SNX17 depletion data set was obtained from McNally et al. (2017). Proteins from this dataset were only included in the comparison if they were identified in at least two of the SNX17 depletion cell surface proteome SILAC experiments. The SNX27 depletion data set was obtained from Steinberg et al. (2013). Unlike the SNX17 dataset, the full proteomics results were not publicly available, with the data presented already pre-filtered to a threshold fold change of 1.4-fold, and with a subcellular localisation annotation of 'integral membrane proteins'. It is unclear to what degree the difference in subcellular localisation annotation made to the comparison. For both imported datasets, proteins were annotated using the same subcellular localisation annotation methodology as for the MEF and neuron data sets. For the comparisons between the MEF or neuron data and the SNX17 or SNX27 depletion data, proteins were only included if were annotated with a plasma membrane annotation and were identified in both datasets being compared.

MEF vs SNX17

211 plasma membrane annotated proteins were identified in both the spastin^{N384K} mutant MEF data and the SNX17 siRNA depletion HeLa data. This represented 37% of MEF plasma membrane annotated data and 44% of SNX17 plasma membrane annotated data.

When filtering proteins by a threshold 1.5-fold change in cell surface abundance, only 2 proteins, Ephb2 and Lama4 showed more than a 1.5-fold reduction from the cell surface in both HET and HOM MEFs and the SNX17 depletion data (**Figure 10A** and **Figure 10B**). However, there were substantially more proteins identified when filtering for proteins that showed a reduction of more than 1.5-fold in only one of the MEF data sets and the SNX17 data (**Figure 10A** and **Figure 10B**). On average, these proteins showed a considerable reduction in abundance at the cell surface, and a low fold-change variation between the samples (**Figure 10C**). Investigations into the functions of these proteins revealed functions in ion and substrate transport, migration and cell adhesion, receptor signalling, and neuronal development and maintenance (**Table 7** (located after **Figure 10** legends)).

For plasma membrane annotated proteins that had an abundance of more than 1.5-fold at the cell surface in both the HET and HOM MEF datasets and the SNX17 depletion, only 1 protein, Gas1, was identified (**Figure 10D** and **Figure 10E**). Furthermore, when relaxing this threshold to including any proteins identified in either the HET or HOM MEF data and the SNX17 data, only 1 additional protein was identified, Gnai2 (**Figure 10D** and **Figure 10E**). Of these proteins, Gas1 showed a high fold change variability, but Gnai2 showed a consistent level of fold change between samples (**Figure 10C**). These proteins were identified to function in development and proliferation (**Table 8** (located after **Figure 10** legends)).

Neurons vs SNX17

258 plasma membrane annotated proteins were identified in both the neuron and SNX17 depletion proteomic analyses. This represented 24% of the neuron plasma membrane annotated data and 54% of the SNX17 plasma membrane annotated data.

When filtering proteins by a threshold 1.5-fold change, 13 proteins were reduced more than 1.5-fold from the cell surface in both HET and HOM neuron data sets, and the SNX17 data **(Figure 10F** and **Figure 10G**). 8 additional proteins were identified when relaxing the filtering criteria to proteins reduced more than 1.5-fold in either the HET or HOM neuron data and the SNX17 data (**Figure 10F** and **Figure 10G**). These proteins showed a high homogeneity of fold change across all samples (**Figure**

10H). The functions of these identified proteins were investigated, revealing proteins involved in neuronal survival, immune activation, and cell adhesion (**Table 9** (located after **Figure 10** legends)).

No proteins had increased cell surface abundance in both the neuron proteomics and the SNX17 data. One potentially explanation for this was the heavy bias of the SNX17 depletion data towards proteins with reduced rather than increased abundance at the cell surface (**Figure 10C** and **Figure 10H**).

A)

MEF vs SNX17 KD Comparison

Threshold: <0.67 Fold Change

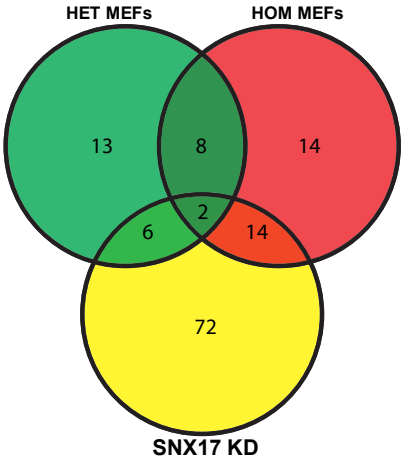

B)

	Het MEFs	HOM MEFs	SNX17 KD	Total Proteins	Protein Names
i	+	+	+	2	**Ephb2, Lama4**
ii	+	+	-	8	Cfl1, Cd276, Msn, Slc44a1, F11r, Mmp14, Pttglip, Erp44
iii	+	-	+	6	Ywhae, Itgb1, Sdc1, Lrp1, Fam129b, Tfrc
iv	-	+	+	14	Slc2a1, Slc38a1, Antxr2, Slc29a1, Efnb2, Dcbld2, Crim1, Igsf3, Slc39a6, Slc20a1, Lrp5, Heg1, Anxa1, Calr

Threshold: >1.5 Fold Change

D)

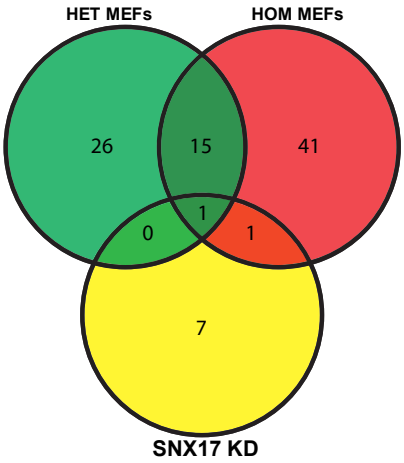

E)

	Het MEFs	HOM MEFs	SNX17 KD	Total Proteins	Protein Names
v	+	+	+	1	**Gas1**
vi	+	+	-	15	Il1rap, Flnc, Cd109, Plxnb2, Itga2, Hbegf, Erbb2, Slc4a2, Piezo1, Itgb5, Myh9, Pfn1, Thy1, Epha7, Slc22a5
	+	-	+	0	-
vii	-	+	+	1	Gnai2

C)

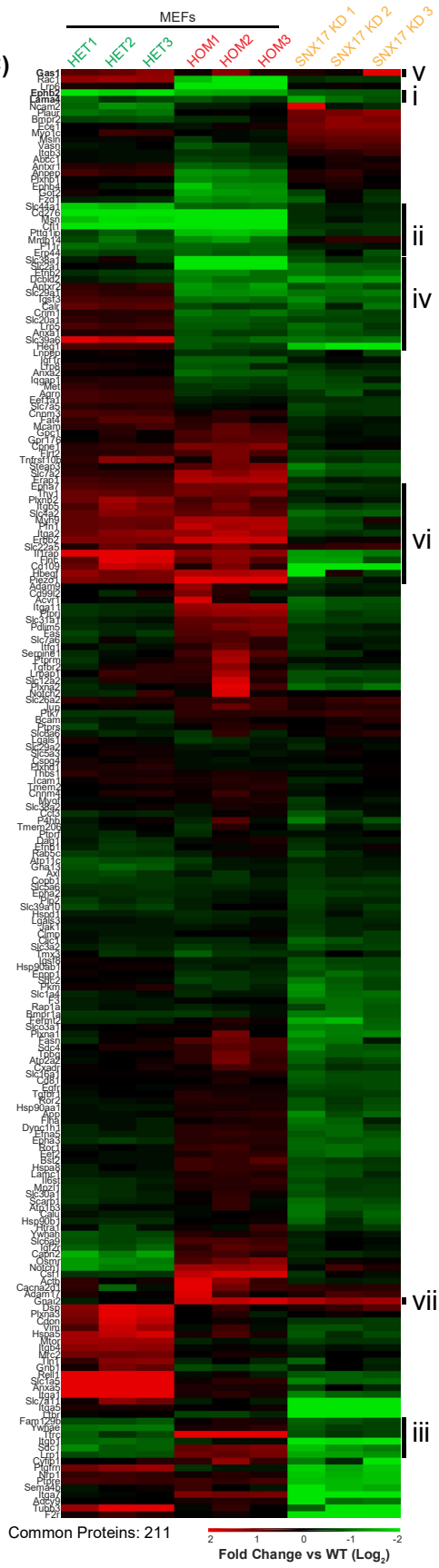

Neurons vs SNX17 KD Comparison

F)

Threshold: <0.67 Fold Change

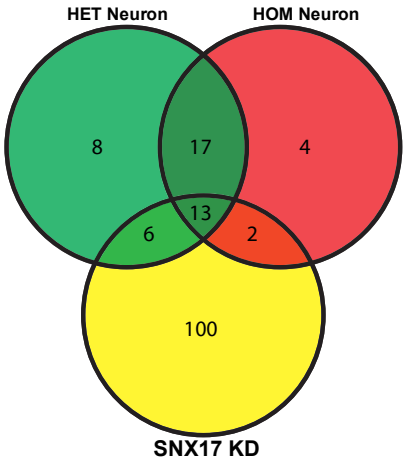

G)

	HET Nrns	HOM Nrns	SNX17 KD	Total Proteins	Protein Names
i	+	+	+	13	**Lamc1, Cd109, Tnc, Anxa1, Ilf2, Enpp1, Cd81, Calr, Ptgfrn, Sdc2, Rala, Bcap31, Heg1**
ii	+	+	-	17	Icam1, Bcam, Clu, Dsp, Sept2, Vdac1, Rhoa, Stmn1, Got2, Erbb2, Arhgdia, Itgb5, Myh10, Gpc1, Slc39a10, Hnrnpc, Dock7
iii	+	-	+	6	Ak2, Pkm, Actn4, Hspa8, Slc29a1, Flna
iv	-	+	+	2	Slc39a6, Atp1b3

Threshold: >1.5 Fold Change

I)

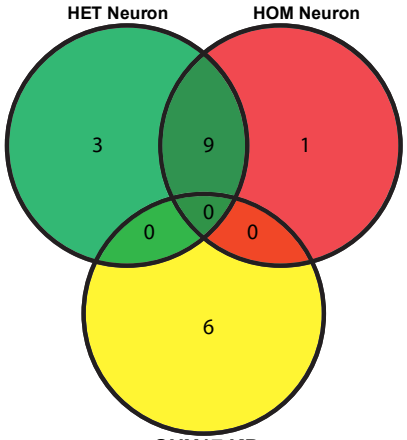

J)

	HET Nrns	HOM Nrns	SNX17 KD	Total Proteins	Protein Names
	+	+	+	0	-
v	+	+	-	9	Met, Htra1, Slc7a11, Itga5, Ptpre, Acvr1, Kctd12, Atp2b4, Cacna2d1
	+	-	+	0	-
	-	+	+	0	-

H)

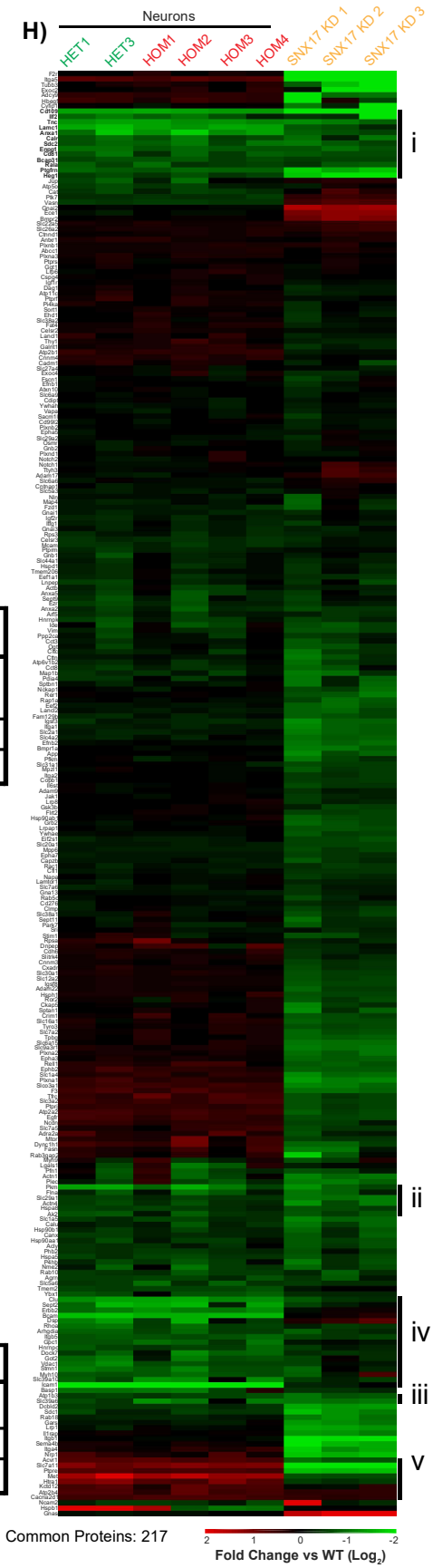

Figure 10 - Comparisons between heterozygous and homozygous spastin^{N384K} mutant MEFs/neurons and SNX17 siRNA depleted HeLa cells reveal proteins that have common cell surface abundance changes.

A) **Analysis showing the common proteins reduced at the cell surface when comparing heterozygous and homozygous spastin^{N384K} mutant MEFs and SNX17 siRNA depleted HeLa cells from McNally et al. (2017)** – A list of proteins identified in both the MEF sample proteomics and the published SNX17 siRNA depleted HeLa cell proteomics was compiled. From this list, lists of plasma membrane annotated proteins with mean HET-WT, mean HOM-WT, and mean Medium/Heavy ratios fold change of <0.67 were generated and plotted in a Venn diagram. 'SNX17 KD' refers to SNX17 siRNA depleted cells.

B) **Table showing the outcome of Figure 10A** – The proteins determined from **Figure 10A** are identified in the table shown. Roman numerals correspond to areas defined in the heatmap (**Figure 10C**).

C) **Heatmap showing all plasma membrane annotated proteins common to both MEF proteomics and SNX17 siRNA depleted HeLa cell proteomics from McNally et al. (2017)** – The fold change of each sample relative to the mean WT peptide abundance was plotted for MEF samples, and for SNX17 siRNA KD samples the Medium/Heavy ratio for each independent experimental repeat was plotted. The heatmap only displays plasma membrane annotated proteins. Data was plotted on a $\log_2$ scale, with maximum/minimum values set at 2 and -2 (equivalent of 4-fold increase and a 0.25-fold decrease) to aid data visualisation. Where a protein was only identified in two independent experiments in the SNX17 siRNA depleted data set, the average of these values was displayed in the third SNX17 KD column to aid data visualisation. Line markers and roman numerals indicate regions of proteins identified in **Figures 10A,B,D,E**. Bold names indicate highlighted proteins.

D) **Analysis showing the common groups of proteins increased at the cell surface when comparing heterozygous and homozygous spastin^{N384K} mutant MEFs and SNX17 siRNA depleted HeLa cells from McNally et al. (2017)** – Methods as in **Figure 10A**, but lists of plasma membrane annotated proteins with mean HET-WT, mean HOM-WT, and mean Medium/Heavy ratios fold change of >1.5 were generated and plotted in a Venn diagram.

E) **Table showing the outcome of Figure 10D** – The proteins determined from **Figure 10D** are identified in the table shown. Roman numerals correspond to areas defined in the heatmap (**Figure 10C**).

F) **Analysis showing the common proteins reduced at the cell surface when comparing heterozygous and homozygous spastin^{N384K} mutant primary cortical neurons and SNX17 siRNA depleted HeLa cells from McNally et al. (2017)** – A list of proteins identified in both the neuron sample proteomics and the published SNX17 siRNA depleted HeLa cell proteomics was compiled. From this list, lists of plasma membrane annotated proteins with mean HET-WT, mean HOM-WT, and mean Medium/Heavy ratios fold change of <0.67 were generated and plotted in a Venn diagram. 'SNX17 KD' refers to SNX17 siRNA depleted cells.

G) **Table showing the outcome of Figure 10F** – The proteins determined from **Figure 10F** are identified in the table shown. Roman numerals correspond to areas defined heatmap in **Figure 10H**.

H) **Heatmap showing all plasma membrane annotated proteins common to both neuron proteomics and SNX17 siRNA depleted HeLa cell proteomics from McNally et al. (2017)** – The fold change of each sample relative to the mean WT peptide abundance was plotted for neuron samples, and for SNX17 siRNA KD samples the Medium/Heavy for each independent experimental repeat was plotted. The heatmap only displays plasma membrane annotated proteins. Data was plotted on a $\log_2$ scale, with maximum values set at 2 and -2 (equivalent to 4-fold increase and 0.25-fold decrease) to aid data visualisation. Where a protein was only identified in two independent experiments in the SNX17 siRNA depleted data set, the average of these values was displayed in the third SNX17 KD column to aid data

visualisation. Line markers and roman numerals indicate proteins identified **in Figures 10F,G,I,J.** Bold names indicate highlighted proteins.

I) **Analysis showing the common proteins increased at the cell surface when comparing heterozygous and homozygous spastin^{N384K} mutant primary neurons and SNX17 siRNA depleted HeLa cells from McNally et al. (2017)** – Methods in **Figure 10F**, but lists of plasma membrane annotated proteins with mean HET-WT, mean HOM-WT, and mean Medium/Heavy ratios fold change of >1.5 were generated and plotted in a Venn diagram.

J) **Table showing the outcome of Figure 10I** – The proteins determined from **Figure 10I** are identified in the table shown. Roman numerals correspond to areas defined heatmap in **Figure 10H**.

Gene Name	Protein Function	Reference	Proteomics Results (Fold Change)
Ephb2	Ephrin-b receptor mediating synaptic transmission and plasticity	Alapin et al. 2018	**Decrease** – HET: 0.26 HOM: 0.36 SNX17: 0.57
Lama4	Neuromuscular junction formation	Chand et al. 2017	**Decrease** – HET: 0.63 HOM: 0.65 SNX17: 0.47
Ywhae	Regulation of neurite formation during cortical development	Cornell et al. 2016	**Decrease** – HET: 0.63 HOM: 0.65 SNX17: 0.64
Itgb1	Integrin associating the cell and the extracellular matrix regulating processes such as migration and adhesion	Margadant et al. 2011	**Mixed** – HET: 0.50 HOM: 1.23 SNX17: 0.25
Sdc1	Regulator of inflammation responses	Bartlett, Hayashida, and Park 2007	**Mixed** – HET: 0.53 HOM: 1.96 SNX17: 0.39
Lrp1	Myelin development, nerve conduction and axonal regeneration	Lin et al. 2017	**Mixed** – HET: 0.60 HOM: 1.92 SNX17: 0.38
Fam129b	Regulator of cell cycle progression by Ras activation	Lee, Ji, and Lu 2016	**Mixed** – HET: 0.62 HOM: 1.15 SNX17: 0.60
Tfrc	Facilities the uptake of iron	van Renswoude et al. 1982	**Mixed** – HET: 0.63 HOM: 5.09 SNX17: 0.66

Gene Name	Protein Function	Reference	Proteomics Results (Fold Change)
Slc2a1	Glucose transporter	Nualart, Godoy, and Reinicke 1999	**Decrease** – HET: 0.94 HOM: 0.14 SNX17: 0.53
Slc38a1	Sodium dependent amino acid transporter	Mackenzie and Erickson 2004	**Decrease** – HET: 0.90 HOM: 0.23 SNX17: 0.66
Antxr2	Necessary for cellular interactions with laminin and the extracellular matrix	Bell et al. 2001	**Mixed** – HET: 1.38 HOM: 0.41 SNX17: 0.58
Slc29a1	Nucleoside transporter	Mangravite, Xiao, and Giacomini 2003	**Mixed** – HET: 1.35 HOM: 0.42 SNX17: 0.49
Efnb2	Ligand for ephrin receptors regulating migration and adhesion during development	Fuller 2003	**Decrease** – HET: 0.70 HOM: 0.46 SNX17: 0.52
Dcbld2	Regulates vascular remodelling	Guo et al. 2009	**Decrease** – HET: 0.78 HOM: 0.49 SNX17: 0.39
Crim1	Modulates bone morphogenetic protein activity	Wilkinson et al. 2003	**Mixed** – HET: 1.27 HOM: 0.50 SNX17: 0.63
Igsf3	Regulates axonal growth and branching during development	Usardi et al. 2017	**Mixed** – HET: 1.54 HOM: 0.51 SNX17: 0.51
Slc39a6	Zinc influx transporter	Taylor et al. 2003	**Mixed** – HET: 3.68 HOM: 0.56 SNX17: 0.50
Slc20a1	Sodium dependent phosphate transporter	Olah et al. 1994	**Mixed** – HET: 1.37 HOM: 0.57 SNX17: 0.66
Lrp5	Regulator of Wnt signalling	Mao et al. 2001	**Mixed** – HET: 1.51 HOM: 0.60 SNX17: 0.59
Heg1	Regulation of endothelial cell-cell junctions for heart formation and blood vessels	Kleaveland et al. 2009	**Mixed** – HET: 1.51 HOM: 0.65 SNX17: 0.25

Gene Name	Protein Function	Reference	Proteomics Results (Fold Change)
Anxa1	Regulator of immunity by actin cytoskeleton rearrangement	D'Acquisto et al. 2007	**Mixed** – HET: 1.22 HOM: 0.67 SNX17: 0.61
Calr	Chaperone to promote protein folding in the ER	Nauseef et al. 1995	**Mixed** – HET: 1.71 HOM: 0.68 SNX17: 0.58

Table 7 - **Common proteins reduced at the cell surface in HET and HOM spastin^{N384K} MEFs and SNX17 depleted data from McNally et al. (2017), or from either a HET or HOM MEF data set and the SNX17 data**. The proteins described are the proteins listed in **Figure 10B**.

Gene Name	Protein Function	Reference	Proteomics Results (Fold Change)
Gas1	Promotes the formation of neurites and neuronal differentiation	Bautista et al. 2018	**Increase** – HET: 1.98 HOM: 1.52 SNX17: 1.73
Gnai2	Promotes epithelial cell proliferation	Villanueva et al. 2015	**Mixed** – HET: 0.91 HOM: 3.37 SNX17: 2.62

Table 8 - **Common proteins increased at the cell surface in HET and HOM spastin^{N384K} MEFs and SNX17 depleted data from McNally et al. (2017), or from either a HET or HOM MEF data set and the SNX17 data.** The proteins described are the proteins listed in **Figure 10E**.

Gene Name	Protein Function	Reference	Proteomics Result (Fold Change)
Lamc1	Laminin that mediates cell adhesion and migration during development	Simon-Assmann 2013	**Decrease** – HET: 0.34 HOM: 0.39 SNX17: 0.65
Cd109	Modulates transforming growth factor beta 1 regulating cell survival	Finnson et al. 2006	**Decrease** – HET: 0.37 HOM: 0.38 SNX17: 0.15
Tnc	Matrix protein regulating neuron migration, neural regeneration, neurite outgrowth, and synaptic plasticity	Martina et al. 2010	**Decrease** – HET: 0.40 HOM: 0.42 SNX17: 0.48
Anxa1	Regulator of immunity by actin cytoskeleton rearrangement	D'Acquisto et al. 2007	**Decrease** – HET: 0.41 HOM: 0.38 SNX17: 0.61

Gene Name	Protein Function	Reference	Proteomics Result (Fold Change)
Ilf2	Regulation of T cell activation	Harashima, Guettouche, and Barber 2010	**Decrease** – HET: 0.50 HOM: 0.62 SNX17: 0.14
Enpp1	Regulation of pyrophosphate levels regulating purinergic signalling	Belli and Goding 1994	**Decrease** – HET: 0.51 HOM: 0.58 SNX17: 0.61
Cd81	Tetraspanin functioning in cell adhesion and immune cell activation	Levy, Todd, and Maecker 1998	**Decrease** – HET: 0.54 HOM: 0.64 SNX17: 0.62
Calr	Chaperone to promote protein folding in the ER	Nauseef et al. 1995	**Decrease** – HET: 0.56 HOM: 0.60 SNX17: 0.58
Ptgfrn	Regulates the activity of prostaglandin F receptor that functions in endothelial cell network formation	Keightley et al. 2010	**Decrease** – HET: 0.56 HOM: 0.57 SNX17: 0.31
Sdc2	Regulation of dendritic initiation and elongation and arborisation	Chen et al. 2011	**Decrease** – HET: 0.57 HOM: 0.54 SNX17: 0.56
Rala	Multifunctional GTPase involved in integrin-dependant membrane raft exocytosis and in growth signalling	Balasubramanian et al. 2010	**Decrease** – HET: 0.60 HOM: 0.65 SNX17: 0.61
Bcap31	ER chaperone protein that recognises abnormally folded proteins and targets them for degradation	Wakana et al. 2008	**Decrease** – HET: 0.64 HOM: 0.64 SNX17: 0.68
Heg1	Regulation of endothelial cell-cell junctions for heart formation and blood vessels	Kleaveland et al. 2009	**Decrease** – HET: 0.66 HOM: 0.68 SNX17: 0.25

Table 9 - **Common proteins reduced at the cell surface in HET and HOM spastin^{N384K} primary cortical neurons and SNX17 depleted data from McNally et al. (2017), or from either a HET or HOM neuron data set and the SNX17 data**. The proteins described are the proteins listed in **Figure 10G**.

MEFs vs SNX27

77 plasma membrane annotated proteins overlapped between the spastin^{N384K} mutant MEF data and the SNX27 siRNA depletion HeLa data. This represented 13% of the MEF plasma membrane annotated data, and 73% of the SNX27 plasma membrane annotated data.

2 proteins were identified when filtering for proteins that had a 1.5-fold reduction in their abundance at the cell surface in both MEF data sets and the SNX27 data (**Figure 11A** and **Figure 11B**). These were Slc44a1 and Sco2a1. 9 addition proteins where identified when relaxing the filter to include proteins reduced more than 1.5-fold in either MEF mutant genotype and the SNX27 data. These 11 proteins showed a substantial reduction in cell surface abundance and low variation between samples (**Figure 11C**). These proteins were identified to function in ion and solute transport, receptor signalling, and lipid transport (**Table 10** (located after **Figure 11** legends)).

Only 1 protein, Itga2, was increased more than 1.5-fold in both MEF mutant genotypes and the SNX27 data (**Figure 11D** and **Figure 11E**). Two additional proteins, Sema4c and Flrt3, were identified by relaxing this criterion to include proteins identified in either mutant genotype and the SNX27 data. All three proteins showed a high level of fold change, and low variability between samples (**Figure 11C**). These proteins were identified to function in cell adhesion and migration, with Sema4c and Flrt3 particularly fulfilling these functions in neurons (**Table 11** (located after **Figure 11** legends)).

Neurons vs SNX27

73 plasma membrane annotated proteins overlapped between the spastin^{N384K} mutant primary cortical neuron data and the SNX27 siRNA depletion HeLa data. This represented 7% of the plasma membrane annotated primary neuron data, and 69% of the plasma membrane annotated SNX27 data set.

5 proteins were reduced more than 1.5-fold in their cell surface abundance in both neuron data sets and the SNX27 data (**Figure 11F** and **Figure 11G**). Two additional proteins were also included when relaxing the filter to include proteins from only one of the mutant genotypes that were also found in the SNX27 data. There was very low intragenotypic and cell type variation between samples (**Figure 11H**). These proteins were identified to function in a diverse range of functions, including cell adhesion and dendritic initiation and elongation (**Table 12** (located after **Figure 11** legends)).

Only 1 protein, Flrt3, was increased more than 1.5-fold at the cell surface in either neuron dataset and the SNX27 data (**Figure 11I** and **Figure 11J**). Flrt3 functions in regulating neuronal interaction with its environment by mediating processes such as adhesion, axon guidance, and neurite

number and length (**Table 13** (located after **Figure 11** legends)). Flrt3 had a good intragenotypic and intergenotypic fold change consistency in the spastin experiments, although the SNX27 results were more variable (**Figure 11H**).

A)

MEF vs SNX27 KD Comparison

Threshold: <0.67 Fold Change

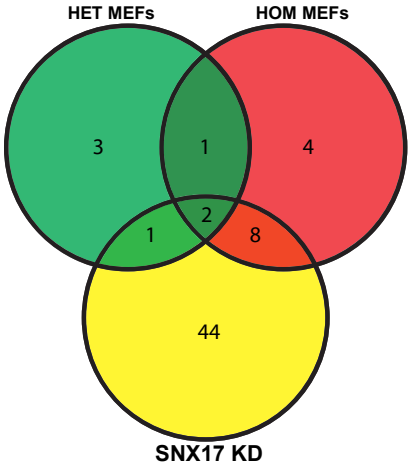

B)

	Het MEFs	HOM MEFs	SNX17 KD	Total Proteins	Protein Names
i	+	+	+	2	**Slc44a1, Slco2a1**
ii	+	+	-	1	Mmp14
iii	+	-	+	1	Atp11c
iv	-	+	+	8	Slc2a1, Slc2a3, Crim1, Adrb2, Slc39a6, Lrp5, Heg1, Tmem30a

Threshold: >1.5 Fold Change

D)

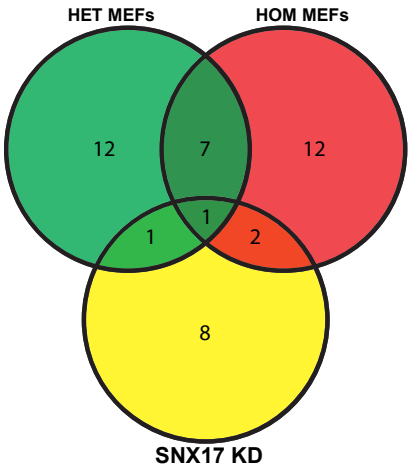

E)

	Het MEFs	HOM MEFs	SNX17 KD	Total Proteins	Protein Names
v	+	+	+	1	**Itga2**
vi	+	+	-	7	Il1rap, Lrfn4, Slc1a3, Slc4a2, Itgb5, Thy1, Slc22a5
vii	+	-	+	1	Sema4c
viii	-	+	+	2	Flrt3

C)

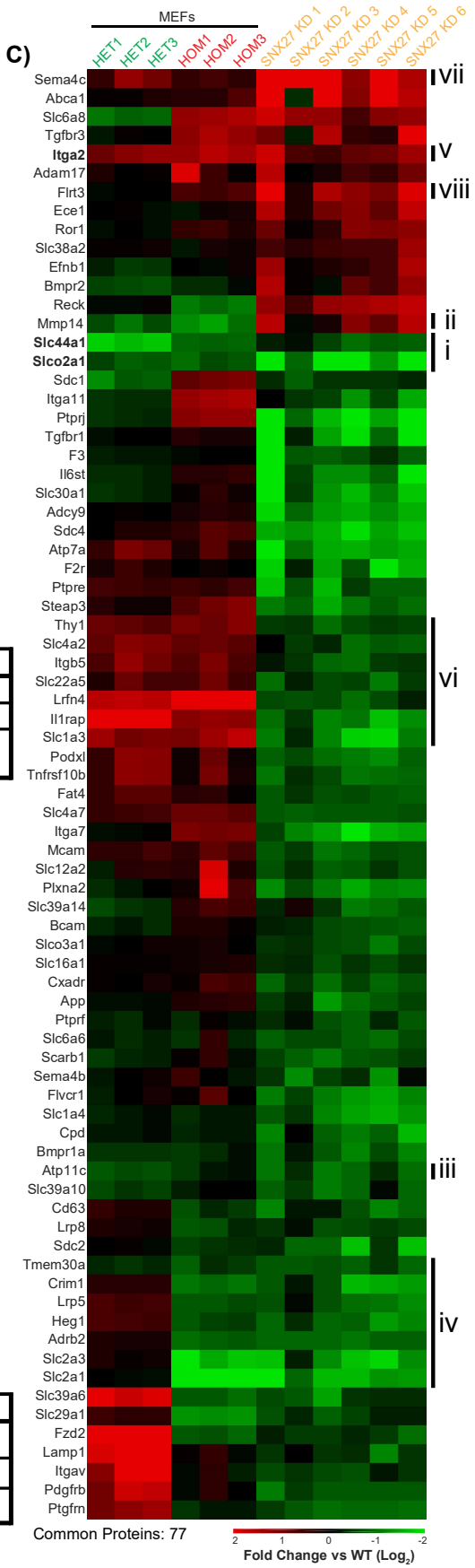

Neurons vs SNX27 KD Comparison

F)

Threshold: <0.67 Fold Change

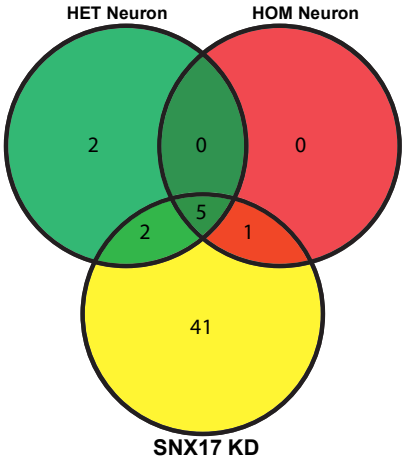

G)

	HET Nrns	HOM Nrns	SNX17 KD	Total Proteins	Protein Names
i	+	+	+	5	**Bcam, Ptgfrn, Sdc2, Itgb5, Slc39a10**
	+	+	-	0	-
ii	+	-	+	2	Cd63, Heg1
iii	-	+	+	1	Slc39a6

Threshold: >1.5 Fold Change

I)

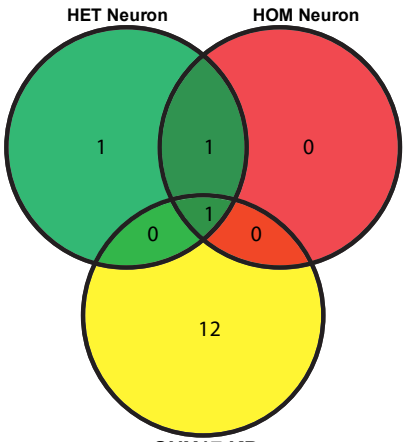

J)

	HET Nrns	HOM Nrns	SNX17 KD	Total Proteins	Protein Names
iv	+	+	+	1	**Flrt3**
v	+	+	-	1	Ptpre
	+	-	+	0	-
	-	+	+	0	-

H)

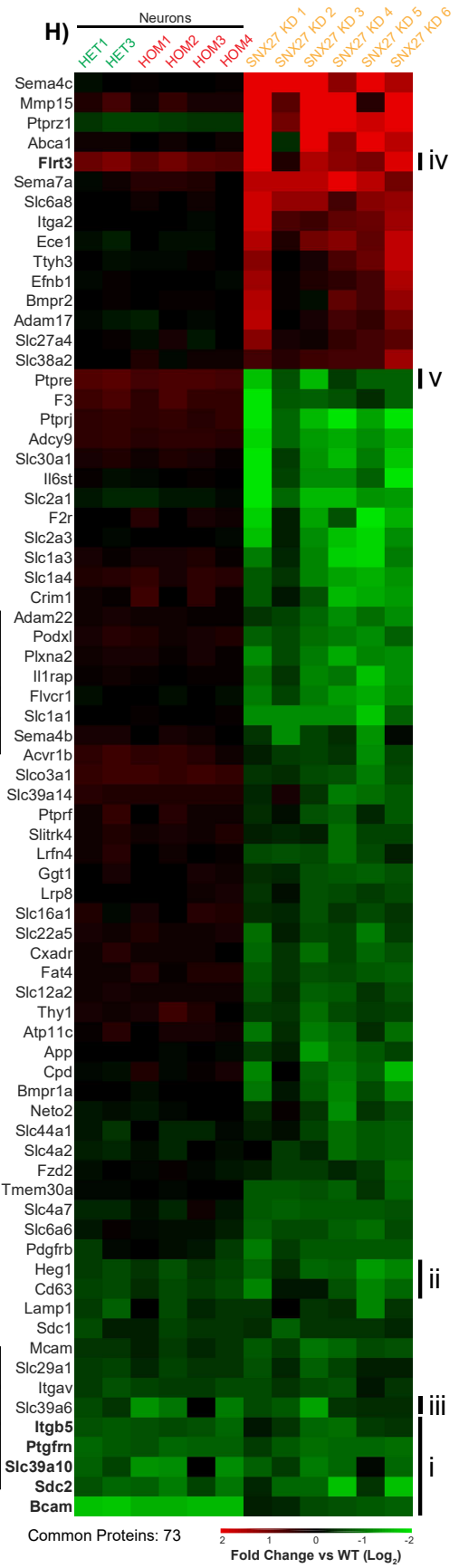

Figure 11 - Comparisons between heterozygous and homozygous spastin^{N384K} mutant MEFs/neurons and SNX27 siRNA depleted HeLa cells reveal proteins that have common cell surface abundance changes.

A) **Analysis showing the common proteins reduced at the cell surface when comparing heterozygous and homozygous spastin^{N384K} mutant MEFs and SNX27 siRNA depleted HeLa cells from Steinberg et al. (2013)** – A list of proteins identified in both the MEF sample proteomics and the published SNX27 siRNA depleted HeLa cell proteomics was compiled. From this list, lists of plasma membrane annotated proteins with mean HET-WT, mean HOM-WT, and mean Medium/Heavy ratios fold change of <0.67 were generated and plotted in a Venn diagram. 'SNX27 KD' refers to SNX27 siRNA depleted cells.

B) **Table showing the outcome of Figure 11A** – The proteins determined from **Figure 11A** are identified in the table shown. Roman numerals correspond to areas defined in the heatmap (**Figure 11C**).

C) **Heatmap showing all plasma membrane annotated proteins common to both MEF proteomics and SNX27 siRNA depleted HeLa cell proteomics from Steinberg et al. (2013)** – The fold change of each sample relative to the mean WT peptide abundance was plotted for MEF samples, and for SNX27 siRNA KD samples the Medium/Heavy ratio for each independent experimental repeat was plotted. The heatmap only displays plasma membrane annotated proteins. Data was plotted on a $\log_2$ scale, with maximum/minimum values set at 2 and -2 (equivalent of 4-fold increase and a 0.25-fold decrease) to aid data visualisation. Where a protein was not identified in all independent experiments in the SNX27 siRNA depleted data set, the average of these values was displayed in the empty SNX27 KD columns to aid data visualisation. Line markers and roman numerals indicate regions of proteins identified in **Figures 11A,B,D,E**. Bold names indicate highlighted proteins.

D) **Analysis showing the common groups of proteins increased at the cell surface when comparing heterozygous and homozygous spastin^{N384K} mutant MEFs and SNX27 siRNA depleted HeLa cells from Steinberg et al. (2013)** – Methods as in **Figure 11A**, but lists of plasma membrane annotated proteins with mean HET-WT, mean HOM-WT, and mean Medium/Heavy ratios fold change of >1.5 were generated and plotted in a Venn diagram.

E) **Table showing the outcome of Figure 11D** – The proteins determined from **Figure 11D** are identified in the table shown. Roman numerals correspond to areas defined in the heatmap (**Figure 11C**).

F) **Analysis showing the common proteins reduced at the cell surface when comparing heterozygous and homozygous spastin^{N384K} mutant primary cortical neurons and SNX27 siRNA depleted HeLa cells from Steinberg et al. (2013)** – A list of proteins identified in both the neuron sample proteomics and the published SNX27 siRNA depleted HeLa cell proteomics was compiled. From this list, lists of plasma membrane annotated proteins with mean HET-WT, mean HOM-WT, and mean Medium/Heavy ratios fold change of <0.67 were generated and plotted in a Venn diagram. 'SNX27 KD' refers to SNX27 siRNA depleted cells.

G) **Table showing the outcome of Figure 11F** – The proteins determined from **Figure 11F** are identified in the table shown. Roman numerals correspond to areas defined heatmap in **Figure 11H**.

H) **Heatmap showing all plasma membrane annotated proteins common to both neuron proteomics and SNX27 siRNA depleted HeLa cell proteomics from Steinberg et al. (2013)** – The fold change of each sample relative to the mean WT peptide abundance was plotted for neuron samples, and for SNX27 siRNA KD samples the Medium/Heavy for each independent experimental repeat was plotted. The heatmap only displays plasma membrane annotated proteins. Data was plotted on a $\log_2$ scale, with maximum values set at 2 and -2 (equivalent to 4-fold increase and 0.25-fold decrease) to aid data visualisation. Where a protein was not identified in all independent experiments in the SNX27 siRNA depleted data set, the average of these values was displayed in the empty SNX27 KD columns to aid

data visualisation. Line markers and roman numerals indicate proteins identified in **Figures 11F,G,I,J**. Bold names indicate highlighted proteins.

I) **Analysis showing the common proteins increased at the cell surface when comparing heterozygous and homozygous spastin^{N384K} mutant primary neurons and SN27 siRNA depleted HeLa cells from Steinberg et al. (2013*)*** – Methods in **Figure 11F**, but lists of plasma membrane annotated proteins with mean HET-WT, mean HOM-WT, and mean Medium/Heavy ratios fold change of >1.5 were generated and plotted in a Venn diagram.

J) **Table showing the outcome of Figure 11I** – The proteins determined from **Figure 11I** are identified in the table shown. Roman numerals correspond to areas defined heatmap in **Figure 11H**.

Gene Name	Protein Function	Reference	Proteomics Results (Fold Change)
Slc44a1	Choline transporter ion channel	Michel and Bakovic 2009	**Decrease** – HET: 0.31 HOM: 0.55 SNX27: 0.65
Slco2a1	Transport of prostaglandins	Nakamura et al. 2018	**Decrease** – HET: 0.60 HOM: 0.58 SNX27: 0.11
Atp11c	Transport of aminophospholipids between leaflets of the plasma membrane	Takatsu et al. 2017	**Decrease** – HET: 0.60 HOM: 0.82 SNX27: 0.56
Slc2a1	Glucose transporter	Nualart et al. 1999	**Decrease** – HET: 0.94 HOM: 0.14 SNX27: 0.36
Slc2a3	Glucose transporter	Seatter et al. 1998	**Mixed** – HET: 1.15 HOM: 0.30 SNX27: 0.36
Crim1	Modulates bone morphogenetic protein activity	Wilkinson et al. 2003	**Mixed** – HET: 1.27 HOM: 0.50 SNX27: 0.47
Adrb2	Adrenergic receptor mediating responses to adrenaline	Allen et al. 1988	**Mixed** – HET: 1.17 HOM: 0.55 SNX27: 0.54
Slc39a6	Zinc influx transporter	Taylor et al. 2003	**Mixed** – HET: 3.68 HOM: 0.56 SNX27: 0.61

Gene Name	Protein Function	Reference	Proteomics Results (Fold Change)
Lrp5	Regulator of Wnt signalling	Mao et al. 2001	**Mixed** – HET: 1.51 HOM: 0.60 SNX27: 0.55
Heg1	Regulation of endothelial cell-cell junctions for heart formation and blood vessels	Kleaveland et al. 2009	**Mixed** – HET: 1.51 HOM: 0.65 SNX27: 0.51
Tmem30a	Transport of aminophospholipids between leaflets of the plasma membrane	Bryde et al. 2010	**Decrease** – HET: 0.76 HOM: 0.66 SNX27: 0.59

Table 10 - **Common proteins reduced at the cell surface in HET and HOM spastin^{N384K} MEFs and SNX27 depleted data from Steinberg et al. (2013), or from either a HET or HOM MEF data set and the SNX27 data**. The proteins described are the proteins listed in **Figure 11B**.

Gene Name	Protein Function	Reference	Proteomics Results (Fold Change)
Itga2	Integrin that allows the binding of collagen functioning in cell attachment and migration	Veit et al. 2011	**Increase** – HET: 2.18 HOM: 2.72 SNX27: 1.92
Sema4c	Semaphorin that functions in axonal guidance and development	Deng et al. 2007	**Increase** – HET: 1.96 HOM: 1.40 SNX27: 3.68
Flrt3	Cell adhesion, cell migration, and axon guidance, mediating spatial organisation of neurons, and mediates neurite number and length	Tsuji et al. 2004	**Mixed** – HET: 0.97 HOM: 1.54 SNX27: 2.23

Table 11 - **Common proteins increased at the cell surface in HET and HOM spastin^{N384K} MEFs and SNX27 depleted data from Steinberg et al. (2013), or from either a HET or HOM MEF data set and the SNX27 data.** The proteins described are the proteins listed in **Figure 11E**.

Gene Name	Protein Function	Reference	Proteomics Result (Fold Change)
Bcam	Laminin receptor functioning in cell adhesion	Udani et al. 1998	**Decrease** – HET: 0.31 HOM: 0.34 SNX27: 0.66
Ptgfrn	Regulates the activity of prostaglandin F receptor that functions in endothelial cell network formation	Keightley et al. 2010	**Decrease** – HET: 0.56 HOM: 0.57 SNX27: 0.55
Sdc2	Regulation of dendritic initiation and elongation and arborisation	Chen et al. 2011	**Decrease** – HET: 0.57 HOM: 0.54 SNX27: 0.46
Itgb5	Integrin involved in cell adhesion, migration and proliferation	Desgrosellier and Cheresh 2010	**Decrease** – HET: 0.59 HOM: 0.60 SNX27: 0.65
Slc39a10	Zinc influx transporter	Kagara et al. 2007	**Decrease** - HET: 0.67 HOM: 0.92 SNX27: 0.59

Table 12 - **Common proteins reduced at the cell surface in HET and HOM spastin^{N384K} primary cortical neurons and SNX27 depleted data from Steinberg et al. (2013), or from either a HET or HOM neuron data set and the SNX27 data**. The proteins described are the proteins listed in **Figure 11G**.

Gene Name	Protein Function	Reference	Proteomics Result (Fold Change)
Flrt3	Cell adhesion, cell migration, and axon guidance, mediating spatial organisation of neurons, and mediates neurite number and length	Tsuji et al. 2004	**Increase** – HET: 2.00 HOM: 1.75 SNX27: 2.23

Table 13 - **Common proteins increased at the cell surface in HET and HOM spastin^{N384K} primary cortical neurons and SNX27 depleted data from Steinberg et al. (2013), or from either a HET or HOM neuron data set and the SNX27 data**. The proteins described are the proteins listed in **Figure 11J**.

5.3 – Discussion

5.3.1 – Summary of results

Quantitative cell surface proteomics was performed on MEFs and primary cortical neurons derived from a spastin^{N384K} mutant mouse. This was done for two main reasons: 1) to investigate whether spastin loss of function would affect the plasma membrane protein landscape; 2) to identify a subset of proteins whose altered cell surface abundance could drive the axonopathy observed in spastin-HSP.

The cell surface proteomic experiments using MEFs and primary cortical neurons were technically successful. The protein abundance data showed the spastin^{N384K} mutation to drive major changes in the cell surface protein landscape in both MEFs and primary cortical neurons in both heterozygous and homozygous genetic backgrounds. These changes were reflected in the substantial increased or decreased abundance of a large number of plasma membrane proteins. Moreover, performing the proteomics on primary cortical neurons allowed the successful identification of a subset of proteins whose changes in surface abundance could drive the axonal degeneration observed in spastin-HSP. In addition, these experiments provided proof of concept that cell surface biotinylation coupled to quantitative TMT-labelling cell surface proteomics could be performed on neurons, as no previous experiments of this type had been performed.

5.3.2 – Spastin loss of function drives major remodelling of the cell surface proteome

Plasma membrane proteins are constantly at flux at the cell surface. Proteins are continually being removed from the plasma membrane by endocytic events but are also constantly being replaced. This replacement comes from either newly synthesised proteins, or proteins that are recycling back to the cell surface after having been internalised.

Disruption to either of these processes causes major changes to the typical cell surface protein landscape. Evidence for this includes proteomic experiments that have analysed the effect of disrupted endocytic cargo sorting on the cell surface proteome. Depletion of the retriever and retromer cargo adaptors, SNX17 and SNX27, both led to a substantial remodelling of protein abundance on the cell surface (McNally et al. 2017; Steinberg et al. 2013). Non-proteomics methods have also regularly shown alterations in protein abundance at the cell surface upon manipulation of the cell surface input or output pathways. Examples include the increased surface abundance of TfnR upon dynamin inhibition (Marks et al. 2001), or the decreased abundance of LDLR at the cell surface upon depletion of the CCC cargo sorting machinery component COMMD1 (Bartuzi et al. 2016).

Like SNX17, SNX27 or COMMD1, spastin plays an important function in the endocytic pathway. Spastin functions specifically to mediate the fission of endosomal recycling tubules (Allison et al. 2017). Loss of functional spastin causes impaired cargo recycling both from the endosome to the cell surface (e.g. TfnR; Allison et al. 2013), and to the TGN (e.g. CI-M6PR; Allison et al. 2017). This results in the mistrafficking of lysosomal hydrolases, and causes lysosomal abnormalities, such as increased lysosomal acidity, swelling, and the presence of an intralumenal substrate that had the appearance of undigested membrane (Allison et al. 2017). As a result of these disruptions to the endocytic pathway, it was predicted that the cells extracted from a spastin mouse expressing a functionally null AAA+ domain would also have a significantly altered plasma membrane proteome.

These predictions were supported by the quantitative cell surface proteomic experiments. A substantial remodelling of the plasma membrane proteome was observed in spastin^{N383K} MEFs and primary neurons from both heterozygous and homozygous backgrounds. This remodelling was in the form of substantial changes to the cell surface abundance of many proteins involved in a diverse range of biological functions. Proteins with both an increased and decreased surface abundance were observed in all the mutant samples, with many proteins having abundance changes in excess of either double or half their wildtype abundance. Gene ontology enrichment analysis identified cell adhesion proteins to have statistically significant changes in their cell surface abundance for both cell types.

The proteomics data from the spastin^{N384K} mutant MEFs showed a large number of cell surface proteins with a statistically robust increased or decreased surface abundance. This result was interesting in that impaired endosomal tubule has been directly identified in these cells (Chapter 3*;* Allison et al. 2017). It should be noted however that this correlation does not imply causality (as discussed below).

Of further note from this MEF dataset was the substantial difference observed between the two spastin mutant genotypes. This difference was not manifested as a less extreme version of the homozygote equivalent samples, but rather as an equally strong effect on a largely different subset of proteins. This is surprising given that spastin-HSP is an autosomal dominant disease that almost certainly functions through loss of function haploinsufficiency (detailed in Introduction Section 1.3.4) and a similar phenomenon was not observed in neuronal data. Currently it is not clear why these differences arose, but they indicate that differing levels of functional spastin have different effects on protein trafficking to and from the cell surface in MEFs.

As for the MEF proteomics, the surface proteomics performed on the primary cortical neurons also showed many proteins with statistically robust increased or decreased abundance at the cell surface. Unlike the MEF data however, these changes were similar irrespective of heterozygosity or homozygosity for the spastin mutant genotypes, with a very strong correlation between the abundance changes observed for almost all proteins between HET and HOM samples.

This data is important for furthering our understanding of the disease mechanism of spastin-HSP as it provides evidence that the axons that undergo degeneration in HSP likely have a highly atypical cell surface protein landscape. This is likely to impact many facets of the biology of these neurons, including their growth and development by changed abundance of receptor proteins, migration and adhesion by changes to protein such as integrins and cadherins, and signal transmission by changes to ion channel abundance. Both cell adhesion pathways and nervous system development related proteins were identified by gene ontology enrichment analysis as being significantly affected by the spastin mutation. A list of proteins whose altered cell surface abundance could have major implications for axonal health were identified and is presented below. In addition, the 1125 plasma membrane proteins identified are likely to represent a substantial part of the embryonic cortical neuronal plasma membrane proteome.

5.3.3 – Spastin's effect on the cell surface proteome is likely to come through multiple pathways

How may spastin loss of function induce such large-scale changes in the protein landscape at the cell surface? As mentioned above, this could result from multiple functional effects on the endo-lysosomal pathway that are a consequence of failed endosomal tubule fission. These effects would include impaired endosomal recycling and altered lysosomal degradation.

Proteomic experiments that have quantified the effect of impaired endocytic cargo sorting on surface protein abundance have been published (McNally et al. 2017; Steinberg et al. 2013). These datasets provide a resource by which the MEF and neuron data can be cross-referenced to provide potential insight into the processes that may be disrupted by the spastin^{N384K} mutation. A high amount of similarity between the MEF or neuron data and one or both of the SNX17 and SNX27 datasets may suggest that surface changes observed in spastin mutant cells were predominately due to direct impairment of endosome to plasma membrane recycling. However, little similarity was observed between either the MEF or neuron datasets and the SNX17 or SNX27 data sets. This was true when comparing proteins that either had increased or decreased abundance at the cell surface. In particular, this was evident when comparing proteins that had increased abundance at the cell surface, with almost no overlap between any of the datasets. One reason for this was that both the SNX17 and SNX27 datasets quantified many more proteins that had decreased rather than increased abundance at the cell surface (McNally et al. 2017; Steinberg et al. 2013).

What may explain this lack of similarity? One reason may be cell type and species-specific differences. Both SNX17 and SNX27 depletion experiments were performed using human HeLa cells, whilst the spastin experiments were performed using mouse fibroblasts and neurons. Comparisons between the MEF and neuron datasets show the clear effect of cell type differences, with relatively few proteins showing similar fold changes between the two datasets.

However, this lack of similarity may also provide some insight into the complex consequence of spastin loss of function beyond a direct inhibition of endocytic recycling. For example, impaired lysosomal function as a result of lysosomal hydrolase mistrafficking may cause a backlog of undigested cargos in the endocytic system, further amplifying the direct impairment of endosome to plasma membrane recycling. Furthermore, lysosome dysfunction may impair related pathways such as autophagy. Autophagic pathways have an intimate association with the cell surface, with one example being that the plasma membrane can act as a source of membrane for autophagosome biogenesis (Pavel and Rubinsztein 2017).

Spastin loss of function is likely to have implications beyond endocytosis which could also impact on protein abundance at the plasma membrane. As described in Introduction Section 1.3.5, spastin has a diverse set of cellular functions. These are likely to relate to spastin's ability to remodel microtubules, either inducing new microtubule formation, increasing microtubule stability, or by severing microtubules (Vemu et al. 2018). Microtubules function in the long-range transport of organelles and vesicles, including during endocytosis (Renard et al. 2015), but also in secretion (Presley et al. 1997; Watson et al. 2005), although the experiments performed in this thesis do not support a secretion-regulating function of spastin (Thesis Chapter 4).

Spastin may impact protein abundance by directly affecting protein synthesis or degradation. A specific block or increased synthesis or degradation of some proteins could lead to their changed abundance on the cell surface. Lysosomal degradation is likely impaired upon spastin loss of function as mentioned above. Spastin has also been shown to be a repressor of transcription (Daftary et al. 2011), although systemic analyses on this function of spastin have not been performed. In summary, it seems probable that the effect of spastin's loss of function on the cell surface proteome results from complex interplay between many disrupted cellular pathways.

5.3.4 – Identification of a subset of proteins whose changed surface abundance could contribute to the axonopathy of spastin-HSP

Cell surface proteins are crucial for cellular health by mediating the interaction between a cell and its environment. This controls processes such as cell survival, proliferation, differentiation, nutrient uptake, ion exchange, migration and adhesion. Cell surface proteins with an aberrant increase or decrease in their surface abundance are therefore good candidates to drive the axonopathy observed in HSP. Top pathological candidates identified from the neuron proteomics were identified by their known functions. These are shown and described below (**Table 14**), with the reasoning behind their inclusion discussed below.

Protein Name	Protein Function	Reference	Neuron Proteomics Result (Fold Change)
Itga8	Integrin functioning cell mediation of cell-cell interaction, cell recruitment, and neurite outgrowth regulation	Denda et al. 1998	**Decrease** – Het:0.37 KI: 0.36
Tnc	Matrix protein regulating neuron migration, neural regeneration, neurite outgrowth, and synaptic plasticity	Martina et al. 2010	**Decrease** – Het: 0.40 KI: 0.42
Erbb4	Central nervous system development and axonal guidance	Carraway et al. 1997	**Decrease** – Het: 0.52 KI: 0.44
Ngfr	Neurotrophin receptor regulating axonal health	Johnson et al. 1986	**Decrease** – Het: 0.47 KI: 0.51
Prom1	Regulation of cell differentiation and proliferation, and regulation of neurite extension	Takenobu et al. 2011	**Decrease** – Het: 0.48 KI: 0.54
Brinp3	Bone morphogenic protein inducible inhibition of neuronal proliferation	Kawano et al. 2004	**Decrease** – Het: 0.41 KI: 0.47
Sdc2	Regulation of dendritic initiation and elongation and arborisation	Chen et al. 2011	**Decrease** – Het: 0.57 KI: 0.54
Rtn4rl2	Nogo receptor that inhibits neurite outgrowth, and dendrite spine and synapse formation, but facilitates axon migration	Wills et al. 2012	**Increase** – Het: 1.76 KI: 1.67
Flrt3	Cell adhesion, cell migration, and axon guidance, mediating spatial organisation of neurons, and mediates neurite number and length	Tsuji et al. 2004	**Increase –** Het: 2.00 KI: 1.75
Slitrk2	Promotes excitatory synapse differentiation and supresses neurite outgrowth	Beaubien et al. 2016	**Increase** – Het: 1.55 KI: 1.58
Unc5c	Netrin receptor required in axonal guidance in the corticospinal tract	Finger et al. 2002	**Increase** – Het: 1.63 KI: 1.51
Icam1	Endothelial cell adhesion during immune response	Smith et al. 1989	**Decrease** – Het: 0.07 KI: 0.07
Bcam	Laminin receptor functioning in cell adhesion	Udani et al. 1998	**Decrease** – Het: 0.31 KI: 0.34
Vcan	Extracellular matrix assembly and cell adhesion regulation	Damasceno et al. 2016	**Decrease** – Het: 0.49 KI: 0.59
Acvr1	Activin receptor that mediates Bone Morphogenic Protein	Kishigami et al. 2004	**Increase** – Het: 1.64

Protein Name	Protein Function	Reference	Neuron Proteomics Result (Fold Change)
	signalling for development and repair		KI: 1.60

Table 14 - **Table showing the top pathological candidate proteins whose altered cell surface abundance could drive the axonopathy observed in spastin-HSP**. Proteins were identified from the neuron proteomics based on their fold change and protein function.

Itga8, Tnc, Erbb4

One method of filtering proteins was analysing whether the proteins of specific pathways were especially altered in their cell surface abundance. This was performed using gene ontology analysis, and in spastin-mutant neurons revealed proteins functioning in cell adhesion and nervous system development. Both of these processes are essential for neuronal health, with focal adhesion proteins mediating essential neuronal processes such as neurite outgrowth (Ivins et al. 2000), axon arborisation (Kalil and Dent 2014), and axonal guidance (Bixby and Harris 1991), and nervous system development proteins essential to allow synapse formation and differentiation (Williams et al. 2010). The magnitude of change for some of these proteins was dramatic, with cell adhesion protein Itga8 and Tnc and nervous system development protein Erbb4 reduced more than 2.5-fold from the cell surface.

Ngfr, Prom1, Brinp3, Sdc2, Rtn4rl2, Flrt3, Slitrk2, Unc5c

Some proteins involved in neuronal maintenance and function were not identified by the gene ontology analysis. One example is the nerve growth factor receptor (Ngfr) which was reduced more than 2-fold from the cell surface in both spastin mutant genotypes. This protein is fundamental to neuronal health. It regulates the survival of sympathetic and sensory neurons during nervous system differentiation (Levi-Montalcini 1987), regulates axonal growth and synapse formation (Harrington and Ginty 2013), regulates the expression of ion channels (Zhang et al. 2005) and neurotransmitters and neuropeptides (Levi-Montalcini et al. 1975). Additionally, it has reported functions in regulating neuronal body size, and axonal and dendritic arborisation (Spillane et al. 2012).

Further examples of proteins important in neuronal health include the protrusion protein Prom1 and the bone morphogenetic protein inducible Brinp3, both of which regulate neuronal proliferation (Kawano et al. 2004; Takenobu et al. 2011), and both of which were reduced at the neuronal cell surface more than 2-fold in both mutant genotypes. Furthermore, the protein Sdc2 was reduced from the cell surface in both spastin-mutant genotypes and the SNX17 and SNX27 data and has been added to the shortlist due to its role in elongation and arborisation of dendrites (Chen et al. 2011).

Looking at proteins with increased abundance at the cell surface potentially related to axonal degeneration, the Nogo receptor (Rtn4rl2) and Flrt3 present themselves as pathological candidates as both are important in the regulation of neurite outgrowth and axon guidance (Tsuji et al. 2004; Wills et al. 2012), with Flrt3 having an increase in abundance in mutant spastin samples and the SNX27 proteomics. Additionally, the proteins Slitrk2 and Unc5c had increased cell surface abundance in both MEF and neuronal data sets, and, given their role in neurite outgrowth (Beaubien et al. 2016) and axonal guidance in the corticospinal tract (Finger et al. 2002), both are pathological candidates.

Icam1, Bcam, Vcan

Beyond this list, some proteins that do not have clear neuronal function are interesting candidates for further investigation. One set of examples are the cell adhesion proteins Icam1 (Smith et al. 1989) and Bcam (Udani et al. 1998). These had the largest reduction in their cell surface abundance of any of the quantified proteins in the neuronal dataset but have no known roles in neuronal health. On a similar theme, the adhesion protein Vcan (Damasceno et al. 2016) was reduced from the cell surface more than 1.5-fold in mutant genotypes from MEF and neuronal datasets.

Acvr1

Previous work on HSP has shown spastin depleted cells to have upregulated BMP signalling (Tsang et al. 2009). This has also been observed in cells and organisms with mutations in other HSP proteins such as atlastin-1 and spartin (Fassier et al. 2010; Nahm et al. 2013; Tsang et al. 2009; X. Wang et al. 2007; Zhao and Hedera 2013). BMP signalling is important in neuronal health as it functions in nervous system development, neural proliferation, neural precursor cell commitment, and nervous system injury (Sabo et al. 2009). A disruption to any of these processes could potential give rise to the axonopathy of HSP. Given this, alterations in the surface abundance of activin receptor 1 (Acvr1 (a BMP signalling receptor)) are interesting, with the protein increased in its cell surface abundance in both spastin mutant neuron genotypes and homozygous spastin-mutant MEFs.

Caveats

One caveat to these experiments was that embryonic neurons were used for experimentation, whilst axonal degeneration in spastin-HSP affects adult neurons (Blackstone et al. 2011). Whilst embryonic neurons are the typical model used in neuronal cell biology experiments (Arbab et al. 2014), their use has the potential to skew results towards proteins involved in axonal development *vs* axonal maintenance. It is not clear how much overlap exists between these processes. However, substantial differences in neuron physiology between development and later stages has been reported, with one example being that the expression of the axonal sodium transport pump Atpb1b1 begins only 15 days after birth (Safronov et al. 1999).

This problem is not unique to studies of HSP and is a general problem affecting most research into adult-onset neurodegenerative diseases (Arbab et al. 2014). Even new strategies using neurons derived from adult IPSCs are unable to produce neurons with entirely the same characteristics as adult neurons (Ho et al. 2016). To help ensure that the neurons used in experimentation were as mature as possible, neurons were only used for experimentation after 14 days *in vitro*. Whilst not equivalent to adult neurons, these neurons have many of the characteristics of maturity, such as the development of dendritic spines that are required for synaptic connectivity and showing responsiveness to NMDA and AMPA neurotransmitters (Edwards et al. 2017).

5.3.5 – Future aims

Verification of cell surface abundance changes

An important future experiment that needs to be performed is the validation of the cell surface abundance changes observed for proteins in **Table 14**. An effective low-to-medium throughput method of doing this would be to use flow cytometry with fluorescent antibodies specific to the extracellular epitopes of these proteins.

Investigations into effects on the synthesis or degradation of proteins upon spastin loss of function

One suggested cause of altered plasma membrane protein abundance was changes in the rate of proteins synthesis or degradation for specific proteins. One way of determining this is by looking at the total cellular protein abundance, irrespective of subcellular localisation. Changes in the total cellular protein abundance could indicate that the changes observed were caused in part by changed synthesis or degradation, in addition to other spastin related-causes. A further refinement would be to determine whether increases in total protein abundances are transcriptionally driven.

These experiments could be performed in an unbiased way by using both further proteomics and transcriptomics. Whole cell lysates labelled with TMT coupled with mass spectrometry could be used to obtain a quantitative representation of total cellular protein abundance, while a measure on the effect of spastin's loss of function on protein synthesis could be obtained by performing whole transcriptome sequencing experiments (RNA-seq). This would provide an unbiased quantitative measure on the mRNA levels corresponding to each protein in wildtype and spastin mutant cells. Alternatively, the use of antibodies and western blotting could be used to determine the total cellular abundance for specific proteins, while quantitative real-time PCR experiments could be used to report specific transcript levels.

Cell compartmentalisation assays

Given the heterogenous anatomy of neurons, it is possible that different endocytic or secretory pathways dominate in different areas of the cell. For example, it has been previously described that neurons have accelerated pathways for neurotransmitter release at synapses (Fei et al. 2008; de Lange et al. 2003). To investigate this, a compartmentalised cell culture device could be used to separate somatodendrities from axons (Cheng et al. 2017), with each compartment then analysed by cell surface proteomics.

Other HSP mouse models

A further extension of the project would be to perform the cell surface proteomics on neurons extracted from mice mutated in other HSP genes. This would allow the production of a list of proteins whose cell surface abundance show similar alterations generally in HSP. These proteins would therefore be high priority candidates in the investigation into the causes of the axonopathy in HSP. Examples of existing HSP mice include the spartin knockout mouse (Renvoisé et al. 2012), and the REEP1 knockout mouse (Beetz et al. 2013), both of which develop the gait abnormalities typical of HSP.

Neuron behaviour assays

Assays could be designed which test the predicted effects that changes in the abundance of proteins in **Table 14** would cause on neuron behaviour. For example, neurite length and arborisation could be tested by simple neuronal immunofluorescence staining and imaging, followed by well-established automated neuronal morphology analysis (Ferreira et al. 2014). Axonal guidance could be measured by using the stripe assay, which uses microscopy to measure the direction of axonal growth relative to the striped pattern of axonal guidance molecules (Knöll et al. 2007). Cell adhesion could be measured by polyacrylamide-traction force microscopy (Khalili and Ahmad 2015). This technique relies on adhesion and spreading of cells grown on polyacrylamide gels to create forces within the gel, leading to displacement of fluorescent beads within the gel. Measuring the displacement of these beads provides a metric of the cell adhesion properties of the cell. In the final analysis, proof of the involvement of a pathway in HSP pathogenesis would be to show that is it perturbed *in vivo* and that rescue of this perturbation improves axonal and gait phenotypes. The spastin^{N384K} mouse would be an ideal tool for these experiments.

Chapter 6 – Final Discussion

6.1 – Overview

In this thesis I have investigated the function of spastin in endosomal tubule fission (Chapter 3) and in cargo secretion from the ER (Chapter 4). I have also performed quantitative unbiased cell surface proteomics on MEFs and primary cortical neurons derived from ATPase defective spastin mutant mice, identifying a list of pathogenic candidate proteins whose cell surface abundance changes may drive HSP (Chapter 5). For each results chapter, I have provided a discussion that both integrates my research into the wider literature, and details future experiments that could be performed. In this Final Discussion, I will therefore discuss how these results further our understanding of the mechanisms underlying spastin-HSP pathogenesis. The topics discussed are: 1) the relationship between endosomal tubule fission and neurodegeneration; 2) whether pathology results directly from dysfunctional microtubule remodelling with endosomal tubule fission and lysosome defects merely epiphenomena; and 3) potential unknown functions of spastin.

6.2 – The relationship between endosomal tubule fission and neurodegeneration

I have shown in fibroblasts that spastin functions in the fission of endosomal recycling tubules. Two observations provide supporting evidence that spastin also has this function in neurons. Firstly, Allison et al. (2013) observed that spastin depletion in zebrafish neurons led to the formation of elongated SNX1 tubules which my works shows is indicative of a defect in tubule fission. Secondly, a suggested outcome of defective endosomal tubule fission is lysosomal dysfunction through the mistrafficking of lysosomal hydrolases, and lysosomal abnormalities were observed in both fibroblasts, in primary cortical neurons from spastin^{N384K} mice, and in IPSC-derived neurons from spastin-HSP patients (Allison et al. 2017).

It is valid therefore to ask how a defect in endosomal tubule fission caused by dysfunctional spastin could result in the axonopathy observed in spastin-HSP. Although defects in spastin could affect neuronal health outside spastin's role in endosomal tubule fission (discussed below), there are at least two major pathogenic consequences of defects in endosomal tubule fission. These are: 1) pathogenicity resulting from lysosome dysfunction, and 2) pathogenicity resulting from a remodelling of the cell surface proteome. It should be noted that these two potential causes of pathology may not be mutually exclusive.

Endosomal tubule fission defects as a cause of lysosome-based neuropathology

Inefficient endosomal tubule fission correlates with the defective endosome-to-Golgi trafficking of M6PR and the aberrant secretion of M6P-tagged lysosomal enzyme from the cell (Allison et al. 2017). Thus, receptor mistrafficking as a result of defective tubule fission likely explains some of the abnormalities observed in the lysosomes of spastin depleted or mutated cell lines and neurons. These abnormalities include an increase in lysosome size and acidity, and the lysosomal lumen containing abundant membrane whorls by electron microscopy that likely represent membrane substrate accumulation (Allison et al. 2017). It should be noted that similar phenotypes have also been associated with an increasing list of HSP proteins, including HSP components of the endolysosomal pathways such as strumpellin (Song et al. 2018), AP5 (Hirst et al. 2015), spastizin (Khundadze et al. 2013), spatacsin (Boutry et al. 2018; Branchu et al. 2017; Renvoisé et al. 2014; Varga et al. 2015), ER-shaping proteins such as REEP1 (Allison et al. 2017), and even the recently discovered mitochondrial HSP protein ATAD3A (Cooper et al. 2017). Collectively therefore, lysosome dysfunction is potentially a unifying mechanism of pathology, and not unique to spastin-HSP pathogenesis.

How may lysosome dysfunction cause neurodegeneration? One established possibility is through an impairment in autophagic flux (Ballabio 2009; Platt et al. 2012; Raben et al. 2009). Autophagosomes function in cells to facilitate the degradation of damaged organelles and toxic cytoplasmic protein aggregates. Once toxic cargos have been internalised, autophagosomes fuse with lysosomes (forming autolysosomes), allowing lysosomal hydrolytic enzymes to degrade lumenal substrates. Impaired lysosomal substrate degradation has been associated with defective autophagy through several mechanisms. Firstly, it has been shown that a lysosomal accumulation of undigested cholesterols inhibits the lysosomal SNARES that mediate lysosome-autophagosome fusion (Fraldi et al. 2010). This could result in an aberrant sequestration of autophagic machinery and membrane into degradation-incompetent autophagosomes. Secondly, an accumulation of ganglioside lipids has been shown to impair the reformation of lysosomes from autolysosomes (Boutry et al. 2018). Similarly, this would generate a backlog in the autophagic pathway, but by creating an imbalance between autophagosome and lysosome abundance. Importantly, impaired autophagic flux has been directly related to neurodegeneration by the decreased ability to clear cytotoxic protein aggregates or damaged organelles (Ashrafi et al. 2014; Gowrishankar et al. 2015; Hara et al. 2006; de Pablo-Latorre et al. 2012; Xie et al. 2015). To test this hypothesis, it will be important to examine whether IPSC-derived neurons from spastin-HSP patients or derived primary cortical neurons from the spastin ATPase defective mouse have alterations in autophagy.

In addition to affecting autophagic flux, non-mutually exclusive alternative models have been proposed of how defective lysosomes can lead to neurodegeneration. These include increased

metabolic stress as a result of sequestered metabolites (Platt et al. 2012), and an accumulation of toxic lipid droplets in the neuronal-support cells, astrocytes (Branchu et al. 2017). In addition, impaired lysosome fusion is also likely to result in a backlog in the endocytic pathway as well as in the autophagic pathway. This could sequester endocytic machinery in late endosomes that were unable to fuse with lysosomes, with this generating further pressure on the early endocytic sorting machinery through an increase in cargo that cannot be lysosomally degraded. This may exacerbate the effect of defective cargo transport generated through inefficient tubule fission by spastin dysfunction, with one potential outcome being a remodelling of proteins on the cell surface (discussed below).

An important test of the relationship between lysosome dysfunction and axonopathy will be to see whether improved lysosome function can rescue the effect of spastin mutation. One potential therapeutic candidate protein is the lysosomal biogenesis master regulator, transcription factor EB (TFEB). Upregulation of TFEB increases autophagic flux and the clearance of undigested lysosomal substrates in cellular models of the lysosomal storage Niemann-Pick disease (Martini-Stoica et al. 2016; Wang et al. 2015). Studies on the increased activity of TFEB could therefore provide insight into the relevance of lysosome dysfunction on spastin-HSP neuropathology, and even a potential therapeutic route for spastin-HSP treatment.

Endosomal tubule fission defects as a cause of cell surface proteome remodelling-based neuropathology

Defective endosomal tubule fission is likely to induce a remodelling of the cell surface proteome. This may arise through a direct impairment of endosome to plasma membrane recycling, or through the wider consequences of lysosome dysfunction or other downstream effects on defective sorting away from the degradative compartment as described above. Through the use of quantitative cell surface proteomics in pathological-relevant primary cortical neurons expressing spastin with a non-functional ATPase, I have shown that cortical neurons have a significantly altered cell surface proteome and have identified a list of pathological candidates that could drive the axonopathy observed in spastin-HSP. Although it remains to be tested, it also probable therefore that mutations in other HSP proteins associated with the endolysosomal pathway would result in similar remodelling of the cell surface protein landscape.

How could changes in the abundance of identified proteins induce neurodegeneration? Cell surface proteins are crucial to facilitate the interaction between the neuron and its environment, and changes in this interaction could have substantial consequences on many facets of a cell's typical function. Three potentially significant groups of proteins whose cell surface abundance changes may

be pathogenic are highlighted below. Although this list is not exhaustive, and the cell surface abundance changes have not yet been validated, it provides an example of the range of neuronal defects that may be caused by plasma membrane remodelling at the neuronal cell surface. To validate their importance in spastin-HSP pathology, manipulations of each protein's cell surface abundance or activity need to be made to see if this can rescue the axonal degeneration phenotype, with the spastin mouse model described previously being a suitable tool for this.

One potentially significant protein that showed increased abundance on the cell surface was the BMP signalling receptor activin-1. Aberrant BMP signalling has been associated with spastin-HSP previously, with spastin identified as an inhibitor of BMP signalling (Tsang et al. 2009), with this recently shown to be specific to the M1 isoform of spastin in zebrafish (Jardin et al. 2018). BMP functions in neuronal development, dendritogenesis, motor axon targeting, in axonal repair after injury, and synaptic function, potentially by altering the stability of the cytoskeleton (Charron and Tessier-Lavigne 2007; Fassier et al. 2010; Jardin et al. 2018; O'Connor-Giles, Ho, and Ganetzky 2008; Sabo, Kilpatrick, and Cate 2009; Wang et al. 2007; Zhong and Zou 2014). The increased abundance of the BMP signalling receptor is likely to promote BMP signalling in neurons. Excessive activation of BMP signalling has been shown to result in the repression of myelin synthesis (Cate et al. 2010; Colak et al. 2008; See et al. 2004), potential autoimmunity (Yoshioka et al. 2012), and defective motor neuron targeting (Jardin et al. 2018), although given the function of BMP signalling in cytoskeletal remodelling, excessive activation of BMP signalling may also affect axonal transport (Ellis et al. 2010; X. Wang et al. 2007). In particular, the function of BMP signalling in axonal transport seems particularly relevant to spastin-HSP, as axonal degeneration is characterised by degeneration of the furthest points of the axon and spastin KO mice show defective axonal transport of some cargos (Kasher et al. 2009). Investigations into defective BMP signalling in spastin-HSP neurons are therefore pertinent and could highlight potential druggable targets if the relationship between BMP signalling and spastin-HSP axonal degeneration was validated.

A second group of proteins that were altered in their cell surface abundance in mutant mouse neurons were proteins involved in cell adhesion. A change in neuronal cell adhesion has been implicated in neurodegeneration, for example in Alzheimer's disease (Bao et al. 2015; Caltagarone et al. 2007). One mechanism of action is through disruption of synaptic junctions, with adhesion proteins critical to facilitate the formation synaptic scaffolds in synapse formation and synaptic plasticity (Washbourne 2004). However, it is also likely that the changed abundance of neuronal adhesion proteins may influence axonal guidance during development, or the retraction of the axon during axonal degeneration (Wang et al. 2012).

Finally, the change in the plasma membrane abundance of neurodevelopmental proteins such as neuronal growth factor receptor (Ngfr) may be significant to spastin-HSP pathology. For example, amongst other functions, NGF signalling is suggested to be neuroprotective after neuronal injury by preventing apoptosis (Lebrun-Julien et al. 2009; María Frade et al. 1996). In addition, the action of NGF can induce axonal regeneration by promoting axonal growth, with a lack of NGF directly associated with axonal degeneration (MacInnis and Campenot 2005). It is therefore potentially pathologically significant that a substantial decreased abundance of Ngfr in spastin-HSP cortical neurons was observed.

Is the pathologically-relevant endosomal tubule fission reaction in the cell body or the axon?

Spastin-HSP pathology is characterised by the distal degeneration of axons (Blackstone et al. 2011). However, it is currently not understood where defects in endosomal tubule fission occur in relation to the distal axon. Two potential non-mutually exclusive models are: 1) that endosomal tubule fission defects occur in the neuronal soma, resulting in directly affected (e.g. recycling endosomal tubules transport) or indirectly affected (e.g. hydrolytic lysosome transport) membrane cargo transport to the distal axon; 2) that endosomal tubule fission defects occur *in situ* at the axon tip, causing localised aberrations in the local axon environment.

Experiments to differentiate between these two models have not yet been performed. However, the evidence that zebrafish lacking spastin have increased endosomal tubulation in axons (Allison et al. 2013), and that mammalian neurons do have SNX1 at the distal axon (Freeman et al. 2013), suggests that endosomal tubule fission defects within the axon itself are possible. Example experiments to test this would involve the live cell imaging of endosomal tubule fission within the axons of neurons derived from wildtype and spastin^{N384K} ATPase defective mice. However, this may be difficult technically, both in relation to the expression of cell markers of endosomal tubules in the axon, and in the resolution of individually endosomal tubule fission events in the narrow axon. An alternative approach could be to use super-resolution SIM microscopy in spastin depleted cells to see if endosomal tubules were elongated.

6.3 – Are endosomal tubule fission defects merely a marker of microtubule defects and not directly related to disease pathology?

As spastin regulates microtubules, a relevant question is whether it is simply defective axonal microtubule remodelling which drives spastin-HSP pathology, with defective endosomal tubule fission and lysosomal dysfunction only non-pathogenic epiphenomena. Indeed, spastin-mediated microtubule remodelling could directly drive many functions of spastin in neurons including axonal growth and pruning.

However, the data suggests that microtubule dysfunction in the axon alone is unlikely to completely explain the axonal degeneration of HSP. Studies of microtubules in the axons of spastin-HSP neurons revealed few obvious differences along the length of the axon compared to wildtype cells (Fassier et al. 2013; Riano et al. 2009), although a systematic study of microtubule posttranslational modifications in the wildtype and spastin dysfunctional neurons has not yet been performed. In addition, whilst lysosome dysfunction has been associated with microtubule-related HSP proteins such as spastin, it has also been observed in mutations of HSP proteins with functions seemingly unrelated to microtubules, such as the mitochondrial HSP protein ATAD3A (Cooper et al. 2017). This suggests that lysosome dysfunction may be a true pathogenic convergence point in HSP. Furthermore, the many cell surface abundance changes identified from the cortical neuron proteomics are also very likely to have at least some pathogenic impact on the cell's interaction with the environment. Thus, a likely scenario seems that defects in spastin's microtubule-regulatory function underpin spastin-HSP, but the best pathological candidate amongst the many cell biological processes linked to this is lysosomal dysfunction and cell surface proteome remodelling caused by defective endosomal tubule fission.

6.4 – Perspectives for further unknown functions of spastin

Major progress has been made in our understanding of spastin since its initially discovery 19 years ago. Remarkably, new functions of spastin continue to be discovered suggesting that more functions may remain to be found. By homology to endosomal tubule fission, these may include fission of other tubular structures in the cell, with candidates including the fission of lysosomal tubules or autophagosomes from the ER membrane. Further investigations in spastin's function will likely continue to use existing powerful tools such as the spastin^{N384K} mouse coupled to high-resolution microscopy, proteomics and transcriptomics, but could also be supplemented by tools supplied by the combined developments in CRISPR and IPSC technology. Together, these approaches will eventually lead to a full understanding of spastin's normal and pathological function in human neurons. Spastin research has progressed remarkably in ~20 years; it will be remarkable how it will have progressed in 20 years more.

Chapter 7 - References

Abou Jamra, Rami, Orianne Philippe, Annick Raas-Rothschild, Sebastian H. Eck, Elisabeth Graf, Rebecca Buchert, Guntram Borck, Arif Ekici, Felix F. Brockschmidt, Markus M. Nöthen, Arnold Munnich, Tim M. Strom, Andre Reis, and Laurence Colleaux. 2011. "Adaptor Protein Complex 4 Deficiency Causes Severe Autosomal-Recessive Intellectual Disability, Progressive Spastic Paraplegia, Shy Character, and Short Stature." *The American Journal of Human Genetics* 88(6):788–95.

Adell, Manuel Alonso Y., Simona M. Migliano, Srigokul Upadhyayula, Yury S. Bykov, Simon Sprenger, Mehrshad Pakdel, Georg F. Vogel, Gloria Jih, Wesley Skillern, Reza Behrouzi, Markus Babst, Oliver Schmidt, Michael W. Hess, John A. G. Briggs, Tomas Kirchhausen, and David Teis. 2017. "Recruitment Dynamics of ESCRT-III and Vps4 to Endosomes and Implications for Reverse Membrane Budding." *ELife* 6.

Akizu, Naiara, Vincent Cantagrel, Jana Schroth, Na Cai, Keith Vaux, Douglas McCloskey, Robert K. Naviaux, Jeremy Van Vleet, Ali G. Fenstermaker, Jennifer L. Silhavy, Judith S. Scheliga, Keiko Toyama, Hiroko Morisaki, Fatma M. Sonmez, Figen Celep, Azza Oraby, Maha S. Zaki, Raidah Al-Baradie, Eissa A. Faqeih, Mohammed A. M. Saleh, Emily Spencer, Rasim Ozgur Rosti, Eric Scott, Elizabeth Nickerson, Stacey Gabriel, Takayuki Morisaki, Edward W. Holmes, and Joseph G. Gleeson. 2013. "AMPD2 Regulates GTP Synthesis and Is Mutated in a Potentially Treatable Neurodegenerative Brainstem Disorder." *Cell* 154(3):505–17.

Alapin, Jessica M., Monica Dines, Maria Vassiliev, Tal Tamir, Alon Ram, Clifford Locke, Ji Yu, and Raphael Lamprecht. 2018. "Activation of EphB2 Forward Signaling Enhances Memory Consolidation." *Cell Reports* 23(7):2014–25.

Alazami, Anas M., Nouran Adly, Hisham Al Dhalaan, and Fowzan S. Alkuraya. 2011. "A Nullimorphic ERLIN2 Mutation Defines a Complicated Hereditary Spastic Paraplegia Locus (SPG18)." *Neurogenetics* 12(4):333–36.

Ali, Shafaqat, Michael Huber, Christian Kollewe, Stephan C. Bischoff, Werner Falk, and Michael U. Martin. 2007. "IL-1 Receptor Accessory Protein Is Essential for IL-33-Induced Activation of T Lymphocytes and Mast Cells." *Proceedings of the National Academy of Sciences* 104(47):18660–65.

Alkam, Duah, Ezra Z. Feldman, Awantika Singh, and Mahmoud Kiaei. 2017. "Profilin1 Biology and Its Mutation, Actin(g) in Disease." *Cellular and Molecular Life Sciences* 74(6):967–81.

Allen, J. M., E. E. Baetge, I. B. Abrass, and R. D. Palmiter. 1988. “Isoproterenol Response Following Transfection of the Mouse Beta 2-Adrenergic Receptor Gene into Y1 Cells.” *The EMBO Journal* 7(1):133–38.

Allison, Rachel, James R. Edgar, Guy Pearson, Tania Rizo, Timothy Newton, Sven Günther, Fiamma Berner, Jennifer Hague, James W. Connell, Jürgen Winkler, Jennifer Lippincott-Schwartz, Christian Beetz, Beate Winner, and Evan Reid. 2017. “Defects in ER–endosome Contacts Impact Lysosome Function in Hereditary Spastic Paraplegia.” *The Journal of Cell Biology* 216(5):1337–55.

Allison, Rachel, Jennifer H. Lumb, Coralie Fassier, James W. Connell, Daniel Ten Martin, Matthew N. J. Seaman, Jamilé Hazan, and Evan Reid. 2013. “An ESCRT–spastin Interaction Promotes Fission of Recycling Tubules from the Endosome.” *The Journal of Cell Biology* 202(3):527–43.

Altan-Bonnet, Nihal, Rachid Sougrat, Wei Liu, Erik L. Snapp, Theresa Ward, and Jennifer Lippincott-Schwartz. 2006. “Golgi Inheritance in Mammalian Cells Is Mediated through Endoplasmic Reticulum Export Activities.” *Molecular Biology of the Cell* 17(2):990–1005.

Anderson, S., A. T. Bankier, B. G. Barrell, M. H. L. de Bruijn, A. R. Coulson, J. Drouin, I. C. Eperon, D. P. Nierlich, B. A. Roe, F. Sanger, P. H. Schreier, A. J. H. Smith, R. Staden, and I. G. Young. 1981. “Sequence and Organization of the Human Mitochondrial Genome.” *Nature* 290(5806):457–65.

Antón, Inés M., Wange Lu, Bruce J. Mayer, Narayanaswamy Ramesh, and Raif S. Geha. 1998. “The Wiskott-Aldrich Syndrome Protein-Interacting Protein (WIP) Binds to the Adaptor Protein Nck.” *Journal of Biological Chemistry* 273(33):20992–95.

Antonicka, Hana, Elsebet Østergaard, Florin Sasarman, Woranontee Weraarpachai, Flemming Wibrand, Anne Marie B. Pedersen, Richard J. Rodenburg, Marjo S. van der Knaap, Jan A. M. Smeitink, Zofia M. Chrzanowska-Lightowlers, and Eric A. Shoubridge. 2010. “Mutations in C12orf65 in Patients with Encephalomyopathy and a Mitochondrial Translation Defect.” *The American Journal of Human Genetics* 87(1):115–22.

Antonny, Bruno, Christopher Burd, Pietro De Camilli, Elizabeth Chen, Oliver Daumke, Katja Faelber, Marijn Ford, Vadim A. Frolov, Adam Frost, Jenny E. Hinshaw, Tom Kirchhausen, Michael M. Kozlov, Martin Lenz, Harry H. Low, Harvey McMahon, Christien Merrifield, Thomas D. Pollard, Phillip J. Robinson, Aurélien Roux, and Sandra Schmid. 2016. “Membrane Fission by Dynamin: What We Know and What We Need to Know.” *The EMBO Journal* 35(21):2270–84.

Apaja, Pirjo M. and Gergely L. Lukacs. 2014. “Protein Homeostasis at the Plasma Membrane.” *Physiology* 29(4):265–77.

Arbab, Mandana, Susanne Baars, and Niels Geijsen. 2014. “Modeling Motor Neuron Disease: The Matter of Time.” *Trends in Neurosciences* 37(11):642–52.

Ashrafi, Ghazaleh, Julia S. Schlehe, Matthew J. LaVoie, and Thomas L. Schwarz. 2014. “Mitophagy of Damaged Mitochondria Occurs Locally in Distal Neuronal Axons and Requires PINK1 and Parkin.” *The Journal of Cell Biology* 206(5):655–70.

Aumeier, Charlotte, Laura Schaedel, Jérémie Gaillard, Karin John, Laurent Blanchoin, and Manuel Théry. 2016. “Self-Repair Promotes Microtubule Rescue.” *Nature Cell Biology* 18(10):1054–64.

Babst, Markus. 2011. “MVB Vesicle Formation: ESCRT-Dependent, ESCRT-Independent and Everything in Between.” *Current Opinion in Cell Biology* 23(4):452–57.

Bacon, Louise, Robert a Eagle, Martina Meyer, Nicholas Easom, Neil T. Young, and John Trowsdale. 2004. “Two Human ULBP/RAET1 Molecules with Transmembrane Regions Are Ligands for NKG2D.” *The Journal of Immunology* 173(2):1078–84.

Bajorek, Monika, Heidi L. Schubert, John McCullough, Charles Langelier, Debra M. Eckert, William-May B. Stubblefield, Nathan T. Uter, David G. Myszka, Christopher P. Hill, and Wesley I. Sundquist. 2009. “Structural Basis for ESCRT-III Protein Autoinhibition.” *Nature Structural & Molecular Biology* 16(7):754–62.

Balasubramanian, Nagaraj, Jeremy A. Meier, David W. Scott, Andrés Norambuena, Michael A. White, and Martin Alexander Schwartz. 2010. “RalA-Exocyst Complex Regulates Integrin-Dependent Membrane Raft Exocytosis and Growth Signaling.” *Current Biology* 20(1):75–79.

Balla, Tamas. 2013. “Phosphoinositides: Tiny Lipids With Giant Impact on Cell Regulation.” *Physiological Reviews* 93(3):1019–1137.

Ballabio, A. 2009. “Disease Pathogenesis Explained by Basic Science: Lysosomal Storage Diseases as Autophagocytic Disorders.” *International Journal of Clinical Pharmacology and Therapeutics* 47 Suppl 1:S34-8.

Bannykh, Sergei I. 1996. “The Organization of Endoplasmic Reticulum Export Complexes.” *The Journal of Cell Biology* 135(1):19–35.

Bao, Xinjie, Gengfeng Liu, Yongshuai Jiang, Qinghua Jiang, Mingzhi Liao, Rennan Feng, Liangcai Zhang, Guoda Ma, Shuyan Zhang, Zugen Chen, Bin Zhao, Renzhi Wang, Keshen Li, and Guiyou Liu. 2015. "Cell Adhesion Molecule Pathway Genes Are Regulated by Cis-Regulatory SNPs and Show Significantly Altered Expression in Alzheimer's Disease Brains." *Neurobiology of Aging* 36(10):2904.e1-2904.e7.

Baram, Dana, Yoseph A. Mekori, and Ronit Sagi-Eisenberg. 2001. "Synaptotagmin Regulates Mast Cell Functions." *Immunological Reviews* 179(1):25–34.

Bard, Frederic, Laetitia Casano, Arrate Mallabiabarrena, Erin Wallace, Kota Saito, Hitoshi Kitayama, Gianni Guizzunti, Yue Hu, Franz Wendler, Ramanuj DasGupta, Norbert Perrimon, and Vivek Malhotra. 2006. "Functional Genomics Reveals Genes Involved in Protein Secretion and Golgi Organization." *Nature* 439(7076):604–7.

Barlowe, Charles. 1994. "COPII: A Membrane Coat Formed by Sec Proteins That Drive Vesicle Budding from the Endoplasmic Reticulum." *Cell* 77(6):895–907.

Barlowe, Charles and Ari Helenius. 2016. "Cargo Capture and Bulk Flow in the Early Secretory Pathway." *Annual Review of Cell and Developmental Biology* 32(1):197–222.

Bartlett, Allison H., Kazutaka Hayashida, and Pyong Woo Park. 2007. "Molecular and Cellular Mechanisms of Syndecans in Tissue Injury and Inflammation." *Molecules and Cells* 24(2):153–66.

Bartuzi, Paulina, Daniel D. Billadeau, Robert Favier, Shunxing Rong, Daphne Dekker, Alina Fedoseienko, Hille Fieten, Melinde Wijers, Johannes H. Levels, Nicolette Huijkman, Niels Kloosterhuis, Henk van der Molen, Gemma Brufau, Albert K. Groen, Alison M. Elliott, Jan Albert Kuivenhoven, Barbara Plecko, Gernot Grangl, Julie McGaughran, Jay D. Horton, Ezra Burstein, Marten H. Hofker, and Bart van de Sluis. 2016. "CCC- and WASH-Mediated Endosomal Sorting of LDLR Is Required for Normal Clearance of Circulating LDL." *Nature Communications* 7(1):10961.

Baumgartner, M. R. 2000. "Hyperammonemia with Reduced Ornithine, Citrulline, Arginine and Proline: A New Inborn Error Caused by a Mutation in the Gene Encoding Delta1-Pyrroline-5-Carboxylate Synthase." *Human Molecular Genetics* 9(19):2853–58.

Bautista, Elizabeth, Natanael Zarco, Nicolás Aguirre-Pineda, Manuel Lara-Lozano, Paula Vergara, Juan Antonio González-Barrios, Raúl Aguilar-Roblero, and José Segovia. 2018. "Expression of Gas1 in Mouse Brain: Release and Role in Neuronal Differentiation." *Cellular and Molecular Neurobiology* 38(4):841–59.

Bayrakli, Fatih, Hatice Gamze Poyrazoglu, Sirin Yuksel, Cengiz Yakicier, Bekir Erguner, Mahmut Samil Sagiroglu, Betul Yuceturk, Bugra Ozer, Selim Doganay, Bahattin Tanrikulu, Askin Seker, Fatih Akbulut, Ali Ozen, Huseyin Per, Sefer Kumandas, Yasemin Altuner Torun, Yasar Bayri, Mustafa Sakar, Adnan Dagcinar, and Ibrahim Ziyal. 2015. "Hereditary Spastic Paraplegia with Recessive Trait Caused by Mutation in KLC4 Gene." *Journal of Human Genetics* 60(12):763–68.

Beaubien, François, Reesha Raja, Timothy E. Kennedy, Alyson E. Fournier, and Jean-François Cloutier. 2016. "Slitrk1 Is Localized to Excitatory Synapses and Promotes Their Development." *Scientific Reports* 6(1):27343.

Beetz, C., A. O. H. Nygren, J. Schickel, M. Auer-Grumbach, K. Burk, G. Heide, J. Kassubek, S. Klimpe, T. Klopstock, F. Kreuz, S. Otto, R. Schule, L. Schols, A. D. Sperfeld, O. W. Witte, and T. Deufel. 2006. "High Frequency of Partial SPAST Deletions in Autosomal Dominant Hereditary Spastic Paraplegia." *Neurology* 67(11):1926–30.

Beetz, Christian, Michael Brodhun, Konstantin Moutzouris, Michael Kiehntopf, Alexander Berndt, Dirk Lehnert, Thomas Deufel, Martin Bastmeyer, and Jörg Schickel. 2004. "Identification of Nuclear Localisation Sequences in Spastin (SPG4) Using a Novel Tetra-GFP Reporter System." *Biochemical and Biophysical Research Communications* 318(4):1079–84.

Beetz, Christian, Nicole Koch, Mukhran Khundadze, Geraldine Zimmer, Sandor Nietzsche, Nicole Hertel, Antje-Kathrin Huebner, Rizwan Mumtaz, Michaela Schweizer, Elisabeth Dirren, Kathrin N. Karle, Andrey Irintchev, Victoria Alvarez, Christoph Redies, Martin Westermann, Ingo Kurth, Thomas Deufel, Michael M. Kessels, Britta Qualmann, and Christian A. Hübner. 2013. "A Spastic Paraplegia Mouse Model Reveals REEP1-Dependent ER Shaping." *Journal of Clinical Investigation* 123(10):4273–82.

Belli, Sabina I. and James W. Goding. 1994. "Biochemical Characterization of Human PC-1, an Enzyme Possessing Alkaline Phosphodiesterase I and Nucleotide Pyrophosphatase Activities." *European Journal of Biochemistry* 226(2):433–43.

Benham, Adam M. 2012. "Protein Secretion and the Endoplasmic Reticulum." *Cold Spring Harbor Perspectives in Biology* 4(8):a012872–a012872.

Benz, Corinna, Caroline Clucas, Jeremy C. Mottram, and Tansy C. Hammarton. 2012. “Cytokinesis in Bloodstream Stage Trypanosoma Brucei Requires a Family of Katanins and Spastin” edited by D. Zilberstein. *PLoS ONE* 7(1):e30367.

Berger, Philipp, Peter Young, and Ueli Suter. 2002. “Molecular Cell Biology of Charcot-Marie-Tooth Disease.” *Neurogenetics* 4(1):1–15.

Beuter, Simone, Ziv Ardi, Omer Horovitz, Jennifer Wuchter, Stefanie Keller, Rinki Saha, Kuldeep Tripathi, Rachel Anunu, Orli Kehat, Martin Kriebel, Gal Richter-Levin, and Hansjürgen Volkmer. 2016. “Receptor Tyrosine Kinase EphA7 Is Required for Interneuron Connectivity at Specific Subcellular Compartments of Granule Cells.” *Scientific Reports* 6(1):29710.

Bi, Xiping, Richard A. Corpina, and Jonathan Goldberg. 2002. “Structure of the Sec23/24–Sar1 Pre-Budding Complex of the COPII Vesicle Coat.” *Nature* 419(6904):271–77.

Bieling, Peter, Liedewij Laan, Henry Schek, E. Laura Munteanu, Linda Sandblad, Marileen Dogterom, Damian Brunner, and Thomas Surrey. 2007. “Reconstitution of a Microtubule Plus-End Tracking System in Vitro.” *Nature* 450(7172):1100–1105.

Bielli, Anna, Charles J. Haney, Gavin Gabreski, Simon C. Watkins, Sergei I. Bannykh, and Meir Aridor. 2005. “Regulation of Sar1 NH 2 Terminus by GTP Binding and Hydrolysis Promotes Membrane Deformation to Control COPII Vesicle Fission.” *The Journal of Cell Biology* 171(6):919–24.

Bishop, Derron L., Thomas Misgeld, Mark K. Walsh, Wen-Biao Gan, and Jeff W. Lichtman. 2004. “Axon Branch Removal at Developing Synapses by Axosome Shedding.” *Neuron* 44(4):651–61.

Bishop, Naomi and Philip Woodman. 2000. “ATPase-Defective Mammalian VPS4 Localizes to Aberrant Endosomes and Impairs Cholesterol Trafficking” edited by J. Bonifacino. *Molecular Biology of the Cell* 11(1):227–39.

Bixby, John L. and William A. Harris. 1991. “Molecular Mechanisms of Axon Growth and Guidance.” *Annual Review of Cell Biology* 7(1):117–59.

Blackstone, Craig, Cahir J. O’Kane, and Evan Reid. 2011. “Hereditary Spastic Paraplegias: Membrane Traffic and the Motor Pathway.” *Nature Reviews Neuroscience* 12(1):31–42.

Boncompain, Gaelle, Severine Divoux, Nelly Gareil, Helene de Forges, Aurianne Lescure, Lynda Latreche, Valentina Mercanti, Florence Jollivet, Graça Raposo, and Franck Perez. 2012. “Synchronization of Secretory Protein Traffic in Populations of Cells.” *Nature Methods* 9(5):493–98.

Bonifacino, Juan S. and Benjamin S. Glick. 2004. “The Mechanisms of Vesicle Budding and Fusion.” *Cell* 116(2):153–66.

Bonnon, C., M. W. Wendeler, J. P. Paccaud, and H. P. Hauri. 2010. “Selective Export of Human GPI-Anchored Proteins from the Endoplasmic Reticulum.” *Journal of Cell Science* 123(10):1705–15.

Boone, Philip M., Bo Yuan, Ian M. Campbell, Jennifer C. Scull, Marjorie A. Withers, Brett C. Baggett, Christine R. Beck, Christine J. Shaw, Pawel Stankiewicz, Paolo Moretti, Wendy E. Goodwin, Nichole Hein, John K. Fink, Moon-Woo Seong, Soo Hyun Seo, Sung Sup Park, Izabela D. Karbassi, Sat Dev Batish, Andrés Ordóñez-Ugalde, Beatriz Quintáns, María-Jesús Sobrido, Susanne Stemmler, and James R. Lupski. 2014. “The Alu-Rich Genomic Architecture of SPAST Predisposes to Diverse and Functionally Distinct Disease-Associated CNV Alleles.” *The American Journal of Human Genetics* 95(2):143–61.

Boot, Rolf G., Marri Verhoek, Wilma Donker-Koopman, Anneke Strijland, Jan van Marle, Hermen S. Overkleeft, Tom Wennekes, and Johannes M. F. G. Aerts. 2007. “Identification of the Non-Lysosomal Glucosylceramidase as β-Glucosidase 2.” *Journal of Biological Chemistry* 282(2):1305–12.

Boucrot, Emmanuel, Adi Pick, Gamze Çamdere, Nicole Liska, Emma Evergren, Harvey T. McMahon, and Michael M. Kozlov. 2012. “Membrane Fission Is Promoted by Insertion of Amphipathic Helices and Is Restricted by Crescent BAR Domains.” *Cell* 149(1):124–36.

Bouhouche, A. 2005. “Mutation in the Epsilon Subunit of the Cytosolic Chaperonin-Containing t-Complex Peptide-1 (Cct5) Gene Causes Autosomal Recessive Mutilating Sensory Neuropathy with Spastic Paraplegia.” *Journal of Medical Genetics* 43(5):441–43.

Boukhris, A., G. Stevanin, I. Feki, P. Denora, N. Elleuch, MI Miladi, C. Goizet, J. Truchetto, S. Belal, A. Brice, and Chokri Mhiri. 2009. “Tunisian Hereditary Spastic Paraplegias: Clinical Variability Supported by Genetic Heterogeneity.” *Clinical Genetics* 75(6):527–36.

Boukhris, Amir, Rebecca Schule, José L. Loureiro, Charles Marques Lourenço, Emeline Mundwiller, Michael A. Gonzalez, Perrine Charles, Julie Gauthier, Imen Rekik, Rafael F. Acosta Lebrigio, Marion Gaussen, Fiorella Speziani, Andreas Ferbert, Imed Feki, Andrés Caballero-Oteyza, Alexandre Dionne-Laporte, Mohamed Amri, Anne Noreau, Sylvie Forlani, Vitor T. Cruz, Fanny Mochel, Paula Coutinho, Patrick Dion, Chokri Mhiri, Ludger Schols, Jean Pouget, Frédéric Darios, Guy A. Rouleau, Wilson Marques, Alexis Brice, Alexandra Durr, Stephan Zuchner, and Giovanni Stevanin. 2013. “Alteration of Ganglioside Biosynthesis Responsible for Complex Hereditary Spastic Paraplegia.” *The American Journal of Human Genetics* 93(1):118–23.

Boulant, Steeve, Comert Kural, Jean-Christophe Zeeh, Florent Ubelmann, and Tomas Kirchhausen. 2011. “Actin Dynamics Counteract Membrane Tension during Clathrin-Mediated Endocytosis.” *Nature Cell Biology* 13(9):1124–31.

Boutry, Maxime, Julien Branchu, Céline Lustremant, Claire Pujol, Julie Pernelle, Raphaël Matusiak, Alexandre Seyer, Marion Poirel, Emeline Chu-Van, Alexandre Pierga, Kostantin Dobrenis, Jean-Philippe Puech, Catherine Caillaud, Alexandra Durr, Alexis Brice, Benoit Colsch, Fanny Mochel, Khalid Hamid El Hachimi, Giovanni Stevanin, and Frédéric Darios. 2018. “Inhibition of Lysosome Membrane Recycling Causes Accumulation of Gangliosides That Contribute to Neurodegeneration.” *Cell Reports* 23(13):3813–26.

Branchu, Julien, Maxime Boutry, Laura Sourd, Marine Depp, Céline Leone, Alexandrine Corriger, Maeva Vallucci, Typhaine Esteves, Raphaël Matusiak, Magali Dumont, Marie-Paule Muriel, Filippo M. Santorelli, Alexis Brice, Khalid Hamid El Hachimi, Giovanni Stevanin, and Frédéric Darios. 2017. “Loss of Spatacsin Function Alters Lysosomal Lipid Clearance Leading to Upper and Lower Motor Neuron Degeneration.” *Neurobiology of Disease* 102:21–37.

Brill, Monika S., Tatjana Kleele, Laura Ruschkies, Mengzhe Wang, Natalia A. Marahori, Miriam S. Reuter, Torben J. Hausrat, Emily Weigand, Matthew Fisher, Andrea Ahles, Stefan Engelhardt, Derron L. Bishop, Matthias Kneussel, and Thomas Misgeld. 2016. “Branch-Specific Microtubule Destabilization Mediates Axon Branch Loss during Neuromuscular Synapse Elimination.” *Neuron* 92(4):845–56.

Bryde, Susanne, Hanka Hennrich, Patricia M. Verhulst, Philippe F. Devaux, Guillaume Lenoir, and Joost C. M. Holthuis. 2010. “CDC50 Proteins Are Critical Components of the Human Class-1 P 4 - ATPase Transport Machinery.” *Journal of Biological Chemistry* 285(52):40562–72.

Bucci, Cecilia, Robert G. Parton, Ian H. Mather, Henk Stunnenberg, Kai Simons, Bernard Hoflack, and Marino Zerial. 1992. “The Small GTPase Rab5 Functions as a Regulatory Factor in the Early Endocytic Pathway.” *Cell* 70(5):715–28.

Burk, D. H. 2002. “Alteration of Oriented Deposition of Cellulose Microfibrils by Mutation of a Katanin-Like Microtubule-Severing Protein.” *THE PLANT CELL ONLINE* 14(9):2145–60.

Butler, R., J. D. Wood, J. A. Landers, and V. T. Cunliffe. 2010. “Genetic and Chemical Modulation of Spastin-Dependent Axon Outgrowth in Zebrafish Embryos Indicates a Role for Impaired Microtubule Dynamics in Hereditary Spastic Paraplegia.” *Disease Models & Mechanisms* 3(11–12):743–51.

Byrne, Paula C., Stewart Webb, Fergus McSweeney, Teresa Burke, Michael Hutchinson, and Nollaig A. Parfrey. 1998. “Linkage of AD HSP and Cognitive Impairment to Chromosome 2p: Haplotype and Phenotype Analysis Indicates Variable Expression and Low or Delayed Penetrance.” *European Journal of Human Genetics* 6(3):275–82.

Caltagarone, John, Zheng Jing, and Robert Bowser. 2007. “Focal Adhesions Regulate Aβ Signaling and Cell Death in Alzheimer’s Disease.” *Biochimica et Biophysica Acta (BBA) - Molecular Basis of Disease* 1772(4):438–45.

Campbell, P. D., K. Shen, M. R. Sapio, T. D. Glenn, W. S. Talbot, and F. L. Marlow. 2014. “Unique Function of Kinesin Kif5A in Localization of Mitochondria in Axons.” *Journal of Neuroscience* 34(44):14717–32.

Campelo, Felix, Harvey T. McMahon, and Michael M. Kozlov. 2008. “The Hydrophobic Insertion Mechanism of Membrane Curvature Generation by Proteins.” *Biophysical Journal* 95(5):2325–39.

Canbaz, Derya, Koray Kırımtay, Esra Karaca, and Arzu Karabay. 2011. “SPG4 Gene Promoter Regulation via Elk1 Transcription Factor.” *Journal of Neurochemistry* 117(4):724–34.

Carlier, Marie France and Dominique Pantaloni. 1981. “Kinetic Analysis of Guanosine 5’-Triphosphate Hydrolysis Associated with Tubulin Polymerization.” *Biochemistry* 20(7):1918–24.

Carlos Martín Zoppino, Felipe, Rodrigo Damián Militello, Ileana Slavin, Cecilia Álvarez, and María I. Colombo. 2010. “Autophagosome Formation Depends on the Small GTPase Rab1 and Functional ER Exit Sites.” *Traffic* 11(9):1246–61.

Carlton, Jez, Miriam Bujny, Brian J. Peter, Viola M. J. Oorschot, Anna Rutherford, Harry Mellor, Judith Klumperman, Harvey T. McMahon, and Peter J. Cullen. 2004. “Sorting Nexin-1 Mediates Tubular Endosome-to-TGN Transport through Coincidence Sensing of High- Curvature Membranes and 3-Phosphoinositides.” *Current Biology* 14(20):1791–1800.

Carr, David B. and D. James Surmeier. 2007. “M 1 Muscarinic Receptor Modulation of Kir2 Channels Enhances Temporal Summation of Excitatory Synaptic Potentials in Prefrontal Cortex Pyramidal Neurons.” *Journal of Neurophysiology* 97(5):3432–38.

Carrasco, Patricia, Jordi Jacas, Ignasi Sahún, Helena Muley, Sara Ramírez, Beatriz Puisac, Pau Mezquita, Juan Pié, Mara Dierssen, and Núria Casals. 2013. “Carnitine Palmitoyltransferase 1C Deficiency Causes Motor Impairment and Hypoactivity.” *Behavioural Brain Research* 256:291–97.

Carraway III, Kermit L., Janet L. Weber, Michelle J. Unger, Jessica Ledesma, Naichen Yu, Martin Gassmann, and Cary Lai. 1997. “Neuregulin-2, a New Ligand of ErbB3/ErbB4-Receptor Tyrosine Kinases.” *Nature* 387(6632):512–16.

Casari, Giorgio, Maurizio De Fusco, Sonia Ciarmatori, Massimo Zeviani, Marina Mora, Patricio Fernandez, Giuseppe De Michele, Alessandro Filla, Sergio Cocozza, Roberto Marconi, Alexandre Dürr, Bertrand Fontaine, and Andrea Ballabio. 1998. “Spastic Paraplegia and OXPHOS Impairment Caused by Mutations in Paraplegin, a Nuclear-Encoded Mitochondrial Metalloprotease.” *Cell* 93(6):973–83.

Castresana, J., M. Lübben, M. Saraste, and D. G. Higgins. 1994. “Evolution of Cytochrome Oxidase, an Enzyme Older than Atmospheric Oxygen.” *The EMBO Journal* 13(11):2516–25.

Cate, Holly S., Jennifer K. Sabo, Daniel Merlo, Dennis Kemper, Tim D. Aumann, Julien Robinson, Toby D. Merson, Ben Emery, Victoria M. Perreau, and Trevor J. Kilpatrick. 2010. “Modulation of Bone Morphogenic Protein Signalling Alters Numbers of Astrocytes and Oligodendroglia in the Subventricular Zone during Cuprizone-Induced Demyelination.” *Journal of Neurochemistry* 115(1):11–22.

Chand, Kirat K., Kah Meng Lee, Nickolas A. Lavidis, and Peter G. Noakes. 2017. “Loss of Laminin-A4 Results in Pre- and Postsynaptic Modifications at the Neuromuscular Junction.” *The FASEB Journal* 31(4):1323–36.

Chang, J., S. Lee, and C. Blackstone. 2013. “Protrudin Binds Atlastins and Endoplasmic Reticulum-Shaping Proteins and Regulates Network Formation.” *Proceedings of the National Academy of Sciences* 110(37):14954–59.

Chappie, Joshua S., Jason A. Mears, Shunming Fang, Marilyn Leonard, Sandra L. Schmid, Ronald A. Milligan, Jenny E. Hinshaw, and Fred Dyda. 2011. “A Pseudoatomic Model of the Dynamin Polymer Identifies a Hydrolysis-Dependent Powerstroke.” *Cell* 147(1):209–22.

Charron, Frédéric and Marc Tessier-Lavigne. 2007. “The Hedgehog, TGF-β/BMP and Wnt Families of Morphogens in Axon Guidance.” Pp. 116–33 in *Axon Growth and Guidance*. New York, NY: Springer New York.

Charvin, Delphine. 2003. “Mutations of SPG4 Are Responsible for a Loss of Function of Spastin, an Abundant Neuronal Protein Localized in the Nucleus.” *Human Molecular Genetics* 12(1):71–78.

Chen, Chiung-Ya, Chia-Wen Lin, Chiung-Ying Chang, Si-Tse Jiang, and Yi-Ping Hsueh. 2011. “Sarm1, a Negative Regulator of Innate Immunity, Interacts with Syndecan-2 and Regulates Neuronal Morphology.” *The Journal of Cell Biology* 193(4):769–84.

Cheng, Mei-Yun, Hsing-Hua Ho, Tsung-Kai Huang, Chih-Fan Chuang, Hui-Yu Chen, Hui-Wen Chung, Wan-Chong Leong, Wen-Cheng Yang, Chien-Chung Fu, Yun-Hsin Hsu, and Yen-Chung Chang. 2017. “A Compartmentalized Culture Device for Studying the Axons of CNS Neurons.” *Analytical Biochemistry* 539:11–21.

Chi, Richard J., Jingxuan Liu, Matthew West, Jing Wang, Greg Odorizzi, and Christopher G. Burd. 2014. “Fission of SNX-BAR–coated Endosomal Retrograde Transport Carriers Is Promoted by the Dynamin-Related Protein Vps1.” *The Journal of Cell Biology* 204(5):793–806.

Chiaruttini, Nicolas, Lorena Redondo-Morata, Adai Colom, Frédéric Humbert, Martin Lenz, Simon Scheuring, and Aurélien Roux. 2015. “Relaxation of Loaded ESCRT-III Spiral Springs Drives Membrane Deformation.” *Cell* 163(4):866–79.

Christ, Liliane, Camilla Raiborg, Eva M. Wenzel, Coen Campsteijn, and Harald Stenmark. 2017. “Cellular Functions and Molecular Mechanisms of the ESCRT Membrane-Scission Machinery.” *Trends in Biochemical Sciences* 42(1):42–56.

Ciccarelli, Francesca D., Christos Proukakis, Heema Patel, Harold Cross, Shakil Azam, Michael A. Patton, Peer Bork, and Andrew H. Crosby. 2003. “The Identification of a Conserved Domain in Both Spartin and Spastin, Mutated in Hereditary Spastic Paraplegia.” *Genomics* 81(4):437–41.

Clarençon, F., E. Touzé, A. Leroy–Willig, H. Turmel, O. Naggara, S. Pavy, A. Brézin, and J. –L. Mas. 2006. “Spastic Paraparesis as a Manifestation of Leber’s Disease.” *Journal of Neurology* 253(4):525–26.

Clarkson, Andrew N., Ben S. Huang, Sarah E. MacIsaac, Istvan Mody, and S. Thomas Carmichael. 2010. “Reducing Excessive GABA-Mediated Tonic Inhibition Promotes Functional Recovery after Stroke.” *Nature* 468(7321):305–9.

CLAUDIANI, P., E. RIANO, A. ERRICO, G. ANDOLFI, and E. RUGARLI. 2005. “Spastin Subcellular Localization Is Regulated through Usage of Different Translation Start Sites and Active Export from the Nucleus.” *Experimental Cell Research* 309(2):358–69.

Cocucci, Emanuele, Raphaël Gaudin, and Tom Kirchhausen. 2014. “Dynamin Recruitment and Membrane Scission at the Neck of a Clathrin-Coated Pit” edited by J. Lippincott-Schwartz and J. Lippincott-Schwartz. *Molecular Biology of the Cell* 25(22):3595–3609.

Cohen, Sarah, Alex M. Valm, and Jennifer Lippincott-Schwartz. 2018. “Interacting Organelles.” *Current Opinion in Cell Biology* 53:84–91.

Colak, D., T. Mori, M. S. Brill, A. Pfeifer, S. Falk, C. Deng, R. Monteiro, C. Mummery, L. Sommer, and M. Gotz. 2008. “Adult Neurogenesis Requires Smad4-Mediated Bone Morphogenic Protein Signaling in Stem Cells.” *Journal of Neuroscience* 28(2):434–46.

Connell, James W., Rachel Allison, and Evan Reid. 2016. “Quantitative Gait Analysis Using a Motorized Treadmill System Sensitively Detects Motor Abnormalities in Mice Expressing ATPase Defective Spastin” edited by A. J. Grierson. *PLOS ONE* 11(3):e0152413.

Connell, James W., Catherine Lindon, J. Paul Luzio, and Evan Reid. 2009. “Spastin Couples Microtubule Severing to Membrane Traffic in Completion of Cytokinesis and Secretion.” *Traffic* 10(1):42–56.

Cooper, Helen M., Yang Yang, Emil Ylikallio, Rafil Khairullin, Rosa Woldegebriel, Kai-Lan Lin, Liliya Euro, Eino Palin, Alexander Wolf, Ras Trokovic, Pirjo Isohanni, Seppo Kaakkola, Mari Auranen, Tuula Lönnqvist, Sjoerd Wanrooij, and Henna Tyynismaa. 2017. “ATPase-Deficient Mitochondrial Inner Membrane Protein ATAD3A Disturbs Mitochondrial Dynamics in Dominant Hereditary Spastic Paraplegia.” *Human Molecular Genetics* 26(8):1432–43.

Cornell, Brett, Tomoka Wachi, Vladimir Zhukarev, and Kazuhito Toyo-oka. 2016. “Regulation of Neuronal Morphogenesis by 14-3-3epsilon (Ywhae) via the Microtubule Binding Protein, Doublecortin.” *Human Molecular Genetics* 25(20):4610–4610.

Corona, P., E. Lamantea, M. Greco, F. Carrara, A. Agostino, D. Guidetti, M. T. Dotti, C. Mariotti, and M. Zeviani. 2002. “Novel Heteroplasmic MtDNA Mutation in a Family with Heterogeneous Clinical Presentations.” *Annals of Neurology* 51(1):118–22.

Corvera, Silvia, Antonello D’Arrigo, and Harald Stenmark. 1999. “Phosphoinositides in Membrane Traffic.” *Current Opinion in Cell Biology* 11(4):460–65.

Coury, F., S. Zenger, A. K. Stewart, S. Stephens, L. Neff, K. Tsang, G. E. Shull, S. L. Alper, R. Baron, and A. O. Aliprantis. 2013. “SLC4A2-Mediated Cl-/HCO3- Exchange Activity Is Essential for Calpain-Dependent Regulation of the Actin Cytoskeleton in Osteoclasts.” *Proceedings of the National Academy of Sciences* 110(6):2163–68.

Coutelier, Marie, Cyril Goizet, Alexandra Durr, Florence Habarou, Sara Morais, Alexandre Dionne-Laporte, Feifei Tao, Juliette Konop, Marion Stoll, Perrine Charles, Maxime Jacoupy, Raphaël Matusiak, Isabel Alonso, Chantal Tallaksen, Mathilde Mairey, Marina Kennerson, Marion Gaussen, Rebecca Schule, Maxime Janin, Fanny Morice-Picard, Christelle M. Durand, Christel Depienne, Patrick Calvas, Paula Coutinho, Jean-Marie Saudubray, Guy Rouleau, Alexis Brice, Garth Nicholson, Frédéric Darios, José L. Loureiro, Stephan Zuchner, Chris Ottolenghi, Fanny Mochel, and Giovanni Stevanin. 2015. "Alteration of Ornithine Metabolism Leads to Dominant and Recessive Hereditary Spastic Paraplegia." *Brain* 138(8):2191–2205.

Crespo-Yàñez, Xènia, Carmen Aguilar-Gurrieri, Anne-Claire Jacomin, Agnès Journet, Magda Mortier, Emmanuel Taillebourg, Emmanuelle Soleilhac, Winfried Weissenhorn, and Marie-Odile Fauvarque. 2018. "CHMP1B Is a Target of USP8/UBPY Regulated by Ubiquitin during Endocytosis" edited by F. Schweisguth. *PLOS Genetics* 14(6):e1007456.

Crow, Yanick, Maha Zaki, Mohamed Abdel-Hamid, Ghada Abdel-Salam, Odile Boespflug-Tanguy, Nuno Cordeiro, Joseph Gleeson, Nirmala Gowrinathan, Vincent Laugel, Florence Renaldo, Diana Rodriguez, John Livingston, and Gillian Rice. 2014. "Mutations in ADAR1, IFIH1, and RNASEH2B Presenting As Spastic Paraplegia." *Neuropediatrics* 45(06):386–91.

Cutrona, Meritxell B., Galina V. Beznoussenko, Aurora Fusella, Oliviano Martella, Pedro Moral, and Alexander A. Mironov. 2013. "Silencing of Mammalian Sar1 Isoforms Reveals COPII-Independent Protein Sorting and Transport." *Traffic* 14(6):691–708.

D'Acquisto, Fulvio, Ahmed Merghani, Emilio Lecona, Guglielmo Rosignoli, Karim Raza, Christopher D. Buckley, Roderick J. Flower, and Mauro Perretti. 2006. "Annexin-1 Modulates T-Cell Activation and Differentiation." *Blood* 109(3):1095–1102.

d'Enfert, C. 1991. "Sec12p-Dependent Membrane Binding of the Small GTP-Binding Protein Sar1p Promotes Formation of Transport Vesicles from the ER." *The Journal of Cell Biology* 114(4):663–70.

Daftary, Gaurang S., Amy M. Tetrault, Elisa M. Jorgensen, Jennifer Sarno, and Hugh S. Taylor. 2011. "A Novel Role for the AAA ATPase Spastin as a HOXA10 Transcriptional Corepressor in Ishikawa Endometrial Cells." *Molecular Endocrinology* 25(9):1539–49.

Damasceno, Karine Araújo, Enio Ferreira, Alessandra Estrela-Lima, Conrado de Oliveira Gamba, Fernanda Freitas Miranda, Mariana Rezende Alves, Rafael Malagoli Rocha, André Luís Branco de Barros, and Geovanni Dantas Cassali. 2016. "HER-2 and EGFR MRNA Expression and Its Relationship with Versican in Malignant Matrix-Producing Tumors of the Canine Mammary Gland" edited by N. K. Karamanos. *PLOS ONE* 11(8):e0160419.

Davenport, Anne, Alexis Bivona, Will Latson, Larry F. Lemanski, and Venugopalan Cheriyath. 2016. "Loss of Maspardin Attenuates the Growth and Maturation of Mouse Cortical Neurons." *Neurodegenerative Diseases* 16(3–4):260–72.

Day, Charles A., Nicholas W. Baetz, Courtney A. Copeland, Lewis J. Kraft, Bing Han, Ajit Tiwari, Kimberly R. Drake, Heidi De Luca, Daniel J. F. Chinnapen, Michael W. Davidson, Randall K. Holmes, Michael G. Jobling, Trina A. Schroer, Wayne I. Lencer, and Anne K. Kenworthy. 2015. "Microtubule Motors Power Plasma Membrane Tubulation in Clathrin-Independent Endocytosis." *Traffic* 16(6):572–90.

Delevoye, Cédric, Stéphanie Miserey-Lenkei, Guillaume Montagnac, Floriane Gilles-Marsens, Perrine Paul-Gilloteaux, Francesca Giordano, François Waharte, Michael S. Marks, Bruno Goud, and Graça Raposo. 2014. "Recycling Endosome Tubule Morphogenesis from Sorting Endosomes Requires the Kinesin Motor KIF13A." *Cell Reports* 6(3):445–54.

Denda, Sumiko, Ulrich Müller, Kathryn L. Crossin, Harold P. Erickson, and Louis F. Reichardt. 1998. "Utilization of a Soluble Integrin-Alkaline Phosphatase Chimera To Characterize Integrin A8β1 Receptor Interactions with Tenascin: Murine A8β1 Binds to the RGD Site in Tenascin-C Fragments, but Not to Native Tenascin-C †." *Biochemistry* 37(16):5464–74.

Deng, S., A. Hirschberg, T. Worzfeld, J. Y. Penachioni, A. Korostylev, J. M. Swiercz, P. Vodrazka, O. Mauti, E. T. Stoeckli, L. Tamagnone, S. Offermanns, and R. Kuner. 2007. "Plexin-B2, But Not Plexin-B1, Critically Modulates Neuronal Migration and Patterning of the Developing Nervous System In Vivo." *Journal of Neuroscience* 27(23):6333–47.

Denton, Kyle R., Ling Lei, Jeremy Grenier, Vladimir Rodionov, Craig Blackstone, and Xue-Jun Li. 2014. "Loss of Spastin Function Results in Disease-Specific Axonal Defects in Human Pluripotent Stem Cell-Based Models of Hereditary Spastic Paraplegia." *STEM CELLS* 32(2):414–23.

Depienne, Christel, Estelle Fedirko, Sylvie Forlani, Cécile Cazeneuve, P. Ribai, Imed Feki, Chantal Tallaksen, Karine Nguyen, Bruno Stankoff, Merle Ruberg, Giovanni Stevanin, Alexandra Durr, and Alexis Brice. 2007. "Exon Deletions of SPG4 Are a Frequent Cause of Hereditary Spastic Paraplegia." *Journal of Medical Genetics* 44(4):281–84.

Derivery, Emmanuel, Emmanuèle Helfer, Véronique Henriot, and Alexis Gautreau. 2012. “Actin Polymerization Controls the Organization of WASH Domains at the Surface of Endosomes” edited by J. Keen. *PLoS ONE* 7(6):e39774.

Derivery, Emmanuel, Carla Sousa, Jérémie J. Gautier, Bérangère Lombard, Damarys Loew, and Alexis Gautreau. 2009. “The Arp2/3 Activator WASH Controls the Fission of Endosomes through a Large Multiprotein Complex.” *Developmental Cell* 17(5):712–23.

Desgrosellier, Jay S. and David A. Cheresh. 2010. “Integrins in Cancer: Biological Implications and Therapeutic Opportunities.” *Nature Reviews Cancer* 10(1):9–22.

Desmaris, Elodie, Marc Keruzore, Amandine Saulnier, Leslie Ratié, Stavroula Assimacopoulos, Sarah De Clercq, Xinsheng Nan, Kaushik Roychoudhury, Shenyue Qin, Sadia Kricha, Clément Chevalier, Thomas Lingner, Kristine A. Henningfeld, David Zarkower, Antonello Mallamaci, Thomas Theil, Kenneth Campbell, Tomas Pieler, Meng Li, Elizabeth A. Grove, and Eric J. Bellefroid. 2018. “DMRT5, DMRT3, and EMX2 Cooperatively Repress Gsx2 at the Pallium–Subpallium Boundary to Maintain Cortical Identity in Dorsal Telencephalic Progenitors.” *The Journal of Neuroscience* 38(42):9105–21.

Destexhe, Alain and Eve Marder. 2004. “Plasticity in Single Neuron and Circuit Computations.” *Nature* 431(7010):789–95.

Dhers, L., L. Ducassou, J. L. Boucher, and D. Mansuy. 2017. “Cytochrome P450 2U1, a Very Peculiar Member of the Human P450s Family.” *Cellular and Molecular Life Sciences* 74(10):1859–69.

Dick, Katherine J., Matthias Eckhardt, Coro Paisán-Ruiz, Aisha Alkhayat Alshehhi, Christos Proukakis, Naomi A. Sibtain, Helena Maier, Reza Sharifi, Michael A. Patton, Wafa Bashir, Roshan Koul, Sandy Raeburn, Volkmar Gieselmann, Henry Houlden, and Andrew H. Crosby. 2010. “Mutation of FA2H Underlies a Complicated Form of Hereditary Spastic Paraplegia (SPG35).” *Human Mutation* 31(4):E1251–60.

Dieck, Chelsea L., Gannie Tzoneva, Farhad Forouhar, Zachary Carpenter, Alberto Ambesi-Impiombato, Marta Sánchez-Martín, Renate Kirschner-Schwabe, Scott Lew, Jayaraman Seetharaman, Liang Tong, and Adolfo A. Ferrando. 2018. “Structure and Mechanisms of NT5C2 Mutations Driving Thiopurine Resistance in Relapsed Lymphoblastic Leukemia.” *Cancer Cell* 34(1):136–147.e6.

Dimitrov, Ariane, Mélanie Quesnoit, Sandrine Moutel, Isabelle Cantaloube, C. Pous, and Franck Perez. 2008. “Detection of GTP-Tubulin Conformation in Vivo Reveals a Role for GTP Remnants in Microtubule Rescues.” *Science* 322(5906):1353–56.

Dingjan, Ilse, Peter T. A. Linders, Danielle R. J. Verboogen, Natalia H. Revelo, Martin ter Beest, and Geert van den Bogaart. 2018. “Endosomal and Phagosomal SNAREs.” *Physiological Reviews* 98(3):1465–92.

Dirkx, Ronald, Annette Thomas, Linsong Li, Åke Lernmark, Robert S. Sherwin, Pietro De Camilli, and Michele Solimena. 1995. “Targeting of the 67-KDa Isoform of Glutamic Acid Decarboxylase to Intracellular Organelles Is Mediated by Its Interaction with the NH 2 -Terminal Region of the 65-KDa Isoform of Glutamic Acid Decarboxylase.” *Journal of Biological Chemistry* 270(5):2241–46.

Dislich, Bastian, Manuel E. Than, and Stefan F. Lichtenthaler. 2011. “Specific Amino Acids in the BAR Domain Allow Homodimerization and Prevent Heterodimerization of Sorting Nexin 33.” *Biochemical Journal* 433(1):75–83.

Dong, Rui, Yasunori Saheki, Sharan Swarup, Louise Lucast, J. Wade Harper, and Pietro De Camilli. 2016. “Endosome-ER Contacts Control Actin Nucleation and Retromer Function through VAP-Dependent Regulation of PI4P.” *Cell* 166(2):408–23.

Dor, Talya, Yuval Cinnamon, Laure Raymond, Avraham Shaag, Naima Bouslam, Ahmed Bouhouche, Marion Gaussen, Vincent Meyer, Alexandra Durr, Alexis Brice, Ali Benomar, Giovanni Stevanin, Markus Schuelke, and Simon Edvardson. 2014. “KIF1C Mutations in Two Families with Hereditary Spastic Paraparesis and Cerebellar Dysfunction.” *Journal of Medical Genetics* 51(2):137–42.

Dransfield, Ian and Sarah Farnworth. 2016. “Axl and Mer Receptor Tyrosine Kinases: Distinct and Nonoverlapping Roles in Inflammation and Cancer?” Pp. 113–32 in *Advances in Experimental Medicine and Biology*.

Drin, Guillaume and Bruno Antonny. 2010. “Amphipathic Helices and Membrane Curvature.” *FEBS Letters* 584(9):1840–47.

Duan, Lei, Yuko Miura, Manjari Dimri, Biswanath Majumder, Ingrid L. Dodge, Alagarsamy L. Reddi, Amiya Ghosh, Norvin Fernandes, Pengcheng Zhou, Karen Mullane-Robinson, Navin Rao, Stephen Donoghue, Rick A. Rogers, David Bowtell, Mayumi Naramura, Hua Gu, Vimla Band, and Hamid Band. 2003. "Cbl-Mediated Ubiquitinylation Is Required for Lysosomal Sorting of Epidermal Growth Factor Receptor but Is Dispensable for Endocytosis." *Journal of Biological Chemistry* 278(31):28950–60.

DuBoff, Brian, Jürgen Götz, and Mel B. Feany. 2012. "Tau Promotes Neurodegeneration via DRP1 Mislocalization In Vivo." *Neuron* 75(4):618–32.

Dunn, K. W. 1989. "Iterative Fractionation of Recycling Receptors from Lysosomally Destined Ligands in an Early Sorting Endosome." *The Journal of Cell Biology* 109(6):3303–14.

Durr, Alexandra, Chantal Tallaksen, and Christel Depienne. 1993. *Spastic Paraplegia 4*. Vol. 4. University of Washington, Seattle.

Eckert, Thomas, Doan Tuong-Van Le, Susanne Link, Lena Friedmann, and Günther Woehlke. 2012. "Spastin's Microtubule-Binding Properties and Comparison to Katanin" edited by A. Hofmann. *PLoS ONE* 7(12):e50161.

Eckert, Thomas, Susanne Link, Doan Tuong-Van Le, Jean-Philippe Sobczak, Anja Gieseke, Klaus Richter, and Günther Woehlke. 2012. "Subunit Interactions and Cooperativity in the Microtubule-Severing AAA ATPase Spastin." *Journal of Biological Chemistry* 287(31):26278–90.

Edwards, Darin, Frank Sommerhage, Bonnie Berry, Hanna Nummer, Martina Raquet, Brad Clymer, Maria Stancescu, and James J. Hickman. 2017. "Comparison of NMDA and AMPA Channel Expression and Function between Embryonic and Adult Neurons Utilizing Microelectrode Array Systems." *ACS Biomaterials Science & Engineering* 3(12):3525–33.

Ellis, J. E., L. Parker, J. Cho, and K. Arora. 2010. "Activin Signaling Functions Upstream of Gbb to Regulate Synaptic Growth at the Drosophila Neuromuscular Junction." *Developmental Biology* 342(2):121–33.

Elo, Jenni M., Srujana S. Yadavalli, Liliya Euro, Pirjo Isohanni, Alexandra Götz, Christopher J. Carroll, Leena Valanne, Fowzan S. Alkuraya, Johanna Uusimaa, Anders Paetau, Eric M. Caruso, Helena Pihko, Michael Ibba, Henna Tyynismaa, and Anu Suomalainen. 2012. "Mitochondrial Phenylalanyl-TRNA Synthetase Mutations Underlie Fatal Infantile Alpers Encephalopathy." *Human Molecular Genetics* 21(20):4521–29.

Elsayed, Liena E. O., Inaam N. Mohammed, Ahlam A. A. Hamed, Maha A. Elseed, Adam Johnson, Mathilde Mairey, Hassab Elrasoul S. A. Mohamed, Mohamed N. Idris, Mustafa A. M. Salih, Sarah M. El-sadig, Mahmoud E. Koko, Ashraf Y. O. Mohamed, Laure Raymond, Marie Coutelier, Frédéric Darios, Rayan A. Siddig, Ahmed K. M. A. Ahmed, Arwa M. A. Babai, Hiba M. O. Malik, Zulfa M. B. M. Omer, Eman O. E. Mohamed, Hanan B. Eltahir, Nasr Aldin A. Magboul, Elfatih E. Bushara, Abdelrahman Elnour, Salah M. Abdel Rahim, Abdelmoneim Alattaya, Mustafa I. Elbashir, Muntaser E. Ibrahim, Alexandra Durr, Anjon Audhya, Alexis Brice, Ammar E. Ahmed, and Giovanni Stevanin. 2017. "Hereditary Spastic Paraplegias: Identification of a Novel SPG57 Variant Affecting TFG Oligomerization and Description of HSP Subtypes in Sudan." *European Journal of Human Genetics* 25(1):100–110.

Erichsen, A. K., E. Inderhaug, M. Mattingsdal, K. Eiklid, and C. M. E. Tallaksen. 2007. "Seven Novel Mutations and Four Exon Deletions in a Collection of Norwegian Patients with SPG4 Hereditary Spastic Paraplegia." *European Journal of Neurology* 14(7):809–14.

Erlich, Yaniv, Simon Edvardson, Emily Hodges, Shamir Zenvirt, Pramod Thekkat, Avraham Shaag, Talya Dor, Gregory J. Hannon, and Orly Elpeleg. 2011. "Exome Sequencing and Disease-Network Analysis of a Single Family Implicate a Mutation in KIF1A in Hereditary Spastic Paraparesis." *Genome Research* 21(5):658–64.

Errico, Alessia. 2002. "Spastin, the Protein Mutated in Autosomal Dominant Hereditary Spastic Paraplegia, Is Involved in Microtubule Dynamics." *Human Molecular Genetics* 11(2):153–63.

Errico, Alessia. 2004. "Spastin Interacts with the Centrosomal Protein NA14, and Is Enriched in the Spindle Pole, the Midbody and the Distal Axon." *Human Molecular Genetics* 13(18):2121–32.

Esteves, Typhaine, Alexandra Durr, Emeline Mundwiller, José L. Loureiro, Maxime Boutry, Michael A. Gonzalez, Julie Gauthier, Khalid H. El-Hachimi, Christel Depienne, Marie-Paule Muriel, Rafael F. Acosta Lebrigio, Marion Gaussen, Anne Noreau, Fiorella Speziani, Alexandre Dionne-Laporte, Jean-François Deleuze, Patrick Dion, Paula Coutinho, Guy A. Rouleau, Stephan Zuchner, Alexis Brice, Giovanni Stevanin, and Frédéric Darios. 2014. "Loss of Association of REEP2 with Membranes Leads to Hereditary Spastic Paraplegia." *The American Journal of Human Genetics* 94(2):268–77.

Evans, K., C. Keller, K. Pavur, K. Glasgow, B. Conn, and B. Lauring. 2006. "Interaction of Two Hereditary Spastic Paraplegia Gene Products, Spastin and Atlastin, Suggests a Common Pathway for Axonal Maintenance." *Proceedings of the National Academy of Sciences* 103(28):10666–71.

Eymard-Pierre, Eleonore, Gaetan Lesca, Sandra Dollet, Filippo Maria Santorelli, Matteo di Capua, Enrico Bertini, and Odile Boespflug-Tanguy. 2002. “Infantile-Onset Ascending Hereditary Spastic Paralysis Is Associated with Mutations in the Alsin Gene.” *The American Journal of Human Genetics* 71(3):518–27.

Faber, Ingrid, Eduardo Rafael Pereira, Alberto R. M. Martinez, Marcondes França Jr, and Hélio Afonso Ghizoni Teive. 2017. “Hereditary Spastic Paraplegia from 1880 to 2017: An Historical Review.” *Arquivos de Neuro-Psiquiatria* 75(11):813–18.

Fabrikant, Gur, Suman Lata, James D. Riches, John A. G. Briggs, Winfried Weissenhorn, and Michael M. Kozlov. 2009. “Computational Model of Membrane Fission Catalyzed by ESCRT-III” edited by V. S. Pande. *PLoS Computational Biology* 5(11):e1000575.

Faelber, Katja, York Posor, Song Gao, Martin Held, Yvette Roske, Dennis Schulze, Volker Haucke, Frank Noé, and Oliver Daumke. 2011. “Crystal Structure of Nucleotide-Free Dynamin.” *Nature* 477(7366):556–60.

Falcone, Carmen and Antonello Mallamaci. 2015. “Tuning of Neocortical Astrogenesis Rates by Emx2 in Meural Stem Cells.” *Neural Regeneration Research* 10(4):550.

Fassier, C., A. Tarrade, L. Peris, S. Courageot, P. Mailly, C. Dalard, S. Delga, N. Roblot, J. Lefevre, D. Job, J. Hazan, P. A. Curmi, and J. Melki. 2013. “Microtubule-Targeting Drugs Rescue Axonal Swellings in Cortical Neurons from Spastin Knockout Mice.” *Disease Models & Mechanisms* 6(1):72–83.

Fassier, Coralie, James A. Hutt, Steffen Scholpp, Andrew Lumsden, Bruno Giros, Fatiha Nothias, Sylvie Schneider-Maunoury, Corinne Houart, and Jamilé Hazan. 2010. “Zebrafish Atlastin Controls Motility and Spinal Motor Axon Architecture via Inhibition of the BMP Pathway.” *Nature Neuroscience* 13(11):1380–87.

Fath, Stephan, Joseph D. Mancias, Xiping Bi, and Jonathan Goldberg. 2007. “Structure and Organization of Coat Proteins in the COPII Cage.” *Cell* 129(7):1325–36.

Fei, Hao, Anna Grygoruk, Elizabeth S. Brooks, Audrey Chen, and David E. Krantz. 2008. “Trafficking of Vesicular Neurotransmitter Transporters.” *Traffic* 9(9):1425–36.

Feng, Yan, Barry Press, and Angela Wandinger-Ness. 1995. “Rab 7: An Important Regulator of Late Endocytic Membrane Traffic.” *Journal of Cell Biology* 131(6 I):1435–52.

Ferreira, Tiago A., Arne V. Blackman, Julia Oyrer, Sriram Jayabal, Andrew J. Chung, Alanna J. Watt, P. Jesper Sjöström, and Donald J. van Meyel. 2014. “Neuronal Morphometry Directly from Bitmap Images.” *Nature Methods* 11(10):982–84.

Figiel, Małgorzata, Hyongi Chon, Susana M. Cerritelli, Magdalena Cybulska, Robert J. Crouch, and Marcin Nowotny. 2011. “The Structural and Biochemical Characterization of Human RNase H2 Complex Reveals the Molecular Basis for Substrate Recognition and Aicardi-Goutières Syndrome Defects.” *Journal of Biological Chemistry* 286(12):10540–50.

Filoteo, A. G. 1995. “Mutants in the Putative Nucleotide-Binding Region of the Plasma Membrane Ca^{2+}-Pump.” *Journal of Biological Chemistry* 270(50):30111–14.

Finger, Jacqueline H., Rod T. Bronson, Belinda Harris, Kenneth Johnson, Stefan a Przyborski, and Susan L. Ackerman. 2002. “The Netrin 1 Receptors Unc5h3 and Dcc Are Necessary at Multiple Choice Points for the Guidance of Corticospinal Tract Axons.” *The Journal of Neuroscience* 22(23):10346–56.

Finnson, Kenneth W., Betty Y. Y. Tam, Kai Liu, Anne Marcoux, Pierre Lepage, Stephane Roy, Albane A. Bizet, and Anie Philip. 2006. “Identification of CD109 as Part of the TGF-β Receptor System in Human Keratinocytes.” *The FASEB Journal* 20(9):1525–27.

Fjorback, A. W., M. Seaman, C. Gustafsen, A. Mehmedbasic, S. Gokool, C. Wu, D. Militz, V. Schmidt, P. Madsen, J. R. Nyengaard, T. E. Willnow, E. I. Christensen, W. B. Mobley, A. Nykjaer, and O. M. Andersen. 2012. “Retromer Binds the FANSHY Sorting Motif in SorLA to Regulate Amyloid Precursor Protein Sorting and Processing.” *Journal of Neuroscience* 32(4):1467–80.

Flanagan, John and Gordon L. E. Koch. 1978. “Cross-Linked Surface Ig Attaches to Actin.” *Nature* 273(5660):278–81.

Fonknechten, N., D. Mavel, P. Byrne, C. S. Davoine, C. Cruaud, D. Bönsch, D. Boentsch, D. Samson, P. Coutinho, M. Hutchinson, P. McMonagle, J. M. Burgunder, A. Tartaglione, O. Heinzlef, I. Feki, T. Deufel, N. Parfrey, A. Brice, B. Fontaine, J. F. Prud’homme, J. Weissenbach, A. Dürr, and J. Hazan. 2000. “Spectrum of SPG4 Mutations in Autosomal Dominant Spastic Paraplegia.” *Human Molecular Genetics* 9(4):637–44.

Forster, Rebecca, Matthias Weiss, Timo Zimmermann, Emmanuel G. Reynaud, Fatima Verissimo, David J. Stephens, and Rainer Pepperkok. 2006. “Secretory Cargo Regulates the Turnover of COPII Subunits at Single ER Exit Sites.” *Current Biology* 16(2):173–79.

Fourtassi, M., S. Jacquin-Courtois, M. C. Scheiber-Nogueira, A. Hajjioui, J. Luaute, K. Charvier, D. Maucort-Boulch, and G. Rode. 2012. “Bladder Dysfunction in Hereditary Spastic Paraplegia: A Clinical and Urodynamic Evaluation.” *Spinal Cord* 50(7):558–62.

Fraldi, Alessandro, Fabio Annunziata, Alessia Lombardi, Hermann-Josef Kaiser, Diego Luis Medina, Carmine Spampanato, Anthony Olind Fedele, Roman Polishchuk, Nicolina Cristina Sorrentino, Kai Simons, and Andrea Ballabio. 2010. “Lysosomal Fusion and SNARE Function Are Impaired by Cholesterol Accumulation in Lysosomal Storage Disorders.” *The EMBO Journal* 29(21):3607–20.

Freeman, C. L., G. Hesketh, and M. N. J. Seaman. 2014. “RME-8 Coordinates the Activity of the WASH Complex with the Function of the Retromer SNX Dimer to Control Endosomal Tubulation.” *Journal of Cell Science* 127(9):2053–70.

Freeman, Caroline, Matthew N. J. Seaman, and Evan Reid. 2013. “The Hereditary Spastic Paraplegia Protein Strumpellin: Characterisation in Neurons and of the Effect of Disease Mutations on WASH Complex Assembly and Function.” *Biochimica et Biophysica Acta (BBA) - Molecular Basis of Disease* 1832(1):160–73.

Friedman, Jonathan R., Jared R. DiBenedetto, Matthew West, Ashley A. Rowland, and Gia K. Voeltz. 2013. “Endoplasmic Reticulum–endosome Contact Increases as Endosomes Traffic and Mature” edited by R. S. Hegde. *Molecular Biology of the Cell* 24(7):1030–40.

Friedman, Jonathan R., Laura L. Lackner, Matthew West, Jared R. DiBenedetto, Jodi Nunnari, and Gia K. Voeltz. 2011. “ER Tubules Mark Sites of Mitochondrial Division.” *Science* 334(6054):358–62.

Fujimoto, Toyoshi and Robert G. Parton. 2011. “Not Just Fat: The Structure and Function of the Lipid Droplet.” *Cold Spring Harbor Perspectives in Biology* 3(3):a004838–a004838.

Fujioka, Yuko, Sho W. Suzuki, Hayashi Yamamoto, Chika Kondo-Kakuta, Yayoi Kimura, Hisashi Hirano, Rinji Akada, Fuyuhiko Inagaki, Yoshinori Ohsumi, and Nobuo N. Noda. 2014. “Structural Basis of Starvation-Induced Assembly of the Autophagy Initiation Complex.” *Nature Structural & Molecular Biology* 21(6):513–21.

Fuller, T. 2003. “Forward EphB4 Signaling in Endothelial Cells Controls Cellular Repulsion and Segregation from EphrinB2 Positive Cells.” *Journal of Cell Science* 116(12):2461–70.

Gallop, Jennifer L., Christine C. Jao, Helen M. Kent, P. Jonathan G. Butler, Philip R. Evans, Ralf Langen, and Harvey T. McMahon. 2006. “Mechanism of Endophilin N-BAR Domain-Mediated Membrane Curvature.” *The EMBO Journal* 25(12):2898–2910.

Gangula, Narmadha Reddy and Subbareddy Maddika. 2013. “WD Repeat Protein WDR48 in Complex with Deubiquitinase USP12 Suppresses Akt-Dependent Cell Survival Signaling by Stabilizing PH Domain Leucine-Rich Repeat Protein Phosphatase 1 (PHLPP1).” *Journal of Biological Chemistry* 288(48):34545–54.

Gao, Boning, Yoshitaka Sekido, Anton Maximov, Mohamad Saad, Eva Forgacs, Farida Latif, Ming H. Wei, Michael Lerman, Jung-Ha Lee, Edward Perez-Reyes, Ilya Bezprozvanny, and John D. Minna. 2000. “Functional Properties of a New Voltage-Dependent Calcium Channel α 2 δ Auxiliary Subunit Gene (CACNA2D2).” *Journal of Biological Chemistry* 275(16):12237–42.

Gasol, Emma, Maite Jiménez-Vidal, Josep Chillarón, Antonio Zorzano, and Manuel Palacín. 2004. “Membrane Topology of System Xc - Light Subunit Reveals a Re-Entrant Loop with Substrate-Restricted Accessibility.” *Journal of Biological Chemistry* 279(30):31228–36.

Gatfield, David. 2003. “Nonsense-Mediated MRNA Decay in Drosophila:At the Intersection of the Yeast and Mammalian Pathways.” *The EMBO Journal* 22(15):3960–70.

Gautreau, Alexis, Ksenia Oguievetskaia, and Christian Ungermann. 2014. “Function and Regulation of the Endosomal Fusion and Fission Machineries.” *Cold Spring Harbor Perspectives in Biology* 6(3):a016832–a016832.

Ge, Liang, David Melville, Min Zhang, and Randy Schekman. 2013. “The ER–Golgi Intermediate Compartment Is a Key Membrane Source for the LC3 Lipidation Step of Autophagosome Biogenesis.” *ELife* 2:e00947.

Ghai, R., M. Mobli, S. J. Norwood, A. Bugarcic, R. D. Teasdale, G. F. King, and B. M. Collins. 2011. “Phox Homology Band 4.1/Ezrin/Radixin/Moesin-like Proteins Function as Molecular Scaffolds That Interact with Cargo Receptors and Ras GTPases.” *Proceedings of the National Academy of Sciences* 108(19):7763–68.

Ghosh, Pradipta, Janice Griffith, Hans J. Geuze, and Stuart Kornfeld. 2003. “Mammalian GGAs Act Together to Sort Mannose 6-Phosphate Receptors.” *The Journal of Cell Biology* 163(4):755–66.

Lo Giudice, Temistocle, Federica Lombardi, Filippo Maria Santorelli, Toshitaka Kawarai, and Antonio Orlacchio. 2014. “Hereditary Spastic Paraplegia: Clinical-Genetic Characteristics and Evolving Molecular Mechanisms.” *Experimental Neurology* 261:518–39.

Gohla, Antje, Jörg Birkenfeld, and Gary M. Bokoch. 2005. “Chronophin, a Novel HAD-Type Serine Protein Phosphatase, Regulates Cofilin-Dependent Actin Dynamics.” *Nature Cell Biology* 7(1):21–29.

Gokool, Suzanne, Daniel Tattersall, and Matthew N. J. Seaman. 2007. “EHD1 Interacts with Retromer to Stabilize SNX1 Tubules and Facilitate Endosome-to-Golgi Retrieval.” *Traffic* 8(12):1873–86.

Goliand, Inna, Shai Adar-Levor, Inbar Segal, Dikla Nachmias, Tali Dadosh, Michael M. Kozlov, and Natalie Elia. 2018. “Resolving ESCRT-III Spirals at the Intercellular Bridge of Dividing Cells Using 3D STORM.” *Cell Reports* 24(7):1756–64.

Goliand, Inna, Dikla Nachmias, Ofir Gershony, and Natalie Elia. 2014. “Inhibition of ESCRT-II–CHMP6 Interactions Impedes Cytokinetic Abscission and Leads to Cell Death” edited by S. Doxsey. *Molecular Biology of the Cell* 25(23):3740–48.

Gomez, Timothy S. and Daniel D. Billadeau. 2009a. “A FAM21-Containing WASH Complex Regulates Retromer-Dependent Sorting.” *Developmental Cell* 17(5):699–711.

Gomez, Timothy S. and Daniel D. Billadeau. 2009b. “A FAM21-Containing WASH Complex Regulates Retromer-Dependent Sorting.” *Developmental Cell* 17(5):699–711.

Goodenough, Daniel A. and David L. Paul. 2009. “Gap Junctions.” *Cold Spring Harbor Perspectives in Biology* 1(1):a002576–a002576.

Gorbsky, G. J. 1987. “Chromosomes Move Poleward in Anaphase along Stationary Microtubules That Coordinately Disassemble from Their Kinetochore Ends.” *The Journal of Cell Biology* 104(1):9–18.

Gordon, David E., Lisa M. Bond, Daniela A. Sahlender, and Andrew A. Peden. 2010. “A Targeted SiRNA Screen to Identify SNAREs Required for Constitutive Secretion in Mammalian Cells.” *Traffic* 11(9):1191–1204.

Gorvel, Jean-Pierre, Philippe Chavrier, Marino Zerial, and Jean Gruenberg. 1991. “Rab5 Controls Early Endosome Fusion in Vitro.” *Cell* 64(5):915–25.

Gowrishankar, Swetha, Peng Yuan, Yumei Wu, Matthew Schrag, Summer Paradise, Jaime Grutzendler, Pietro De Camilli, and Shawn M. Ferguson. 2015. “Massive Accumulation of Luminal Protease-Deficient Axonal Lysosomes at Alzheimer’s Disease Amyloid Plaques.” *Proceedings of the National Academy of Sciences* 112(28):E3699–3708.

Goyal, Uma and Craig Blackstone. 2013. “Untangling the Web: Mechanisms Underlying ER Network Formation.” *Biochimica et Biophysica Acta (BBA) - Molecular Cell Research* 1833(11):2492–98.

Graham, Martin F., Amy Willey, John Adams, Dorne Yager, and Robert F. Diegelmann. 1995. “Role of Ascorbic Acid in Procollagen Expression and Secretion by Human Intestinal Smooth Muscle Cells.” *Journal of Cellular Physiology* 162(2):225–33.

Granger, Elizabeth, Gavin McNee, Victoria Allan, and Philip Woodman. 2014. “The Role of the Cytoskeleton and Molecular Motors in Endosomal Dynamics.” *Seminars in Cell & Developmental Biology* 31:20–29.

Grieve, Adam G. and Catherine Rabouille. 2011. “Golgi Bypass: Skirting Around the Heart of Classical Secretion.” *Cold Spring Harbor Perspectives in Biology* 3(4):a005298–a005298.

Griffiths, Ian. 1998. “Axonal Swellings and Degeneration in Mice Lacking the Major Proteolipid of Myelin.” *Science* 280(5369):1610–13.

Grøvdal, Lene Melsæther, Espen Stang, Alexander Sorkin, and Inger Helene Madshus. 2004. “Direct Interaction of Cbl with PTyr 1045 of the EGF Receptor (EGFR) Is Required to Sort the EGFR to Lysosomes for Degradation.” *Experimental Cell Research* 300(2):388–95.

Guizetti, Julien, Lothar Schermelleh, J. Mantler, Sandra Maar, Ina Poser, Heinrich Leonhardt, T. Muller-Reichert, and Daniel W. Gerlich. 2011. “Cortical Constriction During Abscission Involves Helices of ESCRT-III-Dependent Filaments.” *Science* 331(6024):1616–20.

Guo, Xiaojia, Lei Nie, Leila Esmailzadeh, Jiasheng Zhang, Jeffrey R. Bender, and Mehran M. Sadeghi. 2009. “Endothelial and Smooth Muscle-Derived Neuropilin-like Protein Regulates Platelet-Derived Growth Factor Signaling in Human Vascular Smooth Muscle Cells by Modulating Receptor Ubiquitination.” *Journal of Biological Chemistry* 284(43):29376–82.

Guo, Yusong and Adam D. Linstedt. 2006. “COPII–Golgi Protein Interactions Regulate COPII Coat Assembly and Golgi Size.” *The Journal of Cell Biology* 174(1):53–63.

Gurel, Pinar S., Anna L. Hatch, and Henry N. Higgs. 2014. “Connecting the Cytoskeleton to the Endoplasmic Reticulum and Golgi.” *Current Biology* 24(14):R660–72.

Hanein, Sylvain, Elodie Martin, Amir Boukhris, Paula Byrne, Cyril Goizet, Abdelmadjid Hamri, Ali Benomar, Alexander Lossos, Paola Denora, José Fernandez, Nizar Elleuch, Sylvie Forlani, Alexandra Durr, Imed Feki, Michael Hutchinson, Filippo M. Santorelli, Chokri Mhiri, Alexis Brice, and Giovanni Stevanin. 2008. “Identification of the SPG15 Gene, Encoding Spastizin, as a Frequent Cause of Complicated Autosomal-Recessive Spastic Paraplegia, Including Kjellin Syndrome.” *The American Journal of Human Genetics* 82(4):992–1002.

Hanna, Michael G., Samuel Block, E. B. Frankel, Feng Hou, Adam Johnson, Lin Yuan, Gavin Knight, James J. Moresco, John R. Yates, Randolph Ashton, Randy Schekman, Yufeng Tong, and Anjon Audhya. 2017. "TFG Facilitates Outer Coat Disassembly on COPII Transport Carriers to Promote Tethering and Fusion with ER–Golgi Intermediate Compartments." *Proceedings of the National Academy of Sciences* 114(37):E7707–16.

Hanna, Michael G., Ioanna Mela, Lei Wang, Robert M. Henderson, Edwin R. Chapman, J. Michael Edwardson, and Anjon Audhya. 2016. "Sar1 GTPase Activity Is Regulated by Membrane Curvature." *Journal of Biological Chemistry* 291(3):1014–27.

Hannedouche, Sébastien, Juan Zhang, Tangsheng Yi, Weijun Shen, Deborah Nguyen, João P. Pereira, Danilo Guerini, Birgit U. Baumgarten, Silvio Roggo, Ben Wen, Richard Knochenmuss, Sophie Noël, Francois Gessier, Lisa M. Kelly, Mirka Vanek, Stephane Laurent, Inga Preuss, Charlotte Miault, Isabelle Christen, Ratna Karuna, Wei Li, Dong-In Koo, Thomas Suply, Christian Schmedt, Eric C. Peters, Rocco Falchetto, Andreas Katopodis, Carsten Spanka, Marie-Odile Roy, Michel Detheux, Yu Alice Chen, Peter G. Schultz, Charles Y. Cho, Klaus Seuwen, Jason G. Cyster, and Andreas W. Sailer. 2011. "Oxysterols Direct Immune Cell Migration via EBI2." *Nature* 475(7357):524–27.

Hansen, Jens Jacob, Alexandra Dürr, Isabelle Cournu-Rebeix, Costa Georgopoulos, Debbie Ang, Marit Nyholm Nielsen, Claire-Sophie Davoine, Alexis Brice, Bertrand Fontaine, Niels Gregersen, and Peter Bross. 2002. "Hereditary Spastic Paraplegia SPG13 Is Associated with a Mutation in the Gene Encoding the Mitochondrial Chaperonin Hsp60." *The American Journal of Human Genetics* 70(5):1328–32.

Hanson, Phyllis I., Robyn Roth, Yuan Lin, and John E. Heuser. 2008. "Plasma Membrane Deformation by Circular Arrays of ESCRT-III Protein Filaments." *The Journal of Cell Biology* 180(2):389–402.

Hanson, Phyllis I. and Sidney W. Whiteheart. 2005. "AAA+ Proteins: Have Engine, Will Work." *Nature Reviews Molecular Cell Biology* 6(7):519–29.

Haque, Nazmul, Ryota Ouda, Chao Chen, Keiko Ozato, and J. Robert Hogg. 2018. "ZFR Coordinates Crosstalk between RNA Decay and Transcription in Innate Immunity." *Nature Communications* 9(1):1145.

Hara, Taichi, Kenji Nakamura, Makoto Matsui, Akitsugu Yamamoto, Yohko Nakahara, Rika Suzuki-Migishima, Minesuke Yokoyama, Kenji Mishima, Ichiro Saito, Hideyuki Okano, and Noboru Mizushima. 2006. "Suppression of Basal Autophagy in Neural Cells Causes Neurodegenerative Disease in Mice." *Nature* 441(7095):885–89.

Harashima, Ai, Toumy Guettouche, and Glen N. Barber. 2010. “Phosphorylation of the NFAR Proteins by the DsRNA-Dependent Protein Kinase PKR Constitutes a Novel Mechanism of Translational Regulation and Cellular Defense.” *Genes & Development* 24(23):2640–53.

Harbour, M. E., S. Y. A. Breusegem, R. Antrobus, C. Freeman, E. Reid, and M. N. J. Seaman. 2010. “The Cargo-Selective Retromer Complex Is a Recruiting Hub for Protein Complexes That Regulate Endosomal Tubule Dynamics.” *Journal of Cell Science* 123(21):3703–17.

Harbour, Michael E., Sophia Y. Breusegem, and Matthew N. J. Seaman. 2012. “Recruitment of the Endosomal WASH Complex Is Mediated by the Extended ‘Tail’ of Fam21 Binding to the Retromer Protein Vps35.” *Biochemical Journal* 442(1):209–20.

Harding, A. E. 1983. “CLASSIFICATION OF THE HEREDITARY ATAXIAS AND PARAPLEGIAS.” *The Lancet* 321(8334):1151–55.

Harrington, Anthony W. and David D. Ginty. 2013. “Long-Distance Retrograde Neurotrophic Factor Signalling in Neurons.” *Nature Reviews Neuroscience* 14(3):177–87.

Harterink, Martin, Fillip Port, Magdalena J. Lorenowicz, Ian J. McGough, Marie Silhankova, Marco C. Betist, Jan R. T. van Weering, Roy G. H. P. van Heesbeen, Teije C. Middelkoop, Konrad Basler, Peter J. Cullen, and Hendrik C. Korswagen. 2011. “A SNX3-Dependent Retromer Pathway Mediates Retrograde Transport of the Wnt Sorting Receptor Wntless and Is Required for Wnt Secretion.” *Nature Cell Biology* 13(8):914–23.

Hasdemir, Burcu, Daniel J. Fitzgerald, Ian A. Prior, Alexei V. Tepikin, and Robert D. Burgoyne. 2005. “Traffic of Kv4 K + Channels Mediated by KChIP1 Is via a Novel Post-ER Vesicular Pathway.” *The Journal of Cell Biology* 171(3):459–69.

Hauke, Sebastian, Alexander von Appen, Tooba Quidwai, Jonas Ries, and Richard Wombacher. 2017. “Specific Protein Labeling with Caged Fluorophores for Dual-Color Imaging and Super-Resolution Microscopy in Living Cells.” *Chemical Science* 8(1):559–66.

Hayashi-Nishino, Mitsuko, Naonobu Fujita, Takeshi Noda, Akihito Yamaguchi, Tamotsu Yoshimori, and Akitsugu Yamamoto. 2009. “A Subdomain of the Endoplasmic Reticulum Forms a Cradle for Autophagosome Formation.” *Nature Cell Biology* 11(12):1433–37.

Hazan, Jamilé, Nùria Fonknechten, Delphine Mavel, Caroline Paternotte, Delphine Samson, François Artiguenave, Claire-Sophie Davoine, Corinne Cruaud, Alexandra Dürr, Patrick Wincker, Philippe Brottier, Laurence Cattolico, Valérie Barbe, Jean-Marc Burgunder, Jean-François Prud'homme, Alexis Brice, Bertrand Fontaine, Roland Heilig, and Jean Weissenbach. 1999. "Spastin, a New AAA Protein, Is Altered in the Most Frequent Form of Autosomal Dominant Spastic Paraplegia." *Nature Genetics* 23(3):296–303.

Hein, Marco Y., Nina C. Hubner, Ina Poser, Jürgen Cox, Nagarjuna Nagaraj, Yusuke Toyoda, Igor A. Gak, Ina Weisswange, Jörg Mansfeld, Frank Buchholz, Anthony A. Hyman, and Matthias Mann. 2015. "A Human Interactome in Three Quantitative Dimensions Organized by Stoichiometries and Abundances." *Cell* 163(3):712–23.

Hensiek, Anke, Stephen Kirker, and Evan Reid. 2015. "Diagnosis, Investigation and Management of Hereditary Spastic Paraplegias in the Era of next-Generation Sequencing." *Journal of Neurology* 262(7):1601–12.

Herrera-Marcos, Luis V, Jose M. Lou-Bonafonte, Maria V Martinez-Gracia, Carmen Arnal, María A. Navarro, and Jesus Osada. 2018. "Prenylcysteine Oxidase 1, a pro-Oxidant Enzyme of Low Density Lipoproteins." *Frontiers in Bioscience (Landmark Edition)* 23:1020–37.

Heuer, Heike, Michael K. Maier, Sandra Iden, Jens Mittag, Edith C. H. Friesema, Theo J. Visser, and Karl Bauer. 2005. "The Monocarboxylate Transporter 8 Linked to Human Psychomotor Retardation Is Highly Expressed in Thyroid Hormone-Sensitive Neuron Populations." *Endocrinology* 146(4):1701–6.

Hierro, Aitor, Adriana L. Rojas, Raul Rojas, Namita Murthy, Grégory Effantin, Andrey V. Kajava, Alasdair C. Steven, Juan S. Bonifacino, and James H. Hurley. 2007. "Functional Architecture of the Retromer Cargo-Recognition Complex." *Nature* 449(7165):1063–67.

Hinnerwisch, Jörg, Wayne A. Fenton, Krystyna J. Furtak, George W. Farr, and Arthur L. Horwich. 2005. "Loops in the Central Channel of ClpA Chaperone Mediate Protein Binding, Unfolding, and Translocation." *Cell* 121(7):1029–41.

Hinshaw, Jenny E. and Sandra L. Schmid. 1995. "Dynamin Self-Assembles into Rings Suggesting a Mechanism for Coated Vesicle Budding." *Nature* 374(6518):190–92.

Hirokawa, Nobutaka, Shinsuke Niwa, and Yosuke Tanaka. 2010. "Molecular Motors in Neurons: Transport Mechanisms and Roles in Brain Function, Development, and Disease." *Neuron* 68(4):610–38.

Hirst, Jennifer, James R. Edgar, Typhaine Esteves, Frédéric Darios, Marianna Madeo, Jaerak Chang, Ricardo H. Roda, Alexandra Dürr, Mathieu Anheim, Cinzia Gellera, Jun Li, Stephan Züchner, Caterina Mariotti, Giovanni Stevanin, Craig Blackstone, Michael C. Kruer, and Margaret S. Robinson. 2015. "Loss of AP-5 Results in Accumulation of Aberrant Endolysosomes: Defining a New Type of Lysosomal Storage Disease." *Human Molecular Genetics* 24(17):4984–96.

Hirst, Jennifer, Carol Irving, and Georg H. H. Borner. 2013. "Adaptor Protein Complexes AP-4 and AP-5: New Players in Endosomal Trafficking and Progressive Spastic Paraplegia." *Traffic* 14(2):153–64.

Hirst, Jennifer, Daniel N. Itzhak, Robin Antrobus, Georg H. H. Borner, and Margaret S. Robinson. 2018. "Role of the AP-5 Adaptor Protein Complex in Late Endosome-to-Golgi Retrieval" edited by S. Schmid. *PLOS Biology* 16(1):e2004411.

Ho, Seok-Man, Brigham J. Hartley, Julia TCW, Michael Beaumont, Khalifa Stafford, Paul A. Slesinger, and Kristen J. Brennand. 2016. "Rapid Ngn2-Induction of Excitatory Neurons from HiPSC-Derived Neural Progenitor Cells." *Methods* 101:113–24.

Hobman, Tom C., Baoping Zhao, Honey Chan, and Marilyn Gist Farquhar. 1998. "Immunoisolation and Characterization of a Subdomain of the Endoplasmic Reticulum That Concentrates Proteins Involved in COPII Vesicle Biogenesis." *Molecular Biology of the Cell* 9(6):1265–78.

van der Hoek, Marjanne D., Ole Madsen, Jaap Keijer, and Feike R. van der Leij. 2018. "Evolutionary Analysis of the Carnitine- and Choline Acyltransferases Suggests Distinct Evolution of CPT2 versus CPT1 and Related Variants." *Biochimica et Biophysica Acta (BBA) - Molecular and Cell Biology of Lipids* 1863(8):909–18.

Hong, Zhi, Yanrui Yang, Cheng Zhang, Yang Niu, Ke Li, Xi Zhao, and Jia-Jia Liu. 2009. "The Retromer Component SNX6 Interacts with Dynactin P150Glued and Mediates Endosome-to-TGN Transport." *Cell Research* 19(12):1334–49.

Horgan, Conor P. and Mary W. McCaffrey. 2011. "Rab GTPases and Microtubule Motors." *Biochemical Society Transactions* 39(5):1202–6.

Hsu, FoSheng, Stephanie Spannl, Charles Ferguson, Anthony A. Hyman, Robert G. Parton, and Marino Zerial. 2018. "Rab5 and Alsin Regulate Stress-Activated Cytoprotective Signaling on Mitochondria." *ELife* 7.

Hsu, Victor W., Ming Bai, and Jian Li. 2012. "Getting Active: Protein Sorting in Endocytic Recycling." *Nature Reviews Molecular Cell Biology* 13(5):323–28.

Hu, Junjie and Tom A. Rapoport. 2016. “Fusion of the Endoplasmic Reticulum by Membrane-Bound GTPases.” *Seminars in Cell & Developmental Biology* 60:105–11.

Hu, Junjie, Yoko Shibata, Christiane Voss, Tom Shemesh, Zongli Li, Margaret Coughlin, Michael M. Kozlov, Tom A. Rapoport, and William A. Prinz. 2008. “Membrane Proteins of the Endoplasmic Reticulum Induce High-Curvature Tubules.” *Science* 319(5867):1247–50.

Hu, X., C. Viesselmann, S. Nam, E. Merriam, and Erik W. Dent. 2008. “Activity-Dependent Dynamic Microtubule Invasion of Dendritic Spines.” *Journal of Neuroscience* 28(49):13094–105.

Huang, Da Wei, Brad T. Sherman, and Richard A. Lempicki. 2009a. “Bioinformatics Enrichment Tools: Paths toward the Comprehensive Functional Analysis of Large Gene Lists.” *Nucleic Acids Research* 37(1):1–13.

Huang, Da Wei, Brad T. Sherman, and Richard A. Lempicki. 2009b. “Systematic and Integrative Analysis of Large Gene Lists Using DAVID Bioinformatics Resources.” *Nature Protocols* 4(1):44–57.

Hunt, S. D., A. K. Townley, C. M. Danson, P. J. Cullen, and D. J. Stephens. 2013. “Microtubule Motors Mediate Endosomal Sorting by Maintaining Functional Domain Organization.” *Journal of Cell Science* 126(11):2493–2501.

Hunt, Sylvie D. and David J. Stephens. 2011. “The Role of Motor Proteins in Endosomal Sorting.” *Biochemical Society Transactions* 39(5):1179–84.

Hurtado-Lorenzo, Andrés, Mhairi Skinner, Jaafar El Annan, Masamitsu Futai, Ge Hong Sun-Wada, Sylvain Bourgoin, James Casanova, Alan Wildeman, Shaliha Bechoua, Dennis A. Ausiello, Dennis Brown, and Vladimir Marshansky. 2006. “V-ATPase Interacts with ARNO and Arf6 in Early Endosomes and Regulates the Protein Degradative Pathway.” *Nature Cell Biology* 8(2):124–36.

Ilgaz Aydinlar, Elif, Arndt Rolfs, Mustafa Serteser, and Yesim Parman. 2014. “Mutation in FAM134B Causing Hereditary Sensory Neuropathy with Spasticity in a Turkish Family.” *Muscle & Nerve* 49(5):774–75.

Inloes, J. M., K. L. Hsu, M. M. Dix, A. Viader, K. Masuda, T. Takei, M. R. Wood, and B. F. Cravatt. 2014. “The Hereditary Spastic Paraplegia-Related Enzyme DDHD2 Is a Principal Brain Triglyceride Lipase.” *Proceedings of the National Academy of Sciences* 111(41):14924–29.

Ishihara, Naotada, Maho Hamasaki, Sadaki Yokota, Kuninori Suzuki, Yoshiaki Kamada, Akio Kihara, Tamotsu Yoshimori, Takeshi Noda, and Yoshinori Ohsumi. 2001. "Autophagosome Requires Specific Early Sec Proteins for Its Formation and NSF/SNARE for Vacuolar Fusion" edited by C. Kaiser. *Molecular Biology of the Cell* 12(11):3690–3702.

Ishiura, Hiroyuki, Wataru Sako, Mari Yoshida, Toshitaka Kawarai, Osamu Tanabe, Jun Goto, Yuji Takahashi, Hidetoshi Date, Jun Mitsui, Budrul Ahsan, Yaeko Ichikawa, Atsushi Iwata, Hiide Yoshino, Yuishin Izumi, Koji Fujita, Kouji Maeda, Satoshi Goto, Hidetaka Koizumi, Ryoma Morigaki, Masako Ikemura, Naoko Yamauchi, Shigeo Murayama, Garth A. Nicholson, Hidefumi Ito, Gen Sobue, Masanori Nakagawa, Ryuji Kaji, and Shoji Tsuji. 2012. "The TRK-Fused Gene Is Mutated in Hereditary Motor and Sensory Neuropathy with Proximal Dominant Involvement." *The American Journal of Human Genetics* 91(2):320–29.

Islam, Farhadul, Vinod Gopalan, and Alfred King-yin Lam. 2018. "RETREG1 (FAM134B): A New Player in Human Diseases: 15 Years after the Discovery in Cancer." *Journal of Cellular Physiology* 233(6):4479–89.

Itoh, Masahiko, Hiroyuki Sasaki, Mikio Furuse, Harunobu Ozaki, Toru Kita, and Shoichiro Tsukita. 2001. "Junctional Adhesion Molecule (JAM) Binds to PAR-3." *The Journal of Cell Biology* 154(3):491–98.

Ivins, J. K., P. D. Yurchenco, and A. D. Lander. 2000. "Regulation of Neurite Outgrowth by Integrin Activation." *The Journal of Neuroscience* 20(17):6551–60.

Jackson, Verity A., Shahid Mehmood, Matthieu Chavent, Pietro Roversi, Maria Carrasquero, Daniel del Toro, Goenuel Seyit-Bremer, Fanomezana M. Ranaivoson, Davide Comoletti, Mark S. P. Sansom, Carol V. Robinson, Rüdiger Klein, and Elena Seiradake. 2016. "Super-Complexes of Adhesion GPCRs and Neural Guidance Receptors." *Nature Communications* 7(1):11184.

Jahic, Amir, Anne K. Erichsen, Thomas Deufel, Chantal M. Tallaksen, and Christian Beetz. 2016. "A Polymorphic Alu Insertion That Mediates Distinct Disease-Associated Deletions." *European Journal of Human Genetics* 24(9):1371–74.

Jakobsson, J., F. Ackermann, F. Andersson, D. Larhammar, P. Low, and L. Brodin. 2011. "Regulation of Synaptic Vesicle Budding and Dynamin Function by an EHD ATPase." *Journal of Neuroscience* 31(39):13972–80.

Janke, Carsten and Jeannette Chloë Bulinski. 2011. “Post-Translational Regulation of the Microtubule Cytoskeleton: Mechanisms and Functions.” *Nature Reviews Molecular Cell Biology* 12(12):773–86.

Jardin, Nicolas, François Giudicelli, Daniel Ten Martín, Anaïs Vitrac, Stéphanie De Gois, Rachel Allison, Corinne Houart, Evan Reid, Jamilé Hazan, and Coralie Fassier. 2018. “BMP- and Neuropilin 1-Mediated Motor Axon Navigation Relies on Spastin Alternative Translation.” *Development* 145(17):dev162701.

Jeon, Daejong, Yu-Mi Yang, Myung-Jin Jeong, Kenneth D. Philipson, Hyewhon Rhim, and Hee-Sup Shin. 2003. “Enhanced Learning and Memory in Mice Lacking Na+/Ca2+ Exchanger 2.” *Neuron* 38(6):965–76.

Ji, Wei-ke, Anna L. Hatch, Ronald A. Merrill, Stefan Strack, and Henry N. Higgs. 2015. “Actin Filaments Target the Oligomeric Maturation of the Dynamin GTPase Drp1 to Mitochondrial Fission Sites.” *ELife* 4.

Ji, Young Rae, Sunita Warrier, Tao Jiang, Doris K. Wu, and Katie S. Kindt. 2018. “Directional Selectivity of Afferent Neurons in Zebrafish Neuromasts Is Regulated by Emx2 in Presynaptic Hair Cells.” *ELife* 7.

Jin, Luyuan, Yu Cao, Guoxia Yu, Jinsong Wang, Xiao Lin, Lihua Ge, Juan Du, Liping Wang, Shu Diao, Xiaomeng Lian, Songlin Wang, Rui Dong, and Zhaochen Shan. 2017. “SFRP2 Enhances the Osteogenic Differentiation of Apical Papilla Stem Cells by Antagonizing the Canonical WNT Pathway.” *Cellular & Molecular Biology Letters* 22(1):14.

Jin, Mingjie and Martin D. Snider. 1993. “Role of Microtubules in Transferrin Receptor Transport from the Cell Surface to Endosomes and the Golgi Complex.” *The Journal of Biological Chemistry* 268(24):18390–97.

Jinushi-Nakao, Shiho, Ramanathan Arvind, Reiko Amikura, Emi Kinameri, Andrew Winston Liu, and Adrian Walton Moore. 2007. “Knot/Collier and Cut Control Different Aspects of Dendrite Cytoskeleton and Synergize to Define Final Arbor Shape.” *Neuron* 56(6):963–78.

Johnson, A., N. Bhattacharya, M. Hanna, J. G. Pennington, A. L. Schuh, L. Wang, M. S. Otegui, S. M. Stagg, and A. Audhya. 2015. “TFG Clusters COPII-Coated Transport Carriers and Promotes Early Secretory Pathway Organization.” *The EMBO Journal* 34(6):811–27.

Johnson, Dan, Anthony Lanahan, C. Rand. Buck, Amita Sehgal, Claudia Morgan, Eric Mercer, Mark Bothwell, and Moses Chao. 1986. “Expression and Structure of the Human NGF Receptor.” *Cell* 47(4):545–54.

Jonas, M. C., M. Pehar, and L. Puglielli. 2010. “AT-1 Is the ER Membrane Acetyl-CoA Transporter and Is Essential for Cell Viability.” *Journal of Cell Science* 123(19):3378–88.

Jouet, Monique, André Rosenthal, Giles Armstrong, John MacFarlane, Roger Stevenson, Joan Paterson, Aïda Metzenberg, Victor Ionasescu, Karen Temple, and Susan Kenwrick. 1994. “X–linked Spastic Paraplegia (SPG1), MASA Syndrome and X–linked Hydrocephalus Result from Mutations in the L1 Gene.” *Nature Genetics* 7(3):402–7.

Kaberniuk, Andrii A., Nicholas C. Morano, Vladislav V. Verkhusha, and Erik Lee Snapp. 2017. “MoxDendra2: An Inert Photoswitchable Protein for Oxidizing Environments.” *Chemical Communications* 53(13):2106–9.

Kagara, Naofumi, Natsumi Tanaka, Shinzaburo Noguchi, and Toshio Hirano. 2007. “Zinc and Its Transporter ZIP10 Are Involved in Invasive Behavior of Breast Cancer Cells.” *Cancer Science* 98(5):692–97.

Kaksonen, Marko and Aurélien Roux. 2018. “Mechanisms of Clathrin-Mediated Endocytosis.” *Nature Reviews Molecular Cell Biology* 19(5):313–26.

Kalil, Katherine and Erik W. Dent. 2014. “Branch Management: Mechanisms of Axon Branching in the Developing Vertebrate CNS.” *Nature Reviews Neuroscience* 15(1):7–18.

Kalil, Katherine, Gyorgyi Szebenyi, and Erik W. Dent. 2000. “Common Mechanisms Underlying Growth Cone Guidance and Axon Branching.” *Journal of Neurobiology* 44(2):145–58.

Kanai, Fumihiko, Hui Liu, Seth J. Field, Hares Akbary, Tsuyoshi Matsuo, Glenn E. Brown, Lewis C. Cantley, and Michael B. Yaffe. 2001. “The PX Domains of P47phox and P40phox Bind to Lipid Products of PI(3)K.” *Nature Cell Biology* 3(7):675–78.

Kancheva, Dahlia, Teodora Chamova, Velina Guergueltcheva, Vanio Mitev, Dimitar N. Azmanov, Luba Kalaydjieva, Ivailo Tournev, and Albena Jordanova. 2015. “Mosaic Dominant TUBB4A Mutation in an Inbred Family with Complicated Hereditary Spastic Paraplegia.” *Movement Disorders* 30(6):854–58.

Kasher, Paul R., Kurt J. De Vos, Stephen B. Wharton, Catherine Manser, Ellen J. Bennett, Megan Bingley, Jonathan D. Wood, Roy Milner, Christopher J. McDermott, Christopher C. J. Miller, Pamela J. Shaw, and Andrew J. Grierson. 2009. "Direct Evidence for Axonal Transport Defects in a Novel Mouse Model of Mutant Spastin-Induced Hereditary Spastic Paraplegia (HSP) and Human HSP Patients." *Journal of Neurochemistry* 110(1):34–44.

Kawano, H., T. Nakatani, T. Mori, S. Ueno, M. Fukaya, A. Abe, M. Kobayashi, F. Toda, M. Watanabe, and I. Matsuoka. 2004. "Identification and Characterization of Novel Developmentally Regulated Neural-Specific Proteins, BRINP Family." *Molecular Brain Research* 125(1–2):60–75.

Keating, Thomas J. and Gary G. Borisy. 1999. "Centrosomal and Non-Centrosomal Microtubules." *Biology of the Cell* 91(4–5):321–29.

Keightley, Margaret C., Pamela Brown, Henry N. Jabbour, and Kurt J. Sales. 2010. "F-Prostaglandin Receptor Regulates Endothelial Cell Function via Fibroblast Growth Factor-2." *BMC Cell Biology* 11(1):8.

Kern, Andreas, Ivan Dikic, and Christian Behl. 2015. "The Integration of Autophagy and Cellular Trafficking Pathways via RAB GAPs." *Autophagy* 11(12):2393–97.

Khalili, Amelia and Mohd Ahmad. 2015. "A Review of Cell Adhesion Studies for Biomedical and Biological Applications." *International Journal of Molecular Sciences* 16(8):18149–84.

Khundadze, Mukhran, Katrin Kollmann, Nicole Koch, Christoph Biskup, Sandor Nietzsche, Geraldine Zimmer, J. Christopher Hennings, Antje K. Huebner, Judit Symmank, Amir Jahic, Elena I. Ilina, Kathrin Karle, Ludger Schöls, Michael Kessels, Thomas Braulke, Britta Qualmann, Ingo Kurth, Christian Beetz, and Christian A. Hübner. 2013. "A Hereditary Spastic Paraplegia Mouse Model Supports a Role of ZFYVE26/SPASTIZIN for the Endolysosomal System" edited by G. S. Barsh. *PLoS Genetics* 9(12):e1003988.

Kieffer, Collin, Jack J. Skalicky, Eiji Morita, Ivana De Domenico, Diane M. Ward, Jerry Kaplan, and Wesley I. Sundquist. 2008. "Two Distinct Modes of ESCRT-III Recognition Are Required for VPS4 Functions in Lysosomal Protein Targeting and HIV-1 Budding." *Developmental Cell* 15(1):62–73.

Kim, Dong Wan, Taichi Uetsuki, Yoshito Kaziro, Nobuo Yamaguchi, and Sumio Sugano. 1990. "Use of the Human Elongation Factor 1α Promoter as a Versatile and Efficient Expression System." *Gene* 91(2):217–23.

Kim, U., Y. Wang, T. Sanford, Y. Zeng, and K. Nishikura. 1994. “Molecular Cloning of CDNA for Double-Stranded RNA Adenosine Deaminase, a Candidate Enzyme for Nuclear RNA Editing.” *Proceedings of the National Academy of Sciences* 91(24):11457–61.

Kishigami, Satoshi, Shun-Ichi Yoshikawa, Trisha Castranio, Kenji Okazaki, Yasuhide Furuta, and Yuji Mishina. 2004. “BMP Signaling through ACVRI Is Required for Left–right Patterning in the Early Mouse Embryo.” *Developmental Biology* 276(1):185–93.

Kleaveland, Benjamin, Xiangjian Zheng, Jian J. Liu, Yannick Blum, Jennifer J. Tung, Zhiying Zou, Shawn M. Sweeney, Mei Chen, Lili Guo, Min-min Lu, Diane Zhou, Jan Kitajewski, Markus Affolter, Mark H. Ginsberg, and Mark L. Kahn. 2009. “Regulation of Cardiovascular Development and Integrity by the Heart of Glass–cerebral Cavernous Malformation Protein Pathway.” *Nature Medicine* 15(2):169–76.

Klebe, S., G. Stevanin, and C. Depienne. 2015. “Clinical and Genetic Heterogeneity in Hereditary Spastic Paraplegias: From SPG1 to SPG72 and Still Counting.” *Revue Neurologique* 171(6–7):505–30.

Knöll, Bernd, Christine Weinl, Alfred Nordheim, and Friedrich Bonhoeffer. 2007. “Stripe Assay to Examine Axonal Guidance and Cell Migration.” *Nature Protocols* 2(5):1216–24.

Konishi, Y., L. B. Yang, P. He, K. Lindholm, B. Lu, R. Li, and Y. Shen. 2014. “Deficiency of GDNF Receptor GFR 1 in Alzheimer’s Neurons Results in Neuronal Death.” *Journal of Neuroscience* 34(39):13127–38.

Korobchevskaya, Kseniya, B. Lagerholm, Huw Colin-York, and Marco Fritzsche. 2017. “Exploring the Potential of Airyscan Microscopy for Live Cell Imaging.” *Photonics* 4(4):41.

Korobova, Farida, Timothy J. Gauvin, and Henry N. Higgs. 2014. “A Role for Myosin II in Mammalian Mitochondrial Fission.” *Current Biology* 24(4):409–14.

Korobova, Farida, Vinay Ramabhadran, and Henry N. Higgs. 2013. “An Actin-Dependent Step in Mitochondrial Fission Mediated by the ER-Associated Formin INF2.” *Science* 339(6118):464–67.

Kostelansky, Michael S., Cayetana Schluter, Yuen Yi C. Tam, Sangho Lee, Rodolfo Ghirlando, Bridgette Beach, Elizabeth Conibear, and James H. Hurley. 2007. “Molecular Architecture and Functional Model of the Complete Yeast ESCRT-I Heterotetramer.” *Cell* 129(3):485–98.

Kucharczyk, Roza, Michael Zick, Maïlis Bietenhader, Malgorzata Rak, Elodie Couplan, Marc Blondel, Stéphane-Duvezin Caubet, and Jean-Paul di Rago. 2009. “Mitochondrial ATP Synthase Disorders: Molecular Mechanisms and the Quest for Curative Therapeutic Approaches.” *Biochimica et Biophysica Acta (BBA) - Molecular Cell Research* 1793(1):186–99.

Kung, Leslie F., Silvere Pagant, Eugene Futai, Jennifer G. D’Arcangelo, Roy Buchanan, John C. Dittmar, Robert J. D. Reid, Rodney Rothstein, Susan Hamamoto, Erik L. Snapp, Randy Schekman, and Elizabeth A. Miller. 2012. “Sec24p and Sec16p Cooperate to Regulate the GTP Cycle of the COPII Coat.” *The EMBO Journal* 31(4):1014–27.

Kurup, Naina, Dong Yan, Alexandr Goncharov, and Yishi Jin. 2015. “Dynamic Microtubules Drive Circuit Rewiring in the Absence of Neurite Remodeling.” *Current Biology* 25(12):1594–1605.

Kvainickas, Arunas, Ana Jimenez-Orgaz, Heike Nägele, Zehan Hu, Jörn Dengjel, and Florian Steinberg. 2017. “Cargo-Selective SNX-BAR Proteins Mediate Retromer Trimer Independent Retrograde Transport.” *The Journal of Cell Biology* 216(11):3677–93.

Lacroix, Benjamin, Juliette van Dijk, Nicholas D. Gold, Julien Guizetti, Gudrun Aldrian-Herrada, Krzysztof Rogowski, Daniel W. Gerlich, and Carsten Janke. 2010. “Tubulin Polyglutamylation Stimulates Spastin-Mediated Microtubule Severing.” *The Journal of Cell Biology* 189(6):945–54.

Lacroix, Jerome J., Wesley M. Botello-Smith, and Yun Luo. 2018. “Probing the Gating Mechanism of the Mechanosensitive Channel Piezo1 with the Small Molecule Yoda1.” *Nature Communications* 9(1):2029.

Lafay, F. 1974. “Envelope Proteins of Vesicular Stomatitis Virus: Effect of Temperature-Sensitive Mutations in Complementation Groups III and V.” *Journal of Virology* 14(5):1220–28.

Lai, Chen, Chengsong Xie, Hoon Shim, Jayanth Chandran, Brian W. Howell, and Huaibin Cai. 2009. “Regulation of Endosomal Motility and Degradation by Amyotrophic Lateral Sclerosis 2/Alsin.” *Molecular Brain* 2(1):23.

Landouré, Guida, Peng-Peng Zhu, Charles M. Lourenço, Janel O. Johnson, Camilo Toro, Katherine V. Bricceno, Carlo Rinaldi, Katherine G. Meilleur, Modibo Sangaré, Oumarou Diallo, Tyler M. Pierson, Hiroyuki Ishiura, Shoji Tsuji, Nichole Hein, John K. Fink, Marion Stoll, Garth Nicholson, Michael A. Gonzalez, Fiorella Speziani, Alexandra Dürr, Giovanni Stevanin, Leslie G. Biesecker, John Accardi, Dennis M. D. Landis, William A. Gahl, Bryan J. Traynor, Wilson Marques, Stephan Züchner, Craig Blackstone, Kenneth H. Fischbeck, and Barrington G. Burnett. 2013. "Hereditary Spastic Paraplegia Type 43 (SPG43) Is Caused by Mutation in C19orf12." *Human Mutation* 34(10):1357–60.

de Lange, R. P. J., A. D. G. de Roos, and J. G. G. Borst. 2003. "Two Modes of Vesicle Recycling in the Rat Calyx of Held." *The Journal of Neuroscience* 23(31):10164–73.

Lata, Suman, Guy Schoehn, Ankur Jain, Ricardo Pires, Jacob Piehler, Heinrich G. Gottlinger, and Winfried Weissenhorn. 2008. "Helical Structures of ESCRT-III Are Disassembled by VPS4." *Science* 321(5894):1354–57.

Lauffer, Benjamin E. L., Cristina Melero, Paul Temkin, Cai Lei, Wanjin Hong, Tanja Kortemme, and Mark Von Zastrow. 2010. "SNX27 Mediates PDZ-Directed Sorting from Endosomes to the Plasma Membrane." *Journal of Cell Biology* 190(4):565–74.

Lebrun-Julien, Frédéric, Barbara Morquette, Annie Douillette, H. Uri Saragovi, and Adriana Di Polo. 2009. "Inhibition of P75NTR in Glia Potentiates TrkA-Mediated Survival of Injured Retinal Ganglion Cells." *Molecular and Cellular Neuroscience* 40(4):410–20.

Lee, Jason E., Laura M. Westrate, Haoxi Wu, Cynthia Page, and Gia K. Voeltz. 2016. "Multiple Dynamin Family Members Collaborate to Drive Mitochondrial Division." *Nature* 540(7631):139–43.

Lee, Jong-Ho, Haitao Ji, and Zhimin Lu. 2016. "FAM129B Activates Ras and Promotes Aerobic Glycolysis." *Cell Cycle* 15(11):1391–92.

Lee, Marcus C. S., Lelio Orci, Susan Hamamoto, Eugene Futai, Mariella Ravazzola, and Randy Schekman. 2005. "Sar1p N-Terminal Helix Initiates Membrane Curvature and Completes the Fission of a COPII Vesicle." *Cell* 122(4):605–17.

Lee, Peter L., Maikke B. Ohlson, and Suzanne R. Pfeffer. 2015. "The Rab6-Regulated KIF1C Kinesin Motor Domain Contributes to Golgi Organization." *ELife* 4.

Lenz, J. H., I. Schuchardt, A. Straube, and G. Steinberg. 2006. "A Dynein Loading Zone for Retrograde Endosome Motility at Microtubule Plus-Ends." *The EMBO Journal* 25(11):2275–86.

Lenz, Martin, Sandrine Morlot, and Aurélien Roux. 2009. “Mechanical Requirements for Membrane Fission: Common Facts from Various Examples.” *FEBS Letters* 583(23):3839–46.

Lenzen, Christian U., Diana Steinmann, Sidney W. Whiteheart, and William I. Weis. 1998. “Crystal Structure of the Hexamerization Domain of N-Ethylmaleimide–Sensitive Fusion Protein.” *Cell* 94(4):525–36.

Leo, Lanfranco, Carina Weissmann, Matthew Burns, Minsu Kang, Yuyu Song, Liang Qiang, Scott T. Brady, Peter W. Baas, and Gerardo Morfini. 2017. “Mutant Spastin Proteins Promote Deficits in Axonal Transport through an Isoform-Specific Mechanism Involving Casein Kinase 2 Activation.” *Human Molecular Genetics* 26(12):2321–34.

Leone, M., E. Bottacchi, G. D’Alessandro, and S. Kustermann. 2009. “Hereditary Ataxias and Paraplegias in Valle ĎAosta, Italy: A Study of Prevalence and Disability.” *Acta Neurologica Scandinavica* 91(3):183–87.

Levi-Montalcini, R., L. Aloe, E. Mugnaini, F. Oesch, and H. Thoenen. 1975. “Nerve Growth Factor Induces Volume Increase and Enhances Tyrosine Hydroxylase Synthesis in Chemically Axotomized Sympathetic Ganglia of Newborn Rats.” *Proceedings of the National Academy of Sciences* 72(2):595–99.

Levi-Montalcini, Rita. 1987. “The Nerve Growth Factor 35 Years Later.” *Science* 237(4819):1154–62.

Levy-Rimler, Galit, Paul Viitanen, Celeste Weiss, Rajach Sharkia, Anat Greenberg, Adina Niv, Ariel Lustig, Yacov Delarea, and Abdussalam Azem. 2001. “The Effect of Nucleotides and Mitochondrial Chaperonin 10 on the Structure and Chaperone Activity of Mitochondrial Chaperonin 60.” *European Journal of Biochemistry* 268(12):3465–72.

Levy, Shoshana, Scott C. Todd, and Holden T. Maecker. 1998. “CD81 (TAPA-1): A MOLECULE INVOLVED IN SIGNAL TRANSDUCTION AND CELL ADHESION IN THE IMMUNE SYSTEM.” *Annual Review of Immunology* 16(1):89–109.

Li, Haiying, Yeon Koo, Xicheng Mao, Luis Sifuentes-Dominguez, Lindsey L. Morris, Da Jia, Naoteru Miyata, Rebecca A. Faulkner, Jan M. van Deursen, Marc Vooijs, Daniel D. Billadeau, Bart van de Sluis, Ondine Cleaver, and Ezra Burstein. 2015. “Endosomal Sorting of Notch Receptors through COMMD9-Dependent Pathways Modulates Notch Signaling.” *The Journal of Cell Biology* 211(3):605–17.

Li, L. Y., H. Chen, Y. H. Hsieh, Y. N. Wang, H. J. Chu, Y. H. Chen, H. Y. Chen, P. J. Chien, H. T. Ma, H. C. Tsai, C. C. Lai, Y. P. Sher, H. C. Lien, C. H. Tsai, and M. C. Hung. 2011. "Nuclear ErbB2 Enhances Translation and Cell Growth by Activating Transcription of Ribosomal RNA Genes." *Cancer Research* 71(12):4269–79.

Li, Miaoxin, Philip Wing-Lok Ho, Shirley Yin-Yu Pang, Zero Ho-Man Tse, Michelle Hiu-Wai Kung, Pak-Chung Sham, and Shu-Leong Ho. 2014. "PMCA4 (ATP2B4) Mutation in Familial Spastic Paraplegia" edited by M. Seaman. *PLoS ONE* 9(8):e104790.

Lin, Jing-Ping, Yevgeniya A. Mironova, Peter Shrager, and Roman J. Giger. 2017. "LRP1 Regulates Peroxisome Biogenesis and Cholesterol Homeostasis in Oligodendrocytes and Is Required for Proper CNS Myelin Development and Repair." *ELife* 6.

Lin, Pengfei, Jianwei Li, Qiji Liu, Fei Mao, Jisheng Li, Rongfang Qiu, Huili Hu, Yang Song, Yang Yang, Guimin Gao, Chuanzhu Yan, Wanling Yang, Changshun Shao, and Yaoqin Gong. 2008. "A Missense Mutation in SLC33A1, Which Encodes the Acetyl-CoA Transporter, Causes Autosomal-Dominant Spastic Paraplegia (SPG42)." *The American Journal of Human Genetics* 83(6):752–59.

Lindeboom, Jelmer J., Masayoshi Nakamura, Anneke Hibbel, Kostya Shundyak, Ryan Gutierrez, Tijs Ketelaar, Anne Mie C. Emons, Bela M. Mulder, Viktor Kirik, and David W. Ehrhardt. 2013. "A Mechanism for Reorientation of Cortical Microtubule Arrays Driven by Microtubule Severing." *Science* 342(6163):1245533–1245533.

Lindroth, Anders M., David Shultis, Zuzana Jasencakova, Jörg Fuchs, Lianna Johnson, Daniel Schubert, Debasis Patnaik, Sriharsa Pradhan, Justin Goodrich, Ingo Schubert, Thomas Jenuwein, Sepideh Khorasanizadeh, and Steven E. Jacobsen. 2004. "Dual Histone H3 Methylation Marks at Lysines 9 and 27 Required for Interaction with CHROMOMETHYLASE3." *The EMBO Journal* 23(21):4146–55.

Liu, Yi-Shi, Xin-Yu Guo, Tetsuya Hirata, Yao Rong, Daisuke Motooka, Toshihiko Kitajima, Yoshiko Murakami, Xiao-Dong Gao, Shota Nakamura, Taroh Kinoshita, and Morihisa Fujita. 2018. "N -Glycan–dependent Protein Folding and Endoplasmic Reticulum Retention Regulate GPI-Anchor Processing." *The Journal of Cell Biology* 217(2):585–99.

Llorente, Alicia, Andrzej Rapak, Sandra L. Schmid, Bo van Deurs, and Kirsten Sandvig. 1998. "Expression of Mutant Dynamin Inhibits Toxicity and Transport of Endocytosed Ricin to the Golgi Apparatus." *The Journal of Cell Biology* 140(3):553–63.

Long, Kimberly R., Yasunori Yamamoto, Adam L. Baker, Simon C. Watkins, Carolyn B. Coyne, James F. Conway, and Meir Aridor. 2010. “Sar1 Assembly Regulates Membrane Constriction and ER Export.” *The Journal of Cell Biology* 190(1):115–28.

Lossos, Alexander, C. Stumpfig, Giovanni Stevanin, Marion Gaussen, B. E. Zimmerman, Emeline Mundwiller, Moriya Asulin, Liat Chamma, Ruth Sheffer, Adel Misk, Shlomo Dotan, John M. Gomori, Penina Ponger, Alexis Brice, Israela Lerer, Vardiella Meiner, and Roland Lill. 2015. “Fe/S Protein Assembly Gene IBA57 Mutation Causes Hereditary Spastic Paraplegia.” *Neurology* 84(7):659–67.

Lu, JianPing, Faiza Rashid, and Paula C. Byrne. 2006. “The Hereditary Spastic Paraplegia Protein Spartin Localises to Mitochondria.” *Journal of Neurochemistry* 98(6):1908–19.

Lucas, María, David C. Gershlick, Ander Vidaurrazaga, Adriana L. Rojas, Juan S. Bonifacino, and Aitor Hierro. 2016. “Structural Mechanism for Cargo Recognition by the Retromer Complex.” *Cell* 167(6):1623–1635.e14.

Lukinavičius, Gražvydas, Luc Reymond, Elisa D’Este, Anastasiya Masharina, Fabian Göttfert, Haisen Ta, Angelika Güther, Mathias Fournier, Stefano Rizzo, Herbert Waldmann, Claudia Blaukopf, Christoph Sommer, Daniel W. Gerlich, Hans-Dieter Arndt, Stefan W. Hell, and Kai Johnsson. 2014. “Fluorogenic Probes for Live-Cell Imaging of the Cytoskeleton.” *Nature Methods* 11(7):731–33.

MacDonald, Ewan, Louise Brown, Arnaud Selvais, Han Liu, Thomas Waring, Daniel Newman, Jessica Bithell, Douglas Grimes, Sylvie Urbé, Michael J. Clague, and Tobias Zech. 2018. “HRS–WASH Axis Governs Actin-Mediated Endosomal Recycling and Cell Invasion.” *The Journal of Cell Biology* 217(7):2549–64.

Macedo-Souza, Lúcia Inês, Fernando Kok, Silvana Santos, Luciana Licinio, Karina Lezirovitz, Natale Cavaçana, Clarissa Bueno, Simone Amorim, André Pessoa, Zodja Graciani, Áurea Ferreira, Abdísio Prazeres, Áurea Nogueira de Melo, Paulo Alberto Otto, and Mayana Zatz. 2009. “Spastic Paraplegia, Optic Atrophy, and Neuropathy: New Observations, Locus Refinement, and Exclusion of Candidate Genes.” *Annals of Human Genetics* 73(3):382–87.

MacInnis, Bronwyn L. and Robert B. Campenot. 2005. “Regulation of Wallerian Degeneration and Nerve Growth Factor Withdrawal-Induced Pruning of Axons of Sympathetic Neurons by the Proteasome and the MEK/Erk Pathway.” *Molecular and Cellular Neuroscience* 28(3):430–39.

Mackenzie, Bryan and Jeffrey D. Erickson. 2004. “Sodium-Coupled Neutral Amino Acid (System N/A) Transporters of the SLC38 Gene Family.” *Pflugers Archiv European Journal of Physiology* 447(5):784–95.

Mackenzie, Bryan, Hitomi Takanaga, Nadia Hubert, Andreas Rolfs, and Matthias A. Hediger. 2007. “Functional Properties of Multiple Isoforms of Human Divalent Metal-Ion Transporter 1 (DMT1).” *Biochemical Journal* 403(1):59–69.

Maier, André, Eva Klopocki, Denise Horn, Andreas Tzschach, Teresa Holm, Robert Meyer, and Thomas Meyer. 2014. “De Novo Partial Deletion in GRID2 Presenting with Complicated Spastic Paraplegia.” *Muscle & Nerve* 49(2):289–92.

Maldonado, Eduardo N., Nathan L. Alderson, Paula V. Monje, Patrick M. Wood, and Hiroko Hama. 2008. “FA2H Is Responsible for the Formation of 2-Hydroxy Galactolipids in Peripheral Nervous System Myelin.” *Journal of Lipid Research* 49(1):153–61.

Malhotra, Vivek and Patrik Erlmann. 2015. “The Pathway of Collagen Secretion.” *Annual Review of Cell and Developmental Biology* 31(1):109–24.

Mancuso, Giuseppe and Elena I. Rugarli. 2008. “A Cryptic Promoter in the First Exon of the SPG4 Gene Directs the Synthesis of the 60-KDa Spastin Isoform.” *BMC Biology* 6(1):31.

Mangravite, Lara M., Guangqing Xiao, and Kathleen M. Giacomini. 2003. “Localization of Human Equilibrative Nucleoside Transporters, HENT1 and HENT2, in Renal Epithelial Cells.” *American Journal of Physiology-Renal Physiology* 284(5):F902–10.

Mannan, Ashraf U., Johann Boehm, Simone M. Sauter, Anne Rauber, Paula C. Byrne, Juergen Neesen, and Wolfgang Engel. 2006. “Spastin, the Most Commonly Mutated Protein in Hereditary Spastic Paraplegia Interacts with Reticulon 1 an Endoplasmic Reticulum Protein.” *Neurogenetics* 7(2):93–103.

Mao, Junhao, Jiyong Wang, Bo Liu, Weijun Pan, Gist H. Farr, Christopher Flynn, Huidong Yuan, Shinji Takada, David Kimelman, Lin Li, and Dianqing Wu. 2001. “Low-Density Lipoprotein Receptor-Related Protein-5 Binds to Axin and Regulates the Canonical Wnt Signaling Pathway.” *Molecular Cell* 7(4):801–9.

Margadant, Coert, Hanneke N. Monsuur, Jim C. Norman, and Arnoud Sonnenberg. 2011. “Mechanisms of Integrin Activation and Trafficking.” *Current Opinion in Cell Biology* 23(5):607–14.

María Frade, José, Alfredo Rodríguez-Tébar, and Yves-Alain Barde. 1996. “Induction of Cell Death by Endogenous Nerve Growth Factor through Its P75 Receptor.” *Nature* 383(6596):166–68.

Marks, Bruno, Michael H. B. Stowell, Yvonne Vallis, Ian G. Mills, Adele Gibson, Colin R. Hopkins, and Harvey T. McMahon. 2001. “GTPase Activity of Dynamin and Resulting Conformation Change Are Essential for Endocytosis.” *Nature* 410(6825):231–35.

Marsh, M., G. Griffiths, G. E. Dean, I. Mellman, and A. Helenius. 1986. “Three-Dimensional Structure of Endosomes in BHK-21 Cells.” *Proceedings of the National Academy of Sciences* 83(9):2899–2903.

Martín-Villar, Ester, Francisco G. Scholl, Carlos Gamallo, Maria M. Yurrita, Mario Muñoz-Guerra, Jesús Cruces, and Miguel Quintanilla. 2005. “Characterization of Human PA2.26 Antigen (T1α-2, Podoplanin), a Small Membrane Mucin Induced in Oral Squamous Cell Carcinomas.” *International Journal of Cancer* 113(6):899–910.

Martin, Elodie, Rebecca Schüle, Katrien Smets, Agnès Rastetter, Amir Boukhris, José L. Loureiro, Michael A. Gonzalez, Emeline Mundwiller, Tine Deconinck, Marc Wessner, Ludmila Jornea, Andrés Caballero Oteyza, Alexandra Durr, Jean-Jacques Martin, Ludger Schöls, Chokri Mhiri, Foudil Lamari, Stephan Züchner, Peter De Jonghe, Edor Kabashi, Alexis Brice, and Giovanni Stevanin. 2013. “Loss of Function of Glucocerebrosidase GBA2 Is Responsible for Motor Neuron Defects in Hereditary Spastic Paraplegia.” *The American Journal of Human Genetics* 92(2):238–44.

Martina, Enrico, Martin Degen, Curzio Rüegg, Adrian Merlo, Maddalena M. Lino, Ruth Chiquet-Ehrismann, and Florence Brellier. 2010. “Tenascin-W Is a Specific Marker of Glioma-Associated Blood Vessels and Stimulates Angiogenesis in Vitro.” *The FASEB Journal* 24(3):778–87.

Martini-Stoica, Heidi, Yin Xu, Andrea Ballabio, and Hui Zheng. 2016. “The Autophagy–Lysosomal Pathway in Neurodegeneration: A TFEB Perspective.” *Trends in Neurosciences* 39(4):221–34.

Matanis, Theodoros, Anna Akhmanova, Phebe Wulf, Elaine Del Nery, Thomas Weide, Tatiana Stepanova, Niels Galjart, Frank Grosveld, Bruno Goud, Chris I. De Zeeuw, Angelika Barnekow, and Casper C. Hoogenraad. 2002. “Erratum: Bicaudal-D Regulates COPI-Independent Golgi–ER Transport by Recruiting the Dynein–dynactin Motor Complex.” *Nature Cell Biology* 4(12):986–92.

Matlin, Karl S. and Kai Simons. 1983. “Reduced Temperature Prevents Transfer of a Membrane Glycoprotein to the Cell Surface but Does Not Prevent Terminal Glycosylation.” *Cell* 34(1):233–43.

Mattila, Juha-Pekka, Anna V. Shnyrova, Anna C. Sundborger, Eva Rodriguez Hortelano, Marc Fuhrmans, Sylvia Neumann, Marcus Müller, Jenny E. Hinshaw, Sandra L. Schmid, and Vadim A. Frolov. 2015. “A Hemi-Fission Intermediate Links Two Mechanistically Distinct Stages of Membrane Fission.” *Nature* 524(7563):109–13.

Maxfield, Frederick R. and Timothy E. McGraw. 2004. “Endocytic Recycling.” *Nature Reviews Molecular Cell Biology* 5(2):121–32.

McBride, Heidi M., Vladimir Rybin, Carol Murphy, Angelika Giner, Rohan Teasdale, and Marino Zerial. 1999. “Oligomeric Complexes Link Rab5 Effectors with NSF and Drive Membrane Fusion via Interactions between EEA1 and Syntaxin 13.” *Cell* 98(3):377–86.

McCaughey, Janine, Victoria J. Miller, Nicola L. Stevenson, Anna K. Brown, Annika Budnik, Kate J. Heesom, Dominic Alibhai, and David J. Stephens. 2016. “TFG Promotes Organization of Transitional ER and Efficient Collagen Secretion.” *Cell Reports* 15(8):1648–59.

McCullough, J., R. D. Fisher, F. G. Whitby, W. I. Sundquist, and C. P. Hill. 2008. “ALIX-CHMP4 Interactions in the Human ESCRT Pathway.” *Proceedings of the National Academy of Sciences* 105(22):7687–91.

McCullough, John, Amy K. Clippinger, Nathaniel Talledge, Michael L. Skowyra, Marissa G. Saunders, Teresa V. Naismith, Leremy A. Colf, Pavel Afonine, Christopher Arthur, Wesley I. Sundquist, Phyllis I. Hanson, and Adam Frost. 2015. “Structure and Membrane Remodeling Activity of ESCRT-III Helical Polymers.” *Science* 350(6267):1548–51.

McCullough, John, Adam Frost, and Wesley I. Sundquist. 2018. “Structures, Functions, and Dynamics of ESCRT-III/Vps4 Membrane Remodeling and Fission Complexes.” *Annual Review of Cell and Developmental Biology* 34(1):85–109.

McDermott, Christopher J., Andrew J. Grierson, Jonathan D. Wood, Megan Bingley, Stephen B. Wharton, Katharine M. D. Bushby, and Pamela J. Shaw. 2003. “Hereditary Spastic Paraparesis: Disrupted Intracellular Transport Associated with Spastin Mutation.” *Annals of Neurology* 54(6):748–59.

McGough, I. J., F. Steinberg, M. Gallon, A. Yatsu, N. Ohbayashi, K. J. Heesom, M. Fukuda, and P. J. Cullen. 2014. “Identification of Molecular Heterogeneity in SNX27-Retromer-Mediated Endosome-to-Plasma-Membrane Recycling.” *Journal of Cell Science* 127(22):4940–53.

McHale, D. P., S. Mitchell, S. Bundey, L. Moynihan, D. A. Campbell, C. G. Woods, N. J. Lench, R. F. Mueller, and A. F. Markham. 1999. “A Gene for Autosomal Recessive Symmetrical Spastic Cerebral Palsy Maps to Chromosome 2q24-25.” *The American Journal of Human Genetics* 64(2):526–32.

McKenzie, Jenna E., Brent Raisley, Xin Zhou, Naava Naslavsky, Tomohiko Taguchi, Steve Caplan, and David Sheff. 2012. “Retromer Guides STxB and CD8-M6PR from Early to Recycling Endosomes, EHD1 Guides STxB from Recycling Endosome to Golgi.” *Traffic* 13(8):1140–59.

McNally, Kerrie E. and Peter J. Cullen. 2018. “Endosomal Retrieval of Cargo: Retromer Is Not Alone.” *Trends in Cell Biology* 28(10):807–22.

McNally, Kerrie E., Rebecca Faulkner, Florian Steinberg, Matthew Gallon, Rajesh Ghai, David Pim, Paul Langton, Neil Pearson, Chris M. Danson, Heike Nägele, Lindsey L. Morris, Amika Singla, Brittany L. Overlee, Kate J. Heesom, Richard Sessions, Lawrence Banks, Brett M. Collins, Imre Berger, Daniel D. Billadeau, Ezra Burstein, and Peter J. Cullen. 2017. “Retriever Is a Multiprotein Complex for Retromer-Independent Endosomal Cargo Recycling.” *Nature Cell Biology* 19(10):1214–25.

Mellman, I. 1992. “The Importance of Being Acid: The Role of Acidification in Intracellular Membrane Traffic.” *The Journal of Experimental Biology* 172:39–45.

Mellman, Ira, Renate Fuchs, and Ari Helenius. 1986. “Acidification of the Endocytic and Exocytic Pathways.” *Annual Review of Biochemistry* 55(1):663–700.

Meltzer, Hagar and Oren Schuldiner. 2016. “Cut Your Losses: Spastin Mediates Branch-Specific Axon Loss.” *Neuron* 92(4):677–80.

Michel, Vera and Marica Bakovic. 2009. “The Solute Carrier 44A1 Is a Mitochondrial Protein and Mediates Choline Transport.” *The FASEB Journal* 23(8):2749–58.

Mierzwa, Beata E., Nicolas Chiaruttini, Lorena Redondo-Morata, Joachim Moser von Filseck, Julia König, Jorge Larios, Ina Poser, Thomas Müller-Reichert, Simon Scheuring, Aurélien Roux, and Daniel W. Gerlich. 2017. “Dynamic Subunit Turnover in ESCRT-III Assemblies Is Regulated by Vps4 to Mediate Membrane Remodelling during Cytokinesis.” *Nature Cell Biology* 19(7):787–98.

Miller, Elizabeth A., Traude H. Beilharz, Per N. Malkus, Marcus C. S. Lee, Susan Hamamoto, Lelio Orci, and Randy Schekman. 2003. "Multiple Cargo Binding Sites on the COPII Subunit Sec24p Ensure Capture of Diverse Membrane Proteins into Transport Vesicles." *Cell* 114(4):497–509.

Miller, Elizabeth, Bruno Antonny, Susan Hamamoto, and Randy Schekman. 2002. "Cargo Selection into COPII Vesicles Is Driven by the Sec24p Subunit." *The EMBO Journal* 21(22):6105–13.

Miller, Justin M. and Eric J. Enemark. 2016. "Fundamental Characteristics of AAA+ Protein Family Structure and Function." *Archaea* 2016:1–12.

Mironov, Alexandre A. 2014. "ER–Golgi Transport Could Occur in the Absence of COPII Vesicles." *Nature Reviews Molecular Cell Biology* 15(3):1–1.

Miserey-Lenkei, S., G. Chalancon, S. Bardin, E. Formstecher, B. Goud, and A. Echard. 2010. "Rab and Actomyosin-Dependent Fission of Transport Vesicles at the Golgi Complex." *Nature Cell Biology* 12(7):645–54.

Mitchell, Philip, Elisabeth Petfalski, Andrej Shevchenko, Matthias Mann, and David Tollervey. 1997. "The Exosome: A Conserved Eukaryotic RNA Processing Complex Containing Multiple 3'→5' Exoribonucleases." *Cell* 91(4):457–66.

Mitchison, T. J. 1989. "Polewards Microtubule Flux in the Mitotic Spindle: Evidence from Photoactivation of Fluorescence." *The Journal of Cell Biology* 109(2):637–52.

Mitchison, Tim, Louise Evans, Eric Schulze, and Marc Kirschner. 1986. "Sites of Microtubule Assembly and Disassembly in the Mitotic Spindle." *Cell* 45(4):515–27.

Mitchison, Tim and Marc Kirschner. 1984. "Dynamic Instability of Microtubule Growth." *Nature* 312(5991):237–42.

Mizuno, M. and S. J. Singer. 1994. "A Possible Role for Stable Microtubules in Intracellular Transport from the Endoplasmic Reticulum to the Golgi Apparatus." *Journal of Cell Science* 107 (Pt 5:1321–31.

Monroe, Nicole and Christopher P. Hill. 2016. "Meiotic Clade AAA ATPases: Protein Polymer Disassembly Machines." *Journal of Molecular Biology* 428(9):1897–1911.

du Montcel, Sophie Tezenas, Perrine Charles, Pascale Ribai, Cyril Goizet, Alice Le Bayon, Pierre Labauge, Lucie Guyant-Maréchal, Sylvie Forlani, Celine Jauffret, Nadia Vandenberghe, Karine N'Guyen, Isabelle Le Ber, David Devos, Carlo-Maria Vincitorio, Mario-Ubaldo Manto, François Tison, Didier Hannequin, Merle Ruberg, Alexis Brice, and Alexandra Durr. 2008. "Composite Cerebellar Functional Severity Score: Validation of a Quantitative Score of Cerebellar Impairment." *Brain* 131(5):1352–61.

Montenegro, Gladys, Adriana P. Rebelo, James Connell, Rachel Allison, Carla Babalini, Michela D'Aloia, Pasqua Montieri, Rebecca Schüle, Hiroyuki Ishiura, Justin Price, Alleene Strickland, Michael A. Gonzalez, Lisa Baumbach-Reardon, Tine Deconinck, Jia Huang, Giorgio Bernardi, Jeffery M. Vance, Mark T. Rogers, Shoji Tsuji, Peter De Jonghe, Margaret A. Pericak-Vance, Ludger Schöls, Antonio Orlacchio, Evan Reid, and Stephan Züchner. 2012. "Mutations in the ER-Shaping Protein Reticulon 2 Cause the Axon-Degenerative Disorder Hereditary Spastic Paraplegia Type 12." *Journal of Clinical Investigation* 122(2):538–44.

Morlot, Sandrine, Valentina Galli, Marius Klein, Nicolas Chiaruttini, John Manzi, Frédéric Humbert, Luis Dinis, Martin Lenz, Giovanni Cappello, and Aurélien Roux. 2012. "Membrane Shape at the Edge of the Dynamin Helix Sets Location and Duration of the Fission Reaction." *Cell* 151(3):619–29.

Moughamian, A. J., G. E. Osborn, J. E. Lazarus, S. Maday, and E. L. F. Holzbaur. 2013. "Ordered Recruitment of Dynactin to the Microtubule Plus-End Is Required for Efficient Initiation of Retrograde Axonal Transport." *Journal of Neuroscience* 33(32):13190–203.

Müller, Christoph W. and Georg E. Schulz. 1992. "Structure of the Complex between Adenylate Kinase from Escherichia Coli and the Inhibitor Ap5A Refined at 1.9 Å Resolution." *Journal of Molecular Biology* 224(1):159–77.

Murray, James T., Christina Panaretou, Harald Stenmark, Marta Miaczynska, and Jonathan M. Backer. 2002. "Role of Rab5 in the Recruitment of HVps34/P150 to the Early Endosome." *Traffic* 3(6):416–27.

Nahm, Minyeop, Min-Jung Lee, William Parkinson, Mihye Lee, Haeran Kim, Yoon-Jung Kim, Sungdae Kim, Yi Sul Cho, Byung-Moo Min, Yong Chul Bae, Kendal Broadie, and Seungbok Lee. 2013. "Spartin Regulates Synaptic Growth and Neuronal Survival by Inhibiting BMP-Mediated Microtubule Stabilization." *Neuron* 77(4):680–95.

Nakamura, Fumihiko, Thomas P. Stossel, and John H. Hartwig. 2011. "The Filamins." *Cell Adhesion & Migration* 5(2):160–69.

Nakamura, Yoshinobu, Takeo Nakanishi, Hiroaki Shimada, Junya Shimizu, Rika Aotani, Shio Maruyama, Kei Higuchi, Takashi Okura, Yoshiharu Deguchi, and Ikumi Tamai. 2018. "Prostaglandin Transporter OATP2A1/ SLCO2A1 Is Essential for Body Temperature Regulation during Fever." *The Journal of Neuroscience* 38(24):5584–95.

Nakata, Takao, Shinsuke Niwa, Yasushi Okada, Franck Perez, and Nobutaka Hirokawa. 2011. "Preferential Binding of a Kinesin-1 Motor to GTP-Tubulin–rich Microtubules Underlies Polarized Vesicle Transport." *The Journal of Cell Biology* 194(2):245–55.

Naslavsky, Naava and Steve Caplan. 2018. "The Enigmatic Endosome – Sorting the Ins and Outs of Endocytic Trafficking." *Journal of Cell Science* 131(13):jcs216499.

Nauseef, William M., Sally J. McCormick, and Robert A. Clark. 1995. "Calreticulin Functions as a Molecular Chaperone in the Biosynthesis of Myeloperoxidase." *Journal of Biological Chemistry* 270(9):4741–47.

Neumann, Sylvia and Sandra L. Schmid. 2013. "Dual Role of BAR Domain-Containing Proteins in Regulating Vesicle Release Catalyzed by the GTPase, Dynamin-2." *Journal of Biological Chemistry* 288(35):25119–28.

Newton, Timothy, Rachel Allison, James R. Edgar, Jennifer H. Lumb, Catherine E. Rodger, Paul T. Manna, Tania Rizo, Zacharias Kohl, Anders O. H. Nygren, Larissa Arning, Rebecca Schüle, Christel Depienne, Lisa Goldberg, Christiane Frahm, Giovanni Stevanin, Alexandra Durr, Ludger Schöls, Beate Winner, Christian Beetz, and Evan Reid. 2018. "Mechanistic Basis of an Epistatic Interaction Reducing Age at Onset in Hereditary Spastic Paraplegia." *Brain* 141(5):1286–99.

Nickel, Walter and Catherine Rabouille. 2009. "Mechanisms of Regulated Unconventional Protein Secretion." *Nature Reviews Molecular Cell Biology* 10(2):148–55.

Nicoziani, Paolo, Frederik Vilhardt, Alicia Llorente, Leila Hilout, Pierre J. Courtoy, Kirsten Sandvig, and Bo van Deurs. 2000. "Role for Dynamin in Late Endosome Dynamics and Trafficking of the Cation-Independent Mannose 6-Phosphate Receptor" edited by S. R. Pfeffer. *Molecular Biology of the Cell* 11(2):481–95.

Nielsen, Erik, Savvas Christoforidis, Sandrine Uttenweiler-Joseph, Marta Miaczynska, Frederique Dewitte, Matthias Wilm, Bernard Hoflack, and Marino Zerial. 2000. "Rabenosyn-5, a Novel Rab5 Effector, Is Complexed with HVPS45 and Recruited to Endosomes through a FYVE Finger Domain." *Journal of Cell Biology* 151(3):601–12.

Nielsen, Erik, Fedor Severin, Jonathan M. Backer, Anthony A. Hyman, and Marino Zerial. 1999. “Rab5 Regulates Motility of Early Endosomes on Microtubules.” *Nature Cell Biology* 1(6):376–82.

Nixon-Abell, Jonathon, Christopher J. Obara, Aubrey V. Weigel, Dong Li, Wesley R. Legant, C. Shan Xu, H. Amalia Pasolli, Kirsten Harvey, Harald F. Hess, Eric Betzig, Craig Blackstone, and Jennifer Lippincott-Schwartz. 2016. “Increased Spatiotemporal Resolution Reveals Highly Dynamic Dense Tubular Matrices in the Peripheral ER.” *Science* 354(6311):aaf3928-aaf3928.

Noh, Shin Hye, Heon Yung Gee, Yonjung Kim, He Piao, Jiyoon Kim, Chung Min Kang, Gahyung Lee, Inhee Mook-Jung, Yangsin Lee, Jin Won Cho, and Min Goo Lee. 2018. “Specific Autophagy and ESCRT Components Participate in the Unconventional Secretion of CFTR.” *Autophagy* 14(10):1761–78.

Novarino, G., A. G. Fenstermaker, M. S. Zaki, M. Hofree, J. L. Silhavy, A. D. Heiberg, M. Abdellateef, B. Rosti, E. Scott, L. Mansour, A. Masri, H. Kayserili, J. Y. Al-Aama, G. M. H. Abdel-Salam, A. Karminejad, M. Kara, B. Kara, B. Bozorgmehri, T. Ben-Omran, F. Mojahedi, I. G. E. D. Mahmoud, N. Bouslam, A. Bouhouche, A. Benomar, S. Hanein, L. Raymond, S. Forlani, M. Mascaro, L. Selim, N. Shehata, N. Al-Allawi, P. S. Bindu, M. Azam, M. Gunel, A. Caglayan, K. Bilguvar, A. Tolun, M. Y. Issa, J. Schroth, E. G. Spencer, R. O. Rosti, N. Akizu, K. K. Vaux, A. Johansen, A. A. Koh, H. Megahed, A. Durr, A. Brice, G. Stevanin, S. B. Gabriel, T. Ideker, and J. G. Gleeson. 2014. “Exome Sequencing Links Corticospinal Motor Neuron Disease to Common Neurodegenerative Disorders.” *Science* 343(6170):506–11.

Nualart, Francisco, Alejandro Godoy, and Karin Reinicke. 1999. “Expression of the Hexose Transporters GLUT1 and GLUT2 during the Early Development of the Human Brain.” *Brain Research* 824(1):97–104.

Nwaobi, Sinifunanya E., Vishnu A. Cuddapah, Kelsey C. Patterson, Anita C. Randolph, and Michelle L. Olsen. 2016. “The Role of Glial-Specific Kir4.1 in Normal and Pathological States of the CNS.” *Acta Neuropathologica* 132(1):1–21.

Nyfeler, Beat, Veronika Reiterer, Markus W. Wendeler, Eduard Stefan, Bin Zhang, Stephen W. Michnick, and Hans-Peter Hauri. 2008. “Identification of ERGIC-53 as an Intracellular Transport Receptor of α 1 -Antitrypsin.” *The Journal of Cell Biology* 180(4):705–12.

O’Connor-Giles, Kate M., Ling Ling Ho, and Barry Ganetzky. 2008. “Nervous Wreck Interacts with Thickveins and the Endocytic Machinery to Attenuate Retrograde BMP Signaling during Synaptic Growth.” *Neuron* 58(4):507–18.

Oates, Emily C., Alexander M. Rossor, Majid Hafezparast, Michael Gonzalez, Fiorella Speziani, Daniel G. MacArthur, Monkol Lek, Ellen Cottenie, Mariacristina Scoto, A. Reghan Foley, Matthew Hurles, Henry Houlden, Linda Greensmith, Michaela Auer-Grumbach, Thomas R. Pieber, Tim M. Strom, Rebecca Schule, David N. Herrmann, Janet E. Sowden, Gyula Acsadi, Manoj P. Menezes, Nigel F. Clarke, Stephan Züchner, Francesco Muntoni, Kathryn N. North, and Mary M. Reilly. 2013. "Mutations in BICD2 Cause Dominant Congenital Spinal Muscular Atrophy and Hereditary Spastic Paraplegia." *The American Journal of Human Genetics* 92(6):965–73.

Obita, Takayuki, Suraj Saksena, Sara Ghazi-Tabatabai, David J. Gill, Olga Perisic, Scott D. Emr, and Roger L. Williams. 2007. "Structural Basis for Selective Recognition of ESCRT-III by the AAA ATPase Vps4." *Nature* 449(7163):735–39.

Okada, Hirokazu, Wenzhu Zhang, Corrinne Peterhoff, Jeremy C. Hwang, Ralph A. Nixon, Sung H. Ryu, and Tae-Wan Kim. 2010. "Proteomic Identification of Sorting Nexin 6 as a Negative Regulator of BACE1-Mediated APP Processing." *The FASEB Journal* 24(8):2783–94.

Okamoto, M., K. Kurokawa, K. Matsuura-Tokita, C. Saito, R. Hirata, and A. Nakano. 2012. "High-Curvature Domains of the ER Are Important for the Organization of ER Exit Sites in Saccharomyces Cerevisiae." *Journal of Cell Science* 125(14):3412–20.

Okegawa, Takatsugu, Rey-Chen Pong, Yingming Li, and Jer-Tsong Hsieh. 2004. "The Role of Cell Adhesion Molecule in Cancer Progression and Its Application in Cancer Therapy." *Acta Biochimica Polonica* 51(2):445–57.

OKUMURA, Mayumi, Angela M. KATSUYAMA, Hideki SHIBATA, and Masatoshi MAKI. 2013. "VPS37 Isoforms Differentially Modulate the Ternary Complex Formation of ALIX, ALG-2, and ESCRT-I." *Bioscience, Biotechnology, and Biochemistry* 77(8):1715–21.

Olah, Zoltan, Csaba Lehel, Wayne B. Anderson, Maribeth V. Eiden, and Carolyn A. Wilson. 1994. "The Cellular Receptor for Gibbon Ape Leukemia Virus Is a Novel High Affinity Sodium-Dependent Phosphate Transporter." *The Journal of Biological Chemistry* 269(41):25426–31.

Olmos, Yolanda, Lorna Hodgson, Judith Mantell, Paul Verkade, and Jeremy G. Carlton. 2015. "ESCRT-III Controls Nuclear Envelope Reformation." *Nature* 522(7555):236–39.

Orthmann-Murphy, Jennifer L., Ettore Salsano, Charles K. Abrams, Alberto Bizzi, Graziella Uziel, Mona M. Freidin, Eleonora Lamantea, Massimo Zeviani, Steven S. Scherer, and Davide Pareyson. 2009. "Hereditary Spastic Paraplegia Is a Novel Phenotype for GJA12/GJC2 Mutations." *Brain* 132(2):426–38.

Osborne, Douglas G., Joshua T. Piotrowski, Christopher J. Dick, Jin-San Zhang, and Daniel D. Billadeau. 2015. “SNX17 Affects T Cell Activation by Regulating TCR and Integrin Recycling.” *The Journal of Immunology* 194(9):4555–66.

Osellame, Laura D., Thomas S. Blacker, and Michael R. Duchen. 2012. “Cellular and Molecular Mechanisms of Mitochondrial Function.” *Best Practice & Research Clinical Endocrinology & Metabolism* 26(6):711–23.

Oshikawa, Mio, Ron Usami, and Seishi Kato. 2009. “Characterization of the Arylsulfatase I (ARSI) Gene Preferentially Expressed in the Human Retinal Pigment Epithelium Cell Line ARPE-19.” *Molecular Vision* 15:482–94.

Oz-Levi, Danit, Bruria Ben-Zeev, Elizabeth K. Ruzzo, Yuki Hitomi, Amir Gelman, Kimberly Pelak, Yair Anikster, Haike Reznik-Wolf, Ifat Bar-Joseph, Tsviya Olender, Anna Alkelai, Meira Weiss, Edna Ben-Asher, Dongliang Ge, Kevin V. Shianna, Zvulun Elazar, David B. Goldstein, Elon Pras, and Doron Lancet. 2012. “Mutation in TECPR2 Reveals a Role for Autophagy in Hereditary Spastic Paraparesis.” *The American Journal of Human Genetics* 91(6):1065–72.

de Pablo-Latorre, Raquel, Assunta Saide, Elena V. Polishhuck, Edoardo Nusco, Alessandro Fraldi, and Andrea Ballabio. 2012. “Impaired Parkin-Mediated Mitochondrial Targeting to Autophagosomes Differentially Contributes to Tissue Pathology in Lysosomal Storage Diseases.” *Human Molecular Genetics* 21(8):1770–81.

Palade, G. 1975. “Intracellular Aspects of the Process of Protein Synthesis.” *Science* 189(4206):867–867.

Palmer, Krysten J., Helen Hughes, and David J. Stephens. 2009. “Specificity of Cytoplasmic Dynein Subunits in Discrete Membrane-Trafficking Steps” edited by E. Holzbaur. *Molecular Biology of the Cell* 20(12):2885–99.

Palmer, Sarah E., Iwona I. Smaczynska-de Rooij, Christopher J. Marklew, Ellen G. Allwood, Ritu Mishra, Simeon Johnson, Martin W. Goldberg, and Kathryn R. Ayscough. 2015. “A Dynamin-Actin Interaction Is Required for Vesicle Scission during Endocytosis in Yeast.” *Current Biology* 25(7):868–78.

Papadopoulos, Chrisovalantis, Genny Orso, Giuseppe Mancuso, Marija Herholz, Sentiljana Gumeni, Nimesha Tadepalle, Christian Jüngst, Anne Tzschichholz, Astrid Schauss, Stefan Höning, Aleksandra Trifunovic, Andrea Daga, and Elena I. Rugarli. 2015. “Spastin Binds to Lipid Droplets and Affects Lipid Metabolism” edited by K. Ashrafi. *PLOS Genetics* 11(4):e1005149.

Park, Seong H., Peng-Peng Zhu, Rell L. Parker, and Craig Blackstone. 2010. “Hereditary Spastic Paraplegia Proteins REEP1, Spastin, and Atlastin-1 Coordinate Microtubule Interactions with the Tubular ER Network.” *Journal of Clinical Investigation* 120(4):1097–1110.

Patel, Heema, Harold Cross, Christos Proukakis, Ruth Hershberger, Peer Bork, Francesca D. Ciccarelli, Michael A. Patton, Victor A. McKusick, and Andrew H. Crosby. 2002. “SPG20 Is Mutated in Troyer Syndrome, an Hereditary Spastic Paraplegia.” *Nature Genetics* 31(4):347–48.

Pavel, Mariana and David C. Rubinsztein. 2017. “Mammalian Autophagy and the Plasma Membrane.” *The FEBS Journal* 284(5):672–79.

Pearce, Margaret M. P., Duncan B. Wormer, Stephan Wilkens, and Richard J. H. Wojcikiewicz. 2009. “An Endoplasmic Reticulum (ER) Membrane Complex Composed of SPFH1 and SPFH2 Mediates the ER-Associated Degradation of Inositol 1,4,5-Trisphosphate Receptors.” *Journal of Biological Chemistry* 284(16):10433–45.

Pecci, Alessandro, Xuefei Ma, Anna Savoia, and Robert S. Adelstein. 2018. “MYH9: Structure, Functions and Role of Non-Muscle Myosin IIA in Human Disease.” *Gene* 664:152–67.

Pereira, Jose H., Ryan P. McAndrew, Oksana A. Sergeeva, Corie Y. Ralston, Jonathan A. King, and Paul D. Adams. 2017. “Structure of the Human TRiC/CCT Subunit 5 Associated with Hereditary Sensory Neuropathy.” *Scientific Reports* 7(1):3673.

Peter, Brian J. 2004. “BAR Domains as Sensors of Membrane Curvature: The Amphiphysin BAR Structure.” *Science* 303(5657):495–99.

Phillips-Krawczak, Christine A., Amika Singla, Petro Starokadomskyy, Zhihui Deng, Douglas G. Osborne, Haiying Li, Christopher J. Dick, Timothy S. Gomez, Megan Koenecke, Jin-San Zhang, Haiming Dai, Luis F. Sifuentes-Dominguez, Linda N. Geng, Scott H. Kaufmann, Marco Y. Hein, Mathew Wallis, Julie McGaughran, Jozef Gecz, Bart van de Sluis, Daniel D. Billadeau, and Ezra Burstein. 2015. “COMMD1 Is Linked to the WASH Complex and Regulates Endosomal Trafficking of the Copper Transporter ATP7A” edited by J. E. Gruenberg. *Molecular Biology of the Cell* 26(1):91–103.

Pichlmair, A., O. Schulz, C. P. Tan, J. Rehwinkel, H. Kato, O. Takeuchi, S. Akira, M. Way, G. Schiavo, and C. Reis e Sousa. 2009. “Activation of MDA5 Requires Higher-Order RNA Structures Generated during Virus Infection.” *Journal of Virology* 83(20):10761–69.

Platt, Frances M., Barry Boland, and Aarnoud C. van der Spoel. 2012. “Lysosomal Storage Disorders: The Cellular Impact of Lysosomal Dysfunction.” *The Journal of Cell Biology* 199(5):723–34.

Politz, Joan C. 1999. “Use of Caged Fluorochromes to Track Macromolecular Movement in Living Cells.” *Trends in Cell Biology* 9(7):284–87.

Pols, Maaike S., Eline van Meel, Viola Oorschot, Corlinda ten Brink, Minoru Fukuda, M. G. Swetha, Satyajit Mayor, and Judith Klumperman. 2013. “HVps41 and VAMP7 Function in Direct TGN to Late Endosome Transport of Lysosomal Membrane Proteins.” *Nature Communications* 4(1):1361.

Popoff, Michel R. and Bernard Poulain. 2010. “Bacterial Toxins and the Nervous System: Neurotoxins and Multipotential Toxins Interacting with Neuronal Cells.” *Toxins* 2(4):683–737.

Popow, Johannes, Alexander Schleiffer, and Javier Martinez. 2012. “Diversity and Roles of (t)RNA Ligases.” *Cellular and Molecular Life Sciences* 69(16):2657–70.

Prasad, D. V. R., T. Nguyen, Z. Li, Y. Yang, J. Duong, Y. Wang, and C. Dong. 2004. “Murine B7-H3 Is a Negative Regulator of T Cells.” *The Journal of Immunology* 173(4):2500–2506.

Presley, John F., Nelson B. Cole, Trina A. Schroer, Koret Hirschberg, Kristien J. M. Zaal, and Jennifer Lippincott-Schwartz. 1997. “ER-to-Golgi Transport Visualized in Living Cells.” *Nature* 389(6646):81–85.

Progida, Cinzia and Oddmund Bakke. 2016. “Bidirectional Traffic between the Golgi and the Endosomes – Machineries and Regulation.” *Journal of Cell Science* jcs.185702.

Puthenveedu, Manojkumar A., Benjamin Lauffer, Paul Temkin, Rachel Vistein, Peter Carlton, Kurt Thorn, Jack Taunton, Orion D. Weiner, Robert G. Parton, and Mark von Zastrow. 2010. “Sequence-Dependent Sorting of Recycling Proteins by Actin-Stabilized Endosomal Microdomains.” *Cell* 143(5):761–73.

Qualmann, Britta, Dennis Koch, and Michael Manfred Kessels. 2011. “Let’s Go Bananas: Revisiting the Endocytic BAR Code.” *The EMBO Journal* 30(17):3501–15.

Quarles, Richard H. 2007. “Myelin-Associated Glycoprotein (MAG): Past, Present and Beyond.” *Journal of Neurochemistry* 100(6):1431–48.

Raben, Nina, Lauren Shea, Victoria Hill, and Paul Plotz. 2009. “Chapter 21 Monitoring Autophagy in Lysosomal Storage Disorders.” Pp. 417–49 in *Methods in enzymology*.

Raiborg, Camilla. 2001. “Hrs Recruits Clathrin to Early Endosomes.” *The EMBO Journal* 20(17):5008–21.

Raiborg, Camilla and Harald Stenmark. 2009. “The ESCRT Machinery in Endosomal Sorting of Ubiquitylated Membrane Proteins.” *Nature* 458(7237):445–52.

Raimondi, Andrea, Shawn M. Ferguson, Xuelin Lou, Moritz Armbruster, Summer Paradise, Silvia Giovedi, Mirko Messa, Nao Kono, Junko Takasaki, Valentina Cappello, Eileen O’Toole, Timothy A. Ryan, and Pietro De Camilli. 2011. “Overlapping Role of Dynamin Isoforms in Synaptic Vesicle Endocytosis.” *Neuron* 70(6):1100–1114.

Rainier, Shirley, Melanie Bui, Erin Mark, Donald Thomas, Debra Tokarz, Lei Ming, Colin Delaney, Rudy J. Richardson, James W. Albers, Nori Matsunami, Jeff Stevens, Hilary Coon, Mark Leppert, and John K. Fink. 2008. “Neuropathy Target Esterase Gene Mutations Cause Motor Neuron Disease.” *The American Journal of Human Genetics* 82(3):780–85.

Rainier, Shirley, Jing-Hua Chai, Debra Tokarz, Robert D. Nicholls, and John K. Fink. 2003. “NIPA1 Gene Mutations Cause Autosomal Dominant Hereditary Spastic Paraplegia (SPG6).” *The American Journal of Human Genetics* 73(4):967–71.

Ralston, Evelyn, Thorkil Ploug, John Kalhovde, and Terje Lømo. 2001. “Golgi Complex, Endoplasmic Reticulum Exit Sites, and Microtubules in Skeletal Muscle Fibers Are Organized by Patterned Activity.” *The Journal of Neuroscience* 21(3):875–83.

Rao, Kavitha, Michelle C. Stone, Alexis T. Weiner, Kyle W. Gheres, Chaoming Zhou, David L. Deitcher, Edwin S. Levitan, and Melissa M. Rolls. 2016. “Spastin, Atlastin, and ER Relocalization Are Involved in Axon but Not Dendrite Regeneration” edited by P. Forscher. *Molecular Biology of the Cell* 27(21):3245–56.

Raote, Ishier, Maria Ortega-Bellido, António J. M. Santos, Ombretta Foresti, Chong Zhang, Maria F. Garcia-Parajo, Felix Campelo, and Vivek Malhotra. 2018. “TANGO1 Builds a Machine for Collagen Export by Recruiting and Spatially Organizing COPII, Tethers and Membranes.” *ELife* 7.

Raote, Ishier, Maria Ortega Bellido, Marinella Pirozzi, Chong Zhang, David Melville, Seetharaman Parashuraman, Timo Zimmermann, and Vivek Malhotra. 2017. “TANGO1 Assembles into Rings around COPII Coats at ER Exit Sites.” *The Journal of Cell Biology* 216(4):901–9.

Rapaport, Debora, Wojtek Auerbach, Naava Naslavsky, Metsada Pasmanik-Chor, Emilia Galperin, Amos Fein, Steve Caplan, Alexandra L. Joyner, and Mia Horowitz. 2006. “Recycling to the Plasma Membrane Is Delayed in EHD1 Knockout Mice.” *Traffic* 7(1):52–60.

Raskind, W. H., M. A. Pericak-Vance, F. Lennon, J. Wolff, H. P. Lipe, and T. D. Bird. 1997. “Familial Spastic Paraparesis: Evaluation of Locus Heterogeneity, Anticipation, and Haplotype Mapping of the SPG4 Locus on the Short Arm of Chromosome 2.” *American Journal of Medical Genetics* 74(1):26–36.

Ravid, Tommer, Jill M. Heidinger, Peter Gee, Elaine M. Khan, and Tzipora Goldkorn. 2004. “C-Cbl-Mediated Ubiquitinylation Is Required for Epidermal Growth Factor Receptor Exit from the Early Endosomes.” *Journal of Biological Chemistry* 279(35):37153–62.

Reggiori, Fulvio, Chao-wen Wang, Usha Nair, Takahiro Shintani, Hagai Abeliovich, and Daniel J. Klionsky. 2004. “Early Stages of the Secretory Pathway, but Not Endosomes, Are Required for Cvt Vesicle and Autophagosome Assembly in Saccharomyces Cerevisiae.” *Molecular Biology of the Cell* 15(5):2189–2204.

Reid, E. 1999. “Locusphenotype Correlations in Autosomal Dominant Pure Hereditary Spastic Paraplegia: A Clinical and Molecular Genetic Study of 28 United Kingdom Families.” *Brain* 122(9):1741–55.

Reid, E., C. Grayson, D. C. Rubinsztein, M. T. Rogers, And J. S. Rubinsztein. 1999. “Subclinical Cognitive Impairment in Autosomal Dominant ‘Pure’ Hereditary Spastic Paraplegia.” *Journal of Medical Genetics* 36(10):797–98.

Reid, Evan, James Connell, Thomas L. Edwards, Simon Duley, Stephanie E. Brown, and Christopher M. Sanderson. 2005. “The Hereditary Spastic Paraplegia Protein Spastin Interacts with the ESCRT-III Complex-Associated Endosomal Protein CHMP1B.” *Human Molecular Genetics* 14(1):19–38.

Reid, Evan, Mark Kloos, Allison Ashley-Koch, Lori Hughes, Simon Bevan, Ingrid K. Svenson, Felicia Lennon Graham, Perry C. Gaskell, Andrew Dearlove, Margaret A. Pericak-Vance, David C. Rubinsztein, and Douglas A. Marchuk. 2002. “A Kinesin Heavy Chain (KIF5A) Mutation in Hereditary Spastic Paraplegia (SPG10).” *The American Journal of Human Genetics* 71(5):1189–94.

Reith, Walter and Bernard Mach. 2001. “The Bare Lymphocyte Syndrome and the Regulation of MHC Expression.” *Annual Review of Immunology* 19(1):331–73.

Ren, Xuefeng and James H. Hurley. 2010. “VHS Domains of ESCRT-0 Cooperate in High-Avidity Binding to Polyubiquitinated Cargo.” *The EMBO Journal* 29(6):1045–54.

Renard, Henri-François, Ludger Johannes, and Pierre Morsomme. 2018. “Increasing Diversity of Biological Membrane Fission Mechanisms.” *Trends in Cell Biology* 28(4):274–86.

Renard, Henri-François, Mijo Simunovic, Joël Lemière, Emmanuel Boucrot, Maria Daniela Garcia-Castillo, Senthil Arumugam, Valérie Chambon, Christophe Lamaze, Christian Wunder, Anne K. Kenworthy, Anne A. Schmidt, Harvey T. McMahon, Cécile Sykes, Patricia Bassereau, and Ludger Johannes. 2015. “Endophilin-A2 Functions in Membrane Scission in Clathrin-Independent Endocytosis.” *Nature* 517(7535):493–96.

van Renswoude, J., K. R. Bridges, J. B. Harford, and R. D. Klausner. 1982. “Receptor-Mediated Endocytosis of Transferrin and the Uptake of Fe in K562 Cells: Identification of a Nonlysosomal Acidic Compartment.” *Proceedings of the National Academy of Sciences* 79(20):6186–90.

Renvoisé, Benoît, Jaerak Chang, Rajat Singh, Sayuri Yonekawa, Edmond J. FitzGibbon, Ami Mankodi, Adeline Vanderver, Alice B. Schindler, Camilo Toro, William A. Gahl, Don J. Mahuran, Craig Blackstone, and Tyler Mark Pierson. 2014. “Lysosomal Abnormalities in Hereditary Spastic Paraplegia Types SPG15 and SPG11.” *Annals of Clinical and Translational Neurology* 1(6):379–89.

Renvoisé, Benoît, Rell L. Parker, Dong Yang, Joanna C. Bakowska, James H. Hurley, and Craig Blackstone. 2010. “SPG20 Protein Spartin Is Recruited to Midbodies by ESCRT-III Protein Ist1 and Participates in Cytokinesis” edited by S. Doxsey. *Molecular Biology of the Cell* 21(19):3293–3303.

Renvoisé, Benoît, Julia Stadler, Rajat Singh, Joanna C. Bakowska, and Craig Blackstone. 2012. “Spg20−/− Mice Reveal Multimodal Functions for Troyer Syndrome Protein Spartin in Lipid Droplet Maintenance, Cytokinesis and BMP Signaling.” *Human Molecular Genetics* 21(16):3604–18.

Riano, Elena, Monica Martignoni, Giuseppe Mancuso, Daniele Cartelli, Francesca Crippa, Irene Toldo, Gabriele Siciliano, Daniela Di Bella, Franco Taroni, Maria Teresa Bassi, Graziella Cappelletti, and Elena I. Rugarli. 2009. “Pleiotropic Effects of Spastin on Neurite Growth Depending on Expression Levels.” *Journal of Neurochemistry* 108(5):1277–88.

Rivera, Victor M. 2000. “Regulation of Protein Secretion Through Controlled Aggregation in the Endoplasmic Reticulum.” *Science* 287(5454):826–30.

Roberts, Anthony J., Brian S. Goodman, and Samara L. Reck-Peterson. 2014. “Reconstitution of Dynein Transport to the Microtubule plus End by Kinesin.” *ELife* 3:e02641.

Rodriguez-Gabin, A. G., X. Yin, Q. Si, and J. N. Larocca. 2009. “Transport of Mannose-6-Phosphate Receptors from the Trans-Golgi Network to Endosomes Requires Rab31.” *Experimental Cell Research* 315(13):2215–30.

Rogers, Gregory C., Stephen L. Rogers, Tamara A. Schwimmer, Stephanie C. Ems-McClung, Claire E. Walczak, Ronald D. Vale, Jonathan M. Scholey, and David J. Sharp. 2004. “Two Mitotic Kinesins Cooperate to Drive Sister Chromatid Separation during Anaphase.” *Nature* 427(6972):364–70.

Rojas, Raul, Thijs van Vlijmen, Gonzalo A. Mardones, Yogikala Prabhu, Adriana L. Rojas, Shabaz Mohammed, Albert J. R. Heck, Graça Raposo, Peter van der Sluijs, and Juan S. Bonifacino. 2008. “Regulation of Retromer Recruitment to Endosomes by Sequential Action of Rab5 and Rab7.” *The Journal of Cell Biology* 183(3):513–26.

Roll-Mecak, Antonina and Ronald D. Vale. 2005. “The Drosophila Homologue of the Hereditary Spastic Paraplegia Protein, Spastin, Severs and Disassembles Microtubules.” *Current Biology* 15(7):650–55.

Roll-Mecak, Antonina and Ronald D. Vale. 2006. “Making More Microtubules by Severing: A Common Theme of Noncentrosomal Microtubule Arrays?: Figure 1.” *The Journal of Cell Biology* 175(6):849–51.

Roll-Mecak, Antonina and Ronald D. Vale. 2008. “Structural Basis of Microtubule Severing by the Hereditary Spastic Paraplegia Protein Spastin.” *Nature* 451(7176):363–67.

Rousseaux, M., M. J. Launay, O. Kozlowski, and W. Daveluy. 2007. “Botulinum Toxin Injection in Patients with Hereditary Spastic Paraparesis.” *European Journal of Neurology* 14(2):206–12.

Roux, A., G. Cappello, J. Cartaud, J. Prost, B. Goud, and P. Bassereau. 2002. “A Minimal System Allowing Tubulation with Molecular Motors Pulling on Giant Liposomes.” *Proceedings of the National Academy of Sciences* 99(8):5394–99.

Roux, A., G. Koster, M. Lenz, B. Sorre, J. B. Manneville, P. Nassoy, and P. Bassereau. 2010. “Membrane Curvature Controls Dynamin Polymerization.” *Proceedings of the National Academy of Sciences* 107(9):4141–46.

Roux, Aurélien, Katherine Uyhazi, Adam Frost, and Pietro De Camilli. 2006. “GTP-Dependent Twisting of Dynamin Implicates Constriction and Tension in Membrane Fission.” *Nature* 441(7092):528–31.

Row, Paula E., Han Liu, Sebastian Hayes, Rebecca Welchman, Panagoula Charalabous, Kay Hofmann, Michael J. Clague, Christopher M. Sanderson, and Sylvie Urbé. 2007. “The MIT Domain of UBPY Constitutes a CHMP Binding and Endosomal Localization Signal Required for Efficient Epidermal Growth Factor Receptor Degradation.” *Journal of Biological Chemistry* 282(42):30929–37.

Rowland, Ashley A., Patrick J. Chitwood, Melissa J. Phillips, and Gia K. Voeltz. 2014. “ER Contact Sites Define the Position and Timing of Endosome Fission.” *Cell* 159(5):1027–41.

Ruano, Luis, Claudia Melo, M. Carolina Silva, and Paula Coutinho. 2014. “The Global Epidemiology of Hereditary Ataxia and Spastic Paraplegia: A Systematic Review of Prevalence Studies.” *Neuroepidemiology* 42(3):174–83.

Rueden, Curtis T., Johannes Schindelin, Mark C. Hiner, Barry E. DeZonia, Alison E. Walter, Ellen T. Arena, and Kevin W. Eliceiri. 2017. “ImageJ2: ImageJ for the next Generation of Scientific Image Data.” *BMC Bioinformatics* 18(1):529.

Rui, Yan-Ning, Zhen Xu, Xiaoqian Fang, Miriam R. Menezes, Julien Balzeau, Airu Niu, John P. Hagan, and Dong H. Kim. 2017. “The Intracranial Aneurysm Gene THSD1 Connects Endosome Dynamics to Nascent Focal Adhesion Assembly.” *Cellular Physiology and Biochemistry* 43(6):2200–2211.

Sabo, Jennifer K., Trevor J. Kilpatrick, and Holly S. Cate. 2009. “Effects of Bone Morphogenic Proteins on Neural Precursor Cells and Regulation during Central Nervous System Injury.” *Neurosignals* 17(4):255–64.

Sachse, Martin, Sylvie Urbé, Viola Oorschot, Ger J. Strous, and Judith Klumperman. 2002. “Bilayered Clathrin Coats on Endosomal Vacuoles Are Involved in Protein Sorting toward Lysosomes” edited by J. Bonifacino. *Molecular Biology of the Cell* 13(4):1313–28.

Safronov, Boris V., Matthias Wolff, and Werner Vogel. 1999. “Axonal Expression of Sodium Channels in Rat Spinal Neurones during Postnatal Development.” *The Journal of Physiology* 514(3):729–34.

Saito, Kota, Mei Chen, Fred Bard, Shenghong Chen, Huilin Zhou, David Woodley, Roman Polischuk, Randy Schekman, and Vivek Malhotra. 2009. “TANGO1 Facilitates Cargo Loading at Endoplasmic Reticulum Exit Sites.” *Cell* 136(5):891–902.

Saito, Kota, Koh Yamashiro, Yuki Ichikawa, Patrik Erlmann, Kenji Kontani, Vivek Malhotra, and Toshiaki Katada. 2011. “CTAGE5 Mediates Collagen Secretion through Interaction with TANGO1 at Endoplasmic Reticulum Exit Sites” edited by A. D. Linstedt. *Molecular Biology of the Cell* 22(13):2301–8.

Saito, Kota, Koh Yamashiro, Noriko Shimazu, Tomoya Tanabe, Kenji Kontani, and Toshiaki Katada. 2014. “Concentration of Sec12 at ER Exit Sites via Interaction with CTAGE5 Is Required for Collagen Export.” *The Journal of Cell Biology* 206(6):751–62.

Salvarezza, Susana B., Sylvie Deborde, Ryan Schreiner, Fabien Campagne, Michael M. Kessels, Britta Qualmann, Alfredo Caceres, Geri Kreitzer, and Enrique Rodriguez-Boulan. 2009. “LIM Kinase 1 and Cofilin Regulate Actin Filament Population Required for Dynamin-Dependent Apical Carrier Fission from the Trans -Golgi Network” edited by S. L. Schmid. *Molecular Biology of the Cell* 20(1):438–51.

Samatov, Timur R., Daniel Wicklein, and Alexander G. Tonevitsky. 2016. “L1CAM: Cell Adhesion and More.” *Progress in Histochemistry and Cytochemistry* 51(2):25–32.

Sambuughin, Nyamkhishig, Lev G. Goldfarb, Tatiana M. Sivtseva, Tatiana K. Davydova, Vsevolod A. Vladimirtsev, Vladimir L. Osakovskiy, Al’bina P. Danilova, Raisa S. Nikitina, Anastasia N. Ylakhova, Margarita P. Diachkovskaya, Anna C. Sundborger, Neil M. Renwick, Fyodor A. Platonov, Jenny E. Hinshaw, and Camilo Toro. 2015. “Adult-Onset Autosomal Dominant Spastic Paraplegia Linked to a GTPase-Effector Domain Mutation of Dynamin 2.” *BMC Neurology* 15(1):223.

Sanchez-Wandelmer, J., N. T. Ktistakis, and F. Reggiori. 2015. “ERES: Sites for Autophagosome Biogenesis and Maturation?” *Journal of Cell Science* 128(2):185–92.

Sanderson, Christopher M., James W. Connell, Thomas L. Edwards, Nicholas A. Bright, Simon Duley, Amanda Thompson, J. Paul Luzio, and Evan Reid. 2006. “Spastin and Atlastin, Two Proteins Mutated in Autosomal-Dominant Hereditary Spastic Paraplegia, Are Binding Partners.” *Human Molecular Genetics* 15(2):307–18.

Saraste, J. and K. Svensson. 1991. “Distribution of the Intermediate Elements Operating in ER to Golgi Transport.” *Journal of Cell Science* 100 (Pt 3:415–30.

Saugier-Veber, Pascale, Arnold Munnich, Dominique Bonneau, Jean-Michel Rozet, Martine Le Merrer, Roger Gil, and Odile Boespflug-Tanguy. 1994. “X–linked Spastic Paraplegia and Pelizaeus–Merzbacher Disease Are Allelic Disorders at the Proteolipid Protein Locus.” *Nature Genetics* 6(3):257–62.

Schiel, J. A., K. Park, M. K. Morphew, E. Reid, A. Hoenger, and R. Prekeris. 2011. “Endocytic Membrane Fusion and Buckling-Induced Microtubule Severing Mediate Cell Abscission.” *Journal of Cell Science* 124(10):1769–1769.

Schimmöller, F., B. Singer-Krüger, S. Schröder, U. Krüger, C. Barlowe, and H. Riezman. 1995. “The Absence of Emp24p, a Component of ER-Derived COPII-Coated Vesicles, Causes a Defect in Transport of Selected Proteins to the Golgi.” *The EMBO Journal* 14(7):1329–39.

Schindelin, Johannes, Ignacio Arganda-Carreras, Erwin Frise, Verena Kaynig, Mark Longair, Tobias Pietzsch, Stephan Preibisch, Curtis Rueden, Stephan Saalfeld, Benjamin Schmid, Jean-Yves Tinevez, Daniel James White, Volker Hartenstein, Kevin Eliceiri, Pavel Tomancak, and Albert Cardona. 2012. “Fiji: An Open-Source Platform for Biological-Image Analysis.” *Nature Methods* 9(7):676–82.

Schmidt, Hannes, Matthias Werner, Paul A. Heppenstall, Mechthild Henning, Margret I. Moré, Susanne Kühbandner, Gary R. Lewin, Franz Hofmann, Robert Feil, and Fritz G. Rathjen. 2002. “CGMP-Mediated Signaling via CGKIα Is Required for the Guidance and Connectivity of Sensory Axons.” *The Journal of Cell Biology* 159(3):489–98.

Schnaar, Ronald L. 2010. “Brain Gangliosides in Axon-Myelin Stability and Axon Regeneration.” *FEBS Letters* 584(9):1741–47.

Schöneberg, Johannes, Il-Hyung Lee, Janet H. Iwasa, and James H. Hurley. 2017. “Reverse-Topology Membrane Scission by the ESCRT Proteins.” *Nature Reviews Molecular Cell Biology* 18(1):5–17.

Schuurs-Hoeijmakers, Janneke H. M., Michael T. Geraghty, Erik-Jan Kamsteeg, Salma Ben-Salem, Susanne T. de Bot, Bonnie Nijhof, Ilse I. G. M. van de Vondervoort, Marinette van der Graaf, Anna Castells Nobau, Irene Otte-Höller, Sascha Vermeer, Amanda C. Smith, Peter Humphreys, Jeremy Schwartzentruber, Bassam R. Ali, Saeed A. Al-Yahyaee, Said Tariq, Thachillath Pramathan, Riad Bayoumi, Hubertus P. H. Kremer, Bart P. van de Warrenburg, Willem M. R. van den Akker, Christian Gilissen, Joris A. Veltman, Irene M. Janssen, Anneke T. Vulto-van Silfhout, Saskia van der Velde-Visser, Dirk J. Lefeber, Adinda Diekstra, Corrie E. Erasmus, Michèl A. Willemsen, Lisenka E. L. M. Vissers, Martin Lammens, Hans van Bokhoven, Han G. Brunner, Ron A. Wevers, Annette Schenck, Lihadh Al-Gazali, Bert B. A. de Vries, and Arjan P. M. de Brouwer. 2012. “Mutations in DDHD2, Encoding an Intracellular Phospholipase A1, Cause a Recessive Form of Complex Hereditary Spastic Paraplegia.” *The American Journal of Human Genetics* 91(6):1073–81.

Schwartz, Charles E., Melanie M. May, Nancy J. Carpenter, R. Curtis Rogers, Judith Martin, Martin G. Bialer, Jewell Ward, Javier Sanabria, Silvana Marsa, James A. Lewis, Roberto Echeverri, Herbert A. Lubs, Kytja Voeller, Richard J. Simensen, and Roger E. Stevenson. 2005. "Allan-Herndon-Dudley Syndrome and the Monocarboxylate Transporter 8 (MCT8) Gene." *The American Journal of Human Genetics* 77(1):41–53.

Schwarz, Dianne S. and Michael D. Blower. 2016. "The Endoplasmic Reticulum: Structure, Function and Response to Cellular Signaling." *Cellular and Molecular Life Sciences* 73(1):79–94.

Scott, A., J. Gaspar, M. D. Stuchell-Brereton, S. L. Alam, J. J. Skalicky, and W. I. Sundquist. 2005. "Structure and ESCRT-III Protein Interactions of the MIT Domain of Human VPS4A." *Proceedings of the National Academy of Sciences* 102(39):13813–18.

Scott, Anna, Hyo-Young Chung, Malgorzata Gonciarz-Swiatek, Gina C. Hill, Frank G. Whitby, Jason Gaspar, James M. Holton, Ramya Viswanathan, Sanaz Ghaffarian, Christopher P. Hill, and Wesley I. Sundquist. 2005. "Structural and Mechanistic Studies of VPS4 Proteins." *The EMBO Journal* 24(20):3658–69.

Seaman, M. N. J., M. E. Harbour, D. Tattersall, E. Read, and N. Bright. 2009. "Membrane Recruitment of the Cargo-Selective Retromer Subcomplex Is Catalysed by the Small GTPase Rab7 and Inhibited by the Rab-GAP TBC1D5." *Journal of Cell Science* 122(14):2371–82.

Seaman, Matthew N. J. 2004. "Cargo-Selective Endosomal Sorting for Retrieval to the Golgi Requires Retromer." *The Journal of Cell Biology* 165(1):111–22.

Seaman, Matthew N. J., Eric G. Marcusson, Joan Lin Cereghino, and Scott D. Emr. 1997. "Endosome to Golgi Retrieval of the Vacuolar Protein Sorting Receptor, Vps10p, Requires the Function of the VPS29 , VPS30 , and VPS35 Gene Products." *The Journal of Cell Biology* 137(1):79–92.

Seaman, Matthew N. J., J. Michael McCaffery, and Scott D. Emr. 1998. "A Membrane Coat Complex Essential for Endosome-to-Golgi Retrograde Transport in Yeast." *The Journal of Cell Biology* 142(3):665–81.

Seatter, Michael J., Sarah A. De La Rue, Lisa M. Porter, and Gwyn W. Gould. 1998. "QLS Motif in Transmembrane Helix VII of the Glucose Transporter Family Interacts with the C-1 Position of <scp>d</Scp> -Glucose and Is Involved in Substrate Selection at the Exofacial Binding Site †." *Biochemistry* 37(5):1322–26.

See, Jill, Xianchao Zhang, Nuri Eraydin, Sung-Bin Mun, Polina Mamontov, Jeffrey A. Golden, and Judith B. Grinspan. 2004. “Oligodendrocyte Maturation Is Inhibited by Bone Morphogenetic Protein.” *Molecular and Cellular Neuroscience* 26(4):481–92.

Shanmughapriya, Santhanam, Sudarsan Rajan, Nicholas E. Hoffman, Andrew M. Higgins, Dhanendra Tomar, Neeharika Nemani, Kevin J. Hines, Dylan J. Smith, Akito Eguchi, Sandhya Vallem, Farah Shaikh, Maggie Cheung, Nicole J. Leonard, Ryan S. Stolakis, Matthew P. Wolfers, Jessica Ibetti, J. Kurt Chuprun, Neelakshi R. Jog, Steven R. Houser, Walter J. Koch, John W. Elrod, and Muniswamy Madesh. 2015. “SPG7 Is an Essential and Conserved Component of the Mitochondrial Permeability Transition Pore.” *Molecular Cell* 60(1):47–62.

Shaw, Jonathan D., Hiroko Hama, Farrokh Sohrabi, Daryll B. DeWald, and Beverly Wendland. 2003. “Ptdlns(3,5)P2 Is Required for Delivery of Endocytic Cargo into the Multivesicular Body.” *Traffic* 4(7):479–90.

Shcherbakova, Daria M., Prabuddha Sengupta, Jennifer Lippincott-Schwartz, and Vladislav V. Verkhusha. 2014. “Photocontrollable Fluorescent Proteins for Superresolution Imaging.” *Annual Review of Biophysics* 43(1):303–29.

Shen, Qing-Tao, Amber L. Schuh, Yuqing Zheng, Kyle Quinney, Lei Wang, Michael Hanna, Julie C. Mitchell, Marisa S. Otegui, Paul Ahlquist, Qiang Cui, and Anjon Audhya. 2014. “Structural Analysis and Modeling Reveals New Mechanisms Governing ESCRT-III Spiral Filament Assembly.” *The Journal of Cell Biology* 206(6):763–77.

Sherwood, Nina Tang, Qi Sun, Mingshan Xue, Bing Zhang, and Kai Zinn. 2004. “Drosophila Spastin Regulates Synaptic Microtubule Networks and Is Required for Normal Motor Function” edited by Michael Bate. *PLoS Biology* 2(12):e429.

Shibata, Yoko, Junjie Hu, Michael M. Kozlov, and Tom A. Rapoport. 2009. “Mechanisms Shaping the Membranes of Cellular Organelles.” *Annual Review of Cell and Developmental Biology* 25(1):329–54.

Shim, Joon W., Johanna Sandlund, Mustafa Q. Hameed, Bonnie Blazer-Yost, Feng C. Zhou, Michael Klagsbrun, and Joseph R. Madsen. 2016. “Excess HB-EGF, Which Promotes VEGF Signaling, Leads to Hydrocephalus.” *Scientific Reports* 6(1):26794.

Shim, Soomin, Samuel A. Merrill, and Phyllis I. Hanson. 2008. “Novel Interactions of ESCRT-III with LIP5 and VPS4 and Their Implications for ESCRT-III Disassembly” edited by S. Lemmon. *Molecular Biology of the Cell* 19(6):2661–72.

Shimazaki, Haruo, Junko Honda, Tametou Naoi, Michito Namekawa, Imaharu Nakano, Masahide Yazaki, Katsuya Nakamura, Kunihiro Yoshida, S. -i. Ikeda, Hiroyuki Ishiura, Yoko Fukuda, Yuji Takahashi, Jun Goto, Shoji Tsuji, and Yoshihisa Takiyama. 2014. "Autosomal-Recessive Complicated Spastic Paraplegia with a Novel Lysosomal Trafficking Regulator Gene Mutation." *Journal of Neurology, Neurosurgery & Psychiatry* 85(9):1024–28.

Shimazaki, Haruo, Yoshihisa Takiyama, Hiroyuki Ishiura, Chika Sakai, Yuichi Matsushima, Hideyuki Hatakeyama, Junko Honda, Kumi Sakoe, Tametou Naoi, Michito Namekawa, Yoko Fukuda, Yuji Takahashi, Jun Goto, Shoji Tsuji, Yu-ichi Goto, and Imaharu Nakano. 2012. "A Homozygous Mutation of C12orf65 Causes Spastic Paraplegia with Optic Atrophy and Neuropathy (SPG55)." *Journal of Medical Genetics* 49(12):777–84.

Shoukier, Moneef, Juergen Neesen, Simone M. Sauter, Loukas Argyriou, Nadine Doerwald, DV Krishna Pantakani, and Ashraf U. Mannan. 2009. "Expansion of Mutation Spectrum, Determination of Mutation Cluster Regions and Predictive Structural Classification of SPAST Mutations in Hereditary Spastic Paraplegia." *European Journal of Human Genetics* 17(2):187–94.

Simon-Assmann, Patricia. 2013. "The Laminin Family." *Cell Adhesion & Migration* 7(1):44–47.

Simonetti, Boris, Chris M. Danson, Kate J. Heesom, and Peter J. Cullen. 2017. "Sequence-Dependent Cargo Recognition by SNX-BARs Mediates Retromer-Independent Transport of CI-MPR." *The Journal of Cell Biology* 216(11):3695–3712.

Simonsen, Anne, Jean-Michel Gaullier, Antonello D'Arrigo, and Harald Stenmark. 1999. "The Rab5 Effector EEA1 Interacts Directly with Syntaxin-6." *Journal of Biological Chemistry* 274(41):28857–60.

Simpson, Michael A., Harold Cross, Christos Proukakis, Anna Pryde, Ruth Hershberger, Arnaud Chatonnet, Michael A. Patton, and Andrew H. Crosby. 2003. "Maspardin Is Mutated in Mast Syndrome, a Complicated Form of Hereditary Spastic Paraplegia Associated with Dementia." *The American Journal of Human Genetics* 73(5):1147–56.

Simunovic, Mijo, Emma Evergren, Ivan Golushko, Coline Prévost, Henri-François Renard, Ludger Johannes, Harvey T. McMahon, Vladimir Lorman, Gregory A. Voth, and Patricia Bassereau. 2016. "How Curvature-Generating Proteins Build Scaffolds on Membrane Nanotubes." *Proceedings of the National Academy of Sciences* 113(40):11226–31.

Simunovic, Mijo, Jean-Baptiste Manneville, Henri-François Renard, Emma Evergren, Krishnan Raghunathan, Dhiraj Bhatia, Anne K. Kenworthy, Gregory A. Voth, Jacques Prost, Harvey T. McMahon, Ludger Johannes, Patricia Bassereau, and Andrew Callan-Jones. 2017. "Friction Mediates Scission of Tubular Membranes Scaffolded by BAR Proteins." *Cell* 170(1):172–184.e11.

Słabicki, Mikołaj, Mirko Theis, Dragomir B. Krastev, Sergey Samsonov, Emeline Mundwiller, Magno Junqueira, Maciej Paszkowski-Rogacz, Joan Teyra, Anne-Kristin Heninger, Ina Poser, Fabienne Prieur, Jérémy Truchetto, Christian Confavreux, Cécilia Marelli, Alexandra Durr, Jean Philippe Camdessanche, Alexis Brice, Andrej Shevchenko, M. Teresa Pisabarro, Giovanni Stevanin, and Frank Buchholz. 2010. "A Genome-Scale DNA Repair RNAi Screen Identifies SPG48 as a Novel Gene Associated with Hereditary Spastic Paraplegia" edited by N. Hastie. *PLoS Biology* 8(6):e1000408.

van der Sluijs, Peter, Michael Hull, Paul Webster, Philippe Mâle, Bruno Goud, and Ira Mellman. 1992. "The Small GTP-Binding Protein Rab4 Controls an Early Sorting Event on the Endocytic Pathway." *Cell* 70(5):729–40.

Smalla, K. H., H. Matthies, K. Langnase, S. Shabir, T. M. Bockers, U. Wyneken, S. Staak, M. Krug, P. W. Beesley, and E. D. Gundelfinger. 2000. "The Synaptic Glycoprotein Neuroplastin Is Involved in Long-Term Potentiation at Hippocampal CA1 Synapses." *Proceedings of the National Academy of Sciences* 97(8):4327–32.

Smith, C. W., S. D. Marlin, R. Rothlein, C. Toman, and D. C. Anderson. 1989. "Cooperative Interactions of LFA-1 and Mac-1 with Intercellular Adhesion Molecule-1 in Facilitating Adherence and Transendothelial Migration of Human Neutrophils in Vitro." *Journal of Clinical Investigation* 83(6):2008–17.

Smith, Graham R., Bruno Contreras-Moreira, Xiaodong Zhang, and Paul A. Bates. 2004. "A Link between Sequence Conservation and Domain Motion within the AAA+ Family." *Journal of Structural Biology* 146(1–2):189–204.

Snead, Wilton T., Carl C. Hayden, Avinash K. Gadok, Chi Zhao, Eileen M. Lafer, Padmini Rangamani, and Jeanne C. Stachowiak. 2017. "Membrane Fission by Protein Crowding." *Proceedings of the National Academy of Sciences* 114(16):E3258–67.

Snider, Jamie, Guillaume Thibault, and Walid A. Houry. 2008. "The AAA+ Superfamily of Functionally Diverse Proteins." *Genome Biology* 9(4):216.

Solomons, Julianna, Charles Sabin, Emilie Poudevigne, Yoshiko Usami, David Lutje Hulsik, Pauline Macheboeuf, Bettina Hartlieb, Heinrich Göttlinger, and Winfried Weissenhorn. 2011. "Structural Basis for ESCRT-III CHMP3 Recruitment of AMSH." *Structure* 19(8):1149–59.

Solowska, J. M., M. D'Rozario, D. C. Jean, M. W. Davidson, D. R. Marenda, and P. W. Baas. 2014. "Pathogenic Mutation of Spastin Has Gain-of-Function Effects on Microtubule Dynamics." *Journal of Neuroscience* 34(5):1856–67.

Solowska, J. M., G. Morfini, A. Falnikar, B. T. Himes, S. T. Brady, D. Huang, and P. W. Baas. 2008. "Quantitative and Functional Analyses of Spastin in the Nervous System: Implications for Hereditary Spastic Paraplegia." *Journal of Neuroscience* 28(9):2147–57.

Solowska, Joanna M. and Peter W. Baas. 2015. "Hereditary Spastic Paraplegia SPG4: What Is Known and Not Known about the Disease." *Brain* 138(9):2471–84.

Solowska, Joanna M., James Y. Garbern, and Peter W. Baas. 2010. "Evaluation of Loss of Function as an Explanation for SPG4-Based Hereditary Spastic Paraplegia." *Human Molecular Genetics* 19(14):2767–79.

Song, Lin, Ramesh Rijal, Malte Karow, Maria Stumpf, Oliver Hahn, Laura Park, Robert Insall, Rolf Schröder, Andreas Hofmann, Christoph S. Clemen, and Ludwig Eichinger. 2018. "Expression of N471D Strumpellin Leads to Defects in the Endolysosomal System." *Disease Models & Mechanisms* 11(9):dmm033449.

Sönnichsen, Birte, Stefano De Renzis, Erik Nielsen, Jens Rietdorf, and Marino Zerial. 2000. "Distinct Membrane Domains on Endosomes in the Recycling Pathway Visualized by Multicolor Imaging of Rab4, Rab5, and Rab11." *The Journal of Cell Biology* 149(4):901–14.

de Souza, Paulo Victor Sgobbi, Wladimir Bocca Vieira de Rezende Pinto, Gabriel Novaes de Rezende Batistella, Thiago Bortholin, and Acary Souza Bulle Oliveira. 2017. "Hereditary Spastic Paraplegia: Clinical and Genetic Hallmarks." *The Cerebellum* 16(2):525–51.

Spillane, M., A. Ketschek, C. J. Donnelly, A. Pacheco, J. L. Twiss, and G. Gallo. 2012. "Nerve Growth Factor-Induced Formation of Axonal Filopodia and Collateral Branches Involves the Intra-Axonal Synthesis of Regulators of the Actin-Nucleating Arp2/3 Complex." *Journal of Neuroscience* 32(49):17671–89.

Srayko, Martin, Eileen T. O'Toole, Anthony A. Hyman, and Thomas Müller-Reichert. 2006. "Katanin Disrupts the Microtubule Lattice and Increases Polymer Number in C. Elegans Meiosis." *Current Biology* 16(19):1944–49.

Stachowiak, Jeanne C., Carl C. Hayden, and Darryl Y. Sasaki. 2010. “Steric Confinement of Proteins on Lipid Membranes Can Drive Curvature and Tubulation.” *Proceedings of the National Academy of Sciences* 107(17):7781–86.

Stachowiak, Jeanne C., Eva M. Schmid, Christopher J. Ryan, Hyoung Sook Ann, Darryl Y. Sasaki, Michael B. Sherman, Phillip L. Geissler, Daniel A. Fletcher, and Carl C. Hayden. 2012. “Membrane Bending by Protein–protein Crowding.” *Nature Cell Biology* 14(9):944–49.

Stadel, Daniela, Valentina Millarte, Kerstin D. Tillmann, Jessica Huber, Bat-Chen Tamin-Yecheskel, Masato Akutsu, Alik Demishtein, Bruria Ben-Zeev, Yair Anikster, Franck Perez, Volker Dötsch, Zvulun Elazar, Vladimir Rogov, Hesso Farhan, and Christian Behrends. 2015. “TECPR2 Cooperates with LC3C to Regulate COPII-Dependent ER Export.” *Molecular Cell* 60(1):89–104.

Steegmaier, Martin, Judith Klumperman, Davide L. Foletti, J. S. Yoo, and Richard H. Scheller. 1999. “Vesicle-Associated Membrane Protein 4 Is Implicated in Trans-Golgi Network Vesicle Trafficking” edited by R. W. Schekman. *Molecular Biology of the Cell* 10(6):1957–72.

Steigemann, Patrick and Daniel W. Gerlich. 2009. “Cytokinetic Abscission: Cellular Dynamics at the Midbody.” *Trends in Cell Biology* 19(11):606–16.

Steinberg, Florian, Matthew Gallon, Mark Winfield, Elaine C. Thomas, Amanda J. Bell, Kate J. Heesom, Jeremy M. Tavaré, and Peter J. Cullen. 2013. “A Global Analysis of SNX27–retromer Assembly and Cargo Specificity Reveals a Function in Glucose and Metal Ion Transport.” *Nature Cell Biology* 15(5):461–71.

Stephan, Aaron B., Steven Tobochnik, Michele Dibattista, Crystal M. Wall, Johannes Reisert, and Haiqing Zhao. 2012. “The Na+/Ca2+ Exchanger NCKX4 Governs Termination and Adaptation of the Mammalian Olfactory Response.” *Nature Neuroscience* 15(1):131–37.

Stephens, David J. 2003. “De Novo Formation, Fusion and Fission of Mammalian COPII-Coated Endoplasmic Reticulum Exit Sites.” *EMBO Reports* 4(2):210–17.

Stevanin, Giovanni, Filippo M. Santorelli, Hamid Azzedine, Paula Coutinho, Jacques Chomilier, Paola S. Denora, Elodie Martin, Anne-Marie Ouvrard-Hernandez, Alessandra Tessa, Naïma Bouslam, Alexander Lossos, Perrine Charles, José L. Loureiro, Nizar Elleuch, Christian Confavreux, Vítor T. Cruz, Merle Ruberg, Eric Leguern, Djamel Grid, Meriem Tazir, Bertrand Fontaine, Alessandro Filla, Enrico Bertini, Alexandra Durr, and Alexis Brice. 2007. “Mutations in SPG11, Encoding Spatacsin, Are a Major Cause of Spastic Paraplegia with Thin Corpus Callosum.” *Nature Genetics* 39(3):366–72.

Stinchcombe, Jane. 2004. “Linking Albinism and Immunity: The Secrets of Secretory Lysosomes.” *Science* 305(5680):55–59.

Stone, Michelle C., Michelle M. Nguyen, Juan Tao, Dana L. Allender, and Melissa M. Rolls. 2010. “Global Up-Regulation of Microtubule Dynamics and Polarity Reversal during Regeneration of an Axon from a Dendrite” edited by S. Doxsey. *Molecular Biology of the Cell* 21(5):767–77.

Stone, Michelle C., Kavitha Rao, Kyle W. Gheres, Seahee Kim, Juan Tao, Caroline La Rochelle, Christin T. Folker, Nina T. Sherwood, and Melissa M. Rolls. 2012. “Normal Spastin Gene Dosage Is Specifically Required for Axon Regeneration.” *Cell Reports* 2(5):1340–50.

Story, Randall M. and Thomas A. Steitz. 1992. “Structure of the RecA Protein–ADP Complex.” *Nature* 355(6358):374–76.

Strack, Bettina, Arianna Calistri, Stewart Craig, Elena Popova, and Heinrich G. Göttlinger. 2003. “AIP1/ALIX Is a Binding Partner for HIV-1 P6 and EIAV P9 Functioning in Virus Budding.” *Cell* 114(6):689–99.

Stucchi, Riccardo, Gabriela Plucińska, Jessica J. A. Hummel, Eitan E. Zahavi, Irune Guerra San Juan, Oleg Klykov, Richard A. Scheltema, A. F. Maarten Altelaar, and Casper C. Hoogenraad. 2018. “Regulation of KIF1A-Driven Dense Core Vesicle Transport: Ca 2+ /CaM Controls DCV Binding and Liprin-α/TANC2 Recruits DCVs to Postsynaptic Sites.” *Cell Reports* 24(3):685–700.

Stuchell-Brereton, Melissa D., Jack J. Skalicky, Collin Kieffer, Mary Anne Karren, Sanaz Ghaffarian, and Wesley I. Sundquist. 2007. “ESCRT-III Recognition by VPS4 ATPases.” *Nature* 449(7163):740–44.

Sugawara, Etsuko and Hiroshi Nikaido. 2014. “Properties of AdeABC and AdeIJK Efflux Systems of Acinetobacter Baumannii Compared with Those of the AcrAB-TolC System of Escherichia Coli.” *Antimicrobial Agents and Chemotherapy* 58(12):7250–57.

Sundborger, Anna C., Shunming Fang, Jürgen A. Heymann, Pampa Ray, Joshua S. Chappie, and Jenny E. Hinshaw. 2014. “A Dynamin Mutant Defines a Superconstricted Prefission State.” *Cell Reports* 8(3):734–42.

Svenson, Ingrid K., Allison E. Ashley-Koch, Margaret A. Pericak-Vance, and Douglas A. Marchuk. 2001. “A Second Leaky Splice-Site Mutation in the Spastin Gene.” *The American Journal of Human Genetics* 69(6):1407–9.

Svenson, Ingrid K., Mark T. Kloos, Amy Jacon, Carol Gallione, April C. Horton, Margaret A. Pericak-Vance, Michael D. Ehlers, and Douglas A. Marchuk. 2005. “Subcellular Localization of Spastin: Implications for the Pathogenesis of Hereditary Spastic Paraplegia.” *Neurogenetics* 6(3):135–41.

Sweitzer, Sharon M. and Jenny E. Hinshaw. 1998. “Dynamin Undergoes a GTP-Dependent Conformational Change Causing Vesiculation.” *Cell* 93(6):1021–29.

Tabuchi, M., I. Yanatori, Y. Kawai, and F. Kishi. 2010. “Retromer-Mediated Direct Sorting Is Required for Proper Endosomal Recycling of the Mammalian Iron Transporter DMT1.” *Journal of Cell Science* 123(5):756–66.

Takasu, Hirotoshi, Jun Goo Jee, Ayako Ohno, Natsuko Goda, Kenichiro Fujiwara, Hidehito Tochio, Masahiro Shirakawa, and Hidekazu Hiroaki. 2005. “Structural Characterization of the MIT Domain from Human Vps4b.” *Biochemical and Biophysical Research Communications* 334(2):460–65.

Takatsu, Hiroyuki, Masahiro Takayama, Tomoki Naito, Naoto Takada, Kazuya Tsumagari, Yasushi Ishihama, Kazuhisa Nakayama, and Hye-Won Shin. 2017. “Phospholipid Flippase ATP11C Is Endocytosed and Downregulated Following Ca2+-Mediated Protein Kinase C Activation.” *Nature Communications* 8(1):1423.

Takei, Kohji, Peter S. McPherson, Sandra L. Schmid, and Pietro De Camilli. 1995. “Tubular Membrane Invaginations Coated by Dynamin Rings Are Induced by GTP-ΓS in Nerve Terminals.” *Nature* 374(6518):186–90.

Takenaka, Maisa C., Simon Robson, and Francisco J. Quintana. 2016. “Regulation of the T Cell Response by CD39.” *Trends in Immunology* 37(7):427–39.

Takenobu, H., O. Shimozato, T. Nakamura, H. Ochiai, Y. Yamaguchi, M. Ohira, A. Nakagawara, and T. Kamijo. 2011. “CD133 Suppresses Neuroblastoma Cell Differentiation via Signal Pathway Modification.” *Oncogene* 30(1):97–105.

Takida, Satoshi, Yusuke Maeda, and Taroh Kinoshita. 2008. “Mammalian GPI-Anchored Proteins Require P24 Proteins for Their Efficient Transport from the ER to the Plasma Membrane.” *Biochemical Journal* 409(2):555–62.

Talledge, Nathaniel, John McCullough, Dawn Wenzel, Henry C. Nguyen, Matthew S. Lalonde, Monika Bajorek, Jack Skalicky, Adam Frost, and Wesley I. Sundquist. 2018. “The ESCRT-III Proteins IST1 and CHMP1B Assemble around Nucleic Acids.” *BioRxiv* 386532.

Tang, Shaogeng, Nicholas J. Buchkovich, W. Mike Henne, Sudeep Banjade, Yun Jung Kim, and Scott D. Emr. 2016. “ESCRT-III Activation by Parallel Action of ESCRT-I/II and ESCRT-0/Bro1 during MVB Biogenesis.” *ELife* 5.

Tariq, Huma and Sadaf Naz. 2017. “TFG Associated Hereditary Spastic Paraplegia: An Addition to the Phenotypic Spectrum.” *Neurogenetics* 18(2):105–9.

Tatemoto, K. 2004. “Neuropeptide Y: History and Overview.” Pp. 1–21 in *Handbook of Experimental Pharmacology*.

Taylor, Jennifer L., Susan Roehl White, Brett Lauring, And F. Jo. Kull. 2012. “Crystal Structure Of The Human Spastin AAA Domain.” *Journal Of Structural Biology* 179(2):133–37.

Taylor, Kathryn M., Helen E. Morgan, Andrea Johnson, Lisa J. Hadley, And Robert I. Nicholson. 2003. “Structure–function Analysis of LIV-1, the Breast Cancer-Associated Protein That Belongs to a New Subfamily of Zinc Transporters.” *Biochemical Journal* 375(1):51–59.

Taylor, Marcus J., David Perrais, and Christien J. Merrifield. 2011. “A High Precision Survey of the Molecular Dynamics of Mammalian Clathrin-Mediated Endocytosis” edited by S. L. Schmid. *PLoS Biology* 9(3):e1000604.

Terai, Takuya, Eri Maki, Shigeru Sugiyama, Yoshinori Takahashi, Hiroyoshi Matsumura, Yusuke Mori, and Tetsuo Nagano. 2011. “Rational Development of Caged-Biotin Protein-Labeling Agents and Some Applications in Live Cells.” *Chemistry & Biology* 18(10):1261–72.

Tesson, Christelle, Magdalena Nawara, Mustafa A. M. Salih, Rodrigue Rossignol, Maha S. Zaki, Mohammed Al Balwi, Rebecca Schule, Cyril Mignot, Emilie Obre, Ahmed Bouhouche, Filippo M. Santorelli, Christelle M. Durand, Andrés Caballero Oteyza, Khalid H. El-Hachimi, Abdulmajeed Al Drees, Naima Bouslam, Foudil Lamari, Salah A. Elmalik, Mohammad M. Kabiraj, Mohammed Z. Seidahmed, Typhaine Esteves, Marion Gaussen, Marie-Lorraine Monin, Gabor Gyapay, Doris Lechner, Michael Gonzalez, Christel Depienne, Fanny Mochel, Julie Lavie, Ludger Schols, Didier Lacombe, Mohamed Yahyaoui, Ibrahim Al Abdulkareem, Stephan Zuchner, Atsushi Yamashita, Ali Benomar, Cyril Goizet, Alexandra Durr, Joseph G. Gleeson, Frederic Darios, Alexis Brice, and Giovanni Stevanin. 2012. “Alteration of Fatty-Acid-Metabolizing Enzymes Affects Mitochondrial Form and Function in Hereditary Spastic Paraplegia.” *The American Journal of Human Genetics* 91(6):1051–64.

Tiranti, V. 2000. “A Novel Frameshift Mutation of the MtDNA COIII Gene Leads to Impaired Assembly of Cytochrome c Oxidase in a Patient Affected by Leigh-like Syndrome.” *Human Molecular Genetics* 9(18):2733–42.

Tisher, Annya and Arash Salardini. 2016. “A Case Report of a Woman with Young Onset Cognitive Impairment Associated with Hereditary Spastic Paraplegia Due to a Mutation in the SPAST Gene.” *Journal of the Neurological Sciences* 367:131–32.

Townley, Anna K., Yi Feng, Katy Schmidt, Deborah A. Carter, Robert Porter, Paul Verkade, and David J. Stephens. 2008. “Efficient Coupling of Sec23-Sec24 to Sec13-Sec31 Drives COPII-Dependent Collagen Secretion and Is Essential for Normal Craniofacial Development.” *Journal of Cell Science* 121(18):3025–34.

Traer, Colin J., Anna C. Rutherford, Krysten J. Palmer, Thomas Wassmer, Jacqueline Oakley, Naomi Attar, Jez G. Carlton, Joachim Kremerskothen, David J. Stephens, and Peter J. Cullen. 2007. “SNX4 Coordinates Endosomal Sorting of TfnR with Dynein-Mediated Transport into the Endocytic Recycling Compartment.” *Nature Cell Biology* 9(12):1370–80.

Trotta, Nick, Genny Orso, Maria Giovanna Rossetto, Andrea Daga, and Kendal Broadie. 2004. “The Hereditary Spastic Paraplegia Gene, Spastin, Regulates Microtubule Stability to Modulate Synaptic Structure and Function.” *Current Biology* 14(13):1135–47.

Tsang, Hilda T. H., James W. Connell, Stephanie E. Brown, Amanda Thompson, Evan Reid, and Christopher M. Sanderson. 2006. “A Systematic Analysis of Human CHMP Protein Interactions: Additional MIT Domain-Containing Proteins Bind to Multiple Components of the Human ESCRT III Complex.” *Genomics* 88(3):333–46.

Tsang, Hilda T. H., Thomas L. Edwards, Xinnan Wang, James W. Connell, Rachel J. Davies, Hannah J. Durrington, Cahir J. O’Kane, J. Paul Luzio, and Evan Reid. 2009. “The Hereditary Spastic Paraplegia Proteins NIPA1, Spastin and Spartin Are Inhibitors of Mammalian BMP Signalling.” *Human Molecular Genetics* 18(20):3805–21.

Tsaousidou, Maria K., Karim Ouahchi, Tom T. Warner, Yi Yang, Michael A. Simpson, Nigel G. Laing, Philip A. Wilkinson, Ricardo E. Madrid, Heema Patel, Faycal Hentati, Michael A. Patton, Afif Hentati, Philippa J. Lamont, Teepu Siddique, and Andrew H. Crosby. 2008. “Sequence Alterations within CYP7B1 Implicate Defective Cholesterol Homeostasis in Motor-Neuron Degeneration.” *The American Journal of Human Genetics* 82(2):510–15.

Tsuji, Lyuji, Toshihide Yamashita, Tateki Kubo, Tomas Madura, Hiroyuki Tanaka, Ko Hosokawa, and Masaya Tohyama. 2004. “FLRT3, a Cell Surface Molecule Containing LRR Repeats and a FNIII Domain, Promotes Neurite Outgrowth.” *Biochemical and Biophysical Research Communications* 313(4):1086–91.

Udani, Manisha, Qin Zen, Maisha Cottman, Nicole Leonard, Shawn Jefferson, Carrie Daymont, George Truskey, and Marilyn J. Telen. 1998. “Basal Cell Adhesion Molecule/Lutheran Protein. The Receptor Critical for Sickle Cell Adhesion to Laminin.” *Journal of Clinical Investigation* 101(11):2550–58.

Ullrich, Oliver, Sigrid Reinsch, Sylvie Urbé, Marino Zerial, and Robert G. Parton. 1996. “Rab11 Regulates Recycling through the Pericentriolar Recycling Endosome.” *Journal of Cell Biology* 135(4):913–24.

Usardi, Alessia, Keerthana Iyer, Séverine M. Sigoillot, Antoine Dusonchet, and Fekrije Selimi. 2017. “The Immunoglobulin-like Superfamily Member IGSF3 Is a Developmentally Regulated Protein That Controls Neuronal Morphogenesis.” *Developmental Neurobiology* 77(1):75–92.

Valdmanis, Paul N., Inge A. Meijer, Annie Reynolds, Adrienne Lei, Patrick MacLeod, David Schlesinger, Mayana Zatz, Evan Reid, Patrick A. Dion, Pierre Drapeau, and Guy A. Rouleau. 2007. “Mutations in the KIAA0196 Gene at the SPG8 Locus Cause Hereditary Spastic Paraplegia.” *The American Journal of Human Genetics* 80(1):152–61.

Valenstein, Max L. and Antonina Roll-Mecak. 2016. “Graded Control of Microtubule Severing by Tubulin Glutamylation.” *Cell* 164(5):911–21.

Valm, Alex M., Sarah Cohen, Wesley R. Legant, Justin Melunis, Uri Hershberg, Eric Wait, Andrew R. Cohen, Michael W. Davidson, Eric Betzig, and Jennifer Lippincott-Schwartz. 2017. “Applying Systems-Level Spectral Imaging and Analysis to Reveal the Organelle Interactome.” *Nature* 546(7656):162–67.

Vantaggiato, Chiara, Elena Panzeri, Marianna Castelli, Andrea Citterio, Alessia Arnoldi, Filippo Maria Santorelli, Rocco Liguori, Marina Scarlato, Olimpia Musumeci, Antonio Toscano, Emilio Clementi, and Maria Teresa Bassi. 2019. “ZFYVE26/SPASTIZIN and SPG11/SPATACSIN Mutations in Hereditary Spastic Paraplegia Types AR-SPG15 and AR-SPG11 Have Different Effects on Autophagy and Endocytosis.” *Autophagy* 15(1):34–57.

Vantler, Marius, Michael Huntgeburth, Evren Caglayan, Henrik ten Freyhaus, Petra Schnabel, and Stephan Rosenkranz. 2006. “PI3-Kinase/Akt-Dependent Antiapoptotic Signaling by the PDGF α Receptor Is Negatively Regulated by Src Family Kinases.” *FEBS Letters* 580(30):6769–76.

Varga, Rita-Eva, Mukhran Khundadze, Markus Damme, Sandor Nietzsche, Birgit Hoffmann, Tobias Stauber, Nicole Koch, J. Christopher Hennings, Patricia Franzka, Antje K. Huebner, Michael M. Kessels, Christoph Biskup, Thomas J. Jentsch, Britta Qualmann, Thomas Braulke, Ingo Kurth, Christian Beetz, and Christian A. Hübner. 2015. “In Vivo Evidence for Lysosome Depletion and Impaired Autophagic Clearance in Hereditary Spastic Paraplegia Type SPG11.” edited by G. A. Cox. *PLoS Genetics* 11(8):e1005454.

Vaughan, Kevin T., S. H. Tynan, N. E. Faulkner, C. J. Echeverri, and R. B. Vallee. 1999. “Colocalization of Cytoplasmic Dynein with Dynactin and CLIP-170 at Microtubule Distal Ends.” *Journal of Cell Science* 112 (Pt 1:1437–47.

Veit, Guido, Daniela Zwolanek, Beate Eckes, Stephan Niland, Jarmo Käpylä, Manon C. Zweers, Akemi Ishada-Yamamoto, Thomas Krieg, Jyrki Heino, Johannes A. Eble, and Manuel Koch. 2011. “Collagen XXIII, Novel Ligand for Integrin α 2 β 1 in the Epidermis.” *Journal of Biological Chemistry* 286(31):27804–13.

Vemu, Annapurna, Ewa Szczesna, Elena A. Zehr, Jeffrey O. Spector, Nikolaus Grigorieff, Alexandra M. Deaconescu, and Antonina Roll-Mecak. 2018. “Severing Enzymes Amplify Microtubule Arrays through Lattice GTP-Tubulin Incorporation.” *Science* 361(6404):eaau1504.

Venco, Paola, Massimo Bonora, Carlotta Giorgi, Elena Papaleo, Arcangela Iuso, Holger Prokisch, Paolo Pinton, and Valeria Tiranti. 2015. “Mutations of C19orf12, Coding for a Transmembrane Glycine Zipper Containing Mitochondrial Protein, Cause Mis-Localization of the Protein, Inability to Respond to Oxidative Stress and Increased Mitochondrial Ca^{2+}.” *Frontiers in Genetics* 6:185.

Venditti, Rossella, Tiziana Scanu, Michele Santoro, Giuseppe Di Tullio, Alexander Spaar, Renato Gaibisso, Galina V. Beznoussenko, A. A. Mironov, Alexander Mironov, Leopoldo Zelante, Maria Rosaria Piemontese, Angelo Notarangelo, Vivek Malhotra, Barbara M. Vertel, Cathal Wilson, and Maria Antonietta De Matteis. 2012. “Sedlin Controls the ER Export of Procollagen by Regulating the Sar1 Cycle.” *Science* 337(6102):1668–72.

Venditti, Rossella, Cathal Wilson, and Maria Antonietta De Matteis. 2014. “Exiting the ER: What We Know and What We Don’t.” *Trends in Cell Biology* 24(1):9–18.

Verkerk, Annemieke J. M. H., Rachel Schot, Belinda Dumee, Karlijn Schellekens, Sigrid Swagemakers, Aida M. Bertoli-Avella, Maarten H. Lequin, Jeroen Dudink, Paul Govaert, A. L. van Zwol, Jennifer Hirst, Marja W. Wessels, Coriene Catsman-Berrevoets, Frans W. Verheijen, Esther de Graaff, Irenaeus F. M. de Coo, Johan M. Kros, Rob Willemsen, Patrick J. Willems, Peter J. van der Spek, and Grazia M. S. Mancini. 2009. "Mutation in the AP4M1 Gene Provides a Model for Neuroaxonal Injury in Cerebral Palsy." *The American Journal of Human Genetics* 85(1):40–52.

Verny, Christophe, Naig Guegen, Valerie Desquiret, Arnaud Chevrollier, Adriana Prundean, Frederic Dubas, Julien Cassereau, Marc Ferre, Patrizia Amati-Bonneau, Dominique Bonneau, Pascal Reynier, and Vincent Procaccio. 2011. "Hereditary Spastic Paraplegia-like Disorder Due to a Mitochondrial ATP6 Gene Point Mutation." *Mitochondrion* 11(1):70–75.

Vietri, Marina, Kay O. Schink, Coen Campsteijn, Catherine Sem Wegner, Sebastian W. Schultz, Liliane Christ, Sigrid B. Thoresen, Andreas Brech, Camilla Raiborg, and Harald Stenmark. 2015. "Spastin and ESCRT-III Coordinate Mitotic Spindle Disassembly and Nuclear Envelope Sealing." *Nature* 522(7555):231–35.

Villanueva, Hugo, Adriana P. Visbal, Nadine F. Obeid, Andrew Q. Ta, Adeel A. Faruki, Meng-Fen Wu, Susan G. Hilsenbeck, Chad A. Shaw, Peng Yu, Nicholas W. Plummer, Lutz Birnbaumer, and Michael T. Lewis. 2015. "An Essential Role for Gα I2 in Smoothened-Stimulated Epithelial Cell Proliferation in the Mammary Gland." *Science Signaling* 8(394):ra92-ra92.

Voeltz, Gia K., William A. Prinz, Yoko Shibata, Julia M. Rist, and Tom A. Rapoport. 2006. "A Class of Membrane Proteins Shaping the Tubular Endoplasmic Reticulum." *Cell* 124(3):573–86.

Volkow, Nora D., George F. Koob, and A. Thomas McLellan. 2016. "Neurobiologic Advances from the Brain Disease Model of Addiction" edited by D. L. Longo. *New England Journal of Medicine* 374(4):363–71.

De Vos, Kurt J., Victoria J. Allan, Andrew J. Grierson, and Michael P. Sheetz. 2005. "Mitochondrial Function and Actin Regulate Dynamin-Related Protein 1-Dependent Mitochondrial Fission." *Current Biology* 15(7):678–83.

Voss, Felizia K., Florian Ullrich, J. Munch, Katina Lazarow, D. Lutter, Nancy Mah, Miguel A. Andrade-Navarro, J. P. von Kries, Tobias Stauber, and Thomas J. Jentsch. 2014. "Identification of LRRC8 Heteromers as an Essential Component of the Volume-Regulated Anion Channel VRAC." *Science* 344(6184):634–38.

De Vries, D. D., L. N. Went, G. W. Bruyn, H. R. Scholte, R. M. Hofstra, P. a Bolhuis, and B. a van Oost. 1996. “Genetic and Biochemical Impairment of Mitochondrial Complex I Activity in a Family with Leber Hereditary Optic Neuropathy and Hereditary Spastic Dystonia.” *American Journal of Human Genetics* 58(4):703–11.

Vulinovic, Franca, Victor Krajka, Torben J. Hausrat, Philip Seibler, Daniel Alvarez-Fischer, Harutyun Madoev, Jin-Sung Park, Kishore R. Kumar, Carolyn M. Sue, Katja Lohmann, Matthias Kneussel, Christine Klein, and Aleksandar Rakovic. 2018. “Motor Protein Binding and Mitochondrial Transport Are Altered by Pathogenic TUBB4A Variants.” *Human Mutation* 39(12):1901–15.

Wakana, Yuichi, Sawako Takai, Ken-ichi Nakajima, Katsuko Tani, Akitsugu Yamamoto, Peter Watson, David J. Stephens, Hans-Peter Hauri, and Mitsuo Tagaya. 2008. “Bap31 Is an Itinerant Protein That Moves between the Peripheral Endoplasmic Reticulum (ER) and a Juxtanuclear Compartment Related to ER-Associated Degradation” edited by A. Linstedt. *Molecular Biology of the Cell* 19(5):1825–36.

Wali, Gautam, Ratneswary Sutharsan, Yongjun Fan, Romal Stewart, Johana Tello Velasquez, Carolyn M. Sue, Denis I. Crane, and Alan Mackay-Sim. 2016. “Mechanism of Impaired Microtubule-Dependent Peroxisome Trafficking and Oxidative Stress in SPAST-Mutated Cells from Patients with Hereditary Spastic Paraplegia.” *Scientific Reports* 6(1):27004.

Walsh, Mark K. and Jeff W. Lichtman. 2003. “In Vivo Time-Lapse Imaging of Synaptic Takeover Associated with Naturally Occurring Synapse Elimination.” *Neuron* 37(1):67–73.

Wandinger-Ness, Angela and Marino Zerial. 2014. “Rab Proteins and the Compartmentalization of the Endosomal System.” *Cold Spring Harbor Perspectives in Biology* 6(11):a022616.

Wang, Huajin, Michel Becuwe, Benjamin E. Housden, Chandramohan Chitraju, Ashley J. Porras, Morven M. Graham, Xinran N. Liu, Abdou Rachid Thiam, David B. Savage, Anil K. Agarwal, Abhimanyu Garg, Maria-Jesus Olarte, Qingqing Lin, Florian Fröhlich, Hans Kristian Hannibal-Bach, Srigokul Upadhyayula, Norbert Perrimon, Tomas Kirchhausen, Christer S. Ejsing, Tobias C. Walther, and Robert V. Farese. 2016. “Seipin Is Required for Converting Nascent to Mature Lipid Droplets.” *ELife* 5.

Wang, Jack T., Zachary A. Medress, and Ben A. Barres. 2012. “Axon Degeneration: Molecular Mechanisms of a Self-Destruction Pathway.” *The Journal of Cell Biology* 196(1):7–18.

Wang, Jing, Hui-Qiao Sun, Eric Macia, Tomas Kirchhausen, Hadiya Watson, Juan S. Bonifacino, and Helen L. Yin. 2007. “PI4P Promotes the Recruitment of the GGA Adaptor Proteins to the Trans - Golgi Network and Regulates Their Recognition of the Ubiquitin Sorting Signal” edited by S. Schmid. *Molecular Biology of the Cell* 18(7):2646–55.

Wang, Philip Y. and Robert J. Wenthold. 2009. “Synaptic Adhesion-Like Molecules (SALMs).” Pp. 367–83 in *The Sticky Synapse*. New York, NY: Springer New York.

Wang, Raymond Y., Olaf A. Bodamer, Michael S. Watson, and William R. Wilcox. 2011. “Lysosomal Storage Diseases: Diagnostic Confirmation and Management of Presymptomatic Individuals.” *Genetics in Medicine* 13(5):457–84.

Wang, Wuyang, Qiong Gao, Meimei Yang, Xiaoli Zhang, Lu Yu, Maria Lawas, Xinran Li, Marthe Bryant-Genevier, Noel T. Southall, Juan Marugan, Marc Ferrer, and Haoxing Xu. 2015. “Up-Regulation of Lysosomal TRPML1 Channels Is Essential for Lysosomal Adaptation to Nutrient Starvation.” *Proceedings of the National Academy of Sciences* 112(11):E1373–81.

Wang, Xinnan, W. Robert Shaw, Hilda T. H. Tsang, Evan Reid, and Cahir J. O’Kane. 2007. “Drosophila Spichthyin Inhibits BMP Signaling and Regulates Synaptic Growth and Axonal Microtubules.” *Nature Neuroscience* 10(2):177–85.

Washbourne, Philip. 2004. “Cell Adhesion Molecules in Synapse Formation.” *Journal of Neuroscience* 24(42):9244–49.

Wassmer, T., N. Attar, M. V. Bujny, J. Oakley, C. J. Traer, and P. J. Cullen. 2006. “A Loss-of-Function Screen Reveals SNX5 and SNX6 as Potential Components of the Mammalian Retromer.” *Journal of Cell Science* 120(1):45–54.

Wassmer, Thomas, Naomi Attar, Martin Harterink, Jan R. T. van Weering, Colin J. Traer, Jacqueline Oakley, Bruno Goud, David J. Stephens, Paul Verkade, Hendrik C. Korswagen, and Peter J. Cullen. 2009. “The Retromer Coat Complex Coordinates Endosomal Sorting and Dynein-Mediated Transport, with Carrier Recognition by the Trans-Golgi Network.” *Developmental Cell* 17(1):110–22.

Watson, P. 2006. “Microtubule Plus-End Loading of P150Glued Is Mediated by EB1 and CLIP-170 but Is Not Required for Intracellular Membrane Traffic in Mammalian Cells.” *Journal of Cell Science* 119(13):2758–67.

Watson, Peter, Rebecca Forster, Krysten J. Palmer, Rainer Pepperkok, and David J. Stephens. 2005. "Coupling of ER Exit to Microtubules through Direct Interaction of COPII with Dynactin." *Nature Cell Biology* 7(1):48–55.

Webb, Stewart. 1998. "Cognitive Impairment in Families with Pure Autosomal Dominant Hereditary Spastic Paraparesis." *Brain* 121(5):923–29.

Weekes, Michael P., Peter Tomasec, Edward L. Huttlin, Ceri A. Fielding, David Nusinow, Richard J. Stanton, Eddie C. Y. Wang, Rebecca Aicheler, Isa Murrell, Gavin W. G. Wilkinson, Paul J. Lehner, and Steven P. Gygi. 2014. "Quantitative Temporal Viromics: An Approach to Investigate Host-Pathogen Interaction." *Cell* 157(6):1460–72.

van Weering, Jan R. T., Richard B. Sessions, Colin J. Traer, Daniel P. Kloer, Vikram K. Bhatia, Dimitrios Stamou, Sven R. Carlsson, James H. Hurley, and Peter J. Cullen. 2012. "Molecular Basis for SNX-BAR-Mediated Assembly of Distinct Endosomal Sorting Tubules." *The EMBO Journal* 31(23):4466–80.

van Weering, Jan R. T., Paul Verkade, and Peter J. Cullen. 2010. "SNX–BAR Proteins in Phosphoinositide-Mediated, Tubular-Based Endosomal Sorting." *Seminars in Cell & Developmental Biology* 21(4):371–80.

Welte, Michael A. 2015. "Expanding Roles for Lipid Droplets." *Current Biology* 25(11):R470–81.

Welte, Michael A. and Alex P. Gould. 2017. "Lipid Droplet Functions beyond Energy Storage." *Biochimica et Biophysica Acta (BBA) - Molecular and Cell Biology of Lipids* 1862(10):1260–72.

Wendler, Franz, Alison K. Gillingham, Rita Sinka, Cláudia Rosa-Ferreira, David E. Gordon, Xavier Franch-Marro, Andrew A. Peden, Jean-Paul Vincent, and Sean Munro. 2010. "A Genome-Wide RNA Interference Screen Identifies Two Novel Components of the Metazoan Secretory Pathway." *The EMBO Journal* 29(2):304–14.

Wendler, Petra, Susanne Ciniawsky, Malte Kock, and Sebastian Kube. 2012. "Structure and Function of the AAA+ Nucleotide Binding Pocket." *Biochimica et Biophysica Acta (BBA) - Molecular Cell Research* 1823(1):2–14.

Westphal, Andreas, Weijia Cheng, Jinbo Yu, Guntram Grassl, Martina Krautkrämer, Otto Holst, Niko Föger, and Kyeong-Hee Lee. 2017. "Lysosomal Trafficking Regulator Lyst Links Membrane Trafficking to Toll-like Receptor–mediated Inflammatory Responses." *The Journal of Experimental Medicine* 214(1):227–44.

Wharton, Stephen B., Christopher J. McDermott, Andrew J. Grierson, Jonathan D. Wood, Catherine Gelsthorpe, Paul G. Ince, and Pamela J. Shaw. 2003. “The Cellular and Molecular Pathology of the Motor System in Hereditary Spastic Paraparesis Due to Mutation of the Spastin Gene.” *Journal of Neuropathology & Experimental Neurology* 62(11):1166–77.

White, Susan Roehl, Katia J. Evans, Jeffrey Lary, James L. Cole, and Brett Lauring. 2007. “Recognition of C-Terminal Amino Acids in Tubulin by Pore Loops in Spastin Is Important for Microtubule Severing.” *The Journal of Cell Biology* 176(7):995–1005.

Whittaker, Victor P. 1990. “The Contribution of Drugs and Toxins to Understanding of Cholinergic Function.” *Trends in Pharmacological Sciences* 11(1):8–13.

Wilkinson, Lorine, Gabriel Kolle, Daying Wen, Michael Piper, Julie Scott, and Melissa Little. 2003. “CRIM1 Regulates the Rate of Processing and Delivery of Bone Morphogenetic Proteins to the Cell Surface.” *Journal of Biological Chemistry* 278(36):34181–88.

Williams, Megan E., Joris de Wit, and Anirvan Ghosh. 2010. “Molecular Mechanisms of Synaptic Specificity in Developing Neural Circuits.” *Neuron* 68(1):9–18.

Williams, Roger L. and Sylvie Urbé. 2007. “The Emerging Shape of the ESCRT Machinery.” *Nature Reviews Molecular Cell Biology* 8(5):355–68.

Wills, Zachary P., Caleigh Mandel-Brehm, Alan R. Mardinly, Alejandra E. McCord, Roman J. Giger, and Michael E. Greenberg. 2012. “The Nogo Receptor Family Restricts Synapse Number in the Developing Hippocampus.” *Neuron* 73(3):466–81.

Wilson, Deanna G., Khanhky Phamluong, Li Li, Mei Sun, Tim C. Cao, Peter S. Liu, Zora Modrusan, Wendy N. Sandoval, Linda Rangell, Richard A. D. Carano, Andrew S. Peterson, and Mark J. Solloway. 2011. “Global Defects in Collagen Secretion in a Mia3/TANGO1 Knockout Mouse.” *The Journal of Cell Biology* 193(5):935–51.

Windpassinger, Christian, Michaela Auer-Grumbach, Joy Irobi, Heema Patel, Erwin Petek, Gerd Hörl, Roland Malli, Johanna A. Reed, Ines Dierick, Nathalie Verpoorten, Thomas T. Warner, Christos Proukakis, Peter Van den Bergh, Christine Verellen, Lionel Van Maldergem, Luciano Merlini, Peter De Jonghe, Vincent Timmerman, Andrew H. Crosby, and Klaus Wagner. 2004. “Heterozygous Missense Mutations in BSCL2 Are Associated with Distal Hereditary Motor Neuropathy and Silver Syndrome.” *Nature Genetics* 36(3):271–76.

Wingerchuk, D. M., V. A. Lennon, S. J. Pittock, C. F. Lucchinetti, and B. G. Weinshenker. 2006. “Revised Diagnostic Criteria for Neuromyelitis Optica.” *Neurology* 66(10):1485–89.

Witsch, Esther J., Georg Mahlknecht, Jean Wakim, Rotem Sertchook, Erez Bublil, Yosef Yarden, and Michael Sela. 2011. “Generation and Characterization of Peptide Mimotopes Specific for Anti ErbB-2 Monoclonal Antibodies.” *International Immunology* 23(6):391–403.

Wood, Jonathan D. 2006. “The Microtubule-Severing Protein Spastin Is Essential for Axon Outgrowth in the Zebrafish Embryo.” *Human Molecular Genetics* 15(18):2763–71.

Wu, Haoxi, Pedro Carvalho, and Gia K. Voeltz. 2018. “Here, There, and Everywhere: The Importance of ER Membrane Contact Sites.” *Science* 361(6401):eaan5835.

Wu, Meihui, Mei Chung Moh, and Herbert Schwarz. 2016. “HepaCAM Associates with Connexin 43 and Enhances Its Localization in Cellular Junctions.” *Scientific Reports* 6(1):36218.

Xie, Yuxiang, Bing Zhou, Mei-Yao Lin, Shiwei Wang, Kevin D. Foust, and Zu-Hang Sheng. 2015. “Endolysosomal Deficits Augment Mitochondria Pathology in Spinal Motor Neurons of Asymptomatic FALS Mice.” *Neuron* 87(2):355–70.

Xu, Yue, Heinz Hortsman, Lifong Seet, Siew Heng Wong, and Wanjin Hong. 2001. “SNX3 Regulates Endosomal Function through Its PX-Domain-Mediated Interaction with Ptdlns(3)P.” *Nature Cell Biology* 3(7):658–66.

Yamagata, Masahito, Joshua A. Weiner, and Joshua R. Sanes. 2002. “Sidekicks.” *Cell* 110(5):649–60.

Yamamoto, Yasunori and Toshiaki Sakisaka. 2018. “The Peroxisome Biogenesis Factors Posttranslationally Target Reticulon Homology Domain-Containing Proteins to the Endoplasmic Reticulum Membrane.” *Scientific Reports* 8(1):2322.

Yamamoto, Yasunori, Asuka Yoshida, Naoyuki Miyazaki, Kenji Iwasaki, and Toshiaki Sakisaka. 2014. “Arl6IP1 Has the Ability to Shape the Mammalian ER Membrane in a Reticulon-like Fashion.” *Biochemical Journal* 458(1):69–79.

Yamashita, Atsushi, Tsukasa Kumazawa, Hiroki Koga, Naotaka Suzuki, Saori Oka, and Takayuki Sugiura. 2010. “Generation of Lysophosphatidylinositol by DDHD Domain Containing 1 (DDHD1): Possible Involvement of Phospholipase D/Phosphatidic Acid in the Activation of DDHD1.” *Biochimica et Biophysica Acta (BBA) - Molecular and Cell Biology of Lipids* 1801(7):711–20.

Yang, Dong, Neggy Rismanchi, Benoît Renvoisé, Jennifer Lippincott-Schwartz, Craig Blackstone, and James H. Hurley. 2008. “Structural Basis for Midbody Targeting of Spastin by the ESCRT-III Protein CHMP1B.” *Nature Structural & Molecular Biology* 15(12):1278–86.

Yang, Ying, Wei Liu, Zhipeng Fang, Juan Shi, Fengyu Che, Chunxia He, Libo Yao, Enduo Wang, and Yuanming Wu. 2016. “A Newly Identified Missense Mutation in FARS2 Causes Autosomal-Recessive Spastic Paraplegia.” *Human Mutation* 37(2):165–69.

Yip, Yan Y., Stefano Pernigo, Anneri Sanger, Mengjia Xu, Maddy Parsons, Roberto A. Steiner, and Mark P. Dodding. 2016. “The Light Chains of Kinesin-1 Are Autoinhibited.” *Proceedings of the National Academy of Sciences* 113(9):2418–23.

Yoshida, Akane, Hiroki Hayashi, Kenji Tanabe, and Akikazu Fujita. 2017. “Segregation of Phosphatidylinositol 4-Phosphate and Phosphatidylinositol 4,5-Bisphosphate into Distinct Microdomains on the Endosome Membrane.” *Biochimica et Biophysica Acta - Biomembranes* 1859(10):1880–90.

Yoshioka, Yumiko, Masahiro Ono, Motonao Osaki, Ikuo Konishi, and Shimon Sakaguchi. 2012. “Differential Effects of Inhibition of Bone Morphogenic Protein (BMP) Signalling on T-Cell Activation and Differentiation.” *European Journal of Immunology* 42(3):749–59.

Yu, Gang, Masaki Nishimura, Shigeki Arawaka, Diane Levitan, Lili Zhang, Anurag Tandon, You-Qiang Song, Ekaterina Rogaeva, Fusheng Chen, Toshitaka Kawarai, Agnes Supala, Lyne Levesque, Haung Yu, Dun-Sheng Yang, Erin Holmes, Paul Milman, Yan Liang, Dong Mei Zhang, Dong Hong Xu, Christine Sato, Evgeny Rogaev, Marsha Smith, Christopher Janus, Yanni Zhang, Ruedi Aebersold, Lindsay Farrer, Sandro Sorbi, Amalia Bruni, Paul Fraser, and Peter St George-Hyslop. 2000. “Nicastrin Modulates Presenilin-Mediated Notch/Glp-1 Signal Transduction and BAPP Processing.” *Nature* 407(6800):48–54.

Yu, W., FJ Ahmad, and PW Baas. 1994. “Microtubule Fragmentation and Partitioning in the Axon during Collateral Branch Formation.” *The Journal of Neuroscience* 14(10):5872–84.

Yu, Wenqian, Liang Qiang, Joanna M. Solowska, Arzu Karabay, Sirin Korulu, and Peter W. Baas. 2008. “The Microtubule-Severing Proteins Spastin and Katanin Participate Differently in the Formation of Axonal Branches” edited by E. Holzbaur. *Molecular Biology of the Cell* 19(4):1485–98.

Zaccheo, Oliver, David Dinsdale, Peter A. Meacock, and Paul Glynn. 2004. “Neuropathy Target Esterase and Its Yeast Homologue Degrade Phosphatidylcholine to Glycerophosphocholine in Living Cells.” *Journal of Biological Chemistry* 279(23):24024–33.

Zanetti, Giulia, Simone Prinz, Sebastian Daum, Annette Meister, Randy Schekman, Kirsten Bacia, and John AG Briggs. 2013. “The Structure of the COPII Transport-Vesicle Coat Assembled on Membranes.” *ELife* 2.

Zanni, Ginevra, Chiara Scotton, Chiara Passarelli, Mingyan Fang, Sabina Barresi, Bruno Dallapiccola, Bin Wu, Francesca Gualandi, Alessandra Ferlini, E. Bertini, and Wang Wei. 2013. “Exome Sequencing in a Family with Intellectual Disability, Early Onset Spasticity, and Cerebellar Atrophy Detects a Novel Mutation in EXOSC3.” *Neurogenetics* 14(3–4):247–50.

Zehr, Elena, Agnieszka Szyk, Grzegorz Piszczek, Ewa Szczesna, Xiaobing Zuo, and Antonina Roll-Mecak. 2017. “Katanin Spiral and Ring Structures Shed Light on Power Stroke for Microtubule Severing.” *Nature Structural & Molecular Biology* 24(9):717–25.

Zeng, Ying, T. N. C. Ramya, Anouk Dirksen, Philip E. Dawson, and James C. Paulson. 2009. “High-Efficiency Labeling of Sialylated Glycoproteins on Living Cells.” *Nature Methods* 6(3):207–9.

Zhang, Chuanling, Dan Li, Yan Ma, Jinting Yan, Baiqing Yang, Peng Li, Aiping Yu, Cailing Lu, and Xu Ma. 2012. “Role of Spastin and Protrudin in Neurite Outgrowth.” *Journal of Cellular Biochemistry* 113(7):2296–2307.

Zhang, Dong, Gregory C. Rogers, Daniel W. Buster, and David J. Sharp. 2007. “Three Microtubule Severing Enzymes Contribute to the ‘Pacman-Flux’ Machinery That Moves Chromosomes.” *The Journal of Cell Biology* 177(2):231–42.

Zhang, Haijun, Longbin Zhang, and Tao Sun. 2018. “Cohesive Regulation of Neural Progenitor Development by MicroRNA MiR-26, Its Host Gene Ctdsp and Target Gene Emx2 in the Mouse Embryonic Cerebral Cortex.” *Frontiers in Molecular Neuroscience* 11:44.

Zhang, Peijun and Jenny E. Hinshaw. 2001. “Three-Dimensional Reconstruction of Dynamin in the Constricted State.” *Nature Cell Biology* 3(10):922–26.

Zhang, Xuebao, Juan Cai, Ze Zheng, Lisa Polin, Zhenghong Lin, Aditya Dandekar, Li Li, Fei Sun, Russell L. Finley, Deyu Fang, Zeng-Quan Yang, and Kezhong Zhang. 2015. “A Novel ER–microtubule-Binding Protein, ERLIN2, Stabilizes Cyclin B1 and Regulates Cell Cycle Progression.” *Cell Discovery* 1(1):15024.

Zhang, Xuming, Jiehong Huang, and Peter A. McNaughton. 2005. “NGF Rapidly Increases Membrane Expression of TRPV1 Heat-Gated Ion Channels.” *The EMBO Journal* 24(24):4211–23.

Zhao, Jiali and Peter Hedera. 2013. “Hereditary Spastic Paraplegia-Causing Mutations in Atlastin-1 Interfere with BMPRII Trafficking.” *Molecular and Cellular Neuroscience* 52:87–96.

Zhao, Jiali and Peter Hedera. 2015. “Strumpellin and Spartin, Hereditary Spastic Paraplegia Proteins, Are Binding Partners.” *Journal of Experimental Neuroscience* 9:15–25.

Zhao, X., D. Alvarado, S. Rainier, R. Lemons, P. Hedera, C. H. Weber, T. Tukel, M. Apak, T. Heiman-Patterson, L. Ming, M. Bui, and J. K. Fink. 2001. “Mutations in a Newly Identified GTPase Gene Cause Autosomal Dominant Hereditary Spastic Paraplegia.” *Nature Genetics* 29(3):326–31.

Zhao, Yan G., Yong Chen, Guangyan Miao, Hongyu Zhao, Wenyan Qu, Dongfang Li, Zheng Wang, Nan Liu, Lin Li, She Chen, Pingsheng Liu, Du Feng, and Hong Zhang. 2017. “The ER-Localized Transmembrane Protein EPG-3/VMP1 Regulates SERCA Activity to Control ER-Isolation Membrane Contacts for Autophagosome Formation.” *Molecular Cell* 67(6):974–989.e6.

Zhao, Yan G., Nan Liu, Guangyan Miao, Yong Chen, Hongyu Zhao, and Hong Zhang. 2018. “The ER Contact Proteins VAPA/B Interact with Multiple Autophagy Proteins to Modulate Autophagosome Biogenesis.” *Current Biology* 28(8):1234–1245.e4.

Zheng, Pengli, Qingzhou Chen, Xiaoyu Tian, Nannan Qian, Peiyuan Chai, Bing Liu, Junjie Hu, Craig Blackstone, Desheng Zhu, Junlin Teng, and Jianguo Chen. 2018. “DNA Damage Triggers Tubular Endoplasmic Reticulum Extension to Promote Apoptosis by Facilitating ER-Mitochondria Signaling.” *Cell Research* 28(8):833–54.

Zhong, Jian and Hongyan Zou. 2014. “BMP Signaling in Axon Regeneration.” *Current Opinion in Neurobiology* 27:127–34.

Zhou, Sheng-Li, Ronald E. Gordon, Michael Bradbury, Decherd Stump, Chih-Li Kiang, and Paul D. Berk. 1998. “Ethanol Up-Regulates Fatty Acid Uptake and Plasma Membrane Expression and Export of Mitochondrial Aspartate Aminotransferase in HepG2 Cells.” *Hepatology* 27(4):1064–74.

Zivony-Elboum, Yifat, Wendy Westbroek, Nehama Kfir, David Savitzki, Yishay Shoval, Assnat Bloom, Raya Rod, Morad Khayat, Bella Gross, Walid Samri, Hector Cohen, Vadim Sonkin, Tatiana Freidman, Dan Geiger, Aviva Fattal-Valevski, Yair Anikster, Aoife M. Waters, Robert Kleta, and Tzipora C. Falik-Zaccai. 2012. “A Founder Mutation in Vps37A Causes Autosomal Recessive Complex Hereditary Spastic Paraparesis.” *Journal of Medical Genetics* 49(7):462–72.

Züchner, Stephan, Gaofeng Wang, Khanh-Nhat Tran-Viet, Martha A. Nance, Perry C. Gaskell, Jeffery M. Vance, Allison E. Ashley-Koch, and Margaret A. Pericak-Vance. 2006. “Mutations in the Novel Mitochondrial Protein REEP1 Cause Hereditary Spastic Paraplegia Type 31.” *The American Journal of Human Genetics* 79(2):365–69.